Investigation on the Interaction Mechanism Among Various Soft System

THESIS SUBMITTED IN FULFILLMENT OF REQUIREMENTS
FOR THE DEGREE OF
DOCTOR OF PHILOSOPHY (SCIENCE)
OF
JADAVPUR UNIVERSITY, INDIA
by

RAJU SARDAR, M.Sc.

2025

Department of Chemistry
Jadavpur University
Kolkata-700032
India

Prof. Soumen Ghosh, M. Sc., Ph. D.
Professor of Chemistry & Co-ordinator,
Centre for Surface Science
Department of Chemistry, **Jadavpur University**
Kolkata – 700 032, West Bengal, India

Phone : +91-33-2457 2503
Fax : 91-33-2414 4266
Mob - 9432 075 363
E-Mail – gsoumen17@yahoo.co.in/
soumen.ghosh@jadavpuruniversity.in

Awards of Prof. B. N. Ghosh from ICS, Dr. B. C. Deb from ISCA, Bronze Medal from CRSI, Visiting Chair Professor of St. F. X. University, Canada &
Selected as Top 2% World Ranking Scientist in Chemical Physics by Scientists of Stanford University, USA.

CERTIFICATE FROM THE SUPERVISOR

This is to certify that the thesis entitled **"Investigation on the Interaction Mechanism Among Various Soft System"** submitted by **Sri. Raju Sardar,** who got his name registered on 08.02.2022 for the award of **Ph.D. (Science) degree** of **Jadavpur University**, is absolutely based upon his own work under the supervision of **Prof. Soumen Ghosh** and that neither this thesis nor any part of it has been submitted for any degree/diploma or any other academic award anywhere before.

Soumen Ghosh. 08.09.25
Soumen Ghosh

Centre for Surface Science
Physical Chemistry Section
Department of Chemistry
Jadavpur University
Kolkata- 700032

Prof. Soumen Ghosh
Department of Chemistry
Jadavpur University
Kolkata-700 032, W.B., India

“Be less curious about people and more curious about ideas.”

Marie Curie **(1867 – 1934)**

Dedicated To

My Beloved Grandmother

DECLARATION

I hereby declare that the work incorporated in this dissertation was carried out by me at the Centre for Surface Science, Physical Chemistry Section, Department of Chemistry, Jadavpur University, Kolkata-700032, India. The entire work, or any part of it, has never been submitted before for any prize or degree anywhere.

Raju Sardar
(RAJU SARDAR) 08.09.25

ACKNOWLEDGEMENT

I am profoundly grateful to the individuals whose unwavering support and contributions have been involved in the completion of this dissertation, entitled **"Investigation on the Interaction Mechanism Among Various Soft System,"** conducted at the Centre for Surface Science, Physical Chemistry Section, Department of Chemistry, Jadavpur University, Kolkata, India.

At the outset, I would like to take the privilege of expressing my sincere thanks and deep sense of gratitude to Prof. Soumen Ghosh, Department of Chemistry, Jadavpur University, not only for his unreserved inspiration, affectionate guidance, suggestions, and advice, he gave me maintaining patience and understanding throughout the tenure of the work.

I would like to extend my sincere thanks to Prof. Kajal Krishna Rajak, HOD, Department of Chemistry, Jadavpur University, for providing me with the central instrumental facilities throughout my research work. The author also expresses his heartiest thanks to all the faculty members, Department of Chemistry, Jadavpur University, and also university administration for the smooth running of his research work.

I warmly remember the all-out unconditional cooperation received from my colleagues, Dr. Rajesh Banik, Mr. Bipin Bihari Mondal, Mr. Sumanta Bandyopadhyay, Mr. Rabindranath Paul, Mrs. Tanaya Saha, Mrs. Sudipta Chakraborty, Ms. Kakoli Roy, Ms. Ankita Saha, Dr. Sourav Das, and Dr. Jayabrata Maity for their collaborative spirit, technical expertise, and unwavering encouragement throughout this research journey.

The author is highly indebted to Dr. Soumik Bardhan, Dr. Jayanta Kumar Midya, Mr. Himal Das, and Ms. Sayani Bhunia for their valuable suggestions and discussions throughout this research journey. I also wish to acknowledge Mr. Priyatosh Mandal, Mr. Arijit Bhowmick, Mr. Babusona Maity, Mr. Jit Mondal, and Mr. Prabhat Routh for their unwavering emotional support and for making this journey truly joyful.

Special thanks are due to the Central Instrumentation Facility at IACS and the University of Calcutta for their technical support and provision of necessary instrumentation.

I gratefully acknowledge the financial support provided by the Council of Scientific and Industrial Research (CSIR), Government of India, which enabled the successful execution of this research.

Finally, I express my deepest appreciation to my parents and family members for their unwavering love, encouragement, and sacrifices throughout my academic journey.

Centre for Surface Science

Physical Chemistry Section

Department of Chemistry

Jadavpur University, Kolkata – 700032, India

Raju Sardar

(Raju Sardar) 08.09.25

Investigation on the Interaction Mechanism Among Various Soft System

Raju Sardar

Jadavpur University, 2025

Index No.: 2/22/Chem./27

ABSTRACT

This thesis explores the interaction mechanisms involved among various soft matter systems that are highly relevant to nanotechnology, biotechnology, and pharmaceutical sciences. Key systems examined include graphene oxide (GO)-dye-surfactant assemblies, protein-bile salt interactions, ionic liquid (IL)-based vesicular systems with proteins, drug-surfactant interactions, and graphene/reduced graphene oxide (RGO)-protein complexes. The unique two-dimensional structure and π-conjugated system of GO allow for efficient fluorescence quenching of dye molecules, with surfactants influencing this process by preventing non-specific binding and aggregation. These interactions are essential for developing advanced optical sensing platforms. The study also highlights the role of bile salts as biosurfactants that interact with proteins, affecting physiological processes and enabling uses in drug delivery, proteomics, and pharmaceutical formulations. Surface-active ionic liquids (SAILs), which combine the properties of surfactants and ionic liquids, are examined as versatile and environmentally friendly carriers for proteins and drug compounds because of their amphiphilic and biocompatible characteristics. Mixed micellar systems composed of drugs and surfactants are studied for their ability to improve drug solubility, decrease toxicity, and facilitate targeted delivery. Additionally, the interaction of graphene-based nanomaterials with biological molecules is evaluated to determine their potential in biomedical applications, especially in drug delivery and biosensing. The results presented aid in the rational design of multifunctional soft systems for use in emerging nanobiotechnological and pharmaceutical fields.

Soumen Ghosh.

Signature of the Supervisor

Date: 08.09.25

Prof. Soumen Ghosh
Department of Chemistry
Jadavpur University
Kolkata-700 032, W.B., India

Raju Sardar

Signature of the Candidate

Date: 08.09.25

PREFACE

The intricate interplay between graphene oxide (GO) and fluorescent dyes has garnered significant attention in recent scientific advancements. GO, with its unique 2-D structure and extensive π-conjugated system, exhibits remarkable fluorescence quenching capabilities. The aggregation behavior of dye molecules changes significantly in the presence of graphene oxide (GO), resulting in the modulation of their photophysical properties. However, the presence of surfactants can affect the interaction between graphene oxide (GO) and the dye. These surfactants can prevent non-specific binding and aggregation of dyes on the GO surface, thereby affecting quenching efficiency and, in some cases, enhancing fluorescence intensity. Studying how GO and surfactants control dye fluorescence is crucial for advanced optical sensing platforms and nanotechnology applications.

Bile salts are a unique class of biosurfactants that have recently been employed as substrates for derivatives suitable as building blocks in the construction of innovative superstructures. Investigation on the interaction of bile salts with protein has become increasingly popular due to their rising use in drug delivery and pharmaceuticals. These interactions influence key physiological processes, aiding in metabolic disease research and lipid transport understanding. Their mild detergent properties also support proteomics applications like protein purification and crystallization. Additionally, bile salts improve drug stability, solubility, absorption, and bioavailability in pharmaceutical formulations. Ionic liquids (ILs) are a unique class of salts known for their special physicochemical properties. Over recent decades, they've gained global scientific and industrial interest as sustainable, "green" chemistry solutions for various applications. Surface active ionic liquids (SAILs) are a new type of ionic liquids with long alkyl chains that combine surfactant and IL properties, showing amphiphilic behavior. Environmentally friendly and versatile, SAILs are effective alternatives to traditional surfactants in applications like protein folding, micellar catalysis, drug delivery, and solubilization. SAIL-based vesicular system would be a good delivery system for DNA, protein, and drug molecules due to its biocompatible nature.

Mixed amphiphilic system often shows superior properties compared to their pure components. This mixed system has enormous applications in drug delivery, biomedical applications, enhanced oil recovery, biosensors, food, materials sciences, and other critical fields. In recent years, mixed micelles between amphiphilic drugs with surfactants have become an interesting topic of research due to a lot of advantages. Drug-surfactant mixed amphiphilic systems play an important role in reducing the toxicity, increasing the bioavailability, and targeted delivery of drugs.

Graphene-based nanomaterials, particularly graphene oxide and reduced graphene oxide (RGO), are largely employed in the biomedical field. This nanomaterial acts as a very good delivery system for various drugs. The toxicity of such nanomaterials is relatively lower compared to other nanomaterials which used in biomedical applications. To apply these nanomaterials for biomedical purposes, their interaction study with biological molecules (like protein, DNA, etc) is very important.

CONTENTS

INTRODUCTION

Introduction:

There are soft materials systems all around us. Most of the human body's organs are made up of soft materials. One of the distinguishing features of soft materials is their ability to deform easily under stress and external stimuli. These materials can undergo significant deformation even with just the thermal energy present at ambient temperature.[1, 2] In his 1991 Nobel lecture,[3] Pierre-Gilles de Gennes highlighted "flexibility" as a quality that distinguishes soft materials. Soft materials or soft systems include a variety of substances, such as polymer solutions, surfactants, colloidal suspensions, aerosols, emulsions, foams, gels, liquid crystals (LCs), and biological materials.[4-6] They are commonly found in nature, and scientists and engineers have drawn inspiration from them to design and create stimuli-responsive smart materials and systems for scientific research, aiming to understand fundamental concepts and explore technological applications in devices and healthcare.

Amphiphile:

The term "amphiphile" originated from the Greek words "αμφιζ", amphis, meaning "both" or "double," and "φιλία" (philia), meaning "affinity." The term is used to indicate that the compounds possess a dual affinity, i.e., exhibit both hydrophilic (water-loving) and lipophilic (fat-loving) properties. A typical amphiphile consists of a polar hydrophilic residue, generally called the head, connected with a non-polar hydrophobic group called the tail.[7] Surfactant molecules, as well as diglycerides such as phospholipids (the main component of biological membranes), are typical examples of amphiphiles. Surfactants, also known as surface-active agents, are amphiphilic molecules with interfacial activity. They can lower the surface tension of a liquid or the interfacial tension between two liquids with different polarities by accumulating at the interface. Surfactants are the most common ingredients found in the soaps and detergents used in the laundry and for domestic purposes. This detergent, originally formulated as a "self-activated" cleaning agent in 1907 by a German business company, has been widely utilized as a laundry detergent known as 'PERSIL'. In the past, sodium PERborate, a bleaching agent, and sodium SILicate, a basic washing agent, were combined to form 'PERSIL', however, neither of these components are conventional surfactant that is commonly used as a flexible washing agent. Surfactant molecules tend to move their polar heads toward the interface (air-liquid, solid-liquid, or two immiscible liquid interfaces; Fig. 1), which lowers the interfacial free energy. Surfactants serve as emulsifiers, dispersants, wetting agents, foaming agents, and stabilizing agents in a variety of everyday items (toothpaste, shampoo,

conditioner, shaving foam, facewash, toilet cleanser, glue, hair gel, ink, and so on). They also have excellent detergency properties.

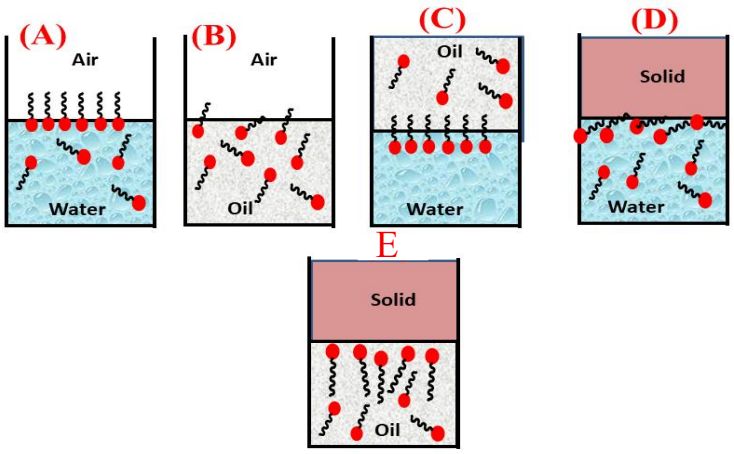

Fig. 1. Adsorption patterns of surfactants at various interfaces: (A) air/water, (B) air/oil, (C) oil/water, (D) solid/water, and (E) solid/oil interface.

A surfactant's hydrophobic tail is typically composed of long alkyl hydrocarbon chains (8-22 carbon atoms),[8] whereas the hydrophilic head group is either cationic,[9-18] anionic,[19-25] nonionic,[26-29] or zwitterionic.[30-32] Unlike regular soaps, which are manufactured by saponifying naturally occurring fatty acids (triglycerides) from vegetable and animal sources, surfactants are derived from petroleum products whose structure can be modulated in various ways.[9-30] Modern detergents consist of 10–20 different components, most of which are salts of fatty acids and surfactants (sodium and potassium salts of C_{12-18} long alkyl chains[8, 33,34]). These salts are extracted through the saponification process from animal fats, palm oil, soybean oil, and coconut oil. Since surfactants can clean a surface more thoroughly, even at low temperatures and with hard water, they are more appealing to use than soaps.

Additionally, surfactants are vital components of our biological system. Biological cell membranes, or lipid bilayers, contain phospholipids,[35] which are also amphiphilic molecules that help ions, proteins, and other molecules move selectively inside and outside of cells. Bile salt (steroidal anionic biosurfactants) is a prominent organic solute in bile juice that helps the intestines absorb dietary fats.[36] The human lungs produce a pulmonary surfactant, also known as pulmonary epithelial lining fluid (ELF), which helps to increase lung compliance and overall lung capacity. ELF contains a lipoprotein-type surfactant, which is secreted from lung epithelial type II cells and delivered to the alveolar space to lower surface tension at the air-liquid boundary in the lung.[37]

Classification of the amphiphiles/surfactants

Based on the head group charge in aqueous solution, surfactants can be classified as follows-

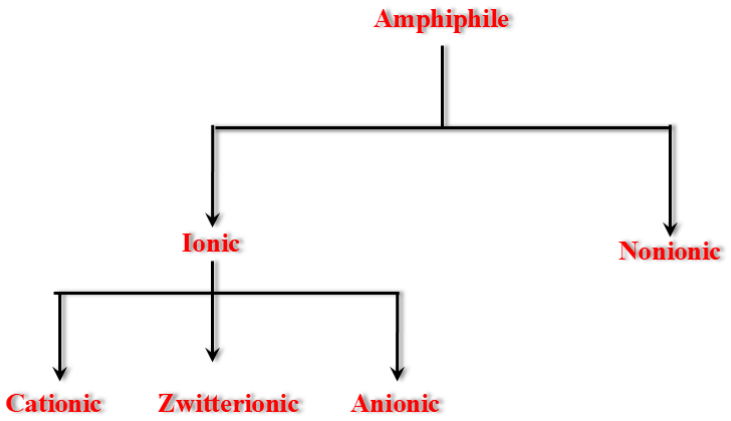

Fig. 2. Schematic representation of classification of amphiphiles/surfactants.

Cationic Surfactants:

These surfactant classes consist of positively charged head groups (alkyl quaternary ammonium salts, amine salts, phosphonium salts, amine oxides, etc.) and negatively charged counterions (primarily Cl^- and Br^-). These surfactants are expensive to prepare; thus, their application is limited.

Example:

Cetyltrimethylammonium bromide (CTAB), Dodecyltrimethylammonium chloride (DTAC), Tetradecyltrimethylammonium bromide (TTAB), etc.

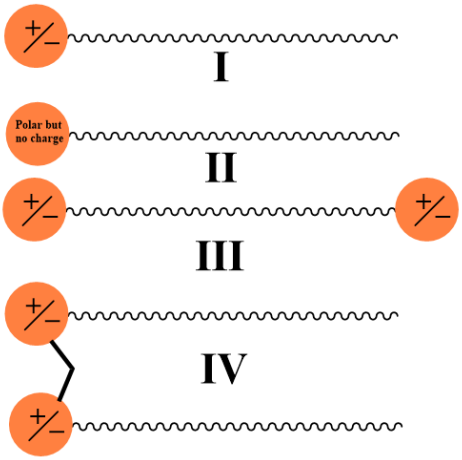

Fig. 3. Schematic representation of (I) Ionic (cationic/anionic), (II) Non-ionic, (III) Zwitterionic (bola electrolyte type), (IV) Gemini type amphiphiles/surfactants.

Anionic Surfactant:

This class of surfactant has a negatively charged head group (sulfonates, sulfosuccinates, alkyl-sulfates, carboxylates, N-acyl amino acid, etc) along with positively charged counterions (alkali metal ion Na^+/K^+ and quaternary ammonium cation). The majority of household detergents contain this anionic surfactant.

Example:

Sodium lauryl sulphate (SLS/SDS), Sodium dodecylbenzene sulfonate (SDBS), sodium tetradecyl sulfate (TSDS), Sodium lauryl sarcosinate (SDDS), etc.

Zwitterionic Surfactant:

These surfactants have both positively and negatively charged centers, making them suitable for use as cationic or anionic surfactants with varying pH values. This class includes imidazole derivatives, phosphatides, and betaines, among others. Normally, here ammonium ions contribute a positive charge, while carboxylates, sulfates, or sulfonate ions contribute towards negative charge. These surfactants exhibit great dermatological properties. The strong foaming characteristics and less sensitivity to skin make zwitterionic surfactants a common ingredient in shampoos, cosmetic products, and hand and dishwashing detergents.

Example:

Lauramidopropyl betaine, 3-[(3-cholamidopropyl) dimethylammonio]-1-propanesulfonate (CHAPS), Lauramidopropyl betaine, etc.

Nonionic Surfactant:

This class of surfactant has no electrical charge on its hydrophilic head group. These compounds have polar functionality in their structures, which makes them miscible in water. This class includes surfactants such as alkylpolyglucosides, polyoxyethylenes, N-based glucamine, and polyglycidols. Following anionic surfactants, they are widely produced in the industrial sector.

Example:

2-[4-(2,4,4-trimethylpentan-2-yl) phenoxy] ethanol (Triton X100), N-decanoyl-N-methylglucamine (MEGA-10), etc.

Other classes of Surfactants:

Surfactants are further divided into a few specific classes in addition to their overall classification. Over the last two decades, these surfactants have received a great deal of attention and investigation.

Gemini Surfactant:

Gemini surfactants are a distinct type of surfactant (Fig. 4), with more surface activity than typical surfactants due to their high hydrophobicity. They consist of a rigid or non-rigid spacer, an extended hydrocarbon chain joined to a polar head group, and another hydrocarbon chain organized sequentially with another polar head group. These two hydrocarbon chains are connected with the general spacer. These polar head groups can be categorized as positive (ammonium),[38] negative (sulfates, carboxylate, etc.),[39] or nonionic (based on carbohydrates).[40] Spacers can be stiff (stilbene) or flexible (saturated hydrocarbon chain), with lengths varying from two to twelve methylene groups. The first Gemini surfactants were synthesized in 1971 by Bunton et al.[41]

Menger et al.[42] first coined the term "Gemini" in 1991. Spacers can be connected to either the middle of the long hydrocarbon tails or both of the same head groups.

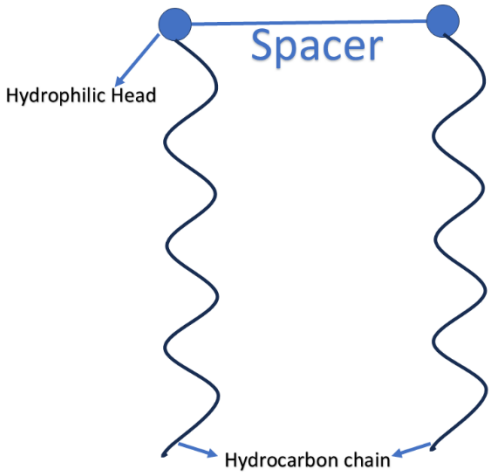

Fig. 4. Schematic representation of Gemini surfactants.

SILICONE Surfactant:

Silicone surfactants, often referred to as siloxane-polyoxyalkylene copolymers, are a special class of surfactants that contain permethylated siloxane hydrophobic groups together with one or more hydrophilic polar groups that can be cationic, anionic, non-ionic, or zwitterionic.

Polyoxyethylene (PEO) and polyoxypropylene (PPO)-based non-ionic groups are the most common types found in nature. Silicon surfactants effectively lower surface tension to 15-20 mN.m-1 in both aqueous and non-aqueous solvents when compared to conventional hydrocarbon surfactants.[43] These surfactants are widely used as stabilizers in polyurethane foams, conditioners in textiles, additives in ink, and emulsifiers in the cosmetics industry because of their unique spreading properties.[44]

Fluoro Surfactant:

They are members of the distant class of surfactants, where at least one hydrogen atom in the alkyne chain is replaced by an F-atom. Fluorosurfactants are widely used in a wide range of fields, such as firefighting, biomedicine, adhesives, and cosmetics.[45-47] The surface activity of these surfactants has been measured by the quantity of fluorine atoms that take the place of the alkyne hydrogens. The surface activity of Fluoro surfactants is higher than that of traditional organic surfactants.

Ionic Liquids:

Ionic Liquids (ILs) are molten salts (purely ionic semi-organic compounds) with melting temperatures less than 100 °C (212 °F).[48] The ordinary table salt (NaCl) has a melting point of about 801 °C, which clearly shows that traditional inorganic salts and ionic liquids differ significantly. This distinction is related to the components (ions) by which they are produced; small symmetrical ions generate ordinary inorganic salts, whereas ionic liquids are formed by big unsymmetrical massive cations with anions (Fig. 5), and charges are dispersed over enormous volumes via resonance.

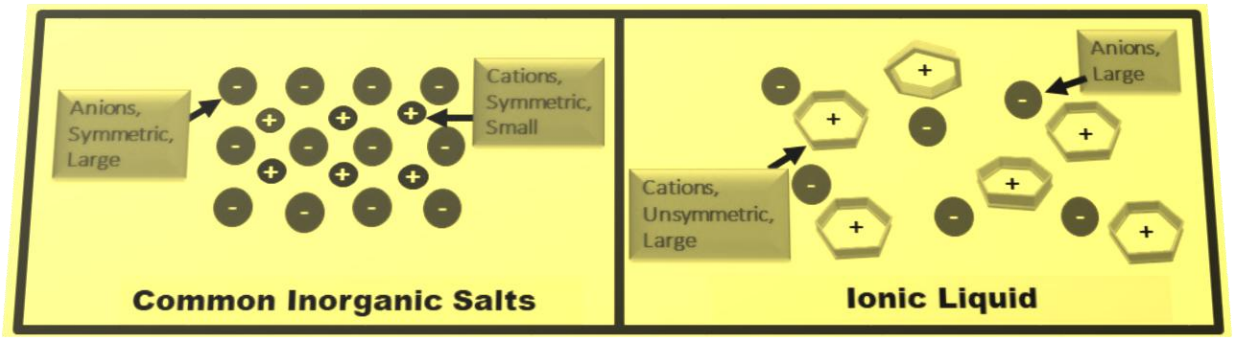

Fig. 5. Comparative diagrams of anions and cations with possible orientation between conventional inorganic salts with ionic liquids.

Gabriel and Weiner reported the first synthetic ionic liquid, ethyl ammonium nitrate (m.p. 52-55 °C), in 1888.[49] Paul Walden, a Russian, Latvian, a German chemist, synthesized room temperature ionic liquid (RTIL) for the first time in 1914.[50] It was ethylammonium nitrate, or (C_2H_5) $NH_3^+ \cdot NO_3$- (m.p. 12 °C). The melting point of ionic liquids varies greatly below 100 °C. While some ionic liquids that contain large organic or inorganic anions are typically liquids at room temperature with melting points even below 0°C (e.g., 1-ethyl-3-methylimidazolium ethylsulfate (m.p.<-20 °C), EMIM dicyanamide (m.p. -21 °C), etc.), others that have long alkyl chains attached to the imidazolium N-atom in combination with halide anions (such as 1-hexadecyl-3-methylimidazolium chloride, m.p. 64-65°C) are solid at room temperature. Conventional organic cations, such as alkyl-imidazolium, -pyridinium, -ammonium, -phosphonium, and -pyrrolidinium types, combined with anions, such as organic triflate, dicyanamide, acetate, trifluoroacetate, and trifluoromethylsulfate, or inorganic halides (bromide or chloride), hexafluorophosphate, nitrate, perchlorate, chloroaluminate, and tetrafluoroborate, form ionic liquids (Fig. 6).[51] Ionic liquids are currently being used with increasing attention because of their considerable conductivity, low volatility, high thermal stability, low vapour pressure, and non-flammability. Because of their many physicochemical properties, ILs can be employed in many applications such as an alternate solvent to conventional organic solvents,[52] drug delivery,[53] micellar catalysis,[54] and antibacterial activities.[55]

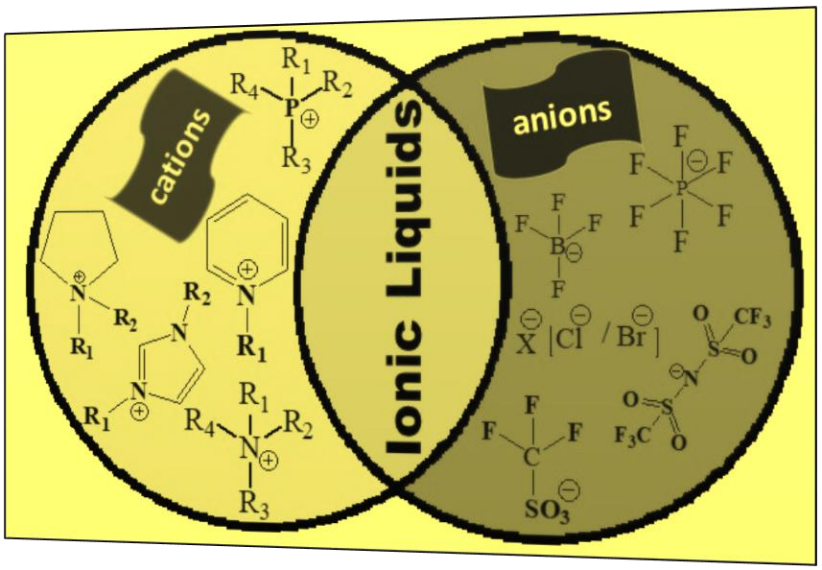

Fig.6. Some commonly used cations and anions forming ionic liquids.

For the past twenty years, ionic liquids (IL) containing fragments of the di-alkyl imidazolium, di-alkyl pyridinium, and alkylammonium types have been referred to as Surface Active Ionic

Liquids (SAILs), a unique class of surfactants. Di-alkyl imidazolium ionic liquids have drawn particular attention among the various cations that form SAILs because they may be made by tuning N-substituents with various alkyl groups and counter anions using a straightforward one-pot synthesis.[56-58] The surface activity of numerous ionic liquids has been documented in earlier research,[59-64] with the majority of these studies being conducted in aqueous solution.

Depending on their structure, various amphiphilic molecules exhibit a balance between hydrophilicity and lipophilicity. This phenomenon, known as hydrophilic lipophilic balance (HLB), is crucial for classifying surfactants as either water soluble or oil soluble based on their relative solubility.

Aggregation of amphiphiles/surfactants:

The most important characteristic of the amphiphiles is self-aggregation in the solution medium. In order to avoid unfavourable interaction with the solvent molecules, amphiphilic molecules arrange themselves in a particular solvent depending upon the nature of the solvent (polar/non-polar). The solvent-induced self-aggregation of amphiphiles generates many microstructures (micelle, reverse micelle, vesicle, etc) depending upon the arrangement of the hydrophilic and hydrophobic moieties of the amphiphiles. In a polar solvent, the hydrophobic residue of the amphiphile experiences an unfavourable interaction with the solvent molecules and a favourable interaction with the other. As a result, arrangements are formed at bulk where hydrophilic heads are exposed to the polar environment and hydrophobic tails (Fig. 7 B) are drawn together into an oil-like core. This type of aggregate, where hydrophilic groups are aligned towards the solvent and the hydrophobic residues are away from the solvent, is known as the Micelle. The size of the micelle may vary from small to large depending on the nature of the amphiphiles. The concentration of amphiphiles/surfactants beyond which a micelle forms is known as the Critical Micelle Concentration (CMC). Micellization is a dynamic process where a rapid equilibrium exists between the free surfactants and the micelle.

Micelles are colloidal in size. McBain was the first to predict that surfactants in solution would self-assemble in 1913.[65] Although he was harshly criticized at the time by a group of scientists at a Royal Society meeting in London, it was later scientifically established that surfactants can practically aggregate in solution, as evidenced by their superior detergency properties, which allow them to easily remove dirt and dissolve it into their hydrophobic core. The major driving force of micellization includes hydrophobic interaction between the hydrophobic tail of the amphiphile; apart from that, electrostatic and van der Waals forces of interaction play important

roles in the micellization process of the ionic type of amphiphile. In the case of ionic-type amphiphiles, the counterion plays a vital role in micellization by entering between the similarly charged micellar head groups, resulting in minimizing the electrostatic repulsion. The micellization process is significantly influenced by positive entropy contribution because the gain in entropy by the free water molecules that were "trapped" in the solvation cage surrounding the surfactant monomers through H-bonding interaction among them outweighs the loss of entropy caused by the aggregate of the surfactant monomers.[66] In essence, CMC, which addresses "inexact" but "convenient" surfactant concentrations, is not a specific surfactant concentration but rather a limited range of surfactant concentrations.[67] Different shapes of micelles can be formed depending on the surfactant type and microenvironment, as detailed above.

Like water droplets in an oil system, reverse micelles form in a solution where the amount of a non-polar solvent (such as alkanes, haloalkanes, aromatic solvents, etc.) is greater than the amount of a polar one. Surfactants are used to stabilize the components in the solution as the amphiphiles aggregate. This technique was applied to make a particular kind of microemulsion.[68] The polar head groups in the reverse micelle (Fig. 7C) are directed around the water molecules in the inner micellar core (often referred to as the "Water pool," or "W" in Fig. 7C), while the hydrophobic portions are exposed outside of the non-polar solvents. The size of reverse micelles, which have nanometer dimensions, can be expanded by adding more water to the solution. These reverse micelle water pools can be utilized to solubilize proteins[69] and create nanomaterials.[70]

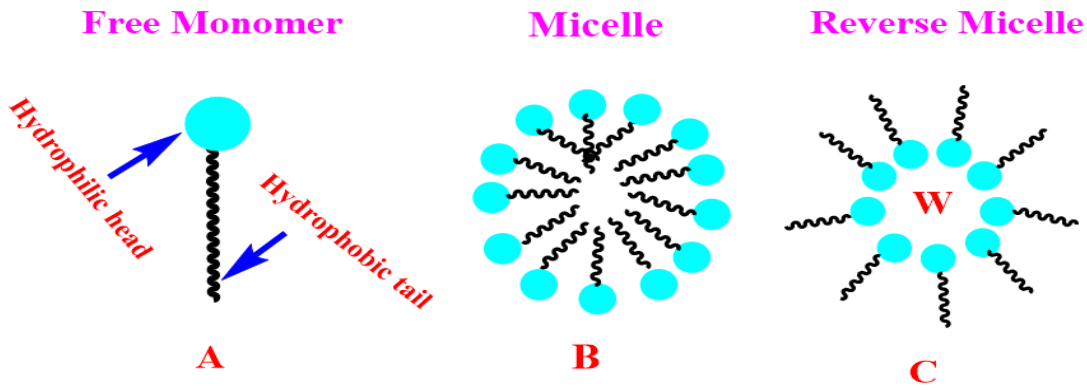

Fig. 7. Various aggregate structures of surfactants in solution: (A) free monomer, (B) normal micelle (spherical structure), (C) reverse micelle.

CMC determination:

The most essential feature of surfactants is their CMC. In the literature, numerous analytical techniques are available for determining CMC. For example, according to Mukerjee and Mysels,[71] there are 71 potential approaches that they have analyzed critically after drawing from various literature. However, the right approach will depend on the equipment available, the investigator's own preferences, and the connection between the technique and the final application.

Numerous techniques, including tensiometry, conductometry, viscometry, turbidimetry, light scattering, vapour pressure osmometry, fluorimetry (including steady-state fluorimetry, steady-state anisotropy, and time-resolved fluorimetry), spectrophotometry, magnetic resonance, calorimetry, etc., can be used to determine CMC. Tensiometry, conductometry, and fluorimetry are the most commonly utilized techniques among them. Conductometry techniques can only be used with ionic surfactants. Various approaches are used to test the physical properties of surfactants in solution, and variations in surfactant concentration result in varied plot appearances across methodologies (Fig. 8).

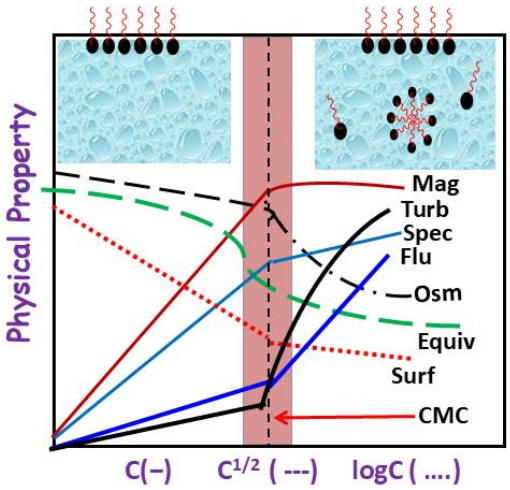

Fig. 8. Determination of CMC of a surfactant with variation of surfactant concentration (C) by various methods: viz., Mag: magnetic resonance; Turb: turbidimetry; Spec: spectrophotometry (plotted against C); Flu: Fluorimetry; Osm: osmotic coefficient (against $C^{1/2}$). Equiv: equivalent conductance; Surf: surface tension (against log C).

The dotted white line represents the distinct breaks that are present in all physical properties and are regarded as CMC. Since CMC is method-dependent, it should be emphasized that it is not merely a point but rather a narrow range (represented by the thin bar). Since the size of the scattering units in solution determines the scattering phenomenon, a significant increase in scattering radiation above CMC is observed employing the light scattering method[72] directly demonstrates large assemblies after CMC. By concentrating on the self-diffusion of monomers following CMC, a nuclear magnetic resonance (NMR) investigation has produced yet another significant demonstration of the compactness of surfactant monomers in micelles.

Micellar characteristic:

Structure, shape, microenvironment, and characteristics:

It was suggested by Hartley[73] in 1936 that micelles are basically spherical. This suggestion also backs up McBain's 1920 publication.[74] The micelles should have between 50 and 100 monomers that are linked in a rather small concentration range, according to Hartley's spherical micelle model. The diameter of this associate structure is around twice the length of the hydrocarbon chain. As explained above, micelle interiors are essentially hydrophobic, but head groups connect with some counterions to prevent being too near because of their repulsive interaction. Many of the characteristics of a single surfactant system with ionic properties were successfully described by the classical Hartley model. The surface charge and zeta potential of ionic micelles allow them to create an electrical double-layer structure[75] that shows electrophoresis in an electric field. Ionic micelles create a "stern layer" in the surrounding environment where head groups and oppositely charged counter ions are close due to electrostatic interaction. However, the "Gouy Chapman layer" forms around the outside of the contents of the "Stern layer." Both of these layers can unbind free monomers, counterions, and water molecules that solvate micelles through ion-dipole interaction. Together, the terms "Stern layer" and "Gouy Chapman layer" have been used to refer to the electrical double layer (Fig. 9). A hydrophobic core of micelles exists inside the 'Stern layer'. The micellar kinetic component is comprised of the Stern layer and the core. The Gouy-Chapman layer is also known as a diffuse layer. The diffuse layer's boundary, which can move with the micelle in solution, is also referred to as a shear or slipping plane. The stability of colloidal dispersions is frequently shown by the zeta potential (ζ), which is the slipping plane potential (Fig. 9). A micellar solution with zeta potential values greater than ± 30 mV is considered stable. Certain

water molecules in nonionic micelles make an H-bonding connection with polyethylene oxide groups, which causes them to halt inside the core right near the head groups (palisade layer).

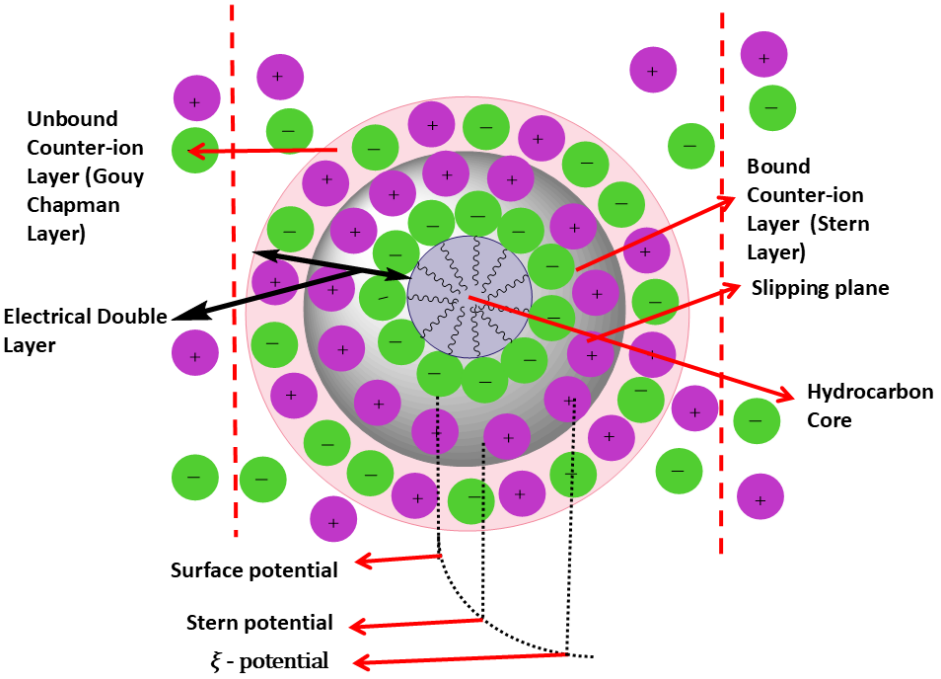

Fig. 9. Schematic representation of ionic micelles demonstrating counterion binding, charge neutralization, micellar core, and electrical double layer, assuming spherical symmetry of micelle.

Beginning with Hartley's idea, contemporary research has created a more practical microscopic image of micelles, which leads to the conclusion that, of course, micelles are dynamic. It is feasible to quickly switch the monomers between the solution phase and micelles. Rather than being smooth and uniform, micelles can be found as irregular molecular clusters if we create a high-resolution camera or freeze the molecules' motion. Since it is unable to account for several experimental phenomena, Hartley's straightforward "two-states" spherical micellar model has gained criticism. The molecular model that Menger[76] has put forward is very different from Hartley's in terms of how non-polar compounds are solubilized in micelles. Water molecules can enter a micelle up to a certain distance, according to Menger's "porous cluster" model (3–4 methylene carbon atoms after the head group); this means that they can enter the micelle more easily and that the interior or core is comparatively smaller, as shown by NMR and fluorescence measurements. In addition to the traditional spherical micelle, other suggested shapes include the worm-like structure,[77] ellipsoid shape,[78] disk or cylindrical structure of

Harkins,[79] rodlike micelle of Debye,[80] lamellar type of Philippoff[81], and spherical bilayer (vesicle) structure.[82] The idea of a packing parameter (P) was put up by Israelachvili et al.[83,84] to differentiate between the various supramolecular assemblies that form in solution. It is possible to determine the micelle's amphiphile packing parameter using the following formula:

$$P = \frac{v}{A_{min} l_c} \quad (1)$$

Where v is the volume of the hydrophobic chain (nm^3), assuming it is incompressible, and A_{min} represents the headgroup's surface area at the micellar-solution interface (nm^2/molecule). l_c is the maximum effective length of the hydrophobic chain of an amphiphile (nm). Tandford's formula is generally used to calculate the effective length and volume of the hydrophobic chain in the case of a pure amphiphile.[85,86]

$$l_c \leq l_{max} \approx (0.154 + 0.126\, n_c) \text{ and } v = (0.0274 + 0.0269 n_c) \quad (2)$$

where, l_{max} is the maximum length of the monomer chain and n_c is the number of carbon atoms in the hydrophobic chain.

Table 1. Packing parameter (P) values for different aggregates are tabulated as follows:

Aggregates	P
Micelles	< 0.333
Non-spherical aggregates	0.333 < P < 0.50
Bilayers and vesicles	0.5 < P <1
Inverted aggregates	>1

Some aggregated molecular geometries have been represented in Fig. 10.

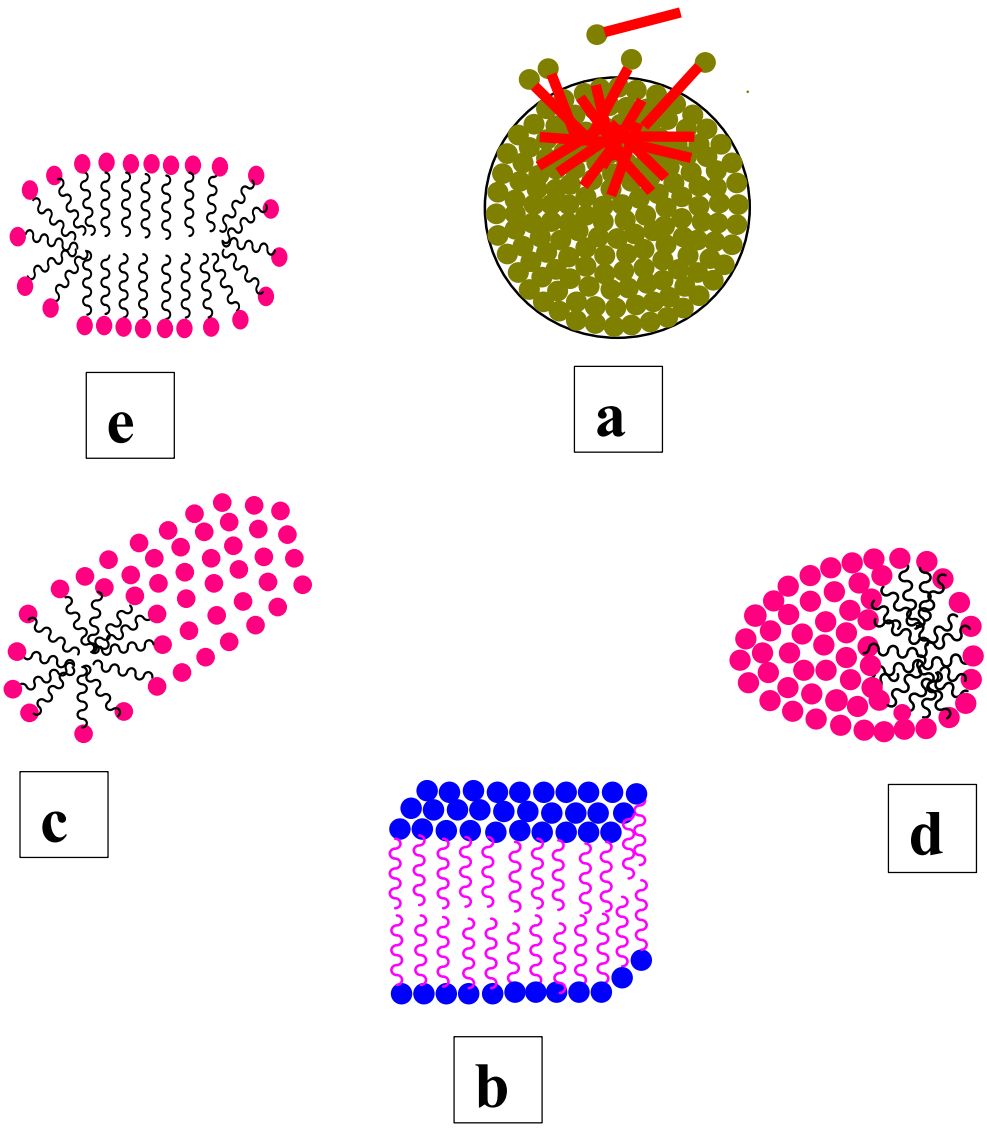

Fig. 10. Schematic representation of geometrical forms of aggregates. a: spherical micelle; b. lamellar or bilayer arrangement; c: rodlike micelle, d: oblate ellipsoid (bisected) micelle, and e: wormlike or cylindrical micelle.

Recent advances in technology have allowed us to gather experimental evidence and images of many types of micelles. By taking into account the size distribution assuming spherical micelles[87] without actually identifying the micellar shape, the dynamic light scattering (DLS) approach allows us to get a firsthand understanding of micellar size (average hydrodynamic diameter) and diffusivity. Atomic force microscopy (AFM), small-angle neutron scattering (SANS), small-angle X-ray scattering (SAXS), cryo-transmission electron microscopy (cryo-TEM), and static light scattering (SLS) can all be used to measure the size and form of a

micelle.[88-91] The only method capable of differentiating between linear and branching micelles is cryo-TEM. When different inorganic and organic salts are present, the shapes of micelles change. The following are a few examples that demonstrate spherical-to-cylindrical and spherical-to-wormlike or rod-like transitions: sodium dodecyl sulfate micelles change from spherical to cylindrical conformation[92] when exposed to concentrated NaCl solution; sodium alkylbenzenesulfonate micelles change from spherical to cylindrical and ultimately multilamellar vesicles[93] when exposed to high concentrations of Na_2SO_4 salt; cetyl trimethyl ammonium bromide, cetyl pyridinium chloride micelles change into wormlike micelles[94,95] when salicylate salts are present, etc.

***Degree of counterion binding*:**

Counterions are an essential component of micelles,[96,97] particularly in the stern layer. To understand the electrical double layer and to calculate the thermodynamic parameters for the micellization process, the degree of counterion binding is a crucial parameter. Depending on amphiphiles, solution media, additives, and other factors, the degree of counterion binding (g) can range from 20 to 80%. The specific conductance value is first influenced by both free surfactant monomers and counterions at low surfactant concentrations. As surfactant concentrations rise, the proportion of monomers and counterions increases monotonically, increasing the specific conductance value (Fig. 11). Nevertheless, certain counterions attach to the micelles following micellization, and the resulting micelles become less mobile because of their increased size. A decreased number of free monomers and unbound counterions is the only factor contributing to specific conductance values (Fig. 11), which causes specific conductance values to be offset. The degree of counterion binding (g) is determined using a straightforward relation based on the two unique slopes of different magnitudes (S_1 and S_2) that are obtained as a result of this conductometric phenomenon.

$$g = 1 - S_2/S_1 \quad (3)$$

Even though this approach is predicated on certain assumptions, it is actually very effective, and the degree of counterion binding uncertainty falls within an acceptable error range (about 2-3%).

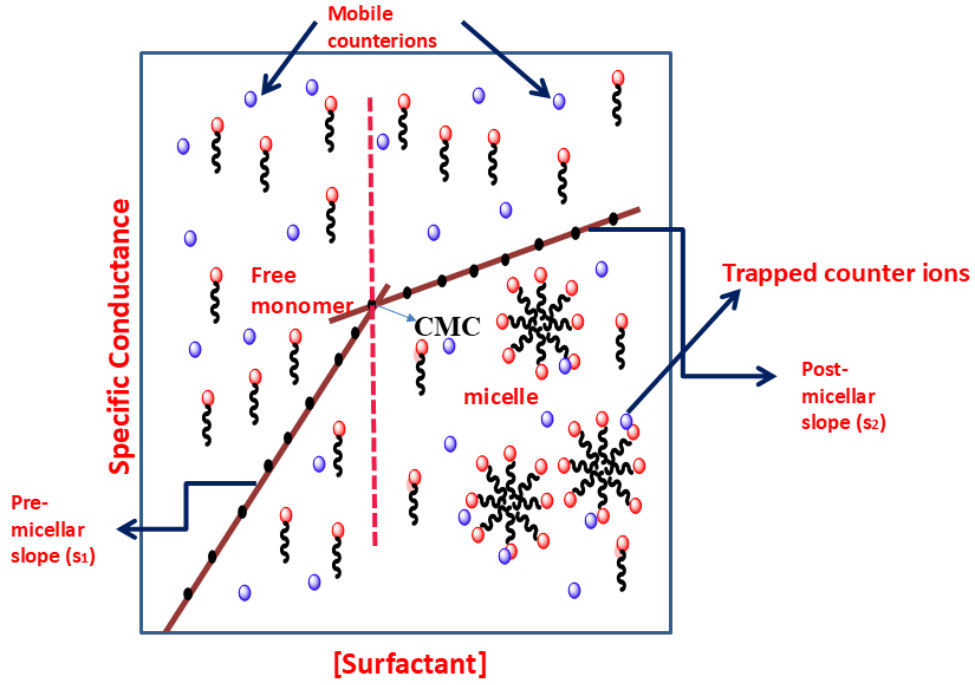

Fig. 11. Specific conductance vs. [Surfactant] profile for determination of CMC and degree of counterion binding using pre (S_1) and post micellar (S_2) slopes.

Thermodynamics of micellization:

The process of micelle formation is energetically regulated by thermodynamic principles. The so-called "iceberg" structure surrounding the surfactant monomer is disrupted during micellization, which raises entropy.[98,99] The mass action model and the phase separation model, often known as the pseudo-phase model,[100,101] are two methods that have been widely employed in classical literature and are recognized as effective micellization models. The mass action model states that following CMC, monomers and micelles are interdependent, with micelle concentration rising in tandem with monomer concentration and vice versa, based on the following equilibrium:

$$nS \overset{K_M}{\leftrightarrow} S_n \text{ or } M \qquad (4a)$$

The symbols S, S_n, n, and K_M stand for surfactant monomers, micelles, aggregation number, and equilibrium micellization constant, respectively, for a nonionic surfactant.

When examining micellization in the context of ionic surfactants, the equilibrium above incorporates the charges and counterions:

$$nS^{\pm} + mZ^{\mp} \underset{K_M}{\leftrightarrow} (S_n Z_m)^{\pm(n-m)} \text{ or } M^{\pm(n-m)} \quad (4b)$$

where Z± and m stand for counterions and the number of counterions that are bonded to the micelle in the equilibrium process mentioned above, for an ionic surfactant.

Therefore, it is expressed as follows: for nonionics, ignoring the activity impact,

$$K_M = \frac{a_M}{a_S^n} \approx \frac{C_M}{C_S^n} \quad (4c)$$

In this case, C represents the concentration, and a is the activity coefficient.

Regarding ionic surfactants,

$$K_M = \frac{a_M^{\pm(n-m)}}{a_{S^{\pm}}^n a_{Z^{\mp}}^m} \approx \frac{C_M^{\pm(n-m)}}{C_{S^{\pm}}^n C_{Z^{\mp}}^m} \quad (4d)$$

The following relation can be used to get the standard Gibbs free energy of micellization for nonionic surfactants:

$$\Delta G_M^0 = -RT \ln K_M = -RT \ln C_M + nRT \ln C_S \quad (5)$$

One way to display the change in the standard Gibbs free energy of micellization per monomeric unit (n) is as follows:

$$\frac{\Delta G_M^0}{n} = \Delta G_{mic}^0 = -\frac{RT}{n} \ln C_M + RT \ln C_S \quad (6)$$

A very small percentage of monomers form micelles at the CMC. Thus, the approximation of equation 6 is as follows:

$$\Delta G_M^0 = RT \ln C_S = RT \ln CMC \quad (7)$$

Regarding ionic surfactants,

$$\Delta G_M^0 = -RT \ln K_M = -RT \ln C_M^{\pm(n-m)} + nRT \ln C_S^{\pm} + mRT \ln C_Z^{\mp} \quad (8)$$

As a result, the typical Gibbs free energy change per monomeric unit can be expressed as follows:

$$\frac{\Delta G_M^0}{n} = \Delta G_{mic}^0 = -\frac{RT}{n} \ln C_M^{\pm(n-m)} + RT \ln C_S^{\pm} + \frac{m}{n} RT \ln C_Z^{\mp} \quad (9)$$

Once more, since the percentage of monomers is extremely low and typically n is high, equation 9 is changed to

$$\Delta G_{mic}^{0} = RT \ln C_S^{\pm} + \frac{m}{n} RT \ln C_Z^{\mp} \quad (10)$$

It can be expressed as follows for common ionizable surfactants:

$$C_S^{\pm} = C_Z^{\mp} \quad (11)$$

Therefore, at CMC, it is evident that

$$C_S^{\pm} = C_Z^{\mp} = CMC \quad (12)$$

so that, $\Delta G_{mic}^{0} = \left(1 + \frac{m}{n}\right) RT \ln CMC = (1 + g)\, RT \ln CMC$ (13)

where g represents the degree or fraction of counterion binding.

When g = 0, counterion binding does not occur in the case of a nonionic surfactant.

$$\Delta G_{mic}^{0} = RT \ln CMC \quad (14)$$

However, if all counterions are bound, g = 1, and Eq. 13 looks like this:

$$\Delta G_{mic}^{0} = 2RT \ln CMC \quad (15)$$

The aforementioned relationship is predicated on multiple reliable approximations and a constant condition of the aggregation number (n).

According to the pseudo-phase concept, monomer concentration stays constant at or above CMC, and micelles are thought to form a new phase at or above CMC.

Based on phase equilibrium, the pseudo-phase model states that the following equilibrium can be granted: **monomer ↔ micelle (Pseudophase)** (16)

The chemical potential of free surfactant monomers (μ_S) in solution is equal to the chemical potential of surfactant monomers in the pseudo micellar phase ($\mu_S^{micelle}$) at a constant temperature.

Consequently, for nonionic surfactants,

$$\mu_S = \mu_S^{micelle} \text{ or } \mu_M \quad (17)$$

One way to write equation 17 for a nonionic surfactant is

$$\mu_S^{0} + RT \ln a_S = \mu_M^{0} + RT \ln a_M \quad (18)$$

or, $\Delta G_m^{0} = \mu_M^{0} - \mu_S^{0} = RT \ln a_S \approx RT \ln CMC$ (19)

Since, a_M (Activity of micelle considering it as a separate pure phase or pseudo phase) = 1,

In the case of ionic surfactants,

$$\mu_S^{\pm} + \frac{m}{n}\mu_Z^{\mp} = \mu_M^{\pm} \tag{20}$$

as, $\mu_S = \mu_M$

As a result, the eq. 20 is transformed to

$$\mu_{S^{\pm}}^0 + RT\ln a_S^{\pm} + \frac{m}{n}\mu_{Z^{\mp}}^0 + \frac{m}{n}RT\ln a_Z^{\mp} = \mu_{M^{\pm}}^0 + RT\ln a_M^{\pm} \tag{21}$$

$$\text{Or, } \left[\mu_{M^{\pm}}^0 - \left(\mu_{S^{\pm}}^0 + \frac{m}{n}\mu_{Z^{\mp}}^0\right)\right] = RT\ln a_S^{\pm} + \frac{m}{n}RT\ln a_Z^{\mp} - RT\ln a_M^{\pm} \tag{22}$$

$$\text{hence, } \Delta G_m^0 = RT\ln a_S^{\pm} + \frac{m}{n}RT\ln a_Z^{\mp} - RT\ln a_M^{\pm} \tag{23}$$

$$\text{Since, } a_M^{\pm} = 1,\ \Delta G_m^0 = RT\ln a_S^{\pm} + \frac{m}{n}RT\ln a_Z^{\mp} = \left(1 + \frac{m}{n}\right)RT\ln CMC \tag{24}$$

$$\text{Or, } \Delta G_m^0 = (1+g)\,RT\ln CMC \tag{25}$$

In equations 20 through 24, $\mu_M^{\pm}$ is actually $\mu_M^{\pm(n-m)}$;for simplicity, the factor (n-m) has been disregarded.

We derive the same equation for ΔG_m^0 from the pseudo-phase model, which we get from the mass action model. For monomers and micelles, the standard chemical potentials are μ_S^0 and μ_M^0, respectively, and the corresponding activities are a_S and a_M.

It should be mentioned that the equilibrium concentration of free monomer (C_S) is regarded as being equal to CMC for the two approaches mentioned above.

In the mass action model, incorporating the contribution of the aggregation number (n),[102] standard Gibbs free energy of micellization (ΔG_{mic}^0), and standard enthalpy of micellization (ΔH_{mic}^0) can be stated by,

$$\Delta G_{mic}^0 = (1+g)\,RT\ln X_{CMC} + \frac{RT}{n}\ln[2n(n+m)] \tag{26}$$

$$\text{and, } \Delta H_{mic}^0 = -RT^2\left[(1+g)\frac{d\ln X_{CMC}}{dT} + \ln X_{CMC}\frac{dg}{dT} + \frac{d\left[\left(\frac{1}{n}\right)\ln\{2n(n+m)\}\right]}{dT}\right] \tag{27}$$

In the two equations above, CMC is represented in mole fractions (X_{CMC}).

In this case, n is the aggregate number, and g is the number of counterion bindings. Equations 26 and 27 typically have small second and third terms. Conceptually, the terms can be omitted in the pseudo-phase model.

Therefore, in the case of ionic micelles,

$$\Delta H_{mic}^{0} = -RT^{2}\left[(1+g)\frac{d\ln X_{CMC}}{dT} + \ln X_{CMC}\frac{dg}{dT}\right] \quad (28)$$

On the other hand, nonionic micelles

$$\Delta H_{mic}^{0} = -RT^{2}\frac{d\ln X_{CMC}}{dT} \quad (29)$$

It is possible to compute the entropy of micellization (ΔS_{mic}^{0}) using the Gibbs-Helmholtz equation.

$$\Delta S_{mic}^{0} = \frac{\Delta H_{mic}^{0} - \Delta G_{mic}^{0}}{T} \quad (30)$$

The evaluation of ΔH_{mic}^{0} and ΔS_{mic}^{0} using equations 26 to 30, whichever applies for different systems, requires that CMC be measured at various temperatures. In general, the values of ΔS_{mic}^{0} are positive. The rupture of the iceberg structure surrounding the monomers to get them into the micelle overshadows the negative entropy contribution from the amphiphilic association in the micelle or the solvation of monomers; this process raises the overall entropy.

It should be noted that CMC should be converted to mole fraction units (as previously indicated) in order to calculate thermodynamic parameters. Equation 29 is used to measure the CMC values at various temperatures in order to compute the standard enthalpy of micellization (ΔH_{mic}^{0}) using the van't Hoff method. ITC (isothermal titration calorimetry) allows for the direct measurement of both CMC and ΔH_{mic}^{0}. The calorimetric method of determining ΔH_{mic}^{0} yields value with great accuracy.[103-106] In general, the enthalpies computed using the direct approach and the van't Hoff method (which determines CMC at various temperatures) are found to differ, particularly for ionic surfactants.[107-109]

For the micellization of surfactant, neither the mass action model nor the pseudo-phase model is exactly right. Both methods assume that the equilibrium concentration of free monomers throughout the micellization process is equal to CMC. Conveniently, it is also believed that the degree of counterion binding and the aggregation number are independent of temperature, or at least independent within the temperature range under investigation. These two models are the simplified versions for figuring out thermodynamic parameters, despite these drawbacks.

There are various methods in addition to the two models mentioned above. For nonionized and noninteracting systems,[100] Hall and Pethica apply a thermodynamic model that Hill established for small systems.[110] Hall has formulated a comprehensive approach to the multicomponent system of interacting aggregates.[111-113] Another thermodynamic method for nonionic surfactant systems has been proposed by Corkill and colleagues.[114-116] On the basis of micelle shape, Tanford[117] has put up an intriguing model for micelle formation. Ruckenstein and Nagarajan[118] further refine this geometrical model, which is expanded by Israelachvili et al.[83]

This topic merits more research because it is difficult to determine thermodynamic parameters with absolute precision due to a number of variables, including changes in aggregation number, micellar shape and size, counterion condensation, and micellar solvation with temperature variations and other environmental changes.

Mixed Amphiphiles system:

A lot of research has been focused on studying mixed amphiphile systems in recent years. Surface and colloidal properties of a mixed amphiphile system may differ from those of the pure constituents. Nonideal mixing of amphiphilic components frequently results in synergy in the properties of the mixes that can be utilized in their applications. A mixed amphiphile system is considered synergistic when its critical micelle concentration (cmc) values are lower than those of its pure constituents.[119] Mixed micelles are therefore frequently utilized in industries, pharmaceutical formulations, and increased oil recovery procedures. Potential skin irritation can be treated with a low dose of a mixed amphiphile/surfactant combination.[120] The use of fewer surfactants to generate mixed micelles is also beneficial to the environment because it reduces the amount of surfactant released.[121] In the human body, mixed micelles have significantly improved the absorption of hydrophobic drugs.[122,123] It is intriguing to note that an equimolar mixture of cationic and anionic surfactants may produce an insoluble ion pair; nevertheless, if the amount of one component in the solution is significantly higher than the other, the ion pair becomes soluble. In the literature, vesicle-like structures have also been observed as a result of catanionic surfactant conjugation.[124-126] A cleaning product that combines cationic and anionic surfactants can decrease water hardness.[127] Mixed micelles comprising ionic-ionic,[128-132] ionic-nonionic[133-136] and nonionic-nonionic[137-139] pairings have been documented in the literature, with uncommon nonionic-nonionic and cationic-cationic pairings. Significant research has also been done on the mixed micelle production of surface-

active ionic liquid (SAIL) in conjunction with cationic,[140-143] anionic,[144-147] nonionic surfactants,[148-151] and amphiphilic drugs.[119, 152, 153]

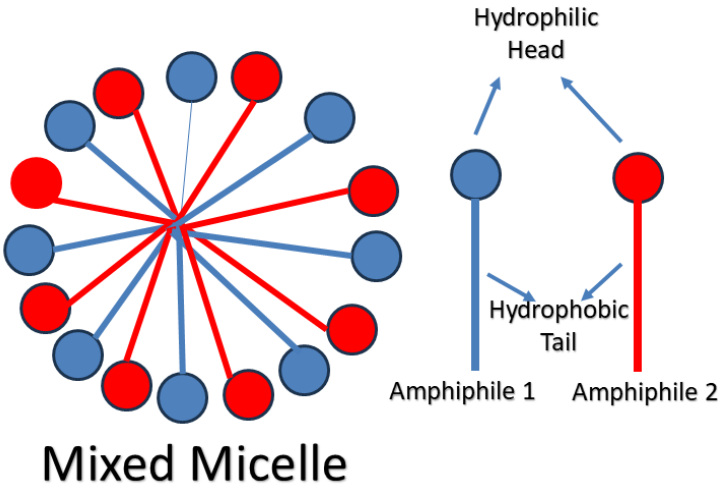

Fig. 12. Schematic representation of a mixed micelle formed by two ionic surfactants (Surfactant 1 (blue) and Surfactant 2 (red)).

Clint[154] proposes a simple hypothesis to determine CMC based on the ideal mixing of monomeric amphiphiles during the formation of mixed micelles. The proposed relation made by Clint's[154] assumption is given here:

$$\frac{1}{(CMC)_{max}} = \sum_i \frac{\alpha_i}{(CMC)_i} \tag{31}$$

In this case, the stoichiometric mole fraction of the i^{th} component is represented by α_i, and its CMC is represented by $(CMC)_i$. The following is the form of Eq. 31 if the mixing of amphiphilic components generating a mixed micelle is not ideal:

$$\frac{1}{(CMC)_i} = \sum_i \frac{\alpha_i}{f_i\,(CMC)_i} \tag{32}$$

where f_i represents the activity coefficient of the i^{th} component.

In cases where nearly ideal mixing, or homologous series of surfactants with similar head groups, might be expected, Clint's[154] theory offers a sufficient explanation. However, it is unable to predict either $(CMC)_{max}$ or the monomeric compositions in the mixed micelle formed by different head groups of surfactants.

Vesicles:

Vesicles are closed amphiphile bilayer structures that are spherical or ellipsoidal and possess an interior cavity that holds the aqueous solution in which they are dispersed (Fig. 13). Normal vesicles are called liposomes when they are made of naturally occurring phospholipids. However, a variety of synthetic amphiphiles and surfactants that can create bilayers can also generate vesicles. Vesicles are generally metastable in aqueous solution; energy is needed to dissolve the amphiphile in water and to cause aggregation (shaking, sonication, extrusion), as well as for the vesicles to flocculate into hydrated multilayers eventually. Their sizes can vary from 20 nm to 10 μm, depending on the experimental preparation circumstances, and they may have one or more onion-like concentric bilayer surfaces.[7] Based on differences in diameter, vesicles can be categorized as small (1-100 nm), large (100 nm- 1 μm), giant (1 μm-10 μm), uni- or multilamellar vesicles, or other sizes.[155] In the 1960s, Alec Bangham and his colleagues were the first to show that phospholipids spontaneously form bilayer vesicles, which they later called liposomes.[156] Over the past several years, a large number of papers on the production of vesicles from single surfactants or from mixes of cationic and anionic surfactants (known as catanionic vesicles) have been published in the literature.[157-159] Vesicles are widely used in biology and colloidal chemistry. Catanionic vesicles are anticipated to be employed as a template for the production of hollow particles as well as vehicles for the regulated delivery of drugs, proteins, genes, etc.[160] The spontaneous generation of catanionic vesicles can be controlled to create aggregates of different sizes by altering the chain length, the polar group type, the surfactant ratio, or the addition of salt. For vesicles made from single or mixed surfactants, it is crucial, though not required, that the packing parameter, P, fall between 1/2 and 1.[83, 161] Apart from catanionic vesicles, niosomes are another important class of surfactant-based vesicles. Non-ionic surfactant vesicles known as niosomes are produced when synthetic nonionic surfactants are hydrated, either with or without cholesterol or related lipids added. Although they have a bilayer and are structurally similar to liposomes, niosomes are more stable due to the materials employed in their creation, and as a result, they have many more benefits than liposomes.[162, 163] They are liposome-like vesicular structures that can transport both lipophilic and amphiphilic drugs.[164-166] Niosomes are biodegradable, biocompatible, and non-immunogenic, and exhibit flexibility in their structural characterization, making them a promising non-ionic drug delivery vehicle. The potential of niosomes for targeted delivery and controlled release in the treatment of viral infections, cancer,[167] and other microbial illnesses[168]

has been extensively studied. Both hydrophilic and lipophilic medications can be captured by niosomes, which can also prolong the drug's circulation throughout the body.

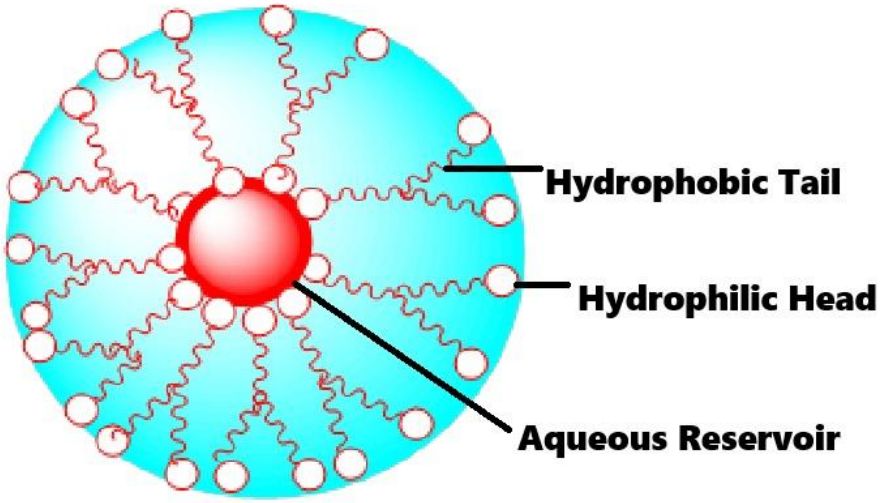

Fig. 13. Schematic representation of Vesicles.

Some Carbon-based nanomaterials as Soft Matter system:

Fullerenes, carbon nanotubes (CNTs), graphene (G) and its derivatives, graphene oxide (GO), reduced graphene oxide (RGO), nanodiamonds (NDs), and carbon-based quantum dots (CQDs) are examples of carbon-based nanomaterials (CBN), some of that acts as hard and some are as soft materials. Carbon nanotube, graphene, nanodiamond etc behaves as hard materials whereas graphene oxide, reduced graphene oxide, carbon-based quantum dots behave as soft materials. The potential biological uses of CBN include drug/gene delivery,[169-172] biosensing,[173-175] stem cell engineering,[176-178] bioimaging,[179-181] fluorescent labelling of cells,[182], and photothermal[183] and photodynamic therapy.[184-186] Carbon-based nanostructures are among the most intriguing possible candidates as biomaterials due to their distinct mechanical, chemical, biological, and physical characteristics.[187, 188] Since carbon-based nanomaterials are stiff and have compact structures, they have excellent mechanical properties.[189, 190] Numerous carbon nanomaterial structures in two and three dimensions have been created both theoretically and practically.[191, 192] Furthermore, carbon-based nanomaterials can easily enter the cellular compartments of living cells due to their small size.[193, 194] They can function as therapeutic or imaging agents and have a high loading capacity for medicines and imaging compounds due to their highly modifiable surface chemistry. After intravenous injection, carbon-based nanomaterials typically have minimal toxicity and controllable

biosafety. Additionally, carbon-based nanostructures are promising materials for biomedical applications due to their ability to diffuse within the body. Due to their distinct biological and physicochemical characteristics, including supramolecular π–π stacking, it is easy of surface modification, photothermal conversion capacity, good adsorption of molecules (such as DNA/RNA, proteins, drugs, and dyes), and potential for theranostic applications.[195, 196] CBNSs have drawn a lot of interest as a nanocarrier system in the field of drug delivery. Many drugs or biomolecules have an aromatic ring, which gives them lipophilicity and facilitates their loading via π–π stacking onto carbon nanomaterials.[197] Additionally, sp^2-based carbon nanomaterials can be biocompatible and harmless when the right dosages are used.[198] Thus, carbon-based nanostructures have emerged as one of the top choices for multimodal drug or biomolecule delivery systems due to the aforementioned physical and chemical characteristics. CNBSs allow various medications to attach, and they can be outfitted with targeted agents and stealth molecules to evade immune system clearance.[199, 200] Additionally, they have a number of benefits over other nanomaterials in drug delivery systems, such as, the ability to combine additional therapeutic and diagnostic components at their internal surface or cavity and a high drug loading capacity that results from their large surface area. Although carbon-based nanomaterials have numerous benefits, they face several challenges when used as biological materials. Carbon-based nanomaterials encounter a number of challenges in bio applications without surface modifications, including low water solubility, low biodegradability, and poor biosafety.[201-203] Carbon's hydrophobicity extends to its nanostructures. This can help in medication delivery by improving penetration across biological membranes. However, low solubility can be a disadvantage. Furthermore, altering the hydrophobic characteristics of carbon-based nanomaterials can change their physicochemical characteristics. Their propensity to aggregate as a result of interactions with biomolecules, which leads to accumulation in human tissues or organs, is another drawback for their use in drug delivery.[204] Consequently, a better comprehension of the interactions between nanomaterials and biomolecules can effectively address the aforementioned issues.[205]

Carbon nanotubes (CNTs):

Carbon nanotubes (CNTs) are seamless, rolled-up graphene sheets with special inherent characteristics. Carbon nanotubes (CNTs) are divided into two categories based on the number of graphene layers in the cylindrical tubes: single-walled (SWCNT) and multi-walled (MWCNT). van der Waals forces govern the interactions between each layer in MWCNTs,[206, 207] and a range of 2D crystal combinations with various electrical, optical, and mechanical

characteristics can form multilayered CNTs to produce various physical phenomena and device functionality. Nonetheless, one of the main obstacles to CNT application in nanomedicine is their poor dispersibility. Consequently, a number of functionalization pathways have been created to spread them and thereby increase their biocompatibility.[208, 209] Defective carbon atoms on the sidewall or at the termination, where oxidation produces carboxylic acid groups or carboxylated fractions that are then chemically changed by amination or esterification,[210] allow for covalent functionalization. Grafting to the surface of carboxylated carbon nanotubes has been accomplished recently using a variety of polymers,[211] metals,[212] and biological molecules.[213] Although it is widely acknowledged that when the surface of CNTs is appropriately functionalized (modified), their cell and tissue compatibility can be greatly enhanced,[214] concerns regarding the biocompatibility (biotoxicity) of CNTs have been raised as a practical issue, and numerous in-depth studies are still ongoing. In a variety of biomedical applications, such as biosensing, disease diagnosis, and treatment, functionalized carbon nanotubes have presented excellent prospects.[215] They enable biomedical imaging, deliver therapeutic compounds like medications and genes,[216] and detect a variety of biological targets.

Graphene and its derivatives:

One of the most significant and difficult fields of study in nanomaterials science in recent years has been the study of graphene and its derivatives. Graphene is a two-dimensional, single-atom-thick nanomaterial containing sp^2 hybridized carbon atoms and a hexagonal honeycomb sheetlike structure (Fig. 14). Graphene, discovered in 2004, has been intensively investigated in various domains. As a result of graphene's intriguing optical, electrical, and chemical characteristics, a number of graphene-based biosensors have been developed to identify biomolecules with great sensitivity.[217-219] For drug delivery applications, graphene's poly-aromatic surface structure with ultrahigh surface area allows for the effective loading of aromatic drug molecules via π-π-stacking.[220] Furthermore, graphene is less harmful than carbon nanotubes (CNTs) in cell cultures derived from platelets, fibroblasts, and lung epithelium.[221] The surface of graphene may contain a mix of hydrophilic and hydrophobic substances. Its extremely adaptable physicochemical characteristics allow for functionalization, which in turn allows for the attachment of various functional groups.[222] For instance, adding PEG to graphene's surface enhanced its biocompatibility and enhanced its circulation period.[223] Individual graphene sheets exhibit remarkable electrical transport capabilities, according to recent research.[224, 225] Using graphene sheets in a nanocomposite material is one way to potentially use these qualities for biomedical purposes. Graphene oxide

(GO), reduced graphene oxide (RGO), few-layer graphene oxide (FLGO), and chemically modified graphene (CCG) are some of the derivatives that have been created since pristine graphene has limited aqueous solubility despite having great electrical conductivity. One of graphene's most significant derivatives, graphene oxide (GO), is produced by strongly oxidizing graphite powder and is both inexpensive and plentiful. Graphene oxide exhibits remarkable optical capabilities because of its huge band gap,[226, 227] which are somewhat constrained in graphene because of its zero band gap. In addition, the graphene oxide sheet's surface and edges contain a variety of oxygen-containing groups (such as carboxyl, epoxy, and hydroxyl)[228] that make it easily functionalized through covalent and non-covalent bonding, changing its many characteristics. The applications of the modified graphene oxides are more advantageous.[229, 230] There are numerous approaches to functionalize GO based on its use. In recent years, interest has risen in the dye–GO nanocomposite, which has numerous uses in drug delivery, biodevices, and optoelectronic materials. For sol-gel chemistry, GO and RGO are far more appropriate, and they make good candidates for the production of biocompatible nanocomposites. The Hummers method can be used to synthesize GO nanosheets from graphite flakes. GO is used in several biotechnologies, including medication delivery,[231] nanoprobes,[232, 233] cellular imaging,[232] and biosensors.[234, 235] The combined effect of the functional groups on GO's surface and edges prevents electron transport.[236] For this reason, GO has a poor electrical conductivity, while RGO, its reduced version, has a higher electrical conductivity. Because of their high drug loading and efficient delivery capability, GO-based nanocarriers have recently drawn a lot of interest for anticancer drug delivery and imaging.[237] Compared to most nanomaterials, their specific surface area is more than double, reaching about 2600 m^2 g^{-1}.[238, 239] Furthermore, GO has a pH-dependent negative surface charge to preserve strong colloidal stability and shows high water dispersibility in contrast to pristine graphene.[240] On the other hand, GO can aggregate in salt media, including phosphate-buffered saline and protein-rich cell culture media.[240] Physisorption through π–π stacking is another intriguing feature of GO that works well for loading a variety of aromatic medicinal compounds, including the powerful anticancer drug doxorubicin.[241] Therefore, GO is a potential candidate for biomedical applications because of its tiny size, intrinsic optical characteristics, large specific surface area, inexpensive cost, and advantageous non-covalent interactions. Additionally, GO can release drug molecules in response to stimuli like NIR light, which enhances its potential as a delivery system.[242] However, more thorough research is needed to completely understand GOs' in vivo

activities, which include their blood circulation, inflammatory reactions, and clearance mechanisms.

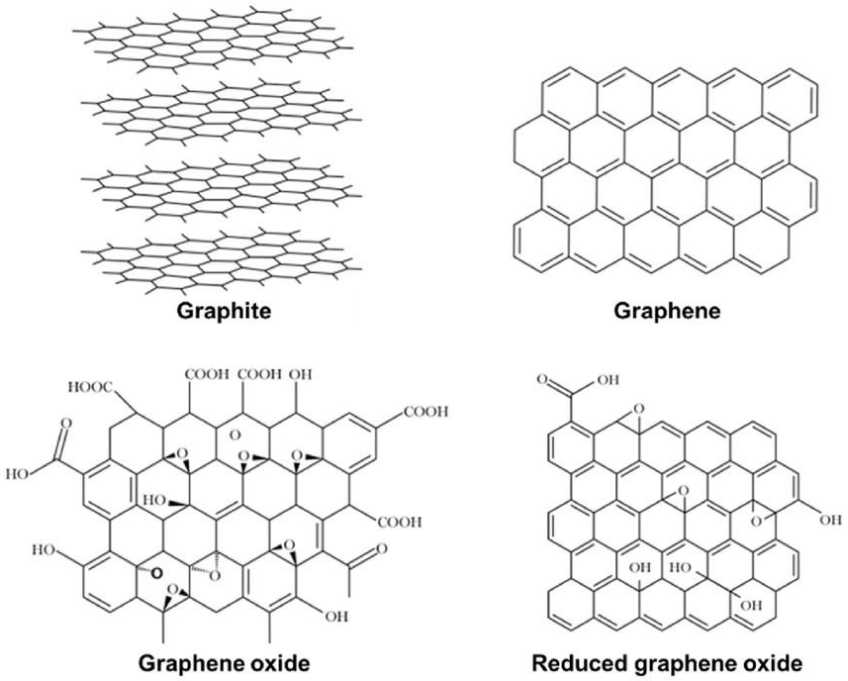

Fig. 14. Structure of graphite, graphene, graphene oxide (GO), and reduced graphene oxide (rGO).[243]

Proteins:

Protein is a very complicated substance found in all living organisms. In addition to having a high nutritional value, proteins play a direct role in chemical processes necessary for life. Early 19th-century chemists recognized the significance of proteins, such as Swedish scientist Jöns Jacob Berzelius, who in 1838 came up with the term "protein," which is derived from the Greek prōteios, which means "holding first place." The proteins of one species are different from those of another because they are species-specific. Additionally, they are organ-specific; for example, the proteins found in muscles, brains, and livers vary within a single organism. Compared to molecules of salt or sugar, a protein molecule is much larger and is made up of several amino acids that are connected to form lengthy chains, much like beads on a string. Proteins contain more than 50 amino acid residues. Among which naturally include roughly 20 distinct amino acids. All of these are α-amino acids with amine groups joined to the (α-carbon atom) adjacent to the carboxyl group in connection with distinct side chains (such as aliphatic, acyclic, aromatic, containing hydroxyl or sulfur, etc.). Except for glycine, which is an achiral amino acid, all naturally occurring amino acids are L-amino acids (chiral). The

characteristics of the amino acids that make up proteins lead to recognized correlations between structure and function, even if it is still impossible to fully explain all of a protein's functions from its amino acid sequence. Plants can synthesize all of the amino acids; animals cannot, even though all of them are essential for life. In addition to having polar groups (hydrophilic character) that may partially dissociate if the side chain is hydrophobic or nonpolar in nature, several of the constituent amino acids can function as weak acids or bases based on pH. Therefore, changing the pH of the solution makes it simple to adjust the protein charge. It is evident that proteins have a negative net charge above and a positive charge below the isoelectric point (pI). Proteins take on their most compact conformations and become less soluble in water at their isoelectric point (pI), which is the pH at which they have zero net charge. Each protein's specific function and structure are determined by its amino acid sequence, often known as the primary structure. Therefore, a polypeptide chain comprises two sections: the N-terminal, which is the amine group of the first amino acid, and the C-terminal, which is the carboxyl group of the last amino acid.[244, 245] When a polypeptide chain assembles into two dimensions, the resulting structure is known as secondary structure. The two types of secondary structural motifs are α-helices and β-sheets (Fig. 15). The fully functional version of the protein, known as the native structure, is produced when these motifs fold into three dimensions; this structure is known as the tertiary structure. The formation of bigger functional complexes from folded proteins is known as the quaternary structure. Typically, animal organs have a significantly higher protein content than blood plasma. Red blood cells, for instance, contain 30% protein, the liver 20–30%, and muscles around 30%. Hair, bones, and other tissues and organs with a low water content have higher protein percentages. The amount of protein in animals is far greater than the amount of free amino acids and peptides; protein molecules are made in cells by the sequential alignment of amino acids and are only released into bodily fluids once synthesis is finished. The primary factor influencing the significance of proteins is their function. Up until now, all enzymes have been found to be proteins. All metabolic reactions are catalysed by enzymes, which allow an organism to accumulate the proteins, nucleic acids, carbohydrates, and lipids its needs for existence, as well as to break them down and transform them into other substances. Enzymes are necessary for life. Numerous hormones made of proteins have significant regulatory roles. The respiratory protein haemoglobin serves as an oxygen carrier in the blood of all vertebrates, carrying oxygen from the lungs to the body's organs and tissues. Albumin, globulins, and fibrinogen are examples of plasma proteins that are essential for osmotic pressure maintenance, material transportation, immune system support, and blood coagulation. A small, water-soluble protein, cytochrome C, is a key electron

carrier in the mitochondrial electron transport chain (ETC), which is vital for cellular respiration and, when released, causes apoptosis. In general, proteins are surface active. Hydrogen bonds, disulfide bridges, electrostatic interactions, complex formation with metal ions, and hydrophobic effects among amino acid residues that favour a folded conformation and overcome the entropy disadvantage can all stabilize proteins. Both specific and non-specific interactions between proteins and numerous substances are possible, and under a variety of environmental conditions, including pH, temperature, pressure, additives, etc., these interactions may result in moderate to large structural or configurational modifications of the protein.

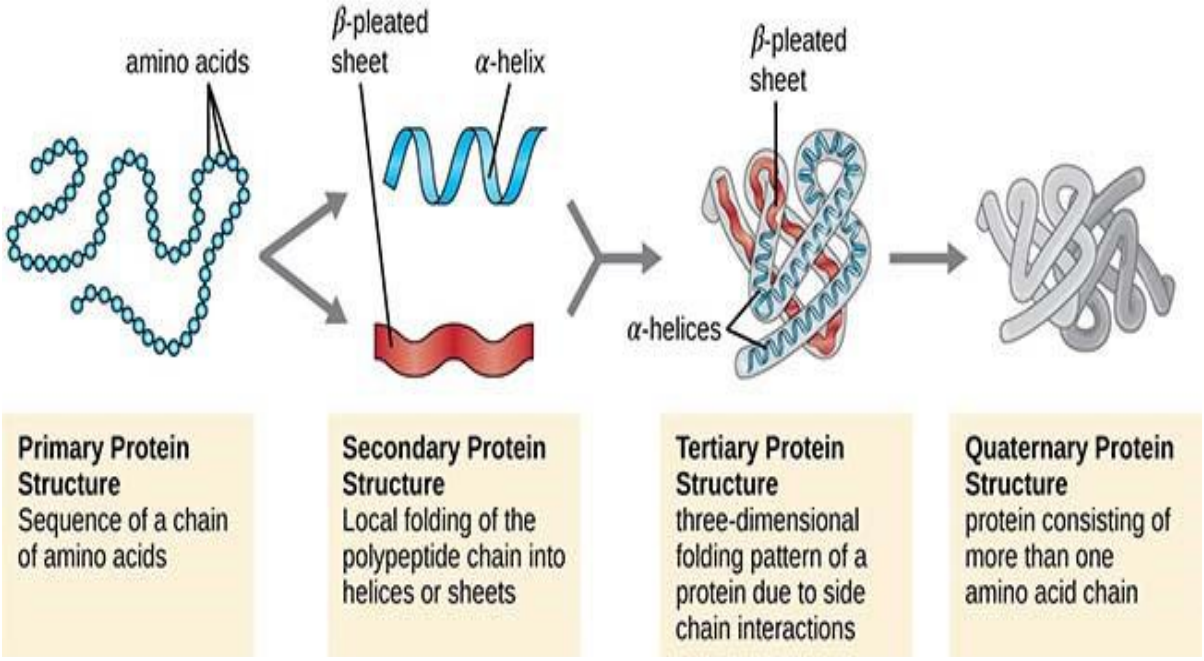

Figure 15: Different protein structures: Primary, Secondary, Tertiary, and Quaternary[246]

Protein-Amphiphile/Surfactant Interaction:

The protein-surfactant interaction has been the focus of a great deal of research in recent decades because of its scientific and technical uses in detergency, drug delivery, cosmetics, food, and other areas.[247-250] Blood serum, for instance, is a mixture of human serum albumin and several other substances, such as molecules with low molecular surface activity. Surface tension of these biological fluids is employed as a diagnostic and therapeutic tool;[251] protein molecular weights are determined by polyacrylamide gel electrophoresis using the complex

between sodium dodecyl sulfate (SDS) and bovine serum albumin (BSA).[252] Two proteinaceous substrates that are commonly exposed to surfactants include human hair and wool. Protein-surfactant interactions have received increased study interest due to their growing biological uses, and numerous polymer surfactants have been developed for protein stabilization, transport, and detection.[253-255] In 1975, Jones[256] published the surfactant-to-protein binding curves for three surfactant concentration regions: the dilute region, where a small number of surfactant molecules first bind to particular high energetic protein binding sites; the intermediate region, where several surfactant molecules bind in a non-cooperative manner; and the concentrated region, where many surfactant molecules cooperatively bind to reach saturation. However, researchers have so far been unable to get a thorough grasp of protein-surfactant interactions, particularly a basic comprehension of complexation behavior and complex structure.[257] The difficulties in investigating protein-surfactant interactions include complex components and binding equilibria present in protein-surfactant mixture solutions, in addition to concentration-dependent binding domains. In addition to several kinds of protein-surfactant complexes, protein-surfactant mixture solutions also contain free protein molecules, free surfactant molecules, and surfactant micelles. It is important to keep in mind that if a protein is present in solution as a multimer, its dissociation could be dynamically accompanied by its attachment. Additionally, the concentrations of the protein and surfactant in the solution have an impact on the association-dissociation equilibrium between these components.[258, 259] To accurately and thoroughly investigate the protein-surfactant interactions therein, particularly the protein-surfactant complexation behavior, it is necessary to combine various analytical techniques and carefully consider variations in the compositions of protein-surfactant solutions for different assay formats due to the complex interaction behavior. When proteins interact with surfactants, hydrophobic and electrostatic forces can cause the proteins to fold, misfold, or refold. In humans, protein misfolding results in serious diseases such as amyotrophic lateral sclerosis, cancer, and Alzheimer's. Therefore, because of their role in biotherapy and medicines, protein-surfactant interactions continue to be a crucial field of study.[260, 261] For industrial use, a growing number of new surfactants with excellent performance and advantageous biological activities have been created. Examples of these include ionic liquid-based surfactants, gemini surfactants, and amino acid-based surfactants. The interactions between new surfactants and functional proteins that have been identified via research and practical applications need more thorough examination. Therefore, choosing the right methods and combining them is essential for examining protein structural alterations, describing new protein-surfactant complexes, and figuring out how they bind. Although the

interaction between proteins and surfactants has been extensively studied and has a significant impact on protein denaturation,[262, 263] the process is generally poorly understood. The majority of the literature describes how proteins interact with the anionic surfactant SDS. Among the proteins examined are trypsin,[264] papain,[265] bromelain,[266] lysozyme,[267] and bovine serum albumin (BSA).[268] Several other surfactants, such as SAILs, gemini surfactants, nonionic surfactants, conventional cationic surfactants, and biosurfactants, have been employed in previous years to clarify protein-surfactant interactions in addition to SDS.[269-273] Unlike traditional denaturants like urea and guanidine hydrochloride (GdnHCl), surfactants denature proteins differently. In contrast to other denaturants like urea and GdnHCl, which have weaker interactions with the protein backbone, surfactants have stronger interactions with proteins. The final state can vary depending on the denaturation technique; in the presence of chemical denaturants, it is usually a completely featureless random coil with significant conformational freedom, whereas the protein's thermally and acid-denatured states are more likely to be compact and retain residual secondary structure.[274] A variety of circumstances influences the interactions between proteins and surfactants. It has been seen that urea and GdnHCl denature proteins at molar concentration, whereas surfactants denature proteins at a millimolar concentration range. Depending on the pH of the solution, proteins can function as polyelectrolytes. A protein has "zero" total charge at its isoelectric pH. It bears a positive charge below the isoelectric pH and a negative one above, promoting interaction between species with opposing charges. Due to charge neutralization, interactions between SDS and proteins with a positive net charge induce the complex to precipitate. Adding too much SDS can usually dissolve the precipitated complex again, however, some protein-surfactant complexes are difficult to dissolve again.[267]

Since the majority of conventional surfactants are toxic and environmentally harmful, various ionic liquid-based surfactants and biosurfactants (e.g., sodium cholate, sodium deoxycholate, etc.) that are less toxic and environmentally friendly have become an interesting topic of research into their interactions with various proteins in recent years. Researchers have recently concentrated a great deal of attention on the manufacture of different ionic liquid-based surfactants and their usage in gene, protein, and drug delivery. Various ionic liquid-based micelles and vesicles have been designed in recent years, and their interaction with protein, DNA, and other biomolecules has gained popularity in the biomedical and biotechnological fields.[155, 275]

Protein-Nanoparticle Interaction:

The swift advancement of nanotechnology in recent decades has created several opportunities for the application of micro- and nanoscale materials in various fields of science, industry, and medicine. For this reason, it is essential to understand the mechanisms behind the interactions between nanoparticles (NPs) and biological objects to apply nanotechnologies safely across a range of sectors. As a result, it is critical to comprehend how NPs enter the body, tissues, and cells, where they go once, they are there, and the effects of their presence. Furthermore, we should address all of the intricate molecular facets of nano-bio interaction if we wish to comprehend the biological influence of NPs completely. One of the most important macromolecules found in living organisms is protein. Therefore, research on the interaction between the nanoparticle and protein molecules is crucial for the safe application of NPs in biomedicine.

Nanoparticles, due to their tiny size and high surface-to-volume ratio, have unique and distinct characteristics from their parent atoms/molecules or bulk materials.[276, 277] These traits are size-dependent and apply to a wide range of phenomena in disciplines such as energy, environment, electronics, and medicine.[278, 279] Nanoparticles are particularly interesting in medical science because they are small enough to interact directly with cellular machinery and efficiently reach previously inaccessible targets.[280] This result opens up the possibility of using nanoparticles for high-level targeted drug delivery and the development of extraordinarily sensitive biosensors.[281] The majority of these functions necessitate the attachment of certain biomolecules to the nanoparticle surface, resulting in unique hybrid nano-biomaterials with synergetic properties desired for probing biological processes crucial for diagnostics and cell function modification.[282] Proteins are the best macromolecules for this purpose since they support almost every element of biological activity and play an important role in nearly every biological process.[283]

Since nanoparticles have a very high surface-to-volume ratio and, therefore, very active surface chemistry, they are typically coated right away by protein molecules upon contact. The interaction of nanoparticles with protein molecules leads to the creation of a biological corona on the nanoparticle surface, which differs significantly from that adsorbed on a flat surface of the same bulk material under similar experimental conditions. The formation of a protein shell on the surface of nanomaterials upon exposure to biological fluids is known as the protein corona, and it is a crucial factor influencing both biocompatibility and nanotoxicity. Several

studies in the literature look at various aspects of this corona production, as well as its effects and applications, in particular nanoparticle–protein systems.[284-288] These can be broadly divided into three classes, which look at (i) how nanoparticles affect protein conformation,[289, 290] (ii) how protein molecules affect the stability and surface functionality of nanoparticles,[285, 291] and (iii) how nanoparticle-protein composites behave in relation to the biological medium.[292, 293] The first problem, where it has been demonstrated that the contact of the nanoparticles can alter the native conformation of the protein and consequently the functional impact (sometimes irreversibly), is the subject of the majority of the investigations. Such surface-driven alterations to the native protein structures have been demonstrated to be largely controlled by the structural and chemical characteristics of both proteins and nanoparticles as well as the strength of their interactions. Additionally, the presence of nanoparticles may regulate the enzymatic activity, protein transport, and interactions between protein molecules in a complex nanoparticle-protein system.[294, 295] However, it's also feasible that protein interactions could change the nanoparticles' colloidal stability and surface characteristics. Proteins may have an impact on several phase changes that occur in the nanoparticles, such as flocculation, glass transition, gelation, and crystallization, which can be utilized to create multifunctional materials.[296, 297] The protein corona has also been demonstrated to affect several additional characteristics of the nanoparticle system, including cellular uptake, accumulation, clearance, inflammation, and degradation.[298] The ability to alter the nanoparticles' biophysical characteristics, which frequently diverge greatly from those of the bare nanoparticles, is the most crucial feature of the nanoparticle-protein interaction.[299] The biological milieu gains a new biological identity as a result of protein adsorption on nanoparticles, and this biological identity, in turn, regulates the nanoparticles' biological response.[300] The exposure of appropriate/target biological entities to transmit avidity effects resulting from the interaction of the composites with the unique epitopes of the medium is made possible by the protein corona. The arrangement of protein molecules on the surface of the nanoparticle is also a critical factor influencing the complex's biological responsiveness at the cellular level.[301]

In recent years, the interaction of different biomolecules with graphene-based nanomaterials, particularly graphene oxide (GO) and reduced graphene oxide (RGO), has become a prominent and intriguing research field. The adsorption of protein molecules on the surface of GO/RGO often leads to the formation of a protein corona, and this protein corona has a large role in the biomedical application of these graphene-based materials. As a result, it is critical to accurately

assess the biological effects of graphene materials, which are known to be heavily influenced by the protein corona due to their critical role in defining cell-nanomaterial interactions, as well as subsequent cellular uptake and cytotoxicity. The protein corona could be made up of several layers of adsorbed proteins. This could include a firmly absorbed inner layer known as the "hard corona" and an outer layer called the "soft" layer made up of proteins that are dynamically exchanging with the main solvent and the nanomaterial. When it comes to graphene oxide (GO), it has been found that the protein corona lessens the cytotoxicity of the material by reducing its interaction with the cell membrane. These interactions have consequences for GO applications in drug delivery since effective drug loading and regulated release in biofluids are crucial factors that are impacted by GO's spontaneous interactions with the biofluids' proteins.

Several recent studies have demonstrated protein corona formation on the GO/RGO nanosheets. Coreas et al[302] recently reported how protein corona formation affects the biological function of reduced graphene oxide (RGO). In their studies, they have incorporated sodium cholate biosurfactant on the surface of RGO to see how this coating can change protein adsorption, also known as protein corona formation. They also looked at how protein corona formation affects cytotoxicity, ROS production, and disruption of mitochondrial function. It was shown by Chong et al.[303] that coating GO with bovine serum albumin (BSA) reduced its toxicity to A549 cells. When BSA bound to GO, they also saw a change in its secondary structure. Liu and coworkers[304] investigated the influence of ionic strength and pH in the formation and conformation of protein corona on GO nanosheets. The model protein HSA was used in their protein corona study under biological conditions. According to Lim et al.,[305] when human serum albumin (HSA) was adsorbed on GO, its maximum fluorescence emission wavelength was redshifted, indicating a change in the protein's conformation.

In several earlier studies, the primary focus was on how the surface characteristics of carbonaceous nanoparticles could affect protein adsorption.[306-308] According to various research, the adsorption of proteins on graphene-based nanomaterials, such as graphene, graphene oxide, and RGO, is primarily driven by hydrophobic and $\pi-\pi$ interactions.[309, 310] The reduction of GO to generate RGO reduces the oxygen-containing functional groups, which increases the probability of hydrophobic, and $\pi-\pi$ interactions with various low molecular weight organic adsorbates.[311, 312] However, it has been observed in multiple studies that the reduction of GO decreases the adsorbent power toward protein molecules.[313]

Amphiphilic Drugs:

Drug molecules are often amphiphilic, possessing both hydrophilic and hydrophobic residues. Numerous tranquilizers, antidepressants, antispasmolytic, anesthetics, and antihistaminic medicines contain amphiphilic drug molecules as their active medicinal ingredients.[314] They make up a large class of chemicals that include drugs like doxorubicin that are used to treat cancer. It is anticipated that their pharmacological action, as well as characteristics pertaining to toxicity and haemolysis, will be significantly influenced by their amphiphilic qualities. Amphiphilic characteristics influence a drug's solubility, bioavailability, integration into and impact on lipid membranes, transport characteristics, and rate of release from formulations.[315] Some research has been done on the self-assembling characteristics of various classes of amphiphilic drugs, but mostly in diluted aqueous solutions and using traditional experimental methods like conductivity, static light scattering, NMR spectroscopy (chemical shifts), and measurements of colliding properties.[314] This has shown connections between the characteristics of aggregates and the structure of medicinal molecules. Generally speaking, the hydrophobicity is mostly caused by aromatic ring configurations, which can reduce the molecules' flexibility in comparison to traditional surfactants that have an aliphatic chain as a hydrophobic tail group. This could affect their ability to self-assemble. In the current study, drug molecules are usually exclusively categorized according to their biological and pharmacological implications. However, in this instance, we tried to classify different types of drugs with colloidal behavior according to their medicinal implications, which are rare.

Amphiphilic drug classes include beta-blockers,[316] peptide[317] and non-peptide[318] antibiotics, tricyclic antidepressants,[319, 320] antihistamines,[321] anticholinergic,[322] local anesthetics (LA),[323, 324] non-steroidal anti-inflammatory drugs,[325] analgesics,[326] phenothiazine,[327, 328] benzodiazepine tranquilizers,[329] and anticancer drugs.[330] Most of these drug molecules contain one or more aromatic ring, while others are of peptide nature. Table 1 lists the CMC and aggregation number (N) of some commonly used non-peptide drugs.

Table 2. Micellar properties of some non-peptide amphiphilic drugs in water

Class	Drug	CMC (mM)	N	Ref.
Analgesics	Dextropropoxyphene	100	7	[331]
Antibiotics	Penicillin G	250	-	[331]
	Sodium fusidate	3.6	-	[332]
	Actinomycin D	0.1	-	[331]
Anticholinergics	Chlorphenoxamine.HCl	45	13	[331]
	Piperidolate.HCl	82	12	[331]
	Orphenadrine.HCl	96	7	[331]
	Penthianate methobromide	220	6	[321]
Antifungal polyenes	Nystatin	0.003	-	[333]
	Amphotericin B	0.0006	-	[334]
Antihistamines	Chlorcyclizine.HCl	127	3	[331]
	Diphenylpyraline.HCl	40	9	[331]
	Tripelennamine.HCl	120	3	[331]
	Thenyldiamine.HCl	100	3	[331]
Antihypertensives (With β-blocking Action)	Oxprenolol.HCl	170	3	[331]
	Propranolol.HCl	100	12	[331]
General anesthetics	Thiopental	7.0	-	[335]
Local anesthetics	Tetracaine.HCl	130	7	[336]
	Dibucaine.HCl	11	9	[337]
Phenothiazines	Promazine.HCl	36	11	[331]
	Thioridazine.HCl	5.9	8	[331]
	Trifluopromazine	4.5	-	[338]
	Chlorpromazine.HCl	19	11	[331]
Thioxanthene Tranquilizers	Flupenthioxl	8.5	19	[331]
Tricyclic antidepressants	Nortriptyline.HCl	23	4	[331]
	Clomipramine.HCl	22	6	[331]
	Imipramine.HCl	47	8	[331]
	Amitriptyline.HCl	36	7	[331]
	Desipramine.HCl	49	7	[331]

Amphiphilic drug-Surfactant interaction:

Over the past few decades, researchers have examined how drugs interact with surfactants.[339, 340] Many types of drugs are hydrophobic, which reduces their bioavailability. When surfactants are added to the drug's formulation, its bioavailability is increased.[341] Micelle production boosts the bioavailability of hydrophobic drugs by facilitating their solubilization.[342] Several methods enhance the solubility of drugs that are not very soluble in water, including the use of surfactants, the formation of drug salts, the application of polymers, and the creation of drug nanoparticles.[343] Among them, surfactants are useful components that can be utilized to stabilize drugs, facilitate their transport, and enhance their solubility in aqueous media.[344, 345] Using surfactants to solubilize medications efficiently minimizes the drug's interaction with inactivating agents, such as enzymes, and so lessens the adverse effects of the medication. Consequently, the amphiphile micelle aggregation is important for dissolving water-insoluble medications to decrease toxicity and boost bioavailability.[346] The micelle structure is concerned with the bio-membrane arrangement. As a result, every researcher is excited to see how drugs, bio-membranes, and other body fluid materials interact. As the study also looks at how drugs and surfactants interact when different kinds of solvents, electrolytes, salt, etc., are present.[347] Surfactants can also be utilized in drug delivery systems to improve the solubility and bioavailability of drug species and to slow down the rate at which drug molecules degrade by interacting with micelles through their interior or exterior surfaces.[348, 349] Surfactants protect medication molecules from the impacts of the biological environment by allowing them to remain in the human body for longer periods.[350, 351] Many medications can generate micelle-like structures in both aqueous and non-aqueous media. Often, a high concentration of amphiphilic drug is required to form a micelle-like structure, which can act as a self-carrier. But high dosages of these medications may create negative side effects by binding to various body regions. In some cases, this amphiphilic drug is not lipophilic enough to form micelle-like aggregates.[352] The most efficient technique for hydrophobic medications to lessen this impact is micellar solubilization with surfactants, which minimizes the drugs' interaction with enzymes such as inactivating species and, consequently, their adverse effects.

Graphene-based nanomaterials- Dye interaction:

The interaction of dye molecules with various graphene-based nanomaterials, especially graphene oxide, has become an intriguing field of research due to its enormous applications in various fields. GO has been extensively employed as the support to fabricate new dyes and

pigments because of the abundance of oxygen-containing functional groups (such as the hydroxyl and epoxy groups on sp^3 hybridized carbon on the basal plane and the carbonyl and carboxyl groups on sp^2 hybridized carbon at the corners of the sheets).[353] GO-based dyes and pigments are a current research frontier and exhibit considerable potential in a variety of sectors, including coatings, supercapacitors, photocatalysis, energy-storage materials, and more, due to their unique structures and capabilities. GO can be used as a quencher for a variety of fluorophore compounds due to its high quenching efficacy. The dye's fluorescence intensity can be altered by regulating the substance's interaction with GO. This feature has led to the usage of the GO–dye composite for a variety of applications, including the selective detection of biomolecules. Therefore, the low-cost preparation and optimization of GO-dye composites for use in GO-based sensors and other applications are important. One of the main areas of study in colloids has always been the control of dye aggregation. Many dye molecules tend to form dimers or aggregates because of a variety of intermolecular non-covalent interactions, including electrostatic interactions, hydrogen bonds, van der Waals interactions, and π–π stacking. The dye molecules can be organized in a variety of ways under various circumstances, giving dyes unique photochemical and photophysical characteristics. Sun et al.[354] used the Langmuir–Blodgett (LB) technique to create a simple way to produce GO-dye composite film. Congo red, methylene blue, and rhodamine B are examples of organic dye molecules that aggregate when exposed to GO sheets with a high specific surface area and many functional groups. Through π–π contact and electrostatic interaction between the negatively charged GO and cationic dye molecules, they can cause dye molecules to self-assemble and create a highly ordered GO-dye LB film with H-aggregates and/or J-aggregates. The LB films exhibit enormous promise for use in optical elements, biological sectors, and other areas. In addition to causing dye molecules to form different aggregates, GO can also lessen the degree of dye aggregation. When dyes are covalently functionalized with GO, their characteristics can be altered in addition to their degree of aggregation. The aromatic characteristics of dyes are disrupted when their organic chromophores are covalently bonded to GO, allowing for the modulation of their optoelectronic characteristics. Additionally, a large specific area of GO allows for the loading of additional organic dyes, which is crucial for enhancing optical limiting. An essential component in the creation of novel dyes is GO. This is due to GO's outstanding platform, which can offer a large number of reactive sites for organic functional dyes, significantly enhancing the functionality of conventional dyes. Due to their special qualities, the dyes as made have found extensive applications in numerous fields. Apart from the fields of photoelectric devices and dyeing, they are widely used in solar-thermal energy

storage. Anthraquinone dyes, polyaniline, and azo dyes are examples of organic pigments and dyes with conjugated structures that can absorb light energy and transform it into thermal energy.[355, 356] Since GO has functional groups that contain oxygen, it is frequently utilized as the starting material for acylation reactions that create graphene-based dyes. In addition to the conventional features of GO, researchers have noted that there are no clear toxic effects in vivo. The use of fluorescent dyes in bioimaging can be significantly increased if they are covalently functionalized onto GO. Blue-green spectral fluorescence can be produced by aminocoumarin dyes, which have high extinction coefficients and large Stokes shifts. By covalently functionalizing them with graphene oxide, they can form a new fluorescent nanohybrid (GO-NH-COUR).[357] GO may be the perfect nanoscale building block for graphene-based hybrid materials because of its distinct performance and chemical makeup. The inclusion of GO significantly impacts the characteristics of graphene-based hybrid materials. For instance, by controlling the degree of dye aggregation, GO can enhance the color performance of dyes. Through the mutual π interactions between GO and dyes, GO can also modify the optoelectronic characteristics of some dyes. As materials research advances, there will likely be more studies on graphene-based dyes, which have a wide range of potential applications in sensing, photoelectronic devices, and dyeing.

Scope and Objective of the work:

Amphiphilic-based soft nano systems (such as micelle, vesicle, reverse micelle, etc) are very useful nanocarriers for drugs, proteins, DNA, and other biomolecules due to their easily modulable structure. To apply these nano-systems as a carrier, a details analysis of the interaction of various biomolecules with such a nanosystem is required. Apart from that, protein-surfactant interactions also have a wide range of utility in the field of biotechnology, cosmetics, the food industry, pharmaceuticals, etc. Graphene-based nanomaterials such as graphene oxide (GO) and reduced graphene oxide (RGO) are also very good nanocarrier systems for biomolecules. Graphene oxide (GO) and reduced graphene oxide (RGO) have recently gained popularity in various applications, such as energy storage, drug delivery, water treatment, biomedicine etc.

Coumarin dyes (1,2-benzopyrone derivatives) are well-known laser dyes in the blue-green region. 7-aminocoumarins (with differently substituted 7-amino groups to the basic coumarin moiety) have a wide range of applications in diverse research areas, as they show quite remarkable excited-state properties. An important homologue of the 7-aminocumarin dyes is

coumarin-153 (C153), a dye that has been used most extensively among different 7-aminocoumarin dyes as a solvatochromic and solvation dynamics probe in various scientific disciplines. The structural rigidity for the 7-amino substituent of the C153 dye, which is a part of the rigid julolidinyl rings, in comparison to the flexible 7-amino coumarin, makes it a stronger fluorescence probe. Coumarin, including C153, are photoactive organic molecule used in the synthesis of dye-sensitized solar cells (DSSC), which convert light energy into electricity. C153 has been investigated for its potential in antibacterial and antifungal activities, as well as in the context of protein-ligand interaction. Coumarin, including C153, has been explored for its use in cancer photochemotherapy and other therapeutic applications.

This study focuses on the role of graphene oxide (GO) nanosheets and two cationic surfactants (CTAB and 16-4-16 gemini) on the photophysical and aggregation properties of the Coumarin-153 dye. Initially, the individual effect of GO nanoparticle and surfactants, and then the combined effect of GO nanoparticle and surfactant micelle on the photophysical and aggregation properties of C153 have been studied. GO was synthesized using the modified Hummer's method and characterized in our lab (refer to the section on the synthesis and characterization of GO). Several physicochemical techniques, including UV-vis spectroscopy, steady-state and time-resolved fluorometry, conductometry, tensiometry, DLS, zeta potential, and TEM, were used in this study. The modulation of the photophysical property of C153 (fluorescence off/on) in the presence of graphene oxide nanosheets and micelle systems will be helpful in various applications of C153, such as chemo sensor, bioimaging, photochemotherapy, laser application, etc. In the literature, a lot of studies present on the fluorescence quenching of various dye molecules by graphene oxide nanosheets. However, only a limited study about the combined effect of graphene oxide nanosheets and micelle systems on the photophysical properties of dye molecules is available in the literature.

Bile salts are naturally occurring amphiphiles (biosurfactants) synthesized in and also released by the liver, as well as stored in the gallbladder. They are compounds containing steroid ring structures, which comprise the hydroxyl group (2/3) with the carboxylic group holding a side chain. They contain both hydrophobic and hydrophilic faces where the b-oriented methyl groups are placed above the plane (convex surface) of the steroid skeleton, while the a-oriented hydroxyl groups lie below it (concave surface). The aggregation pattern of bile salt follows a two-step process; initially, dimeric primary aggregates are formed through the hydrophobic interaction between steroidal domains, and the increasing concentration of bile salt leads to the formation of larger secondary aggregates, formed primarily due to the hydrogen bonding

between hydroxyl and carboxyl groups of different dimeric bile salt units. They solubilize apolar material, in particular cholesterol, lipids, fatty acids, monoglycerides, and fat-soluble vitamins. As such, they play a fundamental role in digestion and gallstone formation. Apart from this, bile salts have played an important role in several steps of protein purification, such as chromatographic separation, selective solubilization of membranes, and reconstitution of proteins.

Cytochrome C is an iron-containing metalloprotein and has been structurally well characterized in both solution and crystalline states. It is a small, globular, water-soluble protein containing a long polypeptide of 104 amino acid residues. The biological respiratory chain depends on cytochrome C, which receives electrons from cytochrome C reductase and transfers them to cytochrome C oxidase. Cyt C activity is crucial for mitochondrial function and is also linked to several other processes, such as cell proliferation, apoptosis, cellular differentiation, and cell cycle regulation. Cyt C also plays a role in the start of apoptosis by aberrant cytoplasmic accumulation, which sets off signalling cascades that result in cell malfunction.

This study focuses on the structural alteration of Cyt C induced by two bile salts, namely sodium cholate (NaC) and sodium deoxycholate (NaDC), using various interfacial, spectroscopic, electrochemical, and morphological measurements. The role of the different hydrophobicities of the two bile salts on the stability and structural change of Cyt C was monitored. Since bile acids and cytochrome C play crucial roles in triggering and regulating cell apoptosis, this interaction study will be helpful in biological and biomedical fields.

Fenbufen, as a derivative of phenylalkanoic (propionic acid), is an orally non-steroidal drug. American Cyanamid introduced it under the trade name **Lederfen** in the 1980s. Fenbufen is available as a capsule or tablet sold under the brand names Cepal, Cinopal, Cybufen, Lederfen, and Reugast. It has been shown to possess analgesic, anti-inflammatory, and antipyretic activity. The mechanism of action of Fenbufen is to prevent the production of prostaglandins that can cause inflammation. Therefore, Fenbufen has been used to treat rheumatoid arthritis, ankylosing spondylitis, and inflammation in osteoarthritis, and it can also relieve symptoms in tendinitis, fibrositis, gout, and periarthritis of the shoulder successfully. Moreover, the fractures, sprains, and backaches can also be treated by Fenbufen. In addition, Fenbufen has an inhibitory effect on human dihydrofolate reductase. Fenbufen is provided with the advantage of a better curative effect than aspirin, lower toxicity than indomethacin, and small side effects on the intestine. Hence, Fenbufen is still widely used

in the field of anti-inflammation. Common side effects of Fenbufen are liver toxicity, nausea, vomiting, and rash. Less common side effects include nausea, vomiting, wheezing, breathlessness, gastrointestinal ulceration, or hemorrhage. To minimize this side effect, Fenbufen should be used with conjugation of various carriers, e.g., surfactant, polymer, etc.

This study presents a comparative analysis of solution phase aggregate formation of two cationic surfactants (CTAB and 16-4-16 gemini surfactants) with Fenbufen drug. Various types of super micellar aggregates were developed between CTAB and Fenbufen at the ideal concentration of Fenbufen. Several physicochemical techniques, including tensiometry, steady-state anisotropy, time-resolved fluorescence, and DLS, were used in this study to investigate the micellar aggregates formed by cationic surfactants and Fenbufen drug across various stoichiometric mole fractions. The morphology of various supermicelle aggregates was characterized by atomic force microscopy (AFM) and TEM measurements. Additionally, a DFT calculation was performed to understand the theoretical binding strength between the surfactants and the Fenbufen drug. This study will be helpful in the field of drug solubilization, distribution, and carriers, as well as minimizing drug toxicity. In the biomedical industry, drug delivery, nanotechnology, and other critical disciplines, supermicelle aggregates have a wide range of applications.

Vesicles are membrane-mimicking structures composed of spherical amphiphilic molecular bilayers (block copolymers, lipids, or surfactants) featuring an internal aqueous reservoir. Over the past few decades, phospholipid-based vesicles have garnered extensive research attention as drug and gene delivery vehicles due to their unique ability to solubilize both hydrophilic and hydrophobic compounds. However, despite their potential as effective drug carriers, phospholipids face challenges such as instability, susceptibility to hydrolysis, high cost, and a complex vesicle-forming process. Consequently, researchers are increasingly interested in developing vesicles without lipids by successfully utilizing various surfactant molecules instead. Nonetheless, most conventional surfactants are toxic and non-eco-friendly, resulting in vesicles formed from these surfactants that are unsuitable as carriers for drugs, proteins, or genes. In recent times, surface-active ionic liquids (SAILs) are a special class of surfactants possessing both surfactant and ionic liquid characteristics, are eco-friendly, and less toxic in nature. So, the SAIL-based vesicles will be the best alternative to conventional surfactant-based vesicles as protein, drug, and gene delivery vehicles. However, only a limited work is reported in the literature about the interaction of SAIL-based vesicles with biomolecules.

This study focuses on the interaction of a SAIL-AOT-based amphiphile (cationic-rich and anionic-rich, respectively) with a model protein HSA in the pre- and post-vesicular concentration at physiological conditions. Several physicochemical techniques, including tensiometry, UV-vis spectroscopy, steady-state and time-resolved fluorescence, isothermal titration calorimetry (ITC), DLS, zeta-potential, and TEM measurements, were performed to characterize the interaction. These types of studies will be very helpful for using vesicles as a nanocarrier system for various biomolecules.

Stem bromelain (BM), a proteolytic enzyme isolated from pineapple (ananus *cosmosus*) stem, belongs to the cysteine proteinase family. This protein belongs to the α + β protein class with 23% helical structure, containing five (5) tryptophan (Trp) units. Bromelain has various health benefits including sinus problems, including reducing inflammation and improving digestion. Bromelain also improves the condition of osteoarthritis and sometimes also impedes the growth of a tumour. Due to these several potential effects, bromelain shows an enormous possibility of research in the present times. In this connection, here we focus on the interaction of two graphene-based nanomaterials, namely graphene oxide (GO) and reduced graphene oxide (RGO), with the bromelain protein in a phosphate buffer medium at pH 7.4. The adsorption of BM on the GO/RGO nanosheets leads to the formation of a protein corona. Several experimental techniques, such as UV-vis spectroscopy, steady-state and time-resolved fluorescence, isothermal titration calorimetry, DLS, zeta potential, and TEM, were employed to understand the adsorption mechanism and characterize the protein corona formation. To use the nanoparticle as a nanocarrier system for BM protein in various therapeutic applications, this interaction study will be very helpful. However, only a limited study available in the literature about the interaction of BM proteins with nanoparticles.

References:

1. Hirst, L. S. *Fundamentals of soft matter science*. (CRC press, 2019).

2. Selinger, J. V. *Introduction to the theory of soft matter: from ideal gases to liquid crystals*. (Springer, 2016).

3. de Gennes, P. Soft matter (Nobel lecture). *Angew. Chemie Int. Ed. English* **31**, 842–845 (1992).

4. FERNANDEZ-NIEVES, A. & PUERTAS, A. M. FLUIDS, COLLOIDS AND SOFT MATERIALS: AN INTRODUCTION TO SOFT MATTER PHYSICS. (2016).

5. Hamley, I. W. & Castelletto, V. Biological soft materials. *Angew. Chemie Int. Ed.* **46**, 4442–4455 (2007).

6. Bisoyi, H. K., Urbas, A. M. & Li, Q. Soft Materials Driven by Photothermal Effect and Their Applications. *Adv. Opt. Mater.* **6**, 1–21 (2018).

7. Sorrenti, A., Illa, O. & Ortuño, R. M. Amphiphiles in aqueous solution: Well beyond a soap bubble. *Chem. Soc. Rev.* **42**, 8200–8219 (2013).

8. Sakamoto, K., Lochhead, R. Y., Maibach, H. I. & Yamashita, Y. *Cosmetic science and technology: theoretical principles and applications*. (Elsevier, 2017).

9. Kaczerewska, O., Martins, R., Figueiredo, J., Loureiro, S. & Tedim, J. Environmental behaviour and ecotoxicity of cationic surfactants towards marine organisms. *J. Hazard. Mater.* **392**, 122299 (2020).

10. Vyas, B., Pillai, S. A., Ray, D., Aswal, V. K., Wang, M. R., Chen, L. J., & Bahadur, P. Interactions of alkyltriphenyl phosphonium based ionic liquids with block copolymer microstructures: a multitechnique study. *J. Mol. Liq.* **300**, 112341 (2020).

11. Saha, A., Mal, A. & Ghosh, S. An elaborate investigation on the transition of rod-like micelle of cetyltrimethylammonium p-toluenesulfonate in presence of different additives. *J. Mol. Liq.* **309**, 113084 (2020).

12. Mondal, S., Pan, A., Patra, A., Mitra, R. K. & Ghosh, S. Ionic liquid mediated micelle to vesicle transition of a cationic gemini surfactant: a spectroscopic investigation. *Soft Matter* **14**, 4185–4193 (2018).

13. Hossain, K. M. Z., Calabrese, V., da Silva, M. A., Bryant, S. J., Schmitt, J., Scott, J. L., & Edler, K. J. Cationic surfactants as a non-covalent linker for oxidised cellulose nanofibrils and starch-based hydrogels. *Carbohydr. Polym.* **233**, 115816 (2020).

14. Ali, A., Farooq, U., Uzair, S. & Patel, R. Conductometric and tensiometric studies on the mixed micellar systems of surface-active ionic liquid and cationic surfactants in aqueous medium. *J. Mol. Liq.* **223**, 589–602 (2016).

15. Pal, N., Saxena, N. & Mandal, A. Synthesis, characterization, and physicochemical properties of a series of quaternary gemini surfactants with different spacer lengths. *Colloid Polym. Sci.* **295**, 2261–2277 (2017).

16. Das, S., Ghosh, S. & Das, B. Formation of mixed micelle in an aqueous mixture of a surface active ionic liquid and a conventional surfactant: experiment and modeling. *J. Chem. Eng. Data* **63**, 3784–3800 (2018).

17. Kumar, V., Pal, N., Jangir, A. K., Manyala, D. L., Varade, D., Mandal, A., & Kuperkar, K. Dynamic interfacial properties and tuning aqueous foamability stabilized by cationic surfactants in terms of their structural hydrophobicity, free drainage and bubble extent. *Colloids Surfaces A Physicochem. Eng. Asp.* **588**, 124362 (2020).

18. Ivanova, A. A., Cheremisin, A. N., Barifcani, A., Iglauer, S. & Phan, C. Molecular insights in the temperature effect on adsorption of cationic surfactants at liquid/liquid interfaces. *J. Mol. Liq.* **299**, 112104 (2020).

19. Kumar, K., Patial, B. S. & Chauhan, S. Conductivity and fluorescence studies on the micellization properties of sodium cholate and sodium deoxycholate in aqueous medium at different temperatures: Effect of selected amino acids. *J. Chem. Thermodyn.* **82**, 25–33 (2015).

20. Mondal, S. & Ghosh, S. Spectroscopic study on the interaction of curcumin with single chain and gemini surfactants. *Chem. Phys. Lett.* **762**, 138144 (2021).

21. Singh, V. & Tyagi, R. Physicochemical properties and effect of organic and inorganic electrolytes on surface properties of C 12 and C 16 alcohol-based bis-sulfosuccinate anionic gemini surfactants. *Colloid Polym. Sci.* **295**, 601–611 (2017).

22. Saha, P., Pyne, D.K., Ghosh, S., Banerjee, S., Das, S., Ghosh, S., Dutta, P. and Halder, A. Effect of an anionic surfactant (SDS) on the photoluminescence of graphene oxide (GO) in acidic and alkaline medium. *RSC Adv.* **8**, 584–595 (2018).

23. Bordes, R. & Holmberg, K. Amino acid-based surfactants–do they deserve more attention? *Adv. Colloid Interface Sci.* **222**, 79–91 (2015).

24. Hu, R., Tang, S., Mpelwa, M., Jin, L., Jiang, Z., Feng, S., & Zheng, Y. Study on the structure–activity relationship between the molecular structure of anionic Gemini surfactants and the rheological properties of their micelle solutions. *J. Dispers. Sci. Technol.* **43**, 490–500 (2022).

25. Patra, N., Ray, D., Aswal, V. K. & Ghosh, S. Exploring physicochemical interactions of different salts with sodium N-dodecanoyl sarcosinate in aqueous solution. *ACS omega* **3**, 9256–9266 (2018).

26. Patist, A., Bhagwat, S. S., Penfield, K. W., Aikens, P. & Shah, D. O. On the measurement of critical micelle concentrations of pure and technical-grade nonionic surfactants. *J. Surfactants Deterg.* **3**, 53–58 (2000).

27. Abe, M., Uchiyama, H., Yamaguchi, T., Suzuki, T., Ogino, K., Scamehorn, J. F., & Christian, S. D. Micelle formation of pure nonionic surfactants and their mixtures. *Langmuir* **8**, 2147–2151 (1992).

28. Pan, A., Mati, S. S., Naskar, B., Bhattacharya, S. C. & Moulik, S. P. Self-aggregation of MEGA-9 (N-nonanoyl-N-methyl-d-glucamine) in aqueous medium: physicochemistry of interfacial and solution behaviors with special reference to formation energetics and micelle microenvironment. *J. Phys. Chem. B* **117**, 7578–7592 (2013).

29. Inoue, T. & Yamakawa, H. Micelle formation of nonionic surfactants in a room temperature ionic liquid, 1-butyl-3-methylimidazolium tetrafluoroborate: surfactant chain length dependence of the critical micelle concentration. *J. Colloid Interface Sci.* **356**, 798–802 (2011).

30. Yoshimura, T., Ichinokawa, T., Kaji, M. & Esumi, K. Synthesis and surface-active properties of sulfobetaine-type zwitterionic gemini surfactants. *Colloids Surfaces A Physicochem. Eng. Asp.* **273**, 208–212 (2006).

31. Banik, R., Das, S., Ghosh, A. & Ghosh, S. Comparative studies on the aggregate formation of synthesized zwitterionic gemini and monomeric surfactants in the presence of the amphiphilic antipsychotic drug chlorpromazine hydrochloride in aqueous solution: an experimental and theoretical approach. *Soft Matter* **19**, 7995–8010 (2023).

32. Kroflič, A., Šarac, B. & Bešter-Rogač, M. Thermodynamic characterization of 3-[(3-cholamidopropyl)-dimethylammonium]-1-propanesulfonate (CHAPS) micellization using isothermal titration calorimetry: temperature, salt, and pH dependence. *Langmuir* **28**, 10363–10371 (2012).

33. Kent, J. A. *Riegel's handbook of industrial chemistry*. (Springer Science & Business Media, 2012).

34. Showell, M. *Handbook of detergents, part D: formulation*. (CRC Press, 2016).

35. Alberts, B., Johnson, A., Lewis, J., Raff, M., Roberts, K., & Walter, P. The shape and structure of proteins. in *Molecular Biology of the Cell. 4th edition* (Garland Science, 2002).

36. Maldonado-Valderrama, J., Wilde, P., Macierzanka, A. & Mackie, A. The role of bile salts in digestion. *Adv. Colloid Interface Sci.* **165**, 36–46 (2011).

37. Veldhuizen, E. J. A. & Haagsman, H. P. Role of pulmonary surfactant components in surface film formation and dynamics. *Biochim. Biophys. acta (bba)-biomembranes* **1467**, 255–270 (2000).

38. Menger, F. M., Keiper, J. S. & Azov, V. Gemini surfactants with acetylenic spacers. *Langmuir* **16**, 2062–2067 (2000).

39. Yoshimura, T. & Esumi, K. Synthesis and surface properties of anionic gemini surfactants with amide groups. *J. Colloid Interface Sci.* **276**, 231–238 (2004).

40. Lin, L.-H. & Lai, Y.-C. Synthesis and physicochemical properties of nonionic Gemini surfactants with a sulfonate spacer. *Colloids Surfaces A Physicochem. Eng. Asp.* **386**, 65–70 (2011).

41. Bunton, C. A., Robinson, L. B., Schaak, J. & Stam, M. F. Catalysis of nucleophilic substitutions by micelles of dicationic detergents. *J. Org. Chem.* **36**, 2346–2350 (1971).

42. Menger, F. M. & Keiper, J. S. Gemini surfactants. *Angew. Chemie Int. Ed.* **39**, 1906–1920 (2000).

43. Li, X., Washenberger, R. M., Scriven, L. E., Davis, H. T. & Hill, R. M. Phase behavior and microstructure of water/trisiloxane E6 and E10 polyoxyethylene surfactant/silicone oil systems. *Langmuir* **15**, 2278–2289 (1999).

44. Hill, R. M. *Silicone surfactants*. vol. 86 (CRC Press, 1999).

45. Sontake, A. R. & Wagh, S. M. The phase-out of perfluorooctane sulfonate (PFOS) and the global future of aqueous film forming foam (AFFF), innovations in fire fighting foam. *Fire Eng.* **39**, 19–23 (2014).

46. Porter, M. R. *Handbook of surfactants*. (Springer, 2013).

47. Renner, R. The long and the short of perfluorinated replacements. at (2006).

48. Hayes, R., Warr, G. G. & Atkin, R. Structure and nanostructure in ionic liquids. *Chem. Rev.* **115**, 6357–6426 (2015).

49. Gabriel, S. & Weiner, J. Ueber einige abkömmlinge des propylamins. *Berichte der Dtsch. Chem. Gesellschaft* **21**, 2669–2679 (1888).

50. Walden, P. Molecular weights and electrical conductivity of several fused salts. *Bull. Acad. Imper. Sci.(St. Petersburg)* **1800**, (1914).

51. Stepnowski, P. Application of chromatographic and electrophoretic methods for the analysis of imidazolium and pyridinium cations as used in ionic liquids. *Int. J. Mol. Sci.* **7**, 497–509 (2006).

52. Rogers, R. D. & Seddon, K. R. Ionic liquids--solvents of the future? *Science (80-.).* **302**, 792–793 (2003).

53. Shamshina, J. L., Barber, P. S. & Rogers, R. D. Ionic liquids in drug delivery. *Expert Opin. Drug Deliv.* **10**, 1367–1381 (2013).

54. Bica, K., Gärtner, P., Gritsch, P. J., Ressmann, A. K., Schröder, C., & Zirbs, R. Micellar catalysis in aqueous–ionic liquid systems. *Chem. Commun.* **48**, 5013–5015 (2012).

55. Docherty, K. M. & Kulpa Jr, C. F. Toxicity and antimicrobial activity of imidazolium and pyridinium ionic liquids. *Green Chem.* **7**, 185–189 (2005).

56. Srour, H., Rouault, H., Santini, C. C. & Chauvin, Y. A silver and water free metathesis reaction: a route to ionic liquids. *Green Chem.* **15**, 1341–1347 (2013).

57. Damilano, G., Kalebić, D., Binnemans, K. & Dehaen, W. One-pot synthesis of symmetric imidazolium ionic liquids N, N-disubstituted with long alkyl chains. *RSC Adv.* **10**, 21071–21081 (2020).

58. Kim, D. J., Oh, K. H. & Park, J. K. A general and direct synthesis of imidazolium ionic liquids using orthoesters. *Green Chem.* **16**, 4098–4101 (2014).

59. Baltazar, Q. Q., Chandawalla, J., Sawyer, K. & Anderson, J. L. Interfacial and micellar properties of imidazolium-based monocationic and dicationic ionic liquids. *Colloids Surfaces A Physicochem. Eng. Asp.* **302**, 150–156 (2007).

60. Dong, B., Zhao, X., Zheng, L., Zhang, J., Li, N., & Inoue, T. Aggregation behavior of long-chain imidazolium ionic liquids in aqueous solution: micellization and characterization of micelle microenvironment. *Colloids Surfaces A Physicochem. Eng. Asp.* **317**, 666–672 (2008).

61. Inoue, T., Ebina, H., Dong, B. & Zheng, L. Electrical conductivity study on micelle formation of long-chain imidazolium ionic liquids in aqueous solution. *J. Colloid Interface Sci.* **314**, 236–241 (2007).

62. Singh, T. & Kumar, A. Aggregation behavior of ionic liquids in aqueous solutions: effect of alkyl chain length, cations, and anions. *J. Phys. Chem. B* **111**, 7843–7851 (2007).

63. Wang, J., Wang, H., Zhang, S., Zhang, H. & Zhao, Y. Conductivities, volumes, fluorescence, and aggregation behavior of ionic liquids [C4mim][BF4] and [C n mim] Br (n= 4, 6, 8, 10, 12) in aqueous solutions. *J. Phys. Chem. B* **111**, 6181–6188 (2007).

64. Wang, H., Zhang, L., Wang, J., Li, Z. & Zhang, S. The first evidence for unilamellar vesicle formation of ionic liquids in aqueous solutions. *Chem. Commun.* **49**, 5222–5224 (2013).

65. McBain, J. W. Micellar formation of aqueous solution. *Trans. Faraday Soc* **9**, 99–112 (1913).

66. Schmid, R. Recent advances in the description of the structure of water, the hydrophobic effect, and the like-dissolves-like rule. *Monatshefte für Chemie/Chemical Mon.* **132**, 1295–1326 (2001).

67. Sheng, J. J. *Modern chemical enhanced oil recovery: theory and practice*. (Gulf Professional Publishing, 2010).

68. Ray, S. & Moulik, S. P. Dynamics and thermodynamics of aerosol OT-aided nonaqueous microemulsions. *Langmuir* **10**, 2511–2515 (1994).

69. Melo, E. P., Aires-Barros, M. R. & Cabral, J. M. S. Reverse micelles and protein biotechnology. (2001).

70. Chaurasiya, R. S. & Hebbar, H. U. Reverse micelles for nanoparticle synthesis and biomolecule separation. in *Nanoscience in Food and Agriculture 4* 181–211 (Springer, 2017).

71. Mukerjee, P. & Mysels, K. Critical micelle concentrations of aqueous surfactant systems, (1971).

72. Anacker, E. W. & Ghose, H. M. Counterions and micelle size. II. Light scattering by solutions of cetylpyridinium salts. *J. Am. Chem. Soc.* **90**, 3161–3166 (1968).

73. Hartley, G. S. & Donnan, F. G. Aqueous solutions of paraffin-chain salts: a study in micelle formation. (1936).

74. McBain, J. W. & Salmon, C. S. Colloidal Electrolytes. Soap solutions and their constitution. 2. *J. Am. Chem. Soc.* **42**, 426–460 (1920).

75. Shaw, D. J. & IT. *Introduction to colloid and surface chemistry*. vol. 123 (Butterworths London, 1970).

76. Menger, F. M. The structure of micelles. *Acc. Chem. Res.* **12**, 111–117 (1979).

77. Rothstein, J. P. & Mohammadigoushki, H. Complex flows of viscoelastic wormlike micelle solutions. *J. Nonnewton. Fluid Mech.* **285**, 104382 (2020).

78. Tchakalova, V., Oliveira, C. L. P. & Figueiredo Neto, A. M. New lyotropic complex fluid structured in sheets of ellipsoidal micelles solubilizing fragrance oils. *ACS omega* **8**, 29568–29584 (2023).

79. Harkins, W. D. & Mittelmann, R. X-ray investigations of the structure of colloidal electrolytes. IV. A new type of micelle formed by film penetration. *J. Colloid Sci.* **4**, 367–381 (1949).

80. Debye, P. & Anacker, E. W. Micelle shape from dissymmetry measurements. *J. Phys. Chem.* **55**, 644–655 (1951).

81. Philippoff, W. Micelles and X-rays. *J. Colloid Sci.* **5**, 169–191 (1950).

82. Walker, S. A., Kennedy, M. T. & Zasadzinski, J. A. Encapsulation of bilayer vesicles by self-assembly. *Nature* **387**, 61–64 (1997).

83. Israelachvili, J. N., Mitchell, D. J. & Ninham, B. W. Theory of self-assembly of hydrocarbon amphiphiles into micelles and bilayers. *J. Chem. Soc. Faraday Trans. 2 Mol. Chem. Phys.* **72**, 1525–1568 (1976).

84. Israelachvili, J. N. *Intermolecular and surface forces*. (Academic press, 2011).

85. Ghosh, S., Ray, G. B. & Mondal, S. Physicochemical investigation on the bulk and surface properties of the binary mixtures of N-methyl-N-dodecanoyl sodium glycinate (SDDS) and N-methyl-N-decanoyl glucamine (MEGA 10) in aqueous medium. *Fluid Phase Equilib.* **405**, 46–54 (2015).

86. Tanford, C. *The hydrophobic effect: formation of micelles and biological membranes 2d ed*. (J. Wiley., 1980).

87. Sutherland, E., Mercer, S. M., Everist, M. & Leaist, D. G. Diffusion in solutions of micelles. What does dynamic light scattering measure? *J. Chem. Eng. Data* **54**, 272–278 (2009).

88. Berclaz, N., Müller, M., Walde, P. & Luisi, P. L. Growth and transformation of vesicles studied by ferritin labeling and cryotransmission electron microscopy. *J. Phys. Chem. B* **105**, 1056–1064 (2001).

89. Pérez, L., Pinazo, A., Infante, M. R. & Pons, R. Investigation of the micellization process of single and gemini surfactants from arginine by SAXS, NMR self-diffusion, and light scattering. *J. Phys. Chem. B* **111**, 11379–11387 (2007).

90. Gustafsson, J., Nylander, T., Almgren, M. & Ljusberg-Wahren, H. Phase behavior and aggregate structure in aqueous mixtures of sodium cholate and glycerol monooleate. *J. Colloid Interface Sci.* **211**, 326–335 (1999).

91. Tavernier, S. M. F., Vonk, C. G. & Gijbels, R. Inverted micellar structure determination of zinc di-isohexadecyl zinc sulfonate in isododecane by small-angle X-ray scattering and vapor pressure lowering. *J. Colloid Interface Sci.* **81**, 341–353 (1981).

92. Hayashi, S. & Ikeda, S. Micelle size and shape of sodium dodecyl sulfate in concentrated sodium chloride solutions. *J. Phys. Chem.* **84**, 744–751 (1980).

93. Rafique, A. S., Khodaparast, S., Poulos, A. S., Sharratt, W. N., Robles, E. S., & Cabral, J. T. Micellar structure and transformations in sodium alkylbenzenesulfonate (NaLAS) aqueous solutions: effects of concentration, temperature, and salt. *Soft Matter* **16**, 7835–7844 (2020).

94. Varade, D., Joshi, T., Aswal, V. K., Goyal, P. S., Hassan, P. A., & Bahadur, P. Effect of salt on the micelles of cetyl pyridinium chloride. *Colloids Surfaces A Physicochem. Eng. Asp.* **259**, 95–101 (2005).

95. Hoffmann, H., Platz, G., Rehage, H. & Schorr, W. The influence of the salt concentration on the aggregation behavior of viscoelastic detergents. *Adv. Colloid Interface Sci.* **17**, 275–298 (1982).

96. Evans, H. C. 117. Alkyl sulphates. Part I. Critical micelle concentrations of the sodium salts. *J. Chem. Soc.* 579–586 (1956).

97. Scamehorn, J. F. Phenomena in mixed surfactant systems. (1986).

98. Némethy, G. & Scheraga, H. A. Structure of water and hydrophobic bonding in proteins. II. Model for the thermodynamic properties of aqueous solutions of hydrocarbons. *J. Chem. Phys.* **36**, 3401–3417 (1962).

99. Kavanau, J. L. Structure and functions of biological membranes. *Nature* **198**, 525–530 (1963).

100. Schick, M. J. *Nonionic surfactants: physical chemistry*. (CRC Press, 1987).

101. Hall, D. G. Thermodynamics of micelle formation. *Nonion. surfactants Phys. Chem. surfactant Sci. Ser.* **23**, 233–296 (1987).

102. Moroi, Y. *Micelles: theoretical and applied aspects*. (Springer Science & Business Media, 2013).

103. Dong, X., Wang, L., Wang, D., Li, C. & Jin, J. Layer-by-layer engineered Co-Al hydroxide nanosheets/graphene multilayer films as flexible electrode for supercapacitor. *Langmuir* **28**, 293–298 (2012).

104. Olofsson, G. & Loh, W. On the use of titration calorimetry to study the association of surfactants in aqueous solutions. at (2009).

105. Kresheck, G. C. Comparison of the Calorimetric and van't Hoff Enthalpy of Micelle Formation for a Nonionic Surfactant in H_2O and D_2O Solutions from 15 to 40° C. *J. Phys. Chem. B* **102**, 6596–6600 (1998).

106. Majhi, P. R. & Moulik, S. P. Microcalorimetric investigation of AOT self-association in oil and the state of pool water in water/oil microemulsions. *J. Phys. Chem. B* **103**, 5977–5983 (1999).

107. Moulik, S. P. & Mitra, D. Energetics of Micelle Formation: Non Agreement between the Enthalpy Change Measured by the Direct Method of Calorimetry and the Indirect Method of van't Hoff. in *Recent Trends In Surface And Colloid Science* 51–68 (World Scientific, 2012).

108. Hait, S. K., Majhi, P. R., Blume, A. & Moulik, S. P. A critical assessment of micellization of sodium dodecyl benzene sulfonate (SDBS) and its interaction with poly (vinyl pyrrolidone) and hydrophobically modified polymers, JR 400 and LM 200. *J. Phys. Chem. B* **107**, 3650–3658 (2003).

109. Chatterjee, A., Moulik, S. P., Sanyal, S. K., Mishra, B. K. & Puri, P. M. Thermodynamics of micelle formation of ionic surfactants: a critical assessment for sodium dodecyl sulfate, cetyl pyridinium chloride and dioctyl sulfosuccinate (Na salt) by microcalorimetric, conductometric, and tensiometric measurements. *J. Phys. Chem. B* **105**, 12823–12831 (2001).

110. Hill, T. L. *Thermodynamics of small systems*. (Courier Corporation, 1994).

111. Hall, D. G. Thermodynamics of solutions of interacting aggregates by methods similar to surface thermodynamics. Part 1.—General equations for multi-component systems. *J. Chem. Soc. Faraday Trans. 2 Mol. Chem. Phys.* **68**, 1439–1447 (1972).

112. Hall, D. G. Thermodynamics of solutions of interacting aggregates by methods similar to surface thermodynamics. Part 2.—Solutions of non-associating macromolecules. *J. Chem. Soc. Faraday Trans. 2 Mol. Chem. Phys.* **70**, 1526–1541 (1974).

113. Hall, D. G. Thermodynamics of solutions of ideal multi-component micelles. Part 1. *Trans. Faraday Soc.* **66**, 1351–1358 (1970).

114. Corkhill, J. M. & Goodman, J. F. The interaction of non-ionic surface-active agents with water. *Adv. Colloid Interface Sci.* **2**, 298–330 (1969).

115. Corkill, J. M. & Herrmann, K. W. Solution structure in concentrated non-ionic surfactant systems. *J. Phys. Chem.* **67**, 934–937 (1963).

116. Corkill, J. M., Goodman, J. F., Walker, T. & Wyer, J. The multiple equilibrium model of micelle formation. *Proc. R. Soc. London. A. Math. Phys. Sci.* **312**, 243–255 (1969).

117. Tanford, C. Theory of micelle formation in aqueous solutions. *J. Phys. Chem.* **78**, 2469–2479 (1974).

118. Nagarajan, R. & Ruckenstein, E. Critical micelle concentration: a transition point for micellar size distribution: a statistical thermodynamical approach. *J. Colloid Interface Sci.* **60**, 221–231 (1977).

119. Patel, R., Khan, A. B., Dohare, N., Maroof Ali, M. & Rajor, H. K. Mixed micellization and interfacial properties of ionic liquid-type imidazolium gemini surfactant with amphiphilic drug amitriptyline hydrochloride and its thermodynamics. *J. Surfactants Deterg.* **18**, 719–728 (2015).

120. Garcia, M. T., Ribosa, I., Sanchez Leal, J. & Comelles, F. Monomer-micelle equilibrium in the diffusion of surfactants in binary systems through collagen films. *J. Am. Oil Chem. Soc.* **69**, 25–29 (1992).

121. Kibbey, T. C. G. & Hayes, K. F. A multicomponent analysis of the sorption of polydisperse ethoxylated nonionic surfactants to aquifer materials: equilibrium sorption behavior. *Environ. Sci. Technol.* **31**, 1171–1177 (1997).

122. Noriyuki, M., Yasuko, N., Mariko, K., Shozo, M. & Hitoshi, S. Mechanism for the inducement of the intestinal absorption of poorly absorbed drugs by mixed micelles II. Effect of the incorporation of various lipids on the permeability of liposomal membranes. *Int. J. Pharm.* **4**, 281–290 (1980).

123. Aungst, B. J. & Phang, S. Metabolism of a neurotensin (8–13) analog by intestinal and nasal enzymes, and approaches to stabilize this peptide at these absorption sites. *Int. J. Pharm.* **117**, 95–100 (1995).

124. Dutta, R., Ghosh, S., Banerjee, P., Kundu, S. & Sarkar, N. Micelle-vesicle-micelle transition in aqueous solution of anionic surfactant and cationic imidazolium surfactants: Alteration of the location of different fluorophores. *J. Colloid Interface Sci.* **490**, 762–773 (2017).

125. Bergström, M. Thermodynamics of vesicle formation from a mixture of anionic and cationic surfactants. *Langmuir* **12**, 2454–2463 (1996).

126. Mal, A., Bag, S., Ghosh, S. & Moulik, S. P. Physicochemistry of CTAB-SDS interacted catanionic micelle-vesicle forming system: An extended exploration. *Colloids Surfaces A Physicochem. Eng. Asp.* **553**, 633–644 (2018).

127. Ogino, K. & Abe, M. *Mixed surfactant systems*. (CRC Press, 1992).

128. Azum, N., Rub, M. A. & Asiri, A. M. Bile salt–bile salt interaction in mixed monolayer and mixed micelle formation. *J. Chem. Thermodyn.* **128**, 406–414 (2019).

129. George, A., Vora, S., Dogra, A., Desai, H. & Bahadur, P. Mixed micelles of cationic surfactants and bile acid salts in aqueous media. *J. Surfactants Deterg.* **1**, 507–514 (1998).

130. Mahbub, S., Rana, S., Rub, M. A., Hoque, M. A., Kabir, S. E., & Asiri, A. M. Influence of alcohol/temperature on the interaction of sodium dodecyl sulfate with cetyltrimethylammonium bromide: Experimental and theoretical study. *J. Chem. Eng. Data* **64**, 4376–4389 (2019).

131. Parekh, P., Varade, D., Parikh, J. & Bahadur, P. Anionic–cationic mixed surfactant systems: micellar interaction of sodium dodecyl trioxyethylene sulfate with cationic gemini surfactants. *Colloids Surfaces A Physicochem. Eng. Asp.* **385**, 111–120 (2011).

132. Moulik, S. P., Haque, M. E., Jana, P. K. & Das, A. R. Micellar properties of cationic surfactants in pure and mixed states. *J. Phys. Chem.* **100**, 701–708 (1996).

133. Sharma, K. S., Rodgers, C., Palepu, R. M. & Rakshit, A. K. Studies of mixed surfactant solutions of cationic dimeric (gemini) surfactant with nonionic surfactant C12E6 in aqueous medium. *J. Colloid Interface Sci.* **268**, 482–488 (2003).

134. Ogino, K., Tsubaki, N. & Abe, M. Solution properties of mixed surfactant system (II): Electric properties of anionic-nonionic surfactants in aqueous solutions. *J. Colloid Interface Sci.* **98**, 78–83 (1984).

135. Mahajan, R. K., Kaur, N. & Bakshi, M. S. Cyclic voltammetry investigation of the mixed micelles of cationic surfactants with pluronic F68 and TritonX-100. *Colloids Surfaces A Physicochem. Eng. Asp.* **255**, 33–39 (2005).

136. Ćirin, D. M., Poša, M. M. & Krstonošić, V. S. Interactions between selected bile salts and Triton X-100 or sodium lauryl ether sulfate. *Chem. Cent. J.* **5**, 1–8 (2011).

137. Ghosh, S. & Chakraborty, T. Mixed micelle formation among anionic gemini surfactant (212) and its monomer (SDMA) with conventional surfactants ($C_{12}E_5$ and $C_{12}E_8$) in brine solution at pH 11. *J. Phys. Chem. B* **111**, 8080–8088 (2007).

138. Guo, L., Colby, R. H., Lin, M. Y. & Dado, G. P. Micellar structure changes in aqueous mixtures of nonionic surfactants. *J. Rheol. (N. Y. N. Y).* **45**, 1223–1243 (2001).

139. Thomas, H. G., Lomakin, A., Blankschtein, D. & Benedek, G. B. Growth of mixed nonionic micelles. *Langmuir* **13**, 209–218 (1997).

140. Qin, L. & Wang, X.-H. Surface adsorption and thermodynamic properties of mixed system of ionic liquid surfactants with cetyltrimethyl ammonium bromide. *RSC Adv.* **7**, 51426–51435 (2017).

141. Pal, A. & Punia, R. Mixed micellization behaviour of tri-substituted surface active ionic liquid and cationic surfactant in aqueous medium and salt solution: experimental and theoretical study. *J. Mol. Liq.* **296**, 111831 (2019).

142. Sharma, R., Mahajan, S. & Mahajan, R. K. Surface adsorption and mixed micelle formation of surface active ionic liquid in cationic surfactants: conductivity, surface tension, fluorescence and NMR studies. *Colloids Surfaces A Physicochem. Eng. Asp.* **427**, 62–75 (2013).

143. Tiwari, A. K. & Saha, S. K. Aggregation behaviour and thermodynamics of mixed micellization of gemini surfactants with a room temperature ionic liquid in water and water-organic solvent mixed media. *J. Chem. Thermodyn.* **60**, 29–40 (2013).

144. Vashishat, R., Sanan, R. & Mahajan, R. K. Bile salt-surface active ionic liquid mixtures: mixed micellization and solubilization of phenothiazine. *RSC Adv.* **5**, 72132–72141 (2015).

145. Wang, X., Wang, R., Zheng, Y., Sun, L., Yu, L., Jiao, J., & Wang, R. Interaction between zwitterionic surface activity ionic liquid and anionic surfactant: Na+-driven wormlike micelles. *J. Phys. Chem. B* **117**, 1886–1895 (2013).

146. Smirnova, N. A., Vanin, A. A., Safonova, E. A., Pukinsky, I. B., Anufrikov, Y. A., & Makarov, A. L. Self-assembly in aqueous solutions of imidazolium ionic liquids and their mixtures with an anionic surfactant. *J. Colloid Interface Sci.* **336**, 793–802 (2009).

147. Jafari-Chashmi, P. & Bagheri, A. The strong synergistic interaction between surface active ionic liquid and anionic surfactant in the mixed micelle using the spectrophotometric method. *J. Mol. Liq.* **269**, 816–823 (2018).

148. Li, N., Zhang, S., Ma, H. & Zheng, L. Role of solubilized water in micelles formed by Triton X-100 in 1-butyl-3-methylimidazolium ionic liquids. *Langmuir* **26**, 9315–9320 (2010).

149. Misono, T., Sakai, H., Sakai, K., Abe, M. & Inoue, T. Surface adsorption and aggregate formation of nonionic surfactants in a room temperature ionic liquid, 1-butyl-3-methylimidazolium hexafluorophosphate (bmimPF6). *J. Colloid Interface Sci.* **358**, 527–533 (2011).

150. Pathan, H., Patil, R., Ray, D., Aswal, V. K., Bahadur, P., & Tiwari, S. Structural changes in non-ionic surfactant micelles induced by ionic liquids and application thereof for improved solubilization of quercetin. *J. Mol. Liq.* **290**, 111235 (2019).

151. Misono, T., Okada, K., Sakai, K., Abe, M. & Sakai, H. Surface adsorption and micelle formation of polyoxyethylene-type nonionic surfactants in mixtures of water and hydrophilic imidazolium-type ionic liquid. *J. Oleo Sci.* **65**, 499–506 (2016).

152. Saha, U., Banerjee, A. & Das, B. Drug-surfactant comicellization: Propranolol hydrochloride-surface active ionic liquid systems in aqueous medium. *J. Mol. Liq.* **309**, 113164 (2020).

153. Farooq, U., Patel, R. & Ali, A. Interaction of a surface-active ionic liquid with an antidepressant drug: Micellization and spectroscopic studies. *J. Solution Chem.* **47**, 568–585 (2018).

154. Clint, J. H. Micellization of mixed nonionic surface active agents. *J. Chem. Soc. Faraday Trans. 1 Phys. Chem. Condens. Phases* **71**, 1327–1334 (1975).

155. Banerjee, C., Roy, A., Kundu, N., Banik, D. & Sarkar, N. A new strategy to prepare giant vesicles from surface active ionic liquids (SAILs): A study of protein dynamics in a crowded environment using a fluorescence correlation spectroscopic technique. *Phys. Chem. Chem. Phys.* **18**, 14520–14530 (2016).

156. Lasic, D. D., Weiner, N., Riaz, M. & Martin, F. Liposomes. in *Pharmaceutical Dosage Forms* 65–77 (CRC Press, 1998).

157. Rosa, M., Rosa Infante, M., Miguel, M. da G. & Lindman, B. Spontaneous formation of vesicles and dispersed cubic and hexagonal particles in amino acid-based catanionic surfactant systems. *Langmuir* **22**, 5588–5596 (2006).

158. Brito, R. O., Marques, E. F., Gomes, P., Falcao, S. & Söderman, O. Self-assembly in a catanionic mixture with an aminoacid-derived surfactant: From mixed micelles to spontaneous vesicles. *J. Phys. Chem. B* **110**, 18158–18165 (2006).

159. Coldren, B. A., Warriner, H., Van Zanten, R., Zasadzinski, J. A. & Sirota, E. B. Lamellar gels and spontaneous vesicles in catanionic surfactant mixtures. *Langmuir* **22**, 2465–2473 (2006).

160. Bramer, T., Göran, K., Edwards, K. & Edsman, K. Effects of pH and ionic strength on catanionic drug-surfactant mixtures used for prolonged release from gels. *J. Drug Deliv. Sci. Technol.* **17**, 285–291 (2007).

161. Engberts, J. B. F. N. & Kevelam, J. Formation and stability of micelles and vesicles. *Curr. Opin. Colloid Interface Sci.* **1**, 779–789 (1996).

162. Baillie, A. J., Florence, A. T., Hume, L. R., Muirhead, G. T. & Rogerson, A. The preparation and properties of niosomes—non-ionic surfactant vesicles. *J. Pharm. Pharmacol.* **37**, 863–868 (1985).

163. Khandare, J. N., Madhavi, G. & Tamhankar, B. M. Niosomes-novel drug delivery system. *East. Pharm.* **37**, 61 (1994).

164. Patel, P., Parashar, A. K., Kaurav, M., Yadav, K., Singh, D., Gupta, G. D., & Kurmi, B. D. Niosome: a vesicular drug delivery tool. in *Nanoparticles and Nanocarriers Based Pharmaceutical Preparations* 333–364 (Bentham Science Publishers, 2022).

165. Arumugam, K. Niosomes: A novel carrier drug delivery system. *J. Drug Deliv. Ther.* **11**, (2021).

166. Chandu, V. P., Arunachalam, A., Jeganath, S., Yamini, K., Tharangini, K., & Chaitanya, G. Niosomes: a novel drug delivery system. *Int. J. Nov. trends Pharm. Sci.* **2**, 25–31 (2012).

167. Liga, S., Paul, C., Moacă, E.-A. & Péter, F. Niosomes: Composition, formulation techniques, and recent progress as delivery systems in cancer therapy. *Pharmaceutics* **16**, 223 (2024).

168. Mehrarya, M., Gharehchelou, B., Haghighi Poodeh, S., Jamshidifar, E., Karimifard, S., Farasati Far, B., Akbarzadeh, I. and Seifalian, A. Niosomal formulation for antibacterial applications. *J. Drug Target.* **30**, 476–493 (2022).

169. Bianco, A., Kostarelos, K. & Prato, M. Applications of carbon nanotubes in drug delivery. *Curr. Opin. Chem. Biol.* **9**, 674–679 (2005).

170. Yang, K., Li, Y., Tan, X., Peng, R. & Liu, Z. Behavior and toxicity of graphene and its functionalized derivatives in biological systems. *Small* **9**, 1492–1503 (2013).

171. Feng, T., Ai, X., An, G., Yang, P. & Zhao, Y. Charge-convertible carbon dots for imaging-guided drug delivery with enhanced in vivo cancer therapeutic efficiency. *ACS Nano* **10**, 4410–4420 (2016).

172. Bao, H., Pan, Y., Ping, Y., Sahoo, N.G., Wu, T., Li, L., Li, J. and Gan, L.H. Chitosan-functionalized graphene oxide as a nanocarrier for drug and gene delivery. *Small* **7**, 1569–1578 (2011).

173. Song, Y., Luo, Y., Zhu, C., Li, H., Du, D., & Lin, Y. Recent advances in electrochemical biosensors based on graphene two-dimensional nanomaterials. *Biosens. Bioelectron.* **76**, 195–212 (2016).

174. Shi, H., Wei, J., Qiang, L., Chen, X. & Meng, X. Fluorescent carbon dots for bioimaging and biosensing applications. *J. Biomed. Nanotechnol.* **10**, 2677–2699 (2014).

175. Soikkeli, M., Kurppa, K., Kainlauri, M., Arpiainen, S., Paananen, A., Gunnarsson, D., Joensuu, J.J., Laaksonen, P., Prunnila, M., Linder, M.B. and Ahopelto, J. Graphene biosensor programming with genetically engineered fusion protein monolayers. *ACS Appl. Mater. Interfaces* **8**, 8257–8264 (2016).

176. Baek, S., Singh, R.K., Khanal, D., Patel, K.D., Lee, E.J., Leong, K.W., Chrzanowski, W. and Kim, H.W. Smart multifunctional drug delivery towards anticancer therapy harmonized in mesoporous nanoparticles. *Nanoscale* **7**, 14191–14216 (2015).

177. Kang, S., Lee, J., Ryu, S., Kwon, Y., Kim, K.H., Jeong, D.H., Paik, S.R. and Kim, B.S. Gold nanoparticle/graphene oxide hybrid sheets attached on mesenchymal stem cells for effective photothermal cancer therapy. *Chem. Mater.* **29**, 3461–3476 (2017).

178. Garcia-Alegria, E., Iliut, M., Stefanska, M., Silva, C., Heeg, S., Kimber, S.J., Kouskoff, V., Lacaud, G., Vijayaraghavan, A. and Batta, K. Graphene Oxide promotes embryonic stem cell differentiation to haematopoietic lineage. *Sci. Rep.* **6**, 25917 (2016).

179. Lin, J., Huang, Y. & Huang, P. Graphene-based nanomaterials in bioimaging. *Biomed. Appl. Funct. Nanomater.* 247–287 (2018).

180. Kim, J., Park, J., Kim, H., Singha, K. & Kim, W. J. Transfection and intracellular trafficking properties of carbon dot-gold nanoparticle molecular assembly conjugated with PEI-pDNA. *Biomaterials* **34**, 7168–7180 (2013).

181. Xu, M., Zhu, J., Wang, F., Xiong, Y., Wu, Y., Wang, Q., Weng, J., Zhang, Z., Chen, W. and Liu, S. Improved in vitro and in vivo biocompatibility of graphene oxide through surface modification: poly (acrylic acid)-functionalization is superior to PEGylation. *ACS Nano* **10**, 3267–3281 (2016).

182. Liu, J.H., Cao, L., LeCroy, G.E., Wang, P., Meziani, M.J., Dong, Y., Liu, Y., Luo, P.G. and Sun, Y.P. Carbon "quantum" dots for fluorescence labeling of cells. *ACS Appl. Mater. Interfaces* **7**, 19439–19445 (2015).

183. Tian, B., Wang, C., Zhang, S., Feng, L. & Liu, Z. Photothermally enhanced photodynamic therapy delivered by nano-graphene oxide. *ACS Nano* **5**, 7000–7009 (2011).

184. Du, D., Wang, K., Wen, Y., Li, Y. & Li, Y. Y. Photodynamic graphene quantum dot: reduction condition regulated photoactivity and size dependent efficacy. *ACS Appl. Mater. Interfaces* **8**, 3287–3294 (2016).

185. Ge, J., Lan, M., Zhou, B., Liu, W., Guo, L., Wang, H., Jia, Q., Niu, G., Huang, X., Zhou, H. and Meng, X. A graphene quantum dot photodynamic therapy agent with high singlet oxygen generation. *Nat. Commun.* **5**, 4596 (2014).

186. Hong, E. J., Choi, D. G. & Shim, M. S. Targeted and effective photodynamic therapy for cancer using functionalized nanomaterials. *Acta Pharm. Sin. B* **6**, 297–307 (2016).

187. Eivazzadeh-Keihan, R., Maleki, A., De La Guardia, M., Bani, M.S., Chenab, K.K., Pashazadeh-Panahi, P., Baradaran, B., Mokhtarzadeh, A. and Hamblin, M.R. Carbon based nanomaterials for tissue engineering of bone: Building new bone on small black scaffolds: A review. *J. Adv. Res.* **18**, 185–201 (2019).

188. Crisan, L., Crisan, B.V., Bran, S., Onisor, F., Armencea, G., Vacaras, S., Lucaciu, O.P., Mitre, I., Baciut, M., Baciut, G. and Dinu, C. Carbon-based nanomaterials as scaffolds in bone regeneration. *Part. Sci. Technol.* **38**, 912–921 (2020).

189. Arash, B., Wang, Q. & Varadan, V. K. Mechanical properties of carbon nanotube/polymer composites. *Sci. Rep.* **4**, 6479 (2014).

190. Wang, K., Shi, L., Linthicum, W., Man, K., He, X., Wen, Q., Rojanasakul, L.W., Rojanasakul, Y. and Yang, Y. Substrate stiffness-dependent carbon nanotube-induced lung fibrogenesis. *Nano Lett.* **19**, 5443–5451 (2019).

191. Zarrintaj, P., Zangene, E., Manouchehri, S., Amirabad, L.M., Baheiraei, N., Hadjighasem, M.R., Farokhi, M., Ganjali, M.R., Walker, B.W., Saeb, M.R. and Mozafari, M. Conductive biomaterials as nerve conduits: recent advances and future challenges. *Appl. Mater. Today* **20**, 100784 (2020).

192. Vatanpour, V., Karimi, H., Ghazanlou, S.I., Mansourpanah, Y., Ganjali, M.R., Badiei, A., Pourbashir, E. and Saeb, M.R. Anti-fouling polyethersulfone nanofiltration membranes aided by amine-functionalized boron nitride nanosheets with improved separation performance. *J. Environ. Chem. Eng.* **8**, 104454 (2020).

193. Das, M., Singh, R. P., Datir, S. R. & Jain, S. Intranuclear drug delivery and effective in vivo cancer therapy via Estradiol–PEG-appended multiwalled carbon nanotubes. *Mol. Pharm.* **10**, 3404–3416 (2013).

194. Panczyk, T., Wolski, P. & Lajtar, L. Coadsorption of doxorubicin and selected dyes on carbon nanotubes. theoretical investigation of potential application as a pH-controlled drug delivery system. *Langmuir* **32**, 4719–4728 (2016).

195. Park, J. S., Goo, N.-I. & Kim, D.-E. Mechanism of DNA adsorption and desorption on graphene oxide. *Langmuir* **30**, 12587–12595 (2014).

196. Wang, H., Sun, Y., Yi, J., Fu, J., Di, J., del Carmen Alonso, A., & Zhou, S. Fluorescent porous carbon nanocapsules for two-photon imaging, NIR/pH dual-responsive drug carrier, and photothermal therapy. *Biomaterials* **53**, 117–126 (2015).

197. Zhuang, W.R., Wang, Y., Cui, P.F., Xing, L., Lee, J., Kim, D., Jiang, H.L. and Oh, Y.K. Applications of π-π stacking interactions in the design of drug-delivery systems. *J. Control. release* **294**, 311–326 (2019).

198. Chang, X.-L., Yang, S.-T. & Xing, G. Molecular toxicity of nanomaterials. *J. Biomed. Nanotechnol.* **10**, 2828–2851 (2014).

199. Kotagiri, N. & Kim, J.-W. Stealth nanotubes: strategies of shielding carbon nanotubes to evade opsonization and improve biodistribution. *Int. J. Nanomedicine* **9**, 85–105 (2014).

200. Miao, W., Shim, G., Lee, S., Lee, S., Choe, Y. S., & Oh, Y. K. Safety and tumor tissue accumulation of pegylated graphene oxide nanosheets for co-delivery of anticancer drug and photosensitizer. *Biomaterials* **34**, 3402–3410 (2013).

201. Al-Jumaili, A., Alancherry, S., Bazaka, K. & Jacob, M. V. Review on the antimicrobial properties of carbon nanostructures. *Materials (Basel).* **10**, 1066 (2017).

202. Notarianni, M., Liu, J., Vernon, K. & Motta, N. Synthesis and applications of carbon nanomaterials for energy generation and storage. *Beilstein J. Nanotechnol.* **7**, 149–196 (2016).

203. Hou, J., Wan, B., Yang, Y., Ren, X. M., Guo, L. H., & Liu, J. F. Biodegradation of single-walled carbon nanotubes in macrophages through respiratory burst modulation. *Int. J. Mol. Sci.* **17**, 409 (2016).

204. Satalkar, P., Elger, B. S., Hunziker, P. & Shaw, D. Challenges of clinical translation in nanomedicine: A qualitative study. *Nanomedicine Nanotechnology, Biol. Med.* **12**, 893–900 (2016).

205. Jiang, W., Kim, B. Y. S., Rutka, J. T. & Chan, W. C. W. Advances and challenges of nanotechnology-based drug delivery systems. *Expert Opin. Drug Deliv.* **4**, 621–633 (2007).

206. Zhbanov, A. I., Pogorelov, E. G. & Chang, Y.-C. Van der Waals interaction between two crossed carbon nanotubes. *ACS Nano* **4**, 5937–5945 (2010).

207. Li, C. & Chou, T.-W. Elastic moduli of multi-walled carbon nanotubes and the effect of van der Waals forces. *Compos. Sci. Technol.* **63**, 1517–1524 (2003).

208. Niyogi, S., Hamon, M.A., Hu, H., Zhao, B., Bhowmik, P., Sen, R., Itkis, M.E. and Haddon, R.C. Chemistry of single-walled carbon nanotubes. *Acc. Chem. Res.* **35**, 1105–1113 (2002).

209. Star, A., Stoddart, J.F., Steuerman, D., Diehl, M., Boukai, A., Wong, E.W., Yang, X., Chung, S.W., Choi, H. and Heath, J.R. Preparation and properties of polymer-wrapped single-walled carbon nanotubes. *Angew. Chemie* **113**, 1771–1775 (2001).

210. Hwang, J. Y., Shin, U. S., Jang, W. C., Hyun, J. K., Wall, I. B., & Kim, H. W. Biofunctionalized carbon nanotubes in neural regeneration: a mini-review. *Nanoscale* **5**, 487–497 (2013).

211. Balasubramanian, K. & Burghard, M. Chemically functionalized carbon nanotubes. *small* **1**, 180–192 (2005).

212. Singh, R.K., Patel, K.D., Kim, J.J., Kim, T.H., Kim, J.H., Shin, U.S., Lee, E.J., Knowles, J.C. and Kim, H.W. Multifunctional hybrid nanocarrier: magnetic CNTs ensheathed with mesoporous silica for drug delivery and imaging system. *ACS Appl. Mater. Interfaces* **6**, 2201–2208 (2014).

213. Yang, W., Thordarson, P., Gooding, J. J., Ringer, S. P. & Braet, F. Carbon nanotubes for biological and biomedical applications. *Nanotechnology* **18**, 412001 (2007).

214. Lacerda, L., Raffa, S., Prato, M., Bianco, A. & Kostarelos, K. Cell-penetrating CNTs for delivery of therapeutics. *Nano Today* **2**, 38–43 (2007).

215. Tasis, D., Tagmatarchis, N., Bianco, A. & Prato, M. Chemistry of carbon nanotubes. *Chem. Rev.* **106**, 1105–1136 (2006).

216. Liu, Z., Robinson, J. T., Tabakman, S. M., Yang, K. & Dai, H. Carbon materials for drug delivery & cancer therapy. *Mater. today* **14**, 316–323 (2011).

217. Zhou, M., Zhai, Y. & Dong, S. Electrochemical sensing and biosensing platform based on chemically reduced graphene oxide. *Anal. Chem.* **81**, 5603–5613 (2009).

218. Dang, Q., Lu, S., Yu, S., Sun, P. & Yuan, Z. Silk fibroin/montmorillonite nanocomposites: effect of pH on the conformational transition and clay dispersion. *Biomacromolecules* **11**, 1796–1801 (2010).

219. Tang, L. A. L., Wang, J. & Loh, K. P. Graphene-based SELDI probe with ultrahigh extraction and sensitivity for DNA oligomer. *J. Am. Chem. Soc.* **132**, 10976–10977 (2010).

220. Liu, Z., Robinson, J. T., Sun, X. & Dai, H. PEGylated nanographene oxide for delivery of water-insoluble cancer drugs. *J. Am. Chem. Soc.* **130**, 10876–10877 (2008).

221. Horvath, L., Magrez, A., Burghard, M., Kern, K., Forró, L., & Schwaller, B. Evaluation of the toxicity of graphene derivatives on cells of the lung luminal surface. *Carbon N. Y.* **64**, 45–60 (2013).

222. Maiti, D., Tong, X., Mou, X. & Yang, K. Carbon-based nanomaterials for biomedical applications: a recent study. *Front. Pharmacol.* **9**, 1401 (2019).

223. McCallion, C., Burthem, J., Rees-Unwin, K., Golovanov, A. & Pluen, A. Graphene in therapeutics delivery: Problems, solutions and future opportunities. *Eur. J. Pharm. Biopharm.* **104**, 235–250 (2016).

224. Novoselov, K.S., Geim, A.K., Morozov, S.V., Jiang, D., Katsnelson, M.I., Grigorieva, I.V., Dubonos, S.V. and Firsov, A.A. Two-dimensional gas of massless Dirac fermions in graphene. *Nature* **438**, 197–200 (2005).

225. Novoselov, K.S., Geim, A.K., Morozov, S.V., Jiang, D.E., Zhang, Y., Dubonos, S.V., Grigorieva, I.V. and Firsov, A.A. Electric field effect in atomically thin carbon films. *Science (80-.).* **306**, 666–669 (2004).

226. Cushing, S. K., Li, M., Huang, F. & Wu, N. Origin of strong excitation wavelength dependent fluorescence of graphene oxide. *ACS Nano* **8**, 1002–1013 (2014).

227. Loh, K. P., Bao, Q., Eda, G. & Chhowalla, M. Graphene oxide as a chemically tunable platform for optical applications. *Nat. Chem.* **2**, 1015–1024 (2010).

228. Szabó, T., Berkesi, O., Forgó, P., Josepovits, K., Sanakis, Y., Petridis, D., & Dékány, I. Evolution of Surface Functional Groups in a Series of Progressively Oxidized Graphite Oxides. *Chem. Mater.* **18**, 2740–2749 (2006).

229. Dong, X., Wang, L., Wang, D., Li, C. & Jin, J. Layer-by-layer engineered Co–Al hydroxide nanosheets/graphene multilayer films as flexible electrode for supercapacitor. *Langmuir* **28**, 293–298 (2012).

230. Hu, R., Gou, H., Mo, Z., Wei, X. & Wang, Y. Highly selective detection of trace Cu2+ based on polyethyleneimine-reduced graphene oxide nanocomposite modified glassy carbon electrode. *Ionics (Kiel).* **21**, 3125–3133 (2015).

231. Sun, X., Liu, Z., Welsher, K., Robinson, J. T., Goodwin, A., Zaric, S., & Dai, H. Nano-graphene oxide for cellular imaging and drug delivery. *Nano Res.* **1**, 203–212 (2008).

232. Guo, C., Book-Newell, B. & Irudayaraj, J. Protein-directed reduction of graphene oxide and intracellular imaging. *Chem. Commun.* **47**, 12658–12660 (2011).

233. Wen, Y., Xing, F., He, S., Song, S., Wang, L., Long, Y., Li, D. and Fan, C. A graphene-based fluorescent nanoprobe for silver (I) ions detection by using graphene oxide and a silver-specific oligonucleotide. *Chem. Commun.* **46**, 2596–2598 (2010).

234. Wang, Z., Huang, P., Bhirde, A., Jin, A., Ma, Y., Niu, G., Neamati, N. and Chen, X. A nanoscale graphene oxide–peptide biosensor for real-time specific biomarker detection on the cell surface. *Chem. Commun.* **48**, 9768–9770 (2012).

235. Liu, Y., Yu, D., Zeng, C., Miao, Z. & Dai, L. Biocompatible graphene oxide-based glucose biosensors. *Langmuir* **26**, 6158–6160 (2010).

236. Gonçalves, G., Vila, M., Bdikin, I., de Andrés, A., Emami, N., Ferreira, R.A., Carlos, L.D., Grácio, J. and Marques, P.A. Breakdown into nanoscale of graphene oxide: confined hot spot atomic reduction and fragmentation. *Sci. Rep.* **4**, 6735 (2014).

237. Zhang, H., Peng, C., Yang, J., Lv, M., Liu, R., He, D., Fan, C. and Huang, Q. Uniform ultrasmall graphene oxide nanosheets with low cytotoxicity and high cellular uptake. *ACS Appl. Mater. Interfaces* **5**, 1761–1767 (2013).

238. Qu, L., Liu, Y., Baek, J. B. & Dai, L. Nitrogen-doped graphene as efficient metal-free electrocatalyst for oxygen reduction in fuel cells. *ACS Nano* **4**, 1321–1326 (2010).

239. Montes-Navajas, P., Asenjo, N. G., Santamaría, R., Menéndez, R., Corma, A., & García, H. Surface area measurement of graphene oxide in aqueous solutions. *Langmuir* **29**, 13443–13448 (2013).

240. Li, D., Müller, M. B., Gilje, S., Kaner, R. B. & Wallace, G. G. Processable aqueous dispersions of graphene nanosheets. *Nat. Nanotechnol.* **3**, 101–105 (2008).

241. Xie, M., Lei, H., Zhang, Y., Xu, Y., Shen, S., Ge, Y., Li, H. and Xie, J. Non-covalent modification of graphene oxide nanocomposites with chitosan/dextran and its application in drug delivery. *RSC Adv.* **6**, 9328–9337 (2016).

242. Zheng, M., Liu, S., Li, J., Qu, D., Zhao, H.F., Guan, X.G., Hu, X.L., Xie, Z.G., Jing, X.B. and Sun, Z.C. Integrating oxaliplatin with highly luminescent carbon dots: an unprecedented theranostic agent for personalized medicine. (2014).

243. Naraprawatphong, R., Chokradjaroen, C., Thiangtham, S., Yang, L. & Saito, N. Nanoscale advanced carbons as an anode for lithium-ion battery. *Mater. Today Adv.* **16**, 100290 (2022).

244. Gauthier, M. A. & Klok, H.-A. Peptide/protein–polymer conjugates: synthetic strategies and design concepts. *Chem. Commun.* 2591–2611 (2008).

245. Gromiha, M. M. *Protein bioinformatics: from sequence to function*. (academic press, 2011).

246. Maminov, A. Short-length peptides contact map prediction using Convolution Neural Networks. *Proc. Sci.* **429**, (2022).

247. Kerstens, S., Murray, B. S. & Dickinson, E. Microstructure of β-lactoglobulin-stabilized emulsions containing non-ionic surfactant and excess free protein: Influence of heating. *J. Colloid Interface Sci.* **296**, 332–341 (2006).

248. Berton, C., Genot, C. & Ropers, M.-H. Quantification of unadsorbed protein and surfactant emulsifiers in oil-in-water emulsions. *J. Colloid Interface Sci.* **354**, 739–748 (2011).

249. Shapiro, A. L., Viñuela, E. & Maizel Jr, J. V. Molecular weight estimation of polypeptide chains by electrophoresis in SDS-polyacrylamide gels. *Biochem. Biophys. Res. Commun.* **28**, 815–820 (1967).

250. Jiang, J., Jin, Y., Liang, X., Piatko, M., Campbell, S., Lo, S. K., & Liu, Y. Synergetic interfacial adsorption of protein and low-molecular-weight emulsifiers in aerated emulsions. *Food Hydrocoll.* **81**, 15–22 (2018).

251. Miller, R., Fainerman, V. B., Makievski, A. V., Krägel, J., Grigoriev, D. O., Kazakov, V. N., & Sinyachenko, O. V. Dynamics of protein and mixed protein/surfactant adsorption layers at the water/fluid interface. *Adv. Colloid Interface Sci.* **86**, 39–82 (2000).

252. Goddard, E. D. & Ananthapadmanabhan, K. P. Interactions of surfactants with polymers and proteins. (1993).

253. Sandanaraj, B. S., Vutukuri, D. R., Simard, J. M., Klaikherd, A., Hong, R., Rotello, V. M., & Thayumanavan, S. Noncovalent modification of chymotrypsin surface using an amphiphilic polymer scaffold: implications in modulating protein function. *J. Am. Chem. Soc.* **127**, 10693–10698 (2005).

254. Tokuda, K., Noda, M., Maruyama, T., Kotera, M. & Nishino, T. A low-fouling polymer surface prepared by controlled segregation of poly (ethylene oxide) and its functionalization with biomolecules. *Polym. J.* **47**, 328–333 (2015).

255. Matsumoto, A., Kataoka, K. & Miyahara, Y. New directions in the design of phenylboronate-functionalized polymers for diagnostic and therapeutic applications. *Polym. J.* **46**, 483–491 (2014).

256. Jones, M. N. A theoretical approach to the binding of amphipathic molecules to globular proteins. *Biochem. J.* **151**, 109–114 (1975).

257. Takeda, K. & Moriyama, Y. Comment on the misunderstanding of the BSA− SDS complex model: concern about publications of an impractical model. *J. Phys. Chem. B* **111**, 1244 (2007).

258. Nielsen, A. D., Borch, K. & Westh, P. Thermal Stability of Humicola i nsolens Cutinase in aqueous SDS. *J. Phys. Chem. B* **111**, 2941–2947 (2007).

259. Sun, Y., Oseliero Filho, P. L. & Oliveira, C. L. P. α-Lactalbumin and sodium dodecyl sulfate aggregates: Denaturation, complex formation and time stability. *Food Hydrocoll.* **62**, 10–20 (2017).

260. Khan, T. A., Mahler, H.-C. & Kishore, R. S. K. Key interactions of surfactants in therapeutic protein formulations: a review. *Eur. J. Pharm. Biopharm.* **97**, 60–67 (2015).

261. Lee, H. J., McAuley, A., Schilke, K. F. & McGuire, J. Molecular origins of surfactant-mediated stabilization of protein drugs. *Adv. Drug Deliv. Rev.* **63**, 1160–1171 (2011).

262. Sehgal, P. & Otzen, D. E. Thermodynamics of unfolding of an integral membrane protein in mixed micelles. *Protein Sci.* **15**, 890–899 (2006).

263. Otzen, D. E. Protein unfolding in detergents: effect of micelle structure, ionic strength, pH, and temperature. *Biophys. J.* **83**, 2219–2230 (2002).

264. Ghosh, S. & Banerjee, A. A multitechnique approach in protein/surfactant interaction study: physicochemical aspects of sodium dodecyl sulfate in the presence of trypsin in aqueous medium. *Biomacromolecules* **3**, 9–16 (2002).

265. Ghosh, S. Physicochemical and conformational studies of papain/sodium dodecyl sulfate system in aqueous medium. *Colloids Surfaces A Physicochem. Eng. Asp.* **264**, 6–16 (2005).

266. Bhattacharya, R. & Bhattacharyya, D. Resistance of bromelain to SDS binding. *Biochim. Biophys. Acta (BBA)-Proteins Proteomics* **1794**, 698–708 (2009).

267. Lad, M. D., Ledger, V. M., Briggs, B., Green, R. J. & Frazier, R. A. Analysis of the SDS− lysozyme binding isotherm. *Langmuir* **19**, 5098–5103 (2003).

268. Turro, N. J., Lei, X.-G., Ananthapadmanabhan, K. P. & Aronson, M. Spectroscopic probe analysis of protein-surfactant interactions: the BSA/SDS system. *Langmuir* **11**, 2525–2533 (1995).

269. Vashishat, R., Chabba, S. & Mahajan, R. K. Surface active ionic liquid induced conformational transition in aqueous medium of hemoglobin. *RSC Adv.* **7**, 13041–13052 (2017).

270. Wang, X., Liu, J., Sun, L., Yu, L., Jiao, J., & Wang, R. Interaction of bovine serum albumin with ester-functionalized anionic surface-active ionic liquids in aqueous solution: a detailed physicochemical and conformational study. *J. Phys. Chem. B* **116**, 12479–12488 (2012).

271. Wu, D., Xu, G., Sun, Y., Zhang, H., Mao, H., & Feng, Y. Interaction between proteins and cationic gemini surfactant. *Biomacromolecules* **8**, 708–712 (2007).

272. Nozaki, Y., Reynolds, J. A. & Tanford, C. The interaction of a cationic detergent with bovine serum albumin and other proteins. *J. Biol. Chem.* **249**, 4452–4459 (1974).

273. Mondal, S., Raposo, M. L., Prieto, G. & Ghosh, S. Interaction of myoglobin with cationic and nonionic surfactant in phosphate buffer media. *J. Chem. Eng. Data* **61**, 1221–1228 (2016).

274. Fersht, A. R. & Daggett, V. Protein folding and unfolding at atomic resolution. *Cell* **108**, 573–582 (2002).

275. Lépori, C. M., Correa, N. M., Silber, J. J., Falcone, R. D., Lopez-Lopez, M., & Moyá, M. L. Use of ionic liquids-like surfactants for the generation of unilamellar vesicles with potential applications in biomedicine. *Langmuir* **35**, 13332–13339 (2019).

276. Cao, G. *Nanostructures and nanomaterials: synthesis, properties and applications*. (World scientific, 2004).

277. Moriarty, P. Nanostructured materials. *Reports Prog. Phys.* **64**, 297 (2001).

278. De, M., Ghosh, P. S. & Rotello, V. M. Applications of nanoparticles in biology. *Adv. Mater.* **20**, 4225–4241 (2008).

279. Niemeyer, C. M. Nanoparticles, proteins, and nucleic acids: biotechnology meets materials science. *Angew. Chemie Int. Ed.* **40**, 4128–4158 (2001).

280. Jiang, W., Kim, B. Y. S., Rutka, J. T. & Chan, W. C. W. Nanoparticle-mediated cellular response is size-dependent. *Nat. Nanotechnol.* **3**, 145–150 (2008).

281. Phillips, R. L., Miranda, O. R., You, C., Rotello, V. M. & Bunz, U. H. F. Rapid and efficient identification of bacteria using gold-nanoparticle–poly (para-phenyleneethynylene) constructs. *Angew. Chemie Int. Ed.* **47**, 2590–2594 (2008).

282. Balazs, A. C., Emrick, T. & Russell, T. P. Nanoparticle polymer composites: where two small worlds meet. *Science (80-.).* **314**, 1107–1110 (2006).

283. Whitford, D. *Proteins: structure and function*. (John Wiley & Sons, 2013).

284. Casals, E., Pfaller, T., Duschl, A., Oostingh, G. J. & Puntes, V. Time evolution of the nanoparticle protein corona. *ACS Nano* **4**, 3623–3632 (2010).

285. Bharti, B., Meissner, J. & Findenegg, G. H. Aggregation of silica nanoparticles directed by adsorption of lysozyme. *Langmuir* **27**, 9823–9833 (2011).

286. Monopoli, M. P., Bombelli, F. B. & Dawson, K. A. Nanoparticle coronas take shape. *Nat. Nanotechnol.* **6**, 11–12 (2011).

287. Monopoli, M. P., Aberg, C., Salvati, A. & Dawson, K. A. Biomolecular coronas provide the biological identity of nanosized materials. *Nano-Enabled Med. Appl.* 205–229 (2020).

288. de Puig, H., Bosch, I., Carré-Camps, M. & Hamad-Schifferli, K. Effect of the protein corona on antibody–antigen binding in nanoparticle sandwich immunoassays. *Bioconjug. Chem.* **28**, 230–238 (2017).

289. Duan, Y., Liu, Y., Shen, W. & Zhong, W. Fluorescamine labeling for assessment of protein conformational change and binding affinity in protein–nanoparticle interaction. *Anal. Chem.* **89**, 12160–12167 (2017).

290. Dennison, J. M., Zupancic, J. M., Lin, W., Dwyer, J. H. & Murphy, C. J. Protein adsorption to charged gold nanospheres as a function of protein deformability. *Langmuir* **33**, 7751–7761 (2017).

291. Mann, S., Shenton, W., Li, M., Connolly, S. & Fitzmaurice, D. Biologically programmed nanoparticle assembly. *Adv. Mater.* **12**, 147–150 (2000).

292. Vertegel, A. A., Siegel, R. W. & Dordick, J. S. Silica nanoparticle size influences the structure and enzymatic activity of adsorbed lysozyme. *Langmuir* **20**, 6800–6807 (2004).

293. Bayraktar, H., Ghosh, P. S., Rotello, V. M. & Knapp, M. J. Disruption of protein–protein interactions using nanoparticles: inhibition of cytochrome c peroxidase. *Chem. Commun.* 1390–1392 (2006).

294. Gagner, J. E., Lopez, M. D., Dordick, J. S. & Siegel, R. W. Effect of gold nanoparticle morphology on adsorbed protein structure and function. *Biomaterials* **32**, 7241–7252 (2011).

295. Chen, Y.-W., Lee, C.-H., Wang, Y.-L., Li, T.-L. & Chang, H.-C. Nanodiamonds as nucleating agents for protein crystallization. *Langmuir* **33**, 6521–6527 (2017).

296. McMillan, R. A., Paavola, C. D., Howard, J., Chan, S. L., Zaluzec, N. J., & Trent, J. D. Ordered nanoparticle arrays formed on engineered chaperonin protein templates. *Nat. Mater.* **1**, 247–252 (2002).

297. Macfarlane, R. J., Lee, B., Jones, M. R., Harris, N., Schatz, G. C., & Mirkin, C. A. Nanoparticle superlattice engineering with DNA. in *Spherical Nucleic Acids* 539–553 (Jenny Stanford Publishing, 2020).

298. Monopoli, M. P., Walczyk, D., Campbell, A., Elia, G., Lynch, I., Baldelli Bombelli, F., & Dawson, K. A. Physical− chemical aspects of protein corona: relevance to in vitro and in vivo biological impacts of nanoparticles. *J. Am. Chem. Soc.* **133**, 2525–2534 (2011).

299. Walkey, C.D., Olsen, J.B., Song, F., Liu, R., Guo, H., Olsen, D.W.H., Cohen, Y., Emili, A. and Chan, W.C. Protein corona fingerprinting predicts the cellular interaction of gold and silver nanoparticles. *ACS Nano* **8**, 2439–2455 (2014).

300. Walczyk, D., Bombelli, F. B., Monopoli, M. P., Lynch, I. & Dawson, K. A. What the cell "sees" in bionanoscience. *J. Am. Chem. Soc.* **132**, 5761–5768 (2010).

301. Maiorano, G., Sabella, S., Sorce, B., Brunetti, V., Malvindi, M. A., Cingolani, R., & Pompa, P. P. Effects of cell culture media on the dynamic formation of protein− nanoparticle complexes and influence on the cellular response. *ACS Nano* **4**, 7481–7491 (2010).

302. Coreas, R., Castillo, C., Li, Z., Yan, D., Gao, Z., Chen, J., Bitounis, D., Parviz, D., Strano, M.S., Demokritou, P. and Zhong, W. Biological Impacts of Reduced Graphene Oxide Affected by Protein Corona Formation. *Chem. Res. Toxicol.* **35**, 1244–1256 (2022).

303. Chong, Y., Ge, C., Yang, Z., Garate, J.A., Gu, Z., Weber, J.K., Liu, J. and Zhou, R. Reduced Cytotoxicity of Graphene Nanosheets Mediated by Blood-Protein Coating. *ACS Nano* **9**, 5713–5724 (2015).

304. Liu, X., Yan, C. & Chen, K. L. Adsorption of Human Serum Albumin on Graphene Oxide: Implications for Protein Corona Formation and Conformation. *Environ. Sci. Technol.* **53**, 8631–8639 (2019).

305. Loh, K. P. & Lim, C. T. Molecular interactions of graphene oxide with human blood plasma proteins. *Nanoscale* **8**, 9425–9441 (2016).

306. Ge, C., Du, J., Zhao, L., Wang, L., Liu, Y., Li, D., Yang, Y., Zhou, R., Zhao, Y., Chai, Z. and Chen, C. Binding of blood proteins to carbon nanotubes reduces cytotoxicity. *Proc. Natl. Acad. Sci.* **108**, 16968–16973 (2011).

307. Wei, X.Q., Hao, L.Y., Shao, X.R., Zhang, Q., Jia, X.Q., Zhang, Z.R., Lin, Y.F. and Peng, Q. Insight into the interaction of graphene oxide with serum proteins and the impact of the degree of reduction and concentration. *ACS Appl. Mater. Interfaces* **7**, 13367–13374 (2015).

308. Gu, Z., Yang, Z., Wang, L., Zhou, H., Jimenez-Cruz, C. A., & Zhou, R. The role of basic residues in the adsorption of blood proteins onto the graphene surface. *Sci. Rep.* **5**, 10873 (2015).

309. Zhang, Y., Zhang, J., Huang, X., Zhou, X., Wu, H., & Guo, S. Assembly of graphene oxide–enzyme conjugates through hydrophobic interaction. *Small* **8**, 154–159 (2012).

310. Wang, F., Duan, L., Wang, F. & Chen, W. Environmental reduction of carbon nanomaterials affects their capabilities to accumulate aromatic compounds. *NanoImpact* **1**, 21–28 (2016).

311. Wang, F., Wang, F., Gao, G. & Chen, W. Transformation of graphene oxide by ferrous iron: Environmental implications. *Environ. Toxicol. Chem.* **34**, 1975–1982 (2015).

312. Tenzer, S., Docter, D., Kuharev, J., Musyanovych, A., Fetz, V., Hecht, R., Schlenk, F., Fischer, D., Kiouptsi, K., Reinhardt, C. and Landfester, K. Rapid formation of plasma protein corona critically affects nanoparticle pathophysiology. in *Nano-enabled medical applications* 251–278 (Jenny Stanford Publishing, 2020).

313. Mu, Q., Liu, W., Xing, Y., Zhou, H., Li, Z., Zhang, Y., Ji, L., Wang, F., Si, Z., Zhang, B. and Yan, B. Protein binding by functionalized multiwalled carbon nanotubes is governed by the surface chemistry of both parties and the nanotube diameter. *J. Phys. Chem. C* **112**, 3300–3307 (2008).

314. Attwood, D. The mode of association of amphiphilic drugs in aqueous solution. *Adv. Colloid Interface Sci.* **55**, 271–303 (1995).

315. Schreier, S., Malheiros, S. V. P. & de Paula, E. Surface active drugs: self-association and interaction with membranes and surfactants. Physicochemical and biological aspects. *Biochim. Biophys. Acta (BBA)-Biomembranes* **1508**, 210–234 (2000).

316. Ruso, J. M., Attwood, D., Rey, C., Taboada, P., Mosquera, V., & Sarmiento, F. Light scattering and NMR studies of the self-association of the amphiphilic molecule propranolol hydrochloride in aqueous electrolyte solutions. *J. Phys. Chem. B* **103**, 7092–7096 (1999).

317. Hwang, P. M. & Vogel, H. J. Structure-function relationships of antimicrobial peptides. *Biochem. Cell Biol.* **76**, 235–246 (1998).

318. Varela, L.M., Rega, C., Suarez-Filloy, M.J., Ruso, J.M., Prieto, G., Attwood, D., Sarmiento, F. and Mosquera, V. Self-association of penicillin V in aqueous solution. *Langmuir* **15**, 6285–6290 (1999).

319. Sarmiento, F., Lopez-Fontan, J. L., Prieto, G., Mosquera, V. & Attwood, D. Mixed micelles of structurally related antidepressant drugs. *Colloid Polym. Sci.* **275**, 1144–1147 (1997).

320. Atherton, A. D. & Barry, B. W. Photon correlation spectroscopy of surface active cationic drugs. *J. Pharm. Pharmacol.* **37**, 854–862 (1985).

321. Causon, D., Gettins, J., Gormally, J., Greenwood, R., Natarajan, N., & Wyn-Jones, E. Ultrasonic relaxations associated with aggregation in drugs. *J. Chem. Soc. Faraday Trans. 2 Mol. Chem. Phys.* **77**, 143–151 (1981).

322. YOKOYAMA, S., FUJINO, Y., KAWAMOTO, Y., KANEKO, A. & FUJIE, T. Micellization of an aqueous solution of piperidolate hydrochloride in the presence of acetylcholine chloride. *Chem. Pharm. Bull.* **42**, 1351–1353 (1994).

323. Fernández, M. S. & Calderón, E. Formation of micelles and membrane action of the local anesthetic tetracaine hydrochloride. *Biochim. Biophys. Acta (BBA)-Biomembranes* **597**, 83–91 (1980).

324. Wakita, M., Kuroda, Y., Fujiwara, Y. & Nakagawa, T. Conformations of dibucaine and tetracaine in small unilamellar phosphatidylcholine vesicles as studied by nuclear Overhauser effects in 1H nuclear magnetic resonance spectroscopy. *Chem. Phys. Lipids* **62**, 45–54 (1992).

325. Rades, T. & Müller-Goymann, C. C. Investigations on the micellisation behaviour of fenoprofen sodium. *Int. J. Pharm.* **159**, 215–222 (1997).

326. Attwood, D. & Tolley, J. A. Self-association of analgesics in aqueous solution: association models for codeine, oxycodone, ethylmorphine and pethidine. *J. Pharm. Pharmacol.* **32**, 761–765 (1980).

327. Wan-Bahdi, W., Mwakibete, H., Bloor, D. M., Palepu, R. & Wyn-Jones, E. Emf and ultrasonic relaxation measurements of premicellar and micellar aggregation in the drug promethazine hydrochloride. *J. Phys. Chem.* **96**, 918–925 (1992).

328. Perez-Villar, V., Vazquez-Iglesias, M. E. & De Geyer, A. Small-angle neutron scattering studies of chlorpromazine micelles in aqueous solutions. *J. Phys. Chem.* **97**, 5149–5154 (1993).

329. Attwood, D., Blundell, R., Mosquera, V. & Garcia, M. Association and surface properties of amphiphilic benzodiazepine and benzothiazepine drugs in aqueous solution. *J. Colloid Interface Sci.* **161**, 19–23 (1993).

330. King, S. P., Basista, A. M. & Torosian, G. Self-association and solubility behaviors of a novel anticancer agent, brequinar sodium. *J. Pharm. Sci.* **78**, 95–100 (1989).

331. Attwood, D. *Surfactant systems: their chemistry, pharmacy and biology*. (Springer Science & Business Media, 2012).

332. Carey, M. C. & Small, D. M. Solution properties of taurine and glycine conjugates of fusidic acid and its derivatives. *Biochim. Biophys. Acta (BBA)-Lipids Lipid Metab.* **306**, 51–57 (1973).

333. Matsuki, H., Ichikawa, R., Kaneshina, S., Kamaya, H. & Ueda, I. Differential scanning calorimetric study on the Krafft phenomenon of local anesthetics. *J. Colloid Interface Sci.* **181**, 362–369 (1996).

334. Dangi, J. S., Vyas, S. P. & Dixit, V. K. Effect of various lipid-bile salt mixed micelles on the intestinal absorption of amphotericin-B in rat. *Drug Dev. Ind. Pharm.* **24**, 631–635 (1998).

335. Seelig, A., Gottschlich, R. & Devant, R. M. A method to determine the ability of drugs to diffuse through the blood-brain barrier. *Proc. Natl. Acad. Sci.* **91**, 68–72 (1994).

336. Matsuki, H., Hashimoto, S., Kaneshina, S. & Yamanaka, M. Surface adsorption and volume behavior of local anesthetics. *Langmuir* **10**, 1882–1887 (1994).

337. Attwood, D. & Fletcher, P. Self-association of local anaesthetic drugs in aqueous solution. *J. Pharm. Pharmacol.* **38**, 494–498 (1986).

338. Atherton, A. D. & Barry, B. W. Micellar properties of phenothiazine drugs: a laser light scattering study. *J. Colloid Interface Sci.* **106**, 479–489 (1985).

339. Aktar, S., Robel Molla, M., Mahbub, S., Rub, M. A., Hoque, M. A., & Islam, D. S. Effect of temperature and salt/alcohol on the interaction of tetradecyltrimethylammonium bromide/Triton X-100 with moxifloxacin hydrochloride: A multitechnique approach. *J. Dispers. Sci. Technol.* **40**, 574–586 (2019).

340. Rub, M. A. & Naqvi, A. Z. Mixed micelle formation between amphiphilic drug amitriptyline hydrochloride and surfactants (conventional and gemini) at 293.15−308.15 K. *J. Phys. Chem. B* **114**, 6354–6364 (2010).

341. Hoque, M.A., Rahman, M.M., Mahbub, S., Hossain, M., Khan, M.A., Amin, M.R., Alqahtani, A.S., Ahmed, M.Z., Alqahtani, M.S. and Almarfadi, O.M. Spectroscopic and cloud point studies of the interaction and thermodynamics of ciprofloxacin hydrochloride+ surfactants mixture in different solvents: effect of temperature and composition. *Korean J. Chem. Eng.* **38**, 1487–1498 (2021).

342. Abdul Rub, M. & Kumar, D. Micellization behavior of antidepressant imipramine hydrochloride drug and hydrotrope (sodium tosylate) mixtures at different compositions and temperatures in different media. *J. Chem. Eng. Data* **65**, 2659–2672 (2020).

343. Deshpande, T. M., Shi, H., Pietryka, J., Hoag, S. W. & Medek, A. Investigation of polymer/surfactant interactions and their impact on itraconazole solubility and precipitation kinetics for developing spray-dried amorphous solid dispersions. *Mol. Pharm.* **15**, 962–974 (2018).

344. Lalthlengliani, J., Gurung, J. & Pulikkal, A. K. Solubilization of aqueous-insoluble phenothiazine drug in TX-100 micellar solution and interactions of cationic/anionic surfactants with phenothiazine–TX-100 system. *J. Mol. Liq.* **354**, 118823 (2022).

345. Rub, M. A., Pulikkal, A. K., Azum, N. & Asiri, A. M. The assembly of amitriptyline hydrochloride+ triton X-45 (non-ionic surfactant) mixtures: Effects of simple salt and urea. *J. Mol. Liq.* **356**, 118997 (2022).

346. Pathania, L. & Chauhan, S. Aggregation and interactional behavior of cationic surfactants in the presence of cephalosporin drug: A thermo-acoustic and spectroscopic approach. *J. Mol. Liq.* **299**, 112210 (2020).

347. Mahbub, S., Shahriar, I., Iqfath, M., Hoque, M.A., Halim, M.A., Khan, M.A., Rub, M.A. and Asiri, A.M. Influence of alcohols/electrolytes on the interaction of reactive red dye with surfactant and removal of dye from solutions. *J. Environ. Chem. Eng.* **7**, 103364 (2019).

348. Fayyaz, S., Ali, S., Khalid, N., Shah, A. & Ullah, F. One pot synthesis and properties of cationic surfactants: N-alkyl-3-methylpyridinium bromide. *J. Surfactants Deterg.* **19**, 841–848 (2016).

349. Farías, T., de Ménorval, L.-C., Zajac, J. & Rivera, A. Solubilization of drugs by cationic surfactants micelles: Conductivity and 1H NMR experiments. *Colloids Surfaces A Physicochem. Eng. Asp.* **345**, 51–57 (2009).

350. Akhter, K., Ullah, K., Talat, R., Haider, A., Khalid, N., Ullah, F., & Ali, S. Synthesis and characterization of cationic surfactants and their interactions with drug and metal complexes. *Heliyon* **5**, (2019).

351. Itoo, F. A., Mir, J. M., Malik, N. A. & Ali, A. Density functional aspects and thermodynamic evaluation of sodium dodecyl sulphate in aqueous tartrazine. *J. King Saud Univ.* **32**, 2505–2512 (2020).

352. Krishnadas, A., Rubinstein, I. & Önyüksel, H. Sterically stabilized phospholipid mixed micelles: in vitro evaluation as a novel carrier for water-insoluble drugs. *Pharm. Res.* **20**, 297–302 (2003).

353. Zu, Y., He, C., Liu, D. & Chen, L. Synthesis of hybrid structures based on metal phthalocyanines/graphene oxide towards nonlinear optical applications. *Dyes. Pigments.* **173**, 107841 (2020).

354. Sun, P., Xu, K., Guang, S. & Xu, H. Monodisperse functionalized GO for water detection in wide range through synergistic enhancement effect. *Dyes. Pigments.* **185**, 108909 (2021).

355. Hu, D., Zhang, J., Gao, G., Sheng, Z., Cui, H., & Cai, L. Indocyanine green-loaded polydopamine-reduced graphene oxide nanocomposites with amplifying photoacoustic and photothermal effects for cancer theranostics. *Theranostics* **6**, 1043 (2016).

356. Tang, B., Wang, L., Xu, Y., Xiu, J. & Zhang, S. Hexadecanol/phase change polyurethane composite as form-stable phase change material for thermal energy storage. *Sol. Energy Mater. Sol. Cells* **144**, 1–6 (2016).

357. Liu, X., Guo, Y., Wang, D., Yang, X., Liu, W., & Qin, W. Graphene oxide functionalization with aminocoumarin nanosheet fluorescent dye: Preparation, electrochemistry, spectroscopy and imaging in the living cells. *Dyes. Pigments.* **113**, 327–335 (2015).

Chapter-I

Exploration of the impact of graphene oxide, acetylenic Gemini, and CTAT on the photophysical and aggregation properties of dipolar coumarin-153

Exploration of the impact of graphene oxide, acetylenic Gemini, and CTAT on the photophysical and aggregation properties of dipolar coumarin-153

Abstract:

Advanced spectroscopy techniques were used to investigate the interaction of laser dye coumarin 153 (C153) with graphene oxide (GO) nanoparticles. GO was synthesized using a modified Hummer process and characterized by UV-vis, Raman laser spectroscopy, FTIR-ATR spectroscopy, FESEM, HR-TEM, and XRD methods. Because of their high contact via stacking and hydrophobic interactions, two aqueous solutions of GO and C153 were mixed to generate GO@C153 composites. In this instance, GO functions as an excellent fluorescence quencher for C153 molecules, causing them to aggregate in an H-type configuration. The Stern-Volmer equation and time-dependent fluorescence experiments were used to investigate the mechanism of fluorescence quenching. According to the findings, both static and dynamic quenching processes are responsible for the decrease in fluorescence intensity. Surface tensiometry, conductometry, UV-vis absorption spectroscopy, steady-state fluorescence measurements, DLS, and time-dependent fluorescence spectroscopy were used to investigate the effect of surfactants (both cetyltrimethylammonium p-toluenesulfonate (CTAT) and synthesized N, N'-dihexadecyl-N, N, N', N'-tetramethyl-N, N'-but-2-ynediyl-di-ammonium chloride (16-4-16) on dye aggregation and photophysical properties. Surfactants alter the microenvironment of the C153 dye, causing spectrum shifting and increased quantum yield, resulting in a rapid increase in fluorescence intensity in the micellar medium. The luminous intramolecular charge transfer (ICT) state of C153 has been observed to stabilize in a micellar medium rather than an aqueous one. Finally, we investigated the photophysical behaviour of the GO-C153-micelle ternary system and noticed that the quenched and blue-shifted (H-type aggregation) fluorescence spectra of C153 (in the presence of GO) began to intensify again and returned to their original peak position in the presence of a micellar medium. The primary use of such research is to create a powerful fluorescence sensor that is both inexpensive and abundant, and this ternary system (GO-C153-micelle) analytical approach can also be utilized to detect the beginning of micelle creation. In wastewater treatment analysis, the GO-C153-Surfactants ternary system concept can be employed to replenish the adsorbent (in this case, GO) by enabling dye molecules to escape the adsorbent and enter the micellar medium.

1. Introduction

In recent years, graphene and its derivatives have emerged as one of the most important and hard fields of research in nanomaterial science. Graphene is a two-dimensional, single-atom-thick nanomaterial composed of sp2-hybridized carbon atoms arranged in a hexagonal honeycomb sheet structure. The first discovery of graphene occurred in 2004, and it has since become a very important subject of research due to its exceptional mechanical and optical properties,[1-6] as well as its various biological[7] and technological implications.[8-10] Because of their wide range of applications, researchers are working hard to discover an economical and effective technique to produce and use graphene derivatives and related materials. Graphene oxide (GO) is one of the most important graphene derivatives, as it is inexpensive and abundant, and it is produced by the intense oxidation of graphite powder. Due to oxidation, graphene oxide has a greater band gap than graphene, which has a zero-band gap. Because of the huge band gap in graphene oxide, it exhibits exceptional optical properties,[11-18] which are somewhat limited in graphene due to its zero-band gap. At the same time, the presence of various oxygen-containing groups (such as hydroxyl, epoxy, and carboxyl) on the surface and edges of graphene oxide sheets[19,20] allows for easy functionalization via covalent and non-covalent bonding, resulting in changes to its varied properties. The modified graphene oxides are more beneficial in various applications.[9,21,22] There are numerous ways to functionalize GO depending on its use. Dye-GO nanocomposite has recently gained popularity as a research area, with numerous applications in biodevices, drug delivery, and optoelectronic materials. Dye-GO nanocomposite production involves a variety of interactions, including electrostatic, π-π, etc.

Currently, we are looking into the impact of surfactant solutions (including synthetic 16-4-16 and conventional CTAT) and GO nanoparticles on the photophysical properties and aggregation of coumarin 153 (C153), a well-known laser dye from the coumarin family. . In this work, we studied the individual and combined effects of surfactants and GO nanoparticles on the aggregation and photophysical behaviour of C153 dye molecules. Because graphene oxide (GO) and graphene are well-known as highly effective fluorescence quenchers for fluorophore molecules,[23-30] it is critical to understand the photophysical behavior of coumarin 153 in the composite, as well as the role of interaction between C153 and graphene oxide. The coumarin 153 dye molecule's ring can easily engage with the vast cloud of graphene oxide via a mechanism known as π-π stacking interaction. The Stern-Volmer (SV) equation is used to analyze the mechanism of fluorescence quenching, which is a process that occurs when the

fluorescence intensity of a fluorophore decreases.[31] Aside from fluorescence quenching, dye molecule aggregation is also significant; spectrum alterations in absorption and fluorescence spectra are detected based on the molecular orientation of the dye molecule in the aggregated state. In general, organic dye molecules exhibit two types of aggregation: H-type aggregation and J-type aggregation.[32,33] In H-type aggregation, the dye molecules are staggered face-to-face, resulting in a blue shift of the absorption peak; while, in J-type aggregation, the dye molecules are aligned edge-to-edge, resulting in a red shift of the absorption peak.[34] The extent of aggregation entirely depends on the temperature, the nature of the dye molecule, and the entire composition of the solution.

However, because the aggregation and photophysical properties of the C153 dye are dependent on the solvent used, solvation dynamics must also be investigated.[35,36] In contrast to a non-polar medium, where the highest fluorescence band changes to a lower wavelength, C153 has a low fluorescence quantum yield and a short fluorescence lifetime in a strongly protic polar solvent. This is because the intramolecular charge transfer (ICT) state in the C153 molecule is less likely to occur in a polar medium vs a non-polar one.[37] The fluorescent ICT state is a form of excited state in which the electron cloud that was mostly located in the amine group (donor group) in the ground state is transferred to the acceptor carbonyl group in the excited state.[38] Because of this unique characteristic, C153 makes a good probe for studying the self-assembly of amphiphile molecules. Furthermore, C153 preferentially dwells in the micelle's center due to its hydrophobic character. This feature, together with C153's photophysical properties, makes it an ideal probe for determining the critical micelle concentration (CMC) of surfactants and other amphiphiles. We utilize a multi-technical approach to study the aggregation and photophysical properties of C153 dye, such as surface tension, conductance, UV-vis absorption, steady-state and time-resolved fluorescence, and so on.

2. Experimental Section

2.1. Chemicals and reagents

Coumarin 153 (C153), hexadecyl trimethyl ammonium p-toluene sulfonate (CTAT), N, N-dimethyl hexadecyl amine, and 1,4-dichloro-2-butyne were purchased from Sigma-Aldrich. Natural graphite flakes (Alfa Aesar), potassium permanganate ($KMnO_4$), sodium nitrate ($NaNO_3$), hydrogen peroxide (30%, H_2O_2), sulphuric acid (H_2SO_4, 98%) were purchased from Merck. For preparing the stock solution of C153 (1.0×10^{-3} M), ethanol was used as solvent. The aqueous solution of C153 was prepared by diluting the stock solution of C153. All the

chemicals mentioned above were used without further purification, and all the experiments were performed at room temperature.

2.2. Instrumentation

2.2.1. Tensiometry

The Krüss (Germany) tensiometer was employed with the ring detachment method for surface tension measurements. Using a Hamilton micro syringe, a concentrated stock solution of surfactants in an aqueous medium was added to water gradually. Each measurement was preceded by a 5-minute equilibration period. To ensure accuracy, each measurement was carried out three times. The method's accuracy was 0.1 $mN.m^{-1}$. Surface tension (γ) vs. log[surfactant] was plotted to determine the CMC, and from the breaks in the plot, the CMC was calculated.

2.2.2. Field Emission Scanning Electron Microscopy (FESEM)

Japan's FESEM, Model FEI INSPECT F50, was used to analyse the surface morphologies of the GO. The drop-casted sample solutions were adequately dried before being gold-plated using the sputtering process for 1 minute at 298±1 K with 5.5 mA current.

2.2.3. Electrical Conductivity Measurements

An Eütech (Singapore) conductivity meter was used to measure electrical conductivity with a cell constant value of 1 cm^{-1}. The temperature of the solution was kept constant at 298 K using a water bath with precision of ± 0.1 K. Using a Hamilton micro syringe, stock solution prepared in the specific solvent (about ∼15 times the CMC) was progressively added to a container containing 6 mL of the solvent. After each addition, followed by homogeneous mixing, the value of the specific conductance (κ) was recorded. Each measurement was carried out three times, and the average result was recorded with an error of 2 s. The CMC values were calculated from the break points in the specific conductance (κ) vs surfactant concentration graphs.

2.2.4. Steady-state spectral measurements

A Shimadzu 1601 UV-Vis spectrophotometer from Japan and a Perkin-Elmer LS 55 fluorescence spectrophotometer from the United States were used to record the absorption and fluorescence emission spectra respectively. The emission spectra of coumarin 153 dye in the aqueous dispersion of GO were measured in the range of 450-700 nm for an excitation

wavelength of 422 nm using an excitation slit width of 10 nm and an emission slit width of 5 nm. All spectroscopic experiments were carried out with freshly prepared solutions containing a low concentration of the dye coumarin 153 (10^{-5}M).

2.2.5. Time-Resolved Fluorescence Study

A Horiba−Jobin−Yvon FluoroCube fluorescence lifetime system was utilised to perform time-resolved fluorescence decay. Coumarin 153 dye was excited by a Nano LED at 450 nm from IBH, UK, and a TBX photon detection module was served as the detector. IBH DAS-6 decay analysis software was used to fit all of the decay data. In place of the sample, the lamp profile was taken using a dilute micellar solution of sodium dodecyl sulphate as a scatterer. The χ^2 values were maintained quite near to unity for the suitable fittings.

2.2.6. Dynamic light scattering (DLS) and zeta potential measurements

DLS and zeta potential measurements were performed in a Zetasizer nano ZS (Malvern, UK) at a scattering angle of 90 º using a He-Ne laser (λ = 632.8 nm). To get rid of bigger particles, all of the solutions were filtered three times via membrane filters with a 0.25 μm porosity. To obtain more precise results, every measurement was repeated twice and the mean values were reported. Standard deviation of the measurements was 5-7 %.

2.2.7. Transmission Electron Microscopy (TEM)

A carbon-coated copper grid with a mesh size of 300 was used to adsorb 10 μL sample solutions of a specific mole fraction. Excess liquid on the copper grid was immediately removed by the filter paper on which it was placed. It was stained negatively using freshly made 0.5 wt% aqueous uranyl acetate. The samples were stored overnight in a desiccator. A JEOL-JEM 2100 transmission electron microscope from Japan was employed, with an accelerating voltage of 100 kV.

2.2.8. Raman Laser Spectroscopy

Raman spectra of the graphite flasks and graphene oxide (GO) were recorded in a Triple Raman spectrometer of model no. T64000 made by Horiba, JobinYvonequipped with 1800 grooves/mm gratings, TE Cooled Synapse CCD (J-Y Horiba) and an open stage Olympus microscope with 100x objective. Samples were excited at λ=532 nm with laser power 1.7 Mw [Ar+ laser (Model: Stabilite 2017, Spectra Physics] and numerical aperture (NA) of 0.9.

2.2.9. Powder X-ray diffraction (PXRD)

Powder X-ray diffraction (PXRD) pattern samples were recorded with a Bruker D8 Advance X-ray diffractometer using monochromatic Ni-filtered Cu Kα (λ =1.5406A^o) radiation. Data were collected from 10^o to 60^o at a scan rate of 0.1^o / minute.

2.2.10. ^{1}H-NMR spectroscopy

1H-NMR spectra were performed using a Bruker DPX-300 (300 MHz) spectrometer at ambient temperature in $CDCl_3$ using tetramethyl silane as an internal standard.

2.2.11. FTIR-ATR spectroscopy

FTIR spectra were recorded on a Perkin Elmer (model no Spectrum Two) FTIR spectrometer using the attenuated total reflectance (ATR) technique. A $LiTiO_3$ detector has been used to record the spectra. Samples were taken on a diamond plate, and pressure was adjusted and measurements were performed between the ranges of 500-4000 cm^{-1} wavelength.

2.3. Synthesis of materials

2.3.1. Synthesis of graphene oxide (GO)

Modified Hummer's method[39] was executed for the synthesis of graphene oxide (GO). The detailed synthesis procedure has been documented in the supplementary.

2.3.2. Synthesis of N, N'-dihexadecyl-N,N,N',N'-tetramethyl-N,N'-but-2-ynediyl-di-ammonium chloride (16-4-16)

Dicationic gemini surfactant N, N'-dihexadecyl-N, N, N', N'-tetramethyl-N, N'-but-2-ynediyl-di-ammonium chloride (16-4-16 gemini) was synthesized as per the procedure mentioned by Menger et. al.[40] and the synthesized gemini surfactant was characterised by 1H-NMR (spectra were given in the supplementary).

2.4. Characterization of GO

The absorbance maximum (cf. Fig. 1a) of GO was observed at around 237 nm for the π-π* transition of the aromatic C-C bond and around 300 nm for the n-π* transition (shoulder band).[41]

GO exhibits a broad peak between (Fig. 1 (b)) 3000 – 3600 cm-1 in the high-frequency region, corresponding to the stretching and bending vibrations of OH groups of water molecules

adsorbed on the graphene oxide layer. The absorption peaks at 2917 cm−1 and 2845 cm−1 represent the symmetric and anti-symmetric stretching vibrations of CH2.42 Two absorption peaks are observed at 1626 cm-1 and 1714 cm-1 due to the stretching vibrations of C=C and C=O from carboxylic acid and carbonyl groups present at the edges of graphene oxide, respectively.41 The absorption peaks at 1052 cm−1, 1216 cm−1, and 1364 cm−1 correspond to the stretching vibrations of C−O from alcohol, C-O-C from epoxy, and C−O from carboxylic acid, respectively. The presence of these oxygen-containing groups indicates that the graphite has been oxidized. Surface hydroxyl groups in GO form hydrogen bonds with the water molecules, further suggesting the hydrophilic nature of GO.

X-Ray diffraction patterns (XRD) of graphite flakes and GO are presented in Fig. 1(c). Graphite shows an intense and sharp peak at $2\theta = 26.6°$ with an interplanar (002) spacing of 0.334 nm.[43] The sharp XRD pattern of graphite implies structural integrity in the layer structures of carbon nanomaterials. In the case of GO, the shifting of the 2θ peak to 10.12° is detected with an increment of interplanar (001) spacing of 0.961 nm, which indicates that the graphite was fully oxidized into graphene oxide.[44] This increment can result from the intercalation of oxide functional groups and water molecules at the carbon basal plane during chemical oxidation reactions.[45]

Raman spectroscopy is a non-destructive technique for determining the order and disorder structures of carbon-based materials. The characteristic G and D peaks and their overtones are the main features of graphite-based materials. The graphite flake demonstrates an intense band (G peak) at 1580 cm^{-1}, with another band appearing at 2722 cm^{-1}. These observations closely align with the values provided in previous literature. The peak at 1348 cm^{-1}, known as the D peak, reveals defects in the sample and is often used to measure the degree of disorder. Raman spectra of GO show a very strong D peak at 1348 cm^{-1}, with an intensity nearly comparable to the G peak at approximately 1600 cm^{-1}. The values of the D and G bands of GO were also found to be in good agreement with earlier literature. The more intense D peak of GO in comparison to graphite indicates a higher presence of structural disorder in GO. The 2D band of GO appears at around 2692 cm^{-1}, with the D+G band at 2914 cm^{-1}. Unlike the D peak, which is Raman active only in GO (in the presence of structural defects), the 2D peak is active for graphite in the absence of defects (cf. Fig. 1(d)).

FESEM micrographs of GO are shown in Fig. 1(e). FESEM shows a two-dimensional sheet-like structure associated with multiple lamellar layers. The smooth leaf-like surface of graphite

is converted into a rough surface after oxidation and forms a porous structure in GO.[46] It is likely to separate the edges of individual sheets, and also possible to determine the length, thickness, and width of the sheet. GO shows (Fig. 1f) a wrinkled and thinly layered structure in the TEM micrographs.

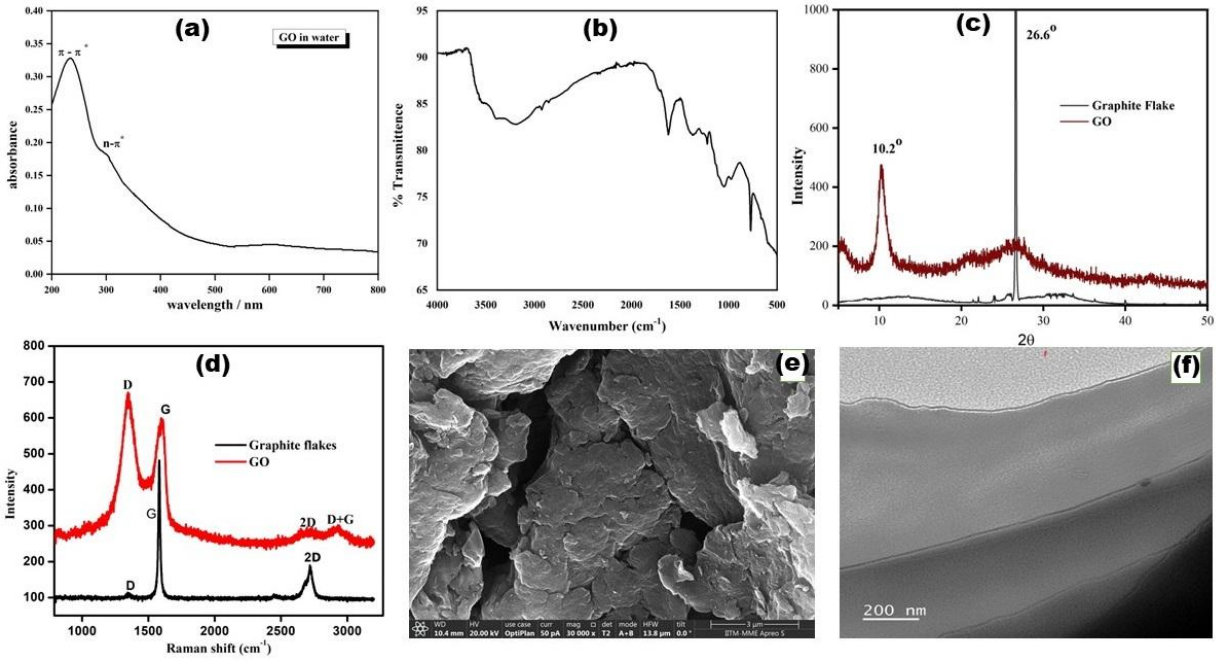

Fig. 1. Characterization of GO by using different experimental techniques: (a)Absorbance; (b) FTIR-ATR; (c) XRD (d) Raman spectroscopy; (e) FESEM; and (f) TEM.

2.5. Preparation of highly stable GO dispersions:

GO nanoparticles were dispersed in deionized water at an average concentration of 0.5 mg/mL, and the dispersion was carried out using an ultrasonic bath for 5 hours. After many sonication processes, the GO dispersion was left undisturbed at room temperature for several days. In this way, large, water-insoluble GO particles were sedimented, and a clear GO dispersion was separated precisely by a decantation process. The GO dispersions produced by this method were homogeneous and very stable. Various concentrations of GO solutions were prepared by diluting the stock solution.

2.6. Preparation of GO-C153 and GO-C153-CTAT/16-4-16 composite in aqueous medium

Various amounts of GO dispersions were mixed with the C153 dye so that the final concentration of C153 in the solution of all composites was 1 x 10^{-5} M. Briefly, a stock C153 dye solution of 1 × 10^{-3} M was pipetted, transferred to a vial, and purged with inert argon gas

to evaporate the solvent. Then, 3 mL of GO solution with different concentrations of GO was added to the vial containing C153. For preparing the GO-C153-CTAT/16-4-16 ternary system, various concentrations of CTAT/16-4-16 were added to the GO-C153 binary system and sonicated well.

3. Results and discussion

3.1. Absorption Studies

The absorption spectra of coumarin 153 dye were collected at various concentrations of graphene oxide to investigate the interaction between the two materials (Fig. 2). According to Figure 2, coumarin 153 displays a characteristic absorption peak at approximately 430 nm, which is consistent with the stated value in the literature.[47] The addition of various GO concentrations can cause an increase in the intensity of the maximum absorption spectra. The absorption peak intensities rise with GO content due to the participation of graphene oxide in the absorbing medium, indicating a considerable increase in absorption intensity.

To further understand the quenching mechanism, we studied the shift and shape of absorption peaks in UV-vis spectra. It is well understood that in static quenching, the formation of a ground-state complex between the quencher and fluorophore shifts the fluorescence's UV-Vis absorption spectrum. For dynamic quenching, however, the absorption spectra should not vary.[48] As shown in Fig. 2, the UV-Vis absorption spectra gradually changed towards blue with the addition of GO, with normalized spectra revealing a significant blue shift of 10 nm at a GO concentration of 0.015 mg/mL. The creation of a non-fluorescent H-aggregate dimer could explain this intriguing finding of the UV-Vis absorption peak changing to the blue.[49] Therefore, the UV-Vis shifting for absorption spectra indicates the presence of ground-state quenching, i.e., static quenching.

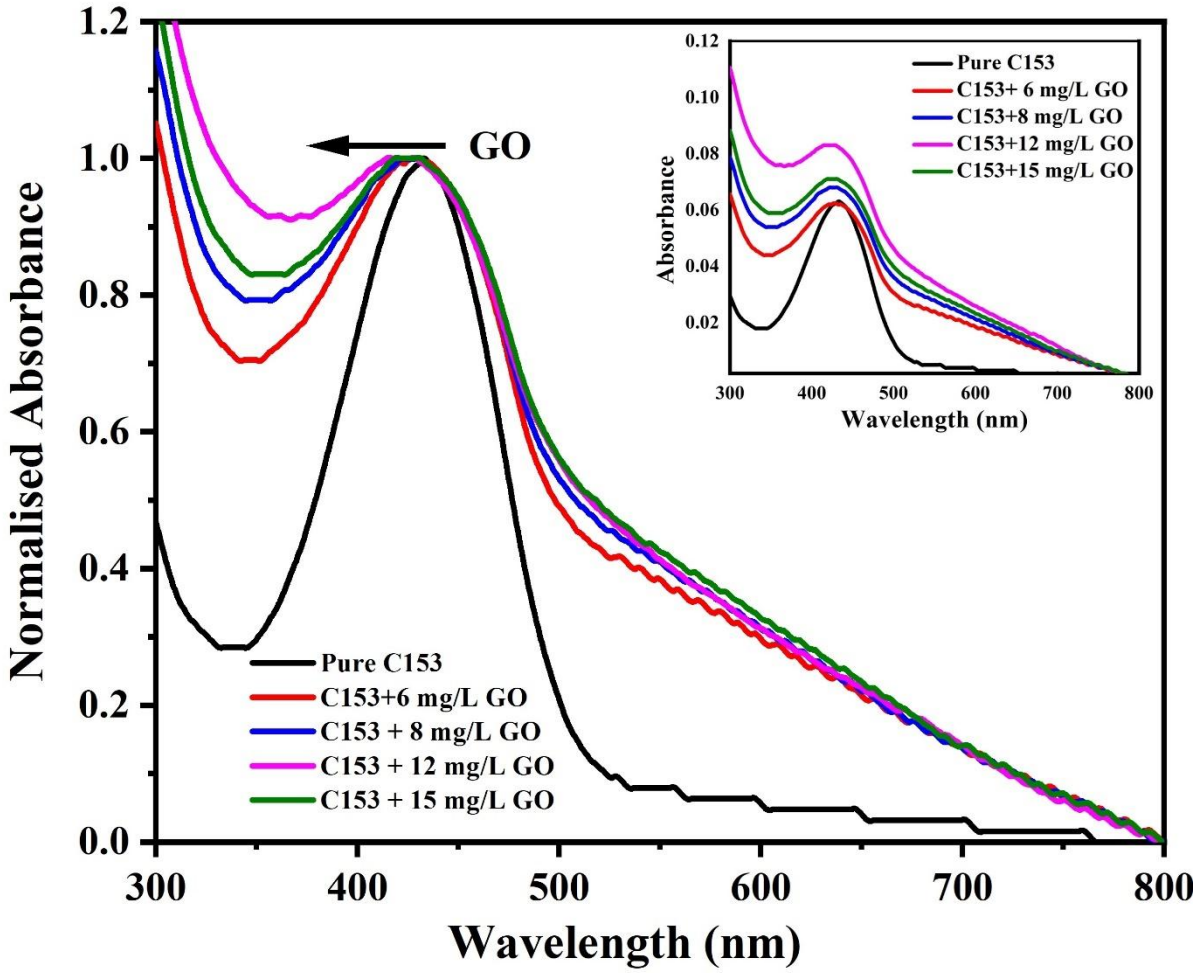

Fig. 2. Normalised UV-vis spectra of 1×10^{-5} M C153 at various concentrations of GO (Inset: UV-vis spectra of C153 at various concentrations of aqueous dispersion of GO).

3.2. Fluorescence Studies

The steady-state fluorescence emission spectra for the coumarin 153 dye in an aqueous GO dispersion were recorded using a light source with a 422 nm excitation. Coumarin 153 exhibited a strong fluorescence emission band in deionized water, peaking at 544 nm.[50] We measured the steady-state emission of the GO@C153 pair at different GO concentrations because the couple's fluorescence emission intensity is significantly reliant on the concentration of GO. The accompanying figure (Fig. 3A) depicts the steady-state emission spectra of the GO@C153 pair at various GO concentrations. According to Fig. 3A, the intensity of coumarin 153 emission decreases as GO concentration increases. Furthermore, an unexpected blue shift of fluorescence peaks to shorter wavelengths is seen. As a result, changing how GO and coumarin 153 interact would allow you to vary the amount of fluorescence emitted. GO was an extremely effective quencher for the C153 fluorophore, as

indicated by the gradual drop in fluorescence emission intensity as GO concentration increased. Furthermore, GO showed no fluorescence at the same excitation wavelength as coumarin 153 (422 nm). This finding clearly shows that the observed quenching of fluorescence emission was induced only by the interaction of the GO and C153, not by reabsorption or any inner filter effect. The fluorescence peak of coumarin 153 moves 32 nm blue with increasing GO content from 0 to 0.01 mg/mL, as shown in the normalised fluorescence spectra (Fig. 3B). This significant blue shift in the fluorescence emission peak could be due to the production of H-aggregates,[51] which are nonfluorescent clumps of dye molecules when GO nanoparticles are present. Blue shifting accelerates with increasing GO levels, but fluorescence emission strength decreases due to the formation of nonfluorescent dimeric aggregation. GO is well-known for its sp^2 hybridized π plane, carboxylic acid groups near the edge, and epoxy and hydroxyl groups on the surface.[52] Coumarin 153 dye, with its aromatic ring and π electrons, can form π-π interactions with GO, resulting in dye-nanoparticle aggregates.

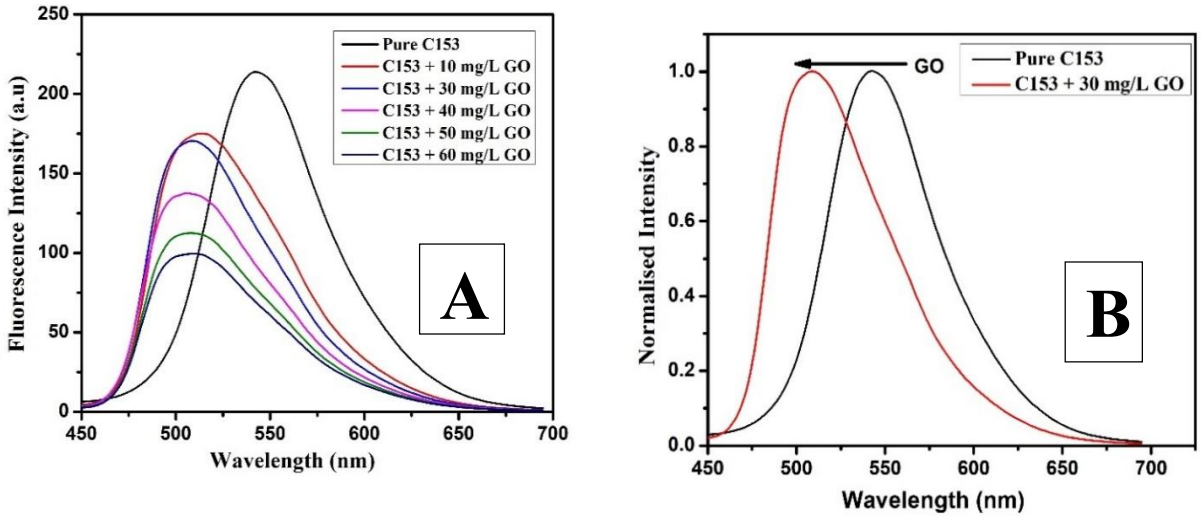

Fig. 3 (A) Fluorescence spectra of 1×10^{-5} M C153 at various concentrations of aqueous dispersed GO with an excitation wavelength of 422 nm (B) Normalised fluorescence spectra of pure C153 and that in presence of 30 mg/L GO aqueous dispersed in C153 solution respectively.

3.3. Binding constant determination

The binding constant of the GO and C153 interactions was evaluated from the steady state fluorescence quenching data by using a modified Stern-Volmer equation.[53,54]

$$\log((F_0\text{-}F)/F) = \log K + n \log[Q] \quad (1)$$

Where K is the binding constant and n is the number of binding sites of nanoparticles on C153. The value of the binding constant (K) can be found from the plot's intercept, and the number of binding sites (n) can be found from the slope when log ((F0-F)/F) vs. log [Q] is plotted (fig. 4). The number of binding sites (n) was around 2.0, and the obtained binding constant (K) for GO and C153 was 4.89 $\times 10^2$ Lg^{-1}. The high binding constant value suggests a strong interaction between GO and C153 molecules.

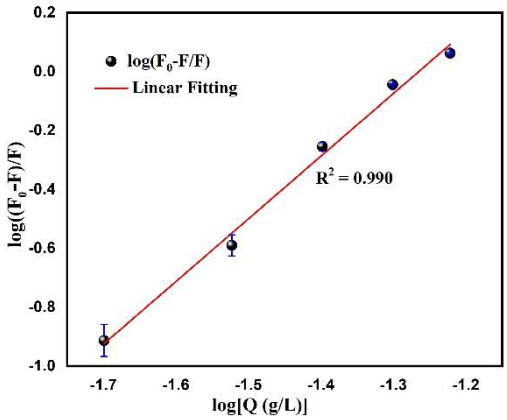

Fig. 4. Modified Stern-Volmer plot, derived from fluorescence data, depicting the binding curves resulting from C153's adsorption on GO.

3.4. Fluorescence quenching analysis

There are two types of quenching processes: static and dynamic. In static quenching, the quencher and fluorophore molecules mix to produce a non-fluorescent ground-state complex. As GO concentration increases, the number of free fluorophores in the ground state that emit fluorescence in the excited state decreases due to complex formation. This causes static quenching, which is the reduction in fluorescence intensity.

In contrast, dynamic quenching produces no ground-state complex. Instead, the quencher molecule forms a compound with the fluorophore in the excited state, deactivating fluorescence emission [55]

To better understand the fluorescence quenching mechanism, we used the Stern-Volmer equation. The Stern-Volmer equation for fluorescence quenching is expressed by the following equation:[56,57]

$$\frac{F_0}{F} = 1 + K_{SV}[Q] \quad (2)$$

Here, F_0 and F represent the fluorophore's fluorescence intensity in the absence and presence of quencher molecules, respectively. K_{SV}, also known as the Stern-Volmer constant, is the binding constant between the fluorophore and the quencher molecule, whereas [Q] represents the quencher concentration. The F_0/F against [Q] plot (Fig. 5) indicates a positive or upward departure from the linear curve for the change in F_0/F of coumarin 153 with GO concentration.

If F_0/F varies linearly with quencher concentration, there can only be one type of quenching: static, dynamic, or both if it deviates from linearity. In our case, it appears that both static and dynamic quenching occurred, as the change in F_0/F of coumarin 153 with GO concentration is bimodal.[58] The blue shift in the absorption spectra is caused by the formation of a ground-state complex between the quencher molecule GO and the dye C153, indicating static quenching. However, to further understand dynamic quenching, we conducted lifetime experiments.

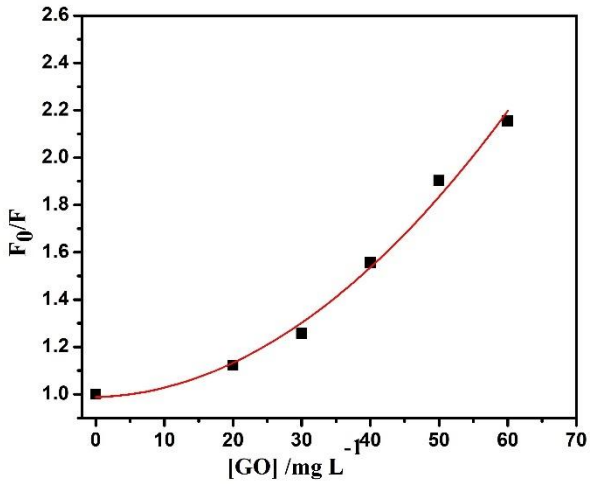

Fig. 5 Stern-Volmer plot for fluorescence quenching of C153 molecule in the presence of various concentrations of graphene oxide aqueous solution.

3.5. Time-resolved fluorescence studies

We used time-dependent fluorescence measurements to investigate how the lifetime of coumarin 153 dye changed in the presence of GO nanoparticles. We used a laser diode with an excitation wavelength of 450 nm and an emission wavelength of 544 nm to measure lifetime. The average lifetime of the coumarin 153 dye in an aqueous medium is 1.89 ns, with a biexponential decay curve.[59] The faster decay component is associated with the dye's aggregation form, whereas the slower decay component corresponds to the dye's monomer form (coumarin153).[60]

We investigated the lifetime of C153 using various GO nanoparticle concentrations. According to Fig. 6A, the fluorescence lifetime of the coumarin 153 dye reduced as the GO concentration increased. The data table (Table 1) shows that when very little GO (0.01 mg/mL) is added, the dye's lifetime is reduced to about half of that in pure deionized water. This suggests that GO is a potent fluorescence quencher for coumarin 153 dye molecules.

The biexponential decay curve shows a progressive increase in the contribution of the faster decay component as GO concentration increases, and a gradual drop in the contribution of the slower decay component. The aggregation of dye molecules in the presence of GO nanoparticles clearly explains this behavior. As previously stated, the faster decay component is related to the H-aggregate form of C153 dye. In the presence of GO, the dye undergoes H-type aggregation, resulting in a faster decay component than the free C153 molecule in an aqueous solution. However, when the concentration of GO grows, the contribution of the slower decay component decreases because GO induces the monomeric form of the C153 molecule to disintegrate and transition into an aggregation. Monomeric coumarin 153 is the cause of the slower decay component, and its contribution decreases as GO concentration increases.

Lifetime measurements were also useful for studying static and dynamic quenching. In the case of static quenching, quencher concentration has no effect on the dye molecule's lifetime, but dynamic quenching shortens it. The following equation represents the change in the dye's fluorescence lifetime with the quencher.

$$\tau_0/\tau = 1 + K_{sv}[Q] \quad (3)$$

Here, τ_0 and τ are the lifetimes of the dye molecule in the absence and presence of the quencher molecule, respectively. K_{sv} is the Stern-Volmer constant, and [Q] is the concentration of the quencher molecule. Fig. 6B reveals that t_0/t gradually changes with GO concentration, not staying constant at $t_0/t = 1$, which is the condition for pure static quenching. Additionally, it does not satisfy the $F_0/F = t_0/t$ condition, which is a need for pure dynamic quenching. In this instance, the variations in t_0/t with GO concentration exhibit an intermediate behaviour, which unequivocally demonstrates the existence of both static and dynamic quenching processes. This observation significantly supports the steady-state Stern-Volmer graphs, which demonstrate both static and dynamic quenching. Thus, the lifetime measuring experiment shows that static and dynamic quenching occur.

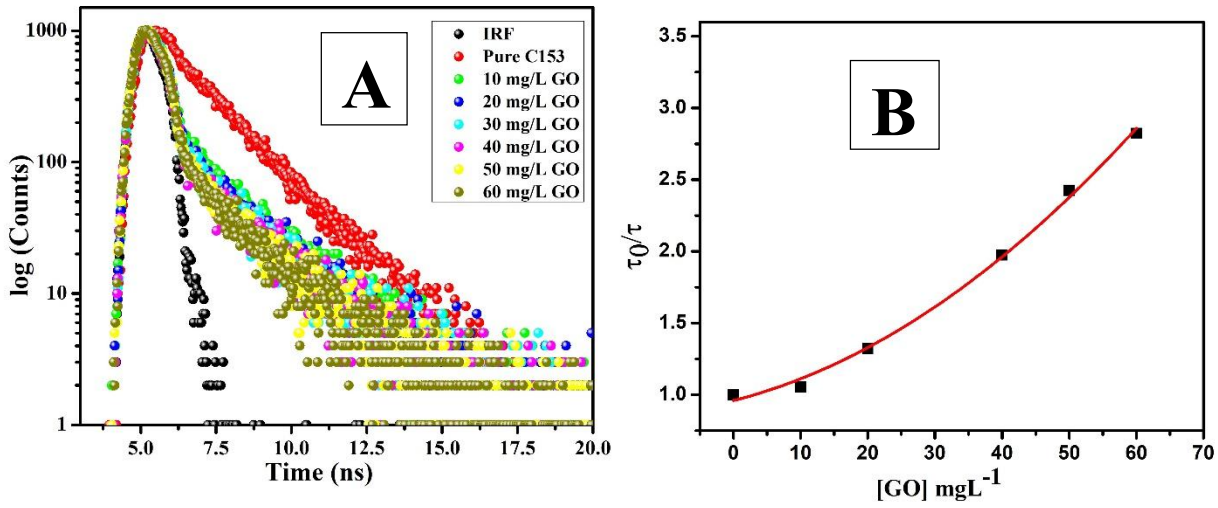

Fig. 6 (A) Time-resolved fluorescence decay of pure C153 (red) and others were due to the presence of various amounts of GO, and the black line was the lamp signal. The wavelength of excitation was 450 nm, and the range of χ^2 was 1.05-1.29; (B) Time-dependent fluorescence quenching Stern-Volmer plot of C153 with various concentrations of GO.

3.6. Mechanistic Details

To investigate the interaction mechanism between coumarin 153 dye and GO, we must first understand the specific structures of the dye and the quencher molecules. The presence of a π ring in the dye molecule increases the likelihood of coumarin 153 undergoing π-π stacking. In contrast, graphene oxide (GO) is composed of numerous hexagonal rings with sp^2 hybridized carbon atoms and a wide range of functional groups. The sp^2 hybridised plane has hydroxyl and epoxy groups, as well as a large number of carboxylic groups along the edges of the hexagonal rings. The structural properties of GO and the dye molecule increase the chance of a π-π contact between the quencher molecule, GO, and coumarin 153 dye.

The observed fluorescence quenching could be explained by energy or electron transfer between the coumarin 153 and the GO quencher molecules. However, the absorption spectra of GO (Fig. 7) show that they do not coincide with the emission spectra of the coumarin 153 dye. This means that there is no potential for energy transfer from the dye molecule to the GO quencher molecule in its ground state.[61] Thus, in the ground state, fluorescence quenching happens via electron transfer from the dye molecule to the GO system. The quenching of fluorescence emission in the excited state could be due to energy transfer from the dye molecule (coumarin 153) to the quencher molecule (GO).

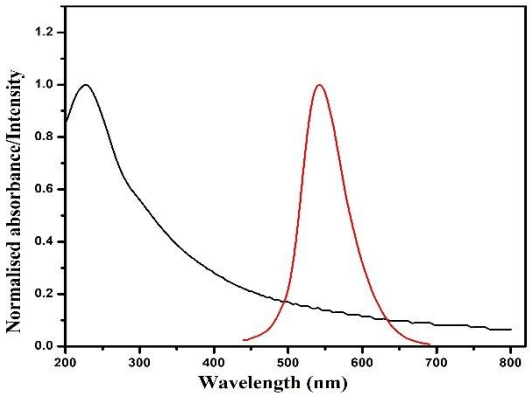

Fig. 7 Normalised UV-vis absorption spectra of GO (black spectrum) and normalised fluorescence spectra of C153 dye molecule (red spectrum).

4. Role of surfactant on the photophysical and aggregation properties of C153 dye

4.1. Conductivity measurements

Specific conductivity measurements were used to investigate the aggregation behaviour of surfactant molecules (both conventional and gemini surfactants) in the presence of dye molecules. Specific conductivity measurements of 16-4-16 and CTAT surfactants were conducted in the absence and presence of the C153 molecule, respectively. The experiment's results were plotted as specific conductivity vs. surfactant concentration. The increased size of 16-4-16 and the larger p-toluene sulfonate counterion group of CTAT resulted in decreased mobility in both surfactants, resulting in low conductivity values.

As seen in Figures 8A and 8B, the conductivity increased rapidly with the addition of surfactant molecules until a certain point, both with and without the C153 molecule. Following that, the slope of the conductivity graph quickly decreased. This point at which the slope reduces is referred to as the critical micellar point for the surfactant molecule. The cmc value of both the pure surfactant and the dye-surfactant complex was calculated using the break point in the specific conductivity vs. surfactant concentration plot.[62] The break point appeared earlier in the presence of the C153 molecule than in its absence, as evidenced by the conductivity plots for both 16-4-16 and CTAT surfactants. This finding suggests that the presence of the C153 molecule promoted micelle formation in both surfactants. This is because the presence of the dye molecule improves overall hydrophobicity, which facilitates micelle formation.

Another intriguing finding from the conductivity plot was that in the presence of the dye molecule C153, both 16-4-16 and CTAT surfactants had higher conductivity than in the absence of the dye molecule. The degree of counterion dissociation (β) can explain this result

by comparing the slope observed in the post-micellar region to that of the pre-micellar region. Table 2 shows that C153 dye significantly increased the degree of counterion dissociation (β) for both 16-4-16 and CTAT surfactants. Complexation between the C153 molecule and surfactant molecules alters the interaction between the counterion and 16-4-16 and CTAT head groups, resulting in increased counterion dissociation and the counterion of 16-4-16 and CTAT becoming looser and faster to dissociate.

Various thermodynamic parameters, such as the standard Gibbs free energy change for micellization (ΔG_m^0), standard enthalpy change of micellization (ΔH_m^0), and standard entropy change of micellization (ΔS^0_m), can be determined from conductivity. The value of ΔG^0_m can be represented by the following relationship[63] (eqn. 4):

$$\Delta G_m^0 = 2.303RT(logCMC - log\omega) \quad (4)$$

Here, 'ω' is known as the molar concentration of water, and its value is 55.3 at 298 K. R is 8.314 J/(mol·K), and T is the temperature on the Kelvin scale.

At the same time, the value of ΔS_m^0 and ΔH^0_m can be calculated using the following equations (Eq. 5 and Eq. 6):

$$\Delta S_m^0 = -\frac{d}{dT}(\Delta G_m^0) \quad (5)$$

$$\Delta H_m^0 = \Delta G_m^0 + T\Delta S_m^0 \quad (6)$$

The data table (Table 2) clearly shows that the presence of C153 leads to a more negative value of the standard Gibbs free energy of micellization (ΔG0m) for both surfactants (16-4-16 and CTAT) compared to the absence of the dye. This finding suggests that the micellization process was favourable when the dye molecule was present. The study revealed that 16-4-16 exhibited a more favourable micellization than CTAT, as indicated by a more negative change in ΔG0m. This is because CTAT has only one chain with sixteen carbons, making it less hydrophobic than 16-4-16, which has two hydrophobic chains linked by a spacer. Similarly, the changes in standard entropy (ΔS_m^0) and standard enthalpy (ΔH_m^0) for micellization can be explained.

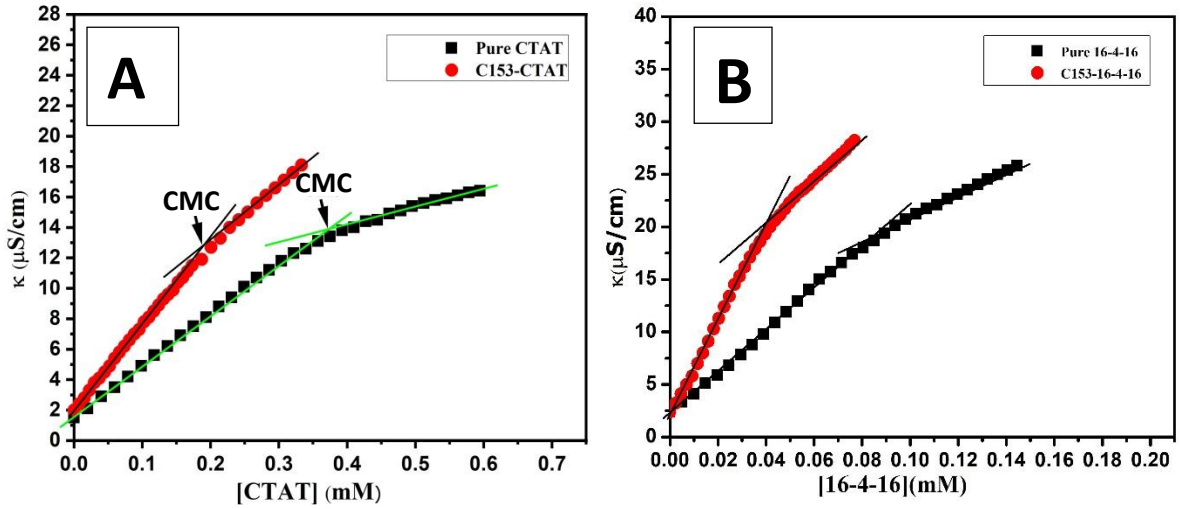

Fig. 8 (A) Specific conductivity vs. CTAT concentration plots in absence and presence of C153 molecule respectively (B) Plots of specific conductivity vs. concentration of 16-4-16 in absence and presence of C153 dye molecule at 298 K.

4.2. Surface tension measurements and determination of various surface parameter

Tensiometry is a very essential tool for studying interfacial changes for the interaction between dye and surfactant molecules. The adsorption of amphiphiles at the air-water interface leads to a decrease in the surface tension of the aqueous phase. The breakdown of H-bonding at the aqueous interface may be the cause of the drop in surface tension observed in the presence of amphiphiles. The surface tension measurements reveal that the formation and adsorption of the C153-surfactant complex have an impact on the overall structure of the surface monolayer and, consequently, the surface tension.[64] Figures 9A and 9B show plots of surface tension variations with bulk surfactant concentration (on a logarithmic scale) for both instances in the presence and absence of C153 dye at 298 K. The figures show that the surface tension lowers when C153 is present, demonstrating that the dye molecule is surface active. Surface tension falls up to a point as surfactant concentration increases, beyond which it remains more or less constant. This threshold is referred to as the critical micelle concentration (CMC). The surface tension graphs clearly illustrate that for both 16-4-16 and CTAT surfactants, the value of CMC is lower in the presence of C153 dye than in its absence. This could be because surfactants and dye molecules form a closed-packed complex, increasing the medium's effective hydrophobicity. As a result, the CMC decreases when the C153 molecule is present.

The surface excess concentration (Γ_{max}) of the amphiphiles[65,66] can be calculated with interface data using Gibbs' equation. For a dilute solution, Gibbs equation can be written as:

$$\Gamma_{max} = -\frac{1}{2.303iRT}\left[\frac{d\gamma}{d\log C}\right] \quad (7)$$

Here, Γ_{max} represents the excess surface concentration of amphiphiles and signifies the packing of the amphiphiles at the interface. *i*.e., the number of species at the air-water interface after the dissociation of amphiphile molecules, R is the universal gas constant, T is the temperature on the Kelvin scale, C is the concentration of amphiphiles in the molar concentration scale, γ is the surface tension in mN/m, and dγ/dlogC represents the slope of the plot of γ vs. logC. The value of n is taken as 2 for CTAT surfactant and 3 for 16-4-16.[67] From the surface excess concentration, we can find A_{min}, which is the minimum area covered by each surfactant molecule at the interface:

$$A_{min} = \frac{10^{18}}{N_A \Gamma_{max}} \tag{8}$$

Here N_A represents Avogadro's number. From the data in Table 3, it can be seen that the low value of Γ_{max} for CTAT surfactant in the presence of the C153 molecule suggests loose packing of the CTAT-C153 complex at the interface; hence, a larger surface area is required for the adsorption of the CTAT-C153 complex. Free CTAT molecules have a high Γ_{max} value, indicating dense packing at the interface. This means that free CTAT molecules require a smaller region to adsorb than when the dye molecule is present. Surprisingly, the reverse phenomenon occurs for the 16-4-16 surfactant. The inclusion of the C153 molecule results in a high Γ_{max} and a low A_{min}, indicating that the 16-4-16-C153 complex requires a tiny region at the air-water interface to adsorb. The absence of the dye molecule results in a low Γ_{max} and a high A_{min}, indicating that free 16-4-16 molecules require a larger surface area for adsorption than the 16-4-16-C153 complex. Because of the high hydrophobicity of the 16-4-16 surfactant, this anomalous behavior could be caused by the development of an unstable complex between C153 and 16-4-16.[64] The effectiveness of surface adsorption is given as a parameter, pC_{20}. Table 3 shows that the value of pC_{20}. for both CTAT and 16-4-16 surfactants decrease in the presence of the C153 molecule. This shows that the dye-surfactant complex has a lesser likelihood to be adsorbed at the interface, resulting in less surface activity than pure surfactant. In the case of oppositely charged dye-surfactant systems, complex formation happens via ion pair complexation, which results in the production of a non-ionic complex that acts as a non-ionic surfactant. Non-ionic surfactants are known to be more surface active than ionic surfactants.[68] In dye-surfactant systems with opposite charges, the presence of the dye molecule leads to an increase in pC_{20}. However, in our case, the surfactant molecules are cationic while the dye molecules (C153) are non-ionic, preventing complex formation via ion pair complexation. Complex formation happens solely through weak hydrophobic interactions

between the dye and surfactant molecules, and the resulting complex has lower surface activity than pure surfactant. In our case, adding the C153 molecule reduces the value of pC_{20} for both surfactants (CTAT and 16-4-16). The presence of the C153 molecule reduces the surface pressure at CMC (π_{cmc}) for both CTAT and 16-4-16 surfactants, as compared to the lack of the dye molecule. This is because the dye-surfactant combination is less likely to be adsorbed at the interface. The presence of the dye molecule reduces the surface activity of surfactants, resulting in an increase in γ_{CMC} compared to the free surfactants. So, tensiometry experiments show that CTAT has a higher surface activity than 16-4-16 Gemini (both with and without C153). This is because, due to their enormous size, 16-4-16 surfactants are loosely packed at the interface, resulting in decreased surface activity when compared to CTAT. However, due to its stronger hydrophobicity, 16-4-16 has a larger micellization capability than CTAT.

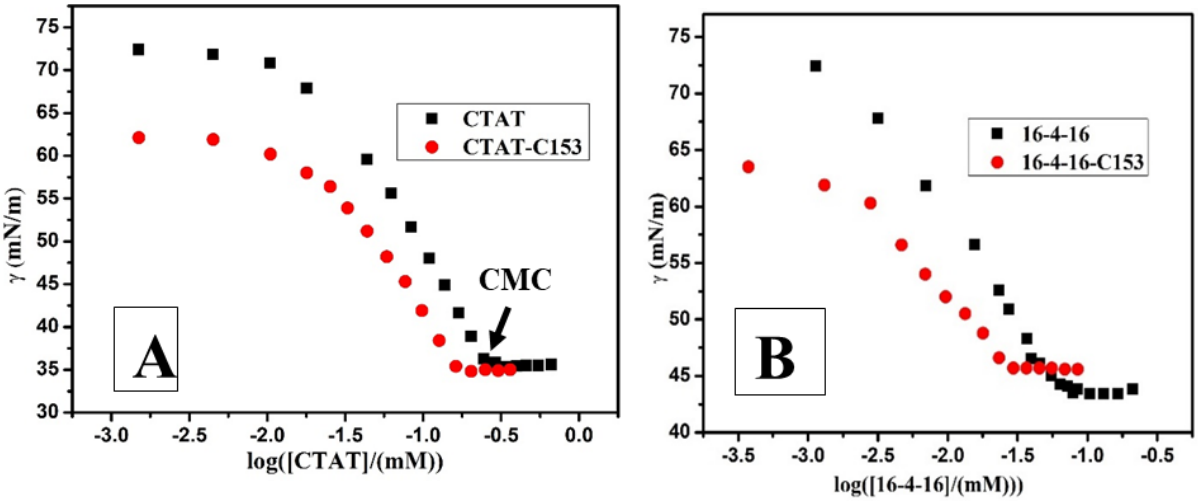

Fig. 9(A) Surface tension vs. concentration of CTAT plots in the absence and presence of 1×10^{-5} (M) C153 molecules; (B) Plots of surface tension vs. 16-4-16 concentration in the absence and presence of C153 dye molecules.

4.3. Steady state spectral studies: As previously stated, C153 has a broad absorption spectrum in an aqueous medium, having a maximum at approximately 430 nm.[47] The absorbance steadily increased with increasing surfactant content (for CTAT and 16-4-16), whereas the maximum absorption peak shifted 6 nm red (Figs. 10A and 10B). The red shift in the absorption band could be due to a change in polarity around the C153 molecule.[69] The polarity of the aqueous dye solution diminishes as the surfactant content increases, resulting in this form of red shift. However, we observed an isosbestic point in the presence of surfactant molecules, which could imply an equilibrium between the C153 molecule's monomeric and higher-order aggregated forms. This sort of aggregation is known as J-type aggregation because the absorbance spectra

show a red shift. The change in absorbance with surfactant concentration produces a perfectly sigmoidal plot (for both CTAT and 16-4-16), from which we easily determined the value of CMC in the presence of the dye molecule, and the results matched well with the CMC values determined by surface tension and conductance, respectively. The rate of increase in absorbance and red sifting of C153 UV-vis spectra is more pronounced in the presence of 16-4-16 than in the absence of CTAT. So, it indicates that 16-4-16 surfactant is more effective at changing the microenvironments of the dye than a monomeric one (CTAT).[70] The fluorescence property of the C153 molecule is highly dependent on solvent polarity. To better understand the effect of CTAT and 16-4-16 surfactants on the fluorescence behaviour of the C153 molecule, we recorded the dye's fluorescence spectra at different surfactant concentrations. In an aqueous solution, C153 has a broad, structureless, low-intensity fluorescence band with a maximum fluorescence at 544 nm. C153 exhibits less strong fluorescence spectra in a highly polar protic solvent, such as an aqueous medium, due to the C153 molecule's H-bonding in the protic polar medium.[71] The ICT state becomes less viable, yielding a weak, broad, and structured fluorescence spectrum. Despite being in a highly polar solvent, the C153 molecule's rigid shape makes twisted intramolecular charge transfer (TICT) less viable.[37] The inclusion of a surfactant solution above its micellar concentration resulted in a considerable increase in fluorescence intensity as well as a blue shift of the emission maxima. The fluorescence property of C153 is dependent on both the concentration and the composition of the surfactants. C153 fluorescence intensity showed no obvious variation in the presence of CTAT surfactant at low concentrations (up to 0.18 mM). However, as CTAT concentration increased, the fluorescence intensity increased rapidly, the spectra shrunk and became crisper, and the emission maxima showed a 6 nm blue shift. As a result, the change in fluorescence intensity with CTAT concentration results in a distinct type of plot, in which the initial intensity was identical to that of water and did not change, but the succeeding fluorescence intensity considerably rose (Fig. 10D). So, based on the figure, we can identify a sharp breakpoint that indicates a shift in the microenvironment surrounding the C153 molecule, and the breakpoints correspond to a supramolecular interaction of CTAT molecules. As a result, surfactant aggregation has a considerable impact on C153's fluorescence properties. The point of intersection could provide vital information regarding the concentration at which surfactant aggregation began, which was known as the critical micelle concentration (CMC). Fluorescence experiments show that CTAT provides a CMC value of 0.185 mM when the C153 molecule is present, which is consistent with surface tension, conductance, and UV-vis absorbance measurements. In contrast, the 16-4-16 surfactant had a more dramatic blue shift and change in fluorescence intensity than the

CTAT surfactant. The increase in fluorescence intensity, together with the progressive blue shift of the emission peak, demonstrates that these surfactants gradually modulate the microenvironment around the C153 fluorophore. The inclusion of the 16-4-16 surfactant caused a significant blue shift (14 nm) (Fig. 10C). This increase in intensity in the presence of the surfactant was caused by the stabilization of the fluorescent ICT state in a micellar medium (because to its hydrophobic nature), while the blue shifting was caused by a change in polarity in the micellar medium compared to an aqueous medium. The variation in fluorescence intensity with gemini concentration results in a more or less sigmoidal curve that differs from the pattern obtained for the CTAT surfactant. The preceding explanation demonstrates that C153's fluorescence behaviour varies in two different surfactant media, implying that the molecule experiences a different microenvironment in each of these two types of surfactant media. The CTAT surfactant contains a single 16-carbon atom hydrophobic chain, but the 16-4-16 surfactant contains two identical 16-carbon atom tails and a 4-carbon atom general spacer with a triple bond, resulting in a more hydrophobic milieu around the C153 probe. As a result, the maximum emission peak shifts more towards blue, and fluorescence intensity increases more rapidly.

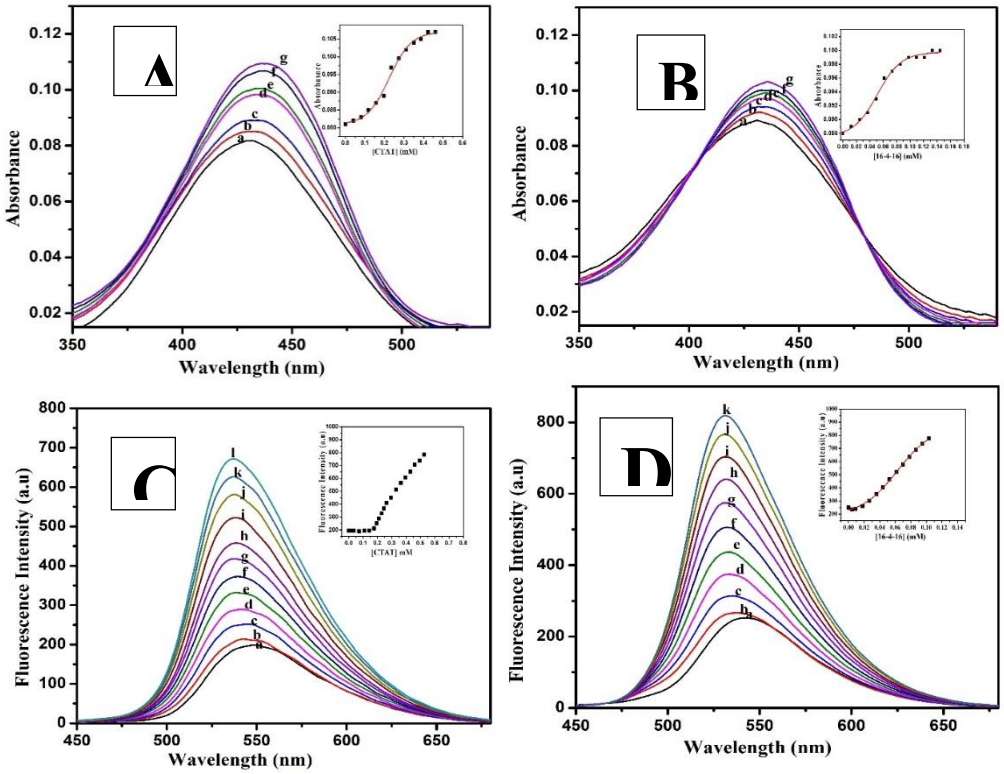

Fig. 10. (A) UV-Vis absorption spectra of 1×10^{-5} M C153 in the presence of (a)-(g) 0, 0.118, 0.196, 0.235, 0.273, 0.349, 0.424 mM CTAT (inset: plots of absorbance vs. concentration of CTAT) (B) UV-Vis absorption plots of C153 in the presence of (a)-(g) 0,

0.037, 0.049, 0.061, 0.085, 0.109, 0.132 mM 16-4-16 (the inset shows a plot of the absorbance of C153 at various concentrations of 16-4-16). (C) Steady-state fluorescence spectra of 1×10^{-5} M C153 in the presence of (a)-(l) 0, 0.176, 0.193, 0.210, 0.228, 0.245, 0.262, 0.295, 0.329, 0.362, 0.395, 0.428 mM CTAT (inset: plots of fluorescence intensity vs. CTAT concentration) (D) Steady-state fluorescence emission spectra of C153 in the presence of (a)-(k) 0, 0.026, 0.035, 0.052, 0.061, 0.069, 0.078, 0.086, 0.094, 0.103, 0.111 mM 16-4-16, (inset represents the plots of fluorescence emission intensity of C153 vs. concentrations of 16-4-16).

4.4. Binding constant determination of dye-surfactant interaction

It is feasible to measure the equilibrium binding constant (K) of the dye-surfactant interaction at different surfactant concentrations. The following reaction can be used to describe the binding of a ligand, (L), to a free dye site, (D), creating an occupied site, (LD):

$$L + D \rightleftarrows LD \tag{9}$$

By designating the dye's absorbance as Abs_0 in the absence of surfactant and Abs in its presence, respectively, the concentration of the occupied sites yields, $[LD] = \Delta Abs/ \varepsilon_{LD} - \varepsilon_D)$

In this case, ε_i represents the absorption coefficient at the chosen wavelength. To examine the data, an extension of the Hildebrand-Benesi equation was used with K = [LD]/[L][D], which was evaluated together with Δε by iterative fits[72]:

$$\frac{C_S C_D}{\Delta Abs} + \frac{\Delta Abs}{\Delta \varepsilon^2} = \frac{1}{K\Delta\varepsilon} + \frac{(C_S + C_D)}{\Delta\varepsilon} \tag{10}$$

Here, C_S and C_D are the concentration of surfactants and dye molecules respectively. In other words, Δε may be found by calculating the reciprocal of the straight line's slope, which matches the fit of the experimental $C_SC_D/\Delta Abs$ values vs. (C_S+C_D), an initial approximation that ignores the $\Delta Abs/\Delta\varepsilon^2$ term. To find the binding constant of the dye-surfactant complex, the first term in equation (10), $(C_S\, C_D /\Delta Abs + \Delta Abs/\Delta\varepsilon^2)$, is reevaluated using the Δε value, and the result is plotted against $(C_S + C_D)$. After going through this process, we were able to determine the equilibrium binding constant values for the C153-CTAT and C153-16-4-16 systems, which are 1.17×10^3 M^{-1} and 14.10×10^3 M^{-1}, respectively. It is evident from the binding constant value that C153 & 16-4-16 have a stronger interaction than C153 & CTAT.

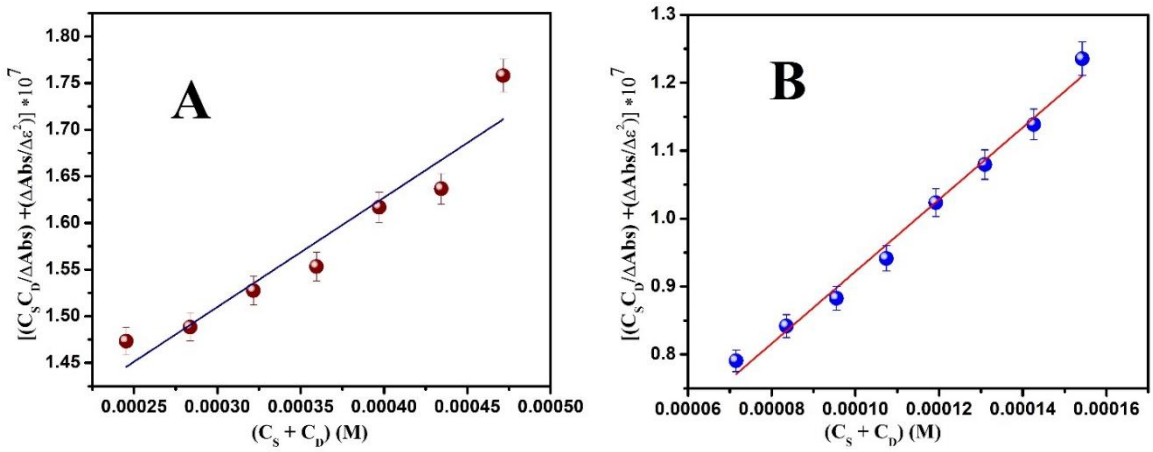

Fig. 11 Analysis of the absorbance titration data for the C153-CTAT/16-4-16 system. C_{C153} = 1×10^{-5} (M), the data are fitted according to the extension of Hildebrand-Benesi model. (A) CTAT-C153, (B) 16-4-16-C153 systems, respectively.

4.5. Fluorescence life time measurements

To investigate the excited-state interaction and changes in the microenvironment surrounding the fluorophore, lifetime measurement is an important method.[73] Differences in solvent relaxation around the fluorophore, as well as the fluorophore's partition into particular regions of crowded environments, can all have an impact on its lifetime.[74] The change in the lifetime of C153 in a multi-component system like a micelle can reveal important information about the fluorophore's position. C153 has a bi-exponential decay curve in both aqueous and micellar environments. As previously stated, the two differing lifetimes correlate to two distinct fluorophore species: monomeric and dimeric. The faster decay component (i.e., shorter lifetime) corresponds to the dimer, whereas the slower decay component (i.e., longer lifetime) belongs to the C153 monomer. In an aqueous media, C153 exists in a substantial dimeric form, which breaks down and transforms to the monomeric form when surfactants are added. However, in the presence of CTAT surfactants at concentrations higher than micellar, 31.76% of the dimeric form with a lifetime of 1.88 ns and 68.24% of the monomeric form with a lifetime of 3.95 ns were detected. In contrast, 16-4-16 surfactants above their micellar concentration exhibited 10.88% dimeric form and 89.12% monomeric form. As a result, in the presence of micelles, C153 disaggregates, increasing the contribution of the monomeric form. Because the micellar core is hydrophobic, C153 molecules disperse uniformly, revealing the monomeric form. 16-4-16 surfactants have a higher monomeric form than CTAT because they

have two hydrophobic tails, resulting in a significantly more hydrophobic environment within the micelle.

The average lifetime of C153 molecules in water and two distinct micellar mediums is as follows: 16-4-16> CTAT > aqueous. The lifetime values of C153 in aqueous and micellar solutions are shown in Tables 5 and 6. The shorter lifetime of C153 in an aqueous media could be due to a stronger perturbation of its electronic state in the polar medium, which is generated by more energy transfer from the fluorophore to the surrounding solvent molecules with high dipole moments. However, in the case of a micellar media, these electronic state perturbations are minimized because less energy is transferred from the fluorophore to its surrounding molecules as the medium's polarity decreases. As a result, C153 has a longer lifetime in the micellar medium.

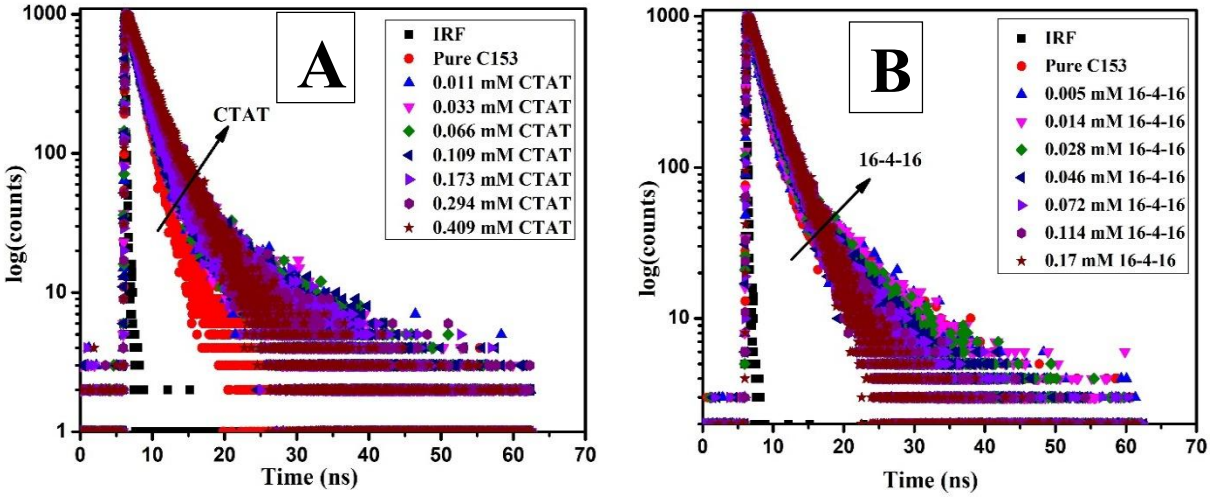

Fig. 12: (A) Time-resolved fluorescence decay of C153 in the presence of various concentrations of CTAT surfactant; (B) in the presence of various concentrations of 16-4-16 surfactant. The wavelength of excitation was 450 nm, and the range of χ^2 was 0.99-1.16.

4.6. Combined effect of GO nanoparticle and surfactant solution

As previously stated, the C153 molecule's fluorescence behavior in GO nanoparticles showed a gradual decrease in emission strength and a significant blue shift in the maximum emission band. Figures 13A and 13B depict the combined effect of GO and micellar solution on the fluorescence behavior of C153. The plot shows that GO reduces fluorescence intensity and produces a blue shift in the peak, but surfactant solution raises intensity and returns it to its original position. In the addition of 40 mg/L GO, the fluorescence peak shifted from 544 nm

to 406 nm, and fluorescence intensity decreased. However, in the presence of 0.1 mM 16-4-16 surfactant, the fluorescence intensity begins to rise again and recovers to its original value of 530 nm, as seen when 16-4-16 surfactant is present at concentrations higher than micellar. A similar observation was made in the presence of CTAT surfactant, however the efficacy of boosting fluorescence intensity and shifting the fluorescence peak back to its original position was lower than with 16-4-16 surfactant.

It is a remarkable finding that dye molecules adsorbed on GO nanosheets split from the nanosheet and enter the micellar medium when a micellar medium is present. The transfer of adsorbed dye molecules from the GO nanosheet to the micellar medium causes an increase in fluorescence intensity. Furthermore, the H-aggregation of dye molecules disintegrates as they reach the micellar medium from the GO nanosheet, leading the dye molecules to disperse uniformly throughout the medium. As a result, the H-aggregate peak shifts back to its original position. These results unequivocally show a significant interaction between surfactants (both 16-4-16 and CTAT) and C153 in the surfactant concentration range at and above the CMC. The combined fluorescence spectra of the samples demonstrate the strong interaction between C153 and surfactant in the combined ternary system (GO-dye-surfactant). The intensity of fluorescence emission is fully dependent on surfactant concentration and increases with the concentration. This behaviour may be characterized in two steps: (1) the addition of GO gradually reduces the fluorescence intensity of C153, and (2) the formation of C153-surfactant micelle complexes causes the fluorescence intensity to increase again. As a result, the interaction between C153 and GO weakens, and the dye is kept separate from graphene oxide. The GO-C153-Surfactants ternary system can be used to regenerate the adsorbent from dye molecules in wastewater treatment analysis because, in the presence of surfactants at and above the CMC, dye molecules leave the adsorbent (GO) and enter the micellar medium. Furthermore, spectroscopic research clearly shows that this GO-C153 composite can be used as a high-performance fluorescence sensor. Given the prominence of C153 as a laser dye, this concept can be applied to the development of effective and low-cost fluorescence sensors for laser applications. The interaction of 16-4-16 surfactants with GO is more prominent than CTAT. There are two reasons for these: (1) electronic charge; (2) $\pi-\pi$ interaction between GO and surfactants. Besides, the electronic charge, 16-4-16 surfactants also have a triple bond in the spacer, which is absent in CTAT surfactants. Due to the presence of π-bonds in 16-4-16, it interacts more strongly with GO than CTAT, and the release of C153 from the GO sheet is more prominent in the presence of 16-4-16 surfactant.

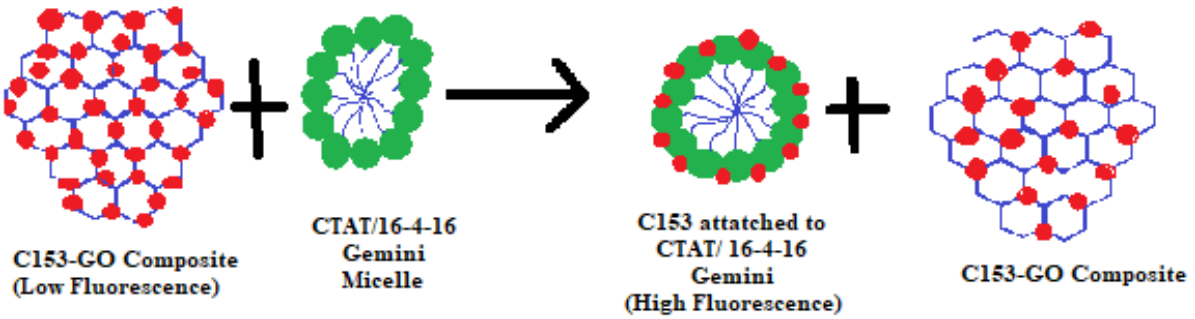

Scheme 1. Representation of C153-GO and C153-GO-CTAT/16-4-16 micelles.

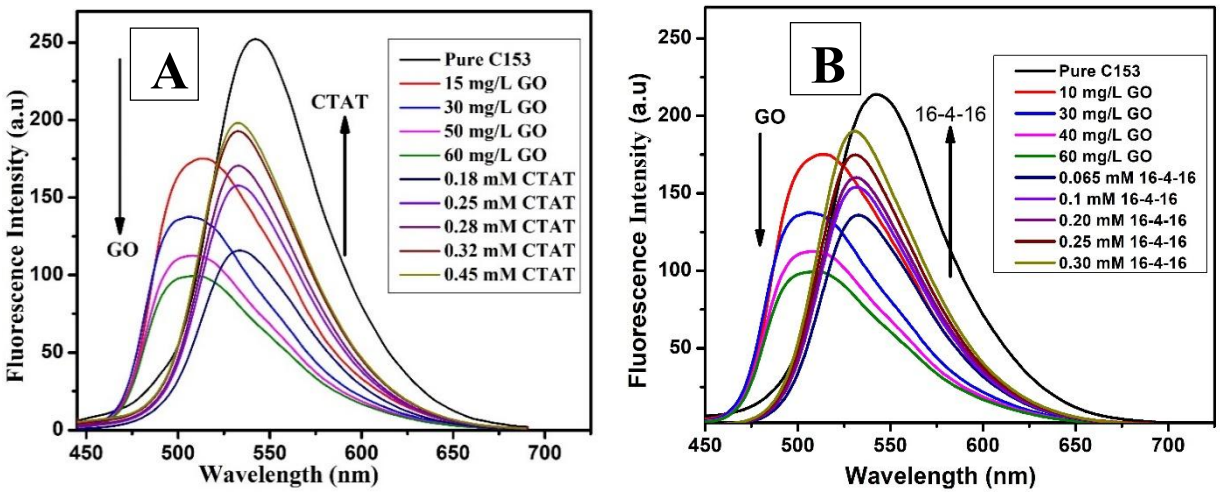

Fig. 13 (A) Fluorescence spectra of C153 in the presence of various concentration of GO and CTAT surfactants (B) Steady-state fluorescence spectra of C153 in the presence of GO and 16-4-16 surfactants.

4.7. Surface Plasmon Resonance (SPR) band analysis:

The produced surface plasmon resonance (SPR) bands of GO in the GO-C153 and GO-C153-CTAT/16-4-16 complexes were monitored over time to determine the complexes' solution phase stability (Fig. S4). GO's UV-vis spectra (Fig. 1a) show two plasmon peaks: one at 237 nm ((π-π^* transition) and the other at 300 nm (n-π*). The dye molecules (C153) exhibit three absorption peaks at wavelengths of 434 nm, 260 nm, and 220 nm. The UV-vis spectra of the GO-C153 system demonstrate that the GO SPR band at 237 nm redshifts and overlaps with the dye peak at 260 nm, generating a new band in the complex at 256 nm. The shifting of the SPR band is due to a significant "π-π" interaction between GO and C153 in the GO-C153 complex. Zhang Y et al.[75] reported a similar SPR band shifting of GO in the tannic acid-GO combination.

The SPR band in the GO-C153-CTAT/16-4-16 complex is slightly more red-shifted (Fig. S4 C&D). To ensure the stability of the complexes, the SPR band change was observed throughout time. This SPR band has been seen to remain consistent throughout time, indicating that GO, C153, and surfactants formed a stable combination. Over time, the complex's absorbance value drops as the dye's adsorption on the graphene oxide nanosheet becomes more visible.

4.8. DLS and Zeta potential measurements of binary and ternary system:

DLS measurements were carried out to investigate the change in GO hydrodynamic diameter (D_h) in the presence of C153 and surfactants. (Fig. 14). The size and surface charge of the complexes have a considerable influence on their stability in solution. GO has a single DLS peak in an aqueous solution at roughly 310 nm, which is consistent with earlier work.[76] C153 caused a modest increase in the D_h of GO (~420 nm). When the surfactants were significantly higher than their CMC, the diameter of the ternary complex (GO-C153-CTAT/16-4-16) increased only slightly in compared to GO. However, there was a relatively large value of D_h when the surfactant concentration was much below the CMC. The diameter of the complexes obtained by TEM coincides well with the DLS (Table 7), despite the fact that the value is slightly less. This discrepancy is caused by the fact that DLS measures the size of the nanoparticles when solvent molecules are still attached to their surface, or their hydrodynamic size. The mean size measurements clearly show that all of the composites have diameters between 300 and 500 nm (Table 7), which indicates that the GO composites are sufficiently colloidally stable in solution. The stability of the complexes was further confirmed by measuring the zeta potential. Due to its numerous oxygen-containing groups, GO has a negative zeta potential (-33.1 mV) in aqueous media. When C153 is present, the negative zeta value of GO slightly drops to -25.7 mV. When the negative potential of the GO-C153 composite vanished in the presence of surfactants, a general positive potential of the complex was seen (both below and above the CMC of surfactants). In this case, the total zeta potential of the composite was between 25 and 40 mV. The colloidal stability of GO complexes in solution is guaranteed by these zeta potential values.

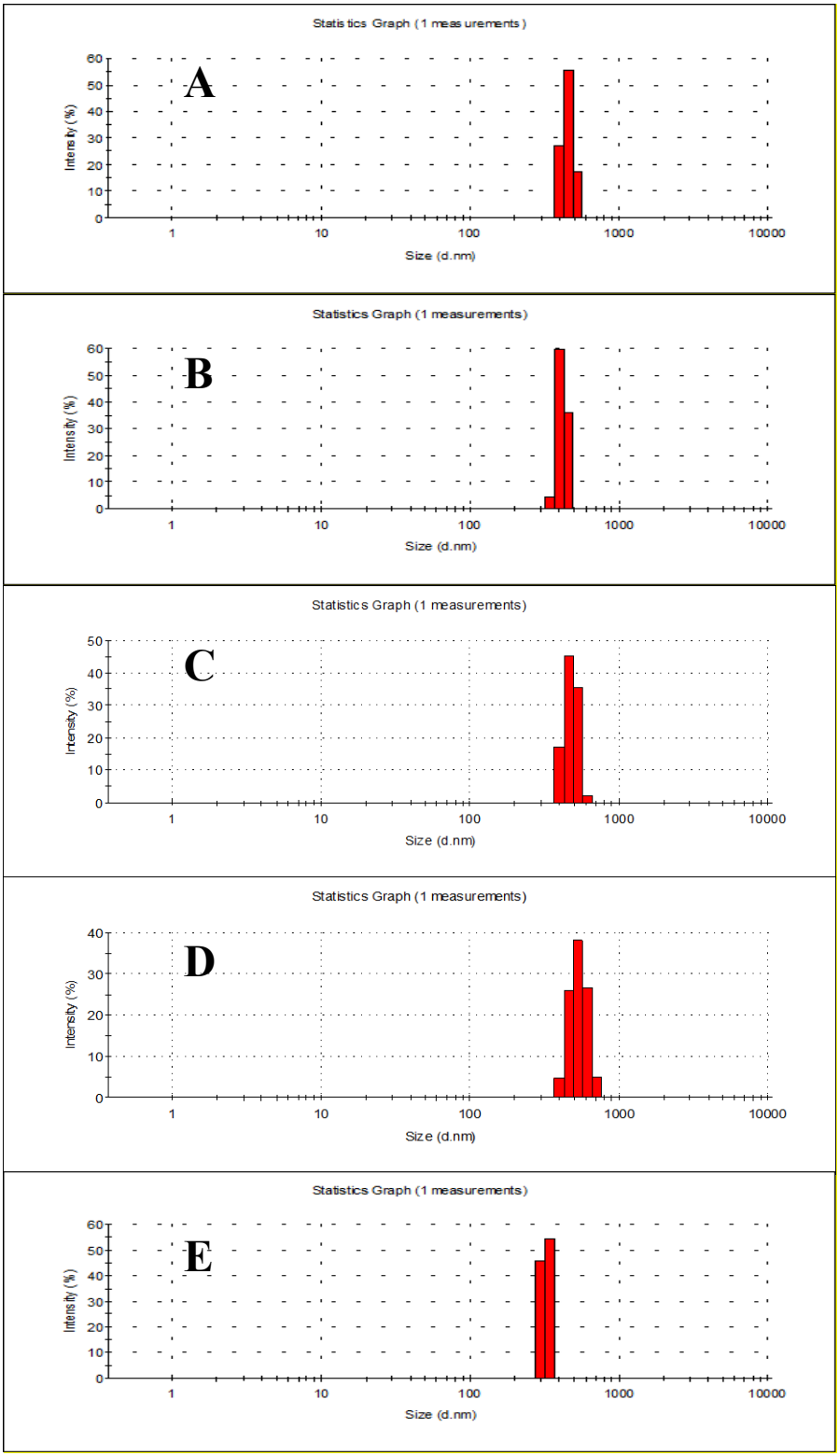

Fig. 14 Variation of hydrodynamic diameter (D_h) of GO in the presence of C153 and surfactants (A) GO-C153, (B) GO-C153-CTAT (below CMC), (C) GO-C153-CTAT (above CMC), (D) GO-C153-16-4-16 (below CMC), (E) GO-C153-16-4-16 (above CMC).

4.9. TEM micrographs analysis (GO-C153 and GO-C153-CTAT/16-4-16)

GO-C153 TEM micrographs (Fig. 15A & 15B) show many strongly contrasted circular black dots in comparison to pure GO flakes (Fig. 1f). The high contrast indicates the aggregation of dye molecules concentrated on the surface of GO sheets, as the aggregate's high charge density blocks the flow of electrons created and accelerated by the microscope. Surprisingly, the bulk of the black spots disappeared and the GO sheets became practically transparent when surfactants were present (above their CMC) (Fig. 15C, 15D, 15E, 15F). This could be the result of dye molecules dissolving in the presence of surfactants. Therefore, it is evident from the TEM micrographs that dye molecules aggregate in the presence of GO and disaggregate in the presence of surfactants in the ternary system.

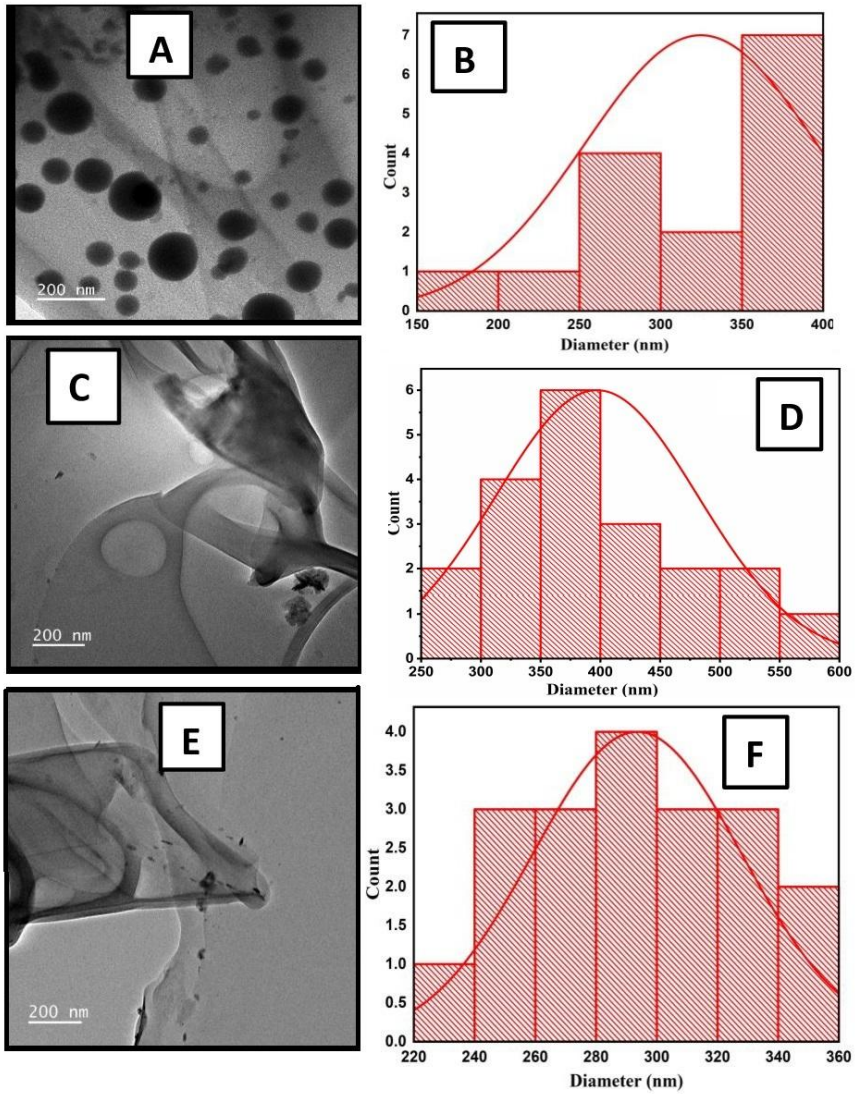

Fig. 15 TEM micrographs and corresponding size distribution plots of (A)&(B) for GO-C153, (C)&(D) for GO-C153-CTAT and (E)&(F) for GO-C153-16-4-16, respectively.

5. Conclusion:

The work investigates the interaction of laser dye C153 with GO nanosheets in an aqueous dispersion, which leads to the creation of GO-C153 composites. The dye's highest absorption peak shifts blue as the GO concentration increases, indicating the creation of an H-aggregate. Fluorescence investigations revealed a drop in fluorescence intensity and a considerable blue shift in the highest fluorescence band, confirming the H-aggregate's formation. UV-Vis and lifetime plots indicate static and dynamic mechanisms that cause fluorescence quenching of C153 in the presence of GO dispersion. The aggregation and photophysical properties of the dye are considerably altered in the presence of surfactant solutions (CTAT and 16-4-16), with gemini surfactant having a larger probability of dye-surfactant aggregate formation than CTAT due to its increased hydrophobicity. The spectroscopic analysis of the GO-C153-CTAT/16-4-16 ternary system revealed a decrease in fluorescence intensity when GO was present, with a significant blue shift in the maximum peak, which is bounced back to its original peak position along with an increase in intensity in the presence of surfactants. This ternary system functions as an optimum fluorescence turn-off/on system. The colloidal stability of the GO-C153 and GO-C153-CTAT/16-4-16 systems was evaluated by measuring the system's SPR band, DLS, and Zeta potential, demonstrating that all GO complexes were sufficiently colloidally stable. The C153-GO composite might be employed as an initial micelle detection fluorescence sensor, which could have applications in biological and biomedical systems.

REFERENCES:

1. C. N. R. Rao, A. K. Sood, K. S. Subrahmanyam and A. Govindaraj, *Angewandte Chemie International Edition*, 2009, **48**, 7752-7777.
2. K. S. Novoselov, A. K. Geim, S. V. Morozov, D. Jiang, M. I. Katsnelson, I. V. Grigorieva, S. V. Dubonos and A. A. Firsov, *Nature*, 2005, **438**, 197-200.
3. K. S. Novoselov, A. K. Geim, S. V. Morozov, D. Jiang, Y. Zhang, S. V. Dubonos, I. V. Grigorieva and A. A. Firsov, *science*, 2004, **306**, 666-669.
4. A. K. Geim and K. S. Novoselov, *Nature Materials*, 2007, **6**, 183-191.
5. K. Novoselov and V. Fal, *Nature*, 2012, **490**, 192-200.
6. A. Geim, *Science* 2009, **324**.

7. S. Zhang, K. Yang, L. Feng and Z. Liu, *Carbon*, 2011, **49**, 4040-4049.

8. L. Qu, Y. Liu, J.-B. Baek and L. Dai, *ACS Nano*, 2010, **4**, 1321-1326.

9. X. Dong, L. Wang, D. Wang, C. Li and J. Jin, *Langmuir*, 2012, **28**, 293-298.

10. X. Wang, L. Zhi, N. Tsao, Ž. Tomović, J. Li and K. Müllen, *Angewandte Chemie International Edition*, 2008, **47**, 2990-2992.

11. G. Eda and M. Chhowalla, *Advanced Materials*, 2010, **22**, 2392-2415.

12. D. Kozawa, Y. Miyauchi, S. Mouri and K. Matsuda, *The Journal of Physical Chemistry Letters*, 2013, **4**, 2035-2040.

13. S. K. Cushing, M. Li, F. Huang and N. Wu, *ACS Nano*, 2014, **8**, 1002-1013.

14. P. Dutta, D. Nandi, S. Datta, S. Chakraborty, N. Das, S. Chatterjee, U. C. Ghosh and A. Halder, *Journal of Luminescence*, 2015, **168**, 269-275.

15. K. P. Loh, Q. Bao, G. Eda and M. Chhowalla, *Nature Chemistry*, 2010, **2**, 1015-1024.

16. C. Galande, A. D. Mohite, A. V. Naumov, W. Gao, L. Ci, A. Ajayan, H. Gao, A. Srivastava, R. B. Weisman and P. M. Ajayan, *Scientific Reports*, 2011, **1**, 85.

17. M. Li, S. K. Cushing, X. Zhou, S. Guo and N. Wu, *Journal of Materials Chemistry*, 2012, **22**, 23374-23379.

18. S. K. Pal, *Carbon*, 2015, **88**, 86-112.

19. T. Szabó, O. Berkesi, P. Forgó, K. Josepovits, Y. Sanakis, D. Petridis and I. Dékány, *Chemistry of Materials*, 2006, **18**, 2740-2749.

20. D. A. Dikin, S. Stankovich, E. J. Zimney, R. D. Piner, G. H. B. Dommett, G. Evmenenko, S. T. Nguyen and R. S. Ruoff, *Nature*, 2007, **448**, 457-460.

21. R. Hu, H. Gou, Z. Mo, X. Wei and Y. Wang, *Ionics*, 2015, **21**, 3125-3133.

22. X. Qi, K.-Y. Pu, X. Zhou, H. Li, B. Liu, F. Boey, W. Huang and H. Zhang, *Small*, 2010, **6**, 663-669.

23. J. Huang, X. Gao, J. Jia, J.-K. Kim and Z. Li, *Analytical Chemistry*, 2014, **86**, 3209-3215.

24. L. Yang, H. Zhao, Y. Li, X. Ran, G. Deng, X. Xie and C.-P. Li, *ACS Applied Materials & Interfaces*, 2015, **7**, 26557-26565.

25. R. Cheng, Y. Liu, S. Ou, Y. Pan, S. Zhang, H. Chen, L. Dai and J. Qu, *Analytical Chemistry*, 2012, **84**, 5641-5644.

26. F. Liu, J. Y. Choi and T. S. Seo, *Biosensors and Bioelectronics*, 2010, **25**, 2361-2365.

27. N. Karousis, A. S. D. Sandanayaka, T. Hasobe, S. P. Economopoulos, E. Sarantopoulou and N. Tagmatarchis, *Journal of Materials Chemistry*, 2011, **21**, 109-117.

28. D. Dinda, B. K. Shaw and S. K. Saha, *ACS Applied Materials & Interfaces*, 2015, **7**, 14743-14749.

29. H. Dong, W. Gao, F. Yan, H. Ji and H. Ju, *Analytical Chemistry*, 2010, **82**, 5511-5517.

30. Y. Liu, C. Liu and Y. Liu, *Applied Surface Science*, 2011, **257**, 5513-5518.

31. X.-F. Zhang and F. Li, *Journal of Photochemistry and Photobiology A: Chemistry*, 2012, **246**, 8-15.

32. K. C. Hannah and B. A. Armitage, *Accounts of Chemical Research*, 2004, **37**, 845-853.

33. M. Kerker, *Journal of Colloid and Interface Science*, 1985, **105**, 297-314.

34. L. Zhang and J. M. Cole, *Journal of Materials Chemistry A*, 2017, **5**, 19541-19559.

35. R. Karmakar and A. Samanta, *The Journal of Physical Chemistry A*, 2002, **106**, 4447-4452.

36. H. Jin, G. A. Baker, S. Arzhantsev, J. Dong and M. Maroncelli, *The Journal of Physical Chemistry B*, 2007, **111**, 7291-7302.

37. M. El-Kemary and W. Rettig, *Physical Chemistry Chemical Physics*, 2003, **5**, 5221-5228.

38. H. Zhu, M. Li, J. Hu, X. Wang, J. Jie, Q. Guo, C. Chen and A. Xia, *Scientific Reports*, 2016, **6**, 24313.

39. S. N. Alam, N. Sharma and L. Kumar, *Graphene*, 2017, **6**, 1-18.

40. F. M. Menger, J. S. Keiper and V. Azov, *Langmuir*, 2000, **16**, 2062-2067.

41. L. Shahriary and A. A. Athawale, *Int. J. Renew. Energy Environ. Eng*, 2014, **2**, 58-63.

42. T. Zhang, D. Zhang and M. Shen, *Materials Letters*, 2009, **63**, 2051-2054.

43. K. Zhang, Y. Zhang and S. Wang, *Scientific Reports*, 2013, **3**, 3448.

44. S. He, X. Liu, P. Yan, A. Wang, J. Su and X. Su, *RSC Advances*, 2019, **9**, 4908-4916.

45. F. Zeng , Z. Sun, X. Sang, D. Diamond, K. T. Lau, X. Liu and D. S. Su, *ChemSusChem*, 2011, **4**, 1587-1591.

46. E. Bozkurt, M. Acar, Y. Onganer and K. Meral, *Physical Chemistry Chemical Physics*, 2014, **16**, 18276-18281.

47. H. Wu, H. Wang, L. Xue and X. Li, *Journal of Colloid and Interface Science*, 2011, **353**, 476-481.

48. J. Zhang, L. Chen, B. Zeng, Q. Kang and L. Dai, *Spectrochimica Acta Part A: Molecular and Biomolecular Spectroscopy*, 2013, **105**, 74-79.

49. M. Şinoforoğlu, B. Gür, M. Arık, Y. Onganer and K. Meral, *RSC Advances*, 2013, **3**, 11832-11838.

50. G. Jones, II and M. A. Rahman, *The Journal of Physical Chemistry*, 1994, **98**, 13028-13037.

51. I. M. Minisy, P. Bober, U. Acharya, M. Trchová, J. Hromádková, J. Pfleger and J. Stejska, *Polymer*, 2019, **174**, 11-17.

52. K. Erickson, R. Erni, Z. Lee, N. Alem, W. Gannett and A. Zettl, *Advanced Materials*, 2010, **22**, 4467-4472.

53. R. Patel, M. U. Mir, J. K. Maurya, U. K. Singh, N. Maurya, M. U. Parray, A. B. Khan, A. Ali., *Luminescence* **30**, 1233–1241 (2015).

54. S. Ghosh, S. Mondal, *Journal of Surface Science and Technology* **2012**, *28* (3-4), 179-195.

55. U. Bhattacharjee, C. Beck, A. Winter, C. Wells and J. W. Petrich, *The Journal of Physical Chemistry B*, 2014, **118**, 8471-8477.

56. N. Patra, B. Mandal, S. Ghosh, *Industrial & Engineering Chemistry Research,* **56**, 10044–10052 (2017).

57. Stern O, Volmer, M. On the quenching-time of fluorescence, Physik Zeitschr 20: 183-188 (1919).

58. H. M. Suresh Kumar, R. S. Kunabenchi, J. S. Biradar, N. N. Math, J. S. Kadadevarmath and S. R. Inamdar, *Journal of Luminescence*, 2006, **116**, 35-42.

59. D. Seth, S. Sarkar and N. Sarkar, *Langmuir*, 2008, **24**, 7085-7091.

60. P. Verma and H. Pal, *The Journal of Physical Chemistry A*, 2014, **118**, 6950-6964.

61. S. Seraj and S. Rouhani, *Journal of Fluorescence*, 2017, **27**, 1877-1883.

62. F. A. Wani, A.B. Khan, A.A Alshehri, M.A. Malik, R. Ahmad and R. Patel, *J. Mol. Liq.* **285**, 270–278 (2019).

63. M. J. Rosen and J. T. Kunjappu, *Surfactants and interfacial phenomena*, John Wiley & Sons 2012.

64. A. Asadzadeh Shahir, S. Javadian, B. B. M. Razavizadeh and H. Gharibi, *The Journal of Physical Chemistry B*, 2011, **115**, 14435-14444.

65. D. K. Chattoraj, *Adsorption and the Gibbs surface excess*, Springer Science & Business Media 2012.

66. R. Patel, A. B. Khan, N. Dohare, M. Maroof Ali & H. K. Rajor, *J. Surfactants Deterg.* **18**, 719–728 (2015).

67. F.A. Wani, Y. Kumar, A. Anand, A.B Bhat, K.A. Alzahrani, M.A. Malik, and R. Patel. *ChemistrySelect* **8**, (2023).

68. B. Gohain and R. K. Dutta, *Journal of Colloid and Interface Science*, 2008, **323**, 395-402.

69. Y. Liu, M. Liu, H. Yan, H. Liu, J. Liu, Y. Zhao, Y. Wu, Y. Zhang and J. Han, *Journal of Molecular Liquids*, 2021, **323**, 115073-115084.

70. T. Sharma, N. Dohare, M. Kumari, U.K. Singh, A.B. Khan, M.S. Borse, and R. Patel. *RSC Adv.* **7**, 16763–16776 (2017).

71. R. Królicki, W. Jarzęba, M. Mostafavi and I. Lampre, *The Journal of Physical Chemistry A*, 2002, **106**, 1708-1713.

72. Grueso, E., López-Pérez, G., Castellano, M. & Prado-Gotor, R. *J. Inorg. Biochem.* **106**, 1–9 (2012).

73. A. Maciejewski, D. R. Demmer, D. R. James, A. Safarzadeh-Amiri, R. E. Verrall and R. P. Steer, *Journal of the American Chemical Society*, 1985, **107**, 2831-2837.

74. T. Bayraktutan and Y. Onganer, *Journal of Luminescence*, 2022, **248**, 118947-1189.

75. Y. Zhang, S. Liu, W. Lu, L. Wang, J. Tian and X. Sun, *Sci. Technol.* **1**, 1142–1144 (2011).

76. I. Roy, D. Rana, G. Sarkar, A. Bhattacharyya, N. R. Saha, S. Mondal, S. Pattanayak, S. Chattopadhyay and D. Chattopadhyay, *RSC Adv.* **5**, 25357–25364 (2015).

Table 1. Time resolved fluorescence decay data of the emission from C153 and C153@GO composite in aqueous medium at room temperature.

[GO] (mg/L)	τ_1 (ps)	τ_2 (ns)	$< \tau >$ (ns)	χ^2
0	186.74 (-13.74)	1.69 (113.74)	1.89	1.29
10	231.61 (66.38)	1.96 (33.62)	0.81	1.05
20	220.62 (71.85)	1.99 (28.15)	0.71	1.23
30	118.36 (76.78)	2.03 (23.22)	0.56	1.19
40	128.93 (78.45)	2.14 (21.55)	0.55	1.20
50	99.88 (79.73)	2.01 (20.27)	0.48	1.08
60	10.03 (79.96)	1.78 (20.04)	0.36	1.17

Table 2. Various thermodynamics parameters of C153-surfactants interaction at room temperature by conductivity measurements

System	β (degree of counter ion dissociation)	$-\Delta G_m^0$ (kJ. mol^{-1})	ΔS_m^0 (J. K^{-1} mol^{-1})	$-\Delta H_m^0$ (kJ. mol^{-1})
CTAT-C153	0.58	14.18	105.02	90.84
CTAT	0.46	13.18	101.72	88.54
16-4-16	0.49	16.23	111.91	95.67
16-4-16-C153	0.56	18.62	119.96	101.34

Table 3. Various surface and micellar parameter of surfactants in absence and presence of C153 molecules

System	CMC (mM)	γ_{CMC} (mN m^{-1})	$10^6 \Gamma_{max}$ (mol m^{-2})	A_{min} ($A^{0\,2}$)	π_{CMC} ($mN\ m^{-1}$)	pC_{20}
CTAT	0.269	35.3	3.39	48.97	38.1	1.12
CTAT-C153	0.181	35.8	3.06	54.25	28.1	1.03
16-4-16	0.079	43.5	1.83	90.72	28.5	1.59
16-4-16-C153	0.030	45.7	2.02	82.19	18.0	1.44

Table 4. Determination of CMC (mM) for surfactants by various methods in the absence and presence of C153 molecules.

System	ST	Conductance	Absorbance	Fluorescence
CTAT	0.269	0.296		
CTAT-C153	0.181	0.185	0.195	0.179
16-4-16	0.079	0.080		
16-4-16-C153	0.030	0.035	0.038	0.031

Table 5. Time-dependent fluorescence decay data of pure C153 in the presence of various concentrations of CTAT surfactants in aqueous medium at 298K

[CTAT](mM)	τ_1 (ns)	τ_2 (ns)	$< \tau >$ (ns)	χ^2
0.011	1.63 (70.55)	7.31 (29.45)	2.12	1.12
0.033	1.67 (69.37)	8.15(30.63)	2.21	1.16
0.066	1.64 (68.24)	7.93(31.76)	2.19	1.08
0.109	1.66 (68.16)	7.74(31.84)	2.2	1.02
0.173	1.7 (65.54)	6.45(34.46)	2.28	1.1
0.294	1.92 (49.64)	4.66(50.36)	2.73	1.11
0.409	1.88 (31.76)	3.95(68.24)	2.93	0.97

Table 6. Time-resolved fluorescence decay data of C153 in the presence of various concentrations of 16-4-16 surfactant.

[16-4-16] (mM)	τ_1 (ns)	τ_2 (ns)	$< \tau >$ (ns)	χ^2
0.005	1.65(60.24)	7.14(34.76)	2.38	1.08
0.014	1.71(61.83)	7.52(38.17)	2.43	0.99
0.028	1.84(61.69)	6.36(38.31)	2.53	1.06
0.046	1.87(56.35)	5.21(43.65)	2.59	1.09
0.072	1.89(47.5)	4.32(52.5)	2.69	1.02
0.114	1.88(30.88)	3.76(69.12)	2.87	1.02
0.17	1.35(10.88)	3.33(89.12)	2.87	1.04

Table 7. A summary of size (diameter) and surface charge measurements of GO in the presence and absence of C153 & surfactants.

Complex	Size (nm)		Zeta potential (mV)
	DLS	TEM	
GO	310	285	-33.1
GO-C153	420	326	-25.7
GO-C153-CTAT (below CMC)	476		24.6
GO-C153-CTAT (above CMC)	415	395	28.8
GO-C153-16-4-16 (below CMC)	515		33.5
GO-C153-16-4-16 (above CMC)	321	296	40.9

The Standard deviations in measuring DLS and Zeta potential are within 7% and 9% respectively.

Supplementary Section

1. Synthesis of graphene oxide using modified Hummer's method:

A temperature-controllable magnetic stirrer was used to continuously stir a mixture of 1 gm of graphite flakes and 0.5 gm of $NaNO_3$ in a 250 mL round bottom flask while adding 25 mL of concentrated H_2SO_4. After two hours, the aforementioned solution was gradually supplemented with 3 g of KMnO4 while maintaining the temperature below 25^0C in an ice bath to prevent overheating and explosion. While the $KMnO_4$ was added, the mixture was continuously stirred. The addition of $KMnO_4$ resulted in the appearance of a greenish hue (Figure S1(A)). Following the addition of $KMnO_4$, the mixture was vigorously agitated at 35°C for a whole night. The resulting solution, which had taken on the appearance of a mass and was coloured brown, was then placed into a 500 mL water beaker while being vigorously mixed. The suspension was then treated with a 10% solution of 30% H_2O_2 to guarantee that the reaction with the KMnO4 was completed. After adding H_2O_2, a pale-yellow glazy look (cf. Figure S1(B)) emerged. The resulting combination was centrifuged and decanted of the supernatant liquid before the brown-

black mass (Figure S1(C)) was taken and placed in a watch glass. The mixture was then washed with HCl and H_2O_2, respectively. Thus, graphene oxide sheets were produced after 4-5 days of drying at temperatures below 50°C. These sheets were broken up in a mortar before being sent through a molecular sieve. Finally, black GO power was attained.

Fig. S1: Synthetic steps of graphene oxide using modified Hummer's method.

2. **Synthesis of N, N'- di hexadecyl - N, N, N', N'- tetramethyl-N, N'-but-2-ynediyl-di-ammonium chloride (16-4-16):**

Di cationic Gemini surfactant was prepared as per the protocol reported by Menger et. al. [40]. N, N-Dimethyl hexadecyl amine (0.5 gm, 3.2 mmol) was transferred into a 250 mL round-bottomed flask and dissolved in 20 mL dry acetone. After dissolution, 0.3 gm (1.4 mmol) 1,4-dichloro-2-butylene was added dropwise to the solution taken in the round-bottomed flask at room temperature with constant stirring. After complete addition, the resultant solution was stirred at room temperature overnight. White solids appeared after the first 2 hours of stirring. After overnight stirring, the obtained white solid was filtered, washed with acetone, dried under a vacuum, and recrystallized with hot acetone. (Yield: 75%, m.p.-215^0 C (dec.))

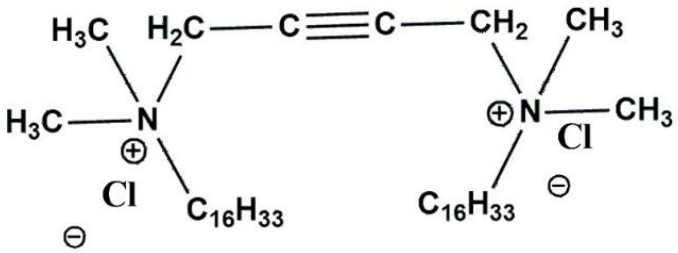

Fig. S2: Structure of synthesized cationic Gemini surfactant (16-4(2-yen)-16) (16 -4-16)

3. Characterisation of 16-4-16 surfactant:

^{1}H NMR:

^{1}H NMR: (300MHz, $CDCl_3$): δ5.17(s,4H), 3.63(t,4H), 3.43(s,12H), 1.75(m,4H), 1.34 1.05(m,52H), 0.85 (t, 6H)

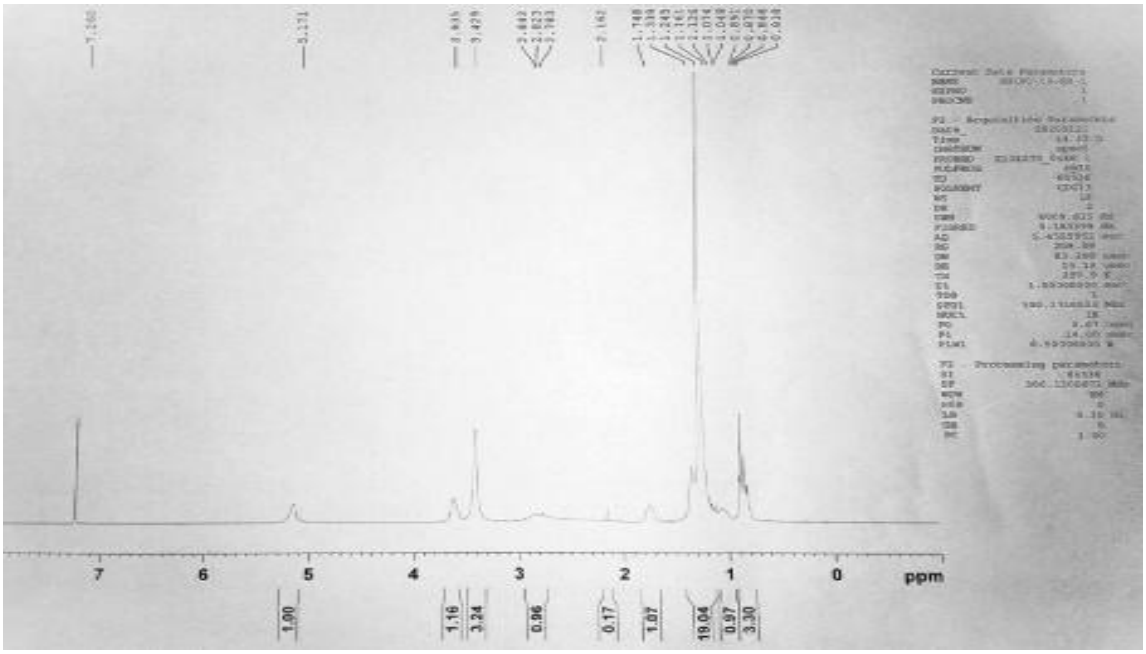

Fig. S3: ^{1}H NMR of synthesised 16-4-16 gemini surfactant

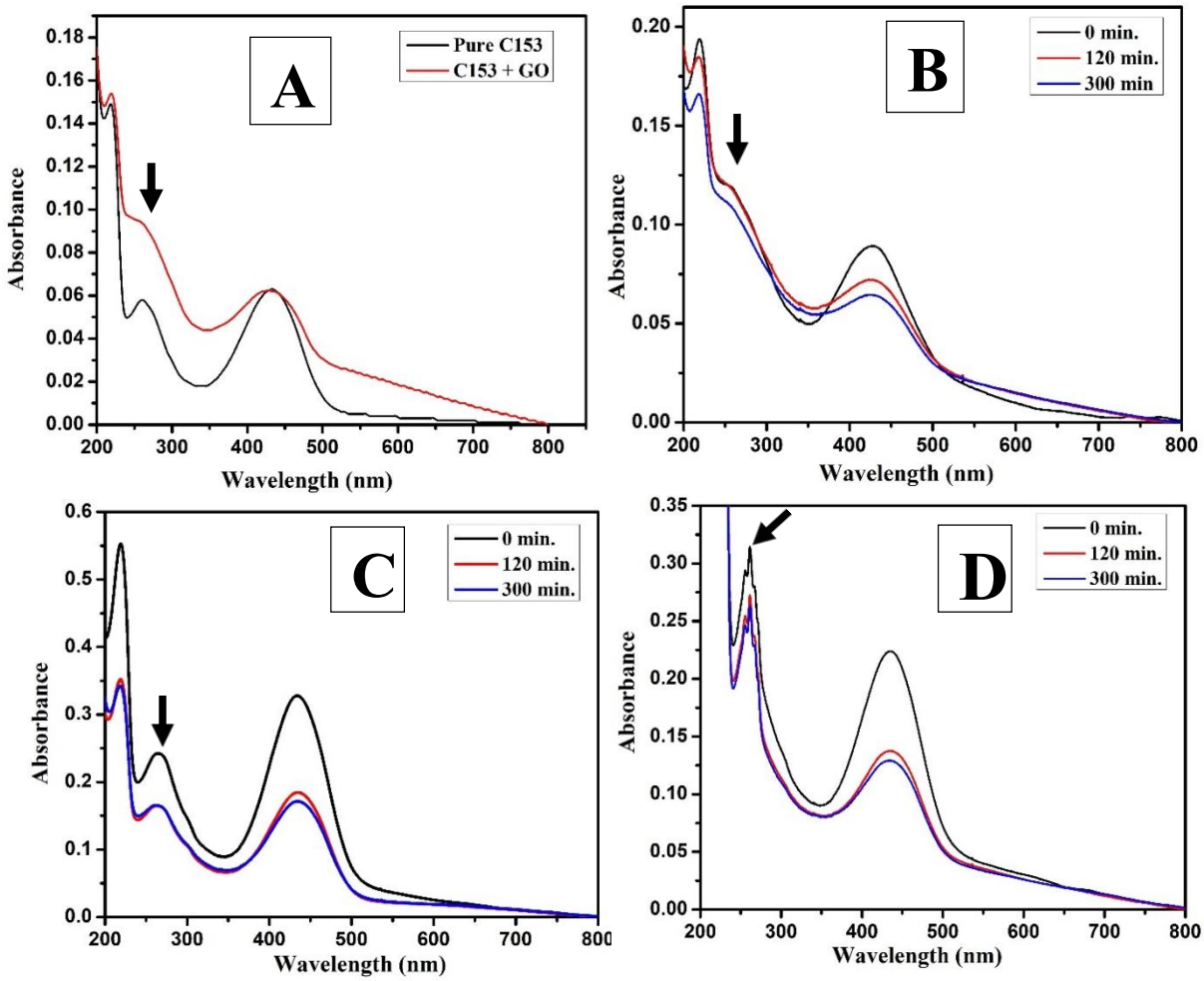

Fig. S4 UV-Vis spectra of C153 & GO-C153 (A). The change in UV-Vis spectra over time of (B) GO-C153, (C) GO-C153-16-4-16, and (D) GO-C153-CTAT to study the change in surface plasmon (SPR) band of GO complexes. The SPR band was highlighted by

Chapter-II

Hydrophobicity-directed structural alteration in cytochrome C induced by bile salts: Physicochemical, spectroscopic, and atomic force microscopy studies with molecular docking analysis

Hydrophobicity-directed structural alteration in cytochrome C induced by bile salts: Physicochemical, spectroscopic, and atomic force microscopy studies with molecular docking analysis

Abstract:

The growing application of bile salts in diverse fields has spurred an investigation into how they interact with biological macromolecules, particularly proteins. The current study shows a comprehensive and comparative analysis of the interaction between the bile salts, sodium cholate (NaC) and sodium deoxycholate (NaDC), with a small heme protein, cytochrome C (Cyt C) in a phosphate buffer medium. Cytochrome C, an iron-containing metalloprotein with a redox characteristic found in cell mitochondria, plays an important part in the cell apoptotic cascade. The interaction was studied using spectroscopic, thermodynamic, and electrochemical measurements and molecular docking analysis. The adsorption isotherm analysis indicates that the presence of Cyt C significantly improves the aggregation behavior and surface activity of bile salts. The binding isotherms based on UV-vis spectroscopy measurements demonstrate that three distinct zones describe the interaction between bile salts and Cyt C, which were also successfully replicated from the variation in steady-state fluorescence intensity of the tryptophan moiety of Cyt C. Both the NaDC-Cyt C and NaC-Cyt C systems showed a distinct calorimetric profile pattern. ITC measurements identified the variations in the enthalpy of micellization of bile salt-Cytochrome C. CD spectroscopy measurements revealed an 8–10% alpha helicity change for Cyt C by exposure to NaC/NaDC. Cyt C's hydrodynamic diameter changed significantly when bile salts were present, according to DLS measurements. As bile salt concentration rose, the contribution of the monomeric peak dropped and the aggregated peak rose as a result of the formation of protein-bile salt complexes. According to electrochemical studies, the presence of NaDC inhibits the electron transfer mechanism at Cyt C's electroactive core. On the other hand, the presence of NaC facilitates this process. The Benesi-Hildebrand equation was used to determine the binding constant for the protein-bile salt interaction system, and the findings indicate that NaDC binds to Cyt C more firmly than NaC. Lastly, we conducted molecular docking investigations, and the outcomes of the molecular simulations matched those of the experiments. The overall experimental analysis's findings suggest that, in addition to electrostatic interaction, bile salt hydrophobicity plays a major role in protein structural change. In biological and biomedical domains, Cyt C's electron transfer mechanism is highly significant when it is modulated in the presence of NaC/NaDC.

1. Introduction:

In recent years, steroidal macrocycle compounds have garnered a lot of attention in domains such as pharmacology, sensing, drug delivery, supramolecular chemistry, and nanotechnology. Due to their exceptional conformational flexibility and ability to host guest molecules, they are essential tools for designing functional and responsive chemical systems. Among the various types of macrocyclic systems, those derived from or inspired by biological molecules, such as bile salts, have emerged as particularly appealing due to their biocompatibility and amphiphilicity. Bile acids and other steroidal components are common building blocks in supramolecular chemistry.[1,2] Bile acid analogues have demonstrated a wide range of biological applications, including anti-tumour, drug carrier, antifungal, and antibacterial action.[3-5] Bile salts, which are unique among biosurfactants, are created by the liver and secreted into the duodenum when food is consumed. They are biologically active amphiphilic molecules having a rigid steroidal backbone and a pliable aliphatic tail. The steroid skeleton has hydrophilic and hydrophobic faces, with α-oriented hydroxyl groups on the concave surface and β-oriented methyl groups on the convex surface.[6-10] Bile salts aid in the solubilization and absorption of fats and other lipid-soluble compounds in the body. Bile salts have more complex aggregation properties than traditional micelle-forming amphiphiles. Several investigations have been conducted to interpret bile salts' self-aggregation behavior. Bile salts form primary aggregates at low concentrations due to the hydrophobic interaction of the monomeric unit's convex surface. The hydrophilic groups of the basic aggregates are thought to face outward.[11] At increasing bile salt concentrations, the main aggregates clump together to produce higher-order aggregates with an extended rod-like structure.[12] Bile salts make excellent host systems for encapsulating a wide range of hydrophobic and hydrophilic guest molecules due to their numerous tuneable binding sites.[13-15] Bile salts are extremely beneficial in a variety of protein purification stages, including chromatographic separation.[16,17] The level of protein purification by bile salts is strongly reliant on the nature of the interaction between proteins and bile salts. As a result, quantitative studies of bile salt-protein interactions are critical for gaining a comprehensive understanding of bile salt-mediated protein purification. The current inquiry of the interactions of bile salts with diverse biological macromolecules, particularly proteins, has been prompted by an increase in the use of bile salts in a variety of fields, particularly medication delivery and pharmaceuticals.[18,19] Protein-bile salt interactions monitor a variety of physiological processes, making them an important first step in identifying new therapeutic targets for the treatment and prevention of metabolic diseases, as well as in understanding intracellular lipid transport.[20] Bile salts can also be used in proteomics, which involves protein

purification, separation, and crystallization, owing to their mild detergent qualities.[21,22] Bile salts are also used in pharmaceutical formulations to keep drugs stable, increase solubility, and improve absorption, permeation, and bioavailability.[23,24] Bile salts have lately been used as substrates for derivatives suitable as building blocks for the construction of new superstructures, sparking inventive concepts for producing supramolecular versions of biological macromolecules.[25,26] Although their physiological roles are well understood, less is known about their ability to act as supramolecular building blocks and molecular hosts for protein molecules.

In parallel, Cyt C is an iron-containing metalloprotein that has been structurally described in both solution and crystalline forms. It is a tiny, globular, water-soluble protein with a long polypeptide of 104 amino acid residues. The heme group of Cyt C is linked to four amino acids (Cys 14, His 18, Met 80, and Cys 17) and non-covalent side chains that stiffen the internal structure around the heme group. As a result, structural changes to the protein in the presence of different ligands are extremely complicated. The presence of the heme group enables Cyt C to perform a redox reaction. The biological respiratory chain relies on cytochrome C, which accepts electrons from cytochrome C reductase and delivers them to cytochrome C oxidase. Cyt c activity is essential for mitochondrial function and is connected to a variety of other activities, including cell proliferation, apoptosis, cellular differentiation, and cell cycle regulation.[27] Cyt C also contributes to the initiation of apoptosis through abnormal cytoplasmic accumulation, which triggers signalling cascades that cause cell dysfunction.[28] Cyt C's release from mitochondria into the cytoplasm has been demonstrated to activate or initiate apoptosis by interacting with cytoplasmic proteins such as caspase, TIB, Bcl-2, and apaf-1.[29] Mitochondrial dysfunction leads to cell death and is connected with a number of illnesses.[30] Furthermore, Cyt C malfunction can affect the mitochondrial membrane potential (MMP), resulting in respiratory chain dysfunction.

The study of bile salt-protein interactions within a macrocyclic framework brings together supramolecular chemistry and bioengineering. It promotes global initiatives in bio-nanomaterials, personalized medicine, and environmentally friendly technology. Bio-derived macrocyclic systems have the potential to minimize reliance on synthetic polymers and boost environmentally friendly chemical processes, making them more important to governance and policy.

There are very few reports in the literature about the influence of bile salts on protein structure and stability. Mukherjee et al.[31] investigated the interaction of HSA proteins with a series of

bile salts, sodium cholate (NaC), sodium deoxycholate (NaDC), and sodium taurocholate (NaTC) in their pre- and post-micellar concentrations and discovered that the hydrophobic residue of bile salts plays an important role in the interaction. Mohanty et al. conducted an intriguing comparison of single and double tryptophan residue-containing proteins (HSA and BSA, respectively) with sodium deoxycholate (NaDC) interactions.[32] Interaction occurs in three zones, although no significant alteration in the α helix was found. Bile acids bind to HSA subdomain IB, disrupting the interhelical π-π stacking interaction between Tyr138 and Tyr166, as observed by Zsila et al.[33]

The majority of study in the literature focuses on the interaction of bile salts and albumin protein. However, it is unlikely that the literature contains a full examination of bile salt interactions with diverse heme proteins. The interaction of the electron transport heme protein Cyt C with bile salts is critical for cell apoptosis (death). Bile salts, particularly at greater concentrations, function as cytotoxic agents in the cell death process. Hydrophobic bile salts can damage the mitochondrial membrane, causing the release of a variety of pro-apoptotic chemicals. Cyt C is a major pro-apoptotic protein produced by mitochondrial cells that is principally responsible for the apoptotic process. Although bile salts and Cyt C do not co-localize, they can emerge upon cell death, increasing the likelihood of contact outside of their original location. Here, We aim to elucidate the interaction between bile salts (sodium cholate (NaC)/sodium deoxycholate (NaDC)) and Cyt C in phosphate buffer at a physiological pH of 7.4. We conducted many interfacial, spectroscopic, thermodynamic, electrochemical, and morphological studies to investigate the specific interaction. Molecular docking studies support the experimental findings. Our findings indicate that bile salts can efficiently regulate the structure and electron transfer mechanism of Cyt C, which is extremely useful in the biological, biomedical, and biotechnological areas.

2. Experimental Section:

2.1 Materials:

Horse heart cytochrome C (Cyt C), sodium cholate (NaC), and sodium deoxycholate (NaDC) were purchased from Sigma-Aldrich Corporation (U. S. A). Bile salts (NaDC/NaC) were recrystallized in ethanolic solution[29] before tensiometric measurements. All sample solutions were prepared in a sodium phosphate buffer (10 mM) with a pH of 7.4. A CL 54 pH meter (Toshniwal Pvt. Ltd., India) was used to test pH with an accuracy of $\pm$ 0.01. The protein solution concentration was maintained at 5 μM throughout the investigation, except for CD spectroscopy, where 2.5 μM proteins were used for instrumentation. The concentration of Cyt

C was estimated using absorption spectral measurements, utilizing the molar extinction coefficient (ε) value of 106100 M^{-1} cm^{-1} at 409 nm for Cyt C.[30]

Sodium dihydrogen phosphate (NaH_2PO_4) and disodium hydrogen phosphate (Na_2HPO_4) were AR-grade products purchased from Merck, India. All experiments were conducted using highly pure double distilled water, with the temperature being maintained at a constant 298 ± 0.2 K.

2.2 Instrumentation

2.2.1 Tensiometry: Using the ring detachment approach, tensiometric measurements have been made using a calibrated du Nouy tensiometer (Kruss, Germany). A platinum ring, cleaned by double distilled water followed by acetone and burned shortly until glowing in a flame of ethanol before every experiment, was used for this purpose. A 5 mL protein solution sample was taken in a corning glass container, and a concentrated (about 15 times the critical micelle concentration (CMC)) bile salt solution was added dropwise using a Hamiltonian micro syringe. Each tensiometric value was taken after a 5-minute equilibration period. The data was collected with a precision of $\pm 1\ mNm^{-1}$.

2.2.2 UV-vis spectroscopy: Absorption spectral measurements were performed using a UV-Vis spectrometer model 1601 (Shimadzu, Japan). A matched set of quartz cuvettes with a 0.5 cm path length was used in this study. To cancel out the contribution of added bile salts to the absorption spectra of Cyt C solution during its optical titration, an equal volume of bile salt was added both in the sample and reference cell (where buffer solution was used as reference). The solution was mixed homogeneously before taking every spectrum. Errors in measurements were within $\pm$ 3 %.

2.2.3 Steady-state fluorescence measurements: Using a PerkinElmer LS 55 (U.S.A) luminescence spectrometer, fluorescence measurements were made. A constant temperature (at $298 \pm 0.1\ K$) was maintained throughout the experiment by using a PerkinElmer fluorescence Peltier system (PTP1) connected to the instrument. A quartz cuvette with a 1 cm path length was filled with 2.5 mL of the Cyt C solution and the emission spectra were recorded in the wavelength range of 295-500 nm. To study the intrinsic fluorescence of Cyt C, the sample was excited at 280 nm using a 5 nm excitation and emission slit. During the experiment, the scan rate was fixed at 250 nm/min.

2.2.4 Circular Dichroism (CD) spectroscopy: To study the conformational changes of protein molecules, CD spectra have been recorded in the far-UV region (200-260 nm) using a Jasco spectropolarimeter (J-815). A pair of quartz cuvettes with a path length of 1 cm was used to

measure the spectra in the nitrogen inert atmosphere. The protein solution concentration was 2.5 μM, and the scan speed was 250 nm/min. Using a Neslab RTE-111 rotating water bath attached to water-jacketed quartz cuvettes, the sample temperature was kept constant at $298 \pm 0.2\,K$. The secondary structures of Cyt C were calculated from CDNN 2.1 software. The following equation has been used to express the CD data as mean residue ellipticity (MRE) in deg$cm^2 dmol^{-1}$.

$$\mathbf{MRE}=\theta_{obs}/\mathbf{10nl[c]} \quad \mathbf{(1)}$$

where [c] is the molar concentration of proteins, n represents the number of amino acid residues present in protein molecules, l is the path length of the cell, and θ_{obs} is CD in mdeg.

2.2.5 Dynamic light scattering (DLS) measurements: DLS measurements were carried out at 632.8 nm a Nano ZS Zetasizer (Malvern, UK) at 90° scattering angle with a He-Ne laser at room temperature. Before starting each measurement, every sample was filtered three times using a Whatman syringe of 0.2 μM pore size. For each experiment, 15 consecutive measurements were made, and their average value was taken. The Stokes-Einstein equation was used to determine the hydrodynamic radius (R_h) of the particles, based on a translational diffusion coefficient and an autocorrelation analysis of scattered light-intensity data

$$\mathbf{D}=K_B\mathbf{T}/3\pi\eta\mathbf{d} \quad \mathbf{(2)}$$

Where D is the diffusion coefficient, T is the Kelvin temperature, K_B is the Boltzmann constant, d is the diameter, and η is the viscosity of the solution.

2.2.6 Cyclic voltammetry (CV) study: Electrochemical measurements were carried out at 298 K using a computer-aided potentiostat/galvanostat instrument from AUTOLAB Company and a standard three-electrode system. A large Pt foil (1 cm x 1 cm) served as the counter electrode, a Pt wire as the working electrode, and a calomel electrode (Hg_2Cl_2) as the reference electrode. All electrochemical data were compared to a saturated calomel electrode (SCE) at 298 K. Cyclic voltammograms of 14 mL of native Cyt C (10 μM) were recorded in a 10 mM phosphate buffer with a pH of 7.4, over a potential range of 50 mV/s. After that, surfactants were added to the native protein solution, and the data was taken after obtaining a steady cycle. Before each experiment, freshly prepared nitrogen gas was purged into the protein solution.

2.2.7 Isothermal titration calorimetry (ITC) measurements: A Microcal ITC-200, Malvern, UK, instrument was employed for the isothermal titration calorimetry (ITC) investigations. During the experiments, the temperature was maintained at 298K. Each ITC experiment comprised 19 injections of bile salt from the syringe into the protein sample in

the cells spaced 180 s apart. 300 mL protein solution (5 μM) was taken in the cell, and 2 μL bile salts (60 mM NaDC and 120 mM NaC) solution were added from a syringe in every single injection. The heat absorbed or emitted at each stage of surfactant addition owing to interaction with protein was recorded, and using ITC software, the collected data was analyzed.

2.2.8 Atomic force microscopy (AFM) measurements: AFM was used to distinguish the tropological change of protein molecules in the presence of bile salts. AFM imaging was performed on the Innova-S2 instrument (Bruker, USA) in the trapping mode. A 10 μM Cyt C solution (in the absence and presence of bile salts above its CMC) was drop cast on mica foil and the sample was dried overnight inside a desiccator. Finally, after suitable drying, the AFM experiments were performed. The AFM image was analyzed using WSxM 5.0 software.

2.2.9 Theoretical: The crystalline structure of cytochrome C was obtained from the RSC Protein Data Bank having PDB ID: 1cgo. The docking studies were done using the Auto Dock 4.2 program based on the Lamarckian Genetic Algorithm (LGA). Optimized structures of sodium deoxycholate (NaDC) and sodium cholate (NaC) were achieved at the DFT//B3LYP/6-311++G (d, p) level of theory using the Gaussian 09 W set of programs, and the obtained geometry was opened in the Auto Dock 4.2 software in an agreeable file format. The grid size was fixed at 126, 126, and 126 Å along the X-, Y-, and Z-axis with a 0.408 Å grid spacing to locate the binding sites of the compounds. The Auto Docking parameters were set up as follows: GA population size = 150; the maximum number of energy evaluations = 2,500,000; GA crossover mode = two points. The minimum energy conformation was selected from a suite of 10 conformations of lowest energy conformers. The docked conformation was illustrated by using the PyMOL software package.

3. Results & Discussion:

3.1 Adsorption isotherm analysis:

Bile salts are a common type of biosurfactant, therefore understanding their micellization and interfacial characteristics in the absence and presence of proteins is critical. Bile salts' micellization mechanism differs significantly from those of other common surfactants due to their unique steroidal structure. The CMC for pure bile salt and mixed protein-bile salt systems is calculated by taking the concentration that corresponds to the last break point in the surface tension (γ) versus logarithm of the total molar bile salt concentration plot. Because of the phosphate buffer medium's high ionic strength, the CMC value for sodium cholate and deoxycholate is lower than that produced in an aqueous medium.[36-38] Figure 1 (A & B) shows

surface tension plots of bile salt (NaDC and NaC) in the presence and absence of cytochrome C. The inset plot clearly depicts the changes in CMC of bile salts in the presence of proteins.

The figures show that in the presence of protein molecules, there are lower surface tension values than in the absence of them, implying that the protein molecules have sufficient surface activity. The plot of γ versus log C for bile salts shows a slight minimum both in the absence and presence of protein molecules. This is attributable to the presence of a small impurity in the sample.[39] Long-chain alcohol may be a contaminant in the bile salt sample provided. Long-chain alcohol has less surface tension than bile salts due to its higher surface activity. As the micelles form, the impurity dissolves in them, lowering the concentration of long-chain alcohol in the bulk and, by extension, at the surface. As a result, the surface tension begins to grow and eventually equals that of pure bile salt solution. The plot of γ vs log C for bile salts reveals a minimum in the presence of contaminants. This tensiometric graph demonstrates that recrystallization does not completely eliminate the impurity.

The variation in CMC value for bile salts type bio-surfactants in the presence of different additives is relatively minor when compared to conventional surfactants.[40,41] The measured CMC value for NaDC and NaC is lower in the presence of Cyt C than in the absence of it, implying that the bile salt aggregation process is facilitated in the presence of Cyt C. This could be due to the presence of an overall positive charge on Cyt C at a fixed pH of 7.4 (the isoelectric pH of Cyt C is 9.6), which reduces electrostatic repulsion between the negatively charged head groups of cholates and deoxycholate monomers, facilitating the micellization process. Because protein molecules include a significant hydrophobic residue, the hydrophobic-hydrophobic interaction between bile salts and proteins also contributes to the reduced CMC value in the presence of protein molecules.[42] To gain a better understanding of the Cyt C and sodium cholate/deoxycholate interaction, interfacial characteristics were estimated at the air/liquid interface. The computed parameters are shown in Table S1.

The inclusion of Cyt C reduces the Π_{CMC} (surface pressure) value of sodium cholate and deoxycholate when compared to the pure ones. This shows that the presence of Cyt C reduces the concentration of bile salts at the air/water interface. The decrease in bile salt population at the interface is most likely due to the formation of a solubilized complex between the bile salts and proteins via both hydrophobic and electrostatic interactions, resulting in some bile salts being transported to the bulk from the interface. Cyt C decreased the Π_{CMC} value for bile salts.

The Γ_{max} (Gibbs surface excess concentration) and A_{min} values for pure bile salts are consistent with the literature.[43] Table S1 shows that the presence of Cyt C results in reduced

Γ_{max} values for sodium cholate and deoxycholate, indicating a decrease in bile salt surface excess concentration. The reduced efficacy of bile salts in populating the air/water interfacial monolayer in the presence of protein molecules suggests the creation of a solubilized Cyt C-bile salt complex at the interface. As a result, the value of A_{min} for two bile salts increases in the presence of Cyt C, implying the formation of a protein-bile salt complex. When comparing the Γ_{max} values of two pure bile salts, NaDC outperforms NaC. This phenomenon can be explained using the hydrophilicity of the two bile salts. NaC is significantly more hydrophilic than NaDC because it has an additional hydroxyl group. NaC is more hydrophilic than NaDC, making it more likely to reach the bulk phase, resulting in a lower Γ_{max} value. The obtained Amin value for bile salts is significantly greater than for conventional surfactants, indicating that bile salts are loosely packed at the interface. Another crucial surface metric is pC_{20}, which indicates how efficiently amphiphiles are adsorbing interfacial. The higher pC_{20} indicates that amphiphiles are more likely to adsorb at the air/water interface. Table S1 shows that the pC_{20} of both bile salts falls in the presence of Cyt C, indicating that bile salts' interfacial adsorption effectiveness reduces in the Cyt C medium. This shows that the generated bile salt-Cyt C complex has a higher propensity to enter the bulk, resulting in certain bile salts moving bulk from the interface via complexation. The Gibbs free energy change for adsorption and micellization was determined using the formulae shown below.[44]

$$\Delta G^0_{mic} = \text{RT ln } X_{cmc} \quad (2)$$

$$\Delta G^0_{ads} = \Delta G^0_{mic} - (\pi_{cmc}/\Gamma_{max}) \quad (3)$$

X_{cmc} represents the critical micelle concentration of the mixture of two components at a given mole fraction. The standard free energy changes (ΔG^0_{mic} and ΔG^0_{ads}) are used to verify whether the process of micellization in the solution and the process of adsorption at the air/liquid interface are enhanced or not in the presence of protein molecules. The negative values of both ΔG^0_{mic} and ΔG^0_{ads} indicate that both processes are spontaneous in the medium. The ΔG^0_{mic} and ΔG^0_{ads} for pure bile-salt and bile salt/Cyt C systems, are given in Table S1.

The values of adsorption-free energy change are much larger than those of micellization in both the presence and absence of the protein molecule, indicating that adsorption is the primary process and micellization is secondary. Thus, air/liquid interface adsorption occurs considerably more spontaneously than micellization in solution. In the presence of protein, both the standard free energy change of micellization and the energy change of adsorption are greater than those of free bile salts. Because protein and bile salt are oppositely charged, the

presence of proteins reduces mutual repulsion between similarly charged head groups of bile salts adsorbed at the interface, resulting in greater spontaneous bile salt adsorption.

The intermolecular or intramolecular hydrophobic interactions between bile salt and Cyt C are considerably preferred, possibly due to protein unfolding and surfactant-protein complex formation, resulting in adsorption at the interface before micelle formation in solution. Furthermore, the standard Gibbs free energy value of micellization for both surfactants is larger in the presence of Cyt C than in the absence of it, demonstrating that Cyt C promotes micellization. Because Cyt C has the opposite charge as bile salt, its presence minimizes electrostatic repulsion between the charged head group of bile salt, resulting in early micellization.

As a result, the tensiometric data support the creation of the bile salt-Cyt C complex while also predicting the nature of the produced protein-bile salt complex (loose/strong). The technique's sensitivity is demonstrated by its ability to detect minor differences in the CMC value of the bile salt in the absence and presence of Cyt C. These findings corroborate the hypothesis that Cyt C greatly increased bile salt surface activity.

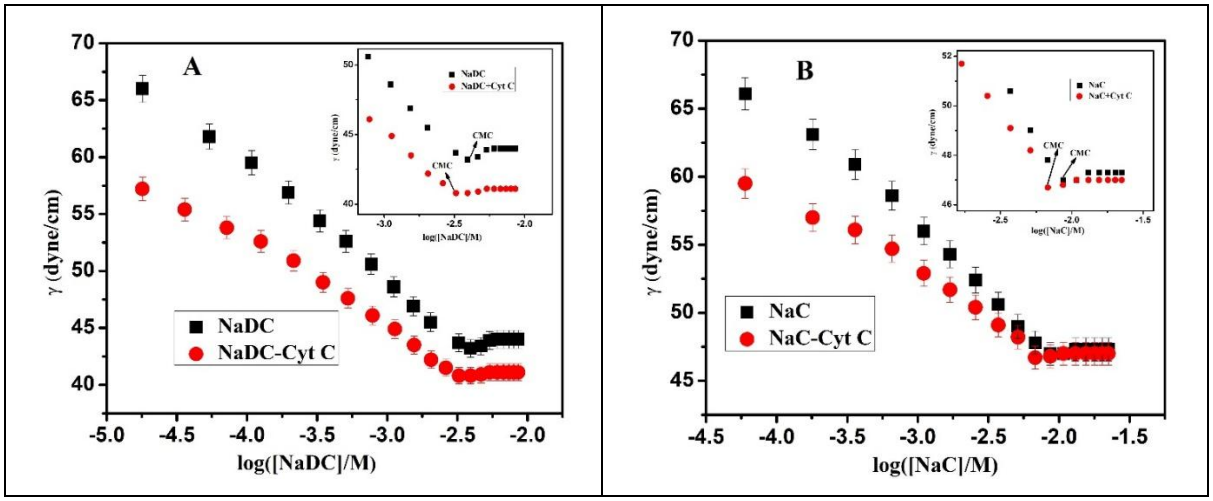

Fig 1. Tensiometric profile of bile salt surfactants (NaDC and NaC) in the absence and presence of heme protein Cyt-C (5 μM) (A) for sodium deoxycholate (NaDC) and (B) sodium cholate (NaC) in phosphate buffer medium (pH 7.4) at 298 K. (Inset plot represents the tensiometric profile in a smaller scale).

3.2 Steady-state spectral analysis:

UV-vis measurements: The native state of Cyt C exhibits a characteristic Soret band with a maximum intensity about 409 nm, indicating the presence of methionine and axial ligands. In the presence of sodium cholate and deoxycholate, a change in the absorbance of the protein at 409 nm was measured, as shown in Figure 2 (A&B). (We provide the UV-Vis spectra in a reduced wavelength scale to clearly visualize the change in absorbance at 409 nm following bile salt addition; the UV-Vis spectra with full wavelength scale are available in the supplementary file in Fig S1 (A&B)). Figure 2 (A&B) shows that in the presence of sodium cholate and sodium deoxycholate, the maximum of the Soret band stays at 409 nm throughout the bile salt concentration range examined, demonstrating the persistence of methionine ligation in Cyt C. Again, when sodium cholate and deoxycholate are added to the protein solution, the absorbance of the Soret peak (at 409 nm) decreases with every addition. The observed drop in absorbance intensity may be attributable to a modification in the electronic transition caused by the protein unfolding near the heme environment.[45] The observed spectral variation could be due to electrostatic disruption or conformational changes caused by bile salt binding, as indicated by the docking-derived distances. Docking investigation reveals that, while there is no direct coordination between the bile salts and Cyt C's heme group, bile salts can indirectly alter the protein's surroundings via long-range electrostatic interactions. Thus, bile salt-induced uncoiling is impacted by both non-polar (non-electrostatic) and electrostatic interactions.

The inset plot of Figure 2 (A&B) shows a substantial drop in absorbance up to 1.03 mM sodium cholate and 0.59 mM sodium deoxycholate. In this area, bile salt monomers interact with the various positively charged amino acid groups of proteins via electrostatic and hydrophobic interactions. The structural modification of the protein is much more dramatic in this location, resulting in a quick drop in absorbance. This is referred to as the critical aggregation concentration (CAC) zone for bile salt. CAC produces a tiny micelle-like cluster with a low aggregation number. Following CAC, the rate of decline in Cyt C absorbance values slows as bile salt concentrations increase, reaching 4.73 mM for sodium cholate and 1.41 mM for sodium deoxycholate. The bile salts in this area have saturated the protein's backbone. This area is known as the saturation concentration (C_S) zone. After C_S, the absorbance decreases much more slowly until CMC, indicating that the structural change of Cyt C is less prominent in this region. In this location, protein-surface-bound bile salt monomers began to cluster among themselves. Following that, the change in Cyt C absorbance value becomes minimal as

bile salt concentration increases. In this case, free bile salt micelles are formed in solution, which have no significant effect on protein structure.

The aforementioned observation shows that structural alteration of Cyt C happens mostly in the presence of free bile salt monomers, with micelles playing a minor role. Furthermore, absorbance measurements (Table 1) revealed three separate breakpoints (CAC, Cs, and CMC), although surface tension measurements did not. UV-vis measurements make it simple to study the interaction zone of bile salts and Cyt C because they are more sensitive to detecting minute changes in protein structure. So, the binding isotherm obtained from UV-vis measurements indicates that bile salts and Cyt C interact in three critical zones.

The UV-vis data provide precise insights into the bile salt-Cyt C interaction, with spectrum shifts corresponding to predicted structural changes. The key breakpoints (CAC, C_S, and CMC) were clearly visible in UV-vis spectra, confirming the technique's sensitivity to tiny structural alterations. These findings support the concept that bile salt monomers have a higher impact on protein conformational changes than bile salt micelles.

Fluorescence analysis: Fluorescence emission is utilized to investigate tertiary structural changes in Cyt C in the presence of bile salts (NaDC/NaC). This is shown in Figures 2C and 2D. Tryptophan (Trp 59) provides the majority of the fluorescence in Cyt C; nevertheless, the porphyrin residue of the protein also emits a minor amount of fluorescence.[46] The emission intensity of native Cyt C is extremely low when compared to other globular proteins. This low fluorescence in natural Cyt C is caused by energy transfer from the fluorophore (Trp 59) to the neighbouring heme group of the porphyrin ring, which reduces the fluorophore's (Trp 59) emission.

In Cyt C, the tryptophan residue (Trp 59) is linked to one of heme's propionic groups. This aromatic Trp 59 residue is primarily responsible for the emission spectra in Cyt C; nevertheless, the emission intensity is significantly low due to the proximity of the heme group to Trp 59, resulting in a Foster Energy Transfer between Trp 59 and the heme group, beginning with the former and progressing to the latter, reducing the emission of the fluorescence spectra.[47,48] The spacing between the heme group and Trp 59 grows, as does the intensity of the protein's fluorescence spectrum.[49] As a result, molecular expansion around heme is usually identified through changes in fluorescence emission intensity.

Figures 2C and 2D indicate that native cytochrome c has a strong emission peak at 342 nm, which can be caused by tryptophan fluorescence. Furthermore, a distinct emission peak near

432 nm is noticed, which is most likely caused by porphyrin fluorescence and is normally weak and largely quenched due to heme's strong absorption capabilities. Cyt C's fluorescence intensity increases as the amounts of both bile salts increase. This could be due to protein unfolding from interactions with bile salts. When the protein unfolds, the spacing between the Trp 59 residue and the heme group increases, limiting the extent of Förster Energy Transfer between them and increasing fluorescence intensity, but also causing a loss in tryptophan structure.

Ahluwalia and his coworkers[50] reported that as the concentration of the anionic surfactant Sodium Dodecyl Sulfate (SDS) increases, so does fluorescence intensity. Singh et al. observed a similar observation regarding the interaction of long-chain imidazolium ionic liquid surfactant with Cyt C.[51] Anionic biosurfactants, sodium cholate, and deoxycholate exhibit a similar phenomenon. In addition to Cyt C's increased fluorescence intensity, the presence of bile salts resulted in a significant red shift in the emission maxima. The red shift in emission maxima is induced by a rise in the polarity of the microenvironment surrounding the fluorophore (tryptophan 59) as it unfolds and is exposed to the solvent.[52] Initially, the tryptophan group resided inside the hydrophobic cavity of proteins, wherein it was in a less polar medium, but when it unfolded, it was exposed to the polar solvent. As a result, the red shift is generated by a polarity variation around the fluorophore (Tr 59) moiety. The molecular docking distance estimate indicates that there is no direct coordination between the heme group and the bile salt. Thus, the long-distance electrostatic force and hydrophobic contact are principally responsible for the tertiary structural variation observed in steady-state fluorescence observations.

The inset plots in Figures (2C & 2D) show the change in Cyt C fluorescence intensity with different amounts of sodium cholate and deoxycholate. This figure shows three well-defined breakpoints for CAC, Cs, and CMC of the bile salts in the presence of Cyt C. Fluorescence intensity increased rapidly until it reached CAC. In this region, the bile salt monomer binds to numerous positively charged protein locations, as previously explained in the UV-vis analysis. After CAC, there is a plateau region known as Cs. In this location, the bile salt monomer completely covered the protein surface. Following this, fluorescence intensity increased significantly up to CMC once more. The fluorescence intensity increased steadily past the CMC. Different reasons may contribute to the increase in protein fluorescence intensity beyond CMC. (1) Protein exists in both monomeric and aggregated forms in aqueous buffer medium (as demonstrated by DLS data). In the presence of bile salt micelles, protein-protein

aggregation may be disturbed due to electrostatic and hydrophobic interactions between the oppositely charged micelle and protein molecules, and the protein monomer is uniformly distributed over the oppositely charged micelle surface. As a result, the proportion of monomeric protein molecules emitting fluorescence in the system may increase, resulting in more fluorescence. (2) The hydrophobic heme moiety can dissolve in the hydrophobic cavity of the bile salt micelle. The solubilization of heme in micelles can increase the distance between heme and Trp59, limiting energy transfer and enhancing fluorescence.[53] The breakpoint results (CAC, Cs, and CMC) closely matched the absorbance readings. As a result, the binding isotherm determined by UV-vis measurements of bile salts and Cyt C interaction is highly reproducible by steady-state fluorescence measurements.

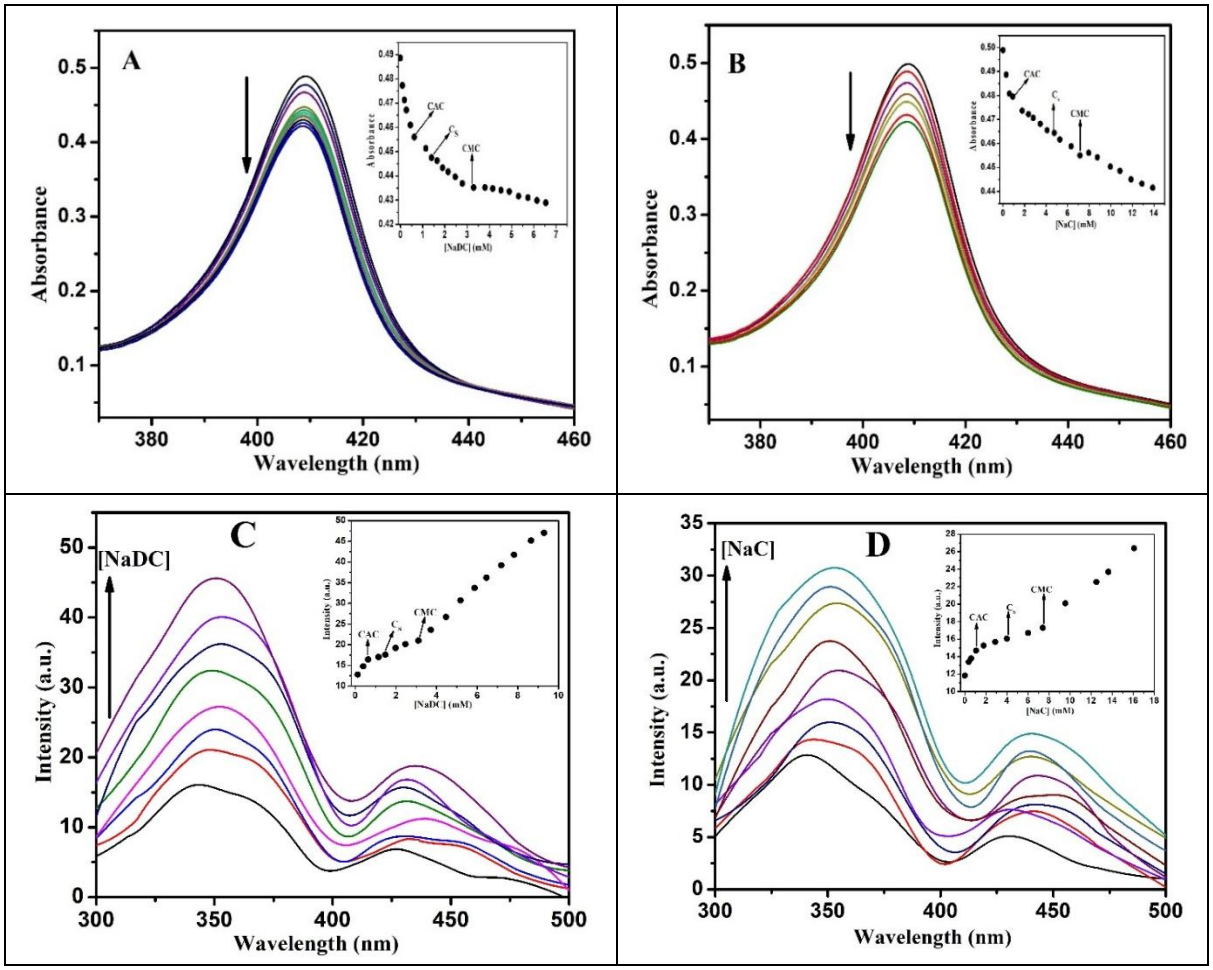

Fig 2. Absorption spectra of Cyt C in the presence of various amounts of (A) NaDC (0, 0.08, 0.17, 0.62, 1.14, 2.46, 3.80, 5.31, 7.31, 8.05 mM respectively), and (B) NaC (0, 0.29, 0.89, 1.77, 2.81, 4.08, 5.27, 7.14, 9.95, 10.88, 13.55, 14.52 mM respectively) at 298 K. (Inset: Plot of the variation in the absorbance of Cyt C (taking absorbance at 409nm) with concentrations of NaDC and NaC respectively). Steady-state fluorescence spectra of Cyt

C in the presence of various amounts of (C) NaDC (0, 0.14, 0.93, 1.97, 3.21, 4.11, 5.99, 9.55 mM respectively) and (D) NaC (0, 0.59, 1.77, 3.99, 6.01, 9.31, 12.49, 16.12, 18.32 mM respectively); at room temperature. (Inset: Changes of fluorescence intensity of Cyt C with the concentration of NaDC and NaC, respectively).

3.3 Benesi-Hildebrand plot analysis:

A quantitative investigation of bile salts (sodium cholate and deoxycholate) interacting with Cyt C was performed using the Benesi-Hildebrand equation, which demonstrates the stoichiometry involved in receptor-ligand interactions.[54]

$$\frac{1}{(I-I_0)} = \frac{1}{(I_1-I_0)} + \frac{1}{(I_1-I_0)k_b\,[\text{bile salt}]} \quad (4)$$

In the above case, I_0 and I depict Cyt C's fluorescence emission intensity in the absence and presence of bile salts; I_1 is the limiting fluorescence emission intensity, and k_b is the binding constant, respectively. Plotting $1/((I-I_0))$ against bile salt concentration yields the Benesi-Hildebrand plot (Figs. 3A and 3B). The graph shows a clear linear trend, demonstrating a 1:1 interaction[55,56] of biosurfactants (sodium cholate and deoxycholate) with Cyt C. The binding constant (k_b) and standard Gibbs free energy change ($\Delta G°$) for sodium deoxycholate are $0.75\times103\ M^{-1}$ and -16.40 kJ mol^{-1}, and $0.41\times10^3\ M^{-1}$ and -14.90 kJ mol^{-1} for sodium cholate respectively, based on the plot's slope and intercept (Table 2). Given the value of the binding constant and the negative Gibbs free energy, it is clear that bile salts and Cyt C interact favourably. The binding constant and Gibbs free energy of the NaDC-Cyt C system are significantly higher than those of NaC-Cyt C, indicating that the NaDC-Cyt C interaction is stronger. Although the charges of the two bile salts are equal, the difference in binding energy and binding constant value is mostly due to the hydrophobicity of the two bile salts. Because NaDC is more hydrophobic than NaC, it has a stronger interaction with Cyt C. The aforementioned data suggest that bile salt hydrophobicity is critical for the interaction between bile salts and Cyt C.

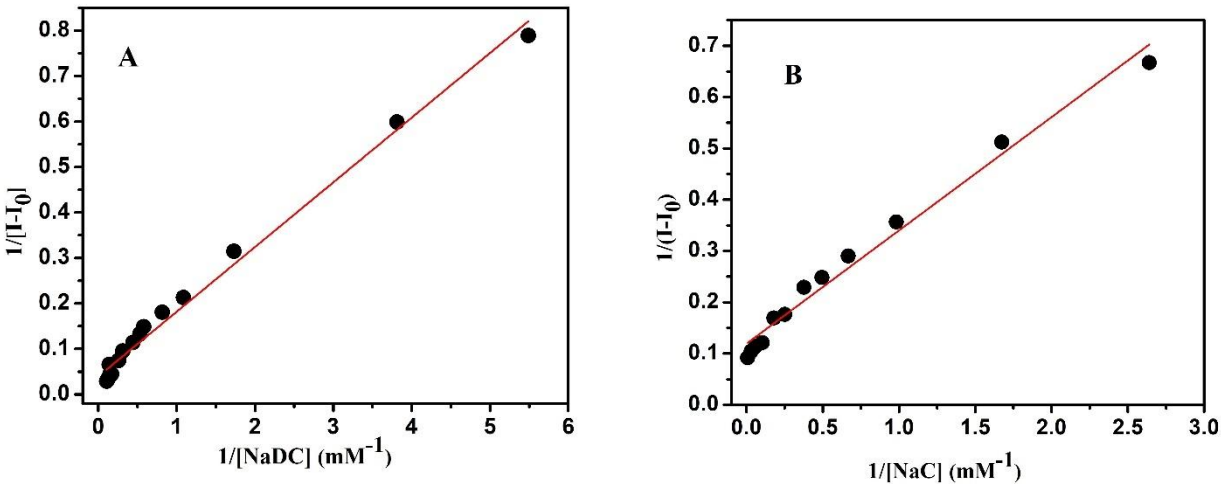

Fig 3. Benesi-Hildebrand plot of 1/(I-I$_0$) against 1/ [bile salt] for binding of Cyt C with bile salts (A) for NaDC and (B) NaC.

3.4 Modification in the secondary structural conformation:

CD spectroscopy is a powerful method for investigating changes in the secondary (far-UV) and tertiary (mid-UV) structures of biological macromolecules.[45] Figures 4A and 4B show far-UV spectra of Cyt C in the presence of sodium cholate and deoxycholate at varying concentrations. Table S2 (Supplementary Section) shows the alterations in the protein's secondary structure, as determined using secondary structure analysis tools. Cyt C exhibits the α-helix structure in its native state, with negative peaks at 208 nm (corresponding to $\pi - \pi^*$ transition) and 220 nm (corresponding to $n - \pi^*$ transition).[57,58] The α-helical structure contributes around 38%, which is consistent with previous studies.[45]

Figure 4 (A&B) demonstrates that when the amounts of sodium cholate and deoxycholate increased, Cyt C's negative ellipticity value dropped. The decrease in negative ellipticity between 208 and 220 nm indicates that Cyt C is losing its α-helical structure over time. The spectral changes suggest partial unfolding or structural relaxation of the protein, rather than a complete transformation to β-sheet, as suggested by CD spectra. This unfolding is most likely driven by electrostatic interactions between positively charged lysine residues near Cyt C's heme crevice and negatively charged carboxylate groups found in bile salts. Binding may disrupt the local helical environment, destabilizing the hydrogen bonding network and resulting in a drop in α-helicity. Furthermore, a minor conformational rearrangement is supported by a little blue shift of the CD band from 220 nm to 218 nm, corresponding to a 2 nm blue shift, which could be caused by a reorganization of the tertiary packing or a change in the local

polarity around aromatic residues. In the presence of bile salts, the secondary structure of proteins changes far less than with ordinary surfactants. Mukherjee et al.[31] discovered that HSA undergoes just a 5% secondary structural change in the presence of bile salts. Mohanty et al.[32] observed that when exposed to the bile salt NaDC, BSA exhibits just a 3% secondary structural alteration. This modest change in protein CD spectra in the presence of bile salts is mostly due to the bile salts' typical steroidal structure, which differs from ordinary surfactants, which have a lengthy hydrophobic chain. This lengthy hydrophobic chain of traditional surfactants can easily infiltrate the numerous hydrophobic pockets of proteins, creating a considerable secondary structural change, resulting in a far bigger change in CD spectra in conventional surfactants than in bile salt surfactants.

The CD data show that sodium deoxycholate and cholate interact with Cyt C in a mild but particular manner, resulting in a moderate decrease in α-helical content without causing full unfolding. The bile salts' rigid steroidal structure appears to restrict the interactions principally electrostatically and sterically. Singh and his colleagues, on the other hand, found an unexpected discovery when researching the interaction of the Cyt C protein and long-chain imidazolium ionic liquid.[51]

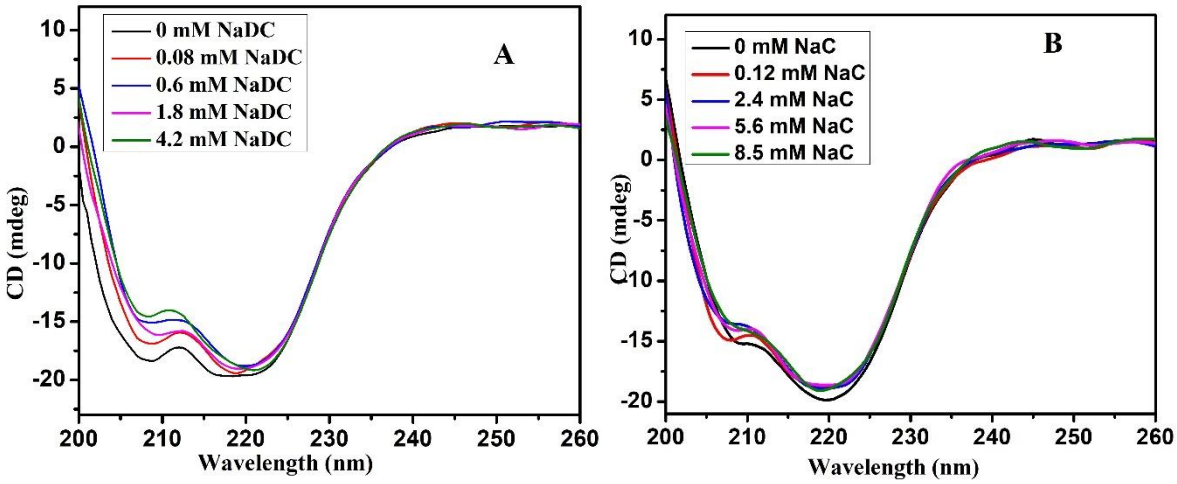

Fig 4. CD spectra of Cyt C at various concentrations of bile salts (A) NaDC and (B) NaC. [Cyt C] =2.5 μM in phosphate buffer medium (pH 7.4) at 298 K.

3.5 Dynamic light scattering (DLS) measurements:

In the presence of ligands, DLS measurements are able to predict protein-ligand interactions based on variations in the protein's hydrodynamic diameter.[59] Figures 5(A&B) show a change in Cyt C's hydrodynamic diameter in the presence of NaDC and NaC. Cyt C has two peaks in

its original state (pH 7.4), with hydrodynamic diameters (Dh) of roughly 4.96 nm and 120 nm (Fig. 5A & B). The smaller one represents the protein's monomeric form, while the larger one represents its aggregation form.[60] Based on the solution NMR structure, Bensi et al. estimated Cyt C's diameter to be 3.6 nm.[61] Our result of a hydrodynamic diameter of ~ 4-5 nm is consistent with the structural NMR investigation, given that the hydration layer thickness is approximately 0.6 nm.[62]

The monomeric form contributes significantly in the native state, but the aggregated form contributes just marginally. The diameter (Dh) of Cyt C's monomeric form has been found to increase in the presence of bile salts (NaDC and NaC). The increase in the size of the monomeric form could be attributed to a number of processes, including (1) denaturation of Cyt C in the presence of bile salts, which induces swelling in the protein structure, and (2) when bile salts are introduced, the protein aggregates into oligomers from its monomeric state. In the presence of sodium deoxycholate, the hydrodynamic diameter of Cyt C increases significantly from 4.96 nm to 10.54 nm, whereas sodium cholate increases only slightly (4.96 nm to 6.42 nm), implying that NaDC is more efficient at forming aggregates and structural changes in Cyt C than NaC. Similarly, the aggregated peak's hydrodynamic diameter (D_h) increased in the presence of NaDC/NaC. Both the intensity and the D_h of the aggregated peak were increased. The possible creation of a bile salt-Cyt C complex could explain the rise in diameter and intensity of the aggregated peak. However, in the presence of a very low concentration of NaDC, the diameter of the aggregated peak was reduced. This could be explained by the breakdown of protein-protein aggregation by negatively charged NaDC. In the presence of NaDC, Figure 5A reveals a peak at ~1 nm alongside the monomeric and aggregated hydrodynamic peak of Cyt C. Sarkar et al.[60] reported that, in addition to monomeric and aggregated peaks, Cyt C has a hydrodynamic peak at 0.6 nm in the presence of denaturant agents' urea and guanidine chloride (GdnCl). One of the proposed reasons for peaks in solutions at 0.6 nm is the hydrolysis of some Cyt C amino acids in the presence of a denaturant. They measured the hydrodynamic diameter of the amino acid tryptophan in the buffer solution and found a distinct peak at 0.8 nm. Based on this discovery, they reasoned that the peak at 0.6 nm could be the result of Cyt C's amino acid hydrolysis. As a result, the hydrodynamic peak about 1 nm of Cyt C in the presence of NaDC could be attributed to protein amino acid residue hydrolysis. Such Cyt C hydrolysis peaks are not found in the presence of NaC, indicating that NaDC functions as a stronger denaturant than NaC. As a result of its high hydrophobicity, NaDC may be considered a more effective denaturant agent for Cyt C than NaC.

Furthermore, the Benesi-Hildebrand plot reveals that the k_b value for the NaDC-Cyt C system is larger than that for the NaC-Cyt C system, suggesting that NaDC binds more strongly to Cyt C, resulting in more structural change and aggregation formation than NaC. Thus, DLS results are supported by Benesi-Hildebrand plots. As a result, it is possible to conclude that the increase in the hydrodynamic diameter of Cyt C in the presence of bile salts indicates that the protein is being unfolded and aggregated, and the DLS data are compatible with those from previous measurements.

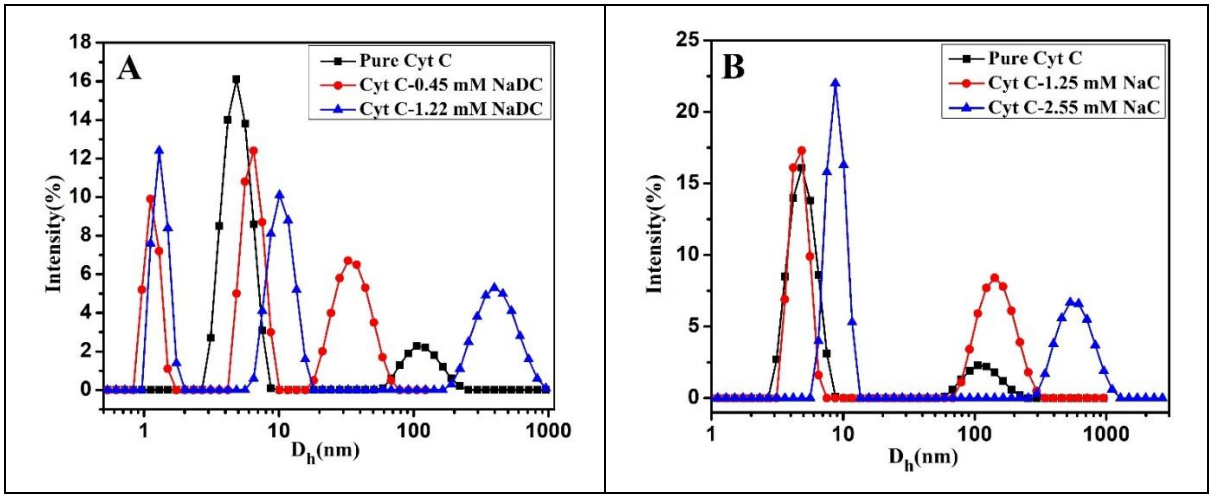

Fig. 5. Variation in the hydrodynamic diameter (D_h) of Cyt C in the presence of different concentrations of NaDC (A) and NaC (B), respectively.

3.6 Microcalorimetry analysis (ITC):

Isothermal titration calorimetry (ITC) is a significant and sensitive tool for evaluating the energy-related features of protein-ligand interactions. Figures 6A and 6B illustrate the calorimetric profiles (enthalpograms) of bile salt (NaDC and NaC) binding to Cyt C. The presented calorimetric profiles are produced by deducting the heat of dilution of bile salts in the buffer medium for an accurate analysis. The enthalpogram was fitted using the 'one set of sites binding model'.

The sodium deoxycholate titration curves are predominantly endothermic. Endothermicity was shown to increase with increasing NaDC concentration in Cyt C solutions up to a point before decreasing with rising bile salt concentration (Fig. 6A). The breakdown of the H-bond (one of the most important forces responsible for protein secondary structure) during the surfactant's contact with the protein molecules could explain the increase in endothermicity observed when sodium deoxycholate concentration increases.[63] After reaching the maximum point (marked as

CMC), the endothermicity of the NaDC-Cyt C ITC curve decreased as the NaDC concentration increased. The latter half of the diagram of NaDC titration in Cyt C is comparable to the pure NaDC titration in a buffer medium (Fig. S4 in the supplemental section), indicating that the latter half of NaDC titration in Cyt C is attributable to the generation of free micelle following the creation of the Cyt C-NaDC complex. Our ITC profile of pure NaDC titration in buffer solution is consistent with the literature.[64]

It is noteworthy to note that sodium cholate followed the opposite trend (Fig. 6B). In this case, the reaction profile's lower panel has exothermic features, crosses zero, and eventually enters the endothermic domain (upper panel). The origin of endothermicity has already been examined (NaC). Exothermicity is caused by an electrostatic/van der Waals contact between Cyt C positively charged amino acid residues and the negatively charged groups of the bile salts.65 The ITC profile of two bile salts (NaDC/NaC) differs significantly in the presence of Cyt C. The first section of the enthalpogram (up to micellization) for the interaction of two bile salts with Cyt C shows a fairly consistent pattern. Exothermicity gradually decreases when bile salts (NaDC/NaC) are introduced, demonstrating that the bile salt monomer binds to Cyt C's highly energetic locations through both hydrophobic and electrostatic interaction. Following their CMC point, two bile salts containing Cyt C exhibit distinct ITC characteristics. NaDC's interaction with Cyt C after the CMC point resulted in a progressive decline in endothermicity, whereas NaC's endothermicity increased modestly. As a result, during the creation of the free micelle, the ITC profile of the interaction between two bile salts and Cyt C changes. Despite having identical structures, the two bile salts (NaDC and NaC) have different micellization processes due to their differential hydrophobicity. As a result, the ITC profile of two bile salts changes during free micelle formation, resulting in a different ITC profile for the two-bile salt in the Cyt C-bile salt interaction.

With the NaDC-Cyt C system, the heat change for micellization ($\Delta H^{\circ}_{micelle}$) is 388.5 J/mol, while it is 585.9 J/mol for the NaC-Cyt C system. The heat change of micellization ($\Delta H^{\circ}_{micelle}$) for both the bile salts in the presence of Cyt C is endothermic in nature. There may be various factors responsible for these endothermic heat changes-

1. Disruption of structured water (Hydration shells):

In the solution phase, both the Cyt C and bile salts are usually surrounded by ordered water molecules. When bile salts form micelles in the presence of Cyt C, some of the structured water

molecules are liberated into the bulk solution. The process of breaking these hydration shells is endothermic since it needs energy

2. Unfolding or rearrangement of protein structure:

Bile salt interactions can lead to partial unfolding or structural changes in Cyt C. This unravelling or rupture of intramolecular bonds (such as hydrogen bonds, van der Waals forces, etc.) absorbs heat and contributes to the endothermic nature.

Despite the endothermic heat change, the micellization process is spontaneous due to the positive enthalpy change. Thus, the micellization process is driven by entropy. The release of water molecules during the interaction of bile salts and Cyt C (the water molecules that surround the protein and bile salts) enhances the system's overall entropy, making the entire process entropically favourable.

The higher the positive value of enthalpy change, the smaller the negative value of Gibbs free energy, indicating that the process is less spontaneous. So, based on the enthalpy change of micellization, it is obvious that the interaction between sodium deoxycholate and Cyt C is more spontaneous than sodium cholate. The inclusion of a hydroxyl group at sodium cholate's 7th position causes a difference in the hydrophobicity of the two bile salts, resulting in the micellization process. So, based on ITC measurements, it is obvious that the hydrophobicity of bile salts is the primary controlling factor for bile salts and Cyt C. Different approaches have shown that sodium deoxycholate binds to Cyt C more effectively than sodium cholate, and calorimetric titration validates this observation.

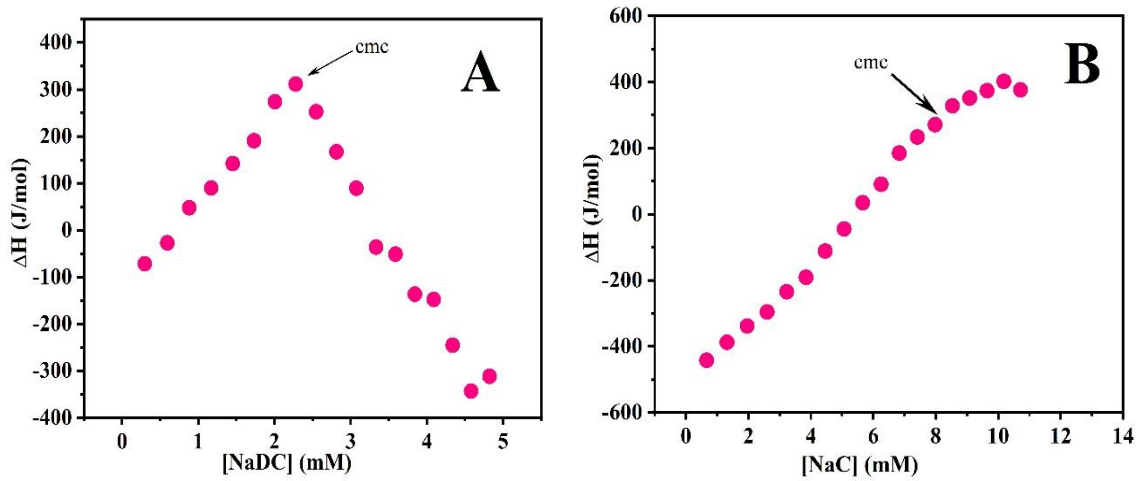

Fig. 6. Plot of integrated heat data after correction of heat of dilution of bile salts against the concentration of the bile salt, for the binding of NaDC (A) and NaC (B) to Cyt C at 298.15 K in phosphate buffer, pH 7.4.

3.7 Cyclic Voltammetry (CV) measurements:

Cyclic voltammetry was employed to evaluate the effect of bile salt ligands on the redox characteristics of Cyt C, an electron transport protein. Figures 7A and 7B show typical cyclic voltammograms of Cyt C (10 μM) in 20 mM phosphate buffer solution in its original state and with bile salts (NaDC and NaC). The figure shows that Cyt C in its original state has distinct oxidation-reduction (redox) peaks on the Pt electrode at a scan speed of 50 mV/s. The primary peak was oxidative at -0.634 V, and the equivalent reductive peak was at -0.96 V with respect to SCE. The separation of peak potential (ΔE_P), or the difference between the peak potential values of the cathode and anode, was ΔE_P = 0.538 V. These redox peaks relate to redox processes occurring at Cyt C's electrochemical centre, which has a formal potential (E°) of 0.313 V in relation to its reference electrode.[66] Cyt C's oxidation peak current changed dramatically in the presence of bile salts (NaC and NaDC). Cyt C was treated with sodium cholate, which raised the oxidative peak current (above and below CMC). Proteins are hydrophobic macromolecules that may bind to surfactant molecules via hydrophobic interactions. The sodium cholate adsorption layer on the Pt electrode causes additional Cyt C to cling to its surface. Furthermore, in the presence of NaC, Cyt C's orientation on the electrode surface could vary, resulting in greater electron transfer leading to the increased peak current.[67] Interestingly, the opposite has been found for sodium deoxycholate. In this situation, peak current decreased as surfactant concentration increased (above and below CMC). The creation of an electro-inactive Cyt C-NaDC complex accounts for the peak current reduction. As a result, Cyt C's electrical activity on the electrode surface decreases globally, disturbing the peak current.[68,69] Cyclic voltammetry data clearly indicate the formation of complexes between Cyt C and bile salts (NaC and NaDC), which is also consistent with fluorescence, CD spectroscopy, DLS, and ITC experiments. Cyclic voltammetry investigations reveal that the interaction between NaC and Cyt C is substantially different from that of NaDC.

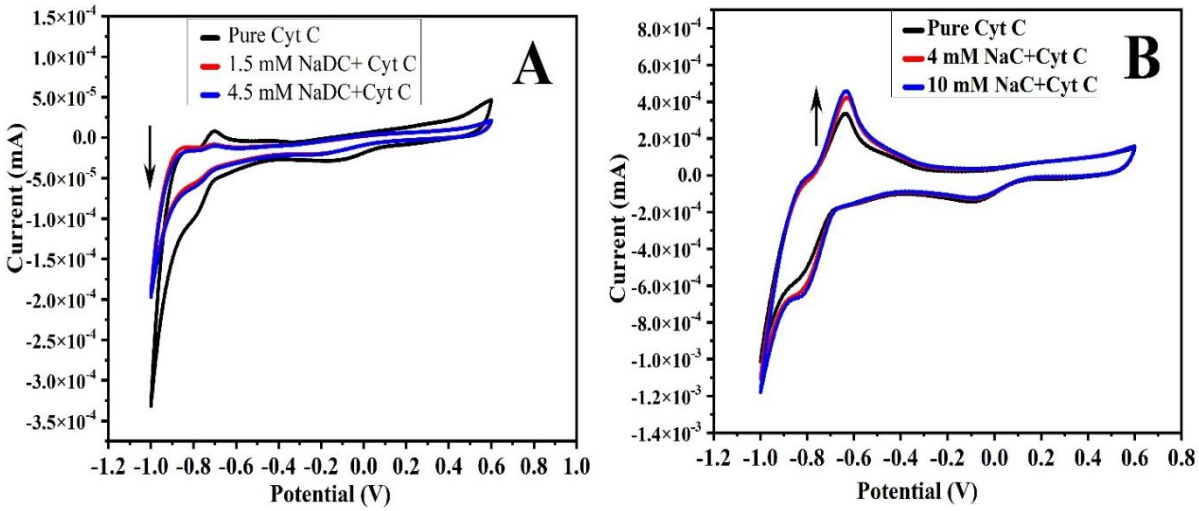

Fig. 7. Cyclic voltammogram of Cyt C (10 μM) in the presence of bile salts, above and below its CMC values (A) NaDC and (B) NaC at 298 K and pH 7.4.

3.8 Morphology analysis of bile salt-Cyt C complex (AFM):

The aggregate formation between the bile salts (NaDC/NaC) and Cyt C has been further confirmed by atomic force microscopy (AFM). The AFM technique has become a crucial tool over other techniques because it provides accurate and direct information about the formation, structural changes, dynamics, topography, and molecular interaction patterns of bio-macromolecules.[70] Fig. 8 shows the AFM topographic images of free Cyt C (Fig. 8(A)) and its mixed system with NaDC/NaC (Fig. 8(B&C)). The AFM micrograph indicates that free Cyt C displays star/sphere-like images, while the addition of bile salts causes Cyt C to display a large aggregated structure. This kind of lump-like AFM micrograph for free hemoglobin was described by Bhat et al.[71] Once more, when NaC was present, a completely distinct micrograph of Cyt C was seen. In this instance, an aggregated morphology that resembled a uniform sheet was seen. Because of its isoelectric pH of around 9.6, Cyt C has a slightly positively charged surface at pH 7.4, which improves the adsorption of negatively charged NaDC/NaC on its surface. Here, a morphological change is caused by the negatively charged tiny micelle cluster of NaDC/NaC attached to Cyt C's backbone.

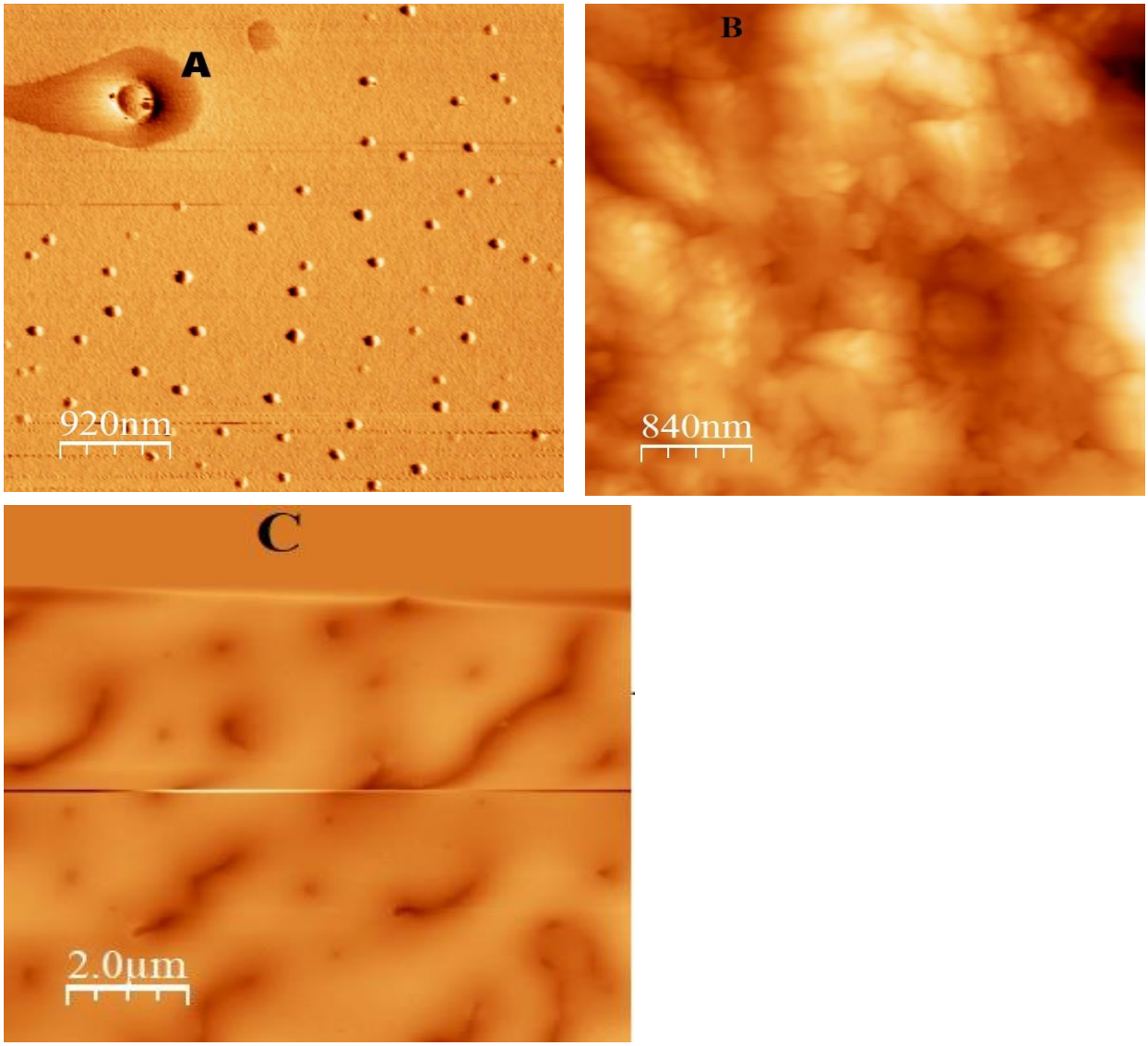

Fig. 8. 2-Dimensional AFM topographic images of Cyt C in the absence and presence of bile salts (A) pure Cyt C, (B) 4.5 mM NaDC, and (C) 8.5 mM NaC at pH 7.4 and ionic strength 10 mM.

3.9 Molecular docking analysis:

The best technique for determining the energy and binding site of a small molecule (ligand) inside a biomacromolecule is molecular docking. Small molecules are attached by the numerous ridges and grooves in the protein structure. By simultaneously searching the entire protein surface, the blind docking method allows us to minimize the energy of the peptide conformations. Cyt C is bound by NaDC and NaC, as seen in Figure 9A-D. The amino acid residues Ala 57, Ala 58, Gly 62, Pro 61, Gly 65, Thr 63, and Lys 4 are directly engaged in the

interaction of NaDC with Cyt C, while Ala 77, Ala 76, Phe 79, Lys 80, Gln 83, Ala 57, Phe 59, Gly 60, Ile 72, and Trp 73 are involved in the interaction with NaC. The docking studies provided free energy values of -0.091 kcal mol^{-1} for NaDC and -0.079 kcal mol^{-1} for NaC, which deviate marginally from the experimental value. This is most likely due to the fact that the protein's crystal structure in the solid state differs from that in the solution in which the studies are conducted. The found negative free energy value suggests that the interaction of bile salt and Cyt C is a spontaneous event. The computed negative free energy for the interaction of NaDC with Cyt C is larger than NaC, indicating that NaDC interacts more strongly with Cyt C. The docking estimated negative free energy value for the interaction of NaDC with HSA was greater than NaC, according to a similar pattern seen by Mukerjee et al..[31] However, compared to the bile salt-Cyt C system, the bile salt-HSA system was projected to have a greater free energy change. NaDC has a greater binding affinity for Cyt C than NaC, as demonstrated by the experimental results, which are mainly supported by theoretical calculations. The estimated distances for the bound bile salts and the heme moiety of Cyt C were 11.0 Å for NaC and 14.4 Å for NaDC, respectively. Both bile salts preferentially attach to surface-accessible areas of Cyt C, away from the heme group, according to these docking studies. These distances imply that bile salt and Cyt C's heme iron do not directly coordinate during their interaction, but that long-range interactions may nevertheless affect the local electrostatic environment or protein conformation. When Bhat et al[72] investigated the interaction of haemoglobin with two cleavable gemini surfactants, they observed a similar type of finding out. According to their docking calculation, the two gemini surfactant residues and haemoglobin’s heme group are separated by 15 Å and 19 Å, respectively. They have also proposed that gemini surfactants cause haemoglobin to alter conformation through long-term hydrophobic and electrostatic interactions. It's important to remember that our molecular docking results are purely computational in nature and lack direct experimental evidence, even if they suggest a potential interaction between the Alcaligenes species Cyt C and NaDC/NaC. Determining the binding affinity or specificity of these interactions is impossible without the use of surface plasmon resonance, radioligand binding tests, or other biophysical investigations. Consequently, rather than being used as proof of molecular interaction, the existing molecular docking data should be seen as an initial tool for creating hypotheses. Taking these factors into account, we recognize the limitations of our research and stress the necessity of additional experimental studies to confirm our computational results. In the literature, a lot of such type’s studies are available where molecular docking is used as a preliminary tool to predict protein-ligand interaction without any experimental validation.[31,72,73]

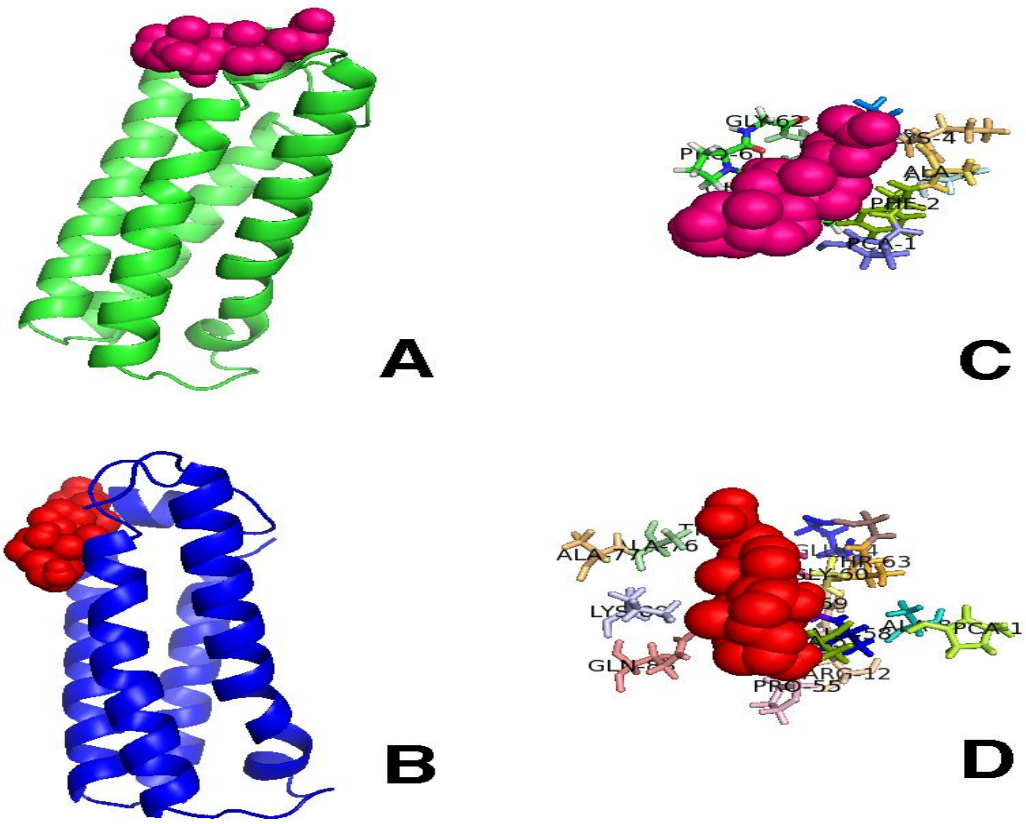

Fig. 9. The lowest energy binding modes of NaDC (A) and NaC (C), with Cyt C, respectively. The structure of Cyt C is displayed by ribbon and tube. Close-up views of binding sites of Cyt C with NaDC (B) and NaC (D) corresponding to (A) and (C), respectively, and the selected amino acid residue is represented by a line model structure.

4. Conclusions:

This study thoroughly investigated the molecular interaction between Cytochrome C and two bile salts (NaDC/NaC) using several kinds of complementary methods which includes tensiometry, UV-vis spectroscopy, fluorescence spectroscopy, circular dichroism (CD), dynamic light scattering (DLS), cyclic voltammetry (CV), isothermal titration calorimetry (ITC), atomic force microscopy (AFM), and molecular docking analysis. Overall, the results indicate that bile salt has a significant effect on Cyt C's physicochemical features, structural integrity, and electrochemical characteristics. Tensiometry studies demonstrate that the interfacial activity of bile salts improves dramatically in the presence of Cyt C, implying the creation of a bile salt-protein complex at a threshold micellar concentration. UV-vis spectroscopy and fluorescence investigations show that the bile salt interacts with Cyt C at three different concentrations, causing the protein structure to partially unfold. The binding

constant value (k_b) for the interaction of NaDC with Cyt C is significantly larger than that of NaC, indicating that NaDC's better hydrophobicity plays a crucial role in the binding process. The CD results showed that Cyt C's α-helical structure decreased after exposure to bile salt media, indicating protein structure destabilization. DLS analysis confirms the change in Cyt C size and the potential production of protein oligomers in bile salt media. ITC results provide thermodynamic evidence for the spontaneous binding of two bile salts to the Cyt C protein. Electrochemical data (CV analysis) indicates that the presence of NaDC decreases Cyt C's oxidative peak current by forming an electro-inactive complex with NaDC. However, in the presence of NaC, the peak current increases, implying that sodium cholate can improve the electron transfer mechanism at Cyt C's electroactive centre by reorienting it around the electrode surface. The AFM findings support the development of the Cyt C-bile salt complex. Molecular docking study predicted the possible binding locations and binding energies of interactions between bile salts and Cyt C, and the results were consistent with the experimental findings.

Overall, this study demonstrates the utility of several methods for analyzing protein-amphiphile interactions and gives light on how bile salts affect the structure and function of Cyt C. These insights will be critical in the cell death process, and the bile salt-protein interaction study will be valuable in a wide range of biological and pharmacological applications. Future studies may look into this interaction using structurally different bile salts or other heme proteins, as well as high-resolution techniques like NMR, SANS, and CDC-PAT, to get more mechanistic insights.

References:

1. Davis, A. P. Cholaphanes. steroids as structural components in molecular engineering. *Chem. Soc. Rev.* **22**, 243–253 (1993).
2. Tamminen, J. & Kolehmainen, E. Bile acids as building blocks of supramolecular hosts. *Molecules* **6**, 21–46 (2001).
3. Mrózek, L., Dvořáková, L., Mandelová, Z., Rárová, L., Řezáčová, A., Plaček, L., Opatřilová, R., Dohnal, J., Paleta, O., Král, V. & Drašar, P. Investigation of new acyloxy derivatives of cholic acid and their esters as drug absorption modifiers. *Steroids* **76**, 1082–1097 (2011).

4. Mishra, S. & Patel, S. Design, synthesis, and anti-bacterial activity of novel deoxycholic acid-amino alcohol conjugates. *Med. Chem. (Los. Angeles).* **16**, 385–391 (2020).

5. Brossard, D., El Kihel, L., Clément, M., Sebbahi, W., Khalid, M., Roussakis, C., & Rault, S. Synthesis of bile acid derivatives and in vitro cytotoxic activity with pro-apoptotic process on multiple myeloma (KMS-11), glioblastoma multiforme (GBM), and colonic carcinoma (HCT-116) human cell lines. *Eur. J. Med. Chem.* **45**, 2912–2918 (2010).

6. Li, R., Santos, C. S., Norsten, T. B., Morimitsu, K. & Bohne, C. Aqueous solubilization of photochromic compounds by bile salt aggregates. *Chem. Commun.* **46**, 1941–1943 (2010).

7. Kundu, N., Banik, D., Roy, A., Kuchlyan, J. & Sarkar, N. Modulation of the aggregat**ion** properties of sodium deoxycholate in presence of hydrophilic imidazolium based ionic liquid: Water dynamics study to probe the structural alteration of the aggregates. *Phys. Chem. Chem. Phys.* **17**, 25216–25227 (2015).

8. Le Dévédec, F., Fuentealba, D., Strandman, S., Bohne, C. & Zhu, X. X. Aggregation behavior of pegylated bile acid derivatives. *Langmuir* **28**, 13431–13440 (2012).

9. Paul, B. K., Ghosh, N. & Mukherjee, S. Direct insight into the nonclassical hydrophobic effect in bile salt:β-cyclodextrin interaction: Role of hydrophobicity in governing the prototropism of a biological photosensitizer. *RSC Adv.* **6**, 9984–9993 (2016).

10. Li, R., Carpentier, E., Newell, E. D., Olague, L. M., Heafey, E., Yihwa, C., & Bohne, C. Effect of the structure of bile salt aggregates on the binding of aromatic guests and the accessibility of anions. *Langmuir* **25**, 13800–13808 (2009).

11. Small, D. M., Penkett, S. A. & Chapman, D. Studies on simple and mixed bile salt micelles by nuclear magnetic resonance spectroscopy. *Biochim. Biophys. Acta (BBA) / Lipids Lipid Metab.* **176**, 178–189 (1969).

12. Small, D. M., Nair, P. P. & Kritchevsky, D. The bile salts. *Plenum Press. New York* (1971).

13. Ridlon, J. M., Kang, D. J. & Hylemon, P. B. Bile salt biotransformations by human intestinal bacteria. *J. Lipid Res.* **47**, 241–259 (2006).

14. Li, G. & McGown, L. B. Model for bile salt micellization and solubilization from studies of a ‘polydisperse’ array of fluorescent probes and molecular modeling. *J. Phys. Chem.* **98**, 13711–13719 (1994).

15. O’Connor, C. J. & Wallace, R. G. Physico-chemical behavior of bile salts. *Adv. Colloid Interface Sci.* **22**, 1–111 (1985).

16. Foster, D. L. & Fillingame, R. H. Energy-transducing H+-ATPase of Escherichia coli. Purification, reconstitution, and subunit composition. *J. Biol. Chem.* **254**, 8230–8236 (1979).

17. Banno, Y., Yada, Y. & Nozawa, Y. Purification and characterization of membrane-bound phospholipase C specific for phosphoinositides from human platelets. *J. Biol. Chem.* **263**, 11459–11465 (1988).

18. Zhuang, S., Li, Q., Cai, L., Wang, C. & Lei, X. Chemoproteomic Profiling of Bile Acid Interacting Proteins. *ACS Cent. Sci.* **3**, 501–509 (2017).

19. Cremers, C. M., Knoefler, D., Vitvitsky, V., Banerjee, R. & Jakob, U. Bile salts act as effective protein-unfolding agents and instigators of disulfide stress in vivo. *Proc. Natl. Acad. Sci. U. S. A.* **111**, (2014).

20. Toke, O. Structural and Dynamic Determinants of Molecular Recognition in Bile Acid-Binding Proteins. *Int. J. Mol. Sci.* **23**, (2022).

21. Banno, Y., Yada, Y. & Nozawa, Y. Purification and characterization of membrane-bound phospholipase C specific for phosphoinositides from human platelets. *J. Biol. Chem.* **263**, 11459–11465 (1988).

22. Foster, D. L. & Fillingame, R. H. Energy-transducing H+-ATPase of Escherichia coli. Purification, reconstitution, and subunit composition. *J. Biol. Chem.* **254**, 8230–8236 (1979).

23. Di Gregorio, M. C., Cautela, J. & Galantini, L. Physiology and physical chemistry of bile acids. *Int. J. Mol. Sci.* **22**, 1–23 (2021).

24. Di Gregorio, M. C., Travaglini, L., Giudice, A. D., Cautela, J., Pavel, N. V. & Galantini, L. Bile Salts: Natural Surfactants and Precursors of a Broad Family of Complex Amphiphiles. *Langmuir* **35**, 6803–6821 (2019).

25. Cautela, J., Stenqvist, B., Schillén, K., Belić, D., Månsson, L.K., Hagemans, F., Seuss, M., Fery, A., Crassous, J.J. and Galantini, L., Supracolloidal atomium. *ACS Nano* **14**, 15748–15756 (2020).

26. Du, G., Belić, D., Del Giudice, A., Alfredsson, V., Carnerup, A.M., Zhu, K., Nyström, B., Wang, Y., Galantini, L. and Schillén, K., Condensed supramolecular helices: The twisted sisters of DNA. *Angew. Chemie* **134**, e202113279 (2022).

27. Li, K., Li, Y., Shelton, J.M., Richardson, J.A., Spencer, E., Chen, Z.J., Wang, X. and Williams, R.S., Cytochrome c deficiency causes embryonic lethality and attenuates stress-induced apoptosis. *Cell* **101**, 389–399 (2000).

28. Chandra, D., Bratton, S.B., Person, M.D., Tian, Y., Martin, A.G., Ayres, M., Fearnhead, H.O., Gandhi, V. and Tang, D.GIntracellular nucleotides act as critical prosurvival factors by binding to cytochrome C and inhibiting apoptosome. *Cell* **125**, 1333–1346 (2006).

29. Zhivotovsky, B., Orrenius, S., Brustugun, O. T. & Døskeland, S. O. Injected cytochrome C induces apoptosis. *Nature* **391**, 449–450 (1998).

30. Maloyan, A., Sanbe, A., Osinska, H., Westfall, M., Robinson, D., Imahashi, K.I., Murphy, E. and Robbins, J. Mitochondrial dysfunction and apoptosis underlie the pathogenic process in α-B-crystallin desmin-related cardiomyopathy. *Circulation* **112**, 3451–3461 (2005).

31. Ghosh, N., Mondal, R. & Mukherjee, S. Hydrophobicity is the governing factor in the interaction of human serum albumin with bile salts. *Langmuir* **31**, 1095–1104 (2015).

32. Mohanty, S., Mishra, S. S., Kuldeep, N., Maharana, J. & Subuddhi, U. Insight into the Effect of Submicellar Concentrations of Sodium Deoxycholate on the Structure, Stability, and Activity of Bovine and Human Serum Albumin: An Interesting Comparison between Single and Double Tryptophan Proteins. *Langmuir* **40**, 5228–5244 (2024).

33. Zsila, F. Circular dichroism spectroscopic detection of ligand binding induced subdomain IB specific structural adjustment of human serum albumin. *J. Phys. Chem. B* **117**, 10798–10806 (2013).

34. Singh, K. and Chauhan, S. Interactional behavior of sodium cholate and sodium deoxycholate in the presence of ceftriaxone sodium: volumetric, compressibility, viscometric, and proton nuclear magnetic resonance studies. *J. Chem. Eng. Data* **65**, 4536–4546 (2020).

35. Janek, T., Czeleń, P., Gudiña, E. J., Rodrigues, L. R. and Czyżnikowska, Ż. Biomolecular interactions of lysosomotropic surfactants with cytochrome c and its effect on the protein conformation: A biophysical approach. *Int. J. Biol. Macromol.* **126**, 1177–1185 (2019).

36. Srivastava, A., Dey, J. & Ismail, K. Interaction of tetracaine hydrochloride with sodium deoxycholate in aqueous micellar phase and at the surface. *Colloids Surfaces A Physicochem. Eng. Asp.* **466**, 181–188 (2015).

37. Menger, F. M. On the Structure of Micelles. *Acc. Chem. Res.* **12**, 111–117 (1979).

38. Chakraborty, T., Chakraborty, I., Moulik, S. P. & Ghosh, S. Physicochemical and conformational studies on BSA - Surfactant interaction in aqueous medium. *Langmuir* **25**, 3062–3074 (2009).

39. Matsuoka, K., Lee, J. & Moroi, Y. Micellization of bile salts and solubilization into the micelles. *J. Surface Sci. and Technol.* **26**, 105–136 (2010).

40. Kumar, K. & Chauhan, S. Surface tension and UV–visible investigations of aggregation and adsorption behavior of NaC and NaDC in water–amino acid mixtures. *Fluid Phase Equilib.* **394**, 165–174 (2015).

41. Chauhan, S., Sharma, V., Singh, K., Chauhan, M. S. & Singh, K. Influence of lactose on the micellar behaviour and surface activity of bile salts as revealed through fluorescence and surface tension studies at varying temperatures. *J. Mol. Liq.* **222**, 67–76 (2016).

42. Aslam, J., Lone, I. H., Radwan, N. R. E., Siddiqui, M. F., Parveen, S., Alnoman, R. B. and Aslam, R. Molecular Interaction of Amino Acid-Based Gemini Surfactant with Human Serum Albumin: Tensiometric, Spectroscopic, and Molecular Docking Study. *ACS Omega* **4**, 22152–22160 (2019).

43. Vashishat, R., Sanan, R. & Mahajan, R. K. Bile salt-surface active ionic liquid mixtures: mixed micellization and solubilization of phenothiazine. *RSC Adv.* **5**, 72132–72141 (2015).

44. Srivastava, A., Uchiyama, H., Wada, Y., Hatanaka, Y., Shirakawa, Y., Kadota, K., & Tozuka, Y. Mixed micelles of the antihistaminic cationic drug diphenhydramine hydrochloride with anionic and non-ionic surfactants show improved solubility, drug release and cytotoxicity of ethenzamide. *J. Mol. Liq.* **277**, 349–359 (2019).

45. Bharmoria, P., Trivedi, T. J., Pabbathi, A., Samanta, A. & Kumar, A. Ionic liquid-induced all-α to α+ β conformational transition in cytochrome c with improved peroxidase activity in aqueous medium. *Phys. Chem. Chem. Phys.* **17**, 10189–10199 (2015).

46. Löwenich, D. & Kleinermanns, K. Porphyrin fluorescence dominates UV photoemission of folded cytochrome c. *Photochem. Photobiol.* **83**, 1308–1312 (2007).

47. Singh, U. K. & Patel, R. Dynamics of Ionic Liquid-Assisted Refolding of Denatured Cytochrome c: A Study of Preferential Interactions toward Renaturation. *Mol. Pharm.* **15**, 2684–2697 (2018).

48. Zaragoza, A., Teruel, J. A., Aranda, F. J., Marques, A., Espuny, M. J., Manresa, A. and Ortiz, A., Interaction of a Rhodococcus sp. Trehalose Lipid Biosurfactant with Model Proteins: Thermodynamic and Structural Changes. *Langmuir* **28**, 1381–1390 (2012).

49. Hamada, D., Hoshino, M., Kataoka, M., Goto, Y. & Fink, A. L. Intermediate Conformational States of Apocytochrome c. *Biochemistry* **32**, 10351–10358 (1993).

50. Ahluwalia, U., Nayeem, S. M. & Deep, S. The non-native conformations of cytochrome c in sodium dodecyl sulfate and their modulation by ATP. *Eur. Biophys. J.* **40**, 259–271 (2011).

51. Singh, U. K., Kumari, M., Khan, S. H., Bohidar, H. B. & Patel, R. Mechanism and Dynamics of Long-Term Stability of Cytochrome c Conferred by Long-Chain Imidazolium Ionic Liquids at Low Concentration. *ACS Sustain. Chem. Eng.* **6**, 803–815 (2018).

52. Singh, U. K., Kumari, M. & Patel, R. Dynamics of cytochrome c in surface active ionic liquid: A study of preferential interactions towards denaturation. *J. Mol. Liq.* **268**, 840–848 (2018).

53. Liu, W., Guo, X. & Guo, R. The interaction between hemoglobin and two surfactants with different charges. *Int. J. Biol. Macromol.* **41**, 548–557 (2007).

54. Paul, B. K., Samanta, A. & Guchhait, N. Exploring hydrophobic subdomain iia of the protein bovine serum albumin in the native, intermediate, unfolded, and refolded states by a small fluorescence molecular reporter. *J. Phys. Chem. B* **114**, 6183–6196 (2010).

55. Kumar, M., Bhardwaj, A., Elahi, D., Singh, O.G., Singh, S.K., Gatasheh, M.K., Irfan, M., Singh, N. and Srivastava, A. Counterion association of ionic drugs with sodium tetradecyl sulfate in the aqueous medium. *ACS omega* **8**, 45942–45951 (2023).

56. Srivastava, A., Yañez, O. & Cantero-López, P. Mixed micellization of bile salts and transglycosylated stevia and enhanced binding and solubility of non-steroidal anti-inflammatory drugs using mixed micelle. *J. Mol. Liq.* **311**, 113341 (2020).

57. Manavalan, P. & Johnson, W. C. Sensitivity of circular dichroism to protein tertiary structure class. *Nature* **305**, 831–832 (1983).

58. Banci, L., Bertini, I., Huber, J. G., Spyroulias, G. A. and Turano, P. Solution structure of reduced horse heart cytochrome c. *J. Biol. Inorg. Chem.* **4**, 21–31 (1999).

59. Chaturvedi, S. K., Ahmad, E., Khan, J. M., Alam, P., Ishtikhar, M. and Khan, R. H., Elucidating the interaction of limonene with bovine serum albumin: A multi-technique approach. *Mol. Biosyst.* **11**, 307–316 (2015).

60. Sarkar, R., Shaw, A. K., Narayanan, S. S., Dias, F., Monkman, A. and Pal, S. K., Direct observation of protein folding in nanoenvironments using a molecular ruler. *Biophys. Chem.* **123**, 40–48 (2006).

61. Banci, L., Bertini, I., Gray, H. B., Luchinat, C., Reddig, T., Rosato, A. and Turano, P. Solution structure of oxidized horse heart cytochrome c. *Biochemistry* **36**, 9867–9877 (1997).

62. Pal, S. K., Peon, J. and Zewail, A. H. Biological water at the protein surface: dynamical solvation probed directly with femtosecond resolution. *Proc. Natl. Acad. Sci.* **99**, 1763–1768 (2002).

63. Akram, M., Bhat, I. A. and Kabir-ud-Din. New insights into binding interaction of novel ester-functionalized m-E2-m gemini surfactants with lysozyme: A detailed multidimensional study. *RSC Adv.* **5**, 102780–102794 (2015).

64. Das, S., Roy, P., Saha Sardar, P. & Ghosh, S. Addressing the interaction of stem bromelain with different anionic surfactants, below, at and above the critical micelle concentration (cmc) in phosphate buffer at pH 7: physicochemical, spectroscopic, & molecular docking study. *Int. J. Biol. Macromol.* **271**, 132368-132387 (2024).

65. Keswani, N. & Kishore, N. Calorimetric and spectroscopic studies on the interaction of anticancer drug mitoxantrone with human serum albumin. *J. Chem. Thermodyn.* **43**, 1406–1413 (2011).

66. Negahdary, M., Sadeghi, S. A., michak, M. H., Zarchi, S. R., Salahi, F., Mohammadi, N., Azargoon, E. and Sayad, A., Direct electron transfer of cytochrome C on cadmium oxide nanoparticles modified carbon paste electrode. *Int. J. Electrochem. Sci.* **7**, 6059–6069 (2012).

67. Wu, Y. & Hu, S. Voltammetric investigation of cytochrome c on gold coated with a self-assembled glutathione monolayer. *Bioelectrochemistry* **68**, 105–112 (2006).

68. Mahajan, S., Sharma, R. & Mahajan, R. K. An investigation of drug binding ability of a surface active ionic liquid: Micellization, electrochemical, and spectroscopic studies. *Langmuir* **28**, 17238–17246 (2012).

69. Sharma, R., Kamal, A. & Mahajan, R. K. A quantitative appraisal of the binding interactions between an anionic dye, Alizarin Red S, and alkyloxypyridinium surfactants: A detailed micellization, spectroscopic and electrochemical study. *Soft Matter* **12**, 1736–1749 (2016).

70. Cohen, S. R. & Bitler, A. Use of AFM in bio-related systems. *Curr. Opin. Colloid Interface Sci.* **13**, 316–325 (2008).

71. Bhat, I. A., Roy, B., Hazra, P. & Kabir-ud-Din. Conformational and solution dynamics of hemoglobin (Hb) in presence of a cleavable gemini surfactant: Insights from spectroscopy, atomic force microscopy, molecular docking and density functional theory. *J. Colloid Interface Sci.* **538**, 489–498 (2019).

72. Bhat, I. A., Roy, B., Hazra, P. & ud-Din, K., Conformational and solution dynamics of hemoglobin (Hb) in presence of a cleavable gemini surfactant: Insights from spectroscopy, atomic force microscopy, molecular docking and density functional theory. *J. Colloid Interface Sci.* **538**, 489–498 (2019).

73. Rudra, S., Dasmandal, S. & Mahapatra, A. Binding interaction of sodium-N-dodecanoyl sarcosinate with hemoglobin and myoglobin: Physicochemical and spectroscopic studies with molecular docking analysis. *J. Colloid Interface Sci.* **496**, 267–277 (2017).

Table 1. Transition concentration of bile salts in the presence of heme protein Cyt C (5 μM) obtained from absorbance measurements at 298 K.

System	CAC (mM)	Cs (mM)	CMC (mM)
NaDC-Cyt C	0.59	1.41	3.18
NaC-Cyt C	1.03	4.73	7.18

Table 2. Binding constant (k_b) and standard Gibbs free energy change (ΔG^0) of bile salts interaction with Cyt C, determined by Benesi-Hildebrand plot at room temperature.

System	k_b $(M^{-1})\times10^{-3}$	$-\Delta G^0$ (kJ/mol)
NaDC-Cyt C	0.75	16.40
NaC-Cyt C	0.41	14.90

Supplementary Section

Calculation of various surface parameters from tensiometry:

Π_{cmc} (surface pressure) was calculated by implementing the equation:

$$\Pi_{CMC} = \gamma_0 - \gamma_{CMC} \quad (1)$$

γ_0 and γ_{CMC} denote the corresponding surface tension values for the solvent and the mixture at CMC, respectively.

The value of Γ_{max} (Gibbs surface excess concentration) was calculated by applying the equation.[1, 2]

$$\Gamma_{max} = -\frac{1}{2.303nRT}\left[\frac{d\gamma}{d\log C}\right] \quad (2)$$

Γ_{max} is the surface excess concentration of the amphiphiles, n stands for the number of species lying at the air-water interface when the amphiphile molecules are dissociated, R is the universal gas constant, and T represents the temperature in the Kelvin scale. C is the amphiphile

concentration in moles/L, γ represents surface tension in mN/m and $\frac{d\gamma}{d\log C}$ represents the slope of the γ vs. log C plot. Here, the value of n is 2 for both the bile salts. A_{min} can also be calculated from Γ_{max}, where A_{min} is the minimum area that is covered by each of the surfactant molecules at the interface: -

$$A_{min} = \frac{10^{20}}{N_A \Gamma_{max}} \quad (3)$$

N_A is the Avogadro number.

Table S1. Surface parameters (micellar parameters) obtained from surface tension measurements for bile salts (NaDC and NaC) in the absence and presence of 5 μM Cyt C in phosphate buffer medium (pH 7.4) at 298 K.

System	CMC (mM)	γ_{CMC} (dyne cm^{-1})	$10^6\ \Gamma_{max}$ ($molm^{-2}$)	A_{min} ($Å^2$)	π_{CMC} (dyne cm^{-1})	pc_{20}	$-\Delta G^0_{micelle}$ (kJ/mol)	$-\Delta G^0_{ads}$ (kJ/mol)
NaDC	3.91	43.2	1.02	161.13	26.3	3.02	21.5	38.40
NaDC-Cyt C	3.18	40.8	0.81	203.24	21.5	2.67	22.2	45.47
NaC	8.67	47.0	0.95	173.34	21.2	2.24	18.62	37.02
NaC-Cyt C	6.85	46.8	0.69	237.17	18.4	2.13	19.07	42.40

The errors in the CMC are ± 2%.

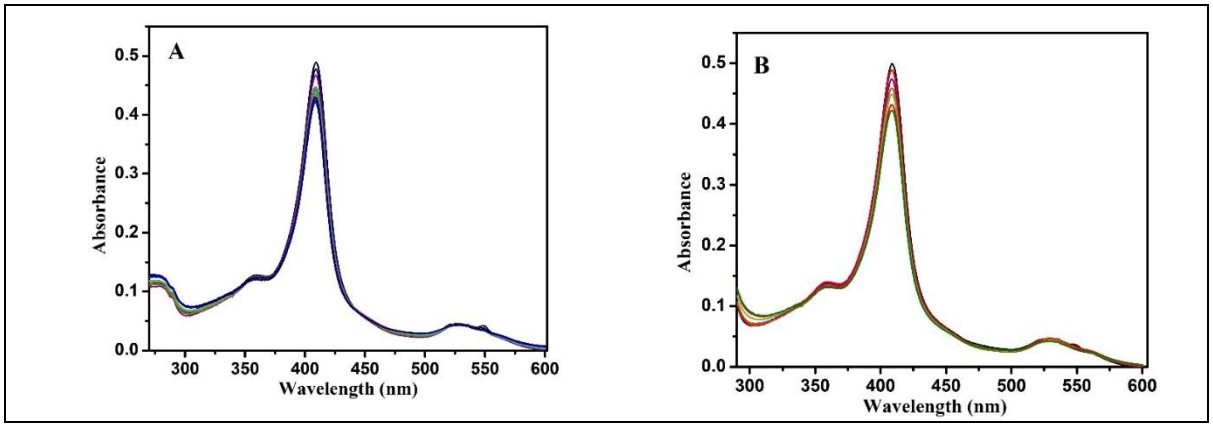

Fig. S1 Variation of UV-Vis spectra of Cyt C in the absence and the presence of bile salts, (A) NaDC and (B) NaC respectively.

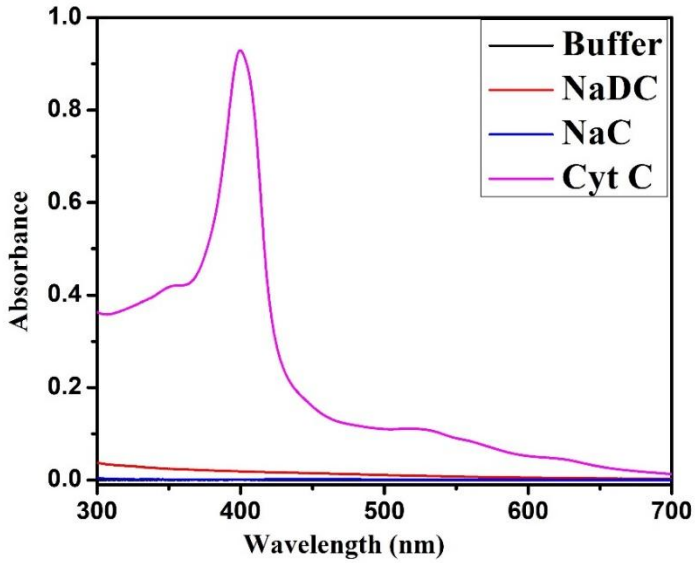

Fig. S2 Absorbance spectra of buffer solution, bile salts (NaDC & NaC), and Cyt C respectively.

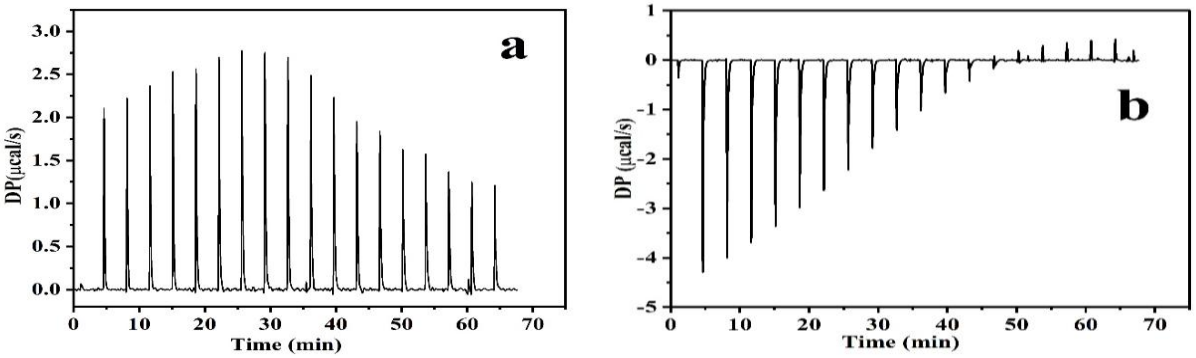

Fig. S3. ITC profile for the binding of NaDC (a) and NaC (b) to Cyt C, indicating the raw data for sequential injection of bile salt to the proteins.

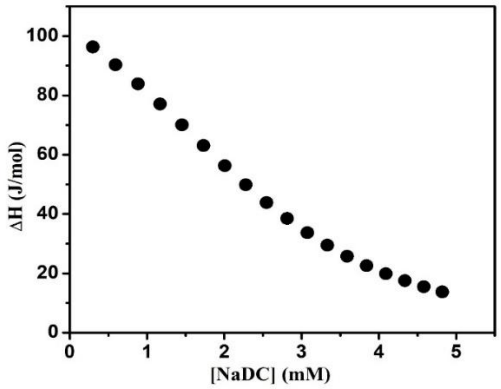

Fig. S4 Plot of variation in the integrated heat data against the concentration of NaDC in phosphate buffer medium at pH 7.4, 298 K.

Table S2 Variation of α-sheet and β-sheet contents of Cyt C in the presence of various amounts of bile salts in pH 7.4, at 298 K.

NaDC			NaC		
C (mM)	α-sheet (%)	β-sheet (%)	C (mM)	α-sheet (%)	β-sheet (%)
0	37.5	16.4	0	37.5	16.4
0.08	36.8	16.8	0.12	37.0	16.6
0.6	35.1	17.1	2.4	35.2	16.7
1.8	34.8	17.6	5.6	34.5	16.9
4.2	33.9	17.9	8.5	34.2	17.1

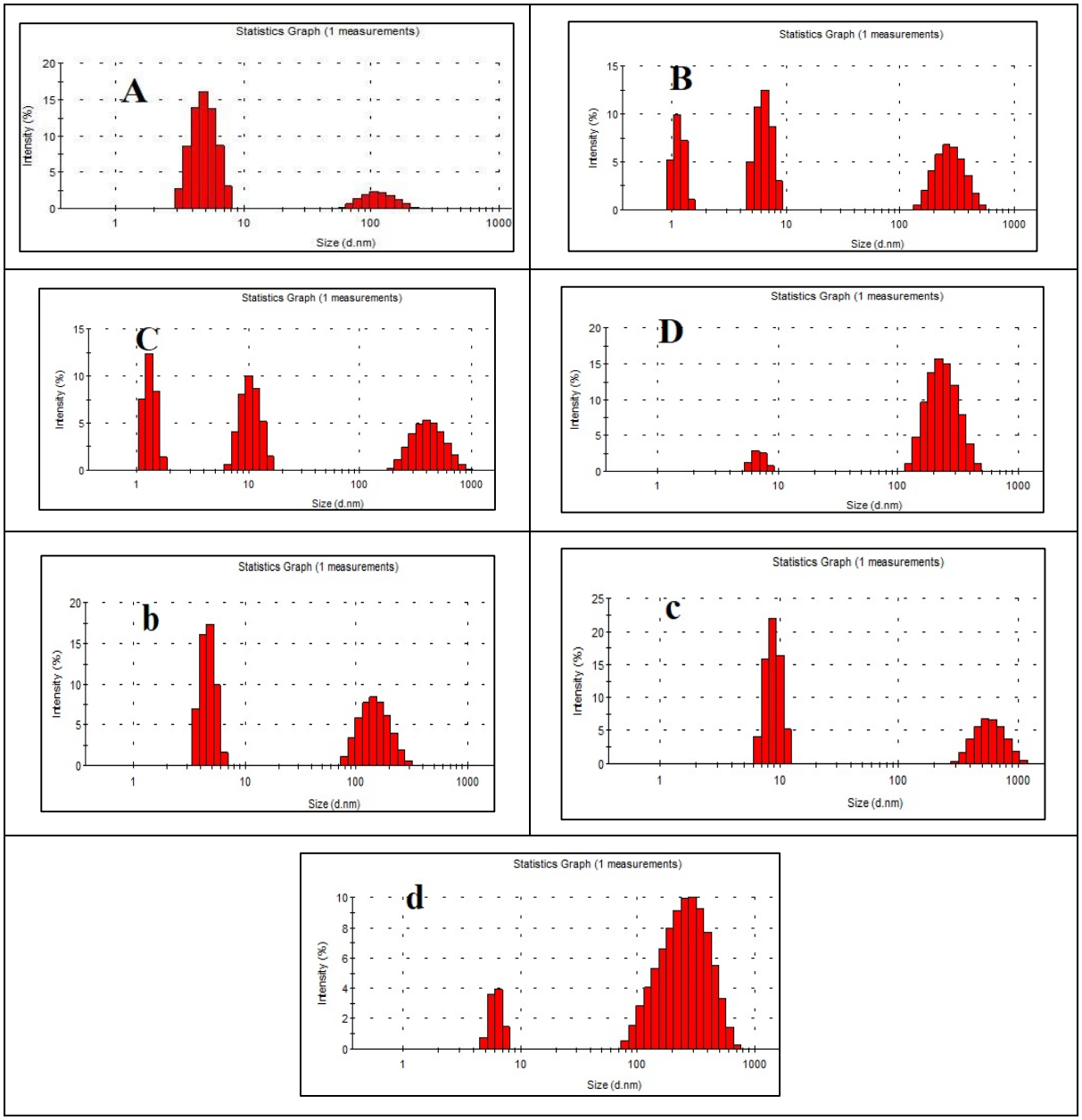

Fig. S5. Instrument generated raw DLS histogram for the variation of hydrodynamic diameter (D_h) of Cyt C in the presence of different concentrations of bile salt, (A) pure Cyt C, (B) 0.45 mM, (C) 1.22 mM, and (D) 3.25 mM NaDC; and (b) 1.25 mM, (c) 2.55 mM and (d) 9.55 mM NaC, respectively.

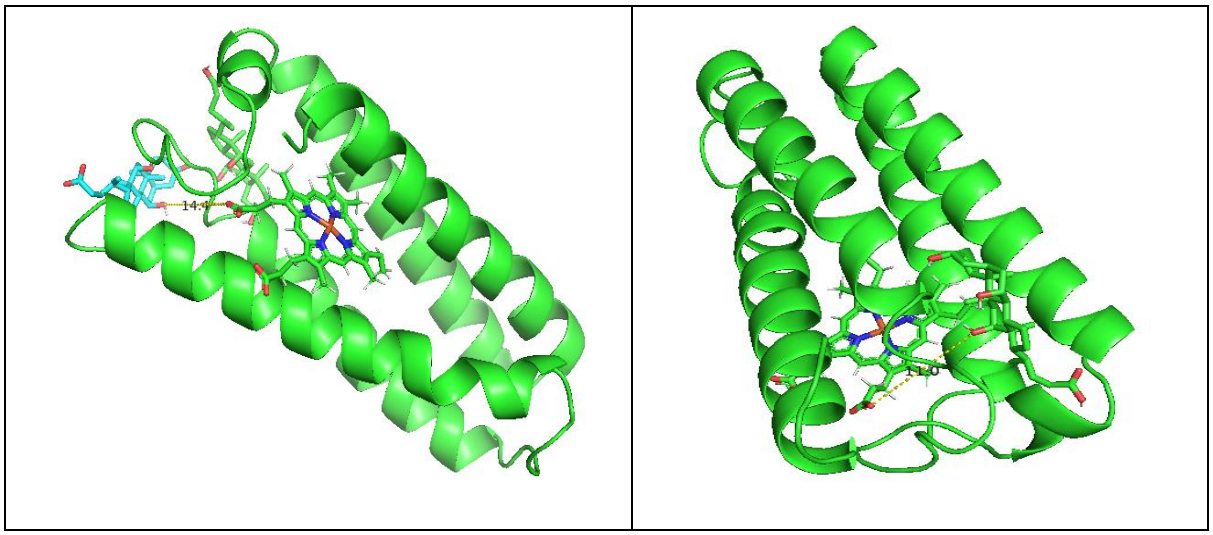

Fig. S6 Docking structure of NaDC (A), and NaC (B) with Cyt C; showing the distance between the bile salt and the heme group of the protein.

References:

1. Sardar, R., Das, S., Banik, R., Bhunia, S. & Ghosh, S. Exploration of the impact of graphene oxide, acetylenic gemini, and CTAT on the photophysical and aggregation properties of dipolar coumarin 153. *Phys. Chem. Chem. Phys.* **26**, 8900–8918 (2024).
2. Banik, R., Das, S., Ghosh, A. & Ghosh, S. Comparative studies on the aggregate formation of synthesized zwitterionic gemini and monomeric surfactants in the presence of the amphiphilic antipsychotic drug chlorpromazine hydrochloride in aqueous solution: an experimental and theoretical approach. *Soft Matter* **19**, 7995–8010 (2023).

Chapter-III

Composition and concentration gradient dependent catanionic vesicle preparation of long-chain ionic liquid and its interaction study with model protein: An HSA case study

Composition and concentration gradient dependent catanionic vesicle preparation of long-chain ionic liquid and its interaction study with model protein: An HSA case study

Abstract:

Soft nanosystems (micelles, vesicles, reverse micelles, etc.) are highly significant in the biomedical field as a delivery system of biomolecules and drugs because of their easily modulable shape. Surface active ionic liquid (SAILs)--based vesicles are increasingly popular due to their eco-friendly and less toxic properties, gaining applications in gene therapy, micellar catalysis, protein and drug delivery, etc. This article presents a comparative study on the interaction of cationic- and anionic-rich vesicles prepared using a SAIL (1-hexadecyl-3-methylimidazolium chloride, C_{16}MimCl) and Aerosol OT (AOT) with a model protein (HSA) in aqueous buffer medium at pH 7.4. The interaction study used various physicochemical, spectroscopic, thermodynamic, and morphological measurements. The steady-state fluorescence spectra of the Trp214 residue of HSA were found to change slightly in cationic-rich vesicles barely but nearly disappeared in anionic-rich vesicles. This suggests that the tertiary structure of HSA was preserved in cationic-rich vesicles, but broken down in anionic-rich vesicles. DLS experiments show that the volume of cationic-rich vesicles rapidly rises (197.32 nm to 1091.31 nm at the addition of about 4 μM HSA) without disrupting their vesicular structure, but anionic-rich vesicles split into smaller vesicles upon protein incorporation. The volume expansion of cationic-rich vesicles during protein adsorption is readily visible in TEM micrographs of the protein-vesicle assembly. Zeta potential measurements indicate that electrostatic attraction plays a major role in protein adsorption on cationic-rich vesicle surfaces, whereas electrostatic repulsion on anionic-rich vesicles leads to the disintegration of vesicle structure during protein adsorption. According to the CD analysis, a little structural alteration (~2%) of HSA occurs in anionic-rich vesicles, while no secondary structural change occurs in cationic-rich vesicles. The overall experimental results reveal that, in cationic-rich vesicles, protein loading preserves both the vesicle and protein structure, making it suitable for use as an injectable drug delivery system (DDS), this is not the case with anionic-rich vesicles. As a result, this vesicular system would play a crucial role in biological and biomedical fields for applications such as drug delivery, protein stability, etc.

1. Introduction:

Ionic liquids (ILs) are a novel class of materials that have garnered global scientific and industrial attention in the last decades due to their special physicochemical qualities that are beneficial for a wide range of applications.[1-6] Owing to these special qualities, these salts are becoming more and more well-liked as the need for sustainable, "green" chemistry grows.[7,8] Interestingly, the constituent ions of ILs can be selectively changed to alter their nature from simple to functional,[9,10] hydrophobic to hydrophilic,[11,12] or electrolytic to surfactant-like.[13] Ionic liquids with shorter alkyl chains behave as electrolytes [14], whereas long alkyl chains act as amphiphiles in the aqueous medium.[15] In recent years, surface active ionic liquids (SAILs), a new class of ionic liquids (ILs) with long alkyl chains that combine the characteristics of surfactants and ILs, [16] and show amphiphilic behaviours, have been used in solution chemistry. Since SAILs are environmentally friendly and amphiphilic in nature, it can be effectively used as a good alternative to conventional surfactants in various applications like protein folding, micellar catalysis, drug delivery, solubilization, etc.[17-20] The SAILs with imidazolium or pyridinium head groups having eight or more carbon atoms exhibit antimicrobial activity in the aqueous medium, and this activity increases with increasing chain lengths of SAILs.[21] Due to these wide ranges of applications, a lot of research groups are involved in the synthesis of SAILs with different approaches.[22,23] The self-assembled of SAILs in aqueous as well as nonaqueous solvents to different kinds of aggregates (such as direct micelle, vesicle, or reverse micelle) is the current topic of interest.[24-26]

Vesicles are membrane-mimicking structures made of spherical amphiphilic molecular bilayers (block copolymers, lipids, or surfactants) with an internal aqueous reservoir.[27] Vesicles can be divided into small (1-100 nm), large (100-1000 nm), giant (1-100 μm), and uni or multilamellar vesicles according to differences in their sizes. Over the past few decades, phospholipid-based vesicles have been the focus of extensive research as drug and gene delivery vehicles due to their unique capacity to solubilize both hydrophilic and hydrophobic compounds.[28,29] However, phospholipids have the potential to be useful drug carriers, but there are challenges due to their instability, hydrolysis susceptibility, high cost, and difficult vesicle-forming process. As a result, researchers are interested in preparing vesicles without the use of lipids, and they have been able to do so by employing various surfactant molecules in place of lipids. Further research on bilayer membranes of catanionic surfactant systems was sparked by Kaler et al.'s [30] initial report on the spontaneous generation of cationic and anionic (catanionic) surfactant vesicles in aqueous medium. When two surfactants with oppositely charged head groups are

mixed in the proper ratio at particular concentrations, soft, spherical, thermodynamically stable materials known as catanionic surfactant vesicles (SVs) spontaneously form in aqueous solution.[31-38] The catanionic vesicle formation by conventional surfactants has been extensively studied in the last three decades due to their huge range of applications. Since most of the surfactants are not eco-friendly and have sufficient toxicity, they limit their application as a constituent of vesicles. As a result, in recent years, IL-like surfactant vesicles have become a popular field of research due to their eco-friendly and less toxic characteristics. Recently, Lepori et. al [39] reported the formation of the unilamellar vesicles by IL-like surfactants with potential application in biomedicine. In the present work, we have focused on preparing a catanionic vesicle by long-chain ionic liquid and Aerosol OT (AOT) in the aqueous medium and studying its interaction with a model protein, Human Serum Albumin (HSA). Here, two different kinds of vesicles were prepared depending on the mole fractions of the two components, (i) cationic-rich vesicles (χ_{AOT}= 0.5), and (ii) anionic-rich vesicles ($\chi_{AOT} = 0.6$), and an interesting comparative study of the interaction of these two vesicular systems with the model protein was performed. To probe the type of interaction involved between the two vesicular systems with HSA, various spectroscopic, thermodynamic, adsorption isotherm, and morphological analyses were done. The overall study suggests that the adsorption of HSA on cationic-rich vesicles is governed by both electrostatic and hydrophobic interactions, whereas in the case of anionic-rich vesicles, only hydrophobic interaction takes place. The steady-state fluorescence and far-UV CD spectra measurements suggest that the tertiary and secondary structures of HSA remain intact in the cationic-rich vesicular system, whereas a structural loss was observed in anionic-rich vesicles. The experimental results infer that the cationic-rich vesicular system can be applied as an effective injectable drug delivery system (DDS). In contrast, the anionic-rich vesicular system is unsuitable for this purpose.

2. Experimental section:

2.1 Materials:

Human Serum Albumin (HSA, 97%), coumarin 153 (C153), and sodium 1,4-bis (2-ethyl-hexyl) sulfosuccinate were purchased from Sigma-Aldrich Corporation (U.S.A) (NaAOT, 98%). 1-hexadecyl-3-methyl imidazolium chloride [C_{16}MimCl, 98%] was procured from Acros Organics (Germany). All the protein samples were prepared in a 10 mM phosphate buffer solution. AOT was used after proper drying in a vacuum (24 h). All the samples are used without further purification.

2.2 Instrumentation:

2.2.1 Turbidity measurements:

Turbidity measurement was done by measuring the transmittance (T) of C_{16}MimCl/AOT solution mixtures at various mole fractions using a Shimadzu (model No. UV-1601 (Japan)) spectrophotometer at 500 nm due to the absence of any absorption of the individual solution of C_{16}MimCl and AOT. Using the relation t = 100-%T, the turbidity of the mixture solution was calculated. All the measurements were performed at 298 K.

2.2.2 Steady-state anisotropy measurements:

Steady-state fluorescence anisotropy was measured using a Perkin Elmer LS55 (USA) fluorescence spectrofluorometer linked to a fluorescence Peltier system PTP-1 with a glass cell with a 1 cm path length. Using 422 nm excitation and 544 nm emission wavelengths, the steady-state fluorescence anisotropy (r) of coumarin 153 was determined. The steady-state anisotropy (r) can be defined as follows:

$$r = \frac{I_v - GI_h}{I_v + 2GI_h} \quad (1)$$

where I_h and I_v represent the horizontally and vertically polarized emission intensities, respectively, that result from the probe's vertically polarized excitation. Factor G can be described as follows:

$$G = \frac{I_v}{I_h}$$

Over a 20-second integration period, the average anisotropy values were calculated.

2.2.3 Dynamic light scattering (DLS) and Zeta potential measurements:

Zetasizer Nano ZS (Malvern, UK) was used to measure zeta potential and DLS at a 90° scattering angle with a He–Ne laser (λ = 632.8 nm). All the solutions were filtered three times via membrane filters with a porosity of 0.25 μm to remove larger particles in DLS measurements. Every measurement was done twice, with the mean values recorded, to produce more accurate findings. The measurements have a 7–9% standard variation.

2.2.4 Transmission electron microscopy (TEM):

Japan-made JEOL-JEM 2100 transmission electron microscope, having a 100 kV accelerating voltage, was used. A 300-mesh carbon-coated copper grid was utilized to adsorb 10 microliters

of sample solutions with a certain mole fraction. Using the filter paper that it was placed on, extra liquid on the copper grid was quickly removed. Freshly prepared 0.5-weight percent aqueous uranyl acetate was used to stain it negatively. A desiccator was used to keep the samples overnight.

2.2.5 Tensiometry:

Surface tension was measured using the ring detachment method with the Krüss tensiometer (Germany). Using a Hamilton micro syringe, a concentrated stock solution of C_{16}MimCl/AOT at a certain mole fraction of AOT was added to the aqueous buffer. Five minutes were given for equilibration before each measurement. All measurements were made three times to ensure accuracy. The precision of the procedure was 0.1 mN m^{-1}. The Critical Vesicle Concentration (CVC) was computed by plotting surface tension (γ) vs. log [mixed surfactant] and analyzing the breaks in the plot.

2.2.6 Steady-state spectral measurements:

The absorption and fluorescence emission spectra were recorded using a Shimadzu 1601 UV-vis spectrophotometer from Japan and a PerkinElmer LS 55 fluorescence spectrophotometer from the United States. The absorbance data of HSA was recorded in the wavelength range of 230-500 nm. The emission spectra of HSA in aqueous buffer were recorded at an excitation wavelength of 295 nm, using an emission and excitation slit width of 5 nm, within the range of 310–500 nm. All experiments were performed in a 10 mM phosphate buffer medium with 5 μM of HSA.

2.2.7 Fluorescence quenching analysis:

The intrinsic fluorescence quenching of HSA by vesicle solution was analysed by using the well-known Stern-Volmer equation [40,41]

$$F_0/F = 1 + K_{SV}[Q] \quad (2)$$

where F_0 and F denote the fluorescence intensity of the fluorophore (HSA) in the absence and presence of a quencher (vesicle) molecule respectively; [Q] is the quencher concentration and K_{SV} is the Stern-Volmer quenching constant.

Additionally, the modified Stern-Volmer equation [40,42] was used to investigate the quenching of emission intensity due to the differential accessibility of the quencher to the fluorophore.

$$\frac{F_0}{F_0-F} = \frac{1}{f} + \frac{1}{f}\frac{1}{K_Q[Q]} \quad (3)$$

Where f is the fractional accessibility of HSA fluorescence to the quencher and K_Q is the modified Stern-Volmer constant.

2.2.8 Time-resolved fluorescence study:

The Horiba-Jobin-Yvon FluoroCube fluorescence lifetime system, which uses a NanoLED at 300 nm (IBH, UK) and a TBX photon detection module as the detector, was used to perform time-resolved fluorescence decay. Each decay data point was fitted using the IBH DAS-6 decay analysis software. Instead of using the sample, a diluted sodium dodecyl sulphate micellar solution was used as a scatter for recording the light profile (IRF). For the appropriate fits, the $\chi 2$ values remained rather close to 1.

2.2.9 Isothermal titration calorimetry (ITC) measurements:

The device used for the isothermal titration calorimetry (ITC) studies was a Microcal ITC-200, Malvern, UK. The experimental temperature was kept constant at 298 K. Each ITC experiment consisted of 21 syringe injections of vesicles into the protein sample in the cells 180 seconds apart. A 300 mL HSA solution (5 μM) was supplied to the cell, and each injection included the addition of 2 μL of [C_{16}Mim] [AOT] mixed solution by syringe. Using ITC software, the data was examined to determine how much heat was absorbed or released due to the interaction with the protein at each stage of mixed surfactant addition.

2.2.10 Circular Dichroism (CD) spectroscopy:

Using a Jasco spectropolarimeter (J-815), CD spectra have been acquired in the far-UV region (200-260 nm) to analyze the conformational changes of HSA molecules. In the nitrogen-inert atmosphere, the spectra were measured using two quartz cuvettes having a path length of 1 cm. The concentration of the HSA solution was 2.5 μM, and the scanning speed was 250 nm/min. The sample temperature was maintained at 298±0.2 K with a Neslab RTE-111 rotating water bath connected to quartz cuvettes with water jackets. Using CDNN 2.1 software, the secondary structures of HSA were computed. After deducting the magnitude of the appropriate buffer solution spectra throughout the 200–260 nm wavelength range, the final CD spectra were recorded. The CD data have been expressed as mean residue ellipticity (MRE) in deg$cm^2 dmol^{-1}$ using the following equation

$MRE=\theta_{obs}/10nl[c]$ **(4)**

where l is the cell's path length, [c] is the molar concentration of proteins, n is the number of amino acid residues in protein molecules, and θ_{obs} is CD in mdeg.

2.3 Preparation of ionic liquid-based catanionic vesicle:

An easy and direct procedure was used to prepare the ionic liquid-based catanionic vesicles. Combining SAILs with oppositely charged AOT in the appropriate concentration and mole fraction. Here, the Clint equation was used to prepare various mixed micelle/vesicle solutions. The aqueous solutions of SAILs were mixed with an AOT solution of the same concentration (a 20 mM stock solution of both amphiphiles) but different in mole fraction, resulting in a mixture that was thoroughly mixed in bath sonication.

3. Results and discussion:

3.1 Characterization of vesicles:

3.1.1 Phase transition study: In the aqueous solution, after a certain concentration of C_{16}MimCl, tiny aggregates are formed called micelles. But, in the presence of oppositely charged Na-AOT, its aggregation behaviours changed depending upon the mole fractions of the two amphiphiles. These changes in aggregation pattern are reflected in their phase behaviour, which is even visible to the naked eye. By monitoring the variation in turbidity of the mixture solution, a UV-Vis spectrophotometer is used to track these visible changes in phase behaviour of [C_{16}Mim] [AOT] mixtures. From the turbidity plot of the [C_{16}Mim] [AOT] mixture (Fig. S1 (A)), it can be seen that the mixture solution stays transparent up to $\chi_{AOT} = 0.4$, indicating the presence of small mixed micellar aggregates. But after that, the solution becomes very turbid ($\chi_{AOT} = 0.5$-0.6), indicating the formation of large aggregates. With further increasing AOT concentration, again, the solutions become transparent, suggesting that large aggregates disintegrate into small ones. The large aggregates indicate the possible existence of mixed aggregates, most notably "vesicles". So, the turbidity analysis suggests that a vesicular solution is obtained at χ_{AOT} = 0.5-0.6, and steady-state anisotropy, DLS, and TEM measurements further validate it.

3.1.2 Steady-state anisotropy: By monitoring the variation in the steady-state fluorescence anisotropy, one can also anticipate morphological changes in amphiphilic aggregates. Here, we have used a hydrophobic C153 probe to assign the nature of aggregate forms in the aqueous solution of [C_{16}Mim] [AOT] mixture. The hydrophobic nature of C153 allows it to be inserted

into the bilayer moiety. Therefore, compared to bulk solvent, its rotational motion is restricted in the bilayer. Thus, a low degree of rotation is associated with a high anisotropy (r) value and vice versa. Fig. S1 (B) shows the variation in steady-state anisotropy of the [C_{16}MimCl] [AOT] aggregates in different mole fractions of AOT. From the figure, it can be observed that with increasing AOT concentration, the anisotropy value of the aggregate system increases at first and becomes maximum at χ_{AOT} = 0.5-0.6, after that anisotropy value decreases with further increasing AOT. So, anisotropy measurements indicate the formation of large and compact aggregates at χ_{AOT} = 0.5-0.6, which are not normal micellar aggregates.

3.1.3 Dynamic light scattering (DLS) and HR-TEM analysis:

The hydrodynamic size distribution profile of [C_{16}Mim] [AOT] mixtures at various χ_{AOT} is presented in Fig. S1 (C). As AOT is introduced into the C_{16}MimCl micellar solution, the hydrodynamic diameter (D_h) of the C_{16}Mim/AOT mixture gradually increases and becomes maximum at χ_{AOT} = 0.5-0.6. The D_h values at χ_{AOT} = 0.5 and χ_{AOT} = 0.6 are 249.36 nm and 244.85 nm, respectively. After χ_{AOT} = 0.6, a decrease in D_h value was observed with further increasing AOT. A temperature-induced transition from micelle to vesicle was reported by Moughton et al.[43] in a previous work, the estimated vesicle size was around 200 nm. So, it can be concluded that the observed aggregate at χ_{AOT} = 0.5-0.6 is mainly due to the formation of vesicles with an average value of D_h ~250 nm. To give direct and microscopic evidence of vesicle formation, HR-TEM measurements were performed with χ_{AOT} = 0.5 and χ_{AOT} = 0.6 mixtures. The TEM micrographs (Fig. S2) indicate the formation of spherical vesicles with bilayer regions. The average size of vesicles obtained from TEM is ~200-250 nm. The results correlate well with the DLS measurements.

3.2 Solution phase stability check of vesicles by zeta potential measurements:

To predict the solution phase stability of formed vesicles, zeta potential measurements were performed at χ_{AOT} = 0.5 and χ_{AOT} = 0.6, and the obtained values were + 66.4 mV and -71.28 mV, respectively. The obtained zeta potential value indicates that both the vesicular systems are highly stable in the solution phase. From that value, it is also clear that the formed vesicle at χ_{AOT} = 0.5 is cationic-rich, whereas at χ_{AOT} = 0.6 it is anionic-rich. So, the zeta potential measurements not only assign the stability of the vesicle, but also predict the overall charge of the two vesicular aggregates.

3.3 Interaction study of formed catanionic vesicle with the model protein (HSA):

3.3.1 Adsorption isotherm analysis:

Tensiometry is a powerful technique to assign the interfacial adsorption of amphiphiles and is also helpful in determining the various surface parameters. The interactions of amphiphiles with proteins not only affect the properties of the bulk phase but also the interfacial activity; so, the study of protein-surfactant interaction by adsorption isotherm is very important. Both electrostatic and hydrophobic interactions are responsible for protein-surfactant complex formation, and the formed complex is surface-active in nature. The surface activity of the [C_{16}Mim] [AOT] mixture was studied in pH=7.4 phosphate buffer (10 mM) at 298 K. Fig. 1 shows the variation of surface tension with the logarithmic concentration of [C_{16}Mim] [AOT] with two different mole fractions of AOT in the absence and presence of HSA. The experimentally obtained critical vesicle concentration (CVC) value of the [C_{16}Mim] [AOT] mixture in both mole fractions of AOT is much lower than the ideal value predicted by the Clint model. Two factors are responsible for the lowering of the CVC value.

1) In the buffer medium, the electrostatic repulsion between the similarly charged groups is minimized (due to high ionic strength), resulting in early aggregation.[44]

2) A highly synergistic interaction between the oppositely charged [C_{16}Mim] and [AOT] causes to appearance of vesicles at lower concentration.

It can be seen from Fig. 1 that with the gradual addition of [C_{16}Mim] [AOT], there was a rapid decrease in surface tension value and ultimately reached a constant value known as CVC. The experimentally obtained CVC values for [C_{16}Mim] [AOT] at χ_{AOT} = 0.5 and χ_{AOT} = 0.6 are 0.0157 mM and 0.0183 mM, respectively (Table S1). In the presence of HSA protein, two distinct breakpoints were found in the tensiometric profile. In this case, initially, there was no significant change in the surface tension value with [C_{16}Mim] [AOT] found (for both χ_{AOT} = 0.5 and χ_{AOT} = 0.6) in the presence of a 5 μM HSA solution. Here, the monomeric [C_{16}Mim] [AOT] interacted with the protein molecule, and a protein surfactant complex was formed, which was less surface-active than pure surfactant. The first breakpoint is known as the critical aggregation concentration (CAC) of the protein surfactant complex, where a protein-bound micelle is formed around the backbone of the biopolymer.[45] The obtained CAC values for [C_{16}Mim] [AOT] at χ_{AOT} = 0.5 and χ_{AOT} = 0.6 are 0.0047 mM and 0.0057 mM respectively (Table S1). After the CAC, with further addition of [C_{16}Mim] [AOT], a critical point is reached

where no change in surface tension value with [C_{16}Mim] [AOT] concentration occurs. This point is known as the critical vesicular concentration (CVC) of the amphiphiles. The CVC for [C_{16}Mim] [AOT] at χ_{AOT} = 0.5 and χ_{AOT} = 0.6 were 0.0157 mM and 0.0183 mM, respectively in the absence of HAS (Table S1). There was a significant change in the CVC value for both surfactants in the presence of protein molecules. In the presence of HSA, the obtained CVC value for [C_{16}Mim] [AOT] at χ_{AOT} = 0.5 and χ_{AOT} = 0.6 was 0.0782 mM and 0.0624 mM, respectively. So, in the presence of HAS, the vesicle formation for both mole fractions of [C_{16}Mim] [AOT] is delayed because at first, some monomeric part interacts with the protein, and after that, the further added surfactant forms the vesicle. The vesicle formation for [C_{16}Mim] [AOT] at χ_{AOT} = 0.5 occurred much later than at χ_{AOT} = 0.6, which suggests that a relatively larger number of [C_{16}Mim] [AOT] units interact with protein for [C_{16}Mim] [AOT] at χ_{AOT} = 0.5 than χ_{AOT} = 0.6. This result can be explained with the help of the isoelectric pH of the HSA protein. Here in the working pH 7.4, the HSA remains anionic (isoelectric pH 5.0),[46] so it can easily interact with the positively charged [C_{16}Mim] [AOT] at χ_{AOT} = 0.5 than χ_{AOT} = 0.6 (which is anionic).

Various surface parameters were calculated at the air/liquid interface and tabulated in Table S1 (supplementary section). The efficiency of interfacial adsorption of [C_{16}Mim] [AOT] was estimated by measuring pC_{20} using the relation

$$pC_{20} = -\log C_{20} \quad (5)$$

where C_{20} denotes the amount of surfactant required to reduce a surface tension value of 20 units. The higher the value of pC_{20}, the greater the adsorption capacity of the amphiphiles at the air/liquid interface. For both the combination of [C_{16}Mim] [AOT] (positively charged at χ_{AOT} = 0.5 and negatively charged at χ_{AOT} = 0.6) in the presence of HSA, there was a decrease in pC_{20} value which signifies that [C_{16}Mim] [AOT]-HSA complex has less tendency to be adsorbed in the interface compare to pure [C_{16}Mim] [AOT] system. If we compare the pC_{20} value for two pure [C_{16}Mim] [AOT], it can be seen that χ_{AOT} = 0.5 has a greater pC_{20} value than χ_{AOT} = 0.6. This phenomenon can be explained with the help of the surface charge of the two components. Since [C_{16}Mim] [AOT] at χ_{AOT} = 0.6 has a greater surface charge (measured by zeta potential) than χ_{AOT} = 0.5, so its tendency to go to the bulk phase is more than χ_{AOT} = 0.5, resulting [C_{16}Mim] [AOT] at χ_{AOT} = 0.6 has less tendency to be adsorbed at the interface and showed less pC_{20} value than at χ_{AOT} = 0.5. Another important surface parameter is π_{CVC}

(i.e., the surface pressure at CVC), which measures the effectiveness of surface tension reduction, and is expressed by the following relation-

$$\Pi_{CVC} = \gamma_0 - \gamma_{CVC} \quad (6)$$

where γ_0 denotes the surface tension in the absence of amphiphiles, and γ_{CVC} is the surface tension at CVC. The Π_{CVC} value for the [C_{16}Mim] [AOT] mixture in the presence of HSA is much lower than in the absence of it (for both the mole-fraction of AOT), which signifies that [C_{16}Mim] [AOT has a lower tendency to adsorbed at the air/water interface in the presence of protein molecule HSA. The number of amphiphilic [C16Mim] [AOT] species in the interface decreases as a result of the formation of a soluble [C16Mim] [AOT]-HSA complex in the presence of protein molecules HSA, which lowers the π_{CVC} value of the amphiphile.

The amount of [C_{16}Mim] [AOT]-HSA adsorbed on the air-water interface is estimated by deriving the surface excess concentration (Γ_{max}) by using the Gibbs adsorption isotherm.[47]

$$\Gamma_{max} = -\frac{1}{2.303nRT}\left[\frac{d\gamma}{d\log C}\right] \quad (7)$$

where 'n' is the number of species at the air-liquid interface after dissociation of amphiphile, *T* is the temperature in Kelvin scale, *R* is the universal gas constant, γ represents surface tension in mN $m^{-1,}$ and $\frac{d\gamma}{d\log C}$ represents the slope of the plot of γ vs. logC. Here, the value of n is 2 for the [C_{16}Mim] [AOT] system. Using the Γ_{max} value, we can find out A_{min} (minimum surface area occupied by each surfactant) by the following relation-

$$A_{min} = 10^{18}/N_A\Gamma_{max} \quad (8)$$

N_A is the Avogadro number. From the Γ_{max} value (in Table S1), it can be seen that [C_{16}Mim] [AOT] at χ_{AOT} = 0.6 has a smaller Γ_{max} value in the presence of HSA, i.e., a larger A_{min} is occupied by the [C_{16}Mim] [AOT]-HSA complex. This is because here [C_{16}Mim] [AOT] and HSA are anionic at pH = 7.4, so due to electrostatic repulsion, a loose complex is formed which occupies a larger area in the interface. But interestingly, an opposite phenomenon was found for [C_{16}Mim] [AOT] at χ_{AOT} = 0.5-HSA system. In this case, the Γ_{max} value increases, i.e., A_{min} decreases compared to pure [C_{16}Mim] [AOT] at χ_{AOT} = 0.5. So, here a compact complex is formed with a low A_{min} value. Because [C_{16}Mim] [AOT] at χ_{AOT} = 0.5 behaves as cationic and

HSA as anionic in nature, a strong electrostatic interaction leads to a stable complex with a low surface area, compared to a pure one.

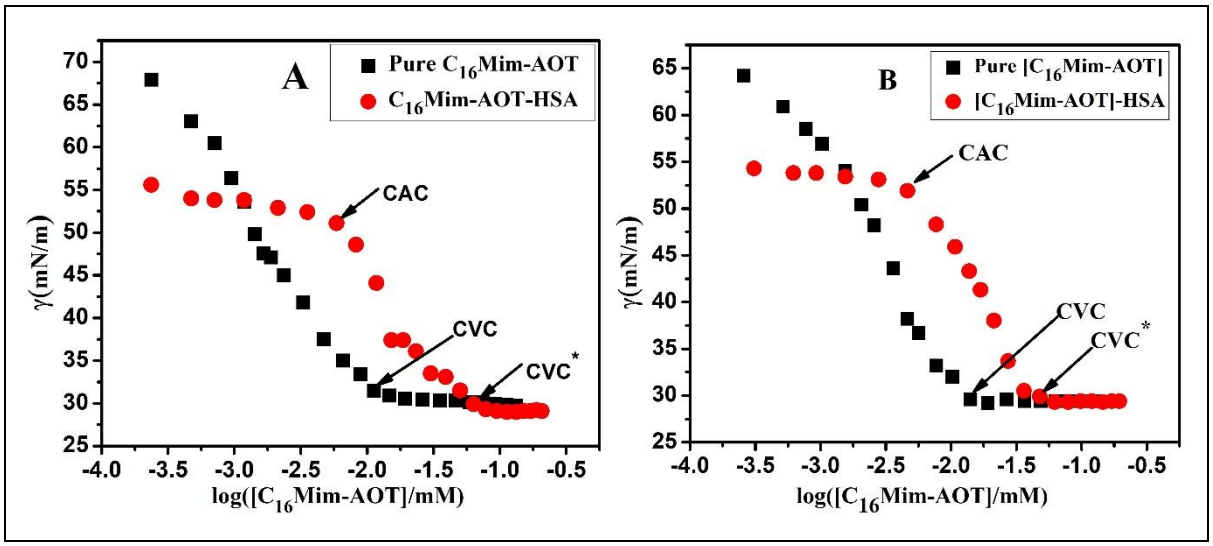

Fig. 1 Tensiometric profile of [C_{16}Mim] [AOT] in the absence and presence of 5 μM HSA, (A) 0.5-mole fraction, and (B) 0.6-mole fraction of AOT at 298 K.

3.3.2 UV-vis Spectroscopy Analysis:

UV-vis spectroscopy is an important technique to predict the interaction between biological macromolecules and ligands in the ground state. The change in absorbance and/or shift in maximum wavelength, Λ_{max} provides useful information about the nature of the complex formed between the vesicle and the HSA molecules. The near UV-vis spectra give an idea about tertiary structure, and the far UV-Vis spectra correspond to the secondary structure of HSA.[48] Here, the absorption spectra of HSA were collected in the absence and presence of [C_{16}Mim] [AOT] in two different mole fractions of AOT (Fig. S3(A) and S3(B) in the supplementary section). It was found that in its native state, HSA exhibits a single peak at 279 nm, which is due to the presence of some aromatic amino acid residue.[49] There was a gradual increase in the absorbance (hyperchromism) value of HSA without any significant shift in the Λ_{max} in the presence of a varying concentration of [C_{16}Mim] [AOT] combination (for both mole fractions of AOT). This observation suggests the formation of the HSA vesicle ground state complex. Since the Λ_{max} of HSA practically remains unchanged in the presence of [C_{16}Mim] [AOT] vesicular solution, it also indicates that in the ground state, there was no change in

hydrophobicity around the amino acid residue of HSA. The binding of the vesicle with HSA was analysed quantitatively by using the Benesi-Hildebrand equation[50]

$$\frac{1}{A-A_0} = \frac{1}{A_{max}-A_0} + \frac{1}{A_{max}-A_0} \times \frac{1}{k_b} \times \frac{1}{[V]} \quad (9)$$

where A & A_0 are the absorbance values of HSA in the presence and absence of vesicles, respectively, Amax is the intermediate absorbance value, and k_b is the binding constant of HSA with [C_{16}Mim] [AOT] vesicle. [V] stands for vesicular concentration. The Benesi-Hildebrand plot of [C_{16}Mim] [AOT] -HSA interaction was presented in Fig. 2A and 2 B. The k_b value for [C_{16}Mim] [AOT] (at χ_{AOT} = 0.6) -HSA and [C_{16}Mim] [AOT] (at χ_{AOT} = 0.5) -HSA systems are 0.76×10^2 M^{-1} and 0.75×10^2 $M^{-1,}$ respectively. The high binding constant value suggests a strong interaction between the [C_{16}Mim] [AOT] vesicle and the HSA molecule. From the binding constant value, it is clear that the extent of interaction of both the vesicular system (cationic and anionic-rich) with the HSA is nearly comparable.

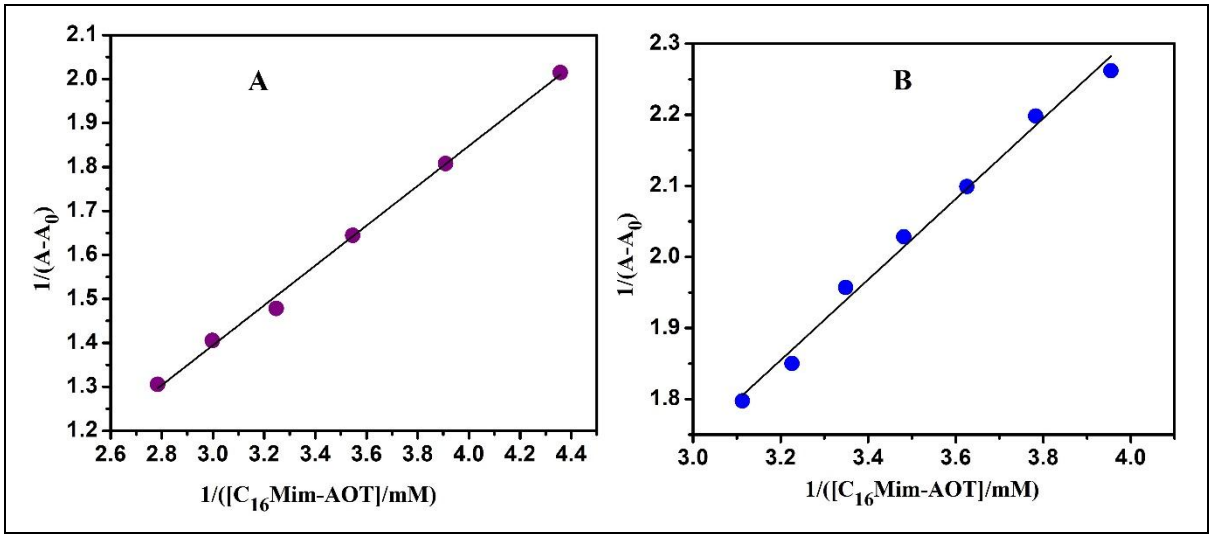

Fig. 2 Benesi-Hildebrand plot of 1/(A-A_0) against 1/ [C_{16}Mim-AOT] for binding of HSA with [C_{16}Mim]/[AOT] (A) 0.5-mole fraction, and (B) 0.6-mole fraction of AOT.

3.3.3 Fluorescence Analysis:

Steady-state fluorescence spectroscopy is an important tool for predicting the tertiary structural alteration of biomolecules. The change in fluorescence behaviour of biomolecules in the presence of ligands suggests structural modification of biomolecules. HSA is a well-known plasma protein with 585 amino acid residues and 17 disulfide bridges.[51] The intrinsic fluorescence of HSA, which is mostly caused by Trp-214, is shown by fluorescence

spectroscopy. This fluorescence indicates the extent of molecule binding and changes in the polarity of the solvent environment, providing information about the binding mechanism in external substances (like ligands, drugs, amphiphiles, etc).[52-54] Figs. 3A and 3B show the change in fluorescence behaviour of HSA in the presence of [C_{16}Mim] [AOT] in its pre- and post-vesicular concentration for two different mole fractions of AOT. In this case, initially, an enhancement of fluorescence intensity along with a noticeable hypsochromic shift (blue shift) of HSA in the pre-vesicular concentration of [C_{16}Mim] [AOT] was observed (in both mole fractions of AOT). The initial increment of the fluorescence intensity also known as photosensitization can be explained at a low concentration of [C_{16}Mim] [AOT], it co-exists with the protein molecule and results in instability in the HSA structure or a loose-packed protein core is generated which results in more chromophoric moiety (Trp214) becoming exposed,[55] resulting slight enhancement of fluorescence intensity. But when [C_{16}Mim] [AOT] was present at or above the vesicular concentration, there was a gradual decrement of fluorescence intensity of the HSA molecule (in both mole fractions of AOT). The fluorescence quenching suggests that the Trp214 residue of HSA becomes more embedded in the hydrophobic bilayer of vesicles which resulting in fewer fluorophores (Trp214) being exposed in the vesicle medium compared to the aqueous medium, resulting in the decrease of fluorescence of HSA in the medium of vesicles. If it is focused on the shifting of fluorescence spectra, it can be seen that in the presence of cationic-rich vesicle ([C_{16}Mim] [AOT] at χ_{AOT} = 0.5), there was no noticeable shifting of HSA fluorescence maxima observed. So, steady-state fluorescence measurements suggest that there is no appreciable change in the microenvironment around the Trp residue of HSA occurring in the presence of cationic-rich vesicles, i.e., the tertiary structure of protein almost remains intact in cationic-rich vesicles. Since in a cationic-rich vesicle, no appreciable tertiary structural loss of HSA takes place, this vesicle might be effective as a protein delivery system (PDS) in the biological and biomedical fields. On the other hand, an entirely different observation was found for anionic-rich vesicle ([C_{16}Mim] [AOT] at χ_{AOT} = 0.6) on the fluorescence shifting of HSA molecules. In this case, at the post-vesicular region, with increasing [C_{16}Mim] [AOT] concentration, there was a remarkable blue shift of the emission spectra of HSA was observed, and ultimately, the emission peak vanished. So, the huge shifting of emission spectra of HSA suggests that the anionic-rich vesicle drastically changes the microenvironment around the Trp residue of HSA, i.e., an appreciable tertiary structural loss of HSA takes place in this case. So, anionic-rich vesicles may not be suitable as PDS, since here the structural conformation change of protein

occurs. The change in CD spectra gives more details about these structural changes (discussed in the latter portion)

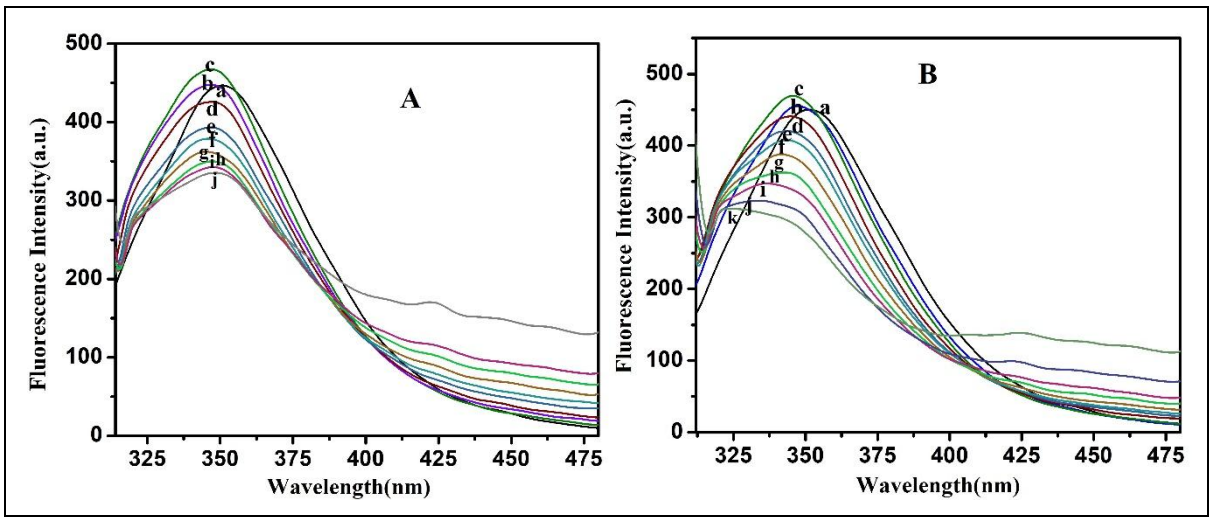

Fig.3 Steady-state fluorescence spectra of HSA in the presence of various amounts of [C_{16}Mim] [AOT]; (A) 0.5-mole fraction (a, b, c, d, e, f, g, h, i, j; 0.0, 0.05, 0.09, 0.14, 0.25, 0.34, 0.45, 0.59, 0.76, 1.62 mM respectively), and (B) 0.6-mole fraction (a, b, c, d, e, f, g, h, i, j, k; 0.0, 0.01, 0.03, 0.09, 0.13, 0.16, 0.24, 0.32, 0.42, 0.68, 1.39 mM respectively) of AOT at 298 K.

3.3.4 Fluorescence quenching analysis:

It is mentioned earlier that the fluorescence intensity of HSA decreased in the presence of the vesicle solution. There are a large number of factors that may be responsible for fluorescence quenching, such as non-fluorescent complex formation between the fluorophore and quencher molecule, fluorescence energy loss through collision, excited state energy transfer, or the molecule undergoing chemical reaction using excited state energy.[56] The fluorescence quenching mechanism can be categorized into two main classes-

1. Static quenching, in which a ground-state non-fluorescent complex is formed between the fluorophore and quencher molecule.
2. Dynamic quenching, which occurs by the excited-state collision.

The Stern-Volmer plot helps to understand the quenching process. The linear Stern-Volmer plot reveals that there is only one type of quenching mechanism present in the system, whereas

a mixed quenching process indicates that there is a positive deviation (upward curvature) in the plot.

In our present system ([C_{16}Mim] [AOT]-HSA), the change of F_0/F with the [C_{16}Mim] [AOT] concentration is shown in Fig.4. From the figure it can be seen that the change in the Stern-Volmer plot for both of the vesicle are downward in nature, i.e. negative deviation from the linearity. The Stern-Volmer plot typically exhibits a negative deviation in several situations, for example, excited state reverse photochemical reaction, the fluorophore experiences a heterogeneous microenvironment in the presence of a quencher, or H-bonded complex formation between the fluorophore and quencher molecules.[40,57] Since in the UV-vis spectra of HSA, there was no such new band appearing in the presence of a vesicle medium (both cationic & anionic), the negative deviation may be arising due to the heterogeneous microenvironment around the protein molecule. It is well known that vesicles have both hydrophobic and hydrophilic moieties along with vesicular holes. So here, the HSA molecule is located at different portions of the vesicle, resulting in it experiencing a heterogeneous environment. Hence, from the negative deviation, it is clear that the protein is successfully loaded at various portions of the vesicle. The magnitude of the Stern-Volmer quenching constant (K_Q) cannot be extracted from the non-linear plot. As a result, the modified form of the Stern-Volmer equation (Eq. 3, mentioned earlier) was used to find out the quenching constant value. Here, the plot of F_0/F_0-F against 1/[C_{16}Mim-AOT] was drawn using the experimental data, as shown in Fig. 4. In this case, a straight-line plot was observed, and from the intercept/slope ratio, the value of quenching constant (K_Q) can be easily found out. The obtained K_Q values for the cationic-rich vesicle-HSA system (χ_{AOT} = 0.5) and anionic-rich vesicle-HSA system (χ_{AOT} = 0.6) were 5.89×10^3 M^{-1} and 4.07×10^3 $M^{-1,}$ respectively, at 298 K.

The computed average lifetime value (τ_0) of HSA in the excited state was 4.67 ns (mentioned in the latter portion). By putting this τ_0 value in the equation $K_{SV} = k_q \times \tau_{0,}$ we can experimentally find out the bimolecular collision quenching constant (k_q) value for the [C_{16}Mim] [AOT]-HSA system. The calculated k_q value for cationic-rich [C_{16}Mim] [AOT]-HSA and anionic-rich [C_{16}Mim] [AOT]-HSA systems was 1.26×10^{12} $M^{-1}s^{-1}$ and 0.87×10^{12} $M^{-1}s^{-1,}$ respectively. For a purely diffusion-controlled process, the maximum limiting k_q value is 2×10^{10} $M^{-1}s^{-1}$; but here the results are very much larger than the limiting value. So, these results suggest a sufficient amount of static quenching present in the system. The UV-vis measurements also supported the static quenching, where the ground state complex formation between the vesicle-HSA was also observed. Hence, static quenching was proved from both

UV-vis measurements and fluorescence quenching analysis. However, the dynamic quenching is not clear from the above discussion. Hence, the lifetime of HSA was measured in the presence of [C_{16}Mim] [AOT] mixture to understand if there is any contribution to the dynamic quenching process (which will be discussed later).

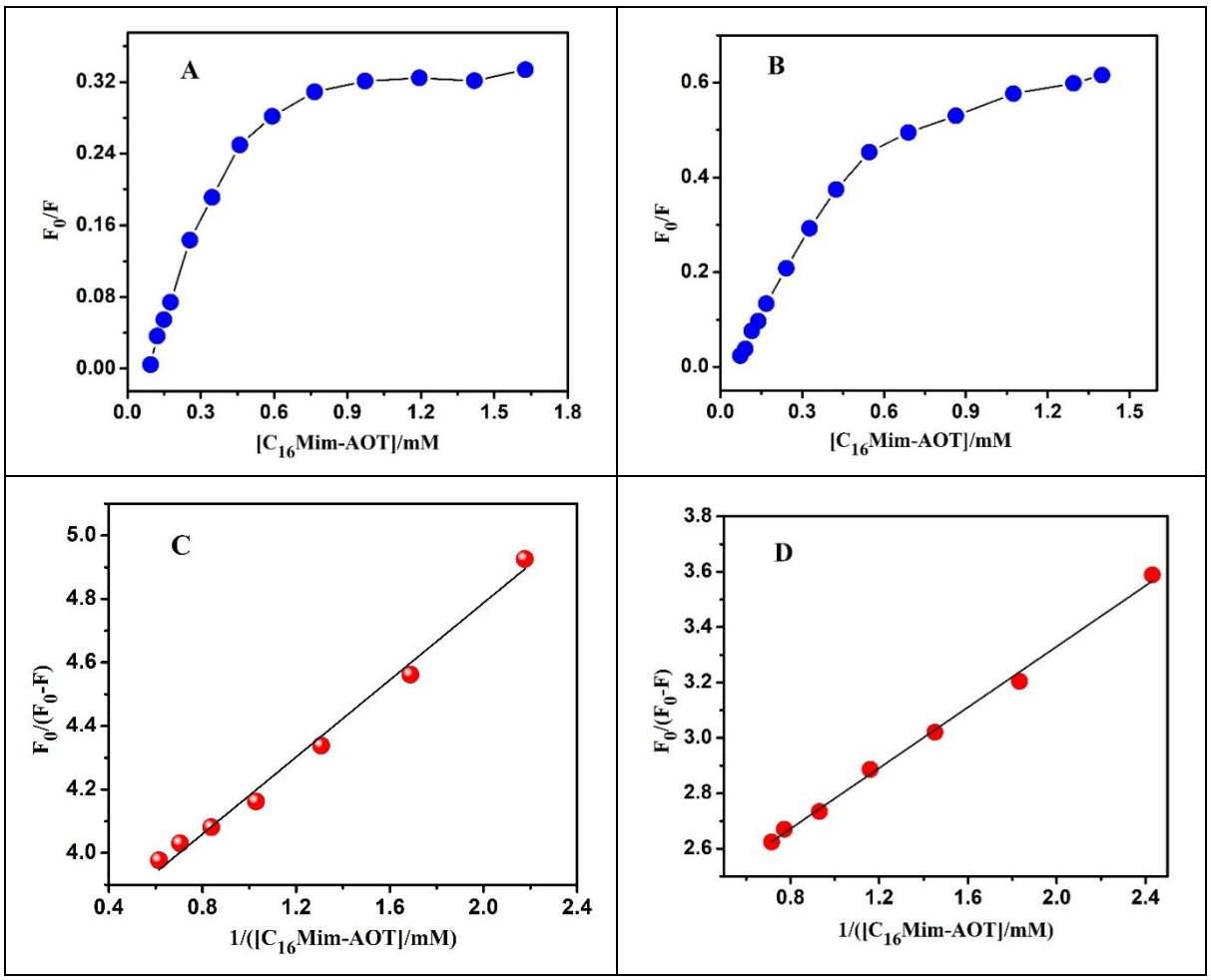

Fig. 4 Representative Stern Volmer plot depicting the variation of F_0/F as a function of [C_{16}Mim-AOT] (A) 0.5-mole fraction, and (B) 0.6-mole fraction of AOT. Corresponding modified Stern Volmer plot (C) 0.5-mole fraction, and (D) 0.6-mole fraction of AOT, depicting the variation of F_0/F_0-F as a function of [C_{16}Mim-AOT] $^{-1}$ monitored at λ_{em} = 350 nm, λ_{exc} = 295 nm, in 10 mM Phosphate buffer of pH 7.4 at 298 K.

3.3.5 Time-resolved fluorescence study of vesicle-HSA interaction:

In the aqueous buffer medium, HSA exhibits a bi-exponential decay pattern with faster decay of about (τ_1) 1.64 ns (24.17%) and a slower decay (τ_2) 5.94 ns (75.83%) components, resulting in about (<τ>) 3.64 ns lifetime on average.[58] The two-phase decay pattern can be explained

based on the rotameric model of tryptophan residue in HSA.[59] There are three possible conformers of Trp (shown in the following picture):

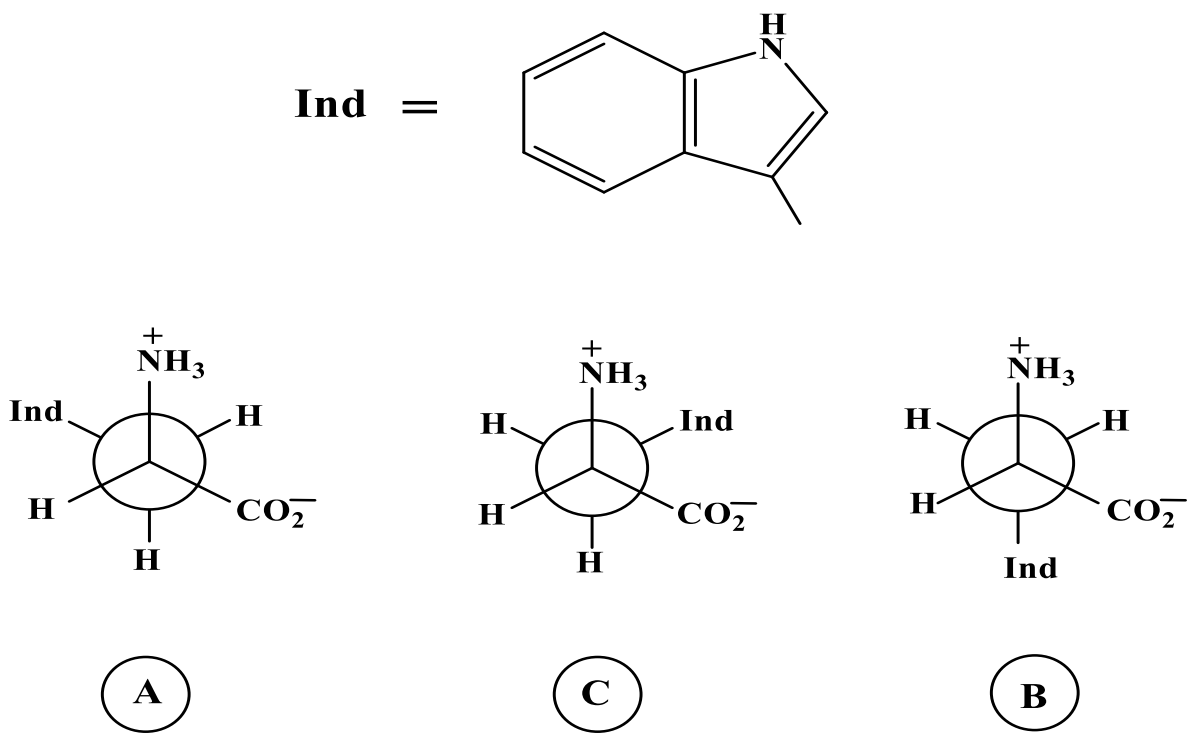

In the bi-exponential decay curve of Trp in the HSA molecule, the faster component is due to the stable conformer (C), whereas the slower one is believed to originate from the rapid interconversion of A & B conformers. The interconversion of stable conformer (C) to either A or B shows difficulty on the nanosecond time scale.[60] In the ground state, the indole ring of tryptophan exists in a slightly puckered conformation, resulting in the orbital overlap between the p(N) & rest π-system of the indole ring being limited. As a result, the electron delocalization throughout the indole ring is hampered in the ground state.[61] In the photoexcited state, this indole ring becomes planar through electron delocalization from the nitrogen lone pair to the aromatic π-ring.[61] The fluorescence intensity of Trp214 very much depends on the solvation; apart from this, the presence of disulfide bond complex, ionic species, methionyl sulphur, etc., acts as a quencher of HSA fluorescence. During the process of quenching, the interaction of quencher molecules with HSA leads to the distortion of the planarity of the indole ring of the Trp residue. This distortion results in a decrease in the lifetime of HSA in the presence of a quencher molecule.[62]

Fig. 5 represents the decay Profile of HSA in the pre- and post-vesicular concentration of [C_{16}Mim] [AOT] (for both $\chi_{AOT} = 0.6$ and $\chi_{AOT} = 0.5$), and the decay parameters are tabulated in Table S2 (Supplementary section). From the decay profile, it is clearly seen that the lifetime

of Trp in HSA decreased gradually with increasing vesicle concentration (for both cationic-rich & anionic-rich vesicles). This indicates that the excited state planarity of the indole ring of Trp is hampered by the presence of the vesicular system, resulting decrease in the regular lifetime.

Since a gradual decrease in fluorescence lifetime was observed for Trp-214 in the presence of both vesicle systems, it might be thought that each vesicle interacts with the Trp residue in a similar way. But from steady-state fluorescence spectra, it is already seen that in cationic-rich vesicles, the fluorescence quenching of Trp 214 occurs without shifting of emission maxima; whereas a huge blue shift along with fluorescence quenching was observed for anionic-rich vesicles. So, this observation clearly suggests that in the excited state, Trp 214 residue interacts with both the vesicular system in a different manner. The Trp residue of HSA is distributed both in buried (hydrophobic) and exposed (hydrophilic) environments, confirmed by short and long-lifetime components.[58] In the case of the cationic-rich vesicle, the protein-vesicle interaction is mainly governed by electrostatic interaction (because, here, HSA is anionic in nature at pH 7.4), so here the vesicle interacts with the hydrophilic part of Trp through electrostatic interaction and there is no appreciable hydrophobic interaction, resulting there is no change in the buried (hydrophobic) component of Trp. This leads to no change in the hydrophobicity along the Trp 214 residue, resulting in no change in fluorescence maxima observed. Here, quenching of the fluorescence intensity and lifetime was observed mainly due to the electrostatic interaction of the vesicle with the hydrophilic part of the Trp residue without significant changes in the microenvironment around the fluorophore of HSA. But in the case of anionic-rich vesicles, no electrostatic interaction is possible. Here, the predominant factor is the hydrophobic interaction with the Trp residue of HSA. Since the hydrophobic residue of Trp is dipped inside the protein core, so, here, interaction takes place by breaking the structure of the protein. The structural alteration of HSA in the presence of anionic-rich vesicles is also clear from the steady-state fluorescence spectral shift. So, from the above discussion, it is clear that both the vesicles interact with the Trp residue in different ways, leading to a gradual decrease in lifetime.

In the case of protein-vesicle assembly, it is extremely difficult to assign separate lifetime contributions; nevertheless, we will attempt to explain the relative amplitudes of the lifetimes. The relative populations of the different conformers present in the excited state have been mostly attributed to the contribution of their lifetimes.

In the native state of HSA data Table S2 shows that the amplitude of the slower decay component (A_2) (~75.83%) was three times greater than the faster component (A_1) (24.17%)

of Trp 214. It was already mentioned that the faster component was for the stable conformer C, and the slower component for the inter-conversion of A & B components. So, in the native state of HSA, the population of A and/or B conformers is very much greater than the C conformers. But in the presence of a vesicle system (both cationic-rich & anionic-rich), the amplitude of the faster decay component increases gradually, and the slower decay component decreases. In the case of cationic-rich vesicles, the amplitude of the faster decay component increases from 24.17% to 45%, and in anionic-rich vesicles, it increases up to 55%. This suggests that the anionic-rich vesicle is more effective in the structural alteration of the HSA protein. It was mentioned earlier that in the native state of HSA, the Trp 214 residue remains buried in the hydrophobic core,[63] resulting in the interconversion of Trp conformers being hindered.[64] But, when the vesicles interact with the indole ring of Trp residue, the flexibility of Trp residue increases compared to when it was buried in the hydrophobic cage of HSA. As a result, the free rotation of the Trp moiety increases in the presence of the vesicle system, which leads to an increase in the interconversion of the conformers of Trp. Since among the three conformers, C is the most stable, the inter-conversion from conformer A or/B to C is suitable in the presence of a vesicle system. So, the increase of the inter-conversion process from A and/or B to C in the presence of a vesicular system leads to an increase in the amplitude of the faster decay component (Table S2). It is suggested that Trp 214 has a shorter lifetime because of accelerated non-radiative decay pathways, which are mostly caused by charge transfer from the indole ring to neighbouring substitutions.

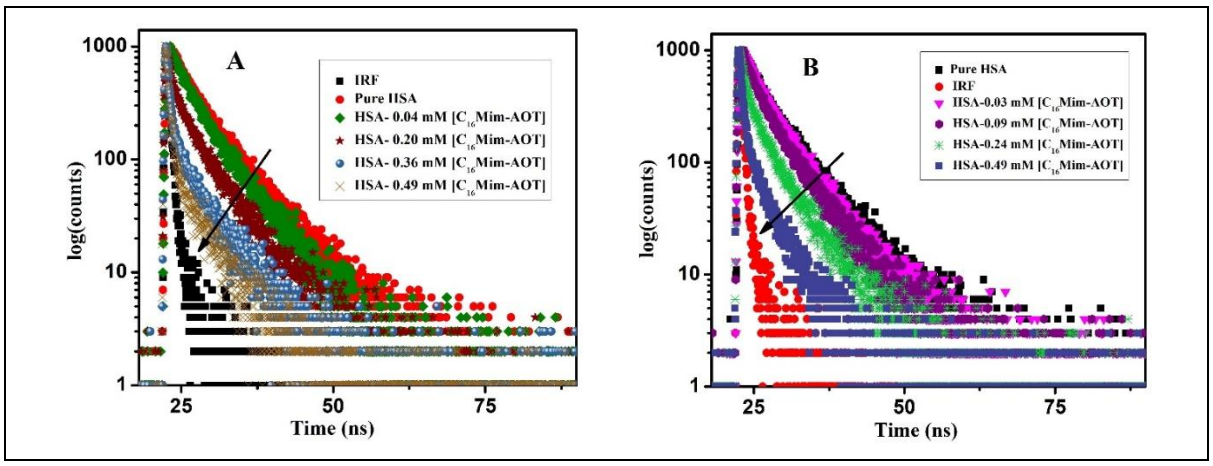

Figure 5. Time-resolved fluorescence decay profile (logarithm of normalized intensity vs time) of HSA (5.0 µM) in the absence and presence of [C_{16}Mim] [AOT] (A) 0.5-mole fraction, and (B) 0.6-mole fraction of AOT at 10 mM Phosphate buffer of pH 7.4 at 298 K, λ_{exc} = 295 nm, and λ_{em} = 350 nm.

3.3.6 ITC measurements:

One of the best methods for defining the kind of interactions that occur between proteins and nano-delivery devices is ITC.[65,66] Using ITC studies, the enthalpy changes associated with the progressive binding of [C_{16}Mim] [AOT] to HSA at 298 K were observed. The enthalpogram of [C_{16}Mim] [AOT] binding to HSA with two distinct mole fractions is displayed in Fig. S4 (Supporting section). To produce the stated enthalpograms accurately, the heat of dilution of [C_{16}Mim] [AOT] in the phosphate buffer medium at pH 7.4 is subtracted from the heat of dilution of [C_{16}Mim] [AOT] in 5 μM HSA solution in the same buffer medium. It was already mentioned in the tensiometric section that the interaction of [C_{16}Mim] [AOT] with HSA occurs sequentially. There are two steps associated with protein- [C_{16}Mim] [AOT] interactions:
(i) monomeric region (aggregation), (ii) vesicular region.

So, it is necessary to understand the enthalpy change involved with each step of protein-[C_{16}Mim] [AOT] interactions. We have displayed integrated heat data against the concentration of [C_{16}Mim] [AOT] in two distinct concentration regions to help better comprehend this sequential interaction of protein- [C_{16}Mim] [AOT] systems and calculate the quantities of heat changes involved in each phase (Fig. 6). The enthalpogram of each vesicular system (cationic-rich and anionic-rich) – HSA interaction is more or less similar in nature. In both cases, the enthalpy changes of HSA-[C_{16}Mim] [AOT] interactions are exothermic, signifying the binding is cooperative in nature[67] and the exothermicity gradually decreases with [C_{16}Mim] [AOT] concentration. In the case of anionic-rich vesicles, the enthalpy associated with each single injection is exothermic in both monomeric and vesicular regions. But, for cationic-rich vesicles, the enthalpy involved with every single injection is exothermic in the monomeric region of [C_{16}Mim] [AOT], gradually crosses zero, and ultimately becomes slightly endothermic in the post-vesicular region. It suggests that the binding of HSA with cationic-rich vesicles is both cooperative and non-cooperative in nature. In contrast, there is only cooperative binding involved in both pre- and post-vesicular concentrations of anionic-rich vesicles. Figures 6A and 6B show strong exothermic enthalpy changes in the monomeric [C_{16}Mim] [AOT]-HSA interaction region for both cationic and anionic-rich vesicular systems. In this region, the enthalpy changes (ΔH) are very high, i.e., -5.90 kcal/mol and -5.89 kcal/mol for anionic-rich and cationic-rich vesicular systems, respectively. In the monomeric regime, $[C_{16}Mim]^+$ and $[AOT]^-$ ions bind to the various charge sites on proteins,[68-69,] which is defined as the critical aggregation concentration. Since in the monomeric region, the interaction of [C_{16}Mim] [AOT] occurs in the specifically high-energy sites of the HSA, resulting in a huge enthalpy change

takes place. After CAC, small exothermic enthalpy changes take place up to vesicle formation, i.e., -0.012 kcal/mol and -0.013 kcal/mol for anionic-rich and cationic-rich vesicles (Figs. 6Aa and 6Bb), respectively. Since all the high-energy binding sites of HSA are already occupied by monomeric [C_{16}Mim] [AOT], in the vesicular region, only adsorption and/or intercalation of HSA on the vesicle surface and/or core takes place, resulting in small enthalpy changes. So, from the enthalpy changes, it can be concluded that both the vesicles have comparable affinity towards the model protein HSA.

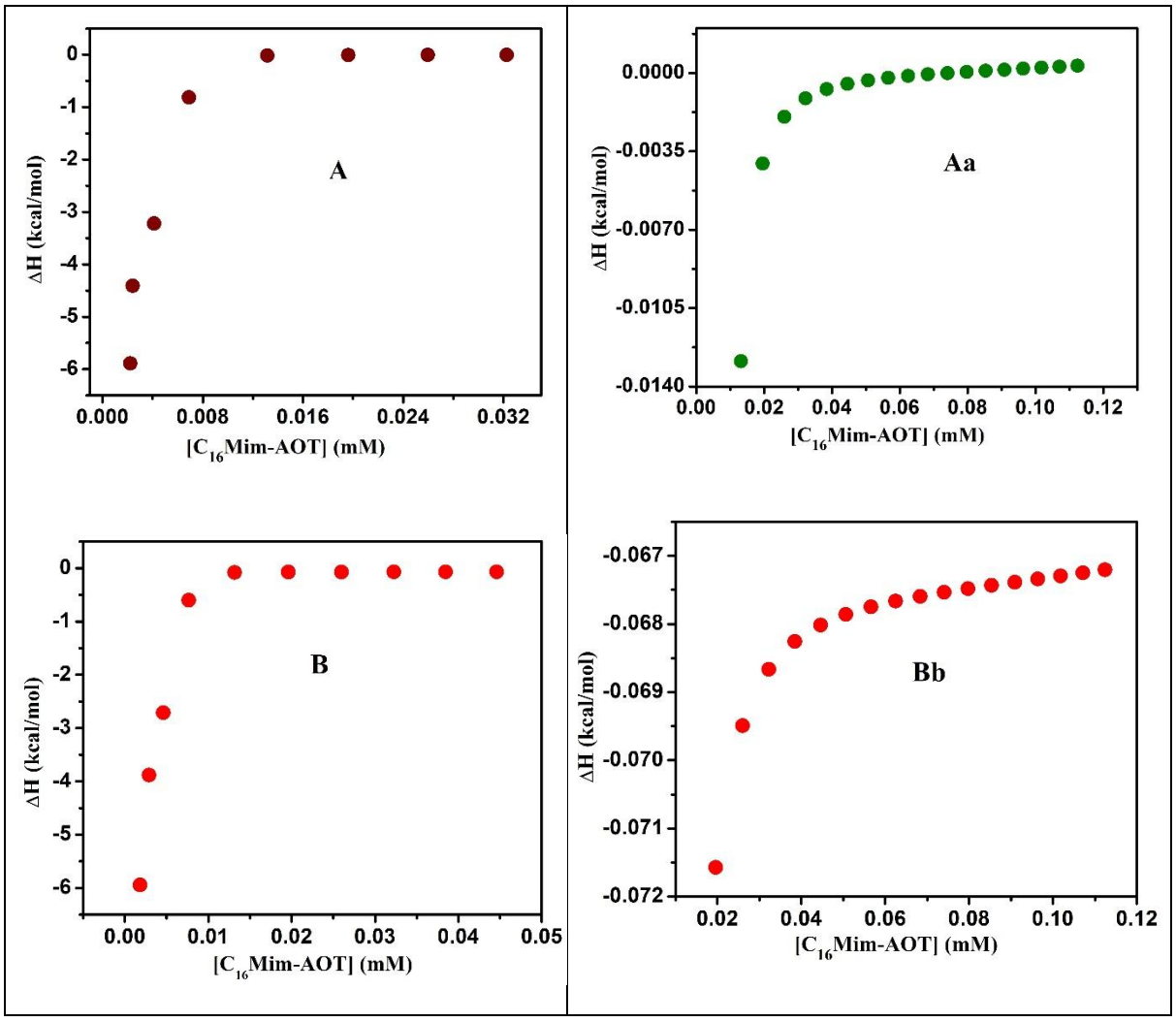

Fig. 6 ITC profile of [C_{16}Mim] [AOT] binding with HSA (A) & (Aa) and (B) & (Bb) are the enthalpy change associated with CAC and CVC of 0.5-mole fraction, and 0.6-mole fraction of AOT in phosphate buffer medium (pH 7.4) at 298 K.

3.3.7 DLS measurements:

To understand the change in the vesicle size in the presence of the HSA molecule, DLS measurements were performed for both the vesicular systems (cationic-rich and anionic-rich). A relatively narrow and monomodal size distribution graph was observed. The variation of hydrodynamic diameter of two vesicular solutions (cationic- and anionic-rich) with HSA concentration was represented in Fig.7. The average hydrodynamic diameter obtained from DLS measurements for cationic-rich and anionic-rich vesicles was around 197.32 nm and 243.48 nm, respectively (Table 1), signifying that anionic-rich vesicles are slightly greater in size. In the presence of the HSA molecule, a gradual expansion of vesicle size was observed for cationic-rich vesicles. In the presence of 3.7 μM HSA, the hydrodynamic size of cationic-rich vesicles drastically increases from 197.32 nm to 1091.31 nm (Table 1). This signifies that a significant number of protein molecules are loaded at the surface and inside the core of vesicles. The adsorption and intercalation of protein molecules lead to an expansion of vesicle size. Both the hydrophobic and electrostatic interactions are responsible for the adsorption and intercalation of HSA molecules in the cationic-rich vesicle.

It was already mentioned that at working pH 7.4, the HSA molecules are anionic in nature. For cationic-rich vesicles, the electrostatic interaction plays a major role, along with hydrophobic interaction, for the adsorption and interaction of protein molecules. It is very interesting to note that a 5 times volume expansion of cationic-rich vesicles was observed upon protein absorption without breaking their structure. So, cationic-rich vesicles can accommodate a large number of HSA molecules without rupturing their vesicle structure, denoting the effectiveness of this vesicle system as an injectable drug delivery system (DDS). So, this vesicular system can be applied in enormous fields like biology, biomedical, biotechnology, etc. But interestingly, an opposite observation was observed in the case of the anionic-rich vesicle. Here, a slight rupture of the vesicle structure was observed upon adsorption of HSA molecules. In the presence of 3.18 μM HSA solution, the size of the anionic-rich vesicle decreases from 243.48 nm to 215.10 nm, i.e., contraction of vesicle size was observed in this case (Table 1). This contraction of vesicle size can be justified by increasing electrostatic repulsion between the polar charge group of the vesicle and the anionic-charged HSA molecule, leading to the rupture of the vesicle into a smaller one. This breakdown of the vesicular structure of anionic-rich vesicles is also clear from the lowering of the negative zeta potential value of vesicles in the presence of HSA molecules (discussed later). Since here, the rapturing of vesicle structure

takes place in the presence of protein molecules, these vesicles are not effective as a drug delivery system (DDS).

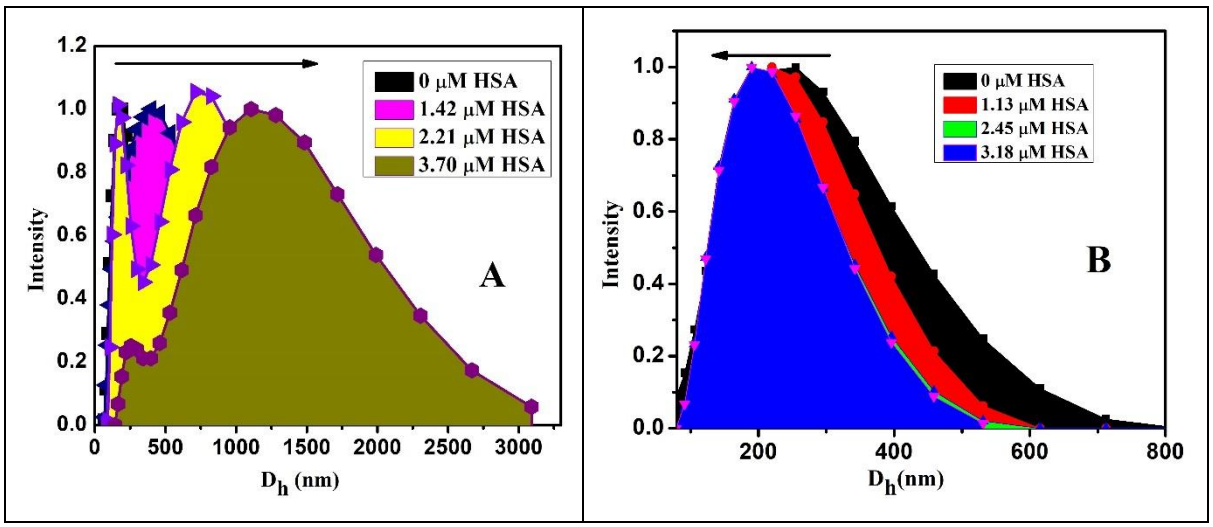

Fig. 7 Variation of hydrodynamic diameter (D_h) of [C_{16}Mim] [AOT] vesicle with increasing concentration of HSA; (A) for the 0.5-mole fraction of AOT, and (B) for the 0.6-mole fraction of AOT, respectively.

3.3.8 Zeta potential measurements:

The change in the zeta potential value of vesicles in the presence of HSA molecules gives important information about the adsorption and intercalation of protein molecules in the vesicle system and also its stability. The variation in zeta potential of two vesicular solutions with increasing HSA concentration was presented in Fig. 8A and 8 B. Here, cationic-rich vesicles had an average zeta potential of +63.51±2.4 mV while anionic-rich vesicles had an average zeta potential of -71.9±3.2 mV, respectively. The zeta potential value of the HSA solution in 10 mM phosphate buffer (at pH 7.4) was -22.1±2.3 mV. There was a gradual decrease in zeta potential value observed for cationic-rich vesicles with increasing HSA concentration, and it even becomes negative at high protein concentration (Fig. 8A). This decrease in the zeta potential value of cationic-rich vesicles suggests that a large number of HSA molecules with anionic charge adsorbed on the surface of the vesicle, leading to a decrease in its positive charge. The aggregation of a huge number of anionic-charged HSA molecules on cationic-rich vesicles nullifies their positive charge, and eventually, the vesicles become negatively charged. So, the zeta potential results strongly suggest that huge protein adsorption takes place on

cationic-rich vesicles, which correlates well with the DLS results. In the case of the anionic-rich vesicle, both the vesicle and protein molecules are anionic in nature, so a gradual increase in the negative zeta potential value of the vesicles is expected with increasing HSA concentration. In the presence of a 4.2 μM HSA solution, the zeta potential value of anionic-rich vesicles goes from -71.9 mV to -31.7 mV. This change in zeta potential value in the presence of HSA molecules can be attributed to the rupture of a large vesicle to a small one, due to increasing electrostatic repulsion between the similarly charged vesicles in the presence of anionic HSA. The rupture of anionic-rich vesicles in the presence of HSA is also observed from DLS measurements.

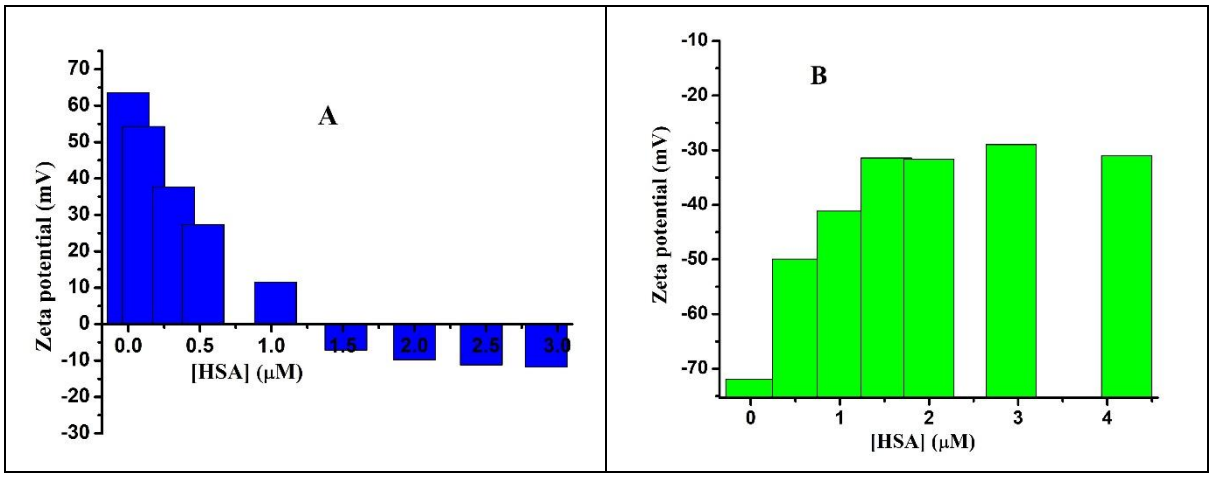

Fig. 8 Variation of zeta potential value of [C_{16}Mim] [AOT] vesicle with increasing concentration of HSA; (A) 0.5 mole fraction, and (B) 0.6 mole fraction of AOT, respectively.

3.3.9 CD spectroscopy analysis:

Far-UV CD spectroscopy is an effective tool for monitoring the secondary structure of proteins. The steady-state fluorescence measurements already confirmed that a drastic tertiary structural change of HSA occurs in the presence of the anionic-rich vesicle, whereas a minute tertiary structural change occurs in the presence of the cationic-rich vesicle. To understand whether there is any effect of two vesicular systems on their below and post-vesicular concentration on the secondary structure of HSA, the far-UV CD spectra of the protein were recorded in the presence of two different vesicular solutions (Fig. 9A and 9B). In the wavelength range of 200-260 nm, ionic liquid-based vesicles have no CD signals, so the entire CD spectra are for HSA.

There are two minima in the CD spectra of native HSA at around 208 nm ($\pi-\pi^*$) and 220 nm ($n-\pi^*$), which is the characteristic α-helical structure of HSA.[70,71] In the native state, ~60% α-helical structure was observed for HSA (Table S3), which agrees well with the previously reported value of having major helical content in its native state (60-67 %).[72,59] On increasing concentration of cationic-rich [C_{16}Mim] [AOT], a superimposed CD spectrum was found both in pre- and post-vesicular concentration, signifying no detectable secondary structural change of HSA in the cationic-rich vesicle. From steady-state fluorescence measurements, we have also seen no appreciable change in the microenvironment around the fluorophore Trp214 moiety of HSA. The above observation suggests that no significant secondary or tertiary structural change of HSA takes place in the presence of cationic-rich vesicles. So, it can be concluded that cationic-rich vesicles are very effective as a protein delivery system (PDS) without altering their secondary structure. On the other hand, in the presence of anionic-rich [C_{16}Mim] [AOT], a slight decrement in the negative ellipticity of HSA was observed, signifying a small decrease in α-helicity of protein in both pre- and post-vesicular concentration. Here, only ~2 % α-helical structural loss of HSA was observed in the presence of anionic-rich vesicles. However, from steady-state fluorescence measurements, a drastic structural change of HSA was observed in the presence of an anionic-rich vesicle. Here, ~40% structural change was observed from fluorescence measurements. This can be attributed to the fact that far-UV CD spectroscopy provides information about global protein structural change, while the fluorescence method is far more sensitive in identifying minute changes in the fluorophore's microenvironments. CD spectroscopy is a global structural reporter, whereas steady-state fluorescence serves as a local structural reporter of proteins. So, it is not likely to draw a direct correlation between the fluorescence measurements and CD spectroscopy data. However, both methods unequivocally demonstrate that in the presence of cationic-rich vesicles, no reportable structural change in HSA was observed. In contrast, a reportable change in the tertiary and secondary structure was observed in the presence of an anionic-rich vesicle.

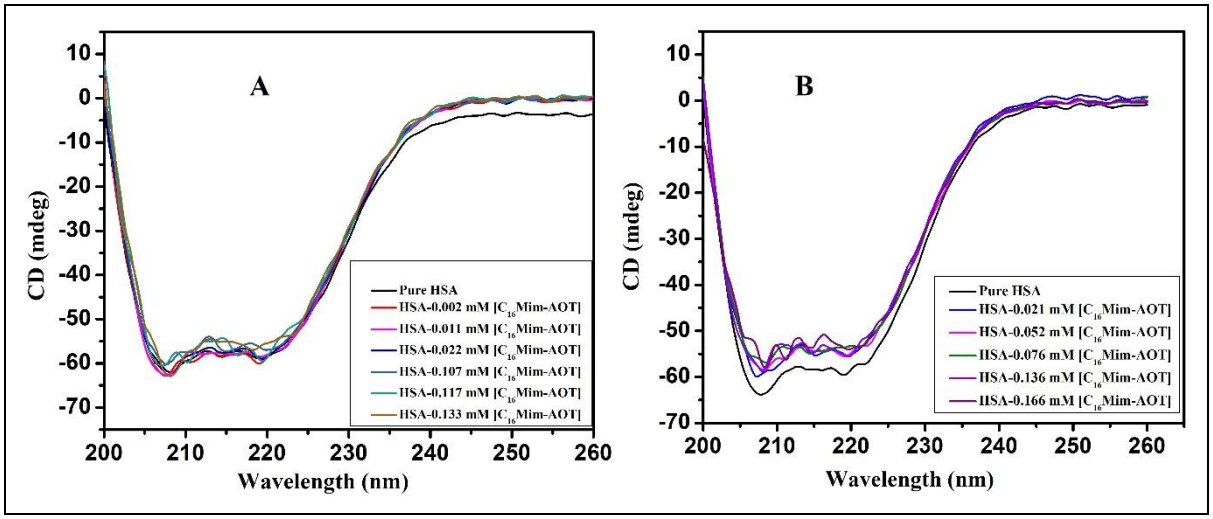

Fig 9. CD spectra of HSA at various concentrations of [C_{16}Mim]/[AOT]; (A) 0.5 mole fraction, and (B) 0.6 mole fraction of AOT. [HSA] =2.5 μM in phosphate buffer medium at 298 K.

3.3.10 TEM analysis of vesicle-protein assembly:

To give direct and microscopic evidence of protein adsorption on the vesicle, TEM measurements were performed. The TEM micrographs of bare vesicles were already mentioned in section 3.1. The micrographs of free HSA show black circles with different sizes, suggesting the protein is present in various aggregated states in the solution (Fig. 10A). In the case cationic-rich vesicle, there was an expansion in the vesicle size was observed in the presence of protein molecules (Fig. 10 B), suggesting a huge number of protein molecules are loaded on vesicle which leads to increase in the size. Since the proteins and vesicles are oppositely charged, both electrostatic and hydrophobic interactions participate in protein adsorption, resulting in many proteins accumulating on the vesicle surface and core. On the other hand, in the case of the anionic-rich vesicle, a size in the vesicle size observed in the presence of protein molecules (Fig. 10C). This suggest that adsorption of protein leads to breakdown of anionic-rich vesicle to small vesicle. It is already mentioned that at pH 7.4, HSA is anionic in nature, and here vesicle is also anionic so here no electrostatic interaction takes place only hydrophobic interaction is present, resulting in a smaller number of protein molecules adsorbed on the vesicle surface. So, TEM measurements clearly show protein adsorption on the vesicle surface without deforming its vesicular structure.

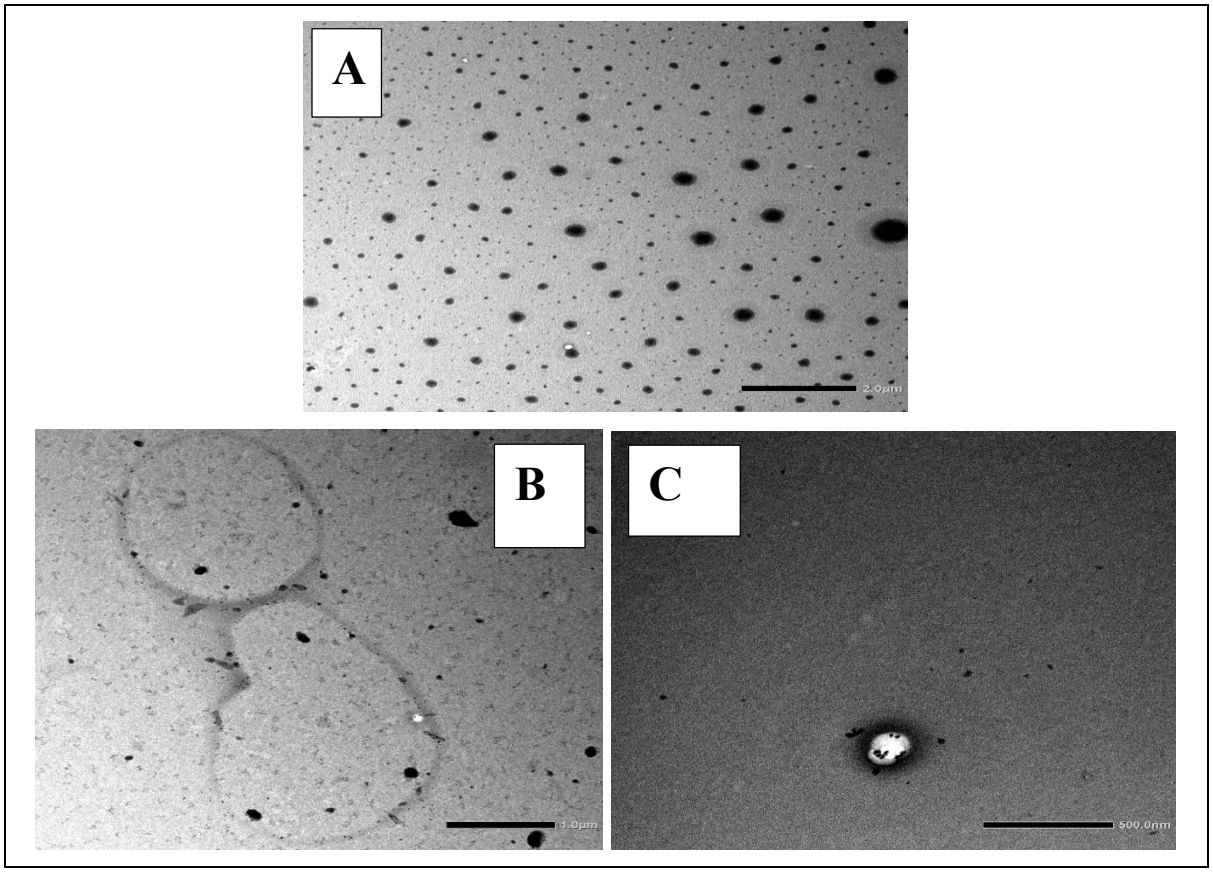

Fig. 10 TEM micrographs of (A) pure HSA, and [C_{16}Mim] [AOT] vesicle-HSA assembly (B) 0.5-mole fraction, (C) 0.6-mole fraction of AOT respectively.

4. Conclusions

In summary, cationic- and anionic-rich vesicles were prepared using SAIL (C_{16}MimCl) and Aerosol OT (AOT) in an aqueous medium, and a detailed interaction study of these vesicular systems with a model protein (HSA) was performed in pre- and post-vesicular concentrations using various experimental techniques. The binding isotherm computed from tensiometry reveals that the [Cl_{16}Mim-AOT] interacts with HSA at two distinct concentration regions of [Cl_{16}Mim-AOT] for both the cationic- and anionic-rich cases. The fluorescence intensity of the Trp214 residue of HSA increased in both cationic- and anionic-rich cases of [C_{16}Mim-AOT] in their pre-vesicular concentration, indicating energy transfer from the ligand to protein molecules. However, there was a progressive decrease in fluorescence intensity in the post-vesicular concentration, which may indicate the formation of a non-fluorescent protein-vesicle combination. The analysis of the fluorescence spectra for the shifting of Trp214 residue emission maximum of HSA in two distinct vesicular media indicates that, in cationic-rich

vesicles, the protein tertiary structure persists, whereas in anionic-rich vesicles, it breaks down. ITC measurements reveal significant enthalpy changes in the pre-vesicular concentration of the HSA-[C_{16}Mim-AOT] interaction, while a small change occurs in the post-vesicular concentration for both cationic and anionic-rich cases. According to the TCSPC study, the interaction between the vesicle and the indole ring of the Trp214 residue makes it easier for Trp214 rotamers to interconvert, which lowers the HSA lifetime. DLS measurements show that protein adsorption in cationic-rich vesicles maintains stable protein and vesicle structures, while anionic-rich vesicles cause instability in both structures. According to CD measurements, no secondary structural change of HSA occurs in cationic-rich vesicles, and a small alteration occurs in the anionic-rich vesicles. Since in cationic-rich vesicles both the protein and vesicle remain stable, it can be effectively used as an injectable DDS. Thus, it can be inferred from the discussion above that the prepared SAIL-based vesicles can be used in biological and biomedical fields as an efficient carrier system for different biomolecules (protein, DNA, drug, etc.).

References:

1. Lei, Z., Chen, B., Koo, Y. M. & Macfarlane, D. R. Introduction: Ionic Liquids. *Chem. Rev.* **117**, 6633–6635 (2017).
2. Mehnert, C. P., Cook, R. A., Dispenziere, N. C. & Afeworki, M. Supported ionic liquid catalysis - A new concept for homogeneous hydroformylation catalysis. *J. Am. Chem. Soc.* **124**, 12932–12933 (2002).
3. Hayes, R., Warr, G. G. & Atkin, R. Structure and Nanostructure in Ionic Liquids. *Chem. Rev.* **115**, 6357–6426 (2015).
4. Domínguez De María, P. 'Nonsolvent' applications of ionic liquids in biotransformations and organocatalysis. *Angew. Chemie - Int. Ed.* **47**, 6960–6968 (2008).
5. Amarasekara, A. S. Acidic Ionic Liquids. *Chem. Rev.* **116**, 6133–6183 (2016).
6. Egorova, K. S., Gordeev, E. G. & Ananikov, V. P. Biological Activity of Ionic Liquids and Their Application in Pharmaceutics and Medicine. *Chem. Rev.* **117**, 7132–7189 (2017).

7. Docherty, K. M. & Kulpa, C. F. Toxicity and antimicrobial activity of imidazolium and pyridinium ionic liquids. *Green Chem.* **7**, 185–189 (2005).

8. Hallett, J. P. & Welton, T. Room-Temperature Ionic Liquids : Solvents for Synthesis and Catalysis . 2. 3508–3576 (2011).

9. Visser, A.E., Swatloski, R.P., Reichert, W.M., Mayton, R., Sheff, S., Wierzbicki, A., Davis Jr, J.H. and Rogers, R.D. Task-specific ionic liquids for the extraction of metal ions from aqueous solutions. *Chem. Commun.* 135–136 (2001) doi:10.1039/b0080411.

10. Li, H., Bhadury, P. S., Song, B. & Yang, S. Immobilized functional ionic liquids: Efficient, green, and reusable catalysts. *RSC Adv.* **2**, 12525–12551 (2012).

11. Yee, P., Shah, J. K. & Maginn, E. J. State of hydrophobic and hydrophilic ionic liquids in aqueous solutions: Are the ions fully dissociated? *J. Phys. Chem. B* **117**, 12556–12566 (2013).

12. Rivera-Rubero, S. & Baldelli, S. Influence of water on the surface of hydrophilic and hydrophobic room-temperature ionic liquids. *J. Am. Chem. Soc.* **126**, 11788–11789 (2004).

13. Greaves, T. L. & Drummond, C. J. Ionic liquids as amphiphile self-assembly media. *Chem. Soc. Rev.* **37**, 1709–1726 (2008).

14. Martinelli, A., Maréchal, M., Östlund, Å. & Cambedouzou, J. Insights into the interplay between molecular structure and diffusional motion in 1-alkyl-3-methylimidazolium ionic liquids: A combined PFG NMR and X-ray scattering study. *Phys. Chem. Chem. Phys.* **15**, 5510–5517 (2013).

15. Inoue, T., Ebina, H., Dong, B. & Zheng, L. Electrical conductivity study on micelle formation of long-chain imidazolium ionic liquids in aqueous solution. *J. Colloid Interface Sci.* **314**, 236–241 (2007).

16. Galgano, P. D. & El Seoud, O. A. Micellar properties of surface active ionic liquids: A comparison of 1-hexadecyl-3-methylimidazolium chloride with structurally related cationic surfactants. *J. Colloid Interface Sci.* **345**, 1–11 (2010).

17. Weingärtner, H., Cabrele, C. & Herrmann, C. How ionic liquids can help to stabilize native proteins. *Phys. Chem. Chem. Phys.* **14**, 415–426 (2012).

18. Bica, K., Gärtner, P., Gritsch, P. J., Ressmann, A. K., Schröder, C., & Zirbs, R. Micellar catalysis in aqueous–ionic liquid systems. *Chem. Commun.* **48**, 5013–5015 (2012).

19. Mahajan, S., Sharma, R. & Mahajan, R. K. An investigation of drug binding ability of a surface active ionic liquid: Micellization, electrochemical, and spectroscopic studies. *Langmuir* **28**, 17238–17246 (2012).

20. Mir, M. A., Chat, O. A., Najar, M. H., Younis, M., Dar, A. A., & Rather, G. M. Solubilization of triphenylamine, triphenylphosphine, triphenylphosphineoxide and triphenylmethanol in single and binary surfactant systems. *J. Colloid Interface Sci.* **364**, 163–169 (2011).

21. Garcia, M. T., Ribosa, I., Perez, L., Manresa, A. & Comelles, F. Aggregation behavior and antimicrobial activity of ester-functionalized imidazolium- and pyridinium-based ionic liquids in aqueous solution. *Langmuir* **29**, 2536–2545 (2013).

22. Lépori, C. M. O., Silber, J. J., Falcone, R. D. & Correa, N. M. Improvement of the amphiphilic properties of a dialkyl phosphate by creation of a protic ionic liquid-like surfactant. *RSC Adv.* **7**, 44743–44750 (2017).

23. Kapitanov, I.V., Jordan, A., Karpichev, Y., Spulak, M., Perez, L., Kellett, A., Kümmerer, K. and Gathergood, N., Synthesis, self-assembly, bacterial and fungal toxicity, and preliminary biodegradation studies of a series of l-phenylalanine-derived surface-active ionic liquids. *Green Chem.* **21**, 1777–1794 (2019).

24. Lépori, C. M. O., Correa, N. M., Silber, J. J., Vaca Chávez, F. & Falcone, R. D. Interfacial properties modulated by the water confinement in reverse micelles created by the ionic liquid-like surfactant bmim-AOT. *Soft Matter* **15**, 947–955 (2019).

25. Villa, C. C., Correa, N. M., Silber, J. J., Moyano, F. & Falcone, R. D. Singularities in the physicochemical properties of spontaneous AOT-BHD unilamellar vesicles in comparison with DOPC vesicles. *Phys. Chem. Chem. Phys.* **17**, 17112–17121 (2015).

26. Lépori, C. M. O., Correa, N. M., Silber, J. J. & Falcone, R. D. How the cation 1-butyl-3-methylimidazolium impacts the interaction between the entrapped water and the reverse micelle interface created with an ionic liquid-like surfactant. *Soft Matter* **12**, 830–844 (2016).

27. Liu, G. & Lecommandoux, S. Nanotechnology Colloids and Colloid Assemblies Nanomaterials Chemistry Synthetic Metal-Containing Polymers Nanofabrication Towards Biomedical Applications The Chemistry of Nanomaterials An Introduction to Plastics. (2006).

28. Singh, R. P., Gangadharappa, H. V. & Mruthunjaya, K. Phospholipids: Unique carriers for drug delivery systems. *J. Drug Deliv. Sci. Technol.* **39**, 166–179 (2017).

29. Grimaldi, N., Andrade, F., Segovia, N., Ferrer-Tasies, L., Sala, S., Veciana, J., & Ventosa, N. Lipid-based nanovesicles for nanomedicine. *Chem. Soc. Rev.* **45**, 6520–6545 (2016).

30. Kaler, E. W., Murthy, A. K., Rodriguez, B. E. & Zasadzinski, J. A. N. Spontaneous vesicle formation in aqueous mixtures of single-tailed surfactants. *Science (80-.).* **245**, 1371–1374 (1989).

31. Hao, J. & Hoffmann, H. Self-assembled structures in excess and salt-free catanionic surfactant solutions. *Curr. Opin. Colloid Interface Sci.* **9**, 279–293 (2004).

32. Kaler, E. W., Herrington, K. L., Murthy, A. K. & Zasadzinski, J. A. N. Phase behavior and structures of mixtures of anionic and cationic surfactants. *J. Phys. Chem.* **96**, 6698–6707 (1992).

33. Jung, H. T., Lee, S. Y., Kaler, E. W., Coldren, B. & Zasadzinski, J. A. Gaussian curvature and the equilibrium among bilayer cylinders, spheres, and discs. *Proc. Natl. Acad. Sci. U. S. A.* **99**, 15318–15322 (2002).

34. Dos Santos, N., Waterhouse, D., Masin, D., Tardi, P. G., Karlsson, G., Edwards, K., & Bally, M. B. Substantial increases in idarubicin plasma concentration by liposome encapsulation mediates improved antitumor activity. *J. Control. Release* **105**, 89–105 (2005).

35. Davies, T. S., Ketner, A. M. & Raghavan, S. R. Self-assembly of surfactant vesicles that transform into viscoelastic wormlike micelles upon heating. *J. Am. Chem. Soc.* **128**, 6669–6675 (2006).

36. Mal, A., Bag, S., Ghosh, S. & Moulik, S. P. Physicochemistry of CTAB-SDS interacted catanionic micelle-vesicle forming system: An extended exploration. *Colloids Surfaces A Physicochem. Eng. Asp.* **553**, 633–644 (2018).

37. Kim, T. H., Song, C., Han, Y. S., Jang, J. D. & Choi, M. C. Spontaneous unilamellar polymer vesicles in aqueous solution. *Soft Matter* **10**, 484–490 (2014).

38. Safran, S. A., Pincus, P. & Andelman, D. Theory of Spontaneous Vesicle Formation in Surfactant Mixtures. *Science (80-.).* **248**, 354–356 (1990).

39. Lépori, C. M., Correa, N. M., Silber, J. J., Falcone, R. D., López-López, M., & Moyá, M. L. Use of Ionic Liquids-like Surfactants for the Generation of Unilamellar Vesicles with Potential Applications in Biomedicine. *Langmuir* **35**, 13332–13339 (2019).

40. Lakowicz, J. R. Principles of fluorescence spectroscopy. *Univ. Maryl. Sch. Med. Balt.* **132**, (2006).

41. Sardar, R., Das, S., Banik, R., Bhunia, S. & Ghosh, S. Exploration of the impact of graphene oxide, acetylenic gemini, and CTAT on the photophysical and aggregation properties of dipolar coumarin 153. *Phys. Chem. Chem. Phys.* **26**, 8900–8918 (2024).

42. Samworth, C. M., Esposti, M. D. & Lenaz, G. Quenching of the intrinsic tryptophan fluorescence of mitochondrial ubiquinol--cytochrome-c reductase by the binding of ubiquinone. *Eur. J. Biochem.* **171**, (1988).

43. Moughton, A. O. & O'Reilly, R. K. Thermally induced micelle to vesicle morphology transition for a charged chain end diblock copolymer. *Chem. Commun.* **46**, 1091–1093 (2010).

44. Menger, F. M. ACCOUNTS OF CHEMICAL RESEARCH On the Structure of Micelles. *Acc. Chem. Res.* **12**, 111–117 (1979).

45. Ghosh, S. & Banerjee, A. A multitechnique approach in protein/surfactant interaction study: physicochemical aspects of sodium dodecyl sulfate in the presence of trypsin in aqueous medium. *Biomacromolecules* **3**, 9–16 (2002).

46. Taboada, P., Gutiérrez-Pichel, M., Barbosa, S. & Mosquera, V. Determination of the interactions between an antidepressant amphiphilic drug and human serum albumin. *Phys. Chem. Chem. Phys.* **6**, 5203–5212 (2004).

47. Chakraborty, T., Chakraborty, I., Moulik, S. P. & Ghosh, S. Physicochemical and conformational studies on BSA - Surfactant interaction in aqueous medium. *Langmuir* **25**, 3062–3074 (2009).

48. Sarangi, A. N. & Gupta, A. N. Impedance Spectroscopy Unveiled the Surfactant-Induced Unfolding and Subsequent Refolding of Human Serum Albumin. *Langmuir* (2024) doi:10.1021/acs.langmuir.4c01886.

49. Abraham, A. N., Sharma, T. K., Bansal, V. & Shukla, R. Phytochemicals as Dynamic Surface Ligands to Control Nanoparticle-Protein Interactions. *ACS Omega* **3**, 2220–2229 (2018).

50. Saraf, A., Sharma, S. & Sachar, S. Insights into the Interactions of Sulfamethoxazole with Organized Assemblies of Ionic and Nonionic Surfactants. *Langmuir* **34**, 14624–14632 (2018).

51. He, X. M. & Carter, D. C. Atomic structure and chemistry of human serum albumin. *Nature* **358**, 209–215 (1992).

52. Mandal, B., Ghosh, S. & Moulik, S. P. Detailed characterization of lysozyme (Lyz)–surfactant (SDDS) interaction and the structural transitions. *New J. Chem.* **40**, 4617–4624 (2016).

53. Kundu, S., Banerjee, C. & Sarkar, N. Inhibiting the fibrillation of serum albumin proteins in the presence of surface active ionic liquids (SAILs) at low pH: spectroscopic and microscopic study. *J. Phys. Chem. B* **121**, 7550–7560 (2017).

54. Vasilescu, M., Angelescu, D., Almgren, M. & Valstar, A. Interactions of globular proteins with surfactants studied with fluorescence probe methods. *Langmuir* **15**, 2635–2643 (1999).

55. Ravikanth Reddy, R., Saha, D., Pan, A., Aswal, V. K., Mati, S. S., Moulik, S. P., & Phani Kumar, B. V. pH-Induced Biophysical Perspectives of Binding of Surface-Active Ionic Liquid [BMIM][OSU] with HSA and Dynamics of the Formed Complex. *Langmuir* **39**, 3729–3741 (2023).

56. Lakowicz, J. R. Principles of fluorescence spectroscopy. *Univ. Maryl. Sch. Med. Balt.* **132**, (2006).

57. Valeur, B. & Berberan-Santos, M. N. *Molecular fluorescence: principles and applications*. (John Wiley & Sons, 2013).

58. Ray, D., Chamlagai, D., Kumar, S., Mukhopadhyay, S., Chakrabarty, S., Aswal, V. K., & Mitra, S. Molecular Insights into the Conformational and Binding Behaviors of Human Serum Albumin Induced by Surface-Active Ionic Liquids. *J. Phys. Chem. B* **128**, 6622–6637 (2024).

59. Maurya, N., Maurya, J.K., Singh, U.K., Dohare, R., Zafaryab, M., Moshahid Alam Rizvi, M., Kumari, M. and Patel, R. In Vitro Cytotoxicity and Interaction of Noscapine with Human Serum Albumin: Effect on Structure and Esterase Activity of HSA. *Mol. Pharm.* **16**, 952–966 (2019).

60. Szabo, A. G. & Rayner, D. M. Fluorescence decay of tryptophan conformers in aqueous solution. *J. Am. Chem. Soc.* **102**, 554–563 (1980).

61. Alcala, J. R., Gratton, E. & Prendergast, F. G. Fluorescence lifetime distributions in proteins. *Biophys. J.* **51**, 597–604 (1987).

62. Petrich, J. W., Chang, M. C., McDonald, D. B. & Fleming, G. R. On the origin of nonexponential fluorescence decay in tryptophan and its derivatives. *J. Am. Chem. Soc.* **105**, 3824–3832 (1983).

63. Moriyama, Y. & Takeda, K. Re-formation of the helical structure of human serum albumin by the addition of small amounts of sodium dodecyl sulfate after the disruption of the structure by urea. A comparison with bovine serum albumin. *Langmuir* **15**, 2003–2008 (1999).

64. Petrich, J. W., Chang, M. C., McDonald, D. B. & Fleming, G. R. On the origin of nonexponential fluorescence decay in tryptophan and its derivatives. *J. Am. Chem. Soc.* **105**, 3824–3832 (1983).

65. Feng, J., Lin, C., Wang, H. & Liu, S. Decoration of gemini alkyl O-glucosides based vesicles by electrostatic deposition of sodium carboxymethyl cellullose: Mechanism, structure and improved stability. *Food Hydrocoll.* **58**, 284–297 (2016).

66. Huang, R., Carney, R. P., Ikuma, K., Stellacci, F. & Lau, B. L. T. Effects of surface compositional and structural heterogeneity on nanoparticle–protein interactions: different protein configurations. *ACS Nano* **8**, 5402–5412 (2014).

67. Li, Y., Wang, X. & Wang, Y. Comparative studies on interactions of bovine serum albumin with cationic gemini and single-chain surfactants. *J. Phys. Chem. B* **110**, 8499–8505 (2006).

68. Li, Y., Wang, X. & Wang, Y. Comparative studies on interactions of bovine serum albumin with cationic gemini and single-chain surfactants. *J. Phys. Chem. B* **110**, 8499–8505 (2006).

69. Bharmoria, P., Trivedi, T. J., Pabbathi, A., Samanta, A. & Kumar, A. Ionic liquid-induced all-α to α + β conformational transition in cytochrome c with improved peroxidase activity in aqueous medium. *Phys. Chem. Chem. Phys.* **17**, 10189–10199 (2015).

70. Hou, H., Qu, X., Li, Y., Kong, Y., Jia, B., Yao, X., & Jiang, B. Binding of citreoviridin to human serum albumin: Multispectroscopic and molecular docking. *Biomed Res. Int.* **2015**, 162391 (2015).

71. Bhakuni, K., Sindhu, A., Bisht, M. & Venkatesu, P. Exploring the counteracting and refolding ability of choline-based ionic liquids toward crowding environment-induced changes in HSA structure. *ACS Sustain. Chem. Eng.* **9**, 422–437 (2020).

72. Rehman, M. T., Shamsi, H. & Khan, A. U. Insight into the binding mechanism of imipenem to human serum albumin by spectroscopic and computational approaches. *Mol. Pharm.* **11**, 1785–1797 (2014).

Table 1. Variation of hydrodynamic diameter (D_h) of [C_{16}Mim]/[AOT] vesicle (χ_{AOT} =0.5 and χ_{AOT} =0.6) with HSA incorporation.

[C_{16}Mim]/[AOT] vesicle (χ_{AOT} =0.5)		**[C_{16}Mim]/[AOT] vesicle (χ_{AOT} =0.6)**	
[HSA] (μM)	**D_h (nm)**	**[HSA] (μM)**	**D_h (nm)**
0	**197.32**	**0**	**243.48**
0.36	**249.26**	**0.48**	**242.68**
0.54	**264.33**	**1.13**	**235.73**
1.07	**308.25**	**2.45**	**217.91**
1.42	**411.27**	**3.18**	**215.10**
2.21	**536.25**		
3.70	**1091.31**		

Supporting information:

1. Characterization of catanionic vesicle:

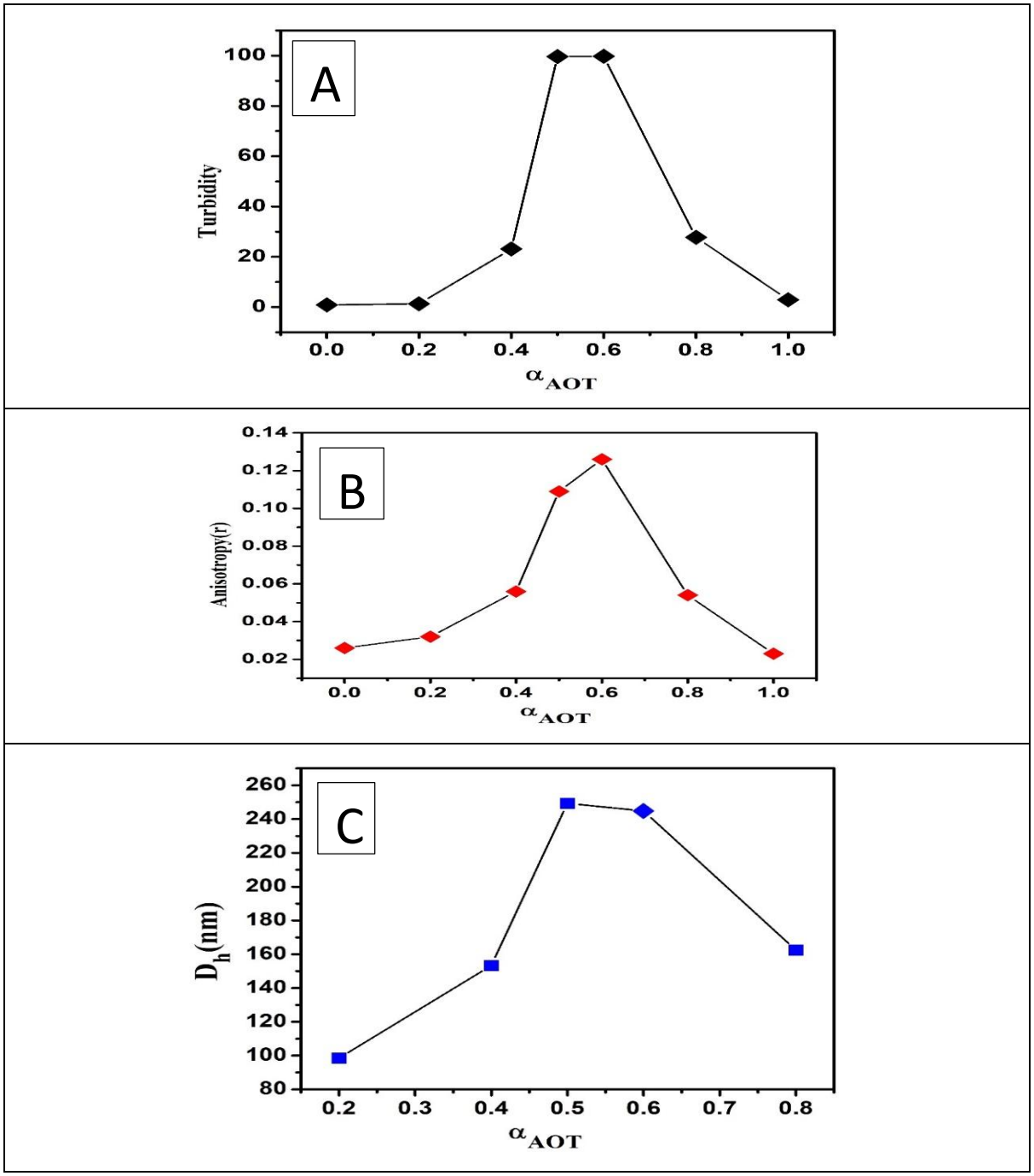

Fig. S1 (A) Variation in turbidity of aqueous [C_{16}Mim] [AOT] mixture at various mole fractions. (B) Variation in steady-state anisotropy of [C_{16}Mim] [AOT] mixture with varying mole fraction of AOT. (C) Change in hydrodynamic diameter (D_h) of [C_{16}Mim] [AOT] aggregate in different mole fractions.

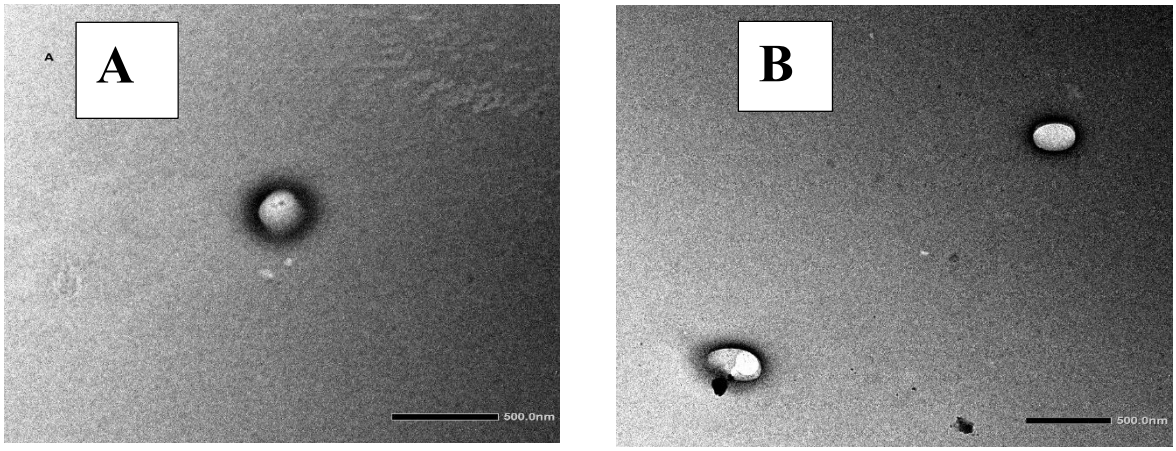

Fig. S2 TEM micrographs of [C_{16}Mim]/[AOT] mixture at (A) 0.5 mole fraction, and (B) 0.6 mole fraction of AOT.

(2) Table S1. Surface parameters (vesicular parameters) obtained from surface tension measurements for [C_{16}Mim] [AOT] at χ_{AOT} = 0.5 and χ_{AOT} = 0.6, in the absence and presence of 5 μM HSA in phosphate buffer medium (pH 7.4) at 298.15 K.

System	CVC (mM)	γ_{CVC} (mN m^{-1})	$10^6\,\Gamma_{max}$ (molm^{-2})	A_{min} (Å^2)	π_{CVC} ($mN\ m^{-1}$)	pC_{20}
[C_{16}Mim] [AOT] (0.6)	0.0183	29.6	1.38	1.20	40.7	2.66
[C_{16}Mim] [AOT] (0.6)-HSA	0.0624	29.3	1.32	1.25	25.9	1.59
[C_{16}Mim] [AOT] (0.5)	0.0157	30.5	0.81	2.04	41.1	2.86
[C_{16}Mim] [AOT] (0.5)-HSA	0.0782	29.3	1.08	1.52	26.7	1.64

(3) Absorbance spectra of HSA in the presence of [C_{16}Mim] [AOT].

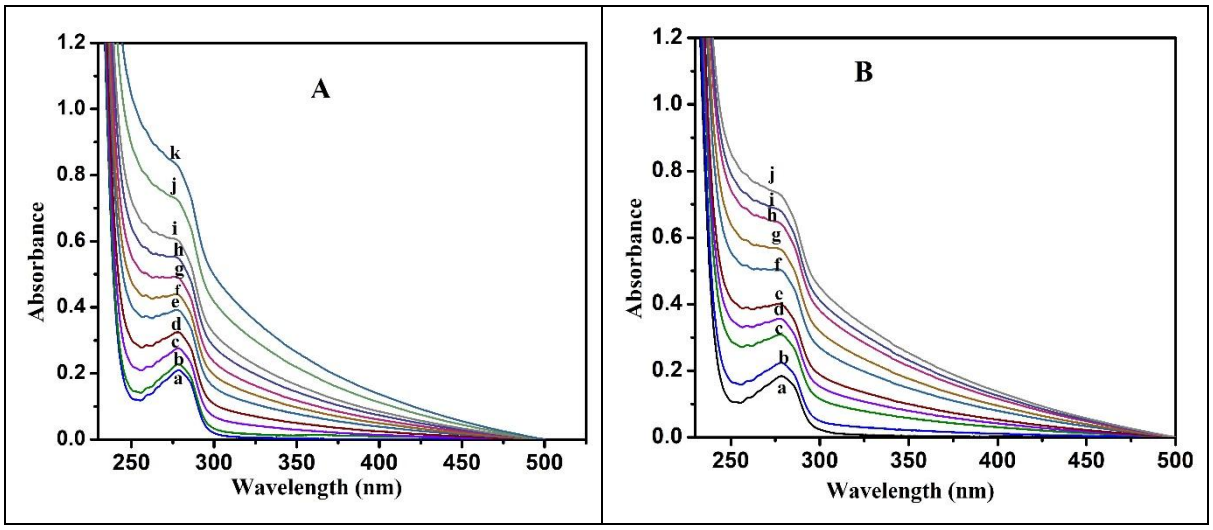

Fig. S3 Absorbance spectra of HSA in the presence of [C_{16}Mim] [AOT], (A) 0.5-mole fraction (a, b, c, d, e, f, g, h, i, j, k; 0.0, 0.05, 0.08, 0.12, 0.15, 0.18, 0.22, 0.28, 0.30, 0.33, 0.35 mM respectively), and (B) 0.6-mole fraction (a, b, c, d, e, f, g, h, i, j; 0.0, 0.04, 0.09, 0.11, 0.13, 0.18, 0.21, 0.26, 0.28. 0.32 mM respectively) of AOT.

(4) Table S2. Time-dependent fluorescence decay profile of HSA in [C_{16}Mim] [AOT] mixed vesicle system for χ_{AOT} =0.5 and, χ_{AOT} =0.6 respectively.

[C_{16}Mim]/[AOT] (mM)(χ_{AOT} =0.5)	τ_1 (ns)	A_1 (%)	τ_2 (ns)	A_2 (%)	$< \tau >$ (ns)
0	1.64	24.17	5.94	75.83	3.64
0.04	1.39	21.97	5.10	78.03	3.21
0.07	1.03	21.75	5.04	78.25	2.74
0.14	0.61	19.72	4.77	80.82	2.04
0.20	0.21	24.22	4.57	75.78	0.77
0.36	0.15	29.72	4.52	70.28	0.48
0.49	0.071	41.08	4.37	58.92	0.17
[C_{16}Mim]/[AOT] (mM)(χ_{AOT} =0.6)					
0.014	1.35	21.86	5.45	78.14	3.28
0.03	1.10	19.23	5.11	80.77	3.04
0.07	1.30	26.63	5.05	73.37	2.86
0.09	1.42	30.21	5.0	69.79	2.85
0.11	1.15	36.12	4.84	63.88	2.24
0.24	0.036	51.82	3.74	48.18	0.07
0.49	0.11	55.49	3.45	44.51	0.19

(5) ITC profile [C_{16}Mim] [AOT] in the presence of HSA solution.

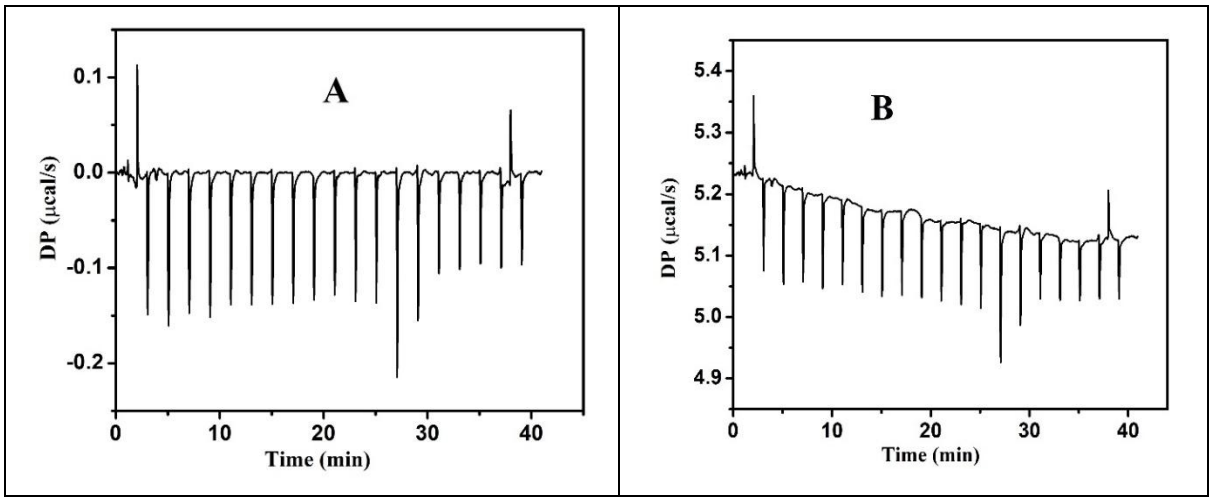

Fig. S4 ITC profile of titration of (A) 0.5, and (B) 0.6- mole fraction of [C_{16}Mim] [AOT] in HSA solution at 298 K.

(6) Variation of hydrodynamic diameter (D_h) of vesicle in the presence of different concentrations of HSA.

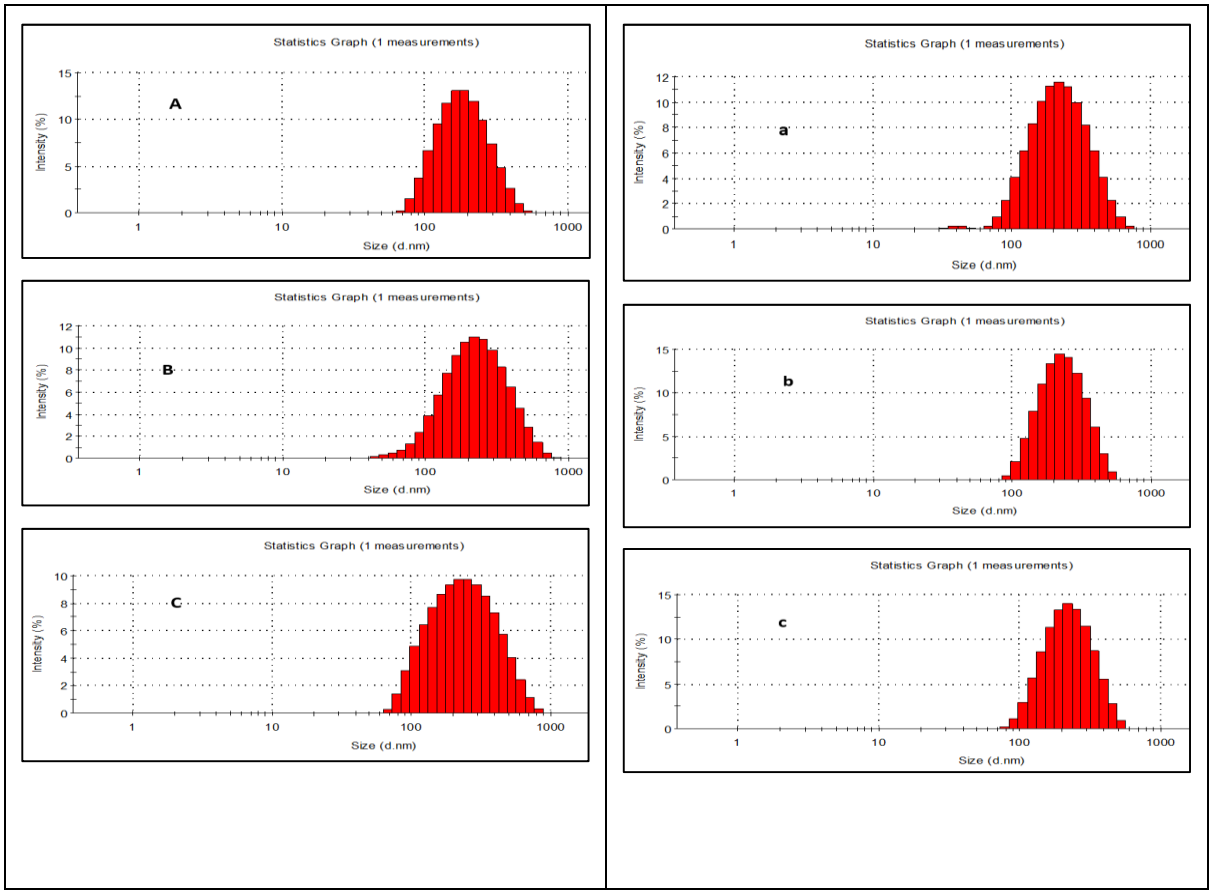

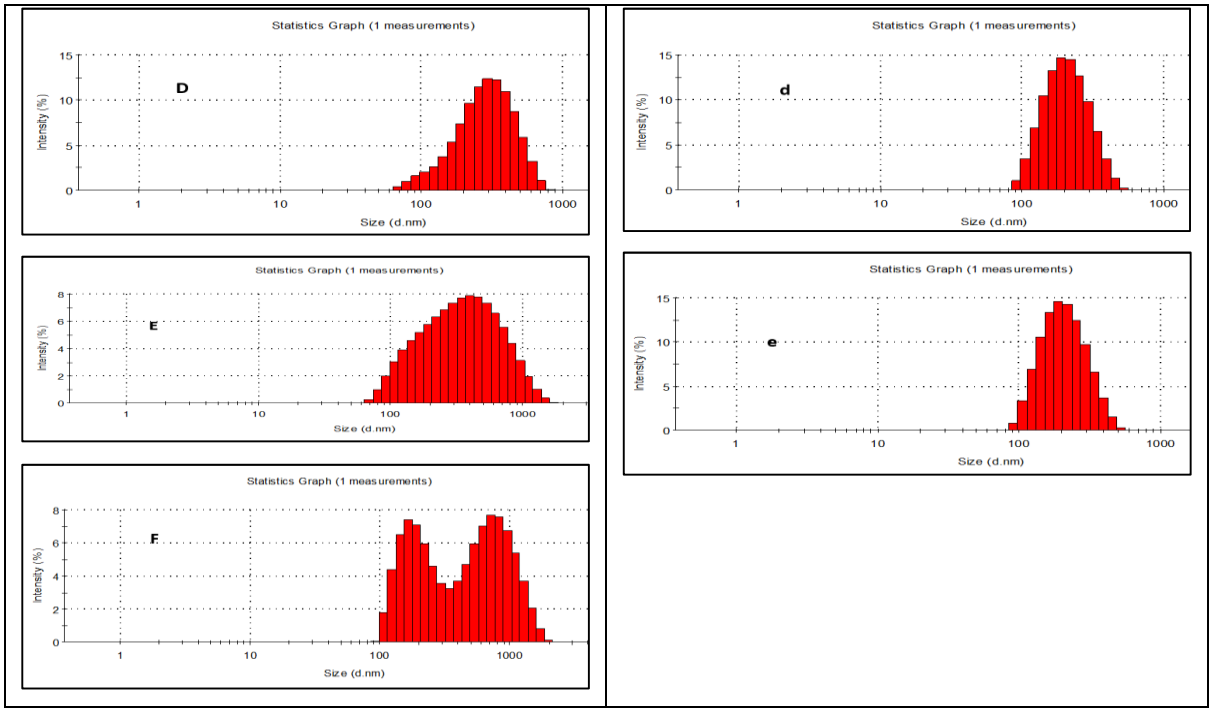

Fig. S5 Variation of hydrodynamic diameter (D_h) of [C_{16}Mim] [AOT] vesicle with increasing concentration of HSA; (A, B, C, D, E, F; 0.0, 0.36, 0.54, 2.21, 3.70 µM of HSA for the 0.5-mole fraction of AOT), and (a, b, c, d, e; 0.0, 0.48, 1.13, 2.45, 3.18 µM of HSA for the 0.6-mole fraction of AOT) respectively.

(7) Table S3. Variation of α-helix contents of HSA in the presence of various amounts of [C_{16}Mim] [AOT] (for χ_{AOT} =0.5 and χ_{AOT} =0.6) in pH 7.4, at 298 K.

[C_{16}Mim] [AOT] (χ_{AOT} =0.5) (mM)	α–helix (%)	[C_{16}Mim] [AOT] (χ_{AOT} =0.6) (mM)	α–helix (%)
0	60.85	0	60.85
0.002	60.85	0.003	59.28
0.011	60.75	0.021	60.21
0.022	60.65	0.052	60.038
0.102	60.53	0.076	59.98
0.107	60.71	0.133	60.09
0.117	60.69	0.136	59.78
0.133	60.48	0.166	59.48
0.186	60.25		

Chapter-IV

Drug-Induced Micelle-to-Supermicelle Transition in CTAB: Comparative Study with Acetylenic Gemini Surfactant via Experimental and DFT Approaches

Drug-Induced Micelle-to-Supermicelle Transition in CTAB: Comparative Study with Acetylenic Gemini Surfactant via Experimental and DFT Approaches

Abstract: Self-assembly or co-assembly of amphiphiles creates a large number of aggregated structures, among which the supermicelle structure is very important for its unique morphology and versatile application in the nanotechnology and biomedicine fields. It is well-known that supermicelles with different morphologies can be created when amphiphilic block copolymers assemble hierarchically in a certain solvent. However, to our knowledge, this is the first instance of the supermicelle formation between a surfactant (cetyltrimethylammonium bromide; CTAB) and an amphiphilic drug (sodium Fenbufen). Here, we present a comprehensive list of supermicelles formed by the co-assembly of the drug and CTAB, including spherical, linear, and cross-linked forms. TEM analysis, along with DLS, anisotropy, and AFM measurements, supported the formation of supermicelles. Along with supermicelle formation, we have also focused on the micellar property of the drug-surfactant mixed system. Here we compared mixed micelle formation between the Fenbufen drug with conventional CTAB and the synthesized acetylenic Gemini surfactants. We have performed a DFT simulation study to understand the molecular interaction between drugs and surfactants. The interaction of Gemini with drug molecules is much stronger than CTAB, according to DFT calculations. However, the Gemini micelle disintegrates into a smaller micelle when the drug molecules are added because of its large size. On the other hand, the modest size of the CTAB micelle allows it to accommodate many drug molecules on its micellar surface and create giant supermicelles with a variety of shapes. These supermicelle aggregates have a variety of uses in the biomedical field, drug delivery, nanotechnology, and other key disciplines.

1. Introduction: One of the most significant properties of nature's building component is amphiphilicity. It has been demonstrated that amphiphilic species, including surfactants, some drug molecules, and block copolymers, may self-assemble a wide range of forms, such as different kinds of micelles, vesicles, tubes, and bilayers[1-6]. Recently, a range of intriguing colloidal materials has been created on a wider length scale using amphiphilic nanostructures like Janus and patchy particles[7]. The self-assembly of the micelle or co-assembly of two different micelles leads to the formation of superstructures, such as supermicelles, nanotubes, and nanosheets[8-13]. The formation of supermicelles and the modification of their supramolecular structure has recently become a very important and fascinating area of

study[14,15]. There have been a few reports in the literature over the last several years on the formation of supermicelles using block copolymer self-assembly. Block copolymers have two or more polymer segments, therefore, when they are placed in solvents that are selective for only one of the segments, the polymer undergoes self-assembly to produce a variety of core-size nanoparticles (micelles). Xiaoyu Li et al. report the formation of complex hierarchical supermicelle structures via the H-bonding interaction of cylindrical block comicelles with crystalline cores as building blocks[16]. Huibin Qiu et al. report the formation of tuneable supermicelles from the hierarchical self-assembly of amphiphilic cylindrical B-A-B triblock comicelles[17]. To the best of our knowledge, however, there are no reports of supermicelle formation by amphiphilic drug-surfactant mixtures in the literature. These supermicelle aggregates have enormous applications in biomedicine, biotechnology, and the nanoscience field. Since these supermicelle aggregates have a lot of nano-micellar channels, they act as effective carriers for hydrophobic or hydrophilic drugs, e.g., by encasing the drug molecules in nano-aqueous pseudo-phase or intercalating them into the aggregate hydrophobic domains. Since the drug builds up at the micellar interface, mixed micelle formation between drug-surfactant mixed systems minimizes the toxicity of the drug and the necessity of a minimum dose[18]. The study of mixed amphiphilic systems has received a lot of attention over the last few decades. A mixed amphiphilic system can have surface and colloidal characteristics that are distinct from those of the pure individual components. Amphiphilic components frequently exhibit synergistic effects when mixed in nonideal ways, which can be used to advantage in certain applications. A system is considered to be synergistic when the critical micelle concentration (CMC) values for mixed amphiphilic systems are lower than those for the pure components alone. Therefore, mixed micelles are frequently used in industries, in pharmaceutical formulations, and enhanced oil recovery procedures[19,20]. In the present work, we have focused on two factors: (1) preparation and characterization of supermicelle aggregates and (2) detailed investigation of mixed micelle formation and its related micellar properties. Here, we made a comparative study of mixed micelle formation between a conventional cetyltrimethylammonium bromide (CTAB) and a synthesized acetylenic Gemini surfactant with Fenbufen drug (FB). Fenbufen is a non-steroidal drug that is a derivative of phenyl alkanoic (propionic acid)[21]. It has analgesic, anti-inflammatory, and antipyretic properties that have been demonstrated. The way that Fenbufen works is by stopping the formation of prostaglandins, which can lead to inflammation[22]. FB has therefore been successfully used to treat rheumatoid arthritis, ankylosing spondylitis, and inflammation in osteoarthritis[23]. It is also effective in relieving the symptoms of fibrositis, gout, tendinitis, and

periarthritis of the shoulder. Although FB is only partially soluble in water, its sodium salt is completely soluble, and its aqueous solution exhibits amphiphilic behaviour. Due to the greater hydrophobicity and electronic charge, Gemini surfactants interact more strongly with the FB drug than CTAB, which is confirmed by DFT calculations. The interaction between FB and surfactants is highly synergistic in nature, so a lower CMC was observed in a mixed system than in a pure one. Although the interactions between FB and Gemini are strong, due to the large size of Gemini's micelles, the incorporation of drugs causes breakdowns of its micellar structure into a large number of small mixed micelles. On the other hand, due to the small size of the CTAB micelle, it can accommodate a large number of FB molecules on its micellar surface, resulting in the formation of a supermicelle solution. To characterize the supermicelle and comprehend the micellar property of the drug-surfactant mixed system, we applied a variety of techniques in this study (e.g., steady-state anisotropy, DLS, zeta potential, tensiometry, lifetime measurements, TEM, and AFM). In addition to doing an experimental study, we also carried out DFT simulations to comprehend the molecular-level interactions between the drug and surfactant molecules.

2. Experimental section:

2.1 Materials: The cationic surfactant cetyltrimethylammonium bromide (CTAB) was purchased from Sigma, USA (99% purity), acetylenic gemini surfactant (N, N’-dihexadecyl-N, N, N’, N’-tetramethyl-N, N’-but-2-ynediyl-di-ammonium chloride (G-16)) was synthesis in our lab and its synthesis procedure, characterization was documented in our previous work.[24] The drug Fenbufen (FB) was the product of TCI with a purity 99%, Acridine orange (AO), used as a probe was a product of Merck India (>98 % purity), Sodium hydroxide (NaOH), and ethanol, used for solution preparation were purchased from Merck India. All the solutions were prepared in aqueous buffer (pH=12.0).

2.2 Instrumentation:

2.2.1 Tensiometry

The surface tension was measured using a Krüss (Germany) tensiometer and the ring detachment method. A concentrated stock solution of surfactants in aqueous medium at a certain mole fraction of drug was added to water with a Hamilton micro syringe, allowing 5 minutes for equilibration before each measurement. To test repeatability, all measurements were repeated three times. The approach had an accuracy of ± 0.1 $mN.m^{-1}$. The cmc was calculated by plotting surface tension (γ) vs. log[surfactant].

2.2.2 Dynamic Light Scattering (DLS) and Zeta potential measurement

DLS measurements were carried out using a He-Ne laser (λ = 632.8 nm) in a Zetasizer nano ZS (Malvern, UK) at a scattering angle of 90°. To remove larger particles, the sample was filtered multiple times. The zeta potential (ζ) and DLS measurement of solutions were repeated twice, and the average values of the results were then reported.

2.2.3 Atomic force microscopy (AFM): The Innova-S2 instrument (Bruker, USA) was used for AFM imaging in the trapping mode. After dropping 30 μL of the FB/CTAB mixed sample onto mica foil, it was left inside a desiccator to dry for the entire night. Ultimately, the AFM experiments were carried out following an appropriate drying period. Using WSxM 5.0, the AFM image was examined.

2.2.4 Transmission Electron Microscopy (TEM):

10 μL sample solutions with concentrations just above the cmc of a certain mole fraction were deposited on a carbon-coated copper grid with a mesh size of 300 to adsorb on it. Excess liquid on the copper grid was immediately removed from the filter paper on which it was placed. To stain it negatively, freshly made 0.5 wt% aqueous uranyl acetate was employed. The samples were dehydrated overnight in a desiccator. A JEOL-JEM 2100 transmission electron microscope from Japan was employed, with an accelerating voltage of 100 kV.

2.2.5 Steady-state fluorescence anisotropy study:

A Perkin Elmer LS55 (USA) fluorescence spectrofluorometer connected to a fluorescence Peltier system PTP-1 with a glass cell with a 1 cm path length was used to assess steady-state fluorescence anisotropy. In the experiment, all solutions with concentrations slightly higher than the cmc at that specific mole fraction were chosen. The steady-state fluorescence anisotropy (r_{ss}) of acridine orange was measured using excitation wavelengths of 480 nm and emission at 530 nm. The definition of r_{ss} is as follows:

$$r_{ss} = \frac{I_v - GI_h}{I_v + 2GI_h} \quad \textbf{(1)}$$

Where I_h and I_v are emission intensities, which are horizontally and vertically polarized, respectively, arise from the vertically polarized excitation of the probe. Factor G is defined as:

$$G = \frac{I_v}{I_h}$$

All the anisotropy values were averaged over an integration time of 20 s.

2.2.6 Time-Resolved Fluorescence Study.

Time-resolved fluorescence decay was performed with the use of a Horiba-Jobin-Yvon FluoroCube fluorescence lifetime system using a NanoLED at 500 nm (IBH, UK), and a TBX photon detection module as the detector. All of the solutions with concentrations that were barely above the cmc at that specific mole fraction were used. Using the IBH DAS-6 decay analysis software, all of the decay data were fitted. Instead of using a sample, a scatterer made from a diluted micellar solution of sodium dodecyl sulfate was used to collect the lamp profile. The $\chi 2$ values were kept somewhat near 1 for suitable fits.

3. Results and discussion:

3.1 Adsorption isotherms analysis:

The adsorption isotherms of pure as well as mixed drug-surfactant systems determined from surface tension (γ) vs. log[amphiphiles] plots are shown in Fig.S1 and Fig.1, respectively. With the gradual addition of a pure or mixed amphiphilic system in an aqueous medium, a sharp decrease in 'γ' values before attaining a plateau above CMC due to interfacial adsorption of amphiphile molecules. The CMC of all pure and mixed systems was defined from the breakpoint in adsorption isotherms. Here, for the first time, we reported the CMC of the sodium Fenbufen drug, and it was 2.67 mM. The CMC of all the mixture systems of CTAB/FB and Gemini/FB fall in the range of 0.1174-0.5176 mM and 0.053-0.254 mM, respectively. Such a low CMC value of the mixture systems compared to parent amphiphiles (CTAB (0.9 mM),[25] Gemini (0.075 mM),[26] and sodium Fenbufen (NaFB)) suggests a very strong synergistic interaction between oppositely charged surfactants and drug molecules in the mixture, causing early aggregation. The CMC values of the mixed surfactants were theoretically determined by using the Client equation[27] at various mole fractions of the drug. It has been observed that the drug-surfactant mixture's CMC significantly deviates from the values predicted by theory, which supports the electrostatic synergistic type interaction between oppositely charged drug and surfactant molecules. The variation of the CMC with the change in the mole fraction of the mixture system is shown in the following figure (Fig. S2 (A-B)).

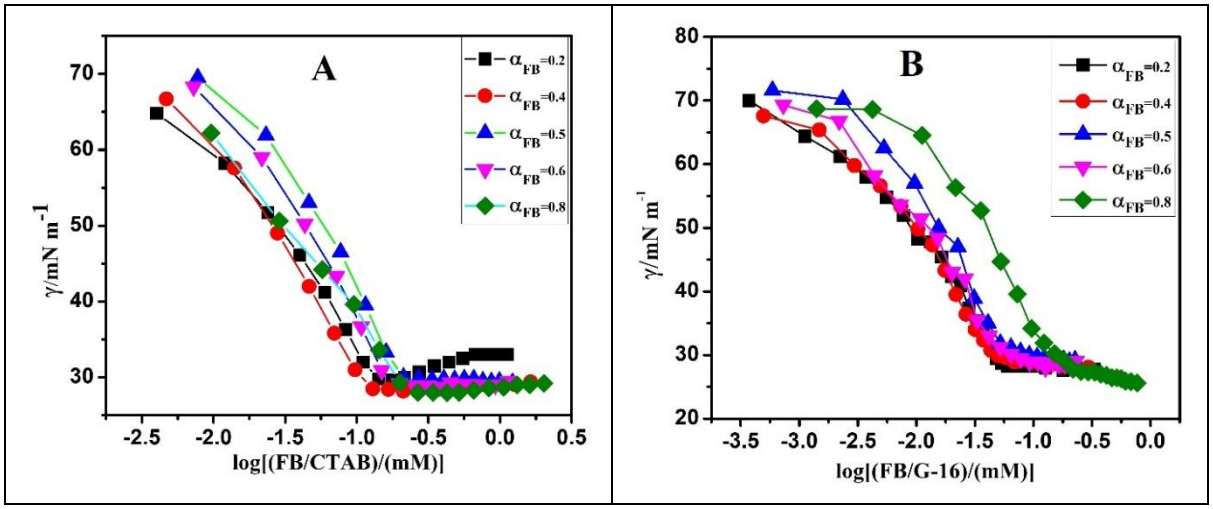

Fig.1 Variation of surface tension (γ) vs. (A) log [FB/CTAB (mM)]; (B) log [FB/G-16 (mM) at different mole fractions of FB in aqueous medium (pH=12.0) at 298.15 K.

Interfacial properties of drug-surfactant mixtures: Tensiometry is a versatile method because it not only measures the CMC values but also provides crucial information regarding the adsorption properties of the amphiphiles at the air-water interface. As a result, the adsorption of CTAB and Gemini surfactant at the aqueous air-water interface has also been observed in the presence of varied FB concentrations. Table S1 shows that the 'γ_{cmc}' value for the CTAB-FB mixture system is significantly lower than that for pure CTAB, indicating that the mixture system's monolayer is densely packed and has more surface activity than pure CTAB. For the Gemini-FB mixture system, the 'γ_{cmc}' values are almost the same as for the pure Gemini, suggesting no significant change in the interfacial activity of the mixture system compared to the pure one. The surface excess concentration (Γ_{max}) of the amphiphilic system can be determined by applying Gibbs' adsorption isotherm to the tensiometric diagrams, and the minimum area covered per amphiphile molecule (A_{min}) at the air-water interface can be calculated from the Γ_{max} value by using the following equation[28] and is presented in Table S1.

$$\Gamma_{max} = -\frac{1}{2.303nRT}\left[\frac{d\gamma}{dlogC}\right] \quad (2)$$

$$A_{min} = \frac{10^{18}}{N_A \Gamma_{max}} \quad (3)$$

Where n is the number of species present at the air-water interface after dissociation of the amphiphiles, R is the universal gas constant (8.314 J/K.mol), T is the Kelvin scale temperature, dγ/dlogC is the slope of the straight-line part in the tensiometric plot, and N_A refers to

Avogadro's number. It is well known that a hydrophilic head group's size plays a significant role in determining the A_{min} value and, thus, the maximum surface excess concentration (Γ_{max}) value of an amphiphile.[29] The lower Γ_{max} value of Gemini surfactant (1.76) compared to CTAB (3.13) can be attributed to the presence of two hydrophilic head groups of Gemini surfactant occupying a relatively larger area on the surface, so the packing of amphiphiles is low. As a result, surface excess concentration (Γ_{max}) per unit area is lower for Gemini than for CTAB. In the presence of drug molecules, initially with increasing concentration of drugs, the value of Γ_{max} increases and A_{min} decreases for CTAB up to a certain mole fraction of $\alpha_{drug = 0.5}$, but beyond that, the Γ_{max} value decreases and A_{min} rises with drug concentration (Table S1). This interesting observation could be explained with the help of intercalation and the accumulation of drug molecules in the CTAB micelle. Initially, with increasing concentration, the drug molecules intercalate the CTAB micelle due to oppositely charged species; as a result, the electrostatic repulsion between similarly charged CTAB head groups minimizes and the compactness of the micelle increases, resulting in a decrease in A_{min} and an increase in Γ_{max} with drug concentration up to $\alpha_{drug = 0.5}$. However, after that, with a further increase in drug concentration, it was unable to penetrate due to the small size of the CTAB micelle and the extra drug molecules that were accommodated on its surface. Due to the accommodation of a large number of similarly charged drug molecules on the micellar surface again enhances the electrostatic repulsion, resulting in loose packing, which leads to an increase in Amin and a decrease in Γ_{max} values. In the case of the Gemini surfactant, only a single type of pattern was observed in the presence of drug molecules. With successive increases in drug concentration, the surface excess concentration (Γ_{max}) increased, while the minimum area per molecule (A_{min}) decreased. This behavior can also be attributed to the opposite charges of the micelles and the drug molecules. The incorporation of oppositely charged drug molecules reduces the electrostatic repulsion between similarly charged head groups of the Gemini surfactant monomers. Consequently, this leads to enhanced micelle compactness, reflected by a decrease in A_{min} and an increase in Γ_{max}. Owing to the relatively large size of Gemini micelles, a substantial number of drug molecules can intercalate into the micelle structure, further reducing electrostatic repulsion and enhancing micelle compactness with progressive drug addition.

Another important surface parameter is surface pressure at CMC (π_{cmc}), which tells about the reduction of surface tension at CMC and is presented by the following equation;

$$\pi_{cmc} = \gamma_0 - \gamma_{cmc} \quad \textbf{(4)}$$

Where γ_0 is the surface tension of pure solvent, and γ_{cmc} is the surface tension of amphiphile solutions at CMC. The π_{cmc} values for the pure system as well as for the drug-surfactant mixed system were calculated and recorded in Table S1. The value of π_{cmc} follows the order (Gemini> CTAB> FB drug), indicating Gemini surfactant is the most surface-active agent, after which CTAB is a moderately surface-active and the drug molecules are the least surface-active agent. In the case of the drug-CTAB mixed system, the π_{cmc} value increases with drug concentration, suggesting that in the presence of drug molecules, the surface activity of CTAB increases. But in the case of Gemini surfactant, there is no appreciable change in π_{cmc} values in the presence of drug molecules. The efficiency of interfacial adsorption is represented by a parameter called $pC_{20,}$ which is given by the following equation.

$$\mathbf{pC_{20} = -\log C_{20}} \qquad \mathbf{(5)}$$

The C_{20} value can be defined as the surfactant concentration required to decrease the surface tension of 20 $mN.m^{-1}$ of a pure solvent. The large value of pC_{20} indicates better adsorption efficiency of the amphiphiles at the air-water interface, hence showing better surface activity. Table S1 shows that the pC_{20} value for Gemini surfactant is much higher than that of CTAB, indicating interfacial adsorption efficiency, i.e., surface activity for Gemini surfactant is better than that of CTAB. Since Gemini surfactant has two hydrophobic groups, its micellization as well as interfacial adsorption power are high compared to CTAB, resulting in a higher pC_{20} value for Gemini surfactant. The pC_{20} value for the drug-CTAB mixed system is much higher than pure CTAB, indicating that in the presence of drugs, the interfacial adsorption of CTAB increases, i.e., the surface activity of CTAB rises. However, in the case of Gemini surfactant, there is no appreciable change in pC_{20} value in the presence of the drug because Gemini itself is very surface active, so no appreciable change was found. The following relationship has been used to derive the packing parameter (p), which dictates the geometry of the micelle[30]

$$\mathbf{P} = \frac{\boldsymbol{V_0}}{\boldsymbol{l_c A_{min}}} \qquad \mathbf{(6)}$$

Due to the difficulty in precisely estimating and determining the cross-sectional area occupied by the hydrophilic group at the micelle-solution interface, A_{min} was used in this instance instead of a_0 (cross-sectional area). Here, l_c is the maximum effective hydrophobic chain length inside the core of the micelle, and v_0 is the volume of the hydrophobic groups in the micellar core. The values of l_c and v_0 can be determined by using Tanford formulas [31]

$$\mathbf{L_c = (0.154 + 0.1265 C_n)\ nm} \qquad \mathbf{(7)}$$

$$V_0 = (0.0274 + 0.0269C_n)\ nm^3 \quad (8)$$

Where C_n is the number of carbon atoms in the saturated hydrocarbon chains of the amphiphiles. For the mixed amphiphilic system, the packing parameter was determined by using the Israelachvili equation.[32]

$$P_{eff} = \left(\frac{v_0}{l_c A_{min}}\right)_{eff} = \frac{\sum v_i X_i}{(\sum A_i X_i) l_c} \quad (9)$$

Table S1 shows that the packing parameters (p) for pure Gemini and drugs are less than 0.33, indicating that these two form a spherical micelle; however, for pure CTAB, the packing parameter is greater than 0.33, indicating that CTAB creates a non-spherical micelle. The typical conventional surfactant (here, CTAB) often forms non-spherical micelles at higher concentration (10 times its CMC or more). In the case of CTAB micelles, the addition of oppositely charged drug molecules leads to a gradual increase in packing efficiency, reaching a maximum at a drug mole fraction of 0.5. This enhancement in packing efficiency can be attributed to the intercalation of the drug molecules within the micelle, which effectively reduces the electrostatic repulsion among the positively charged head groups of the CTAB surfactants. However, beyond $\alpha_{drug = 0.5}$, a decline in packing efficiency is observed with further increases in drug concentration. This decrease is likely due to the limited capacity of the relatively small CTAB micelles to accommodate drug molecules internally. As a result, excess drug molecules tend to localize on the micellar surface. The accumulation of similarly charged drug molecules on the surface leads to renewed electrostatic repulsion, which disrupts the micellar packing and reduces overall packing efficiency. In the case of Gemini micelles, a continuous increase in packing efficiency is observed with increasing concentrations of drug molecules. This behavior is attributed to the fact that the drug molecules carry a charge opposite to that of the Gemini micelles. As a result, incorporation of the drug molecules reduces electrostatic repulsion between the similarly charged head groups of the Gemini monomers, thereby enhancing micellar packing efficiency.

Furthermore, due to the inherently larger size of Gemini micelles compared to CTAB micelles, they can accommodate a greater number of drug molecules. This allows for the progressive intercalation of drug molecules, leading to a consistent increase in micellar compactness—i.e., packing efficiency—as the drug concentration rises.

Thermodynamic analysis of micellization and interfacial adsorption: To study the effect of FB drug on the micellization and adsorption behaviour of CTAB and Gemini surfactant, the

change of Gibbs' free energy of micellization (ΔG^0_m) and the standard Gibbs' free energy of adsorption (ΔG^0_{ad}) were calculated by using the equations below: equations:[33]

$$\Delta G^0_m = RT \ln \chi_{cmc} \quad (10)$$

$$\Delta G^0_{ad} = \Delta G^0_m - (\pi_{cmc}/\Gamma_{max}) \quad (11)$$

Where χ_{cmc} is the CMC value in the mole fraction scale. As can be seen from Table S1, the value of ΔG^0_m is negative for pure CTAB, pure Gemini, and their mixtures with drugs, indicating micellization is a thermodynamically spontaneous process. The negative ΔG^0 values of three pure components follow the order of ΔG^0_m (Gemini)> ΔG^0_m (CTAB)> ΔG^0_m (drug), suggesting that micellization is much easier for Gemini surfactant compared to CTAB or pure drug. In the presence of drugs, the negative ΔG^0_m value increases for CTAB, indicating micellization becomes easier because of the minimization of the electrostatic repulsion between similar charged head groups of CTAB. For the drug-CTAB mixture system, the ΔG^0_m value decreases with increasing drug concentration, suggesting that at low drug concentrations, micellization is favoured, but at very high drug concentrations, micellization is not so favourable. The drug molecules initially intercalate the micelle and reduce the repulsion between the head groups of surfactants since they have opposite charges, making micellization easier. However, as drug concentration rises further, extra drugs adsorb on CTAB micelles, causing a repulsion between the similarly charged carboxyl groups of FB substances and impeding micellization. In the case of the drug-Gemini mixed system, a similar type of phenomenon was also found. Table S1 also showed that ΔG^0_{ad} values are negative throughout, suggesting the adsorption process takes place spontaneously both in the presence and absence of FB molecules. The negative value of ΔG^0_{ad} for CTAB increases in the presence of the drug, so adsorption on the air-water interface becomes favourable. However, in the case of Gemini, a different pattern was seen. Here, the ΔG^0_{ad} values drop in the presence of drug molecules, making Gemini's adsorption on the air-water interface unfavourable. The ΔG^0_{ad} values are also more negative than their corresponding ΔG^0_m values, indicating that adsorption, rather than micellization, is the primary process when a micelle is formed. This is because work must be done to transfer the surfactant molecules from the surface, where they are in monomeric form, to the micellar stage through the aqueous medium. To quantify the synergism in the mixed adsorbed monolayer formation at equilibrium, Sugihara et al.[34] proposed a thermodynamic parameter called the free energy of a surface at equilibrium (G^S_{min}).

$$G^{S}_{min} = \gamma_{cmc} A_{min} N_A \quad (12)$$

The lower value of G^{S}_{min} suggests that a thermodynamically more stable surface is being formed or showing better surface activity. The G^{S}_{min} value is the maximum for drug molecules, indicating less surface activity or a thermodynamically less stable surface film is formed by drug molecules compared to surfactant. In the presence of drug molecules, the G^{S}_{min} value decreases for both CTAB and Gemini surfactants, resulting in more surface activity in the mixed system than in the pure one. So, the surface activity of both surfactants improved in the presence of the FB drug.

3.2 Structural Investigations Utilising DLS and Zeta Potential: DLS measurements were performed to explore the changes in the shape of the mixed aggregate from cationic-rich surfactants to anionic-dominated drug ones, as well as to understand the type of aggregated species present in the aqueous solution of the drug-surfactant combination. DLS, also known as light scattering, is a method for measuring the translational diffusion of particles under Brownian motion. The size of the particles is determined by measuring the intensity fluctuations of the scattered light, expressed as hydrodynamic diameter (D_h).[35] The average hydrodynamic diameters (D_h) of pure FB drugs and synthesized Gemini surfactants were 280 nm and 190.1 nm, respectively, in a solution containing 10 times their CMC values. A tiny micelle with a diameter of around 1 nm and a considerable peak at around 280 nm, which corresponds to a large aggregate, are the two separate DLS peaks that can be seen in pure drug micelles (Fig. S3 (R)), suggesting the presence of two different types of aggregates. DLS measurement indicates the drug-induced non-spherical micelle to large aggregated mixed micelle transition of CTAB, and the size distribution graphs of the drug-surfactant mixed system at a varied concentration of drug are presented in Figure 2 A-B. For the drug-CTAB mixed system, when $\alpha_{drug = 0.0}$, i.e., pure CTAB micelle, we observed a single DLS peak around 1.39 nm (Fig. S3 (A)), which is in good agreement with the literature-reported value.[36] It has been noted that when drugs are added to CTAB micellar solution, the primary peak's intensity gradually declines while the intensity of the supplementary peak sharpens. Two separate peaks in the size distribution are seen for the drug-CTAB mixed system up to $\alpha_{drug = 0.4}$, signifying the presence of pure and mixed micelles. The intensity of the micellar peak decreases gradually as drug concentration rises, and mixed micellar peaks become prominent. However, beyond $\alpha_{drug = 0.4}$, with further increasing the drug concentration, the micellar peaks vanish, and only a mixed micellar peak is observed in the size distribution graph of the drug-CTAB mixed system. A maximum D_h of about 548 nm at $\alpha_{drug = 0.6\text{-}0.8}$, which denotes the presence of large aggregated

species, could be seen if we observed the change in the average hydrodynamic diameter (D_h) with various mole fractions of drugs (Fig. 2A). Contrarily, in the drug-Gemini mixed system, there was a very modest increase in D_h values up to $\alpha_{drug = 0.4}$, but after that, with an increase in FB concentration, there was a sharp decline in D_h value. The mixed micellar peaks with increasing drug concentration begin to break down to smaller peaks after $\alpha_{drug = 0.4}$, as seen by the size distribution plot of the drug-Gemini mixed system (Fig. 2B). Due to the large size of the Gemini micelle, it cannot accommodate many numbers of drug molecules on its micellar surface, resulting in the incorporation of excess drug molecules leads to the breaking down of its micellar structure. Hence, the drug-Gemini mixed system is not capable of producing large aggregates. Although DLS measurements can give a general indication of aggregate size, they are unable to reveal any details about aggregate shape. To better understand the geometry of the drug-CTAB supermicelle aggregate, we performed TEM and AFM investigations.

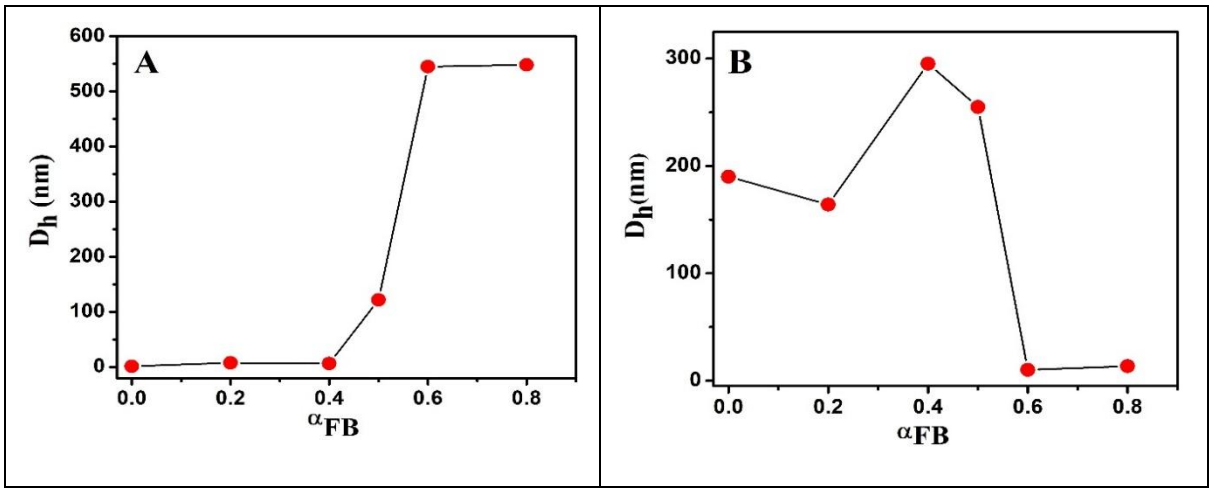

Fig. 2 Changes in hydrodynamic diameter (D_h) of CTAB/FB mixed system (A) and G-16-FB system (B), at different mole fractions of FB at 298.15 K.

We also performed zeta potential (ζ) measurements to comprehend the stability of the colloidal system. The zeta potential represents the difference in potential between the dispersion medium and the stationary layer of solution affixed to the dispersed micellar aggregates. The change in $\zeta\varepsilon\tau\alpha$ potential of the aqueous micellar solution of CTAB and Gemini with the addition of BF drugs is shown in Fig. 3(A-B). For the drug-CTAB mixed system, initially, with the addition of drugs, the slight decrease in zeta potential value clearly indicates the electrostatic interaction of the FB anion with the surface charge of cationic CTA micellar aggregates. But, interestingly, at $\alpha_{drug = 0.4}$, a significant enhancement in the ζ value is observed. This abnormal behaviour can be explained by the fact that the inclusion of Na^+ cation in the Stern layer of the CTAB micelle

effectively enhanced the overall positive charge of the aggregates.[37] Further addition of the FB drugs leads to a decrease in the overall positive charge of the CTAB micelles due to the neutralization of charge density, indicating intercalation of the drug molecules in the micelle. At $\alpha_{drug = 0.6}$, the charge density becomes almost zero (1.02 mV), so here, charge-neutralized larger aggregates are formed. In cationic surfactant systems, aggregates with lower excess charge typically transform into aggregates with less curved morphologies, like vesicles, lamellae, or precipitation.[38] There is a clear link between aggregate size and surface potential: usually, larger aggregates have a smaller surface potential, and vice versa.[39] The higher value of D_h is caused by Na+ ions being highly hydrated due to their tiny size, leading to a stronger negative charge of FB exposure and charge neutralization. So, the ζ value for the drug-CTAB mixed system ($\alpha_{drug = 0.6)}$ clearly indicates the formation of large aggregates with low surface charge, and it fully supports the DLS measurements. Moreover, the positive ζ value at $\alpha_{drug = 0.6}$ indicates the predominance of CTAB monomers in the resultant supermicelle aggregates. Beyond $\alpha_{drug = 0.6}$, anionic-rich aggregates are formed with a negative zeta-potential value. In the case of the drug-Gemini mixed system, initially, with the addition of the FB drug, there was a rapid increase in the ζ value up to $\alpha_{drug = 0.2}$. There are two potential explanations for these abnormalities: (1) The inclusion of Na^+ ions in the stern layer of the Gemini micelle effectively increases the positive charge of the mixed micelle, (2) Due to the effective screening of the electrostatic repulsion between the Gemini head groups by the anionic FB molecules, more Gemini monomers can be linked to the mixed aggregates than to pure Gemini micelles, increasing the overall positive charge. The value gradually decreased after $\alpha_{drug = 0.2}$ with increasing FB concentration, crossing zero potential and eventually reaching the negative potential zone, showing electrostatic interaction between the oppositely charged drug-surfactant mixed systems. The negative zeta potential for $\alpha_{drug = 0.8}$ is lower than that at drug 0.6, indicating that some drug molecules leave the aggregate due to electrostatic repulsion between carboxylate head groups. As a result, the negative value of the zeta potential at $\alpha_{drug = 0.8}$ is slightly less than at $\alpha_{drug = 0.6}$. In conclusion, zeta potential measurements of CTAB, Gemini, and their mixing with FB drugs provide insight into the morphological change of the drug-surfactant aggregates.

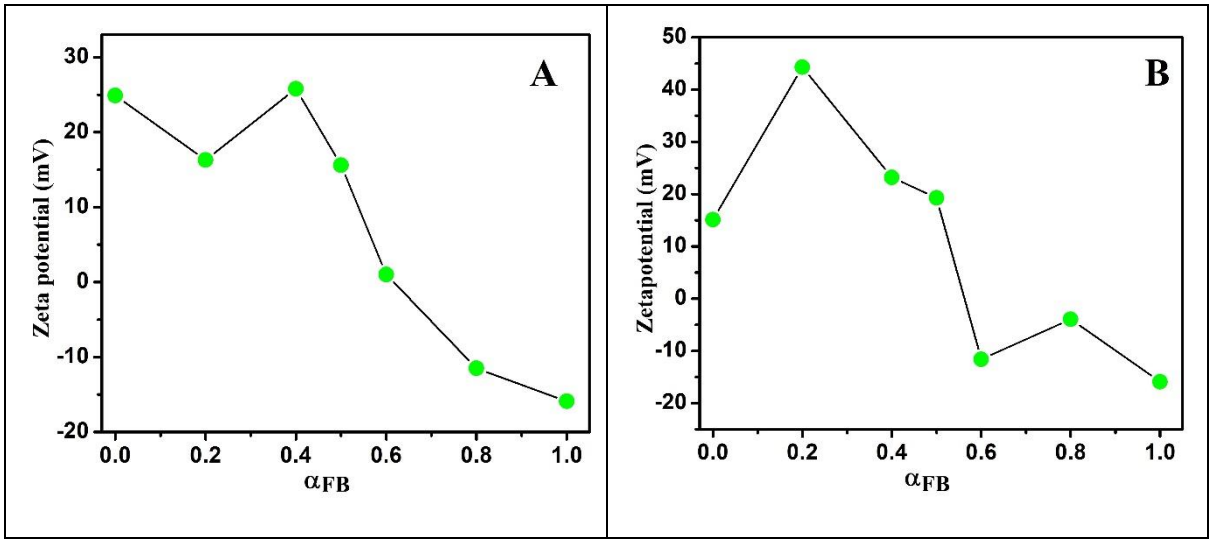

Fig. 3 Zeta potential (ζ) of (A) FB/CTAB and (B) FB/G-16 systems at different mole fractions of FB.

3.3 Structural investigation using Spectroscopic analysis:

Steady-state anisotropy measurement: The steady-state fluorescence anisotropy change can be used to anticipate the morphological change in amphiphile aggregates.[40] As a probe molecule, we employed acridine orange (AO) to assign the kind of aggregates that would form in an aqueous solution of the drug-surfactant mixture. At pH > 10, AO exists as a basic acridine orange (AOB) whose fluorescence behaviour is slightly different from that of AO.[41] Since we utilised a basic pH in our experiment (pH = 12.0), AO is present here as AOB. Although AO is a cationic-charged probe, its basic form (AOB) is non-ionic in nature, allowing it to easily penetrate the charged micelle and provide detailed information about the morphology of aggregates. In comparison to the bulk solution, the rotating motion of the probe molecules is somewhat constrained when they enter a micellar medium. As a result, a high steady-state anisotropy value of the probe molecule is associated with a low degree of rotation of the fluorescence probe in the micellar medium. Therefore, the variation in the microenvironment around the probe is manifested through the change in the anisotropy value (r). The change in the 'r' value for the FB-CTAB and FB-Gemini mixtures at different compositions is shown in Figs. 4A and 4B, respectively. As demonstrated in Fig. 4A, the 'r' value of AOB steadily rises with increases in drug concentration in the FB-CTAB mixed system and reaches a maximum at $\alpha_{drug = 0.6}$ following which the 'r' value slightly declines. These findings imply that the rigidity of the FB-CTAB mixed micellar system increased with increasing drug concentration and

reached its maximum at $\alpha_{drug = 0.6\text{-}0.8}$, following which rigidity slightly decreased. As a result, the probe molecule (AOB) encounters a more rigid environment in the FB-CTAB mixed system as the drug concentration rises, which increases the 'r' value. So, anisotropy measurements clearly indicate that in the presence of the drug FB, the flexible CTAB micelle transformed into more rigid and larger mixed micellar aggregates. Contrarily, we see a completely different trend in the anisotropy (r) value for the FB-Gemini mixed system. The 'r' value, in this case, increased marginally with increasing drug concentration up to $\alpha_{drug = 0.4}$, but then gradually decreased after that. With increasing rigidity of the micelle, fewer water molecules can penetrate the micelle, resulting in less confinement of the probe molecules and an increase in the 'r' value. The repulsion between the same charged head groups of the surfactant is reduced in the presence of negatively charged drug molecules, increasing the micelle's compactness. As a result, drug molecules make micelles more compact, which reduces water molecule penetration and restricts probe confinement, raising the anisotropy value. Because of this, the CTAB micelle's anisotropy value increases with increasing drug concentration and reaches its maximum at $\alpha_{drug = 0.6\text{-}0.8}$. Thereafter, a slight decrease in the anisotropy value caused by repulsion between drugs with the same charged carboxyl group minimized the micelle's compactness in the drug-rich region. On the other hand, the Gemini micelle initially becomes slightly more compact when drug molecules are present, but due to its huge size, its micelle structure weakens as drug concentration rises, causing a drop in the anisotropy value.

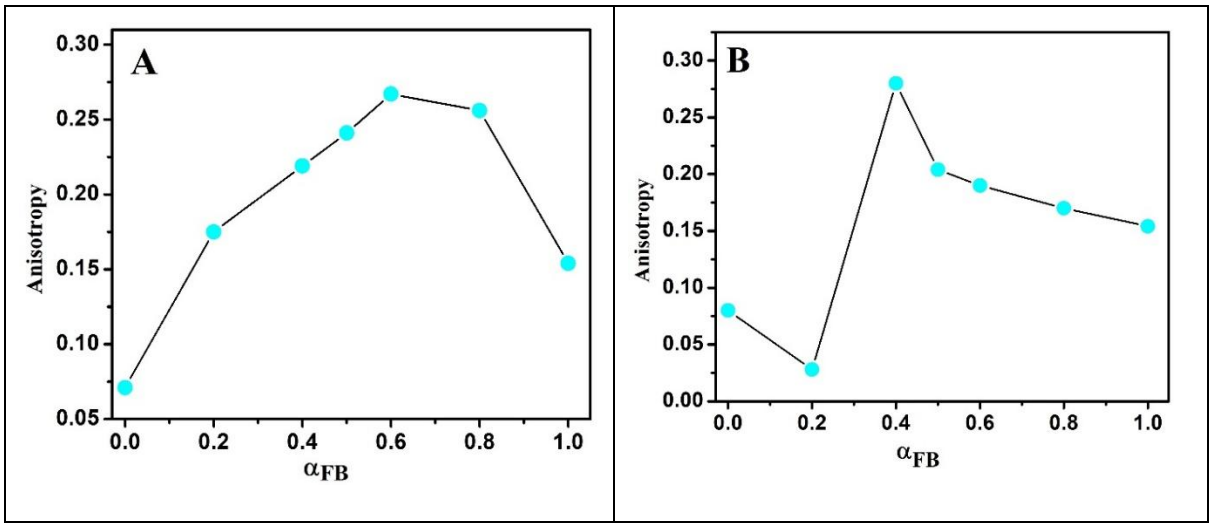

Fig.4 Variation of the steady-state anisotropy value of (A) FB/CTAB and (B) FB/G-16 systems at different mole fractions of FB.

Time-resolved fluorescence study: Time-dependent fluorescence measurements are a valuable tool for understanding the nature of the complex formed between the drugs and surfactant at various drug doses. In this instance, we examined the decay profile of AOB in the absence and presence of the drug-surfactant mixed system. Here, AOB exhibits a mono-exponential decay curve with a lifetime of 5.8 ns, which is consistent with the literature in the absence of any micellar systems.[42] One type of emitting species may exist in the medium, according to the mono-exponential decay curve. AOB only exists in monomeric form in aqueous media with a pH of 12.0.[41] The decay profile (Figs. 5A and 5B) shows that a bi-exponential decay curve was obtained in the presence of pure surfactants or their combined system with drugs, which may indicate the presence of two distinct emitting species. Two emitting species of AOB, monomeric and aggregated, are found in the micellar medium. According to Table S2, the contribution of the monomeric form to the drug-CTAB mixed system decreases as drug concentration increases, while the contribution of the aggregated form increases, reaching its maximum at $\alpha_{drug = 0.6}$. In the bi-exponential decay profile, the faster decay component is for the aggregated form of AOB, and the slower one is for the monomeric form. The aggregated form is weakly fluorescent, and its lifetime is very short.[43] Therefore, as drug concentration rises, the aggregated form's contribution also rises, reducing the lifetime of the fluorophores. The AOB dye interacts with the drug-CTAB mixed micelle to its greatest extent at $\alpha_{drug = 0.6\text{-}0.8}$, according to lifetime measurements, which are in perfect agreement with the anisotropy data. Lifetime data give inferential evidence of substantial aggregation development in the drug-CTAB mixture. The reported lifetime for aggregated AOB is ~ 1.67 ns.[42] The lifetime of AOB in the drug-CTAB mixed system at $\alpha_{drug = 0.6\text{-}0.8}$ is 1.80 ns, showing that the majority of the dye molecules are in the mixed micelle and undergoing dimerization. In contrast, for the Gemini micelle, the contribution of the dimeric form rises in the presence of the FB drug and reaches its maximum at $\alpha_{drug = 0.4\text{-}0.5}$, but this increase is very slight. As drug concentration further increases after $\alpha_{drug = 0.4\text{-}0.5}$, the dimeric form of AOB dye decreases gradually, indicating micelle breakdown into a smaller one. In the drug-CTAB mixed system, the maximal aggregated form of AOB is approximately 95% (at $\alpha_{drug = 0.6}$), whereas in the drug-Gemini mixed system, it is only 52% (at $\alpha_{drug = 0.4}$). So, according to this finding, large aggregates are generated in the drug-CTAB mixed system, however, this was not the case in the drug-Gemini mixed system.

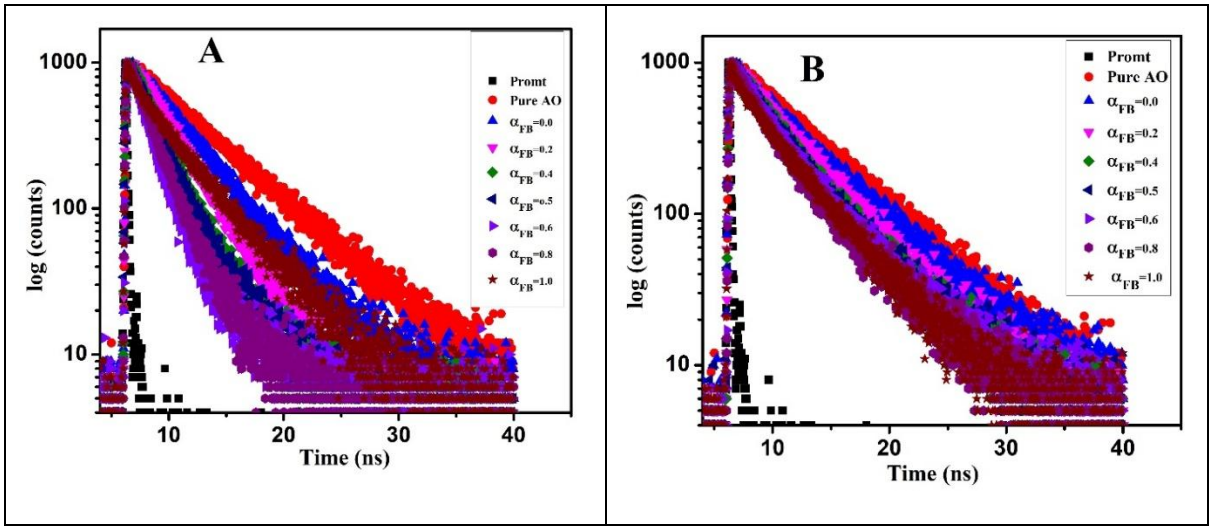

Fig. 5 Time-resolved fluorescence decay profile of the probe acridine orange in aqueous buffer (pH=12.0) of (A) FB/CTAB and (B) FB/G-16 systems at varied mole fraction of FB.

3.4 Aggregate characterization by TEM and AFM: TEM measurements were carried out to provide direct evidence of supermicelle formation and to better understand the microstructure of the drug-surfactant aggregates. The micrographs of FB-CTAB aqueous mixture at $\alpha_{drug = 0.6}$ and $\alpha_{drug = 0.8}$ have been presented in Figure 6 (A-G, H-I). At $\alpha_{drug = 0.6}$, different kinds of supermicelles with sizes between 200 and 500 nm were found. These sorts of aggregate size distributions, which have aggregates with diameters of about 200 nm and over 500 nm, are supported by DLS data. Here, a linear supermicelle with a size of around 200 nm and a spherical supermicelle with tentacle-like arms of approximately 500 nm is obtained. This kind of supermiceller structure created by the hierarchical self-assembly of block copolymers was also reported by E.C. Gould et al.[44] In addition, we have found various other sorts of supermicelle structures, including those that are cross-linked, comet-like, and ribbon-shaped. A similar type of report was made by Xiaoyu Li et al. regarding the formation of cross-linked supermicelles by P-H-P triblock co-micelles.[45] Huibin Qui et al. reported cross-linked supermicelle formation from the hierarchical self-assembly of amphiphilic cylindrical B-A-B triblock co-micelles.[17] At higher drug concentrations ($\alpha_{drug = 0.8}$), nanoflowers and petal-like micrographs were observed by TEM measurements.

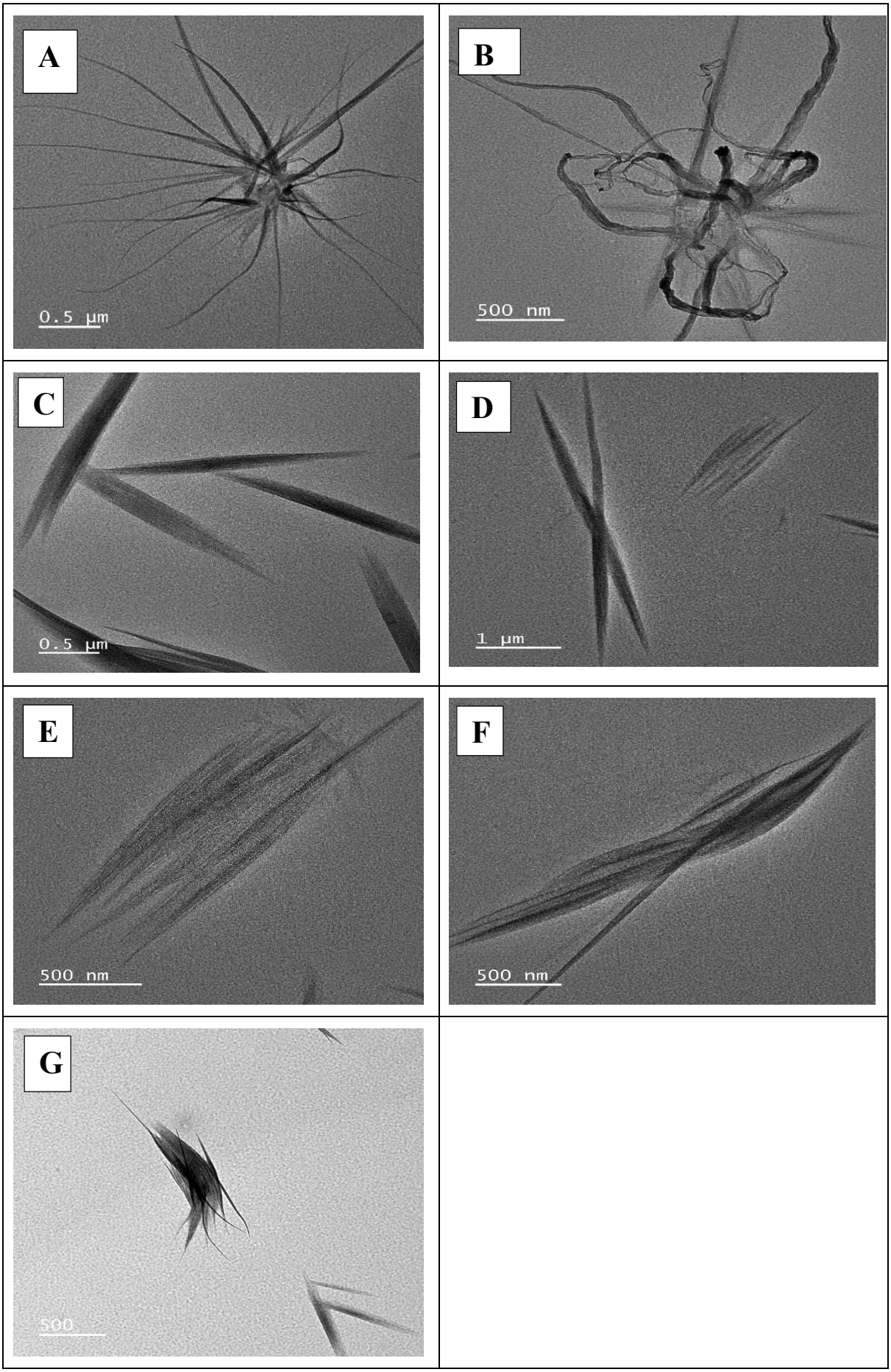
A
0.5 µm
B
500 nm
C
0.5 µm
D
1 µm
E
500 nm
F
500 nm
G
500

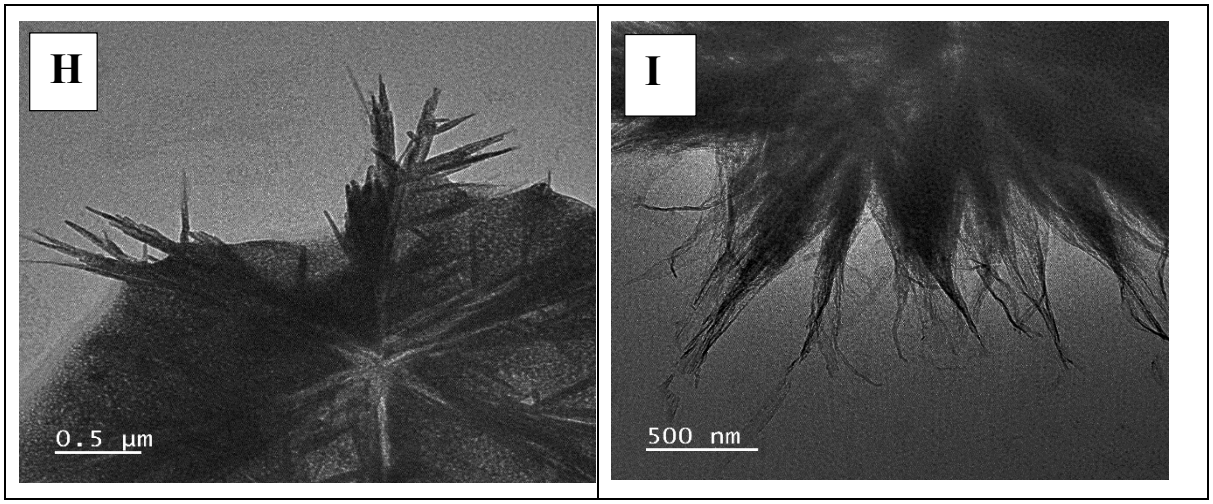

Fig. 6 TEM micrographs of the FB/CTAB system at (A)-(G) α_{FB} =0.6 and (H)-(I) α_{FB} = 0.8.

To validate the supermicelle formation and also to visualise their shape, AFM measurements were performed as well. Regarding the height, diameter, and surface roughness of micellar aggregates, AFM offers crucial information. Here, different types of supermicelle aggregates with a diameter of roughly 400–500 nm were observed by AFM measurements (Figs 7 (A-C)), and these aggregates agree well with the TEM micrographs. AFM measurements revealed a spherical supermicelle with tentacle-like arms that was 70 nm in height; these types of supermicelles are quite obvious in TEM images. AFM measurements confirm the emergence of several non-spherical superstructures depicted in TEM micrographs. Here, we observed a ribbon-shaped supermicelle with a height of roughly 130 nm and a supermicelle that resembled a comet with cylinder micelle-like arms that are 120 nm in height. As a result, the shape and development of supermicelle aggregates in the drug-CTAB mixture are clearly shown by TEM and AFM studies.

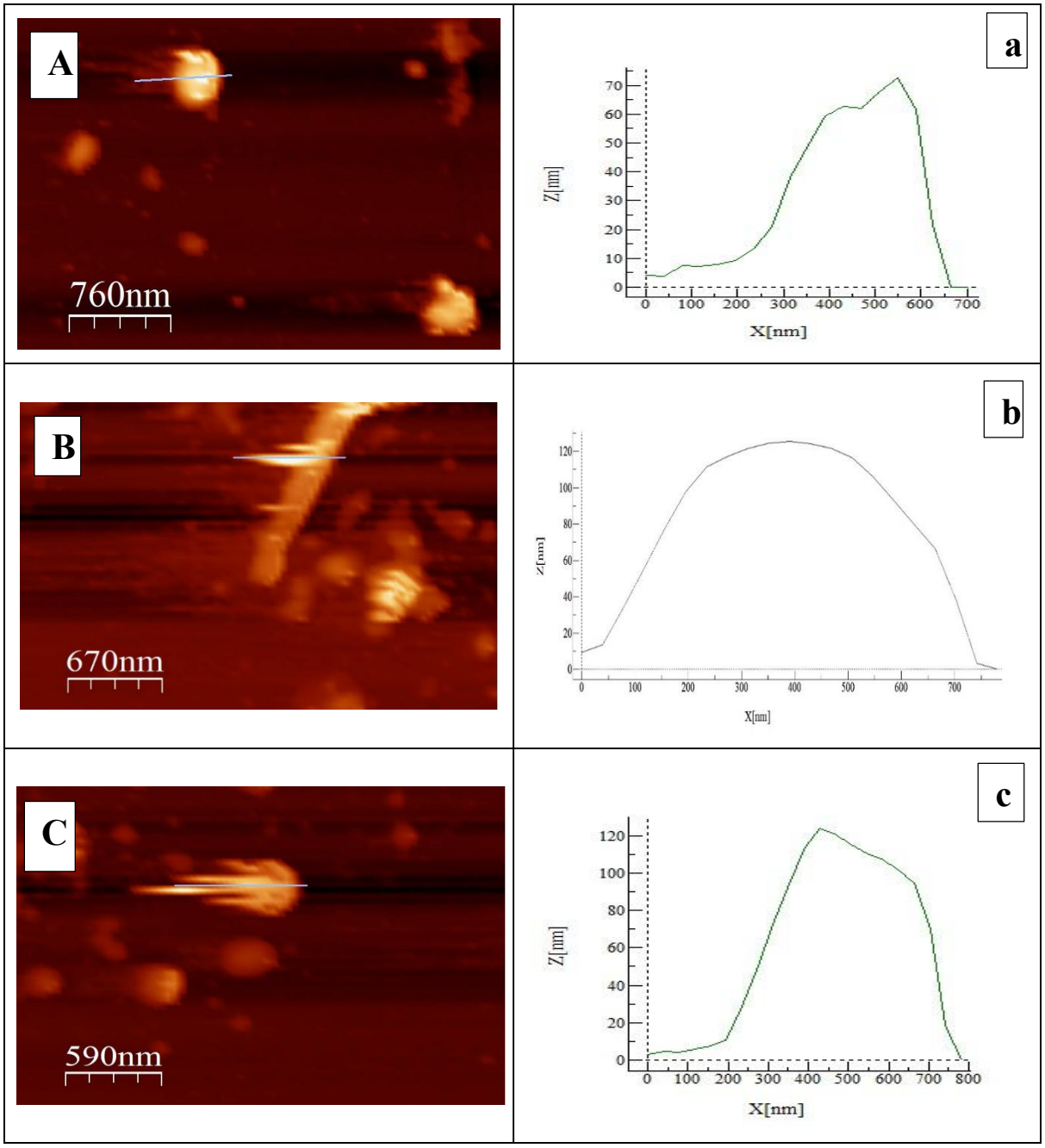

Fig. 7 (A)-(C) 2-Dimensional AFM topographic images of FB/CTAB system and (a)-(c) corresponding size distribution plots.

3.5 Computational Study:

A qualitative study of three-body interaction energies is done for the chemical species considered here, i.e., the surfactant, the drug, and the water molecule. Before moving into electronic energy calculations, we did a conformational sampling for the surfactants to select

the most probable conformer in an aqueous solution to mimic the environment of the experimental studies. The conformational sampling is done by the CREST[46] program. Both Gemini and CTAB resulted in a linear conformation. We did the electronic structure calculations in ORCA 5.0[(47)] with the linear candidates of the surfactants. Geometry optimization and frequency calculation are done on all the molecules to ensure complete optimization. All the frequencies from the frequency analysis of all the moieties came out positive, ensuring minima. With the help of the electronic energies, the interaction energies for the trimer are computed using a many-body expansion formula, which is defined for our case as follows:

$$\boldsymbol{E_{sdw}^{int} = E_{sdw}^{el} - E_{s}^{el} - E_{d}^{el} - E_{w}^{el}} \quad \textbf{(13)}$$

Here, E^{int} and E^{el} refer to the many-body interaction energy and the electronic energies, respectively. The keys *s*, *d,* and *w* refer to the surfactant candidate, drug, and water, respectively. The electronic energy calculations are performed with Density Functional Theory (DFT). The chosen exchange-correlation functional is B3LYP[48-51], and the basis set is def2-TZVP[52,53]. To take the non-covalent or secondary interactions of the moieties into account, we added Stefan Grimme's Dispersion (D3)[54,55] correction term to all the calculations. The electronic energies are tabulated in the supplementary information.

Using the defined formula from equation 12, we computed the interaction energy of the trimers, Gemini-Fenbufen-Water and CTAB-Fenbufen-Water, which is shown in Table 1:

The numbers clearly indicate that the Gemini-trimer interacts more strongly than the CTAB-trimer.

The optimized structures for the molecules and moieties are presented in the following Figure 8:

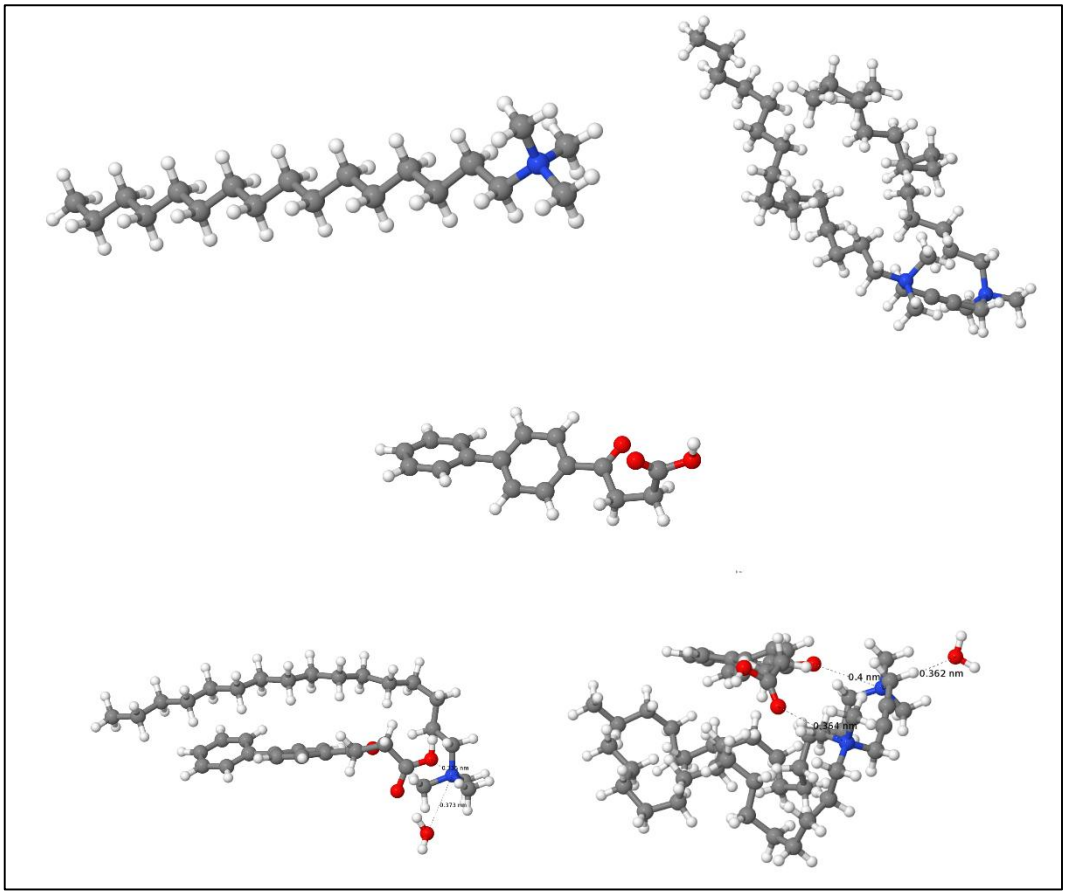

Figure 8: All the geometry-optimized structures of the molecules and moieties are given here; CTAB (top-left), Gemini(top-right), Fenbufen drug(centre), CTAB-Fenbufen-Water(bottom-left), and Gemini-Fenbufen-Water(bottom-right)

4. Concluding Remarks: In summary, we have demonstrated the drug-induced supermicelle formation of a cationic surfactant, CTAB, when the drug is added at a slightly larger than equimolecular concentration. The formation of a large aggregate in the drug-CTAB mixture is suggested by DLS, anisotropy, and lifetime studies, and supermicelle structure was confirmed by TEM and AFM measurements. To investigate the drug's mixed micellar behaviours in the presence of two different surfactants (CTAB and acetylenic Gemini), we also used tensiometry measurements in this case. The experimental results suggest that the interaction of FB drugs with surfactants is highly synergistic in nature. The DFT study confirmed that FB interacts more strongly with Gemini than CTAB due to the higher hydrophobicity and electronic charge of Gemini surfactant. However, the CTAB micelle's small size can build a sizable supermicelle aggregate with FB, whereas the Gemini micelle's huge size prevents it from doing so. In the

biomedical industry, drug delivery, nanotechnology, and other critical disciplines, these supermicelle aggregates have a wide range of applications.

References:

1. Tadros, T. F. *Self-organized surfactant structures*. (John Wiley & Sons, 2011).
2. Alexandridis, P. & Lindman, B. *Amphiphilic block copolymers: self-assembly and applications*. (Elsevier, 2000).
3. Myers, D. *Surfactant science and technology*. (John Wiley & Sons, 2020).
4. Israelachvili, J. N., Mitchell, D. J. & Ninham, B. W. Theory of self-assembly of hydrocarbon amphiphiles into micelles and bilayers. *J. Chem. Soc. Faraday Trans. 2 Mol. Chem. Phys.* **72**, 1525–1568 (1976).
5. Zhang, X. & Wang, C. Supramolecular amphiphiles. *Chem. Soc. Rev.* **40**, 94–101 (2011).
6. Wang, C., Wang, Z. & Zhang, X. Amphiphilic building blocks for self-assembly: from amphiphiles to supra-amphiphiles. *Acc. Chem. Res.* **45**, 608–618 (2012).
7. Lattuada, M. & Hatton, T. A. Synthesis, properties and applications of Janus nanoparticles. *Nano Today* **6**, 286–308 (2011).
8. Gröschel, A. H. & Müller, A. H. E. Self-assembly concepts for multicompartment nanostructures. *Nanoscale* **7**, 11841–11876 (2015).
9. Walther, A. & Müller, A. H. E. Janus particles: Synthesis, self-assembly, physical properties, and applications. *Chem. Rev.* **113**, 5194–5261 (2013).
10. Erhardt, R., Zhang, M., Boker, A., Zettl, H., Fredrik, P., Krausch, G., Abetz, V., & Muller, Axel.H.E. Amphiphilic Janus micelles with polystyrene and poly(methacrylic acid) hemispheres. *J. Am. Chem. Soc.* **125**, 3260–3267 (2003).
11. Voets, I. K., Fokkink, R., Hellweg, T., King, S.M., Waard, p.d., Keizer, A.D., & Stuart, M.A.C. Spontaneous symmetry breaking: Formation of Janus micelles. *Soft Matter* **5**, 999–1005 (2009).
12. Qiu, H., Hudson, Z. M., Winnik, M. A. & Manners, I. Multidimensional hierarchical self-assembly of amphiphilic cylindrical block comicelles. *Science (80-.).* **347**, 1329–1332 (2015).

13. Gröschel, A. H., Schacher, F.H., Schmalz, H., Borisov, O.V., Zhulina, E.B., Walther, A., & Muller, A.H.E. Precise hierarchical self-assembly of multicompartment micelles. *Nat. Commun.* **3**, 710 (2012).

14. Shrestha, R., Elsabahy, M., Luehmann, H., Samarajeewa, S., Florez-Malaver, S., Lee, N.S., Welch, M.J., Liu, Y., & Wooley, K.L. Hierarchically assembled theranostic nanostructures for siRNA delivery and imaging applications. *J. Am. Chem. Soc.* **134**, 17362–17365 (2012).

15. Schacher, F. H., Rupar, P. A. & Manners, I. Functional block copolymers: nanostructured materials with emerging applications. *Angew. Chemie Int. Ed.* **51**, 7898–7921 (2012).

16. Li, X., Gao, Y., Harniman, R., Winnik, M. & Manners, I. Hierarchical Assembly of Cylindrical Block Comicelles Mediated by Spatially Confined Hydrogen-Bonding Interactions. *J. Am. Chem. Soc.* **138**, 12902–12912 (2016).

17. Qiu, H., Russo, Glu., Rupar, P.A., Chabanne, Lau., Winnik, M.A., Manners Ian. Tunable supermicelle architectures from the hierarchical self-assembly of amphiphilic cylindrical B-A-B triblock Co-micelles. *Angew. Chemie - Int. Ed.* **51**, 11882–11885 (2012).

18. Lian, T. & Ho, R. J. Y. Trends and developments in liposome drug delivery systems. *J. Pharm. Sci.* **90**, 667–680 (2001).

19. Holland, P. M. & Rubingh, D. N. Mixed surfactant systems: an overview. (1992).

20. Ghosh, S. & Moulik, S. P. Interfacial and micellization behaviors of binary and ternary mixtures of amphiphiles (Tween-20, Brij-35, and sodium dodecyl sulfate) in aqueous medium. *J. Colloid Interface Sci.* **208**, 357–366 (1998).

21. Kurkov, S. V & Perlovich, G. L. Thermodynamic studies of fenbufen, diflunisal, and flurbiprofen: Sublimation, solution and solvation of biphenyl substituted drugs. *Int. J. Pharm.* **357**, 100–107 (2008).

22. Vane, J. R. Inhibition of prostaglandin biosynthesis as the mechanism of action of aspirin-like drugs. *Adv Biosci* **9**, 395–411 (2014).

23. Brtogden, R. N., Heel, R. C., Speight, T. M. & Avery, G. S. Fenbufen: A Review of its Pharmalogical Properties and Therapeutic Use in Rheumatic Dieases and Acute Pain. *Drugs* **21**, 1–22 (1981).

24. Sardar, R., Das, S., Banik, R., Bhunia, S. & Ghosh, S. Exploration of the impact of graphene oxide, acetylenic gemini, and CTAT on the photophysical and aggregation properties of dipolar coumarin 153. *Phys. Chem. Chem. Phys.* **26**, 8900–8918 (2024).

25. Chakraborty, T., Ghosh, S. & Moulik, S. P. Micellization and related behavior of binary and ternary surfactant mixtures in aqueous medium: Cetyl pyridinium chloride (CPC), Cetyl trimethyl ammonium bromide (CTAB), and polyoxyethylene (10) cetyl ether (Brij-56) derived system. *J. Phys. Chem. B* **109**, 14813–14823 (2005).

26. Menger, F. M., Keiper, J. S. & Azov, V. Gemini surfactants with acetylenic spacers. *Langmuir* **16**, 2062–2067 (2000).

27. Clint, J. H. J. Chem. Soc., Faraday Trans. (1975).

28. Rosen, M. J. & Dahanayake, M. Solution. **25**, 541–545 (1982).

29. Zhao, M. & Zheng, L. Micelle formation by N-alkyl-N-methylpyrrolidinium bromide in aqueous solution. *Phys. Chem. Chem. Phys.* **13**, 1332–1337 (2011).

30. Israelachvili, J. N. *Intermolecular and surface forces*. (Academic press, 2011).

31. Tanford, C. *The hydrophobic effect: formation of micelles and biological membranes 2d ed*. (J. Wiley., 1980).

32. Ghosh, S. & Chakraborty, T. Mixed micelle formation among anionic gemini surfactant (212) and its monomer (SDMA) with conventional surfactants (C12E5 and C12E8) in brine solution at pH 11. *J. Phys. Chem. B* **111**, 8080–8088 (2007).

33. Mahajan, R. K., Mahajan, S., Bhadani, A. & Singh, S. Physicochemical studies of pyridinium gemini surfactants with promethazine hydrochloride in aqueous solution. *Phys. Chem. Chem. Phys.* **14**, 887–898 (2012).

34. Oida, T., Nakashima, N., Nagadome. *S., Ko, J., OH, Se-Wo, Sugihara, G.,* Adsorption and Micelle Formation of Mixed Surfactant Systems in Water. III. A Comparison between Cationic Gemini/Cationic and Cationic Gemini/Nonionic Combinations. *J. Oleo Sci.* **52**, 509–522 (2003).

35. Hassan, P. A., Rana, S. & Verma, G. Making sense of Brownian motion: Colloid characterization by dynamic light scattering. *Langmuir* **31**, 3–12 (2015).

36. Ghosh, S., Ghatak, C., Banerjee, C., Mandal, S., Kuchlyan, J., & Sarkar, N.,. Spontaneous transition of micelle-vesicle-micelle in a mixture of cationic surfactant and anionic surfactant-like ionic liquid: A pure nonlipid small unilamellar vesicular template used for solvent and rotational relaxation study. *Langmuir* **29**, 10066–10076 (2013).

37. Gehlot, P. S., *Rao, K.S., Bharmoria, P., Damarla, K., Gupta, H., Drechsler, M., & Kumar, A.,*. Spontaneous Formation of Multiarchitecture Vesicles of [C8mim]Br + [Na]DBS in Aqueous Medium: Synergic Interplay of Electrostatic, Hydrophobic, and π-π Stacking Interactions. *J. Phys. Chem. B* **119**, 15300–15309 (2015).

38. Jiang, L., Wang, K., Deng, M., Wang, Y. & Huang, J. Bile salt-induced vesicle-to-micelle transition in catanionic surfactant systems: steric and electrostatic interactions. *Langmuir* **24**, 4600–4606 (2008).

39. Egelhaaf, S. U. & Schurtenberger, P. Micelle-to-vesicle transition: a time-resolved structural study. *Phys. Rev. Lett.* **82**, 2804 (1999).

40. Coutinho, P. J. G., Castanheira, E. M. S., Céu Rei, M. & Real Oliveira, M. E. C. D. Nile Red and DCM fluorescence anisotropy studies in C12E7/DPPC mixed systems. *J. Phys. Chem. B* **106**, 12841–12846 (2002).

41. Falcone, R. D., Correa, N. M., Biasutti, M. A. & Silber, J. J. Acid-base and aggregation processes of acridine orange base in n-heptane/AOT/water reverse micelles. *Langmuir* **18**, 2039–2047 (2002).

42. Sayed, M., Gubbala, G. K. & Pal, H. Contrasting interactions of DNA-intercalating dye acridine orange with hydroxypropyl derivatives of β-cyclodextrin and γ-cyclodextrin hosts. *New J. Chem.* **43**, 724–736 (2019).

43. Sayed, M., Jha, S. & Pal, H. Complexation induced aggregation and deaggregation of acridine orange with sulfobutylether-β-cyclodextrin. *Phys. Chem. Chem. Phys.* **19**, 24166–24178 (2017).

44. Gould, O. E. C. *, Lunn,D., Rowden,J., Harniman, R.L., Hudson, Z.M., Winnik, M.A., Miles, M.J, & Manners, Ian.* Transformation and patterning of supermicelles using dynamic holographic assembly. *Nat. Commun.* **6**, 1–7 (2015).

45. Li, X., *Gao, Y., Boott, C.E., Hayward, D.W., Harniman, R., Whittell, G.R., Richardson, R.M., Winnik, M.A., & Manners, Ian.* 'Cross' Supermicelles via the Hierarchical Assembly of Amphiphilic Cylindrical Triblock Comicelles. *J. Am. Chem. Soc.* **138**, 4087–4095 (2016).

46. Pracht, P., Bohle, F. & Grimme, S. Automated exploration of the low-energy chemical space with fast quantum chemical methods. *Phys. Chem. Chem. Phys.* **22**, 7169–7192 (2020).

47. Neese, F. Software update: The ORCA program system—Version 5.0. *Wiley Interdiscip. Rev. Comput. Mol. Sci.* **12**, e1606 (2022).

48. Becke, A. D. Density-functional thermochemistry. I. The effect of the exchange-only gradient correction. *J. Chem. Phys.* **96**, 2155–2160 (1992).

49. Lee, C., Yang, W. & Parr, R. G. Development of the Colle-Salvetti correlation-energy formula into a functional of the electron density. *Phys. Rev. B* **37**, 785 (1988).

50. Vosko, S. H., Wilk, L. & Nusair, M. Accurate spin-dependent electron liquid correlation energies for local spin density calculations: a critical analysis. *Can. J. Phys.* **58**, 1200–1211 (1980).

51. Stephens, P. J., Devlin, F. J., Chabalowski, C. F. & Frisch, M. J. Ab initio calculation of vibrational absorption and circular dichroism spectra using density functional force fields. *J. Phys. Chem.* **98**, 11623–11627 (1994).

52. Weigend, F. & Ahlrichs, R. Balanced basis sets of split valence, triple zeta valence and quadruple zeta valence quality for H to Rn: Design and assessment of accuracy. *Phys. Chem. Chem. Phys.* **7**, 3297–3305 (2005).

53. Weigend, F. Accurate Coulomb-fitting basis sets for H to Rn. *Phys. Chem. Chem. Phys.* **8**, 1057–1065 (2006).

54. Grimme, S., Antony, J., Ehrlich, S. & Krieg, H. A consistent and accurate ab initio parametrization of density functional dispersion correction (DFT-D) for the 94 elements H-Pu. *J. Chem. Phys.* **132**, (2010).

55. Grimme, S., Ehrlich, S. & Goerigk, L. Effect of the damping function in dispersion corrected density functional theory. *J. Comput. Chem.* **32**, 1456–1465 (2011).

Table 1: Interaction energies calculated using equation 1 are given here

Trimer	Interaction Energies (kJ/mol)
Gemini-Fenbufen-Water	-230
CTAB-Fenbufen-Water	-150

Supplementary Section

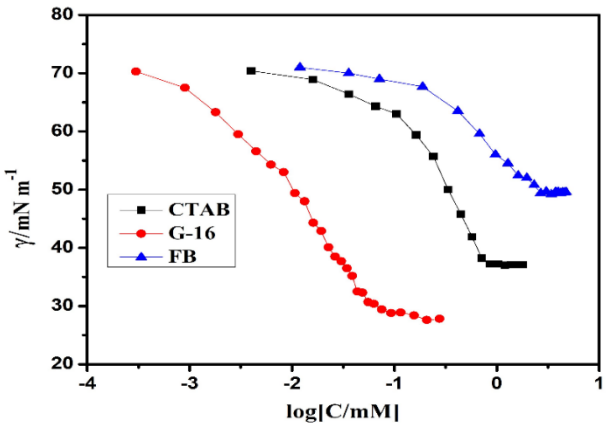

Fig.S1 Variation of surface tension (γ) vs. log [pure components/mM] in aqueous medium (pH= 12.0) at 298.15 K.

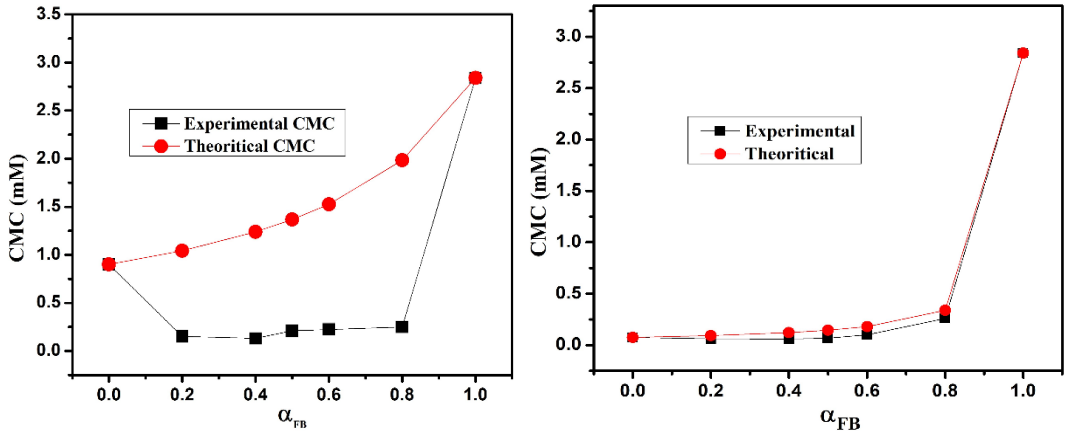

Fig. S2 Comparison of the experimentally obtained CMC value with the theoretically calculated value (using client equation) vs. various mole fraction of the drug; (A) FB-CTAB mixed system and (B) FB-G-16 system respectively.

Table S1. Various physicochemical, surface and thermodynamic parameters, obtained from tensiometric diagram of FB/CTAB and FB/G-16 mixed systems, respectively.

α_{FB}	CMC (mM) (ideal)	CMC (mM) (exp.)	$10^6\Gamma_{max}$ ($mol.m^{-2}$)	A_{min} ($nm^2 molecule^{-1}$)	π_{CMC} ($mN.m^{-1}$)	γ_{CMC} ($mN.m^{-1}$)	pC_{20}	G^S_{min} ($kJ.mol^{-1}$)	$-\Delta G^0_m$ ($kJ.mol^{-1}$)	$-\Delta G^0_{ad}$ ($kJ.mol^{-1}$)	p
FB/CTAB											
0		0.9	3.13	0.530	34.6	37.2	0.50	11.87	24.67	35.72	0.38
0.2	1.04	0.15	3.15	0.527	40.1	29.6	1.54	9.39	29.61	42.34	0.39
0.4	1.23	0.14	3.17	0.523	41.0	28.5	1.57	8.97	29.37	42.30	0.40
0.5	1.36	0.21	3.84	0.432	41.6	30.0	1.27	7.80	28.15	38.98	0.48
0.6	1.52	0.22	2.81	0.590	42.1	28.9	1.36	10.26	27.99	42.97	0.35
0.8	1.98	0.25	2.26	0.734	41.7	28.0	1.49	12.37	27.58	46.03	0.28
1.0		2.84	1.82	0.912	23.1	49.4		27.13	21.86	34.55	0.23
FB/G-16											
0		0.075	1.76	0.94	42.1	28.8	2.0	16.30	30.71	54.61	0.22
0.2	0.093	0.061	2.11	0.78	42.6	28.2	2.05	14.01	31.31	51.49	0.26
0.4	0.122	0.060	2.27	0.73	42.1	28.9	2.03	12.72	30.95	49.49	0.28
0.5	0.146	0.068	2.99	0.55	42.2	29.7	1.84	10.02	29.82	43.93	0.38
0.6	0.180	0.10	2.40	0.69	42.9	28.0	1.93	11.65	29.43	47.30	0.30
0.8	0.339	0.260	3.05	0.54	43.3	27.4	1.35	8.97	27.69	41.88	0.38
1.0		2.84	1.82	0.912	23.1	49.4		27.13	21.86	34.55	0.23

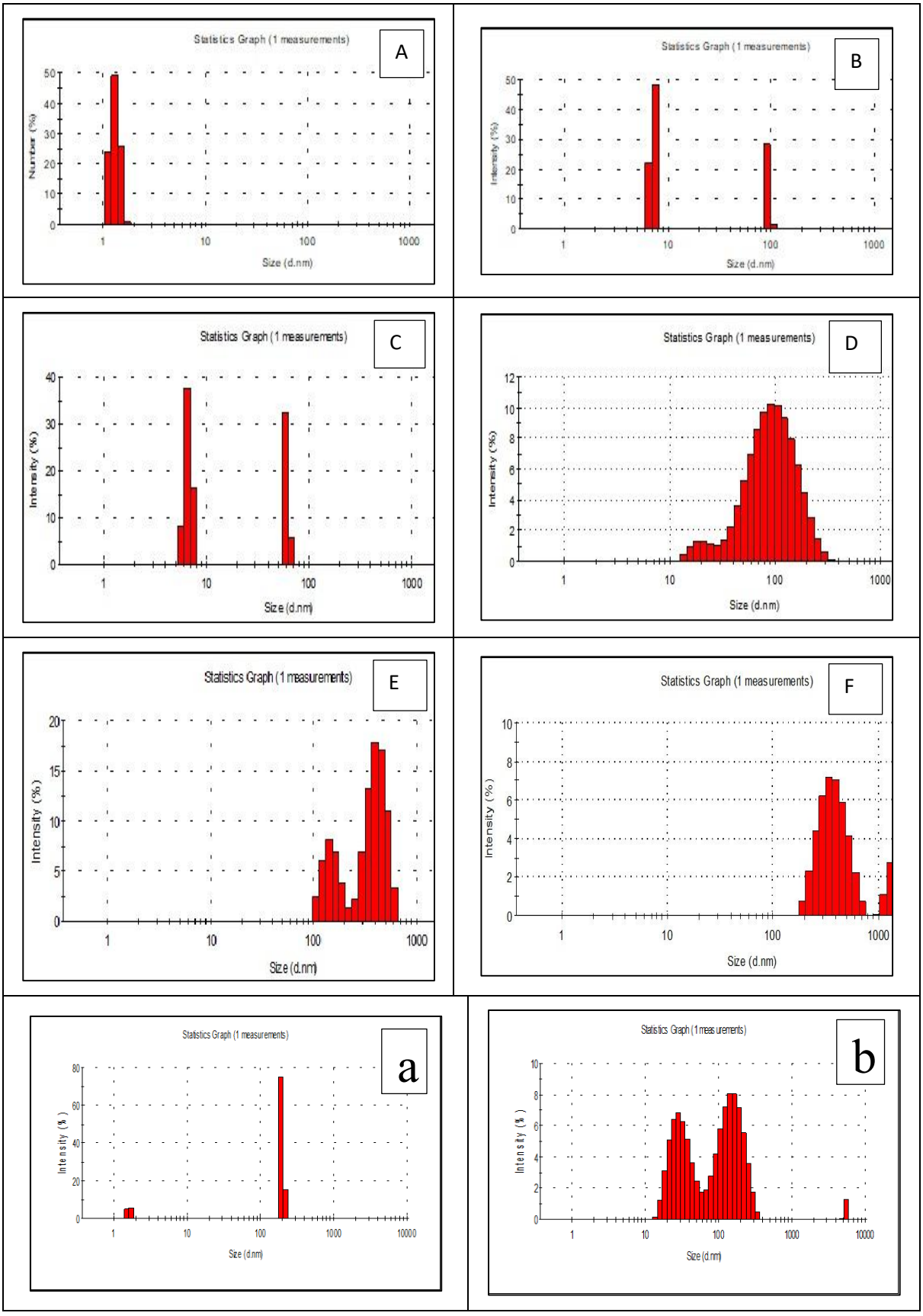
Statistics Graph (1 measurements)
A
Number (%)
Size (d.nm)
Statistics Graph (1 measurements)
B
Intensity (%)
Size (d.nm)
Statistics Graph (1 measurements)
C
Intensity (%)
Size (d.nm)
Statistics Graph (1 measurements)
D
Intensity (%)
Size (d.nm)
Statistics Graph (1 measurements)
E
Intensity (%)
Size (d.nm)
Statistics Graph (1 measurements)
F
Intensity (%)
Size (d.nm)
Statistics Graph (1 measurements)
a
Intensity (%)
Size (d.nm)
Statistics Graph (1 measurements)
b
Intensity (%)
Size (d.nm)

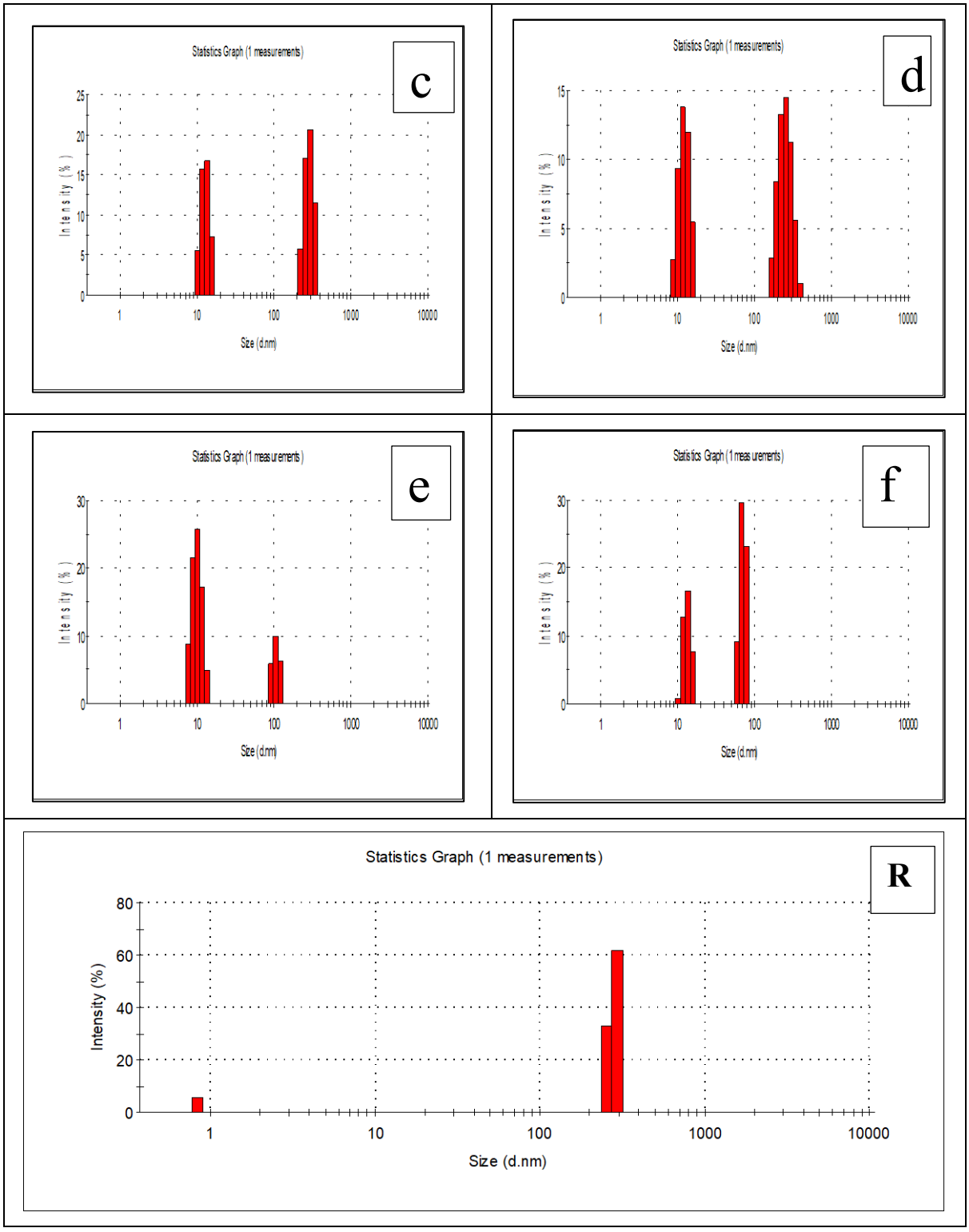

Fig. S3 Size distribution plot of the pure and mixed drug/surfactant system; (A) Pure CTAB, (B) 0.2, (C) 0.4, (D) 0.5, (E) 0.6, and (F) 0.8 FB/CTAB; (a) Pure G-16, (b) 0.2, (c) 0.4, (d) 0.5, (e) 0.6, (f) 0.8 FB/G-16 and (R) Pure FB drug.

Table S2. Time-dependent fluorescence decay profile of acridine orange (AO) in FB/CTAB and FB/G-16 mixed micelles system, respectively.

α_{FB}	τ_1 (ns)	A_1	τ_2 (ns)	A_2	τ_{avg} (ns)	χ^2
FB/CTAB						
0	**0.77**	**0.16**	**4.13**	**0.84**	**3.61**	**0.99**
0.2	**0.57**	**0.13**	**3.11**	**0.87**	**2.78**	**1.11**
0.4	**0.34**	**0.09**	**2.38**	**0.91**	**2.20**	**1.12**
0.5	**1.97**	**0.83**	**4.16**	**0.12**	**2.13**	**1.12**
0.6	**1.43**	**0.95**	**5.37**	**0.05**	**1.62**	**1.19**
0.8	**1.65**	**0.86**	**3.21**	**0.14**	**1.87**	**1.05**
1.0	**0.45**	**0.4**	**4.20**	**0.6**	**2.71**	**1.22**
FB/G-16						
0	**1.37**	**0.14**	**5.54**	**0.86**	**4.96**	**1.07**
0.2	**2.56**	**0.21**	**4.83**	**0.79**	**4.35**	**1.18**
0.4	**3.0**	**0.69**	**6.08**	**0.21**	**3.94**	**1.09**
0.5	**2.55**	**0.61**	**5.56**	**0.39**	**3.73**	**1.04**
0.6	**2.27**	**0.56**	**5.32**	**0.44**	**3.59**	**0.97**
0.8	**2.17**	**0.70**	**5.85**	**0.30**	**3.25**	**1.07**

Table S3: Electronic energies with D3 and dispersion correction energies(individually) obtained from DFT-D3 with B3LYP functional and def2-TZVP basis sets and values are given here

Moieties	Electronic Energy + D3 (hartree)	Dispersion Correction [D3](hartree)
Gemini	**-1682.1907**	**-0.2499**
CTAB	**-803.6754**	**-0.0960**
Water	**-76.4266**	**-0.0006**
Fenbufen	**-843.7387**	**-0.0691**
Gemini-Fenbufen-Water	**-2602.4434**	**-0.3640**
CTAB-Fenbufen-Water	**-1723.8977**	**-0.2056**

Chapter-V

Deciphering the role of concentration and reduction of graphene oxide towards its interaction and protein corona (PC) formation with Bromelain proteins: A spectroscopic and biophysical approach

Deciphering the role of concentration and reduction of graphene oxide towards its interaction and protein corona (PC) formation with Bromelain proteins: A spectroscopic and biophysical approach

Abstract:

Graphene oxide (GO) and its reduced form (RGO) are a novel class of applied materials that have recently gained global attention in various fields, particularly biomedicine, due to their excellent properties. To apply this nanomaterial in biomedical fields, a thorough understanding of its interaction with biomacromolecules is essential. Keeping in mind the therapeutic importance of bromelain (BM) proteins, here we examined how graphene oxide's concentration and reduction impact its interaction with the bromelain, using a variety of spectroscopic and biophysical approaches. The results indicate that the adsorption of BM proteins on the surface of GO/RGO occurs spontaneously and rapidly, forming a protein corona (PC). The binding affinity of BM with GO is much higher than its reduced form (RGO). The binding of BM with GO occurs through cooperative interaction, whereas both cooperative and anti-cooperative binding is observed in the BM/RGO system. The adsorption of BM on GO is driven by both covalent (the epoxy group of GO covalently bonds with the surface amino acids of BM) and non-covalent (H-bonding, electrostatic) interactions. On the other hand, hydrophobic interaction is the primary driving force behind BM adsorption on the RGO surface. Distinct kinds of corona were observed in the BM-GO/RGO system based on the types of interactions involved (such as electrostatic, hydrophobic, H-bonding, covalent bond formation, etc.) between the protein and nanoparticles. A hard protein corona formation was observed for the adsorption of BM on the GO surface, whereas a soft PC formation occurs in the presence of RGO nanoparticles. The therapeutic utility of this protein nanoparticle will be heavily dependent on its PC formation, which will be the focus of future research. This study lays the groundwork for future PC investigations on the diverse range of protein nanoparticles utilized in nanomedicine and environmental applications.

1. Introduction:

Graphene-based nanomaterials, particularly graphene oxide (GO) and reduced graphene oxide (RGO), have recently gained popularity in various applications, such as energy storage,[1] drug delivery,[2-5] water treatment,[6,7] biomedicine,[8,9] etc. Due to the growing manufacturing and use of GO and RGO, there is now more accidental and deliberate human exposure to these nanoparticles worldwide.[10-13] Consequently, it is essential to accurately evaluate the biological impacts of graphene materials, which are known to be heavily impacted by the protein corona

because of their crucial function in defining the interactions between cells and nanomaterials, as well as the cellular uptake and cytotoxicity that follow.[14-17]

The formation of a protein shell on the surface of nanomaterials upon exposure to biological fluids is known as the protein corona, and it is a crucial factor influencing both biocompatibility and nanotoxicity. GO nanosheets are no different, forming a variety of "coronas," such as the hard protein corona (HPC), which firmly adheres to the surface of the nanoparticles. This HPC changes the physicochemical characteristics and surface conformation of GO, which affects how it interacts with biological entities like cells and tissues and eventually determines the cellular and tissue response.[18,19] The formation of protein coronas will mask the initial surface characteristics of nanomaterials and transform them into the actual material that human organs and cells initially encounter.[20,21] Consequently, regardless of how accurately nanomaterials are originally engineered, their fate in vivo becomes complex. Nonspecific interactions can also alter the function and confirmation of specific bioactive proteins, which can impact immune system responses and cell responses.[22,23] Therefore, a thorough understanding of the interactions between nanoparticles and biological proteins is crucial for improved practical application of nanomaterials.

The study of NP-protein interactions is becoming increasingly significant in biomedical applications, particularly drug delivery. The nanomaterial is first exposed to blood as a physiological environment after intravenous delivery. As a result, the investigations that are currently accessible in the literature primarily concentrate on how NPs interact with plasma proteins. Since peptides and proteins may remain weakly accessible after oral treatment, NPs may also find significant usage as possible oral delivery vehicles for proteins. Their interaction with NPs is one tactic that can be employed to increase the bioavailability of the proteins. Thus, in addition to plasma proteins, other proteins, like bromelain (BM) have antidematous, antithrombotic, anti-inflammatory, antitumoral, fibrinolytic, immunomodulator, antiinvasive, and antimetastic qualities and can be taken orally, should also be investigated in connection with NPs. In essence, the therapeutic significance of BM spurred us to study how it interacts with GO/RGO nanosheets.

In this study, we looked at how the concentration and reduction of GO nanosheets to RGO affected the adsorption of BM proteins. The extent of binding of BM proteins on the GO/RGO nanosheets and the cooperativity of the binding were assigned by fluorescence measurement using the Hill isotherm model. Using the Stern-Volmer equation, the mechanism of

fluorescence quenching was determined, and time-resolved fluorescence measurements and UV-vis were used to validate it. The nature of the force involved (H-bonding, π-π, or hydrophobic interaction) during the adsorption of BM on the GO/RGO nanosheets was assigned by the ITC measurements. The stability of proteins on the GO/RGO nanosheets was determined by CD and Tm measurements, and the kind of PC formation (hard or soft corona) was confirmed by DLS measurements. Here, we provide a complete picture of the complexation process and mechanism involved in the adsorption of BM proteins on the GO/RGO nanosheets, which will be helpful in the biomedical application of the BM-GO/RGO bio-interface complex.

2. Experimental Section:

2.1 Materials:

Bromelain (BM) from pineapple stem, B4882 was purchased from Sigma Aldrich. Natural graphite flakes (Alfa Aesar) were purchased from Merck. Graphene oxide (GO) was self-synthesized (using the modified Hummer's method) and the details of characterization were mentioned in our previous paper.[24] Reduced graphene oxide (RGO) was synthesized by gamma radiation in an ethanolic saturation solution of graphene oxide (the details of synthesis and characterization of RGO were documented in the supporting file). All the experiment was performed in 10 mM sodium phosphate buffer solution (pH 7.4).

2.2 Instrumentations:

2.2.1 Fluorescence quenching measurements:

The fluorescence emission of BM was measured in the absence and presence of GO/RGO nanosheets using a PerkinElmer LS 55 (U.S.A.) luminescence spectrometer. The interaction between BM and GO/RGO nanosheets was investigated by mixing a set concentration of BM (400 mg/L) with increasing concentrations of GO/RGO at a constant temperature of 298 K. PerkinElmer fluorescence Peltier system (PTP1) connected to the instrument was used to maintain the constant temperature throughout the experiment. The emission spectra of BM were recorded at an excitation wavelength of 295 nm with a 5 nm excitation and emission slit, and the spectra were recorded in the wavelength range of 310-500 nm.

2.2.2 UV-vis spectroscopy:

The absorption spectral measurements of BM with and without GO/RGO nanoparticles were measured using a Shimadzu 1601 spectrophotometer (Japan). A set of quartz cuvettes with 0.5

cm path length was used in this study. The absorption spectra of BM were recorded in the wavelength range of 250-500 nm.

2.2.3 Time-resolved Fluorescence measurements:

The time-resolved fluorescence decay of BM was measured using a Horiba-Jobin-Yvon FluoroCube fluorescence lifetime system, which includes a 300 nm NanoLED (IBH, UK) and a TBX photon detecting module. The decay analysis software IBH DAS-6 was used to fit each decay data point. The light profile was collected using a diluted sodium dodecyl sulphate (SDS) micellar solution as a scatter. For proper fitting, the χ^2 value was kept close to 1.

2.2.4 Isothermal titration calorimetry (ITC) measurements:

A Microcal ITC-200, Malvern, UK, instrument was used to perform ITC measurements. In a standard titration experiment, 19 injections of BM (titrant, 2 μL per injection from a 30 μM stock) were made into the sample cell (volume = 300 μL) that contained the GO/RGO solution (100 mg/L) at 180-second intervals. The data was analysed using ITC software to assess how much heat was absorbed or released as a result of the nanoparticle interaction at each stage of BM addition. Throughout the ITC experiment, a constant temperature of 298 K was maintained.

2.2.5 Dynamic light scattering (DLS) and Zeta potential measurements:

The Zetasizer Nano ZS dynamic light scattering (DLS) instrument (Malvern, UK) was used to measure the hydrodynamic diameters (Dh) and zeta potential of the GO/RGO system, both with and without varying concentrations of BM. The size measurement was performed using a fixed scattering angle of 90°. The equipment uses a fixed wavelength He-Ne laser (λ = 632.8 nm) to characterize aggregate sizes. To remove bigger particles during DLS measurements, all solutions were filtered three times using 0.25 μm membrane filters. A 1.5 mL filtered bubble-free sample was taken in a quartz cuvette and placed inside the sample chamber of the DLS instrument. We have prepared the sample for DLS measurements by adding 30, 60, 90, and 120 μL of BM solution to 1.5 ml of GO/RGO solution. To obtain more precise results, each measurement was repeated twice and the mean values were recorded.

2.2.6 Circular dichroism (CD) spectroscopy analysis:

The conformational variation of BM in the presence of GO/RGO nanoparticles was monitored by measuring the change in the far-UV CD spectra (195-260 nm) of BM using a Jasco

spectropolarimeter (J-815). The spectra were recorded in a fixed concentration of BM (100 mg/L) with varying concentrations of GO/RGO nanoparticles in a nitrogen-inert atmosphere with a scan rate of 250 nm/min. Using a Neslab RTE-111 rotating water bath attached to quartz cuvettes with water jackets, the sample temperature was kept at 298±0.2 K.

2.2.7 Thermal Melting Studies:

The effect of GO and RGO on the thermal stability of BM proteins was investigated by means of thermal melting studies in the pre-mentioned buffer by monitoring the change in absorbance at 280 nm against temperature. This thermal melting study was carried out in UV-1900 spectrophotometer (Shimadzu Co., Japan) where the initial and final temperatures were pre-fixed in highly sensitive temperature controller device (Model No. LF13751, USA) of which the stability lies within the order of ±0.002°C. The temperature scanning rate was mentioned at 1°C/min. All the thermal melting experiments were performed at air-equilibrated condition.

2.2.8 Transmission electron microscopy (TEM):

The variation in surface morphology of GO/RGO nanosheets after BM incubation was observed by analyzing TEM micrographs taken with a JEOL 2100 Plus electron microscope operating at 100 kV. 10 microliters of the sample were drop-cast onto a copper TEM grid coated with carbon (300-mesh), and the samples were then allowed to dry overnight in a desiccator.

3. Results and discussion:

3.1 Fluorescence measurements and quenching analysis:

Fluorescence spectroscopy is commonly used to study protein structure and conformation. The common chromophore residues present in proteins include tryptophan (Trp), tyrosine (Tyr), and phenylalanine, which serve as intrinsic fluorescence probes. Interestingly, the microenvironmental conditions greatly influence these aromatic amino acid residues (Trp, Tyr, etc). It is well known that the emission properties of amino acid residues are connected to modifications in their microenvironment since proteins bind and undergo conformational changes when they interact with molecules and nanomaterials.[25] The binding mechanism between the quencher and the fluorophore can be clarified by fluorescence quenching studies, which can also disclose the availability of a quencher to the fluorophore in the biomolecules. Recent studies have shown that GO can quench fluorescence when interacting with emission-active biomolecules such as proteins, peptides, and amino acids.[27] Therefore, using highly sensitive fluorescence spectroscopy, it is possible to determine the state and conformation of

bromelain proteins (BM) upon binding GO/RGO nanosheets by observing changes in the fluorescence emission intensity. Here, we examined how the concentration and reduction of GO nanosheets affect the intrinsic fluorescence behavior of BM proteins (Fig. 1 (A&B)). BM has five Trp residues (Trp 8, Trp 27, Trp 67, Trp 176, and Trp 180) across the entire polypeptide chain[28] that are mainly responsible for its intrinsic fluorescence. Three of the five Trp residues may be buried in the BM's hydrophobic core, while the remaining two are near the surface.[29,30] In its native state, BM exhibits fluorescence spectra with an emission maximum (l_{max}) of about 360 nm in the presence of the buffer (Fig.1 (A&B)). A decrease in the emission intensity of BM was observed upon incubation with GO/RGO nanosheets. As the GO and RGO concentrations increased, BM's fluorescence intensity gradually decreased without a shift in l_{max}. The obvious quenching effect in the presence of GO/RGO nanosheets implies the possibility of direct interaction between the nanoparticles and the chromophore residue of BM, which in this case are Trp. Many mechanisms can contribute to fluorescence quenching, including ground-state complex formation, excited state reaction, energy transfer, and collision quenching.[31] In fact, the adsorption of BM onto the GO/RGO nanosheets may have contributed to the decreases in emission intensity since it reduced the distance between the quenching agent GO/RGO, and the BM proteins' active fluorescence emitters. We have used the Stern-Volmer model to determine the precise mechanism underlying the fluorescence quenching of BM in the presence of GO/RGO nanosheets. In the presence of 0.3-17 mg/L of GO, and 0.7-100 mg/L of RGO nanosheets we have monitored the fluorescence quenching of BM proteins. However, we observed that BM followed the S-V linearity relationship only up to 9.0 mg/L of GO, while in the presence of RGO, the linearity is maintained up to a high concentration range. We have used the S-V equation[32] to understand the mechanism of quenching-

$$F_0 / F = 1 + K_{SV}[Q]$$

where F_0 and F are the fluorescence intensity without and with the quencher, respectively, K_{SV} is the Stern-Volmer quenching constant, and [Q] is the quencher concentration. As was previously said, the GO/RGO nanosheets may use ground-state compound formation, excited-state reactions, or collision quenching to quench the protein's fluorescence. Quenching mechanisms might be static, dynamic, or both. Static quenching results in the formation of a ground-state nonfluorescent compound between the fluorophore and quencher. Dynamic quenching can, however, occur when the fluorophore and the quenching agent collide in the excited state. A linear relationship between F_0/F and [Q] implies that just one form of quenching is present, but a non-linear plot indicates that the system has both static and dynamic

quenching. The Stern-Volmer figure for the GO-BM system shows good non-linearity, indicating that fluorescence quenching is caused by both static and dynamic quenching. Here, the Stern-Volmer plot displays an upward curve concave towards the Y-axis (Fig. 1C). However, in the RGO-BM system, good linearity is obtained across a wide range of nanoparticle concentrations (Fig. 1D). Still, considerable non-linearity is observed at extremely high concentrations of RGO nanosheets, implying that one kind of quenching is prevalent here. The absorption spectra of BM in the presence of GO/RGO nanosheets can provide vital information on the quenching mechanism. A detailed inspection of the fluorophore's absorption spectra can easily distinguish between static and dynamic quenching. Collision quenching solely affects the fluorophore's excited states; hence, no change in absorption spectra is expected. In general, static quenching alters the fluorophore's absorption spectra by forming a ground state complex between the fluorophore and the quencher.[33] Furthermore, time-dependent fluorescence spectroscopy also gives important information about the quenching mechanism. Below, we have discussed the change in BM's absorption and time-resolved fluorescence spectra in the presence of GO/RGO nanosheets to get more information about the quenching mechanism. For both the systems (BM-GO and BM-RGO), we have taken the linear concentration zone of GO/RGO nanosheets for our Stern-Volmer model calculation. The calculated Stern-Volmer K_{SV} values for BM-GO and BM-RGO systems are 0.085 L/mg and 0.008 L/mg respectively (Table 1). So, the calculated K_{SV} value for the GO-BM system is nearly 10 times higher than the RGO-BM system. This result suggests that GO acts as a very effective fluorescence quencher for BM compared to its reduced form. In the presence of 18 mg/L of GO nanosheets, there was a ~60% decrease in the fluorescence intensity of BM observed whereas in the presence of the same amount of RGO nanosheets, only a ~13% decrease in the emission intensity was observed.

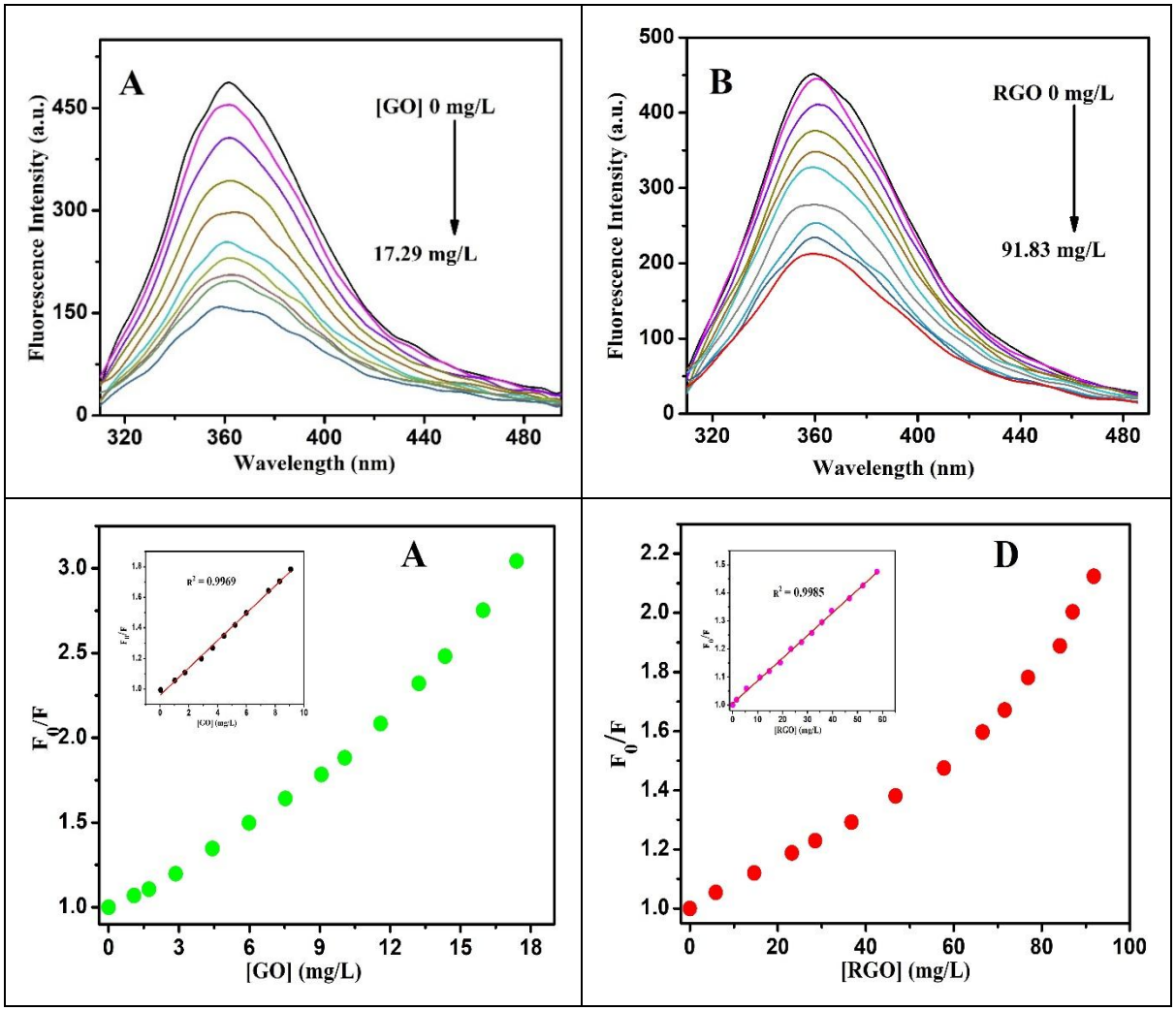

Fig. 1 Fluorescence quenching of BM proteins by GO/RGO nanosheets. Emission spectra of BM in the absence and presence of increasing concentration of (A) GO, and (B) RGO nanosheets. The concentration of BM proteins was kept constant at 400 mg/L, whereas that of GO nanosheets varied from 0 to 17.29 mg/L and RGO from 0 to 91.83 mg/L. Stern-Volmer plots of fluorescence quenching of the BM proteins with varying concentration of (C) GO, and (D) RGO nanosheets. Inset plots represent the linear regime of the Stern-Volmer plot at low quencher concentration.

We have employed the Hill isotherm model to investigate the GO/RGO-BM interactions' binding affinity and cooperativity in more detail. Assuming that the binding of the proteins to GO/RGO nanosheets takes place under equilibrium conditions, this model was used to calculate several important parameters that describe the interactions between the BM proteins and GO/RGO nanomaterials, including the Hill coefficient n, binding dissociation constant K_D, and binding association constant K_A. We have determined the required parameters based on

the Hill equation by fitting the non-linear curve[34] of the fluorescence quenching of BM by the GO/RGO nanosheets (Fig. 2 (A&B)), as shown below.

$$Q = Q_{max} \cdot \frac{[GO]^n}{K_D^n + [GO]^n}$$

$$Q_{max} = \frac{I_0 - I}{I_0}$$

Where I_0 and I represent the protein's fluorescence intensity in the absence and presence of GO/RGO nanosheets, respectively, Qmax is the saturation value of Q, K_D is the dissociation constant that characterizes the relative strength of the GO/RGO-protein interaction, and n is the Hill coefficient that establishes the cooperative nature of the GO/RGO-protein association. The GO-BM and RGO-BM systems have an estimated equilibrium dissociation constant (K_D) of 20.58 mg/L and 255.68 mg/L, respectively (Table 1). Following the formulation of K_D, we quantitatively calculated the equilibrium association constant (K_A) between BM and GO/RGO nanosheets. Since K_A is the reciprocal of K_D, a reversal trend was expected. The K_A value obtained for the GO-BM system (0.048 L/mg) is about 10 times more than that found for the RGO-BM system (0.0039 L/mg) (Table 1). This suggests that the BM protein has a stronger affinity for GO nanosheets than its reduced form (RGO), implying that GO reduction weakens the protein-nanoparticle interaction. The driving forces of the BM protein and GO nanosheet association include covalent interaction, H-bond formation, electrostatic, hydrophobic, and π-π stacking interaction. As we all know, GO consists of a large number of oxygens containing functional groups, such as hydroxyl, carboxyl, and epoxy groups on the surface and edges of the nanosheets. Under mild conditions, the epoxy groups can undergo a nucleophilic addition reaction with an amine,[35] resulting in many covalent bond formations expected between the epoxy groups of GO nanosheets and the different amino acid residues of BM proteins during their interaction. Aside from that, GO nanosheets also include a large number of hydroxyl and carboxyl groups, which favours hydrogen bonding interactions with BM proteins. As a result, we may anticipate that covalent bond formation and H-bond formation will be the primary driving forces for BM-GO nanosheet interaction. The complexation of BM and GO nanosheets is also significantly influenced by electrostatic interaction. There is a considerable possibility of electrostatic interaction since the GO nanosheets are negatively charged and the BM proteins are positive (IP = 9.2) at the working pH 7.4. The reduction of GO nanosheets causes a decrease in oxygen-containing functional

groups, making hydrogen bond interaction and covalent bond formation with BM proteins less viable. Furthermore, the reduction of GO nanosheets decreases their negative surface charge, resulting in less electrostatic interaction with BM proteins. So, the above-mentioned reasons are mostly responsible for the decreased K_A value for BM protein complexation with RGO compared to GO nanosheets. Here, we observed that the fluorescence quenching efficiency of the BM proteins by GO/RGO nanosheets correlated with the binding interaction of GO/RGO-BM systems. For instance, compared to its reduced form, BM has a stronger association with the GO nanosheets. At the same time, GO nanosheets exhibited the maximum efficiency in decreasing BM's intrinsic fluorescence. On the other hand, RGO nanosheets showed the weakest association and, as a result, the weakest fluorescence quenching of BM. All of this revealed that a higher rate of fluorescence quenching (represented by a larger K_{SV}) may be attributed to the attached protein's chromophore residues being closer to the adsorbing surface of a nanosheet (expressed by a higher K_A). We examined the cooperative and multifunctional character of the binding of BM proteins and GO/RGO nanosheets to gain a better understanding of the extent of the binding interaction between these two materials. It is quite likely that proteins include several binding sites for ligands. As a result, the interaction of BM proteins with GO/RGO nanosheets may exhibit a certain level of cooperativity. In order to clarify this, we looked at the Hill coefficient (n) of the complexation of BM with GO/RGO nanosheets. This is a crucial metric that describes the binding cooperativity, or the degree of molecular interaction independence between several binding sites. The BM-GO/RGO system's Hill coefficient was determined using the above Hill equation based on the fluorescence quenching data. We observed anti-cooperative binding or negative cooperativity ($n < 1$) when BM proteins were complexed with RGO nanosheets. In contrast, the BM-GO complexation displayed cooperative binding with positive cooperativity. A Hill coefficient (n) value of less than one indicates an anti-cooperative binding. This indicates that the strength of the binding between the proteins and the surface of the nanomaterial gradually decreases as further proteins adsorb onto it. In contrast, for a positively cooperative process ($n>1$), a single protein molecule adsorbed on the nanomaterial surface stimulates the adsorption of additional protein molecules. The BM-RGO system's anti-cooperativity shows that once BM molecules are adsorbed on the RGO surface, its activity steadily declines, indicating a change in the physicochemical features of the RGO surface with progressive BM protein adsorption. When BM proteins bind to RGO nanosheets, they may undergo a slight conformational change that prevents the BM protein's inner binding sites from being fully exposed to the nanosheets; in other words, the multiple binding sites are unable to participate in the interaction between the protein and the

nanoparticle. As a result, non-cooperativity may arise for the BM-RGO system. As the Hill coefficient for the BM-RGO system is so close to one, some cooperative interaction is feasible. However, the positive cooperativity of the GO-BM interaction could be attributable to the many binding sites engaged in the interaction of BM with GO nanosheets. BM may have several binding sites for GO nanosheets, some of which may be buried within protein core structures. A conformational change to the protein structure occurs as soon as BM attaches to GO nanosheets, exposing the protein's inner binding sites to the nanosheets. As a result, the BM-GO system has a steadily higher binding affinity, forming a cooperative binding association.

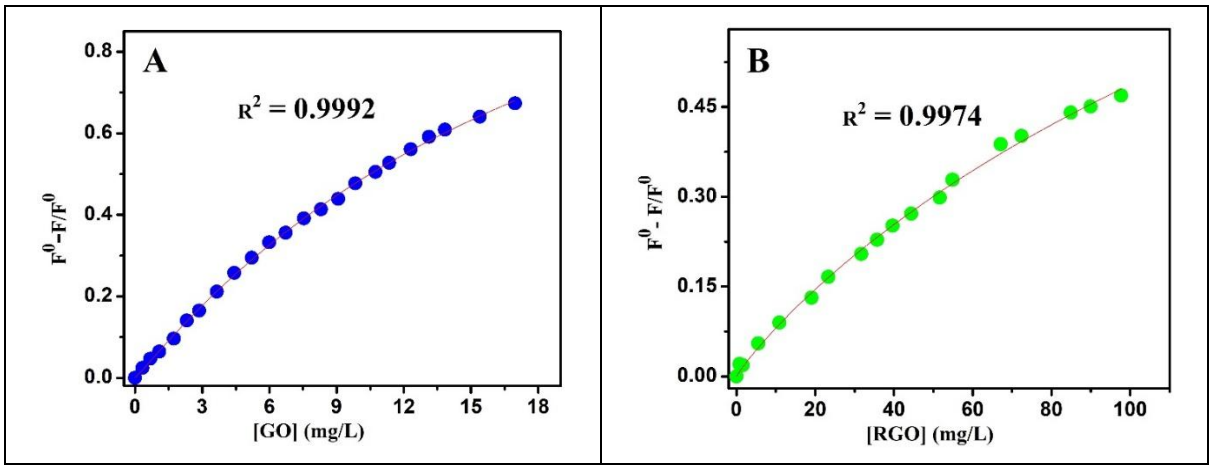

Fig. 2 BM proteins fluorescence quenching properties by GO/RGO nanosheets and the corresponding binding parameters of GO/RGO–BM complexes. Hill plots of the fluorescence quenching of BM in the presence of (A) GO, and (B) RGO nanosheets with increasing concentration. Experimental data were fitted using the Hill mathematical model, as shown in equations (2) and (3).

3.2 UV-vis measurements:

Furthermore, UV-vis spectroscopy measurements are an essential tool for distinguishing the binding mechanism involved between NPs and proteins, as well as understanding the conformational changes that occur in proteins as a result of ground state complex formation with NPs.[36] The aromatic amino acid residues of proteins such as tryptophan (Trp) and tyrosine (Tyr) contribute to their UV-Vis absorbance at 280 nm with respect to their n-π^* transition. Variations in the protein's conformation, particularly in the microenvironment of chromophores (such as Trp and Tyr), can cause variations in the absorption spectra. These changes can be

seen as shifts in wavelength or decreases and increases in the absorbance intensity around the protein's A_{max}. In an aqueous buffer medium, BM exhibits a UV-Vis spectrum with A_{max} about 280 nm,[37] indicating that the BM's Trp and/or Tyr residues absorb UV-vis radiation. BM protein has 5 Trp and 14 Tyr residues, which are responsible for its absorbance. Fig. 3 (A&B) shows that an increase in the absorbance of BM was observed with the addition of GO/RGO nanosheets. This suggests that a ground state complex formation between BM and GO/RGO nanosheets takes place, which leads to an increase in the absorbance of BM. No discernible changes in the absorbance maxima are seen, indicating that complexation with GO/RGO nanosheets does not significantly alter the polarity surrounding BM chromophore residue (such as Trp, Tyr, etc.). When BM is exposed to GO, its absorbance increases much faster than that of RGO nanosheets. The addition of 24 mg/L GO increased the absorbance of BM by approximately 61%, but the same quantity of RGO only increased the absorbance by 4%. This observation is in line with our fluorescence data and implies that GO's binding effectiveness with BM is significantly higher than that of RGO nanosheets. Therefore, the UV-vis measurements, which validate the formation of a ground state complex between BM and GO/RGO nanosheets, clearly show the participation of static quenching of BM in the presence of GO/RGO.

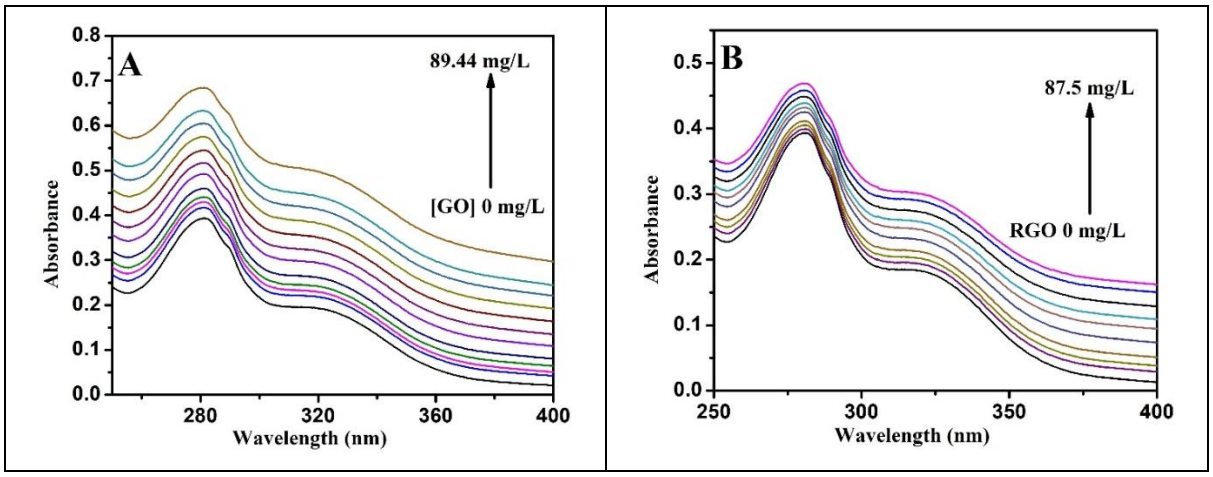

Fig. 3 UV-vis spectra of BM before and after incubation with (A) GO, and (B) RGO nanosheets with increasing nanoparticle concentration.

3.3 Time-resolved fluorescence analysis:

The fluorescence lifetime is the most precise and convenient way to distinguish between static and dynamic quenching. Fluorescence lifetime experiments confirmed the quenching mechanism involved in GO/RGO nanosheet interactions with BM proteins. UV-vis measurements have already verified the formation of a ground-state complex between BM and GO/RGO nanosheets, indicating the role of static quenching. However, there is no particular evidence of the role of dynamic quenching in the interaction of GO nanosheets with BM proteins. It is commonly recognized that the formation of a ground-state complex (static quenching) does not affect the decay period of the uncomplexed fluorophore since only the lifetime of unquenched fluorophores is detected in time-resolved fluorescence analysis. Dynamic quenching, on the other hand, reduces the mean decay time of the entire excited-state population by operating on the entire excited state.[38] Figure 4 shows the decay curve of BM with and without different concentrations of GO nanosheets, and Table S1 lists the corresponding decay data. In an aqueous phosphate buffer medium, native BM exhibits a bi-exponential decay profile with a shorter and longer lifetime component. The bi-exponential decay profile suggests that there are two different emitting components present in BM protein. There are five Trp residues in the total polypeptide chain of BM, which is the primary fluorophore residue in the protein, as was previously mentioned. The longer lifetime component of BM proteins may be attributed to the three Trp residues buried in the hydrophobic core of the protein, whereas the shorter lifetime component may be attributed to the two residues at the protein's surface. As can be shown in Table S1, the average lifetime of BM decreases when GO is added to the BM solution. This suggests that the presence of GO nanosheets perturbed the excited state of BM. It's interesting to note that while there was no discernible change in the lifetime of BM when RGO nanosheets were present, there was a modest decrease in BM lifetime when RGO concentrations were extremely high. Thus, the time-resolved fluorescence decay analysis unequivocally shows that dynamic quenching plays a major role in the fluorescence quenching of BM by GO. In contrast to the fluorescence quenching of BM by RGO nanosheets, dynamic quenching has only a minor influence. Table S1 reveals that in the presence of GO nanosheets, the longer lifetime component of BM reduces while the shorter lifetime component increases. In the presence of GO, the cavity containing the Trp residue of BM may be exposed, resulting in a decrease in the contribution of the cavity containing Trp, which leads to a decrease in the longer lifetime component of BM (because the longer lifetime component is due to the cavity containing the Trp residue). The increase in the

contribution of BM's shorter lifetime component (due to surface Trp residue) in the presence of GO can be explained similarly. Thus, this observation indicates that a significant conformational change of BM occurs when GO nanosheets are present. However, no such change in the lifetime component of BM protein was observed when RGO nanosheets were present, indicating that no significant conformational change occurred. Therefore, in addition to providing insight into the quenching mechanism, the time-resolved fluorescence study provides important details regarding the conformational change of BM in the presence of GO/RGO nanosheets.

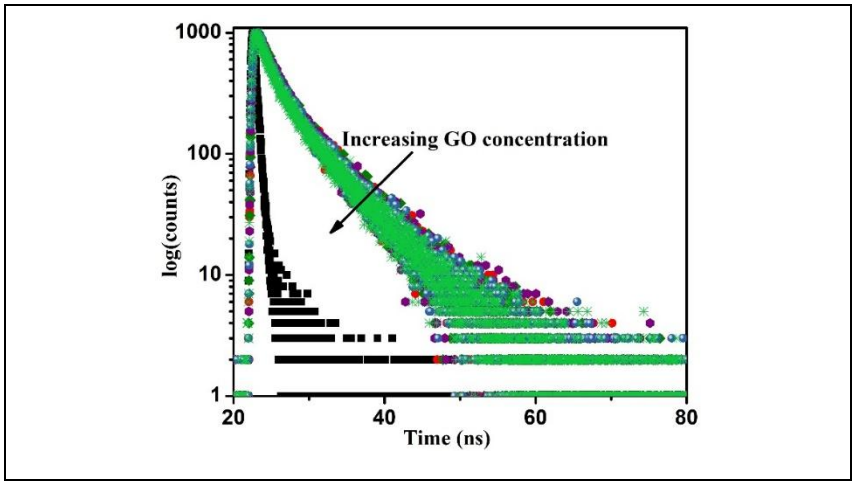

Fig. 4 Time-resolved fluorescence decay profile (logarithm of normalized intensity vs time) of BM protein (400 mg/L) in the absence and presence of various concentrations of GO nanosheets.

3.4 ITC analysis of GO/RGO-BM system:

The protein-NP interaction is commonly characterized by ITC, which directly offers several thermodynamic parameters of the complexation, including entropy, enthalpy, and free energy.[39,40] ITC has been employed in several protein corona studies to clearly characterize the physicochemical aspects of the protein-NP interaction, as ITC analysis has been more and more focused on protein adsorption mechanisms in recent years.[17,41,42] NPs-protein interaction is a complicated process that not only includes a variety of noncovalent forces, such as electrostatic, hydrogen bonding, π-π stacking, and hydrophobic interaction, but also involves the desolvation of proteins and NPs as well as the solvation of the newly formed NPs-protein complex.[43] Depending on the specific protein's structure and the type of nanoparticle surface, different forces contribute differently. The enthalpogram of the complexation of BM proteins with GO and RGO is shown in Fig. 5 (A&B), respectively. The complete complexation process of BM

with GO is exothermic, whereas the process of RGO is initially endothermic but becomes exothermic at high protein concentrations. This suggests that BM-GO complexation is entirely cooperative, whereas RGO-BM complexation contains both cooperative and non-cooperative interactions. As we have already seen from the Hill coefficient (n) value (derived from fluorescence measurements), non-cooperative binding predominates in the RGO-BM system ($n<1$), while cooperative binding occurs between BM and GO ($n> 1$). Thus, our ITC results are consistent with the fluorescence measurements in the steady state. The enthalpogram for the interaction of BM with GO differs significantly from that of RGO, showing that the force involved in the complexation of BM with two nanoparticle systems (GO and RGO) is distinct. The enthalpy change for the complexation of BM with GO is found to be negative ($\Delta H < 0$), whereas this value was found to be positive ($\Delta H > 0$) for RGO (Table 2). In a similar fashion, the change in entropy for the interaction of BM with GO was found to be negative ($\Delta S <0$), and a positive entropy change ($\Delta S >0$) was observed for the RGO-BM complexation. Non-covalent bond formation (e.g., van der Waals force, electrostatic interaction, or hydrogen bonds) is typically an exothermic process ($\Delta H <0$) that occurs more frequently on hydrophilic surfaces, whereas desolvation (the release of the hydration layer from the surface of proteins and NPs) is an endothermic process ($\Delta H >0$) that occurs more frequently on hydrophobic surfaces due to hydrophobic interaction.[44] Similarly, protein adsorption on the surface of nanoparticles results in an unfavourable entropy change ($\Delta S <0$) due to conformational constraint and loss of rotational freedom, whereas desolvation increases the system's entropy ($\Delta S >0$) provided the protein retains its shape. The presence of various oxygen-functional groups (e.g., epoxy, hydroxyl, carboxyl, etc.) at the surface and edges of GO makes it significantly more hydrophilic than its reduced counterpart (RGO). As a result of the presence of oxygen-functional groups and GO's significant surface charge, numerous non-covalent interactions (such as hydrogen bonding, electrostatic, and so on) can be formed with the protein molecule BM. The formation of non-covalent bonds between the protein molecule BM and GO during complexation results in a negative enthalpy change ($\Delta H < 0$). On the other hand, RGO interacts with the BM molecule mostly through hydrophobic interactions, resulting in an endothermic heat change ($\Delta H >0$). During BM-GO complexation, the protein's rotational motion is restricted due to the formation of different non-covalent bonds, resulting in a negative change in the entropy value observed for the GO-BM complex. However, the complexation of BM with RGO occurs via hydrophobic interaction; the hydration layer of both the BM and RGO should be removed first to allow for a hydrophobic complexation reaction. As a result,

the RGO-BM complexation showed a positive entropy change (ΔS > 0). As a result, we may conclude that BM complexation with GO nanoparticles is an enthalpy-driven process, whereas complexation with RGO nanosheets is an entropy-driven activity. The free energy change (ΔG) for BM complexation with both nanoparticles (GO and RGO) is negative, indicating that both complexation processes occur spontaneously.

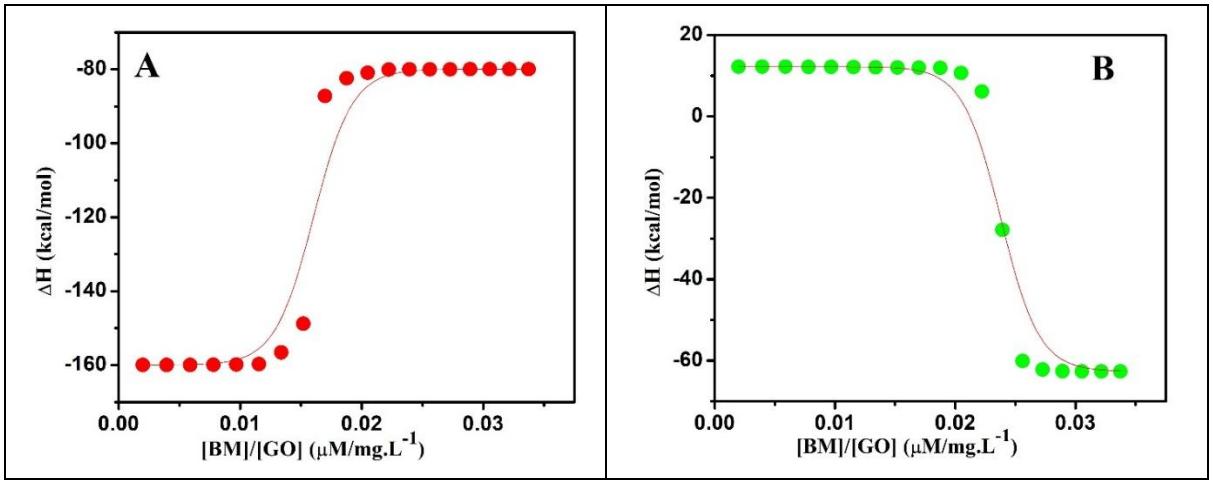

Fig. 5 ITC profile of BM-GO/RGO complexation. Integrated heat data for the reaction of BM proteins with (A) GO and (B) RGO nanosheets.

3.5 DLS measurements:

The hydrodynamic diameter (D_h) of NPs and/or their protein complexes can be found using the popular DLS approach. When proteins are present, the D_h of NPs changes, providing important information on specific protein binding and non-specific adsorption on the NPs' surface.[45] In Figure 6 (A&B), the size distribution of the GO/RGO and GO/RGO-BM complex is displayed. The exact size of GO and RGO can change based on how they are synthesized. The measured D_h values for GO and RGO in our case were 397 nm and 455 nm, respectively (Table 3). The GO/RGO showed a change in size distribution after mixing with BM, as shown in Fig. 6 (A&B). Upon BM incubation, the DLS peak's size and intensity changed, with the change being significantly more noticeable for GO than for its reduced form (RGO). We used varying concentrations of BM (2–8% in the interval of 2) to be adsorbed on the GO/RGO surface. In the presence of 2% BM, the size of GO increased significantly from 397 nm to 1023 nm. However, for 4, 6, and 8% of BM, the GO size was 1325, 1402, and 1497 nm, respectively (Table 3). The significant size increase of GO after incubation with BM may be largely attributed to the formation of protein coronas (PC) surrounding GO. The large thickness of the PC suggests multiple-layer adsorption of BM on the GO surface. Only the adsorption of BM

molecules on the NPs surface is unable to explain such a huge increase in the size of GO upon BM incubation. Apart from BM adsorption on the GO surface, GO agglomeration may occur in the presence of BM which also contributes to the increase in D_h value of GO upon BM incubation. Since, at working pH 7.4, the BM molecules are slightly positively charged, resulting in the negative charge of the GO surface decreases in the presence of protein molecules, which facilitates the NPs agglomeration. Interestingly, the size of RGO only increases moderately upon BM incubation. The size of RGO increased from 455 nm to 474, 484, 594, and 574 nm in the presence of 2, 4, 6, and 8% of BM, respectively (Table 3). These results suggest that RGO is less effective than GO for BM adsorption and protein corona formation. The increase in the size of the NP-protein complex with increasing BM concentration is not regular in the case of RGO. Particularly at high-protein concentrations, a fluctuation in the complex size of the RGO-BM was observed. A rapid equilibrium may exist between the free BM present in the solution and the RGO-BM complex at high protein concentrations, resulting in a fluctuation in the complex size observed. The main driving force for the adsorption of BM on the RGO surface is hydrophobic interaction and this is a weak force, resulting in a loose RGO-BM complex forming. So, here soft protein corona formation takes place in the case of RGO upon BM incubation. On the other hand, in the case of GO, a regular enhancement in the complex size is observed with increasing protein incubation. This suggests a strong complexation occurs between GO and BM, i.e., a hard protein corona formation occurs in this case. Since the adsorption of BM on the GO surface occurs through various strong non-covalent forces (e.g., H-bonding, electrostatic, etc.), as a result, here hard protein coronas formation takes place.

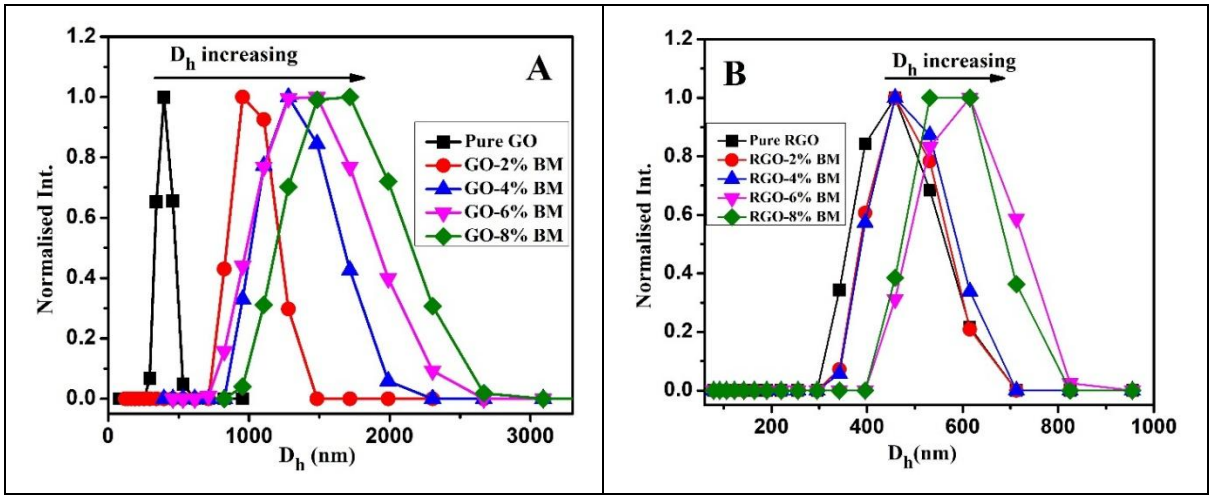

Fig. 6 Variation in the hydrodynamic diameter (D_h) of (A) GO, and (B) RGO nanosheets upon incubation with various concentrations (in %) of BM proteins.

3.6 Zeta potential measurements:

To understand the role of the surface charge of the GO/RGO on the protein corona formation, we have measured the zeta potential (ZP). The obtained ZP for the GO and RGO was -33.4 and -22.6 mV, respectively, suggesting both the NPs possess a negative surface charge. The addition of BM to the GO solution causes a progressive drop in the ZP value of the GO nanosheets. After achieving a minimal ZP value (~-10 mV), the GO-BM complex's ZP value remained constant as BM concentration increased. The above results suggest that a strong electrostatic interaction is present between the GO and BM, and a stable GO-BM complex is formed. So, in the case of GO, a stable hard protein corona formation takes place. Interestingly, the ZP value of RGO decreased in the presence of a low concentration of BM, reaching a minimum of about -15.0 mV. However, a fluctuation in the ZP value of the RGO-BM system was noted at higher BM concentrations. This shows that the formed RGO-BM complex is unstable and a rapid equilibrium exists between the free BM and the RGO-BM complex, resulting in ZP value fluctuations. In the case of RGO, an unstable soft protein corona is formed. The reported ZP results are consistent with the DLS findings, which show a hard corona for GO-BM and a soft PC formation for RGO-BM.

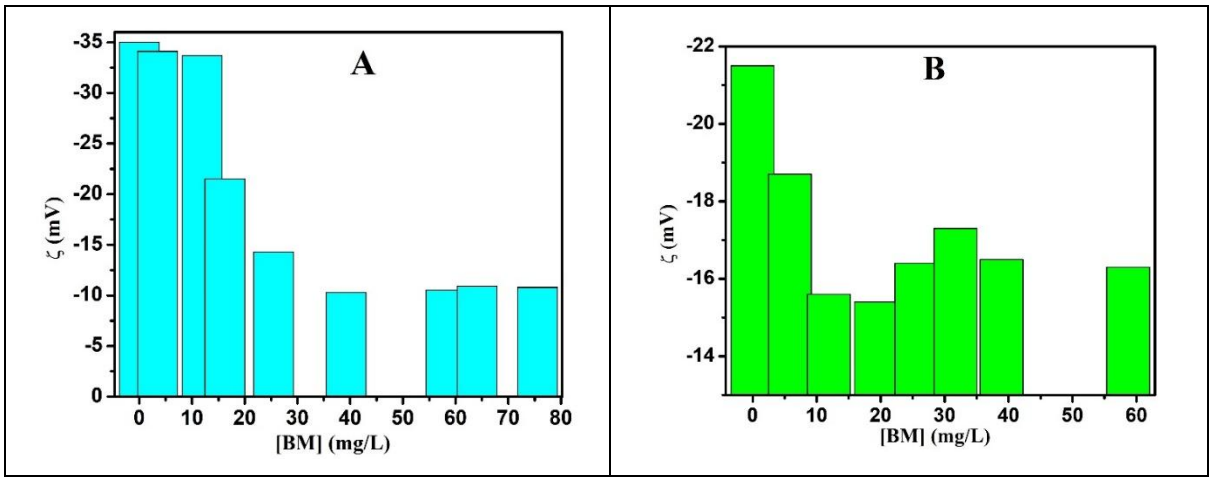

Fig. 7 Variation in the zeta potential value of GO (A) and RGO (B) nanosheets in the presence of different concentrations of BM.

3.7 CD spectroscopy analysis:

Adsorption of proteins onto the nanoparticle surface is a key mechanism in nanoparticle-protein interaction. Some proteins may experience conformational changes or denaturation of

their tertiary and/or secondary structure as a result of surface interaction, while others retain their native structure. In most circumstances, protein interactions with solid surfaces can result in significant structural changes, potentially changing protein function and biological activity. On this basis, it is critical to investigate the nature of the conformational changes undergone by BM proteins during their interaction with the GO/RGO nanosheets. We have observed the far UV CD spectra of the BM proteins with and without GO/RGO nanosheets to get insight into the secondary structural modification of the proteins (Fig. 8 (A&B)). The circular dichroism (CD) spectrum in the far UV region (190-260) can probe the secondary structure of proteins. As seen in Fig. 8 (A&B), BM displays bands at 207, 215, and 222 nm in its native state, with a stronger CD signal at 207 nm and the results agree well with the literature.[46] These bands imply that BM is a typical α+β-class of the enzyme as it is composed of α-helix and β-sheet regions.[47] The stability of the secondary structure of BM in the presence of GO/RGO nanosheets is revealed by the change in the ellipticity in the CD spectrum at the distinctive wavelengths. Based on the obtained CD data, we found that the negative ellipticity of the CD spectrum of BM proteins was slightly enhanced against its native form when a very low quantity of GO was present. This suggests that when GO nanosheets are present in small amounts, the secondary structure of BM gains additional stability. The GO-induced compactness in the BM's helical structure is most likely the cause of this. However, when the GO concentration increased, the ellipticity value of the CD spectra of BM decreased rapidly, indicating that a strong molecular interaction between GO nanosheets and BM proteins disrupts the protein's secondary structure. Although the ellipticity value of BM decreased noticeably, there were no significant variations in peak position identified after GO incubation. The BM proteins retain their α-helix structure after incubation with GO, indicating no significant secondary structural loss. Surprisingly, the ellipticity value of the CD spectra of BM did not change significantly in the presence of RGO, implying that the secondary structure of proteins stays nearly intact. The complexation of the GO-BM system involves strong covalent (the epoxy group of GO forms a crosslink with the surface amino acids of BM) and non-covalent (H-bonding, electrostatic) interactions, which leads to a noticeable secondary structural change. However, in the case of the RGO-BM system, only hydrophobic interaction (weak force) plays a crucial role in complexation, resulting in no significant change in CD ellipticity value observed. Another way to predict the type of protein corona formation—hard or soft—is to look at how the protein's CD spectra change when nanoparticles are present. When hard PC formation occurs, there is a noticeable change in the protein's CD signals; but when soft PC

formation occurs, there are no noticeable changes in the CD signals.[48] In our case, an appreciable change in the CD spectra of BM was observed upon incubation with GO, but no appreciable changes in CD signals were observed upon incubation with RGO. These CD findings suggest that a hard PC formation for GO and a soft PC for RGO occur in the presence of BM. Therefore, our CD results are in good agreement with the DLS data, which also indicate that in the presence of BM proteins, a soft PC formation occurs for RGO and a hard PC formation happens for GO.

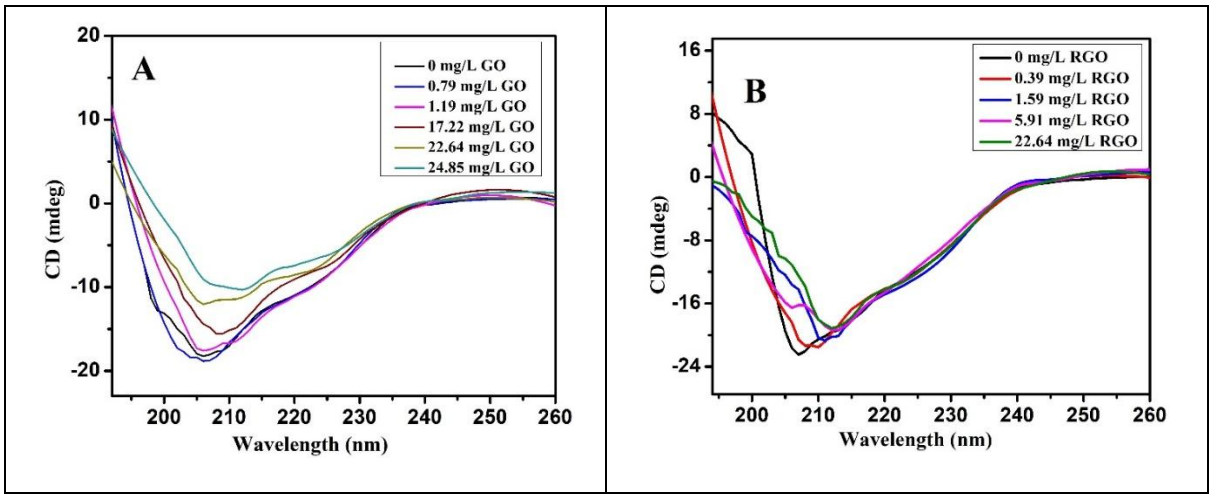

Fig. 8 Far-UV CD spectra of BM protein in the absence and presence of various concentration of (A) GO, and (B) RGO nanoparticles in phosphate buffer medium (pH 7.4) at 298 K. The protein concentration was kept constant at 100 mg/L.

3.8 Optical Melting Study.

The optical melting study is one of the efficient tools to analyse the thermal stability (i.e., resistivity against heat-induced structural alteration) as well as phase transition energetics of biomacromolecules like proteins, nucleic acids, etc.[49,50] In general, the thermal stability of proteins is known to be altered by the association of ligands, which is manifested by the change in helix-coil phase transition temperature. Thermal denaturation leads to an unwinding of the helical geometry of proteins which, in turn, results in abrupt or discontinuous increment in absorbance value at the absorption maxima of proteins. Melting temperature (T_m) is defined as the temperature at which half of the helical conformer is destroyed and becomes a random coiled structure, i.e., halfway of the phase transition or midpoint of the melting profile. Fig. 9A and Fig. 9B depict the thermal melting profile of BM protein in the presence of GO and RGO,

respectively. The corresponding phase transition temperatures are listed in Table 4. Native BM protein exhibited a sharp thermal melting profile with a melting temperature of ~71°C, which indicates substantial thermal stability of the protein owing to its high helical content. At a small concentration of GO nanoparticles (at 5 mg/L), a slight stabilization of BM was evident as the increase in the T_m value (Fig. 9A and Table 4). This is probably because of the occurrence of GO-induced compactness of the helical structure of the protein, which was also supported by the previously mentioned CD study, which evinced a mild enhancement of the negative ellipticity of BM protein in such a low GO-concentration regime. Surprisingly, at sufficiently high concentrations of GO nanoparticles, thermal melting showed a reverse transition pattern as evident from the figure. The opposite thermal melting pattern can probably be attributed to the formation of native-like structure upon the formation of the corona by adsorption of protein residues on the nanoparticle surfaces[51] driven by strong non-covalent (like H-bonding, electrostatic, etc) as well as covalent interactions (cross-linking bond formation between amino acid and epoxy groups). However, the melting temperature was found to be sufficiently decreased in the presence of a high concentration of GO nanoparticles. This decrease in T_m value and so also the thermal stability of BM protein in such a high concentration range is accompanied by the unfolding of helical polypeptide chains with concomitant exposure of hydrophobic cavities containing aromatic amino acid residues ([49,50]). This strong unfolding of BM protein in the presence of a higher concentration of GO nanoparticles is also quite consistent with the lowering of negative ellipticity value at such a high concentration regime.

However, from Fig. 9B (and from Table 4), it is clear that the association of RGO with BM protein hardly alters the T_m values and hence thermal stability of the protein. As RGO forms soft corona with the BM proteins through weak hydrophobic interactions, the complexation barely affected the secondary structure of the protein, which eventually did not impart any sort of unfolding tendency to the protein through exposure of hydrophobic side chains towards the solvent. This resistance of BM protein against unfolding in the presence of RGO went in line with the CD spectroscopic result. Hence, the optical melting study supports the previous experimental results regarding the satisfactory interaction of BM protein with GO and RGO.

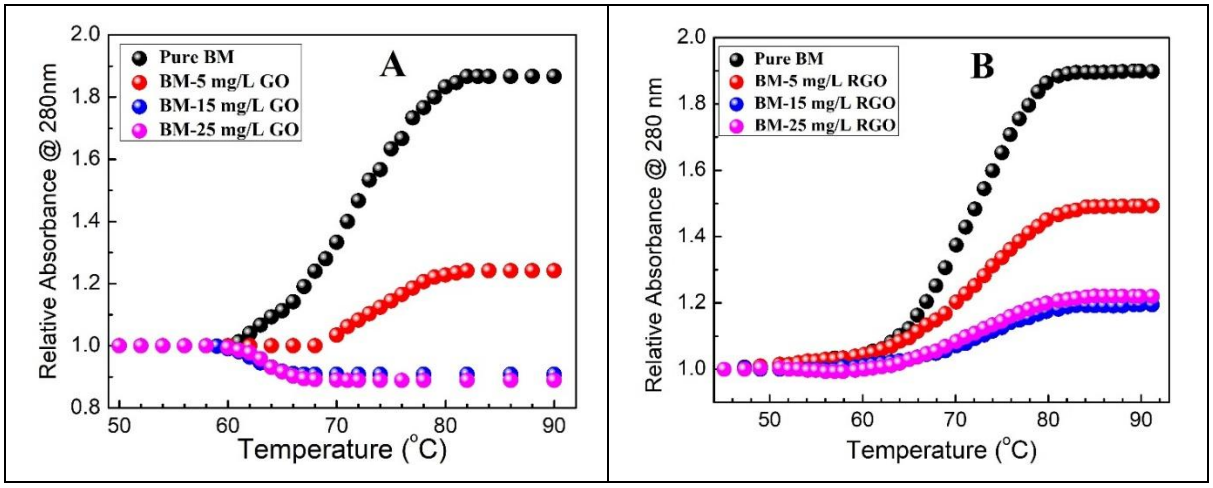

Fig. 9 Thermal melting (T_m) profile of BM proteins in the absence and presence of various concentrations of (A) GO, and (B) RGO nanosheets in 10 mM phosphate buffer medium of pH 7.4.

3.9 TEM analysis:

The morphological change of the nanoparticles after protein incubation was used to validate the adsorption of BM protein onto the GO/RGO nanosheets. The TEM micrographs of free and incubated GO/RGO nanosheets with BM proteins are shown in Fig. 10 (A-D). The TEM micrographs indicate a more wrinkle-like structure with a smaller number of edges visible in RGO than in GO, showing that GO is reduced, which removes many oxygen-containing functional groups. Many black spots were observed on the RGO surface upon incubation with BM proteins, suggesting the adsorption of protein molecules on the nanoparticle surface with high charge densities. A very thick layer was seen on the GO surface upon incubation with BM, indicating multilayered protein adsorption onto the GO surface with extremely high electron densities. So, the TEM micrographs show that a high number of BM proteins strongly adsorbed and formed a multilayer on the GO surface, implying that a hard PC was formed in this circumstance. On the other hand, there was significantly less BM adsorption on the RGO surface, and there were no multiple layers of protein adsorption, indicating the formation of a soft PC. Thus, it is also evident from the TEM micrographs that both soft and hard PC form when BM is incubated on GO/RGO nanosheets.

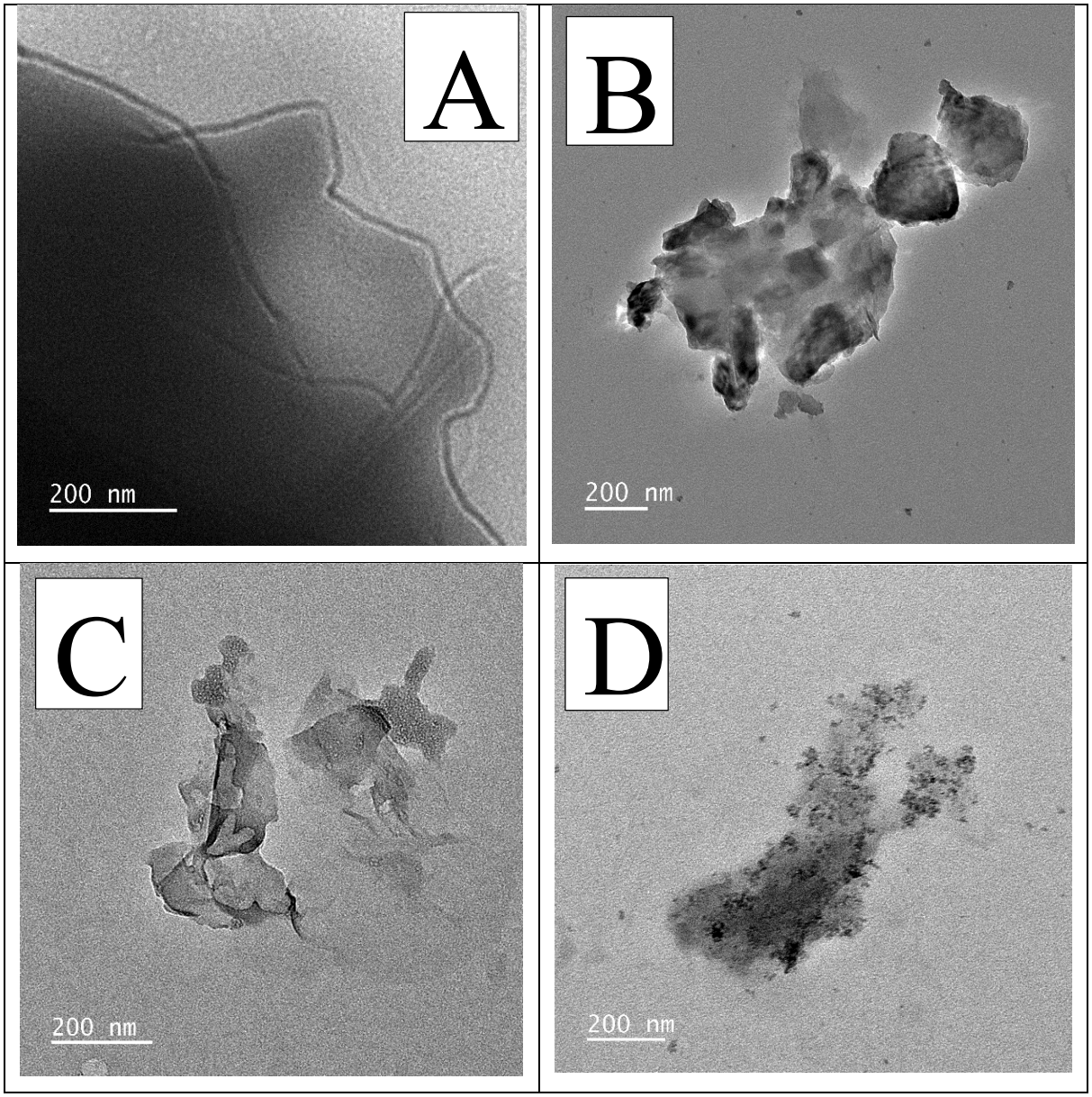

Fig. 10 (A) HR-TEM of pure GO, (B) BM-GO complex, (C) Pure RGO, and (D) BM-RGO complex respectively.

4. Conclusion:

In summary, using various experimental techniques under biologically relevant conditions, we have investigated the molecular interaction of steam bromelain with graphene oxide (GO) and its reduced form (RGO). Our findings indicate that GO has a considerably stronger ability to quench the intrinsic fluorescence of BM than RGO. Both static and dynamic quenching are involved in the fluorescence quenching of BM by GO nanosheets, while static quenching is primarily responsible for the fluorescence quenching of BM in the presence of RGO

nanosheets. The complexation of BM with GO is significantly stronger than that of RGO, as evidenced by the equilibrium association constant (K_A) for the GO-BM system (0.048 L/mg), which is nearly ten times higher than the value obtained for the RGO-BM system (0.0039 L/mg). The binding cooperativity calculated by the Hill isotherm model suggests that BM binds cooperatively with GO nanosheets; however, anti-cooperativity is observed when interacting with RGO nanosheets. Both covalent (bond formation between the surface epoxy group of GO and amino acid residue of protein) and non-covalent forces (electrostatic, H-bonding, etc.) are involved in the complexation of BM with GO nanosheets. In contrast, only hydrophobic interaction (weak non-covalent force) dominates in the complexation process of BM with RGO. The binding of BM with GO nanosheets resulted in a negative enthalpy (DH) change, while the interaction with RGO produced a positive enthalpy change. This suggests that the complexation of BM with GO is enthalpy-driven, while the complexation between BM and RGO is entropy-driven. No significant structural alterations of BM were observed upon its adsorption onto RGO, as indicated by CD spectroscopy and T_m measurements. Conversely, the BM structure was found to be slightly stabilized at very low GO concentrations, while at high GO concentrations, the protein underwent a substantial structural alteration. A progressive increase in the hydrodynamic diameter (D_h) of GO/RGO nanosheets was noted with BM incubation; in the case of GO, this increase was more pronounced. The formation of protein corona (PC) is mainly responsible for this increase in the size of the BM-GO/RGO complex. A hard PC formation was observed for the adsorption of BM onto the GO nanosheets, whereas a soft PC formation was observed for the BM-RGO system, indicated by DLS and CD spectroscopy measurements. These results are important for guiding the practical use of the GO/RGO-BM nano-bio interface complex in biomedical fields. Since GO and RGO have different selectivity toward the BM, these nanomaterial systems can be utilized for the purification and separation process of BM proteins. The high affinity of BM protein for GO/RGO nanosheets makes it suitable for long-term delivery in therapeutics. A thorough understanding of protein corona formation will be useful for applying the BM-GO/RGO system to therapeutic applications.

References:

1. Xu, J., Wang, K., Zu, S.-Z., Han, B.-H. & Wei, Z. Hierarchical nanocomposites of polyaniline nanowire arrays on graphene oxide sheets with synergistic effect for energy storage. *ACS Nano* **4**, 5019–5026 (2010).

2. Xu, Z., Wang, S., Li, Y., Wang, M., Shi, P., & Huang, X. Covalent functionalization of graphene oxide with biocompatible poly (ethylene glycol) for delivery of paclitaxel. *ACS Appl. Mater. Interfaces* **6**, 17268–17276 (2014).

3. Kurapati, R. & Raichur, A. M. Near-infrared light-responsive graphene oxide composite multilayer capsules: a novel route for remote controlled drug delivery. *Chem. Commun.* **49**, 734–736 (2013).

4. Liu, Z., Robinson, J. T., Sun, X. & Dai, H. PEGylated nanographene oxide for delivery of water-insoluble cancer drugs. *J. Am. Chem. Soc.* **130**, 10876–10877 (2008).

5. Kim, H., Lee, D., Kim, J., Kim, T. & Kim, W. J. Photothermally triggered cytosolic drug delivery via endosome disruption using a functionalized reduced graphene oxide. *ACS Nano* **7**, 6735–6746 (2013).

6. Perreault, F., De Faria, A. F. & Elimelech, M. Environmental applications of graphene-based nanomaterials. *Chem. Soc. Rev.* **44**, 5861–5896 (2015).

7. Hu, M. & Mi, B. Enabling graphene oxide nanosheets as water separation membranes. *Environ. Sci. Technol.* **47**, 3715–3723 (2013).

8. Sun, X. Liu, Z., Welsher, K., Robinson, J.T., Goodwin, A., Zaric, S., & Dai, H. Nano-graphene oxide for cellular imaging and drug delivery. *Nano Res.* **1**, 203–212 (2008).

9. Shim, G., Kim, M.-G., Park, J. Y. & Oh, Y.-K. Graphene-based nanosheets for delivery of chemotherapeutics and biological drugs. *Adv. Drug Deliv. Rev.* **105**, 205–227 (2016).

10. Bhattacharya, K. Mukherjee, S. P., Gallud, A., Burkert, S. C., Bellucci, S., Bottini, M., Star, A. & Fadeel, B. Biological interactions of carbon-based nanomaterials: From coronation to degradation. *Nanomedicine Nanotechnology, Biol. Med.* **12**, 333–351 (2016).

11. Hu, X., Li, D. & Mu, L. Biotransformation of graphene oxide nanosheets in blood plasma affects their interactions with cells. *Environ. Sci. Nano* **4**, 1569–1578 (2017).

12. Zhang, Q., Liu, X., Meng, H., Liu, S. & Zhang, C. Reduction pathway-dependent cytotoxicity of reduced graphene oxide. *Environ. Sci. Nano* **5**, 1361–1371 (2018).

13. Xu, M., Zhu, J., Wang, F., Xiong, Y., Wu, Y., Wang, Q., Weng, J., Zhang, Z., Chen W., & Liu, S. Improved in vitro and in vivo biocompatibility of graphene oxide through surface modification: poly (acrylic acid)-functionalization is superior to PEGylation. *ACS Nano* **10**, 3267–3281 (2016).

14. Docter, D., Westmeier, D., Markiewicz, M., Stolte, S., Knauer, S. K., & Stauber, R. H. The nanoparticle biomolecule corona: lessons learned–challenge accepted? *Chem. Soc. Rev.* **44**, 6094–6121 (2015).

15. Lundqvist, M., Stigler, J., Elia, G., Lynch, I., Cedervall, T., & Dawson, K. A. Nanoparticle size and surface properties determine the protein corona with possible implications for biological impacts. *Proc. Natl. Acad. Sci.* **105**, 14265–14270 (2008).

16. Del Pino, P., Pelaz, B., Zhang, Q., Maffre, P., Nienhaus, G. U., & Parak, W. J. Protein corona formation around nanoparticles–from the past to the future. *Mater. Horizons* **1**, 301–313 (2014).

17. Cedervall, T., Lynch, I., Lindman, S., Berggard, T., Thulin, E., Nilsson, H., Dawson, K. A., & Linse, S. Understanding the nanoparticle–protein corona using methods to quantify exchange rates and affinities of proteins for nanoparticles. *Proc. Natl. Acad. Sci.* **104**, 2050–2055 (2007).

18. Quagliarini, E., Pozzi, D., Cardarelli, F. & Caracciolo, G. The influence of protein corona on Graphene Oxide: implications for biomedical theranostics. *J. Nanobiotechnology* **21**, 267 (2023).

19. Hajipour, M. J., Raheb, J., Akhavan, O., Arjmand, S., Mashinchian, O., Rahman, M., Abdolahad, M., Serpooshan, V., Laurent, S., & Mahmoudi, M. Personalized disease-specific protein corona influences the therapeutic impact of graphene oxide. *Nanoscale* **7**, 8978–8994 (2015).

20. Walczyk, D., Bombelli, F. B., Monopoli, M. P., Lynch, I. & Dawson, K. A. What the cell "sees" in bionanoscience. *J. Am. Chem. Soc.* **132**, 5761–5768 (2010).

21. Monopoli, M. P., Aberg, C., Salvati, A. & Dawson, K. A. Biomolecular coronas provide the biological identity of nanosized materials. *Nano-Enabled Med. Appl.* 205–229 (2020).

22. Zolnik, B. S., González-Fernández, Á., Sadrieh, N. & Dobrovolskaia, M. A. Minireview: nanoparticles and the immune system. *Endocrinology* **151**, 458–465 (2010).

23. Deng, Z. J., Liang, M., Monteiro, M., Toth, I. & Minchin, R. F. Nanoparticle-induced unfolding of fibrinogen promotes Mac-1 receptor activation and inflammation. *Nat. Nanotechnol.* **6**, 39–44 (2011).

24. Sardar, R., Das, S., Banik, R., Bhunia, S. & Ghosh, S. Exploration of the impact of graphene oxide, acetylenic gemini, and CTAT on the photophysical and aggregation properties of dipolar coumarin 153. *Phys. Chem. Chem. Phys.* **26**, 8900–8918 (2024).

25. Roach, P., Farrar, D. & Perry, C. C. Interpretation of protein adsorption: surface-induced conformational changes. *J. Am. Chem. Soc.* **127**, 8168–8173 (2005).

26. Ling, X., Xie, L., Fang, Y., Xu, H., Zhang, H., Kong, J., Dresselhaus, M.S., Zhang, J. & Liu, Z. Can graphene be used as a substrate for Raman enhancement? *Nano Lett.* **10**, 553–561 (2010).

27. Li, S., Aphale, A. N., Macwan, I. G., Patra, P. K., Gonzalez, W. G., Miksovska, J., & Leblanc, R. M. Graphene oxide as a quencher for fluorescent assay of amino acids, peptides, and proteins. *ACS Appl. Mater. Interfaces* **4**, 7069–7075 (2012).

28. Ritonja, A., Rowan, A. D., Buttle, D. J., Rawlings, N. D., Turk, V., & Barrett, A. J. Stem bromelain: amino acid sequence and implications for weak binding of cystatin. *FEBS Lett.* **247**, 419–424 (1989).

29. Bisht, M., Jha, I. & Venkatesu, P. Comprehensive evaluation of biomolecular interactions between protein and amino acid based-ionic liquids: A comparable study between [Bmim][Br] and [Bmim][Gly] ionic liquids. *ChemistrySelect* **1**, 3510–3519 (2016).

30. Das, S., Roy, P., Sardar, P. S. & Ghosh, S. Addressing the interaction of stem bromelain with different anionic surfactants, below, at and above the critical micelle concentration (cmc) in phosphate buffer at pH 7: Physicochemical, spectroscopic, & molecular docking study. *Int. J. Biol. Macromol.* **271**, 132368 (2024).

31. Lakowicz, J. R. Principles of fluorescence spectroscopy. *Univ. Maryl. Sch. Med. Balt.* **132**, (2006).

32. Hu, Y.-J., Liu, Y., Zhang, L.-X., Zhao, R.-M. & Qu, S.-S. Studies of interaction between colchicine and bovine serum albumin by fluorescence quenching method. *J. Mol. Struct.* **750**, 174–178 (2005).

33. Hu, Y.-J., Liu, Y. & Xiao, X.-H. Investigation of the interaction between berberine and human serum albumin. *Biomacromolecules* **10**, 517–521 (2009).

34. Lacerda, S. H. D. P., Park, J. J., Meuse, C., Pristinski, D., Becker, M. L., Karim, A., & Douglas, J. F Interaction of gold nanoparticles with common human blood proteins. ACS Nano 4 (1): 365–379. at (2010).

35. Azizi, N. & Saidi, M. R. Highly chemoselective addition of amines to epoxides in water. *Org. Lett.* **7**, 3649–3651 (2005).

36. Baral, A., Satish, L., Das, D. P., Sahoo, H. & Ghosh, M. K. Construing the interactions between MnO 2 nanoparticle and bovine serum albumin: insight into the structure and stability of a protein–nanoparticle complex. *New J. Chem.* **41**, 8130–8139 (2017).

37. Kumar, P. K., Bisht, M., Venkatesu, P., Bahadur, I. & Ebenso, E. E. Exploring the effect of choline-based ionic liquids on the stability and activity of stem bromelain. *J. Phys. Chem. B* **122**, 10435–10444 (2018).

38. Upadhyaya, J., Singh, I. R., Pun, B., Baishya, H. J., Kumar, S., Joshi, S. R., & Mitra, S. Therapeutic Advantages of Nanoparticle-Impregnated Lysozyme Conjugates toward Amyloid-β Fibrillation and Antimicrobial Activity. *J. Phys. Chem. B* (2025).

39. De, M., Miranda, O. R., Rana, S. & Rotello, V. M. Size and geometry dependent protein–nanoparticle self-assembly. *Chem. Commun.* 2157–2159 (2009).

40. Lindman, S., Lynch, I., Thulin, E., Nilsson, H., Dawson, K. A., & Linse, S. Systematic investigation of the thermodynamics of HSA adsorption to N-iso-propylacrylamide/N-tert-butylacrylamide copolymer nanoparticles. Effects of particle size and hydrophobicity. *Nano Lett.* **7**, 914–920 (2007).

41. Henzler, K., Haupt, B., Lauterbach, K., Wittemann, A., Borisov, O., & Ballauff, M. Adsorption of β-lactoglobulin on spherical polyelectrolyte brushes: direct proof of counterion release by isothermal titration calorimetry. *J. Am. Chem. Soc.* **132**, 3159–3163 (2010).

42. Chen, K., Xu, Y., Rana, S., Miranda, O.R., Dubin, P.L., Rotello, V.M., Sun, L. & Guo, X. Electrostatic selectivity in protein–nanoparticle interactions. *Biomacromolecules* **12**, 2552–2561 (2011).

43. De, M., You, C.-C., Srivastava, S. & Rotello, V. M. Biomimetic interactions of proteins with functionalized nanoparticles: a thermodynamic study. *J. Am. Chem. Soc.* **129**, 10747–10753 (2007).

44. Prozeller, D., Morsbach, S. & Landfester, K. Isothermal titration calorimetry as a complementary method for investigating nanoparticle–protein interactions. *Nanoscale* **11**, 19265–19273 (2019).

45. Tsai, D.H., DelRio, F.W., Keene, A.M., Tyner, K.M., MacCuspie, R.I., Cho, T.J., Zachariah, M.R. & Hackley, V.A. Adsorption and conformation of serum albumin protein on gold nanoparticles investigated using dimensional measurements and in situ spectroscopic methods. *Langmuir* **27**, 2464–2477 (2011).

46. Jha, I. & Venkatesu, P. Deciphering the interactions of bromelain with carbon nanotubes: role of protein as well as carboxylated multiwalled carbon nanotubes in a complexation mechanism. *J. Phys. Chem. C* **120**, 15436–15445 (2016).

47. Arroyo-Reyna, A., Hernandez-Arana, A. & Arreguin-Espinosa, R. Circular dichroism of stem bromelain: a third spectral class within the family of cysteine proteinases. *Biochem. J.* **300**, 107–110 (1994).

48. Ko, I. & Mcgillivray, D. J. Soft and Hard Interactions between Polystyrene Nanoplastics and Human Serum Albumin Protein Corona. (2019) doi:10.1021/acs.bioconjchem.9b00015.

49. Ovung, A., Mavani, A., Ghosh, A., Chatterjee, S., Das, A., Suresh Kumar, G., Ray, D., Aswal, V.K. & Bhattacharyya, J. Heme protein binding of sulfonamide compounds: a correlation study by spectroscopic, calorimetric, and computational methods. *ACS omega* **7**, 4932–4944 (2022).

50. Basu, A. & Suresh Kumar, G. Binding and inhibitory effect of the dyes amaranth and tartrazine on amyloid fibrillation in lysozyme. *J. Phys. Chem. B* **121**, 1222–1239 (2017).

51. El-Baba, T. J., Woodall, D. W., Raab, S. A., Fuller, D. R., Laganowsky, A., Russell, D. H., & Clemmer, D. E. Melting proteins: evidence for multiple stable structures upon thermal denaturation of native ubiquitin from ion mobility spectrometry-mass spectrometry measurements. *J. Am. Chem. Soc.* **139**, 6306–6309 (2017).

Table 1. Binding parameters of the BM-GO/RGO system calculated from fluorescence measurements.

Complex	K_{SV} (L/mg)	K_D (mg/L)	K_A(L/mg)	n
GO-BM	0.085	20.58	0.048	1.2
RGO-BM	0.008	255.68	0.0039	0.94

Table 2 Thermodynamic parameters of the interaction of BM proteins with GO/RGO nanosheets derived from ITC measurements.

Complex	ΔH (kcal/mol)	ΔG (kcal/mol)	TΔS (kcal/mol)
GO-BM	-80	-12.8	-67.2
RGO-BM	74.8	-16.4	91.2

Table 3. Variation in the DLS size of GO/RGO nanosheets upon incubation with various concentrations of BM proteins.

System	D_h(nm)	System	D_h(nm)
Pure GO	397	Pure RGO	455
GO-2% BM	1023	RGO-2% BM	474
GO-4% BM	1325	RGO-2% BM	484
GO-6% BM	1402	RGO-2% BM	594
GO-8% BM	1497	RGO-2% BM	574

Table 4. Thermal melting temperature values of BM protein in the absence and presence of various concentrations of GO/RGO in the previously mentioned buffer.

System	**Nanoparticle concentration (mg/L)**	**T_m (°C)**
BM-GO	0	71.6
	5	73.5
	15	62.4
	25	63.3
BM-RGO	0	71.6
	5	71.7
	15	72.0
	25	72.4

Supporting Information:

Synthesis and characterization of gamma-reduced GO (RGO):

1.5 g of GO nanosheets were dispersed in 10 mL of 15 % isopropanol solution through ultrasonication in a test tube. Then, the test tube with dispersed GO solution was placed inside the gamma chamber. Gamma irradiation was carried out at a rate of 1.175 kGy/hr for a duration of one hour. Following the gamma irradiation process, the test tubes containing the GO solution were removed from the chamber, and the resulting solution was filtered and dried in a freeze-dryer. The finally obtained product was termed gamma-reduced graphene oxide (RGO).[1,2] The gamma irradiation setup had the following characteristics: the source of gamma irradiation was Cobalt-60, the strength was 3.7 kCi, and the irradiation chamber had a diameter of 10.6 cm and a height of 14.2 cm.

Characterization:

UV-vis analysis was first employed to monitor the reduction of GO towards RGO (Fig. S1 (A)). The UV-vis spectrum of the GO solution exhibits two bands: one at a shorter wavelength of 235 nm due to the $\pi-\pi^*$ transition of aromatic C-C bonds, and a shoulder band was observed at 302 nm, which is assigned to the n-π^* transition of C=O bonds. In the case of RGO, the absorption peak is red-shifted to 270 nm, suggesting a successful reduction of GO towards RGO and the restoration of C=C bonds in the RGO nanosheets.[3,4]

Fig. S1(B) represents the combined FTIR spectra of the synthesized GO and RGO, respectively. From the figure, it can be seen that the peak at 3436 cm^{-1} (due to the -OH group) becomes less broad in RGO compared to GO, implying significant removal of the hydroxyl group of GO upon its reduction to RGO. It was also found that in RGO, the intensity of other peaks at 1028, 1230, 1573, and 1720 became less than those peaks at the same position in FTIR spectra of GO, signifying the removal of various oxygen-containing functional groups. As a result, the oxygen-containing functional groups were successfully eliminated to a certain extent, and the RGO's edge and basal plane still contained small amounts of functional group residue.[5]

XRD analysis further confirms the conversion of GO towards RGO (Fig. S1(C)). The shift in the characteristic 002 reflection peak from 2Θ = 10.28 to 26.45 and the broadening in peak confirm the reduction of GO. The broadness of the RGO's (002) reflection peak can be explained by either the formation of a single or a few layers of RGO during the reduction of

GO or the random arrangement of the crystal sheets due to incomplete oxidation.[6] A second peak was also seen at 42.52°, which was explained by the existence of carbon materials' turbostratic bands in the RGO.[5]

HR-TEM measurement was performed to understand the morphological change of GO to RGO. The TEM micrograph (Fig. S1(D)) indicates a more wrinkle-like structure with a smaller number of edges visible in RGO than in GO, showing that GO is reduced, which removes many oxygen-containing functional groups.[7]

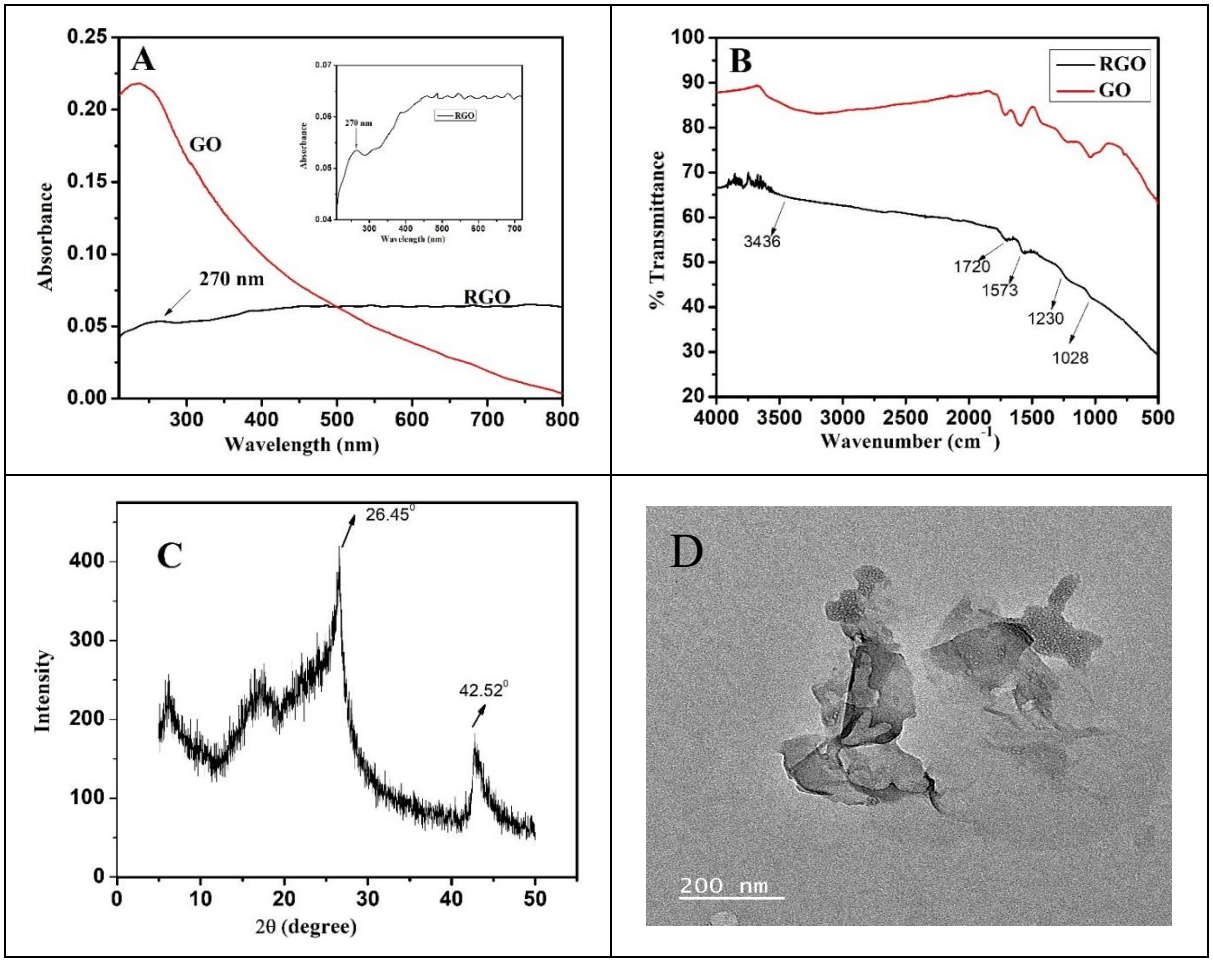

Fig. S1 (A) UV-vis spectra of GO and RGO, (B) FTIR spectra of GO and RGO, (C) XRD of RGO and (D) HR-TEM image of RGO nanosheet.

Table S1. Variation in the lifetime component (TCSPC) of the BM proteins in the presence of different concentrations of GO/RGO nanosheet.

[GO] (mg/L)	τ_1(ns)	A_1(%)	τ_2(ns)	A_2(ns)	$<\tau>$(ns)
0	1.89	28.08	6.20	71.92	3.78
0.79	1.69	35.45	5.95	64.55	3.14
4.74	1.60	34.51	5.88	65.49	3.06
13.89	1.55	32.82	5.75	67.18	3.05
33.69	1.56	35.08	5.90	64.92	2.98
67.77	1.43	33.07	5.80	66.93	2.88
113.41	1.40	34.78	5.78	65.22	2.77
[RGO] (mg/L)					
0.79	1.89	28.28	6.18	71.72	3.77
4.74	1.92	28.74	6.24	71.51	3.79
13.89	1.91	29.68	6.3	70.05	3.75
67.77	1.84	28.98	6.25	70.38	3.69
113.41	1.82	28.95	6.11	71.78	3.68

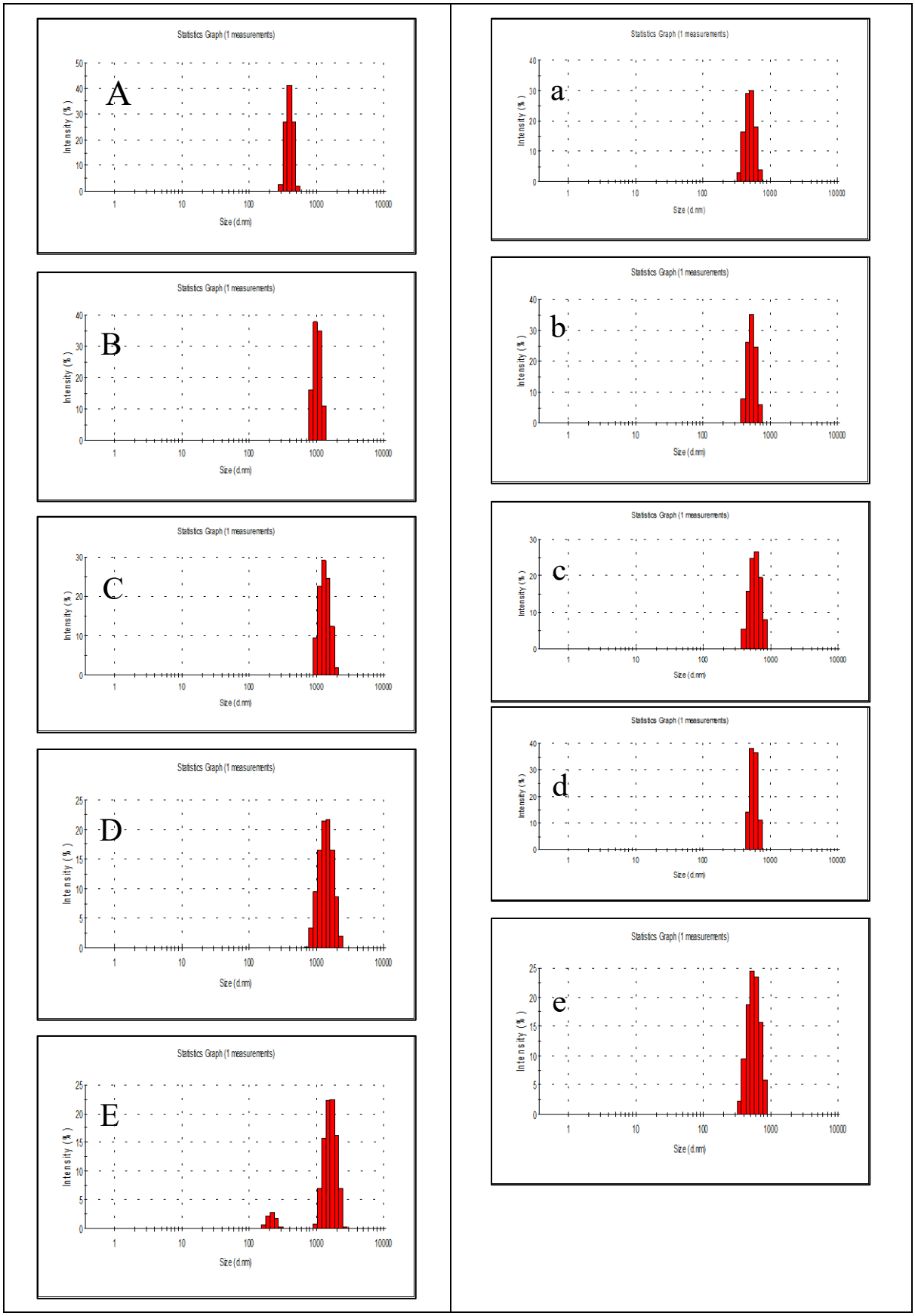

Fig. S2 Variation in the DLS intensity plot of GO (A-E), and RGO (a-e) upon incubation with different concentration of BM proteins.

References:

1. Zhang, Y., Ma, H. L., Zhang, Q., Peng, J., Li, J., Zhai, M., & Yu, Z. Z. Facile synthesis of well-dispersed graphene by γ-ray induced reduction of graphene oxide. *J. Mater. Chem.* **22**, 13064–13069 (2012).

2. Shahriary, L. & Athawale, A. A. Synthesis of graphene using gamma radiations. *Bull. Mater. Sci.* **38**, 739–745 (2015).

3. Zhao, X., Zhang, Q., Chen, D. & Lu, P. Enhanced mechanical properties of graphene-based poly (vinyl alcohol) composites. *Macromolecules* **43**, 2357–2363 (2010).

4. Paredes, J. I., Villar-Rodil, S., Martínez-Alonso, A. & Tascon, J. M. D. Graphene oxide dispersions in organic solvents. *Langmuir* **24**, 10560–10564 (2008).

5. Hidayah, N. M. S., Liu, W. W., Lai, C. W., Noriman, N. Z., Khe, C. S., Hashim, U., & Lee, H. C. Comparison on graphite, graphene oxide and reduced graphene oxide: Synthesis and characterization. in *AIP conference proceedings* vol. 1892 (AIP Publishing, 2017).

6. Sharma, N., Sharma, V., Jain, Y., Kumari, M., Gupta, R., Sharma, S. K., & Sachdev, K. Synthesis and characterization of graphene oxide (GO) and reduced graphene oxide (rGO) for gas sensing application. in *Macromolecular symposia* vol. 376 1700006 (Wiley Online Library, 2017).

7. Fu, C., Zhao, G., Zhang, H. & Li, S. Evaluation and characterization of reduced graphene oxide nanosheets as anode materials for lithium-ion batteries. *Int. J. Electrochem. Sci.* **8**, 6269–6280 (2013).

Summary and conclusions

The first chapter begins by discussing the synthesis and characterization of graphene oxide (GO) nanosheets, followed by a systematic study of how these GO nanosheets and two cationic surfactants affect the photophysical and aggregation properties of the popular laser dye Coumarin 153 (C153). This investigation employs various spectroscopic and physicochemical techniques. The experimental results indicate that GO serves as a strong fluorescent quencher of the C153 dye. In the presence of GO nanosheets, C153 experiences H-type aggregation, leading to significant changes in its photophysical properties. The aggregation of C153 molecules is disrupted by the presence of surfactants at and above their critical micelle concentration (CMC). The 16-4-16 Gemini surfactant demonstrates a greater effectiveness in altering the photophysical and aggregation properties of C153 compared to the CTAT surfactant. Moreover, the quenched fluorescence spectra of the GO-C153 system begin to intensify again in the presence of surfactants, indicating that the GO-C153-Surfactant ternary system can be effectively applied in laser spectroscopy.

The discussion of the second chapter includes the structural alteration of Cytochrome C (Cyt C) induced by two bile salts, namely NaDC and NaC, using various analytical techniques. In this context, bile salts act as mild denaturants, causing a loss of helical structures in Cyt C. Both electrostatic and hydrophobic interactions are responsible for the structural alterations of Cyt C by bile salts. The binding affinity of NaDC for Cyt C is greater than that of NaC, suggesting that the hydrophobicity of bile salts plays a crucial role in the interaction process. The electron transfer process of Cyt C is greatly modified in the presence of the two bile salts. This interaction study will indirectly contribute to understanding the cell apoptosis process.

The systematic study in Chapter three includes the preparation and characterization of long-chain ionic liquid-based vesicles ([C16Mim] [AOT]) and the interaction of this vesicular system with a model protein, HSA, using various physicochemical and spectroscopic techniques. Experimental results suggest that at $\alpha_{AOT} = 0.5$ and $\alpha_{AOT} = 0.6$, a cationic-rich and an anionic-rich vesicle is formed, respectively. The incorporation of the HSA protein in the cationic-rich vesicle results enhancement of vesicular size, signifying the formation of vesicle-HSA complex. In the HSA-cationic-rich vesicle complex both the protein and vesicle structure remain intact. But in the case of anionic-rich vesicle upon HSA incorporation its vesicular structure breaks down into small vesicle and also structural alteration of protein is observed.

Overall results indicates that in this case cationic-rich vesicle can be employed as an injectable drug delivery system (DDS).

The discussion of the fourth chapter includes Fenbufen assisted micelle to supermicelle aggregate formation of CTAB surfactants using various analytical techniques. Here a comparative analysis of the mixed micelle formation between the Fenbufen drug with a conventional CTAB and synthesized G-16 Gemini surfactants was studied. A small size of CTAB micelle allows it to accommodate large number of drug molecules on its micellar structure resulting formation of large supermiceller aggregate structure. Various types of supermicelle aggregate like spherical, linear, cross-linked etc, was observed. On the other hand, due to the large size of Gemini micelle it cannot hold many drugs molecules, resulting incorporation of the excess drug molecules leas to breaks down its micellar structure into small micelle. So, in the case of Gemini micelle no supermicelle type large aggregate formation takes place upon incorporation of drug molecules.

The systematic study of the fifth chapter includes the effect of the concentration and reduction of graphene oxide (GO) nanosheets on the stability and structural alteration of bromelain (BM) protein. The results indicate that BM interact more strongly with GO nanosheet compared to its reduced form (RGO). The BM protein cooperatively bind with GO whereas both cooperative and non-cooperative interaction involved between BM and RGO nanosheet. Both the covalent and non-covalent interaction present during the complexation of BM with GO nanosheets but mainly hydrophobic interaction plays crucial role during the complexation of BM with RGO nanosheets. In the presence of GO nanosheets a substantial structural alteration of BM observed whereas a minor structural change occurs in the presence of RGO. The adsorption of BM protein on the GO and RGO nanosheets leads to formation of a hard and soft protein corona, respectively.

Appendix
Basic Data

Chapter-I

1.1. Modified Stern-Volmer plot data, derived from fluorescence data, depicting the binding curves resulting from the adsorption of C153 on GO.

log [GO]	log[(F_0-F)/F]
-1.69897	-0.91349
-1.52288	-0.59063
-1.39794	-0.25519
-1.30103	-0.04466
-1.22185	0.06221

1.2. Stern-Volmer plot data for fluorescence quenching of C153 molecule in presence of various concentrations of graphene oxide aqueous solution.

[GO] /mg L^{-1}	F_0/F
0	1
20	1.122354
30	1.25664
40	1.55562
50	1.90224
60	2.15395

1.3. Time-dependent fluorescence quenching Stern-Volmer plot data of C153 with various concentrations of GO.

[GO] mgL^{-1}	τ_0/τ
0	1
10	1.05275
20	1.32223
40	1.9744
50	2.42489
60	2.82142

1.4. Variation in the absorbance data of C153 with the concentration of CTAT and 16-4-16 Gemini surfactant, respectively.

[CTAT] (mM)	Absorbance	[16-4-16] (mM)	Absorbance
0	0.081	0	0.088
0.03987	0.082	0.01246	0.089
0.07947	0.083	0.02483	0.09
0.11881	0.085	0.03713	0.091
0.15789	0.087	0.04934	0.093
0.19672	0.089	0.06148	0.096
0.23529	0.097	0.07353	0.097
0.27362	0.0996	0.0855	0.098
0.31169	0.102	0.0974	0.099
0.34951	0.104	0.10922	0.099
0.3871	0.105	0.12097	0.099
0.42444	0.107	0.13264	0.1
0.46154	0.107	0.14423	0.1

1.5. Variation in the fluorescence intensity data of C153 with the concentration of CTAT and 16-4-16 Gemini surfactant, respectively.

[CTAT] (mM)	Intensity	[16-4-16] (mM)	Intensity
0	195.66625	0	251.7519
0.01796	194.58159	0.00449	236.7031
0.03586	194.86703	0.00896	240.2679
0.07143	191.32028	0.01786	260.7338
0.10672	194.99536	0.02668	301.0224
0.14173	196.9715	0.03543	353.6692
0.17647	213.26737	0.04412	403.3851
0.19374	251.78945	0.05273	464.9397
0.21094	288.3975	0.06128	521.4678
0.22807	328.87214	0.06977	577.308
0.24514	369.10831	0.07819	636.2148
0.26214	410.82244	0.08654	688.9025
0.29594	449.91459	0.09483	734.7843
0.32948	512.12174	0.10305	775.9156
0.36276	564.94812	0.11122	809.867
0.39579	608.39505	0.11932	841.7174
0.42857	651.74948	0.12736	872.7796
0.4611	707.65347	0.13534	894.0487
0.49338	737.74196		
0.52542	784.01828		

1.6. The data of the extension of Hildebrand-Benesi model for CTAT-C153, and 16-4-16-C153 systems, respectively.

$C_S + C_D$ (M) (CTAT)	$[(C_S C_D/\Delta Abs) + (\Delta Abs/\Delta\varepsilon^2)]$	$C_S + C_D$ (M) (16-4-16 Gemini)	$[(C_S C_D/\Delta Abs) + (\Delta Abs/\Delta\varepsilon^2)]$
2.45E-04	1.47E-07	7.15E-05	7.91E-08
2.84E-04	1.47E-07	8.35E-05	8.42E-08
3.22E-04	1.49E-07	9.55E-05	8.83E-08
3.60E-04	1.52E-07	1.07E-04	9.16E-08
3.97E-04	1.62E-07	1.19E-04	1.02E-07
4.34E-04	1.64E-07	1.31E-04	1.13E-07
4.72E-04	1.78E-07	1.43E-04	1.14E-07
		1.54E-04	1.24E-07

Chapter-II

2.1. Absorbance data of Cyt C (taking absorbance at 409nm) with concentrations of NaDC and NaC respectively.

[NaDC] (mM)	Absorbance	[NaC] (mM)	Absorbance
0	0.48866	0	0.4989
0.08982	0.47731	0.2994	0.48865
0.17928	0.47133	0.59761	0.48073
0.26839	0.46718	0.89463	0.47955
0.44554	0.461	1.77866	0.47365
0.6213	0.456	2.3622	0.4722
1.14035	0.45134	2.81279	0.47066
1.39535	0.44749	3.47035	0.4682
1.6474	0.44632	4.0856	0.46552
1.89655	0.44336	4.75923	0.46442
2.14286	0.4417	5.27908	0.4617
2.46692	0.43958	6.32184	0.45882
2.78612	0.43689	7.14286	0.45499
2.46692	0.43958	7.95455	0.45612
2.78612	0.43689	8.75706	0.45424
3.29058	0.4352	9.95647	0.45035
3.80591	0.4352	10.85343	0.44858

4.15512	0.43475	11.87845	0.44501
4.52509	0.4341	12.88848	0.44324
4.89305	0.43355	13.88385	0.44153
5.31746	0.43164		
5.73298	0.43102		
6.1399	0.42984		
6.53846	0.42891		

2.2. Fluorescence intensity data of Cyt C with the varying concentration of NaDC and NaC, respectively.

[NaDC] (mM)	Intensity	[NaC] (mM)	Intensity
0.11486	12.7541	0	11.83905
0.38668	14.77596	0.36709	13.38579
0.63358	16.43716	0.59761	13.79112
1.14035	17.02493	1.07262	14.69672
1.47969	17.57985	1.77866	15.25862
1.97897	19.21193	2.89451	15.67213
2.46692	20.11221	3.99578	16.05246
3.10056	20.99368	6.01688	16.70328
3.7156	23.59614	7.41445	17.29481
4.45946	26.70019	9.55056	20.09526
5.17699	30.73204	12.49789	22.53115
5.86957	33.70937	13.63636	23.68942
6.45503	36.20765	16.07143	26.38953
7.18487	39.20672		
7.80992	41.75719		
8.65105	45.19976		
9.29101	47.04918		

2.3. Benesi-Hildebrand plot data of $1/(I-I_0)$ against 1/ [bile salt] for binding of Cyt C with NaDC and NaC, respectively.

1/[NaDC] (mM^{-1})	$1/(I-I_0)$	1/[NaC] (mM^{-1})	$1/(I-I_0)$
5.48956	0.78902	2.64057	0.6671
3.81224	0.59869	1.67333	0.51228
1.73074	0.31467	0.98201	0.3565
1.08716	0.21287	0.66733	0.28995
0.81668	0.18066	0.49484	0.24825
0.57884	0.14844	0.37717	0.22911
0.52909	0.13246	0.25183	0.176
0.44359	0.11377	0.18016	0.16907
0.31368	0.09529	0.10471	0.12112
0.26055	0.07462	0.05789	0.11296
0.13891	0.06557	0.03076	0.10443
0.17037	0.04477	0.00766	0.0918
0.15294	0.04527		
0.13891	0.03877		
0.12804	0.03566		
0.11559	0.03061		
0.10576	0.02891		

Chapter-III

3.1. Variation in turbidity data of aqueous [C_{16}Mim] [AOT] mixture at various mole fractions of AOT.

α_{AOT}	Turbidity
0	0.834
0.2	1.33
0.4	23.08
0.5	99.689
0.6	99.777
0.8	27.74
1	2.925

3.2. Variation in steady-state anisotropy data of [C_{16}Mim] [AOT] mixture with varying mole fraction of AOT.

α_{AOT}	Anisotropy
0	0.026
0.2	0.032
0.4	0.056
0.5	0.109
0.6	0.126
0.8	0.054
1	0.023

3.3. Change in hydrodynamic diameter (D_h) data of [C_{16}Mim] [AOT] aggregate in different mole fractions.

α_{AOT}	Diameter (nm)
0.2	98.52
0.4	153.34
0.5	249.36
0.6	244.82
0.8	162.36

3.4. Benesi-Hildebrand plot data of 1/(A-A_0) against 1/ [C_{16}Mim-AOT] for binding of HSA with [C_{16}Mim]/[AOT] with the 0.5-mole fraction, and 0.6-mole fraction of AOT.

1/([C_{16}Mim-AOT]/mM) (α_{AOT} = 0.5)	1/A-A_0	1/([C_{16}Mim-AOT]/mM) (α_{AOT} = 0.6)	1/A-A_0
4.35721	2.01495	3.95472	2.26183
3.90875	1.80789	3.78282	2.19804
3.54652	1.64441	3.62571	2.09899
3.24785	1.47811	3.48156	2.02827
2.99735	1.40542	3.34883	1.95718
2.78424	1.30548	3.22621	1.85021
		3.11259	1.79753

3.5. Stern Volmer plot data, variation of (F_0- F)/F of HSA as a function of [C_{16}Mim-AOT] at 0.5-mole fraction, and 0.6-mole fraction of AOT.

([C_{16}Mim-AOT]/mM) (α_{AOT} = 0.5)	$(F^0-F)/F$	/([C_{16}Mim-AOT]/mM) (α_{AOT} = 0.6)	$(F^0-F)/F$
0.09473	0.00463	0.07312	0.02369
0.12211	0.03644	0.09119	0.03818
0.14927	0.0548	0.11514	0.07649
0.17622	0.0743	0.13894	0.09683
0.25584	0.14354	0.16848	0.13371
0.34642	0.19126	0.24134	0.20846
0.4594	0.24985	0.32692	0.29283
0.59243	0.28178	0.42432	0.3745
0.76542	0.30898	0.54582	0.45356
0.97169	0.32099	0.68891	0.49491
1.19426	0.32455	0.86294	0.53005
1.41922	0.3215	1.07438	0.57661
1.62756	0.33377	1.29446	0.59863
		1.3991	0.61574

3.6. Modified Stern Volmer plot data of 0.5-mole fraction, and 0.6-mole fraction of AOT binding with HSA, depicting the variation of F_0/F_0-F as a function of [C_{16}Mim-AOT] $^{-1}$

1/([C_{16}Mim-AOT]/mM) (α_{AOT} = 0.5)	F_0/F_0-F	1/([C_{16}Mim-AOT]/mM) (α_{AOT} = 0.6)	F_0/F_0-F
2.17674	4.9259	2.43116	3.58866
1.68796	4.56164	1.83212	3.20477
1.30647	4.33836	1.45157	3.02055
1.02913	4.1623	1.15883	2.8866
0.83734	4.08116	0.93077	2.73429
0.70461	4.03049	0.77252	2.67049
0.61442	3.97672	0.71475	2.62406

3.7. Variation of zeta potential value data of [C_{16}Mim] [AOT] vesicle with increasing concentration of HSA; (A) 0.5 mole fraction, and (B) 0.6 mole fraction of AOT, respectively.

[HSA] (μM)	Zeta potential (mV) ($\alpha_{AOT=0.5}$)	[HSA] (μM)	Zeta potential (mV) (($\alpha_{AOT=0.6}$)
0	63.5	0	-71.9
0.10541	54.3	0.52113	-49.9
0.31445	37.6	1.02778	-41.1
0.52113	27.3	1.52055	-31.4
1.02778	11.6	2	-31.7
1.52055	-7.12	2.92105	-29
2	-9.74	4.21519	-31
2.46667	-11.2		
2.92105	-11.8		

Chapter-IV

4.1. Hydrodynamic diameter (D_h) data of CTAB/FB and G-16-FB mixed system at different mole fractions of FB at 298.15 K.

α_{AOT}	D_h(nm) (CTAB-FB System)	D_h(nm) (G-16-FB System)
0	1.294	190.1
0.2	7.531	164
0.4	6.503	295.3
0.5	122	255
0.6	545	10.1
0.8	548.3	13.54

4.2. Zeta potential (ζ) data of FB/CTAB and FB/G-16 systems at different mole fractions of FB.

α_{AOT}	Zeta potential (mV) (CTAB-FB System)	Zeta potential (mV) (G-16-FB System)
0	24.9	15.1
0.2	16.3	44.3
0.4	25.8	23.2
0.5	15.6	19.3
0.6	1.02	-11.6
0.8	-11.5	-3.93
1	-15.9	-15.9

4.3. Steady-state anisotropy data of FB/CTAB and FB/G-16 systems at different mole fractions of FB.

α_{AOT}	Anisotropy (CTAB-FB System)	Anisotropy (G-16-FB System)
0	0.071	0.08
0.2	0.175	0.028
0.4	0.219	0.28
0.5	0.241	0.204
0.6	0.267	0.19
0.8	0.256	0.17
1	0.154	0.154

Chapter-V

5.1. Data of the Stern-Volmer plots of the fluorescence quenching of the BM with varying concentrations of GO and RGO nanosheets, respectively.

[GO] (mg/L)	F_0/F	[RGO] (mg/L)	F_0/F
0	1	0	1
1.08239	1.06886	5.90273	1.05454
1.72481	1.10645	14.64355	1.12055
2.85941	1.19764	23.19787	1.18803
4.43038	1.34698	28.49878	1.22973
5.98897	1.49842	36.7555	1.29208
7.53532	1.6421	46.76549	1.38066
9.06959	1.7826	57.77149	1.47541
10.07395	1.88183	66.55785	1.59656
11.59893	2.08333	71.59278	1.6711
13.22652	2.32104	76.89822	1.78126
14.34632	2.48228	84.1217	1.88842
15.96869	2.75273	87.01095	2.0032
17.39107	3.04303	91.83359	2.12321

5.2. Hill plots data of the fluorescence quenching of BM in the presence of GO and RGO nanosheets with increasing concentration.

[GO] mg/L	$(F_0- F)/F_0$	[RGO] mg/L	$(F_0- F)/F_0$
0	0	0	0
0.32245	0.02425	0.7984	0.02069
0.67688	0.04701	1.59363	0.01861
1.08239	0.06442	5.52268	0.05515
1.72481	0.09621	10.89494	0.08989
2.30446	0.1406	19.04762	0.1314
2.85941	0.16502	23.35217	0.16607
3.64645	0.21149	31.67587	0.20447
4.43038	0.2576	35.70128	0.22801

[GO] mg/L	$(F_0- F)/F_0$	[RGO] mg/L	$(F_0- F)/F_0$
0	0	0	0
5.21121	0.29473	39.63964	0.25162
5.98897	0.33263	44.38708	0.27159
6.72552	0.35589	51.65667	0.29873
7.53532	0.39102	54.85676	0.32845
8.30396	0.4134	67.09527	0.38786
9.06959	0.43902	72.39618	0.40159
9.83223	0.4771	84.9034	0.4405
10.73618	0.50499	89.96003	0.4508
11.34862	0.52758	97.67932	0.46901
12.31246	0.56072		
13.12569	0.59126		
13.83278	0.6088		
15.39918	0.64055		
16.97257	0.67331		

5.3. ITC data of BM-GO/RGO complexation. Integrated heat data for the reaction of BM proteins with GO, and RGO nanosheets.

[BM]/[GO] $\mu M/mg.\ L^{-1}$	ΔH (kcal/mol)	[BM]/[RGO] $\mu M/mg.\ L^{-1}$	ΔH (kcal/mol)
0.00199	-159.98328	0.00199	12.2172
0.00395	-159.97065	0.00395	12.21021
0.00588	-159.94745	0.00588	12.19624
0.00779	-159.91055	0.00779	12.17529
0.00968	-159.85151	0.00968	12.14735
0.01154	-159.74023	0.01154	12.11242
0.01338	-156.5847	0.01338	12.07051
0.01519	-148.82514	0.01519	12.0216
0.01698	-87.21311	0.01698	11.96567
0.01875	-82.43169	0.01875	11.90267
0.0205	-80.95628	0.0205	10.68033
0.02222	-80.04492	0.02222	6.13115
0.02393	-80.01694	0.02393	-27.85923
0.02561	-80.00113	0.02561	-60.06557
0.02727	-79.99049	0.02727	-62.20492
0.02892	-79.98236	0.02892	-62.61061
0.03054	-79.97554	0.03054	-62.61646
0.03214	-79.96946	0.03214	-62.62251
0.03373	-79.96377	0.03373	-62.6288

5.4. Zeta potential (ζ) value of GO and RGO nanosheets in the presence of different concentrations of BM.

[BM] (mg/L)	ζ (mV)	[BM] (mg/L)	ζ (mV)
0	-35	0	-21.5
3.41	-34.1	5.8	-18.7
11.92	-33.7	11.9	-15.6
16.23	-21.5	19.28	-15.4
25.44	-14.3	25.6	-16.4
39.22	-10.3	31.7	-17.3
58.12	-10.5	38.92	-16.5
64.1	-10.9	58.7	-16.3
75.5	-10.8		

List of

Publications and Reprints

For Thesis:

1. Exploration of the impact of graphene oxide, acetylenic gemini, and CTAT on the photophysical and aggregation properties of dipolar coumarin 153, **R. Sardar, S.** Das, R. Banik, S. Bhunia, and S. Ghosh. ***Physical Chemistry Chemical Physics***, 2024, *26*(11), 8900-8918.

2. Hydrophobicity-directed structural alteration in cytochrome C induced by bile salts: physicochemical, spectroscopic, and atomic force microscopic studies with molecular docking analysis, **R. Sardar**, R. Banik, S. Chowdhury, and S. Ghosh. ***New J. Chem***. **49**, 12289–12305 (2025)

Other Publications:

3. Comparative study of the aggregation behavior of some ionic surfactants with Nonionic Triton X-114 in Water and a Water/2, 2, 2-Trifluoroethanol mixture; R. Banik, B. B. Mondal, **R. Sardar** and S. Ghosh, ***Industrial & Engineering Chemistry Research***, 2024, *63*(7), 3057-3071.

4. A physicochemical investigation of the complex formation by β-cyclodextrin with Triton X-100 and Triton X-114 and their aggregation behaviour in aqueous solution: an experimental approach. R. Banik, **R. Sardar,** B. B Mondal, and S. Ghosh (2025). ***Physical Chemistry Chemical Physics*.**

5. An inclusive comparison regarding aggregation of surface-active ionic liquid and conventional surfactant with a cationic dye Acridine Red exposed in view of spectroscopic and theoretical study, S. Bandyopadhyay, R. Banik, **R. Sardar,** and S. Ghosh, (2024). ***Journal of Molecular Liquids,*** *411*, 125684.

6. Aggregation and characterization of the microenvironment of solvatochromic eosin yellow dye in the presence of zwitterionic, cationic, and anionic surfactants: A spectroscopic and theoretical approach; S. Bandyopadhyay, R. Banik, **R. Sardar** and S. Ghosh (2025). ***Journal of Molecular Liquids,*** 127953.

Poster Presentation:

1. Presented a poster at the 21th National Conference on Surfactants, Emulsions & Biocolloids (NATCOSEB – XXI) on 23-25th November, 2023. **(Topic: Explore the impact of Graphene Oxide (GO), Acetylenic Gemini, and CTAT on the Photophysical and Aggregation Properties of Dipolar Coumarin-153).**

2. Presented a poster at the International Conference on Emerging Trends in Chemical Sciences Towards Sustainability & Interdisciplinarity (ETCSTSI-2025) on 10-11th January, 2025. **(Topic: Hydrophobicity Directed Structural Alteration of Cyt C Induced by Bile Salt).**

PCCP

PAPER

View Article Online
View Journal | View Issue

Cite this: *Phys. Chem. Chem. Phys.*, 2024, **26**, 8900

Exploration of the impact of graphene oxide, acetylenic gemini, and CTAT on the photophysical and aggregation properties of dipolar coumarin 153†

Raju Sardar, Sourav Das, Rajesh Banik, Sayani Bhunia and Soumen Ghosh *

Advanced spectroscopic techniques have been utilized to study the interaction between the laser dye coumarin 153 (C153) and graphene oxide (GO) nanoparticles. GO was synthesized using a modified Hummers' method and characterized by UV-vis spectroscopy, Raman laser spectroscopy, FTIR-ATR spectroscopy, FESEM, HR-TEM, and XRD techniques. The GO@C153 composite was formed by mixing two aqueous solutions of GO and C153 due to their strong interaction through stacking and hydrophobic interactions. In this case, GO acts as an effective fluorescence quencher for C153 molecules, which undergo H-type aggregation in the presence of GO. The Stern–Volmer equation and time-dependent fluorescence studies were utilized to analyse the mechanism of fluorescence quenching. According to the findings, both static and dynamic quenching processes are responsible for the reduction in fluorescence intensity. The effect of surfactants (both cetyltrimethylammonium *p*-toluenesulfonate (CTAT) and synthesized *N*,*N*′-dihexadecyl-*N*,*N*,*N*′,*N*′-tetramethyl-*N*,*N*′-but-2-ynediyl-di-ammonium chloride (16-4-16)) on the aggregation and photophysical properties of the dye was investigated using surface tensiometry, conductometry, UV-vis absorption spectroscopy, steady-state fluorescence measurements, DLS, and time-dependent fluorescence spectroscopy. Surfactants change the microenvironment of the C153 dye, leading to spectrum shifting and a higher quantum yield, which causes a rapid rise in fluorescence intensity in the micellar medium. It has been noted that in a micellar medium rather than in an aqueous one, the luminous intramolecular charge transfer (ICT) state of C153 stabilises. Lastly, we investigated the photophysical behavior of the GO–C153–micelle ternary system and discovered that, in the presence of a micellar medium, the quenched and blue-shifted (H-type aggregation) fluorescence peak of C153 (in the presence of GO) began to intensify once more. The main goal of this work is to create an effective and fairly cost powerful fluorescence sensor. Additionally, the ternary system (GO–C153–micelle) analytical idea can be employed to identify the onset of micelle formation. In wastewater treatment analysis, the GO–C153–surfactant ternary system concept can also be used to regenerate the adsorbent (in this case, GO) from dye molecules by allowing the dye molecules to exit the adsorbent and enter the micellar medium.

Received 5th November 2023,
Accepted 15th February 2024

DOI: 10.1039/d3cp05361j

rsc.li/pccp

1. Introduction

In recent years, investigation of graphene and its derivatives has been one of the most important and challenging areas of research in nanomaterials science. Graphene is a two-dimensional, single-atom, thick nano-material having sp^2 hybridized carbon atoms with a hexagonal honey-comb sheet-like structure. Since graphene was discovered in 2004, its exceptional mechanical and optical properties,[1–6] numerous biological applications,[7] and technological uses[8–10] have made graphene research a very significant subject of study. Efforts are being made to establish a low-cost and efficient method of synthesizing and using graphene derivatives and related materials because of the vast array of applications of graphene. Graphene oxide (GO) is one of the most important derivatives of graphene, which is cheap and abundant and synthesized by the strong oxidation of graphite powder. Due to oxidation, the band gap of graphene oxide is larger than that of graphene, which has a zero-band gap. As a result of its large band gap, graphene oxide shows extraordinary optical properties,[11–18] which are somehow limited in the case of graphene due to its zero-band

Centre for Surface Science, Physical Chemistry Section, Department of Chemistry, Jadavpur University, Kolkata 700032, India. E-mail: gsoumen70@hotmail.com

† Electronic supplementary information (ESI) available. See DOI: https://doi.org/10.1039/d3cp05361j

gap. At the same time, due to the presence of various oxygen-containing groups (such as hydroxyl, epoxy, and carboxyl) on the surface and edges of the graphene oxide sheet,[19,20] it can be functionalized easily by covalent and non-covalent bonding, and its various properties are changed. The modified graphene oxides are more useful for applications.[9,21,22] There are a huge number of ways in which GO can be functionalized depending on its application. In recent times, the dye–GO nanocomposite has become a popular research topic with a lot of applications in biodevices, drug delivery, and optoelectronic materials. There are various types of interactions involved in dye–GO nanocomposite formation, such as electrostatic interactions, π–π interactions, and other types of interactions.

Currently, we investigate the effects of surfactant solutions (including synthetic 16-4-16 and traditional CTAT) and GO nanoparticles on the photophysical characteristics and aggregation of coumarin 153 (C153), a well-known laser dye from the coumarin family. In this experiment, we have investigated the individual, as well as the combined, impacts of surfactants and GO nanoparticles on the aggregation and photophysical behaviours of C153 dye molecules. Understanding the photophysical behavior of coumarin 153 in a composite and the interaction between C153 and graphene oxide is crucial due to their efficacy as fluorescence quenchers.[23–30] The large π-cloud of graphene oxide can be easily interacted with the coumarin 153 dye molecule's π-cloud through a process known as 'π–π stacking interaction'. The quenching of fluorescence emission is a process that indicates a decrease in the fluorescence intensity of a fluorophore, and the mechanism of fluorescence quenching is analysed using the Stern–Volmer (SV) equation.[31] Apart from fluorescence quenching, the aggregation of the dye molecule is also very important; spectral shifts are observed in the absorption and fluorescence spectra depending upon the molecular orientation of the dye molecule in the aggregated state. In organic dye molecules, generally, two types of aggregation are observed, namely H-type aggregation and J-type aggregation.[32,33] In H-type aggregation, the dye molecule is staggered in a face-to-face fashion, and a blue shift of the absorption peak is observed, but in the case of J-type aggregation, the dye molecule is aligned in an edge-to-edge configuration, and a red shift of the absorption peak is observed.[34] The extent of aggregation entirely depends on the temperature, the nature of the dye molecule, and the entire composition of the solution.

However, because the aggregation and photophysical characteristics of the C153 dye rely on the kind of solvent, it is equally crucial to analyse solvation dynamics.[35,36] In contrast to a non-polar medium, which shows a maximum fluorescence band that shifts to a lower wavelength, C153 exhibits a low fluorescence quantum yield and a short fluorescence lifetime in a strongly protic polar solvent. This is due to the fact that the intramolecular charge transfer (ICT) state of the C153 molecule is less likely to occur in a polar medium than in a non-polar one.[37] The fluorescent ICT state is a special type of excited state in which the electron cloud localized mostly in the amine group (donor group) in the ground state is transferred to the acceptor carbonyl group in the excited state.[38] Due to this special property, C153 is an excellent probe for researching the self-assembly of amphiphile molecules. Additionally, because C153 is a hydrophobic molecule, it preferentially resides in the core of the micelle. This photophysical characteristics of C153 make it an excellent probe for figuring out the critical micelle concentration (CMC) of surfactants and other amphiphiles. Here, we use a multi-technical method to investigate the aggregation and photophysical characteristics of the C153 dye, including surface tension, conductance, UV-vis absorption, steady-state and time-resolved fluorescence, *etc.*

2. Experimental section

2.1. Chemicals and reagents

Coumarin 153 (C153), hexadecyl trimethyl ammonium *p*-toluene sulfonate (CTAT), *N*,*N*-dimethyl hexadecyl amine, and 1,4-dichloro-2-butyne were purchased from Sigma-Aldrich. Natural graphite flakes (Alfa Aesar), potassium permanganate ($KMnO_4$), sodium nitrate ($NaNo_3$), hydrogen peroxide (30%, H_2O_2), and sulphuric acid (H_2SO_4, 98%) were purchased from Merck. For preparing the stock solution of C153 (1.0×10^{-3} M), ethanol was used as solvent. The aqueous solution of C153 was prepared by diluting the stock solution of C153. All the chemicals mentioned above were used without further purification and all the experiments were performed at room temperature.

2.2. Instrumentation

2.2.1. Tensiometry. The Krüss (Germany) tensiometer was employed with the ring detachment method for surface tension measurements. Using a Hamilton microsyringe, a concentrated stock solution of surfactants in an aqueous medium was added to water gradually. Each measurement was preceded by a 5-minute equilibration period. To ensure accuracy, each measurement was carried out three times. The method's accuracy was 0.1 mN m^{-1}. Surface tension (γ) *vs.* log[surfactant] was plotted to determine the CMC, and from the breaks in the plot, the CMC was calculated.

2.2.2. Field emission scanning electron microscopy (FESEM). An FESEM, Model FEI INSPECT F50 (Japan), was used to analyse the surface morphologies of GO. The drop-cast sample solutions were adequately dried before being gold-plated using the sputtering process for 1 minute at 298 ± 1 K at 5.5 mA current.

2.2.3. Electrical conductivity measurements. An Eütech (Singapore) conductivity meter was used to measure electrical conductivity with a cell constant value of 1 cm^{-1}. The temperature of the solution was kept constant at 298 K using a water bath with a precision of ±0.1 K. Using a Hamilton microsyringe, stock solution prepared in a specific solvent (about ~15 times the CMC) was progressively added to a container containing 6 mL of the solvent. After each addition, followed by homogeneous mixing, the value of the specific conductance (κ) was recorded. Each measurement was carried out three times, and the average result was recorded with an

error of 2 s. The CMC values were calculated from the break points in the specific conductance (κ) *vs.* surfactant concentration graphs.

2.2.4. Steady-state spectral measurements. A Shimadzu 1601 UV-vis spectrophotometer from Japan and a PerkinElmer LS 55 fluorescence spectrophotometer from the United States were used to record the absorption and fluorescence emission spectra respectively. At an excitation wavelength of 422 nm, the emission spectra of coumarin 153 dye in the aqueous dispersion of GO were recorded within the range of 450–700 nm, using an emission slit width of 5 nm and an excitation slit width of 10 nm. All spectroscopic experiments were carried out with freshly prepared solutions containing a low concentration of the dye coumarin 153 (10^{-5} M).

2.2.5. Time-resolved fluorescence study. A Horiba–Jobin–Yvon FluoroCube fluorescence lifetime system was utilised to perform time-resolved fluorescence decay measurements. The coumarin 153 dye was excited by a NanoLED at 450 nm from IBH, UK, and a TBX photon detection module served as the detector. The IBH DAS-6 decay analysis software was used to fit all of the decay data. The lamp profile was recorded using a dilute micellar solution of sodium dodecyl sulphate as a scatter in place of the sample. The χ^2 values were maintained quite near to unity for the suitable fittings.

2.2.6. Dynamic light scattering (DLS) and zeta potential measurements. DLS and zeta potential measurements were performed using a Zetasizer Nano ZS (Malvern, UK) at a scattering angle of 90° using an He–Ne laser (λ = 632.8 nm). To get rid of bigger particles, all of the solutions were filtered three times using membrane filters with 0.25 μm porosity. To obtain more precise results, each measurement was repeated twice and the mean values were reported. Standard deviation of the measurements was 7–9%.

2.2.7. Transmission electron microscopy (TEM). A carbon-coated copper grid with a mesh size of 300 was used to adsorb 10 μL of sample solutions with a specific mole fraction. Excess liquid on the copper grid was immediately removed using the filter paper on which it was placed. It was stained negatively using freshly made 0.5 wt% aqueous uranyl acetate. The samples were stored overnight in a desiccator. A JEOL-JEM 2100 transmission electron microscope from Japan was employed, with an accelerating voltage of 100 kV.

2.2.8. Raman laser spectroscopy. Raman spectra of the graphite flakes and graphene oxide (GO) were recorded on a Triple Raman spectrometer of model no. T64000 made by Horiba, Jobin Yvone equipped with 1800 grooves per mm gratings, a TE Cooled Synapse CCD (J-Y Horiba) and an open stage Olympus microscope with a 100× objective. Samples were excited at λ = 532 nm with a laser power of 1.7 mW [Ar^+ laser (Model: Stabilite 2017), Spectra Physics] and a numerical aperture (NA) of 0.9.

2.2.9. Powder X-ray diffraction (PXRD). Powder X-ray diffraction (PXRD) patterns of the samples were recorded with a Bruker D8 Advance X-ray diffractometer using monochromatic Ni-filtered Cu Kα (λ = 1.5406 Å) radiation. Data were collected from 10° to 60° at a scan rate of 0.1° per minute.

2.2.10. ^{1}H-NMR spectroscopy. ^{1}H-NMR spectra were recorded using a Bruker DPX-300 (300 MHz) spectrometer at ambient temperature in $CDCl_3$ using tetramethyl silane as an internal standard.

2.2.11. FTIR-ATR spectroscopy. FTIR spectra were recorded on a PerkinElmer (model no. Spectrum Two) FTIR spectrometer using the attenuated total reflectance (ATR) technique. An $LiTiO_3$ detector was used to record the spectra. The process involved obtaining samples on a diamond plate, adjusting the pressure, and conducting measurements within the wavelength range of 500 to 4000 cm^{-1}.

2.3. Synthesis of materials

2.3.1. Synthesis of graphene oxide (GO). A modified Hummers' method[39] was executed for the synthesis of graphene oxide (GO) (Fig. S1, ESI†). The detailed synthesis procedure is documented in the ESI.†

2.3.2. Synthesis of *N*,*N*′-dihexadecyl-*N*,*N*,*N*′,*N*′-tetramethyl-*N*,*N*′-but-2-ynediyl-di-ammonium chloride (16-4-16). The dicationic gemini surfactant *N*,*N*′-dihexadecyl-*N*,*N*,*N*′,*N*′-tetramethyl-*N*,*N*′-but-2-ynediyl-di-ammonium chloride (16-4-16 gemini) was synthesized as per the procedure mentioned by Menger *et al.*[40] and the synthesized gemini surfactant was characterised by ^{1}H-NMR (spectra are given in the ESI,† Fig. S2 and S3).

2.4. Characterization of GO

The absorbance maximum (*cf.* Fig. 1(a)) of GO was observed at around 237 nm for the π–π* transition of the aromatic C–C bond and at around 300 nm for the n–π* transition (shoulder band).[41]

GO shows a broad peak (Fig. 1(b)) between 3000 and 3600 cm^{-1} in the high-frequency region, corresponding to the stretching and bending vibrations of OH groups of water molecules adsorbed on the graphene oxide layer. The absorption peaks at 2917 cm^{-1} and 2845 cm^{-1} represent the symmetric and anti-symmetric stretching vibrations of CH_2.[42] The presence of two absorption peaks was observed at 1626 cm^{-1} and 1714 cm^{-1} due to the stretching vibration of C=C and C=O of carboxylic acid and carbonyl groups present at the edges of graphene oxide, respectively.[41] The absorption peaks at 1052 cm^{-1}, 1216 cm^{-1} and 1364 cm^{-1} correspond to the stretching vibrations of C–O of alcohol, C–O–C of epoxy, and C–O of carboxylic acid, respectively. The presence of these oxygen-containing groups indicates that the graphite has been oxidized. Further evidence of GO's hydrophilic nature comes from the hydrogen bonds that its surface hydroxyl groups make with water molecules.

X-ray diffraction patterns (XRD) of graphite flakes and GO are presented in Fig. 1(c). Graphite shows an intense and sharp peak at 2θ = 26.6° with an interplanar (002) spacing of 0.334 nm.[43] The sharp XRD pattern of graphite implies structural integrity in the layer structures of carbon nanomaterials. In the case of GO, the shifting of the 2θ peak to 10.12° is detected with an increment of interplanar (001) spacing of 0.961 nm, which indicates that the graphite is fully oxidized into graphene oxide.[44] This increment can result from

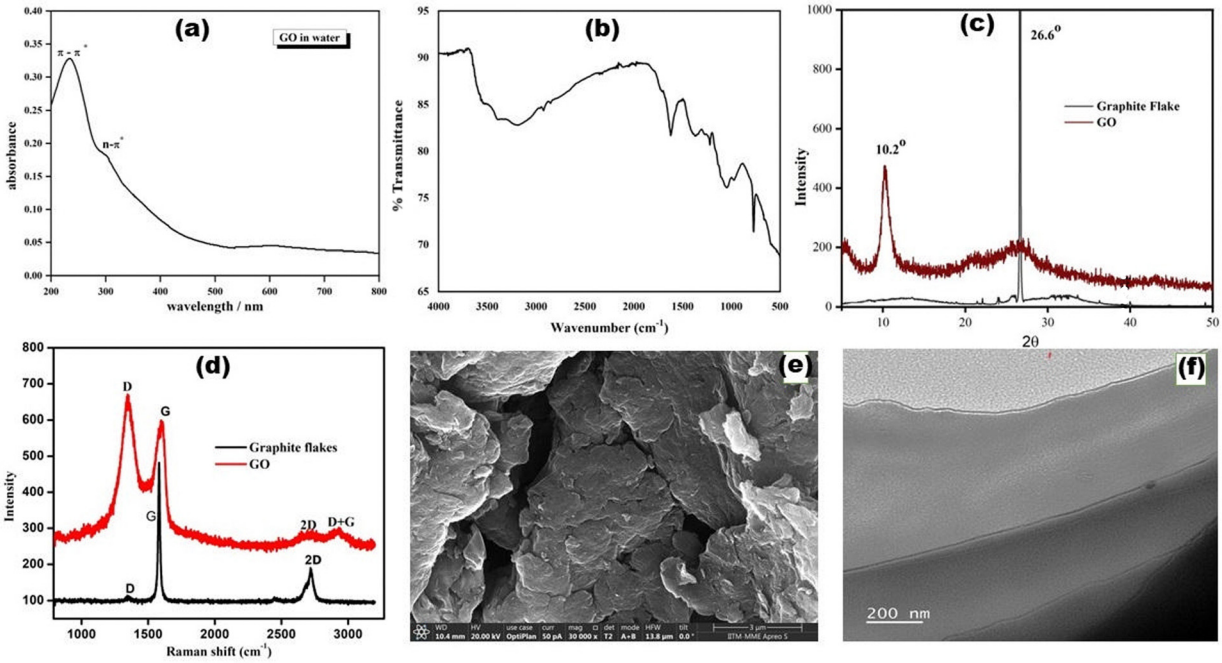

Fig. 1 Characterization of GO by using different experimental techniques: (a) absorbance, (b) FTIR-ATR, (c) XRD, (d) Raman spectroscopy, (e) FESEM, and (f) TEM.

the intercalation of oxide functional groups and water molecules at the carbon basal plane during chemical oxidation reactions.[45]

Raman spectroscopy is a non-destructive technique for the characterization of the ordered and disordered structures of carbon-based materials. The characteristic G and D peaks and their overtones are the main features of graphite-based materials.[46] A band at 2722 cm^{-1} and a strong band (G peak) at 1580 cm^{-1} are visible in graphite flakes. These values are very similar to those given in the earlier literature.[41,46] A peak at 1348 cm^{-1} is also called the D peak, which reveals defects in the sample, and is often used for the measurement of the degree of disorder. Raman spectra of GO show the presence of a very strong D peak at 1348 cm^{-1} with an intensity nearly comparable to the G peak at ~1600 cm^{-1}. The values of the D and G bands of GO were also found to be in good agreement with the earlier literature.[41,46] The more intense D peak of GO in comparison with graphite demonstrates the presence of more structural disorder in GO. The 2D band of GO is found at around 2692 cm^{-1} and the D + G band at 2914 cm^{-1}. Unlike the D peak, which is Raman active only in GO (in the presence of defects in structure), 2D is active for graphite in the absence of defects (*cf.* Fig. 1(d)).

FESEM micrographs of GO are shown in Fig. 1(e). FESEM shows two-dimensional sheet-like structure of GO with multiple lamellar layers. The smooth leaf-like surface of graphite is converted into a rough surface after oxidation and forms a porous structure in GO.[46] It is possible to separate the edges of individual sheets and also to determine the length, thickness, and width of the sheets. GO shows a wrinkled and thin layered structure in the TEM micrographs (Fig. 1(f)).

2.5. Preparation of highly stable GO dispersions

GO nanoparticles were dispersed in deionized water at an average concentration of 0.5 mg mL^{-1}, and the dispersion was carried out using an ultrasonic bath for 5 hours. After many sonication processes, the GO dispersion was left undisturbed at room temperature for several days. In this way, large water-insoluble GO particles were sedimented, and a clear GO dispersion was separated precisely by a decantation process. The GO dispersions produced by this method were homogeneous and very stable. Various concentrations of GO solutions were prepared by diluting this stock solution.

2.6. Preparation of GO–C153 and GO–C153–CTAT/16-4-16 composites in aqueous medium

Various amounts of GO dispersions were mixed with the C153 dye so that the final concentration of C153 in the solution of all composites was 1×10^{-5} M. Briefly, a stock C153 dye solution of 1×10^{-3} M was pipetted, transferred to a vial, and purged with inert argon gas to evaporate the solvent. Then, 3 mL of GO solution with different concentrations of GO was added to the vial containing C153. For preparing the GO–C153–CTAT/16-4-16 ternary system, various concentrations of CTAT/16-4-16 were added to the GO–C153 binary system and sonicated well.

3. Results and discussion

3.1. Absorption studies

Absorption spectra of the coumarin 153 dye were collected at various concentrations of graphene oxide in order to examine the interaction between the two materials (Fig. 2). According to

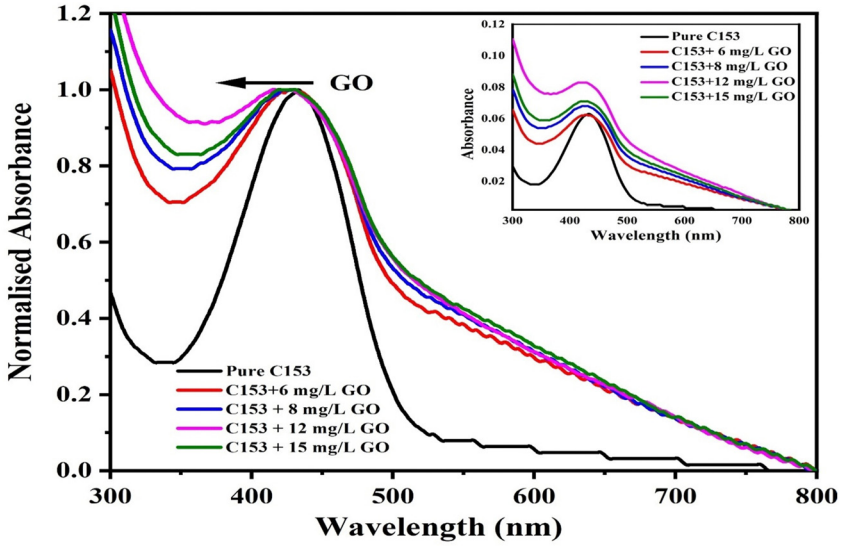

Fig. 2 Normalised UV-vis spectra of 1×10^{-5} M C153 at various concentrations of GO (inset: UV-vis spectra of C153 at various concentrations of aqueous dispersion of GO).

Fig. 2, coumarin 153 has a characteristic absorption peak at a wavelength of about 430 nm, which is in good agreement with the reported value in the literature.[47] It is possible to see a rise in the maximum absorption intensities of the spectra with the addition of various GO concentrations. The absorption peak intensities increase with GO concentration due to graphene oxide's involvement in the absorbing medium, indicating a significant increase in absorption intensity.

To understand the quenching mechanism, we investigated the shift and shape of absorption peaks in the UV-vis absorption spectra. It is known that in static quenching, forming a ground-state complex between the quencher and fluorophore would shift the fluorophore's UV-vis absorption spectrum. On the other hand, there should be no change in the absorption spectra for dynamic quenching.[48] The addition of GO caused a steady change in the UV-vis absorption spectra towards blue, as seen in Fig. 2. The normalised spectra showed a significant blue shift of 10 nm at a GO concentration of 0.015 mg mL^{-1}. The formation of a non-fluorescent H-aggregate dimer could explain this intriguing finding of the UV-vis absorption peak shifting to the blue end.[49] Therefore, the shifting of UV-vis absorption spectra indicates the presence of ground-state quenching, *i.e.*, static quenching.

3.2. Fluorescence studies

Using a light source with a 422 nm excitation wavelength, the steady-state fluorescence emission spectra of the coumarin 153 dye in the aqueous dispersion of GO were captured. In deionized water, coumarin 153 displayed an intense fluorescence emission band with a maximum emission at 544 nm.[50] We measured the steady-state emission of the GO@C153 pair at various GO concentrations since the fluorescence emission intensity of the couple is highly dependent on the concentration of GO. The steady-state emission spectra of the GO@C153 pair at various GO concentrations are shown in the accompanying figure (Fig. 3(A)). According to Fig. 3(A), the emitted intensity of coumarin 153 gradually declines as GO concentration rises. Additionally, an intriguing blue shift of the fluorescence peaks to shorter wavelengths is seen. As a result, the intensity of fluorescence emission could be controlled by changing the interaction between GO and coumarin 153. The C153 fluorescence is effectively quenched by GO, as seen by the steady decline in fluorescence emission spectra that occurs as GO concentration rises. Additionally, it was noted that GO did not exhibit any fluorescence at the same excitation wavelength as coumarin 153 (422 nm). This finding makes it abundantly evident that the observed quenching of fluorescence emission was caused exclusively by the interaction of GO and C153, not by reabsorption or any inner filter effect.

As the GO concentration increases from 0 to 0.01 mg mL^{-1}, the fluorescence peak of coumarin 153 shows blue shifting by 32 nm, as seen by the normalised fluorescence spectra (Fig. 3(B)). This large blue shift of the fluorescence emission peak could be attributed to the formation of H-aggregates,[51] which are nonfluorescent clumps formed between the dye molecules when GO nanoparticles are present. Blue shifting gets stronger as GO levels rise, but nonfluorescent dimeric aggregates are produced, which lowers fluorescence emission intensity. It is well known that GO has an sp^2 hybridized π plane, along with carboxylic acid groups at the edge and epoxy and hydroxyl groups on the surface.[52] The coumarin 153 dye, with its aromatic ring with π electrons, may form π–π interactions with GO, forming dye–nanoparticle aggregates.

3.3. Binding constant determination

The binding constant of the GO and C153 interactions was evaluated from the steady state fluorescence quenching data using a modified Stern–Volmer equation.[53,54]

$$\log((F_0 - F)/F) = \log K + n \log[Q] \quad (1)$$

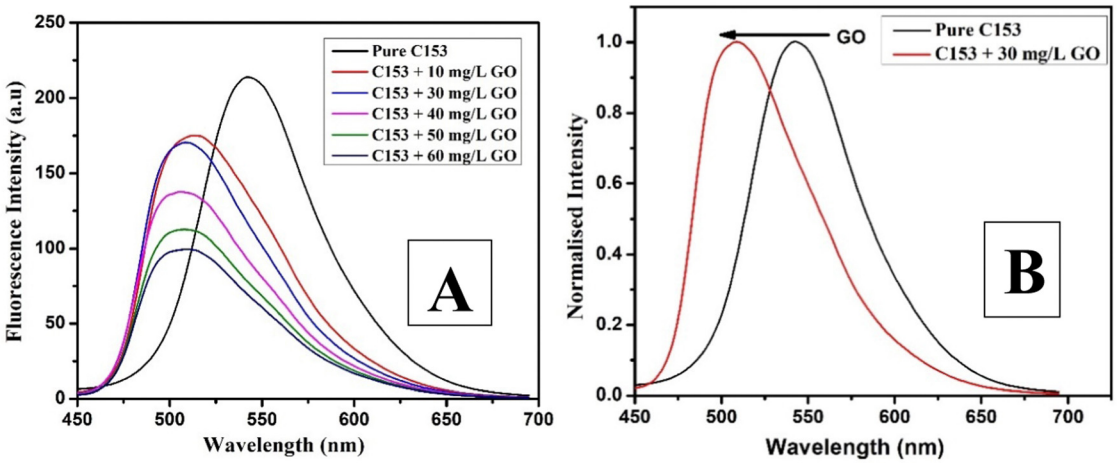

Fig. 3 (A) Fluorescence spectra of 1×10^{-5} M C153 at various concentrations of aqueous dispersed GO with an excitation wavelength of 422 nm and (B) normalised fluorescence spectra of pure C153 and that in the presence of 30 mg L^{-1} GO aqueous dispersed in C153 solution respectively.

where K is the binding constant and n is the number of binding sites of nanoparticles on C153. The value of the binding constant (K) can be found from the intercept of the plot, and the number of binding sites (n) can be found from the slope when $\log((F_0 - F)/F)$ *vs.* $\log[Q]$ is plotted (Fig. 4). The number of binding sites (n) was around 2.0, and the obtained binding constant (K) for GO and C153 was 4.89×10^2 L g^{-1}. The high binding constant value suggests a strong interaction between GO and C153 molecules.

3.4. Fluorescence quenching analysis

The quenching process can be divided into two categories: static quenching and dynamic quenching. In static quenching, the quencher and fluorophore molecule combine to form a nonfluorescent ground-state complex. The number of free fluorophores in the ground state that emit fluorescence in the excited state decreases with increasing GO concentration due to complex formation. This leads to the quenching of fluorescence intensity, known as static quenching.

On the other hand, in dynamic quenching, no ground-state complex is formed. Instead, the quencher molecule forms a complex with the fluorophore in the excited state, leading to the deactivation of fluorescence emission.[55]

To understand the fluorescence quenching mechanism, we used the Stern–Volmer equation of fluorescence quenching. The Stern–Volmer equation of fluorescence quenching can be represented by the following equation:[56,57]

$$\frac{F_0}{F} = 1 + K_{SV}[Q] \quad (2)$$

Here, F_0 and F are the fluorescence intensities of the fluorophore in the absence and presence of quencher molecules, respectively. K_{SV} is the binding constant between the fluorophore and quencher molecule, also known as the Stern–Volmer constant, and the quencher concentration is represented as [Q]. According to the F_0/F *versus* [Q] plot (Fig. 5), there is a positive

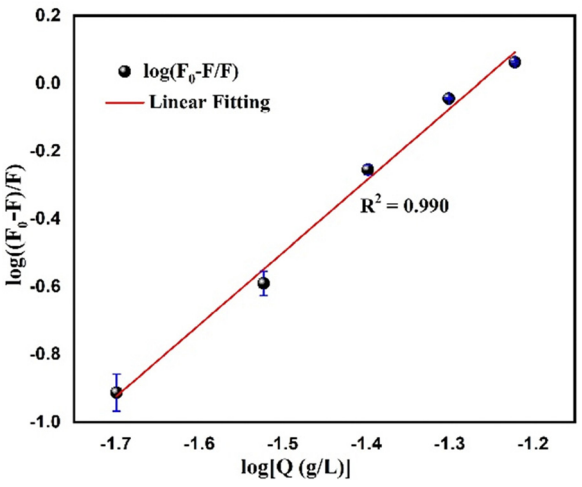

Fig. 4 Modified Stern–Volmer plot, derived from fluorescence data, depicting the binding curves resulting from the adsorption of C153 on GO.

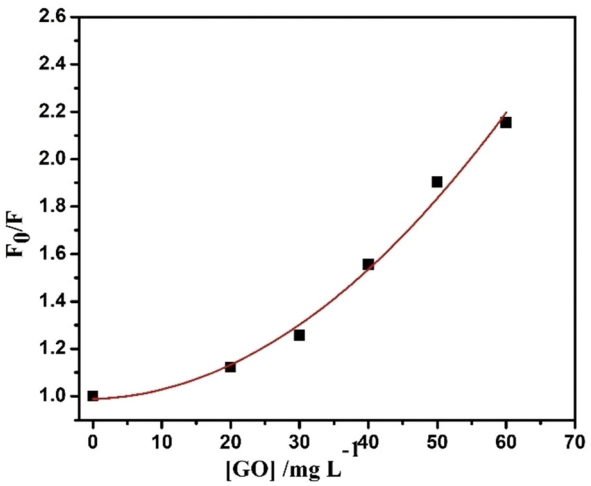

Fig. 5 Stern–Volmer plot for fluorescence quenching of the C153 molecule in the presence of various concentrations of graphene oxide aqueous solution.

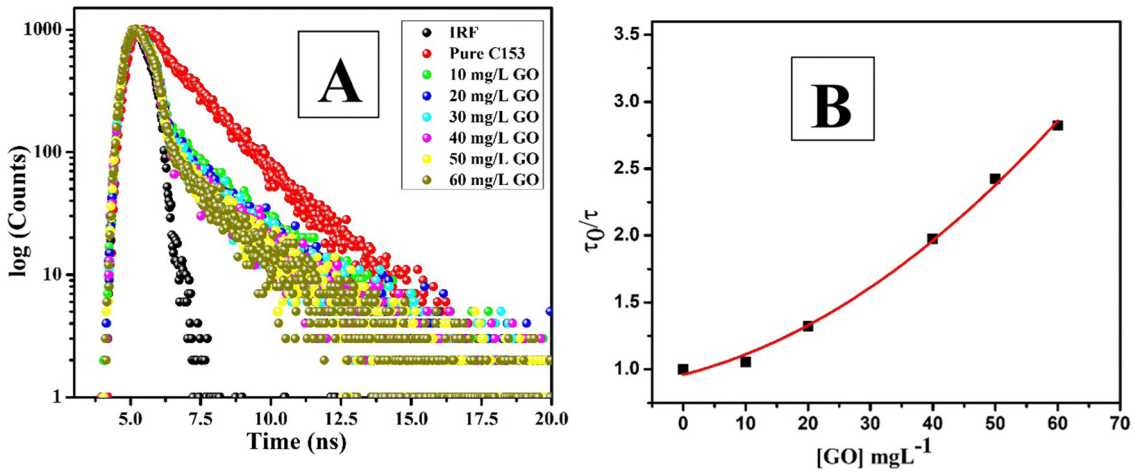

Fig. 6 (A) Time-resolved fluorescence decay of pure C153 (red) and others were due to the presence of various amounts of GO and the black line was the lamp signal. The wavelength of excitation was 450 nm and the range of χ^2 was 1.05–1.29 and (B) time-dependent fluorescence quenching Stern–Volmer plot of C153 with various concentrations of GO.

or upward deviation from the linear curve for the change in F_0/F of coumarin 153 with GO concentration.

If F_0/F changes linearly with quencher concentration, there can only be one form of quenching: static or dynamic, or both if it deviates from linearity. It appears that both static and dynamic quenching occurred in our instance because the change in F_0/F of coumarin 153 with GO concentration is bimodal.[58] The blue shift in the absorption spectra, which results from the creation of a ground-state complex between the quencher molecule GO and the dye C153, is indicative of static quenching. However, to understand the dynamic quenching, we performed lifetime experiments.

3.5. Time resolved fluorescence studies

To study the change in the lifetime of the coumarin 153 dye in the presence of GO nanoparticles, we performed time-dependent fluorescence studies. In this case, we employed a laser diode with an excitation wavelength of 450 nm and an emission wavelength of 544 nm to measure the lifetime. The average lifetime of the coumarin 153 dye in an aqueous medium is 1.89 ns, and it displays a biexponential decay curve.[59] The faster decay component corresponds to the aggregate form of the dye, while the slower decay component corresponds to the monomer form of the coumarin 153 dye.[60]

Here, using different GO nanoparticle concentrations, we assessed the lifetime of the dye coumarin 153. According to Fig. 6(A), the fluorescence lifetime of the coumarin 153 dye decreased as the concentration of GO increased. The data table (Table 1) demonstrates that when very little GO (0.01 mg mL^{-1}) is added, the dye's lifetime decreases to almost half of what it was in pure deionized water. This implies that GO is an extremely effective fluorescence quencher for coumarin 153 dye molecules.

The biexponential decay curve exhibits a gradual increase in the contribution of the faster decay component with increasing GO concentration and a gradual decrease in the contribution of the slower decay component. The aggregation development between the dye molecules in the presence of GO nanoparticles provides a clear explanation for this behaviour. As mentioned earlier, the faster decay component is due to the H-aggregate form of the C153 dye. The dye experiences H-type aggregation in the presence of GO; hence, the quicker decay component rises in comparison to that of the free C153 molecule in an aqueous solution. On the other hand, as GO concentration increases, the contribution of the slower decay component diminishes because GO causes the C153 molecule's monomeric form to degrade and transform into an aggregate form. As monomeric coumarin 153 is the cause of the slower decay component, its contribution falls off as GO concentration increases.

Table 1 Time resolved fluorescence decay data of the emission from C153 and the C153@GO composite in aqueous medium at room temperature

[GO] (mg L^{-1})	τ_1 (ps)	τ_2 (ns)	$\langle\tau\rangle$ (ns)	χ^2
0	186.74 (−13.74)	1.69 (113.74)	1.89	1.29
10	231.61 (66.38)	1.96 (33.62)	0.81	1.05
20	220.62 (71.85)	1.99 (28.15)	0.71	1.23
30	118.36 (76.78)	2.03 (23.22)	0.56	1.19
40	128.93 (78.45)	2.14 (21.55)	0.55	1.20
50	99.88 (79.73)	2.01 (20.27)	0.48	1.08
60	10.03 (79.96)	1.78 (20.04)	0.36	1.17

Lifetime measurement was also helpful in understanding static and dynamic quenching. The lifetime of the dye molecule is unaffected by quencher concentration in the case of static quenching, whereas it is shortened in the case of dynamic quenching. The change in the fluorescence lifetime of the dye with the quencher can be represented by the following equation:

$$\tau_0/\tau = 1 + K_{SV}[Q] \quad (3)$$

Here, τ_0 and τ are the lifetimes of the dye molecule in the absence and presence of the quencher molecule, respectively. K_{SV} is the Stern–Volmer constant, and [Q] is the concentration

of the quencher molecule. Fig. 6(B) reveals that τ_0/τ gradually changes with GO concentration, not staying constant at $\tau_0/\tau = 1$, which is the condition for pure static quenching. Additionally, it does not satisfy the $F_0/F = \tau_0/\tau$ condition, which is the criteria for pure dynamic quenching. In this instance, the variations in τ_0/τ with GO concentration exhibit an intermediate behaviour, which unequivocally demonstrates the existence of both static and dynamic quenching processes. The steady-state Stern–Volmer graphs, which show both static and dynamic quenching, are strongly supported by this observation. Thus, it is evident from the lifetime measurement experiment that both static and dynamic quenching occur.

3.6. Mechanistic details

To study the interaction mechanism between coumarin 153 dye and GO, we need to clearly understand the individual structures of the dye molecule and the quencher molecule. The presence of a π ring in the dye molecule raises the probability of coumarin 153 undergoing π–π stacking. In contrast, GO comprises many hexagonal rings with sp^2 hybridized carbon atoms and a variety of functional groups. The sp^2 hybridised plane has hydroxyl and epoxy groups as well as a sizable number of carboxylic groups at the edges of the hexagonal rings. The structural characteristics of GO and the dye molecule create a high likelihood of π–π interaction between the quencher molecule, GO, and coumarin 153 dye.

The observed fluorescence quenching could be attributed to energy transfer or electron transfer from the coumarin 153 molecule to the GO quencher molecule. However, it is evident that the absorption spectra of GO (Fig. 7) do not overlap with the emission spectra of the coumarin 153 dye. This indicates that there is no possibility of energy transfer from the dye molecule to the GO quencher molecule in the ground state.[61] Therefore, in the ground state, fluorescence quenching occurs through electron transfer from the dye molecule to the GO system. The quenching of fluorescence emission in the excited state may be caused by energy transfer from the dye molecule (coumarin 153) to the quencher molecule (GO).

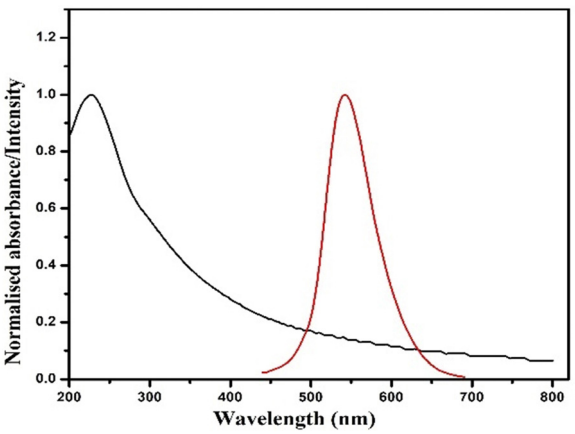

Fig. 7 Normalised UV-vis absorption spectra of GO (black spectrum) and normalised fluorescence spectra of the C153 dye molecule (red spectrum).

4. Effect of surfactants on the photophysical and aggregation properties of the C153 dye

4.1. Conductivity measurements

In order to study the aggregation behaviour of surfactant molecules (both conventional and gemini surfactants) in the presence of dye molecules, specific conductivity measurements were performed. Specific conductivity measurements of 16-4-16 and CTAT surfactants were performed both in the absence and presence of the C153 molecule, respectively. The results of the experiment were represented by the plot of specific conductivity *vs.* concentration of surfactants. The increased size of 16-4-16 and the larger *p*-toluene sulfonate counterion group of CTAT resulted in the lower mobility of 16-4-16 and CTAT, which in turn led to small conductivity values for both surfactants.

As demonstrated in Fig. 8(A) and (B), the conductivity increased quickly with the addition of surfactant molecules up to a certain point, both with and without the C153 molecule. After that point, there was a rapid decrease in the slope of the conductivity graph. This break point, after which the slope decreased, is known as the critical micellar point of the surfactant molecule. The CMC values of pure surfactant and the dye–surfactant complex were obtained from the break point in the plot of specific conductivity *vs.* surfactant concentration.[62] The break point manifested earlier in the presence of the C153 molecule compared to its absence, as shown by the conductivity plots of both 16-4-16 and CTAT surfactants. This result suggests that micelle formation was facilitated for both surfactants in the presence of the C153 molecule. This is because the presence of the dye molecule increases the overall hydrophobicity, making micelle formation easier.

Another interesting observation from the conductivity plot is that in the presence of the dye molecule C153, both 16-4-16 and CTAT surfactants exhibited higher conductivity compared to that in the absence of the dye molecule. This observation can be explained by the degree of counterion dissociation (β), which is determined from the ratio of the slope obtained in the post-micellar region to that in the pre-micellar region. According to Table 2, the presence of the C153 dye considerably increased the degree of counterion dissociation (β) for both 16-4-16 and CTAT surfactants. The counterion of 16-4-16 and CTAT is affected by interactions between the C153 molecule and surfactant molecules, resulting in greater counterion dissociation and the counterion of 16-4-16 and CTAT becoming loose and accelerating its dissociation.

Various thermodynamic parameters for micellization, such as the standard Gibbs free energy change for micellization (ΔG^0_m), standard entropy change of micellization (ΔS^0_m), and standard enthalpy change of micellization (ΔH^0_m), can be determined from conductivity measurements. The value of ΔG^0_m can be represented by the following relationship[63] (eqn (4)):

$$\Delta G^0_m = 2.303RT(\log \mathrm{CMC} - \log \omega) \quad (4)$$

Here, 'ω' is the molar concentration of water, and its value is 55.3 at 298 K. R is 8.314 J $(\mathrm{mol\ K})^{-1}$ and T is the temperature on the Kelvin scale.

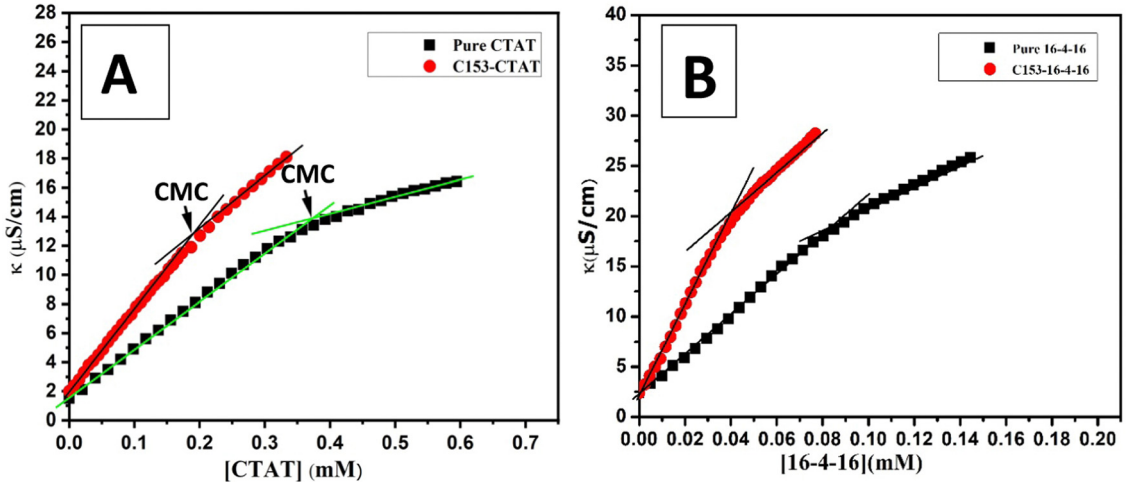

Fig. 8 (A) Specific conductivity *vs.* CTAT concentration plots in the absence and presence of the C153 molecule respectively. (B) Plots of specific conductivity *vs.* concentration of 16-4-16 in the absence and presence of the C153 dye molecule at 298 K.

Table 2 Various thermodynamic parameters of C153–surfactant interaction at room temperature determined by conductivity measurements

System	β (degree of counter ion dissociation)	$-\Delta G_m^0$ (kJ mol^{-1})	ΔS_m^0 (J K^{-1} mol^{-1})	$-\Delta H_m^0$ (kJ mol^{-1})
CTAT–C153	0.58	14.18	105.02	90.84
CTAT	0.46	13.18	101.72	88.54
16-4-16	0.49	16.23	111.91	95.67
16-4-16–C153	0.56	18.62	119.96	101.34

At the same time, the values of ΔS_m^0 and ΔH_m^0 can be calculated using the following equations (eqn (5) and (6)):

$$\Delta S_m^0 = -\frac{d}{dT}(\Delta G_m^0) \quad (5)$$

$$\Delta H_m^0 = \Delta G_m^0 + T\Delta S_m^0 \quad (6)$$

The data table (Table 2) makes it clear that the presence of C153 results in a greater negative value of the standard Gibbs free energy of micellization (ΔG_m^0) for both surfactants (16-4-16 and CTAT) than the absence of the dye. This finding indicates that the micellization process was favourable when the dye molecule was present. The study found that 16-4-16 showed a more favourable micellization compared to CTAT, as evidenced by a more negative change in ΔG_m^0. This is because CTAT only has one chain with sixteen carbons, which is less hydrophobic than 16-4-16, which has two hydrophobic chains connected by a spacer. Similarly, the changes in standard entropy (ΔS_m^0) and standard enthalpy (ΔH_m^0) of micellization can be explained.

4.2. Surface tension measurements and determination of various surface parameters

Tensiometry is a very important method for studying the interaction between dye and surfactant molecules. The adsorption of amphiphiles at the air–water interface results in a decrease in the surface tension of the aqueous phase. The breakdown of H-bonding at the aqueous interface may be the cause of the drop in surface tension observed in the presence of amphiphiles. The surface tension measurements reveal that the formation and adsorption of the C153–surfactant complex have an impact on the overall structure of the surface monolayer and, consequently, the surface tension.[64] The plots of the variation of surface tension with the bulk concentrations of surfactants (on a logarithmic scale) for both cases in the presence and absence of the C153 dye at 298 K are presented in the following figures (Fig. 9(A) and (B)). The figures show that the surface tension decreases when C153 is present, indicating the dye molecule's surface activity. Surface tension decreases up to a certain point when surfactant concentration increases, after which it becomes more or less constant. This break point is known as the critical micelle concentration (CMC). The surface tension graphs clearly show that for both 16-4-16 and CTAT surfactants, the values of CMC are lower in the presence of the C153 dye than those in the dye molecule's absence. This may be due to the close-packed complex formation between surfactants and the dye molecule, which increases the effective hydrophobicity of the medium. As a result, the CMC is smaller when the C153 molecule is present.

The surface excess concentration (Γ_{max}) of the amphiphiles[65,66] can be calculated from interface data using the Gibbs equation. For a dilute solution, the Gibbs equation can be written as:

$$\Gamma_{max} = -\frac{1}{2.303iRT}\left[\frac{d\gamma}{d\log C}\right] \quad (7)$$

Here, Γ_{max} represents the excess surface concentration of amphiphiles and signifies the packing of the amphiphiles at the interface, *I.e.*, the number of species at the air–water interface after the dissociation of amphiphile molecules, R is the universal gas constant, T is the temperature on the Kelvin scale, C is the concentration of amphiphiles on the molar concentration scale, γ is the surface tension in mN m^{-1}, and $d\gamma/d\log C$ represents the slope of the plot of γ *vs.* $\log C$. The value of n is

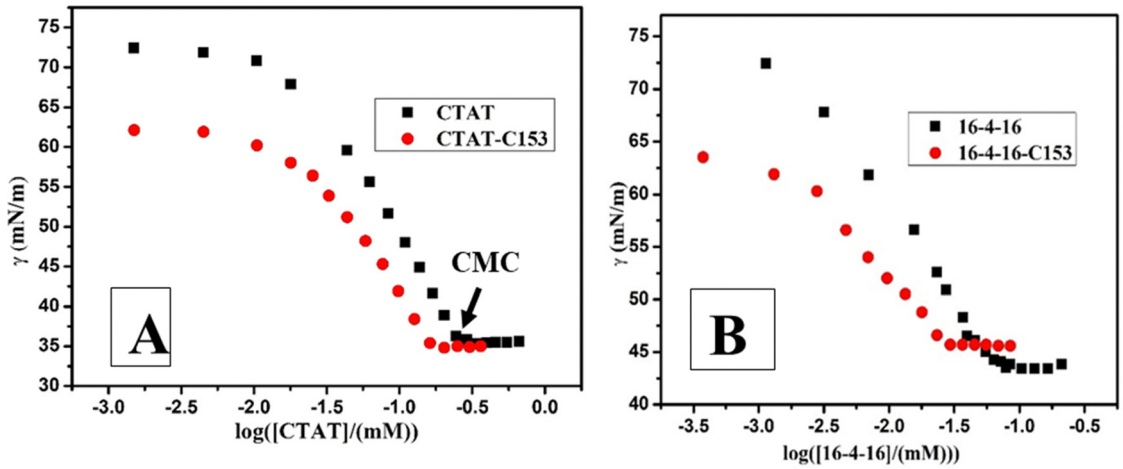

Fig. 9 (A) Surface tension *vs.* concentration of CTAT plots in the absence and presence of 1×10^{-5} (M) C153 molecules; (B) plots of surface tension *vs.* 16-4-16 concentration in the absence and presence of C153 dye molecules.

taken as 2 for the CTAT surfactant and 3 for 16-4-16.[67] From the surface excess concentration, we can find A_{min}, which is the minimum area covered by each surfactant molecule at the interface:

$$A_{min} = \frac{10^{18}}{N_A \Gamma_{max}} \quad (8)$$

Here N_A represents Avogadro's number. From the data in Table 3, it can be seen that the low value of Γ_{max} for the CTAT surfactant in the presence of the C153 molecule suggests loose packing of the CTAT–C153 complex at the interface; hence, a larger surface area is required for the adsorption of the CTAT–C153 complex. On the other hand, for free CTAT molecules, a high value of Γ_{max} is found, which suggests strong packing of CTAT molecules at the interface. This means a smaller area is required for the adsorption of free CTAT molecules compared to that in the presence of the dye molecule. Interestingly, the opposite phenomenon is observed for the 16-4-16 surfactant. In this case, a high value of Γ_{max} and a low value of A_{min} are observed in the presence of the C153 molecule, suggesting that a small area is required at the air–water interface for the adsorption of the 16-4-16–C153 complex. However, in the absence of the dye molecule, a low value of Γ_{max} and a high value of A_{min} are observed, which mean a high surface area is required for the adsorption of free 16-4-16 molecules compared to that of the 16-4-16–C153 complex. This abnormal behavior may be due to the unstable complex formation between C153 and 16-4-16 because of the high hydrophobicity of the 16-4-16 surfactant.[64]

The efficiency of interface adsorption is expressed in terms of the parameter, pC_{20}. From Table 3, it can be seen that the value of pC_{20} for both CTAT and 16-4-16 surfactants decrease in the presence of the C153 molecule. This suggests that the dye–surfactant complex has a lower tendency to be adsorbed at the interface, hence showing less surface activity compared to the pure surfactant. In the case of oppositely charged dye–surfactant systems, complex formation occurs through ion pair complexation, resulting in the formation of a non-ionic complex that behaves as a non-ionic surfactant. It is known that non-ionic surfactants are more surface-active than ionic surfactants.[68] Therefore, in the case of oppositely charged dye–surfactant systems, the value of pC_{20} increases in the presence of the dye molecule. However, in our case, the surfactant molecules are cationic and the dye molecules (C153) are non-ionic, inhibiting complex formation through ion pair complexation. Here, complex formation occurs only through weak hydrophobic interactions between the dye and surfactant molecules, and the resultant complex is less surface-active compared to the pure surfactant. As a result, in our case, the addition of the C153 molecule lowers the value of pC_{20} for both surfactants (CTAT and 16-4-16). It is also observed that the value of π_{cmc} (*i.e.*, the surface pressure at CMC) decreases in the presence of the C153 molecule for both CTAT and 16-4-16 surfactants compared to that in the absence of the dye molecule. This is because the dye–surfactant complex has a lower tendency to be adsorbed at the interface. As a result, in the presence of the dye molecule, the surface activity of surfactants decreases, *i.e.*, γ_{CMC} increases compared to the free surfactant. So, from the tensiometry measurements, it can be seen that the surface activity of CTAT is greater than that of 16-4-16 gemini (both in the presence and absence of C153). This is because due to the large size of the 16-4-16 surfactant, it is loosely packed at the

Table 3 Various surface and micellar parameters of surfactants in the absence and presence of C153 molecules

System	CMC (mM)	γ_{CMC} (mN m^{-1})	$10^6\Gamma_{max}$ (mol m^{-2})	A_{min} (Å^2)	π_{CMC} (mN m^{-1})	pC_{20}
CTAT	0.269	35.3	3.39	48.97	38.1	1.12
CTAT–C153	0.181	35.8	3.06	54.25	28.1	1.03
16-4-16	0.079	43.5	1.83	90.72	28.5	1.59
16-4-16–C153	0.030	45.7	2.02	82.19	18.0	1.44

interface, resulting in low surface activity compared to CTAT. However, due to the greater hydrophobicity of 16-4-16, its micellization capacity is higher than CTAT.

4.3. Steady state spectral studies

It was mentioned earlier that in an aqueous medium, C153 shows a broad absorption spectrum with a maximum of about 430 nm.[47] The absorbance was found to gradually increase with increasing surfactant concentration (for CTAT and 16-4-16), and at the same time, a 6 nm red shift of the highest absorption peak was seen (Fig. 10(A) and (B)). This red shifting of the absorption band may be due to a change in polarity around the C153 molecule.[69] With increasing surfactant concentration, the polarity of the aqueous dye medium decreases, which is responsible for this type of red shifting. However, we also saw an isosbestic point in the presence of surfactant molecules, which may indicate an equilibrium between the C153 molecule's monomeric form and higher-order aggregated form. Since there was a red shift in the absorbance spectra, this type of aggregation is called J-type aggregation. The change in absorbance with the concentration of surfactants gives a perfectly sigmoidal plot (for both CTAT and 16-4-16), from which we easily determined the value of CMC in the presence of the dye molecule, and the results matched well with the CMC value determined from surface tension and conductance, respectively. The rate of increase in absorbance and also the red shifting of the UV-vis spectra of C153 are more pronounced in the presence of 16-4-16 compared to CTAT. So, this indicates that 16-4-16 gemini is more effective at changing the microenvironments of the dye than the monomeric one (CTAT).[70]

The fluorescence properties of the C153 molecule greatly depend on the solvent polarity. Hence, to understand the effect of CTAT and 16-4-16 surfactants on the fluorescence behaviour of the C153 molecule, we recorded the fluorescence spectra of the dye at various concentrations of the surfactants. In an aqueous medium, C153 exhibits a broad, structure-less, and low-intensity fluorescence band with maximum fluorescence at around 544 nm. In a highly polar protic solvent such as an aqueous medium, C153 exhibits less intense fluorescence spectra due to the H-bonding of the C153 molecule in a protic

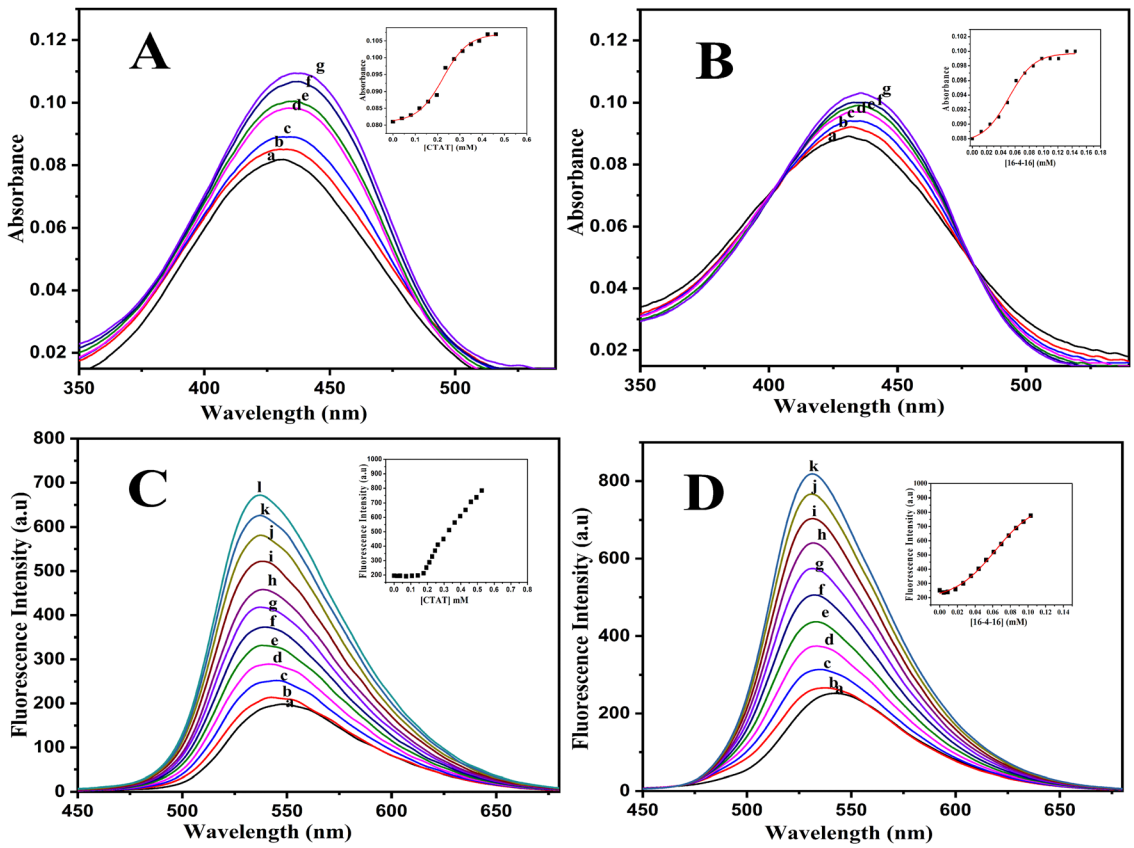

Fig. 10 (A) UV-vis absorption spectra of 1×10^{-5} M C153 in the presence of (a)–(g) 0, 0.118, 0.196, 0.235, 0.273, 0.349, and 0.424 mM CTAT (inset: plots of absorbance *vs.* concentration of CTAT). (B) UV-vis absorption plots of C153 in the presence of (a)–(g) 0, 0.037, 0.049, 0.061, 0.085, 0.109, and 0.132 mM 16-4-16 (the inset shows a plot of the absorbance of C153 at various concentrations of 16-4-16). (C) Steady-state fluorescence spectra of 1×10^{-5} M C153 in the presence of (a)–(l) 0, 0.176, 0.193, 0.210, 0.228, 0.245, 0.262, 0.295, 0.329, 0.362, 0.395, and 0.428 mM CTAT (inset: plots of fluorescence intensity *vs.* CTAT concentration). (D) Steady-state fluorescence emission spectra of C153 in the presence of (a)–(k) 0, 0.026, 0.035, 0.052, 0.061, 0.069, 0.078, 0.086, 0.094, 0.103, and 0.111 mM 16-4-16 (inset represents the plots of fluorescence emission intensity of C153 *vs.* concentrations of 16-4-16).

Table 4 Determination of CMC (mM) of surfactants by various methods in the absence and presence of C153 molecules

System	ST	Conductance	Absorbance	Fluorescence
CTAT	0.269	0.296		
CTAT–C153	0.181	0.185	0.195	0.179
16-4-16	0.079	0.080		
16-4-16–C153	0.030	0.035	0.038	0.031

polar medium.[71] The ICT state becomes less feasible, resulting in a weak, broad, and structured fluorescence spectrum. Although the C153 molecule is in a highly polar solvent, the twisted intramolecular charge transfer (TICT) state is less feasible due to its rigid structure.[37] In the presence of a surfactant solution above its micellar concentration, a significant increase in the fluorescence intensity, along with a blue shifting of the emission maximum, was observed. The fluorescence properties of C153 depend on the concentration and the nature of the surfactants. There was no discernible difference in the fluorescence intensity of C153 in the presence of the CTAT surfactant at low concentrations (up to 0.18 mM). However, as CTAT concentration grew above this, the fluorescence intensity quickly increased, the spectra shrank and became crisp, and a 6 nm blue shift of the emission maxima was noticed. As a result, the change in fluorescence intensity with the concentration of CTAT produces a unique form of plot, where the initial intensity was similar to that of water and did not change, but the subsequent fluorescence intensity significantly increased (Fig. 10(D)). So, from the plot, we can see a sharp breakpoint that signals a shift in the microenvironment around the C153 molecule, and the breakpoints correlate to the supramolecular interaction of CTAT molecules. As a result, the aggregation behaviour of surfactants has a significant impact on the fluorescence properties of C153. The point of intersection could provide important information about the concentration above which the aggregation process of surfactant started, and the concentration at which aggregation started is known as the critical micelle concentration (CMC). According to fluorescence studies, CTAT produces a CMC value of 0.185 mM when the C153 molecule is present, which is compatible with surface tension, conductance, and UV-vis absorbance data (Table 4).

In contrast, the maximum emission peak's blue shift and change in fluorescence intensity were more pronounced for the 16-4-16 surfactant than for the CTAT surfactant. The enhancement of fluorescence intensity, along with the gradual blue shifting of the emission peak, suggests a gradual modulation of the microenvironment around the C153 fluorophore in the presence of these surfactants. In the presence of the 16-4-16 surfactant, a remarkable blue shift (14 nm) was observed (Fig. 10(C)). This enhancement of intensity in the presence of the surfactant was due to the stabilization of the fluorescent ICT state in a micellar medium (due to its hydrophobic nature), and the blue shifting was due to a change in polarity in the micellar medium compared to that in an aqueous medium. The change in fluorescence intensity with the concentration of gemini gives a more or less sigmoidal plot, which differs from the plot obtained for the CTAT surfactant.

The aforementioned explanation makes it evident that C153's fluorescence behaviour varies in two different surfactant media, indicating that the molecule experiences a different microenvironment in each of these two types of surfactant media. The CTAT surfactant has a single 16-carbon atom hydrophobic chain, while the 16-4-16 surfactant has two identical 16-carbon atom tails and a 4-carbon atom general spacer with a triple bond, creating a more hydrophobic microenvironment around the C153 probe. As a result, the maximum emission peak shifts more towards blue, and the fluorescence intensity rises more quickly.

4.4. Determination of the binding constant of dye–surfactant interaction

It is feasible to measure the equilibrium binding constant (K) of the dye–surfactant interaction at different surfactant concentrations. The following reaction can be used to describe the binding of a ligand, (L), to a free dye site, (D), creating an occupied site (LD):

$$\mathrm{L} + \mathrm{D} \rightleftarrows \mathrm{LD} \tag{9}$$

By designating the dye's absorbance as Abs_0 in the absence of surfactant and Abs in its presence, respectively, the concentration of the occupied sites is, $[\mathrm{LD}] = \Delta\mathrm{Abs}/\varepsilon_{\mathrm{LD}} - \varepsilon_{\mathrm{D}}$.

In this case, ε_i represents the absorption coefficient at the chosen wavelength. To examine the data, an extension of the Hildebrand–Benesi equation was used with $K = [\mathrm{LD}]/[\mathrm{L}][\mathrm{D}]$, which was evaluated together with $\Delta\varepsilon$ by iterative fits:[72]

$$\frac{C_S C_D}{\Delta\mathrm{Abs}} + \frac{\Delta\mathrm{Abs}}{\Delta\varepsilon^2} = \frac{1}{K\Delta\varepsilon} + \frac{(C_S + C_D)}{\Delta\varepsilon} \tag{10}$$

Here, C_S and C_D are the concentrations of surfactants and dye molecules respectively. In other words, $\Delta\varepsilon$ may be found by calculating the reciprocal of the straight line's slope. This matches the fit of the experimental $C_S C_D/\Delta\mathrm{Abs}$ values *vs.* $(C_S + C_D)$, an initial approximation ignoring the $\Delta\mathrm{Abs}/\Delta\varepsilon^2$ term. To find the binding constant of the dye–surfactant complex, the first term in eqn (10), $(C_S C_D/\Delta\mathrm{Abs} + \Delta\mathrm{Abs}/\Delta\varepsilon^2)$, is re-evaluated using the $\Delta\varepsilon$ value, and the result is plotted against $(C_S + C_D)$. From this plot, it is possible to determine the equilibrium binding constant values of the C153–CTAT and C153–16-4-16 systems, which are $1.17 \times 10^3\ \mathrm{M}^{-1}$ and $14.10 \times 10^3\ \mathrm{M}^{-1}$, respectively. It is evident from the binding constant values that C153 and 16-4-16 have a stronger interaction than C153 and CTAT (Fig. 11).

4.5. Fluorescence lifetime measurements

To study the excited-state interaction and changes in the microenvironment around the fluorophore, lifetime measurement serves as a crucial tool.[73] Differences in solvent relaxation around the fluorophore and/or the division of the fluorophore into specific regions of crowded environments can affect the fluorophore's lifetime.[74] The change in the lifetime of C153 in a multi-component system such as a micelle can provide valuable information about the fluorophore's location. It has been

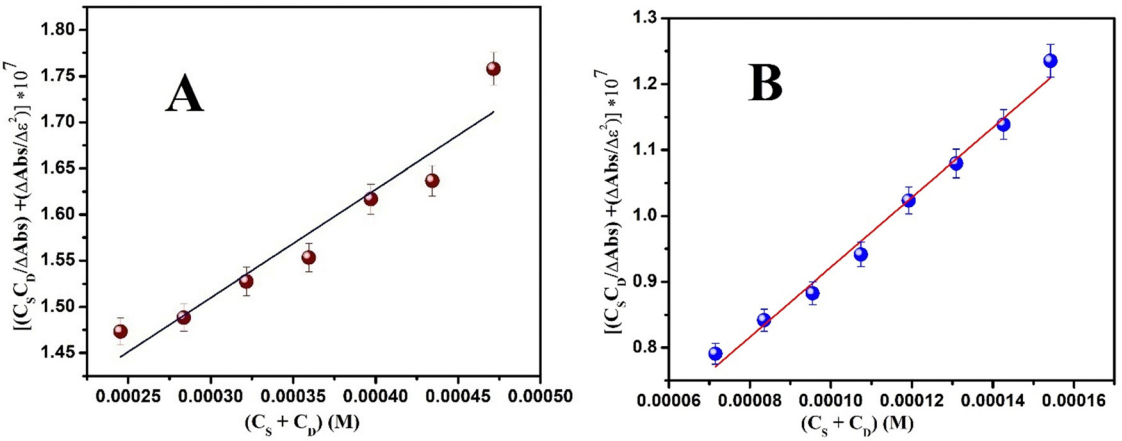

Fig. 11 Analysis of the absorbance titration data for the C153–CTAT/16-4-16 system. $C_{C153} = 1 \times 10^{-5}$ (M), the data are fitted according to the extension of the Hildebrand–Benesi model. (A) CTAT–C153 and (B) 16-4-16–C153 systems, respectively.

observed that C153 exhibits a bi-exponential decay curve in both aqueous and different micellar media. As mentioned earlier, the two different lifetimes correspond to two species: the monomeric and dimeric forms of the fluorophore. The faster decay component (*i.e.*, shorter lifetime) corresponds to the dimer, while the slower decay component (*i.e.*, longer lifetime) is attributed to the monomer of C153. In an aqueous medium, C153 has a significant dimeric form, and with the addition of surfactants, the dimeric form breaks down and converts into the monomeric form. However, in the presence of the CTAT surfactant above its micellar concentration, 31.76% of the dimeric form with a lifetime of 1.88 ns and 68.24% of the monomeric form with a lifetime of 3.95 ns were observed. On the other hand, the 16-4-16 surfactant above its micellar concentration showed 10.88% of the dimeric form and 89.12% of the monomeric form. Therefore, it can be observed that in the presence of micelles, C153 undergoes disaggregation and the contribution of the monomeric form increases. Since the micellar core is hydrophobic, C153 molecules disperse themselves homogeneously, and the monomeric form becomes prominent. In the case of the 16-4-16 surfactant, the monomeric form is greater than that of CTAT because 16-4-16 has two hydrophobic tails, creating a much more hydrophobic environment within the 16-4-16 micelle.

The average lifetimes of C153 molecules in aqueous medium and two different micellar media follow the order 16-4-16 > CTAT > aqueous. The lifetime values of C153 in aqueous and micellar solutions are presented in Tables 5 and 6. The shortening of the lifetime of C153 in an aqueous medium may be attributed to a higher perturbation of its electronic state in the polar medium, caused by greater energy transfer from the fluorophore to the surrounding solvent molecules with high dipole moments. However, in the case of a micellar medium, these perturbations of the electronic state are reduced, as less energy transfer occurs from the fluorophore to its surrounding molecules due to a decrease in the polarity of the medium. As a result, the lifetime of C153 increases in the micellar medium (Fig. 12).

Table 5 Time-dependent fluorescence decay data of pure C153 in the presence of various concentrations of CTAT surfactant in aqueous medium at 298 K

[CTAT] (mM)	τ_1 (ns)	τ_2 (ns)	$\langle\tau\rangle$ (ns)	χ^2
0.011	1.63 (70.55)	7.31 (29.45)	2.12	1.12
0.033	1.67 (69.37)	8.15 (30.63)	2.21	1.16
0.066	1.64 (68.24)	7.93 (31.76)	2.19	1.08
0.109	1.66 (68.16)	7.74 (31.84)	2.2	1.02
0.173	1.7 (65.54)	6.45 (34.46)	2.28	1.1
0.294	1.92 (49.64)	4.66 (50.36)	2.73	1.11
0.409	1.88 (31.76)	3.95 (68.24)	2.93	0.97

Table 6 Time-resolved fluorescence decay data of C153 in the presence of various concentrations of 16-4-16 surfactant

[16-4-16] (mM)	τ_1 (ns)	τ_2 (ns)	$\langle\tau\rangle$ (ns)	χ^2
0.005	1.65 (60.24)	7.14 (34.76)	2.38	1.08
0.014	1.71 (61.83)	7.52 (38.17)	2.43	0.99
0.028	1.84 (61.69)	6.36 (38.31)	2.53	1.06
0.046	1.87 (56.35)	5.21 (43.65)	2.59	1.09
0.072	1.89 (47.5)	4.32 (52.5)	2.69	1.02
0.114	1.88 (30.88)	3.76 (69.12)	2.87	1.02
0.17	1.35 (10.88)	3.33 (89.12)	2.87	1.04

4.6. Combined effect of GO nanoparticles and surfactant solution

As was previously mentioned, the C153 molecule's fluorescence behaviour in GO nanoparticles demonstrated a progressive decline in emission intensity and a sizable blue shift in the maximum emission band. Fig. 13(A) and (B) show the combined impact of GO and micellar solution on the fluorescence behaviour of C153. The plot reveals that GO causes the fluorescence intensity to decrease with a blue shift of the peak, but with surfactant solution, the fluorescence intensity increases and returns to its original value. The fluorescence peak of the studied system shifts from 544 nm to 406 nm in the presence of 40 mg L^{-1} GO, along with a decrease in fluorescence intensity. However, in the presence of 0.1 mM 16-4-16 surfactant, the fluorescence intensity starts to rise once more and returns to its

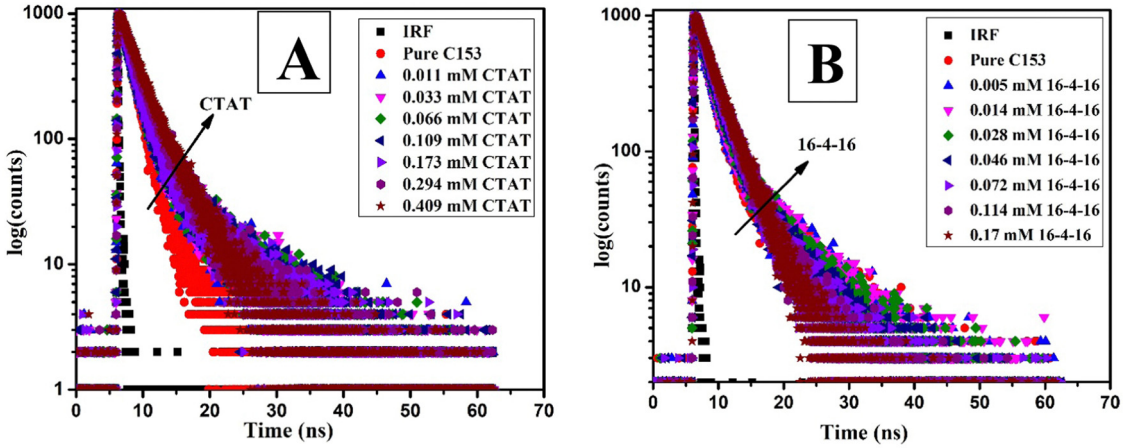

Fig. 12 (A) Time-resolved fluorescence decay of C153 in the presence of various concentrations of CTAT surfactant and (B) in the presence of various concentrations of 16-4-16 surfactant. The wavelength of excitation was 450 nm, and the range of χ^2 was 0.99–1.16.

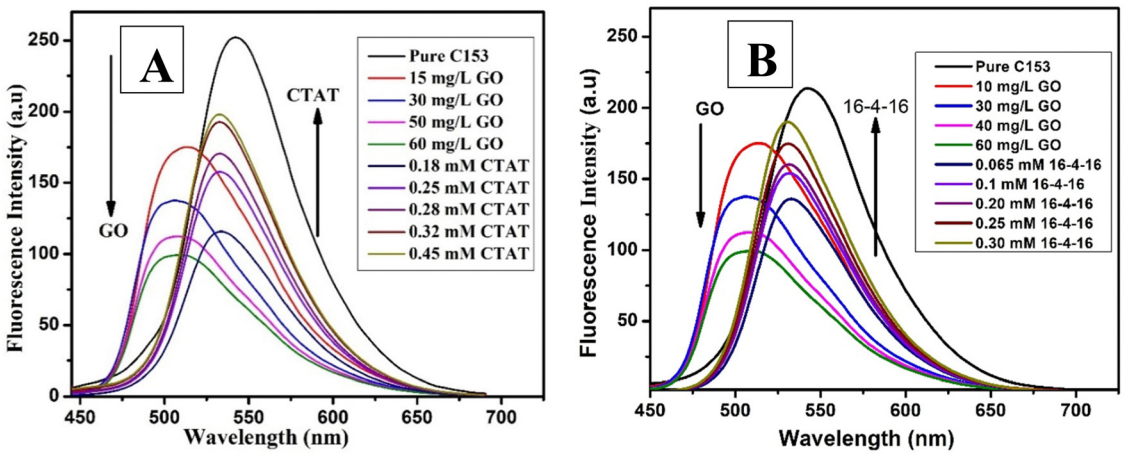

Fig. 13 (A) Fluorescence spectra of C153 in the presence of various concentrations of GO and CTAT surfactants. (B) Steady-state fluorescence spectra of C153 in the presence of GO and the 16-4-16 surfactant.

original value of 530 nm, which is seen when the 16-4-16 surfactant is present at levels above its micellar concentration. A similar observation was made in the presence of the CTAT surfactant, although the efficiency of increasing fluorescence intensity and shifting the fluorescence peak back to its original position was lower compared to the 16-4-16 surfactant.

It is an intriguing finding that dye molecules adsorbed on GO nanosheets separate off the nanosheet and go into the micellar medium when a micellar medium is present (Scheme 1). This transfer of adsorbed dye molecules from the GO nanosheet to the micellar medium leads to an increase in fluorescence intensity. Additionally, the H-aggregation of dye molecules disintegrates as the dye molecules enter the micellar medium from the GO nanosheet, causing the dye molecules to be disseminated uniformly throughout the micellar medium. Consequently, the H-aggregate peak shifts back to its original position. These findings unequivocally demonstrate a substantial interaction between surfactants (both 16-4-16 and CTAT) and C153 in the range of surfactant concentrations at and above the CMC. The combined fluorescence spectra of the samples clearly illustrate the robust interaction between C153 and surfactant in the combined ternary system (GO–dye–surfactant). The intensity of fluorescence emission depends entirely on the concentration of surfactant and increases rapidly with surfactant concentration. This behaviour may be described in two steps: (1) the addition of GO gradually reduces the fluorescence intensity of C153 and (2) the creation of C153–surfactant micelle complexes causes the fluorescence intensity to begin to rise again. As a result, the interaction between C153 and GO becomes weaker, and the dye is kept away from graphene oxide. The idea of the GO–C153–surfactant ternary system can be applied for the regeneration of the adsorbent from dye molecules in wastewater treatment analysis because, in the presence of surfactants at and above the CMC, the dye molecules leave the adsorbent (in this case, GO) and enter the micellar medium. Additionally, spectroscopic analysis clearly indicates that this GO–C153 composite can be utilized as a highly effective fluorescent sensor. Considering C153's popularity as a laser dye, it can be used to construct efficient and inexpensive fluorescent sensors in laser applications. The

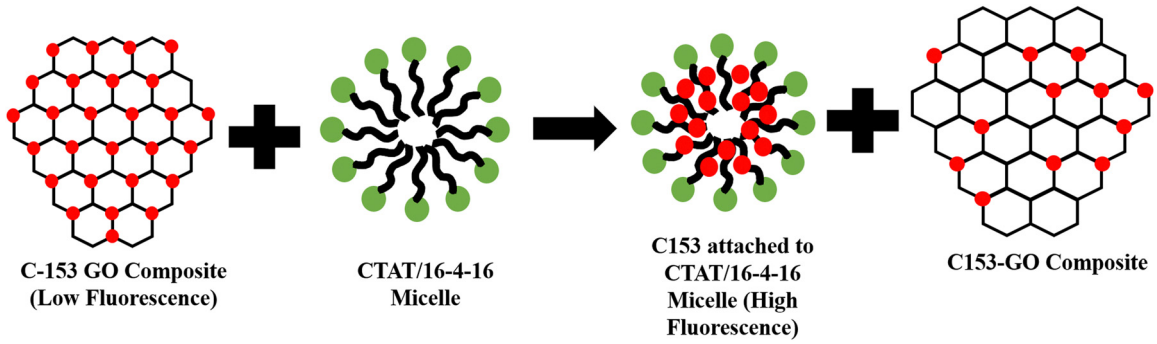

Scheme 1 Representation of C153–GO and C153–GO–CTAT/16-4-16 micelles.

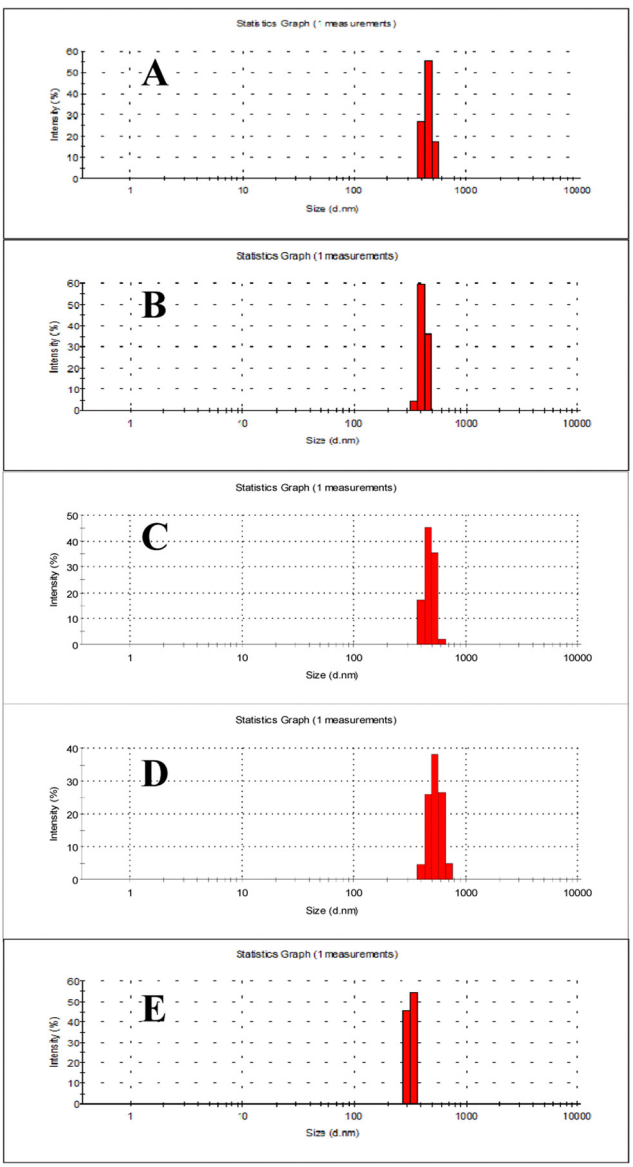

Fig. 14 Variation of the hydrodynamic diameter (D_h) of GO in the presence of C153 and surfactants: (A) GO–C153, (B) GO–C153–CTAT (below CMC), (C) GO–C153–CTAT (above CMC), (D) GO–C153–16-4-16 (below CMC), and (E) GO–C153–16-4-16 (above CMC).

interaction of the 16-4-16 surfactant with GO is more prominent than that of CTAT. There are two reasons for this: (1) electronic charge and (2) π–π interaction between GO and surfactants. Besides the electronic charge, the 16-4-16 surfactant also has a triple bond in the spacer, which is absent in the CTAT surfactant. Due to the presence of π-bonds in 16-4-16, it interacts more strongly with GO than CTAT, and the release of C153 from the GO sheet is more prominent in the presence of the 16-4-16 surfactant.

4.7. Surface plasmon resonance (SPR) band analysis

The generated surface plasmon resonance (SPR) bands of GO in the GO–C153 and GO–C153–CTAT/16-4-16 complexes were observed over time in order to determine the solution phase stability of the complexes (Fig. S4, ESI†). The UV-vis spectra of GO (Fig. 1(a)) reveal that it has two plasmon peaks, one at 237 nm (π–π* transition) and the other at 300 nm (n–π*). Three absorption peaks can be seen for the dye molecules (C153) at wavelengths of 434 nm, 260 nm, and 220 nm, respectively. The UV-vis spectra of the GO–C153 system show that the GO SPR band at 237 nm becomes red-shifted and overlaid with the dye peak at 260 nm, forming a new band for the complex at 256 nm. A substantial π–π interaction between GO and C153 in the GO–C153 complex is the reason for the shifting of the SPR band. A similar type of SPR band shifting of GO in the tannic acid–GO complex was also noted by Y. Zhang *et al.*[75] The SPR band of the GO–C153–CTAT/16-4-16 complex is a little bit more red-shifted (Fig. S4(C) and (D), ESI†). In order to verify the stability of the complexes, the SPR band change of the complex was monitored over time. This SPR band has been found to remain steady over

Table 7 A summary of size (diameter) and surface charge measurements of GO in the presence and absence of C153 and surfactants

Complex	Size (nm)		Zeta potential (mV)
	DLS	TEM	
GO	310	285	−33.1
GO–C153	420	326	−25.7
GO–C153–CTAT (below CMC)	476		24.6
GO–C153–CTAT (above CMC)	415	395	28.8
GO–C153–16-4-16 (below CMC)	515		33.5
GO–C153–16-4-16 (above CMC)	321	296	40.9

The standard deviations in measuring DLS and zeta potential are within 7% and 9% respectively.

time, suggesting that GO, C153, and surfactants formed a stable complex. Over time, the absorbance value of the complex decreases as the dye's adsorption on the graphene oxide nanosheet becomes more noticeable.

4.8. DLS and zeta potential measurements of binary and ternary systems

DLS measurements were performed to study the change in GOs' hydrodynamic diameter (D_h) in the presence of C153 and surfactants (Fig. 14). The size and surface charge of the complexes have a significant impact on their stability in the solution phase. GO exhibits a single DLS peak in an aqueous medium at around 310 nm, which is in good agreement with the value reported in the previous literature.[76] A small increase in the D_h of GO ($\sim$420 nm) was seen in the presence of C153. There was a very slight increase in diameter in comparison to GO in the case of the ternary complex (GO–C153–CTAT/16-4-16) when the concentrations of surfactants were considerably

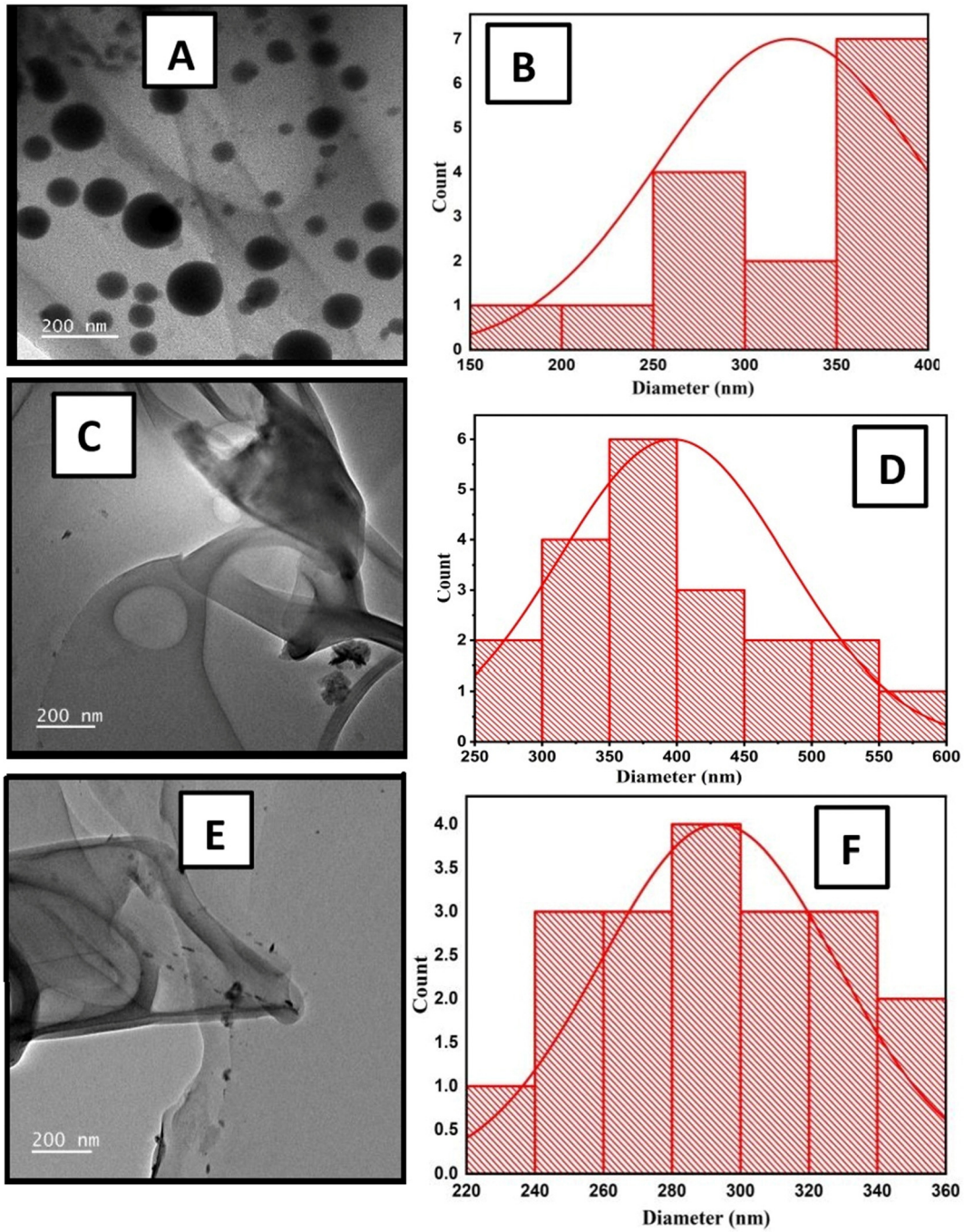

Fig. 15 TEM micrographs and corresponding size distribution plots of (A) and (B) GO–C153, (C) and (D) GO–C153–CTAT and (E) and (F) GO–C153–16-4-16, respectively.

above their CMC. However, a relatively large value of D_h was observed when the surfactant concentration was much below the CMC. Although the value is marginally less, the diameter of the complexes obtained by TEM coincides well with DLS (Table 7). The reason for this disparity is because DLS quantifies the size of the nanoparticles when solvent molecules are still attached to their surface, or their hydrodynamic size. It is evident from the mean size measurements that all of the composites have diameters between 300 and 500 nm (Table 7). This size distribution shows that the GO composites are sufficiently colloidally stable in solution. By measuring the zeta potential, the stability of the complexes was further confirmed. GO exhibits a negative zeta potential (−33.1 mV) in aqueous medium, because it contains a variety of oxygen-containing groups. The negative zeta value of GO decreases somewhat (−25.7 mV) in the presence of C153. A general positive potential of the complex was observed (both below and above the CMC of surfactants) when the negative potential of the GO–C153 composite disappeared in presence of surfactants. Here, the composite's total zeta potential lies at ±25–40 mV. This zeta potential value ensures the colloidal stability of GO complexes in solution.

4.9. TEM micrograph analysis of GO–C153 and GO–C153–CTAT/16-4-16

The TEM micrographs of GO–C153 (Fig. 15(A) and (B)) show multiple strongly contrasted circular black spots in comparison to pure GO flakes (Fig. 1(f)). The high contrast would suggest the aggregation of dye molecules concentrated on the surface of GO sheets as the high charge density of the aggregate prevents the passage of electrons generated and accelerated by the microscope. Interestingly, however, the majority of the black spots disappeared and the GO sheets became nearly transparent when surfactants were present (above their CMC) (Fig. 15(C)–(F)). This might be the result of the dye molecules disintegrating in the presence of surfactants. Therefore, it is evident from the TEM micrographs that dye molecules aggregate in the presence of GO and disaggregate in the presence of surfactants in the ternary system.

5. Conclusion

This study explores the interaction of the laser dye C153 with GO nanosheets in an aqueous dispersion, resulting in the formation of the GO–C153 composite. The maximum absorption peak of the dye shows a blue shift with increasing GO concentration, indicating the formation of the H-aggregate. Fluorescence measurements show a decrease in fluorescence intensity and a significant blue shift in the maximum fluorescence band, confirming the H-aggregate's development. UV-vis and lifetime plots reveal both static and dynamic mechanisms responsible for fluorescence quenching of C153 in the presence of GO dispersion. The aggregation and photophysical characteristics of the dye significantly change in the presence of surfactant solutions (CTAT and 16-4-16), with the gemini surfactant having a higher probability of dye–surfactant aggregate formation than CTAT due to its higher hydrophobicity. The spectroscopic analysis of the GO–C153–CTAT/16-4-16 ternary system revealed a drop in fluorescence intensity when GO was present, with a significant blue shift of the maximum peak and the blue shifted peak is bounced back to its original peak position along with an increase in intensity in the presence of surfactants. This ternary system behaves as an ideal fluorescence turn-off/turn-on system. The colloidal stability of GO–C153 and GO–C153–CTAT/16-4-16 systems was verified by measuring the SPR band, DLS and zeta potential of the systems, indicating sufficient colloidal stability of all the GO complexes. The C153–GO composite could be used as a fluorescent sensor for initial micelle detection, potentially useful in biological and biomedical systems.

Conflicts of interest

There are no conflicts to declare.

Acknowledgements

R. S., S. D. and R. B. thank CSIR, India for the senior research fellowship.

References

1 C. N. R. Rao, A. K. Sood, K. S. Subrahmanyam and A. Govindaraj, *Angew. Chem., Int. Ed.*, 2009, **48**, 7752–7777.
2 K. S. Novoselov, A. K. Geim, S. V. Morozov, D. Jiang, M. I. Katsnelson, I. V. Grigorieva, S. V. Dubonos and A. A. Firsov, *Nature*, 2005, **438**, 197–200.
3 K. S. Novoselov, A. K. Geim, S. V. Morozov, D. Jiang, Y. Zhang, S. V. Dubonos, I. V. Grigorieva and A. A. Firsov, *Science*, 2004, **306**, 666–669.
4 A. K. Geim and K. S. Novoselov, *Nat. Mater.*, 2007, **6**, 183–191.
5 K. Novoselov and V. Fal, *Nature*, 2012, **490**, 192–200.
6 A. Geim, *Science*, 2009, **324**, 1530–1534.
7 S. Zhang, K. Yang, L. Feng and Z. Liu, *Carbon*, 2011, **49**, 4040–4049.
8 L. Qu, Y. Liu, J.-B. Baek and L. Dai, *ACS Nano*, 2010, **4**, 1321–1326.
9 X. Dong, L. Wang, D. Wang, C. Li and J. Jin, *Langmuir*, 2012, **28**, 293–298.
10 X. Wang, L. Zhi, N. Tsao, Ž. Tomović, J. Li and K. Müllen, *Angew. Chem., Int. Ed.*, 2008, **47**, 2990–2992.
11 G. Eda and M. Chhowalla, *Adv. Mater.*, 2010, **22**, 2392–2415.
12 D. Kozawa, Y. Miyauchi, S. Mouri and K. Matsuda, *J. Phys. Chem. Lett.*, 2013, **4**, 2035–2040.
13 S. K. Cushing, M. Li, F. Huang and N. Wu, *ACS Nano*, 2014, **8**, 1002–1013.
14 P. Dutta, D. Nandi, S. Datta, S. Chakraborty, N. Das, S. Chatterjee, U. C. Ghosh and A. Halder, *J. Lumin.*, 2015, **168**, 269–275.

15 K. P. Loh, Q. Bao, G. Eda and M. Chhowalla, *Nat. Chem.*, 2010, **2**, 1015–1024.
16 C. Galande, A. D. Mohite, A. V. Naumov, W. Gao, L. Ci, A. Ajayan, H. Gao, A. Srivastava, R. B. Weisman and P. M. Ajayan, *Sci. Rep.*, 2011, **1**, 85.
17 M. Li, S. K. Cushing, X. Zhou, S. Guo and N. Wu, *J. Mater. Chem.*, 2012, **22**, 23374–23379.
18 S. K. Pal, *Carbon*, 2015, **88**, 86–112.
19 T. Szabó, O. Berkesi, P. Forgó, K. Josepovits, Y. Sanakis, D. Petridis and I. Dékány, *Chem. Mater.*, 2006, **18**, 2740–2749.
20 D. A. Dikin, S. Stankovich, E. J. Zimney, R. D. Piner, G. H. B. Dommett, G. Evmenenko, S. T. Nguyen and R. S. Ruoff, *Nature*, 2007, **448**, 457–460.
21 R. Hu, H. Gou, Z. Mo, X. Wei and Y. Wang, *Ionics*, 2015, **21**, 3125–3133.
22 X. Qi, K.-Y. Pu, X. Zhou, H. Li, B. Liu, F. Boey, W. Huang and H. Zhang, *Small*, 2010, **6**, 663–669.
23 J. Huang, X. Gao, J. Jia, J.-K. Kim and Z. Li, *Anal. Chem.*, 2014, **86**, 3209–3215.
24 L. Yang, H. Zhao, Y. Li, X. Ran, G. Deng, X. Xie and C.-P. Li, *ACS Appl. Mater. Interfaces*, 2015, **7**, 26557–26565.
25 R. Cheng, Y. Liu, S. Ou, Y. Pan, S. Zhang, H. Chen, L. Dai and J. Qu, *Anal. Chem.*, 2012, **84**, 5641–5644.
26 F. Liu, J. Y. Choi and T. S. Seo, *Biosens. Bioelectron.*, 2010, **25**, 2361–2365.
27 N. Karousis, A. S. D. Sandanayaka, T. Hasobe, S. P. Economopoulos, E. Sarantopoulou and N. Tagmatarchis, *J. Mater. Chem.*, 2011, **21**, 109–117.
28 D. Dinda, B. K. Shaw and S. K. Saha, *ACS Appl. Mater. Interfaces*, 2015, **7**, 14743–14749.
29 H. Dong, W. Gao, F. Yan, H. Ji and H. Ju, *Anal. Chem.*, 2010, **82**, 5511–5517.
30 Y. Liu, C. Liu and Y. Liu, *Appl. Surf. Sci.*, 2011, **257**, 5513–5518.
31 X.-F. Zhang and F. Li, *J. Photochem. Photobiol., A*, 2012, **246**, 8–15.
32 K. C. Hannah and B. A. Armitage, *Acc. Chem. Res.*, 2004, **37**, 845–853.
33 M. Kerker, *J. Colloid Interface Sci.*, 1985, **105**, 297–314.
34 L. Zhang and J. M. Cole, *J. Mater. Chem. A*, 2017, **5**, 19541–19559.
35 R. Karmakar and A. Samanta, *J. Phys. Chem. A*, 2002, **106**, 4447–4452.
36 H. Jin, G. A. Baker, S. Arzhantsev, J. Dong and M. Maroncelli, *J. Phys. Chem. B*, 2007, **111**, 7291–7302.
37 M. El-Kemary and W. Rettig, *Phys. Chem. Chem. Phys.*, 2003, **5**, 5221–5228.
38 H. Zhu, M. Li, J. Hu, X. Wang, J. Jie, Q. Guo, C. Chen and A. Xia, *Sci. Rep.*, 2016, **6**, 24313.
39 S. N. Alam, N. Sharma and L. Kumar, *Graphene*, 2017, **6**, 1–18.
40 F. M. Menger, J. S. Keiper and V. Azov, *Langmuir*, 2000, **16**, 2062–2067.
41 L. Shahriary and A. A. Athawale, *Int. J. Renewable Energy Environ. Eng.*, 2014, **2**, 58–63.
42 T. Zhang, D. Zhang and M. Shen, *Mater. Lett.*, 2009, **63**, 2051–2054.
43 K. Zhang, Y. Zhang and S. Wang, *Sci. Rep.*, 2013, **3**, 3448.
44 S. He, X. Liu, P. Yan, A. Wang, J. Su and X. Su, *RSC Adv.*, 2019, **9**, 4908–4916.
45 F. Zeng, Z. Sun, X. Sang, D. Diamond, K. T. Lau, X. Liu and D. S. Su, *ChemSusChem*, 2011, **4**, 1587–1591.
46 E. Bozkurt, M. Acar, Y. Onganer and K. Meral, *Phys. Chem. Chem. Phys.*, 2014, **16**, 18276–18281.
47 H. Wu, H. Wang, L. Xue and X. Li, *J. Colloid Interface Sci.*, 2011, **353**, 476–481.
48 J. Zhang, L. Chen, B. Zeng, Q. Kang and L. Dai, *Spectrochim. Acta, Part A*, 2013, **105**, 74–79.
49 M. Şinoforoğlu, B. Gür, M. Arık, Y. Onganer and K. Meral, *RSC Adv.*, 2013, **3**, 11832–11838.
50 G. Jones, II and M. A. Rahman, *J. Phys. Chem.*, 1994, **98**, 13028–13037.
51 I. M. Minisy, P. Bober, U. Acharya, M. Trchová, J. Hromádková, J. Pfleger and J. Stejska, *Polymer*, 2019, **174**, 11–17.
52 K. Erickson, R. Erni, Z. Lee, N. Alem, W. Gannett and A. Zettl, *Adv. Mater.*, 2010, **22**, 4467–4472.
53 R. Patel, M. U. Mir, J. K. Maurya, U. K. Singh, N. Maurya, M. U. Parray, A. B. Khan and A. Ali, *Luminescence*, 2015, **30**, 1233–1241.
54 S. Ghosh and S. Mondal, *J. Surf. Sci. Technol.*, 2012, **28**(3–4), 179–195.
55 U. Bhattacharjee, C. Beck, A. Winter, C. Wells and J. W. Petrich, *J. Phys. Chem. B*, 2014, **118**, 8471–8477.
56 N. Patra, B. Mandal and S. Ghosh, *Ind. Eng. Chem. Res.*, 2017, **56**, 10044–10052.
57 O. Stern and M. Volmer, On the quenching-time of fluorescence, *Phys. Z.*, 1919, **20**, 183–188.
58 H. M. Suresh Kumar, R. S. Kunabenchi, J. S. Biradar, N. N. Math, J. S. Kadadevarmath and S. R. Inamdar, *J. Lumin.*, 2006, **116**, 35–42.
59 D. Seth, S. Sarkar and N. Sarkar, *Langmuir*, 2008, **24**, 7085–7091.
60 P. Verma and H. Pal, *J. Phys. Chem. A*, 2014, **118**, 6950–6964.
61 S. Seraj and S. Rouhani, *J. Fluoresc.*, 2017, **27**, 1877–1883.
62 F. A. Wani, A. B. Khan, A. A. Alshehri, M. A. Malik, R. Ahmad and R. Patel, *J. Mol. Liq.*, 2019, **285**, 270–278.
63 M. J. Rosen and J. T. Kunjappu, *Surfactants and interfacial phenomena*, John Wiley & Sons, 2012.
64 A. Asadzadeh Shahir, S. Javadian, B. B. M. Razavizadeh and H. Gharibi, *J. Phys. Chem. B*, 2011, **115**, 14435–14444.
65 D. K. Chattoraj, *Adsorption and the Gibbs surface excess*, Springer Science & Business Media, 2012.
66 R. Patel, A. B. Khan, N. Dohare, M. Maroof Ali and H. K. Rajor, *J. Surf. Deterg.*, 2015, **18**, 719–728.
67 F. A. Wani, Y. Kumar, A. Anand, A. B. Bhat, K. A. Alzahrani, M. A. Malik and R. Patel, Exploration of Cloxacillin Sodium interaction with Aggregates of Benzimidazolium Gemini Surfactants: Spectroscopic and Biophysical Analysis, *ChemistrySelect*, 2023, **8**, e202301764.
68 B. Gohain and R. K. Dutta, *J. Colloid Interface Sci.*, 2008, **323**, 395–402.

69 Y. Liu, M. Liu, H. Yan, H. Liu, J. Liu, Y. Zhao, Y. Wu, Y. Zhang and J. Han, *J. Mol. Liq.*, 2021, **323**, 115073.
70 T. Sharma, N. Dohare, M. Kumari, U. K. Singh, A. B. Khan, M. S. Borse and R. Patel, Comparative effect of cationic gemini surfactant and its monomeric counterpart on the conformational stability and activity of lysozyme, *RSC Adv.*, 2017, **7**, 16763–16776.
71 R. Królicki, W. Jarzęba, M. Mostafavi and I. Lampre, *J. Phys. Chem. A*, 2002, **106**, 1708–1713.
72 E. Grueso, G. López-Pérez, M. Castellano and R. Prado-Gotor, Thermodynamic and structural study of phenanthroline derivative ruthenium complex/DNA interactions: Probing partial intercalation and binding properties, *J. Inorg. Biochem.*, 2012, **106**, 1–9.
73 A. Maciejewski, D. R. Demmer, D. R. James, A. Safarzadeh-Amiri, R. E. Verrall and R. P. Steer, *J. Am. Chem. Soc.*, 1985, **107**, 2831–2837.
74 T. Bayraktutan and Y. Onganer, *J. Lumin.*, 2022, **248**, 118947.
75 Y. Zhang, S. Liu, W. Lu, L. Wang, J. Tian and X. Sun, *Sci. Technol.*, 2011, **1**, 1142–1144.
76 I. Roy, D. Rana, G. Sarkar, A. Bhattacharyya, N. R. Saha, S. Mondal, S. Pattanayak, S. Chattopadhyay and D. Chattopadhyay, *RSC Adv.*, 2015, **5**, 25357–25364.

NJC

ROYAL SOCIETY OF CHEMISTRY

PAPER

Cite this: *New J. Chem.*, 2025, **49**, 12289

Hydrophobicity-directed structural alteration in cytochrome *C* induced by bile salts: physicochemical, spectroscopic, and atomic force microscopic studies with molecular docking analysis†

Raju Sardar, Rajesh Banik, Susmita Chowdhury and Soumen Ghosh *

Received 9th March 2025,
Accepted 18th June 2025

DOI: 10.1039/d5nj01078k

rsc.li/njc

Despite the biological relevance of bile salts in digestion and cellular signaling, their interaction with biological macromolecules, particularly with proteins, remains poorly understood. The current study shows a comprehensive and comparative analysis of the interaction between the bile salts, sodium cholate (NaC) and sodium deoxycholate (NaDC), and a small heme protein, cytochrome *C* (Cyt *C*), in aqueous phosphate buffer medium. Adsorption isotherm analysis suggests that the aggregation behavior and the surface activity of bile salts are significantly improved in the presence of Cyt *C*. Based on UV-vis spectroscopy measurements, the binding isotherms show that three different zones describe the interaction between bile salts and Cyt *C*, which are also replicated successfully from the steady-state fluorescence measurements. The calorimetric profile (ITC) of Cyt *C*'s interaction with the two bile salts exhibited a distinct pattern, indicating a different mode of interaction involved for the two bile salts. An 8–10% alpha helicity change was observed for Cyt *C* by exposure to NaC/NaDC, as indicated by CD spectroscopy measurements. DLS results indicate that swelling in protein structure and protein oligomer formation occur in the presence of bile salts. Electrochemical results reveal that the electron transfer process at the electroactive center of Cyt *C* is greatly modified in the presence of bile salts. The calculated binding constant value indicates that NaDC binds more strongly with Cyt *C* than NaC. Finally, we performed molecular docking studies, and the results were in agreement with the experimental results. The results of the entire experimental analysis imply that hydrophobicity of bile salts is a significant factor in protein structure modification in addition to electrostatic interaction. As bile salts have an indirect effect on the process of cell apoptosis, and cytochrome *C* plays a direct function in it, their interaction is of great importance in relation to cell apoptosis. Also, the modulation of the electron transfer process of Cyt *C* in the presence of NaC/NaDC makes it very important in biological and biomedical fields.

1. Introduction

In recent years, steroidal macrocycle compounds have garnered a lot of attention in domains such as pharmacology, sensing, drug delivery, supramolecular chemistry, and nanotechnology. Due to their exceptional conformational flexibility and ability to host guest molecules, they are essential tools for designing functional and responsive chemical systems. Among the various types of macrocyclic systems, those derived from or inspired by biological molecules, such as bile salts, have emerged as particularly appealing due to their biocompatibility and amphiphilicity. Bile acids and other steroidal components are common building blocks in supramolecular chemistry.[1,2] Bile acid analogues have demonstrated a wide range of biological applications, including anti-tumour, drug carrier, antifungal, and antibacterial applications.[3–5]

Particularly unique to biosurfactants, bile salts are produced by the liver and secreted into the duodenum upon ingestion of food. They are biologically active amphiphilic molecules with a rigid steroidal backbone and a flexible aliphatic tail. They have both hydrophilic and hydrophobic faces, with the α-oriented hydroxyl groups at the concave surface and the β-oriented methyl groups above the plane (convex surface) of the steroid skeleton.[6–10] Bile salts play an important role in the solubilization and absorption of fats and other lipid-soluble substances

Centre for Surface Science, Physical Chemistry Section, Department of Chemistry, Jadavpur University, Kolkata-700032, India. E-mail: gsoumen70@hotmail.com

† Electronic supplementary information (ESI) available. See DOI: https://doi.org/10.1039/d5nj01078k

in the body. The aggregation properties of bile salts are very complex compared to conventional micelle-forming amphiphiles. Various studies have been performed to interpret the self-aggregation behavior of bile salts. The primary aggregates of bile salts are formed at low concentration due to the hydrophobic interaction of the convex surface of the monomeric unit. The hydrophilic groups of the primary aggregates are believed to face outwards.[11] At higher concentrations of bile salts, the primary aggregates undergo aggregation to form higher-order aggregates with an elongated rod-like morphology.[12] Due to a large number of different tunable binding sites, bile salts serve as very good host systems for encapsulating a wide variety of hydrophobic and hydrophilic guest molecules.[13–15] Bile salts are very useful in several protein purification steps, such as the chromatographic separation of proteins.[16,17] The degree of protein purification by bile salts is highly dependent on the nature of the interaction between proteins and bile salts. Consequently, quantitative studies of bile salt–protein interactions are of great importance for a complete understanding of bile salt-mediated protein purification. The current investigation of the interactions of bile salts with different biological macromolecules, especially proteins, has been spurred by a rise in the applications of bile salts in various domains, particularly drug delivery and pharmaceuticals.[18,19] The interactions between proteins and bile salts are used to monitor several physiological processes, making them a valuable first step in finding new therapeutic targets for the management and prevention of metabolic diseases and also becoming increasingly important in understanding intracellular lipid transport.[20] Furthermore, bile salts can also be employed in proteomics, which includes protein purification, separation, and crystallization due to their mild detergent properties.[21,22] Bile salts are also commonly utilized in various pharmaceutical formulations to maintain drug stability, increase drug solubility, and enhance drug absorption, permeation, and bioavailability.[23,24] Bile salts have recently been employed as substrates for derivatives appropriate as building blocks for the construction of innovative superstructures, inspiring creative ideas of developing supramolecular versions of biological macromolecules.[25,26] Although their physiological functions are well established, little is known about their ability to function as supramolecular building blocks and molecular hosts for protein molecules.

In parallel, Cyt *C* is an iron-containing metalloprotein and has been structurally well characterized in both solution and crystalline states. It is a small, globular, water-soluble protein containing a long polypeptide of 104 amino acid residues. The heme group of Cyt *C* is attached to four amino acids (Cys 14, His 18, Met 80, and Cys 17) and is linked to non-covalent side chains that rigidify the internal structure around the heme group. Therefore, structural alterations of the protein in the presence of various ligands are highly complex. The presence of the heme group allows Cyt *C* to undergo a redox reaction. The biological respiratory chain depends on cytochrome *C*, which receives electrons from cytochrome *C* reductase and transfers them to cytochrome *C* oxidase. Cyt *C* activity is crucial for mitochondrial function and is also linked to several other processes, such as cell proliferation, apoptosis, cellular differentiation, and cell cycle regulation.[27] Cyt *C* also plays a role in the start of apoptosis by aberrant cytoplasmic accumulation, which sets off signaling cascades that result in cell malfunction.[28] It has been shown that the release of Cyt *C* from the mitochondria into the cytoplasm can either trigger or initiate apoptosis by interacting with cytoplasmic proteins such as caspase, TIB, Bcl-2, and apaf-1.[29] Mitochondrial malfunction causes cell apoptosis and is associated with a variety of diseases.[30] Furthermore, malfunction of Cyt *C* can alter the mitochondrial membrane potential (MMP) and result in respiratory chain dysfunction.

The study of bile salt–protein interactions within a macrocyclic framework links supramolecular chemistry and bioengineering. It supports international initiatives for bionanomaterials, customized medicine, and environmentally friendly technology. Bio-derived macrocyclic systems have the potential to reduce dependence on synthetic polymers and promote sustainable chemical processes, making them more broadly relevant to governance and policy.

There are very limited reports available in the literature about the effect of bile salts on the structure and stability of proteins. Mukherjee *et al.*[31] have investigated the interaction of HSA proteins with a series of bile salts, sodium cholate (NaC), sodium deoxycholate (NaDC), and sodium taurocholate (NaTC), at their pre- and post-micellar concentration and showed that the hydrophobic residue of bile salts plays an important role in the interaction process. Mohanty *et al.* have made an interesting comparative study between the single tryptophan and double tryptophan residue-containing proteins (HSA and BSA, respectively) with sodium deoxycholate (NaDC) interactions.[32] Interaction takes place in three different zones, and no appreciable change in the α helix was observed. Zsila *et al.* noted that the interhelical π–π stacking interaction between Tyr138 and Tyr166 is disrupted when bile acids bind to subdomain IB of HSA.[33]

The majority of the research in the literature focuses on the interaction of bile salts with the albumin protein. However, a comprehensive analysis of bile salts interacting with various heme proteins is unlikely to be found in the literature. The interaction of the electron transport heme protein Cyt *C* with bile salts is particularly important for cell apoptosis (cell death). Bile salts, especially at higher concentrations, act as cytotoxic agents involved in the cell death process. Hydrophobic bile salts can disrupt the mitochondrial membrane, leading to the release of various pro-apoptotic molecules. Cyt *C* is the key pro-apoptotic protein released by mitochondrial cells, primarily responsible for the apoptotic process. Although bile salts and Cyt *C* do not co-localize, they can come outside during cell death, increasing the probability of interaction outside of their initial compartments.

Here, we seek to clarify the interaction between the bile salts (sodium cholate (NaC)/sodium deoxycholate (NaDC)) and Cyt *C* in phosphate buffer at a physiological pH of 7.4. Here, we performed several interfacial, spectroscopic, thermodynamic,

electrochemical, and morphological studies to probe the details of the interaction. Molecular docking studies further validate the experimental results. Our experimental results suggest that bile salts can effectively modulate the structure and electron transfer process of Cyt *C*, which is very beneficial in the biological, biomedical, and biotechnological fields.

2. Experimental section

2.1. Materials

Horse heart cytochrome *C* (Cyt *C*) (CAS No. 9007-43-6, purity: 95%), sodium cholate (NaC) (CAS No. 206986-87-0, purity: 99%), and sodium deoxycholate (NaDC) (CAS No. 302-95-4, purity: 97%) were purchased from Sigma-Aldrich Corporation (USA). Sodium dihydrogen phosphate (NaH_2PO_4) (CAS No. 7558-80-7, purity: 99.9%) and disodium hydrogen phosphate (Na_2HPO_4) (CAS No. 7558-79-4, purity: 99.9%) were AR-grade products purchased from Merck, India. All experiments were conducted using highly pure double-distilled water. Bile salts (NaDC/NaC) were recrystallized in ethanolic solution[34] before tensiometric measurements. Several early studies found a minimum in the tensiometric profile of bile salts due to the presence of impurities in the purchased sample.[34] To remove these impurities, the bile salt sample was recrystallized.

All sample solutions were prepared in a sodium phosphate buffer (10 mM) with a pH of 7.4. A CL 54 pH meter (Toshniwal Pvt. Ltd, India) was used to test pH with an accuracy of ±0.01. The temperature is maintained at a constant value of 298 ± 0.2 K.

The Cyt *C* solution concentration was maintained at 5 μM throughout the investigation, except for CD spectroscopy, where 2.5 μM proteins were used for instrumentation. In the CD experiment, high concentration of the sample causes voltage fluctuations, resulting in noise in the CD spectra. To circumvent problems in the CD experiment, we have chosen a comparatively low concentration of Cyt *C* (2.5 μM) compared to the other experiments. The concentration of Cyt *C* was estimated using absorption spectral measurements, utilizing the molar extinction coefficient (ε) value of 106 100 M^{-1} cm^{-1} at 409 nm for Cyt *C*.[35]

2.2. Instrumentation

2.2.1. Tensiometry. Surface tension was measured using a calibrated du Noüy ring tensiometer (Kruss, Germany) with a platinum ring. Before each experiment, the ring was washed with double-distilled water and acetone and then flame-treated with ethanol. A 5 mL Cyt *C* solution was taken into a Corning glass container, followed by the dropwise addition of stock bile salt solutions (having a concentration of 15× CMC) using a Hamilton micro-syringe. Following a 5-minute equilibration period, measurements were conducted with a precision of ±1 mN m^{-1}.

2.2.2. UV-vis spectroscopy. A Shimadzu UV-vis spectrophotometer (Model 1601) and a matching quartz cuvette (0.5 cm path length) were used to record the absorbance spectra of Cyt *C*. During the optical titration of Cyt *C*, an equal amount of bile salt solution was applied to the reference and sample cuvettes to avoid bile salt absorption. Measurements were performed after complete mixing, with an error margin of ±0.3%.

2.2.3. Steady-state fluorescence spectroscopy. Fluorescence measurements were conducted using a PerkinElmer LS 55 spectrofluorometer connected with a PTP1 Peltier setup. A quartz cuvette (1 cm path length) containing 2.5 mL of Cyt *C* solution was excited at 280 nm, and emission spectra were recorded from 295 to 500 nm with 5 nm excitation and emission slits. The scan rate was fixed at 250 nm min^{-1}.

2.2.4. Circular dichroism (CD) spectroscopy. Protein conformational changes were studied using CD spectra recorded in the far-UV region using a Jasco spectropolarimeter and 1 cm quartz cuvettes in a nitrogen inert atmosphere. The sample temperature was maintained at 298 ± 0.2 K using a Neslab RTE-111 rotating water bath and water-jacketed quartz cuvettes. The secondary structures of Cyt *C* were calculated using CDNN 2.1 software. The following equation has been used to express the CD data as mean residue ellipticity (MRE) in deg cm^2 $dmol^{-1}$.

$$\mathrm{MRE} = \theta_{\mathrm{obs}}/10nl[\mathrm{c}] \quad (1)$$

where [c] is the molar concentration of proteins, n represents the number of amino acid residues present in protein molecules, l is the path length of the cell, and θ_{obs} is CD in mdeg.

2.2.5. Dynamic light scattering (DLS) measurements. DLS measurements were carried out at 632.8 nm using a Nano ZS Zetasizer (Malvern, UK) at a 90° scattering angle with a He–Ne laser at room temperature. Samples were filtered three times using a 0.2 μM pore size syringe before each measurement. 15 consecutive runs were made for each experiment, and their average value was recorded.

2.2.6. Cyclic voltammetry (CV) study. CV measurements were performed using an AUTOLAB potentiostat/galvanostat with a three-electrode system: Pt foil (counter), Pt wire (working), and saturated calomel electrode (SCE) (reference) at 298 K. Cyt *C* (10 μM) in 10 mM phosphate buffer (pH 7.4) was used. Scans were run at 50 mV s^{-1}. After bile salt addition, data were recorded post-equilibration. Nitrogen gas was purged into the solution before each measurement.

Electrode preparation. The Pt wire was first cleaned with distilled water, followed by sonication in ethanol and double-distilled water to eliminate any organic impurities. In addition, before beginning each experiment, the Pt wire was electrochemically cleaned. To eliminate surface contaminants, the Pt-foil was first washed with distilled water and then immersed in concentrated HNO_3 for 15 minutes. It was then carefully washed and dried. SCE was used as received and frequently examined for leaks and correct filling. When it is not used, it is kept in saturated KCl.

2.2.7. Isothermal titration calorimetry (ITC) measurements. ITC measurements were performed using a Microcal ITC-200, Malvern, UK, instrument at 298 K. Each ITC experiment comprised 19 injections of bile salt from the syringe into

the protein sample in the cells spaced 180 s apart. 300 mL of protein solution (5 μM) was taken in the cell, and 2 μL of bile salt (60 mM NaDC and 120 mM NaC) solution was added from a syringe in every single injection. The heat absorbed or emitted at each stage of surfactant addition, owing to interaction with protein, was recorded, and using ITC software, the collected data were analyzed.

2.2.8. Atomic force microscopy (AFM) measurements. Topographical investigation of Cyt *C* in the absence and presence of NaDC/NaC was performed with an Innova-S2 AFM (Bruker, USA) in tapping mode. Cyt *C* solutions (5 μM) were drop-cast on mica and dried overnight in a desiccator. WSxM 5.0 software was used to analyze the images.

2.2.9. Theoretical. From the RCSB Protein Data Bank, the crystal structure of Cyt *C* (PDB ID: 1CGO) was obtained. Docking experiments were carried out using AutoDock 4.2 and the Lamarckian Genetic Algorithm (LGA). DFT was used to optimize the NaDC and NaC structures at the B3LYP/6-311++G(d,p) level using Gaussian 09W. The docking settings used a grid box (126 × 126 × 126 Å, spacing 0.408 Å) with a GA population of 150. PyMOL was used to depict the conformation with the lowest energy from the 10 runs. A large grid box was employed to ensure comprehensive exploration of all potential binding sites, particularly around the heme center. Similar approaches have been adopted in various previous studies, where such types of large grid boxes have been used to understand the protein–ligand interaction. For example, Mukherjee *et al.*[31] have taken a grid box of (126 × 126 × 126 Å) in their docking studies of several bile salts with HSA protein.

2.3. Uncertainty of the various measurements

However, multi-technical approaches provide a deeper understanding of the bile salt–Cyt *C* interaction, each method introduces specific uncertainty. Tensiometry is highly sensitive in monitoring the interfacial changes; however, its accuracy highly depends on the purity of the sample and handling. UV-vis spectroscopy and fluorescence can accurately predict the structural and microenvironmental changes of protein, but their sensitivity may be influenced by spectral overlap or the inner filter effect. CD spectroscopy can accurately predict the change in the helical structure of protein, although its sensitivity may be hampered by voltage fluctuation or absorption of CD radiation by the buffer medium. DLS provides size distribution; however, its accuracy may be influenced by aggregate formation in solution. ITC can directly provide various thermodynamic parameters; however, it assumes a uniform binding model and is sensitive to the buffer medium. To mitigate these uncertainties, we have recrystallized the bile salt to remove the impurity for tensiometric measurements. We have properly made the baseline before taking the UV-vis spectra to eliminate the solvent contribution. We have also removed the bile salt absorption from the original absorption spectra by adding the same amount of bile salt to both the sample and reference cuvette. We have subtracted the buffer absorption spectra from the original sample spectra in CD measurements to cancel any contribution from the buffer. Before DLS measurements, we filtered the sample three times to remove the larger aggregates. In CV measurements, we have properly washed all the electrodes to avoid any contamination. All the experiments were also repeated to fix the various uncertainty issues. Despite these limitations, the consistency across independent measurements supports the robustness of our conclusion.

3. Results and discussion

3.1. Adsorption isotherm analysis

Since bile salts are a typical class of bio-surfactants, the study of their micellization and interfacial properties in the absence and presence of proteins is very important. The mechanism of micellization of bile salts is very different than the other standard surfactants due to their unique steroidal structure. The concentration that corresponds to the last break point in the surface tension (γ) *versus* logarithm of the total molar bile salt concentration plot is used to determine the CMC for both the pure bile salt and mixed protein–bile salt systems. The CMC value for sodium cholate and deoxycholate in phosphate buffer is lower than that obtained in an aqueous medium,[36–38] and this is due to the high ionic strength of the phosphate buffer medium. The plots of surface tension of bile salts (NaDC and NaC) in the presence and absence of cytochrome *C* are presented in Fig. 1(A and B). The inset plot is used to clearly visualize the variation in the CMC of bile salts in the presence of proteins.

From the plots, it can be seen that in the presence of protein molecules, there are lower surface tension values compared to their absence, suggesting that the protein molecules have sufficient surface activity. The plot of γ *vs.* $\log C$ for bile salts shows a modest minimum both in the absence and presence of protein molecules, which is attributed to the presence of a little impurity in the sample.[39] The supplied bile salt sample may contain a long-chain alcohol as an impurity. Because of its greater surface activity, the long-chain alcohol has a lower surface tension than bile salts. The impurity becomes dissolved in the micelles as they start forming, which lowers the concentration of long-chain alcohol in the bulk and, consequently, at the surface as well. As a result, the surface tension starts to rise and eventually reaches that of the pure bile salt solution. This explains why the plot of γ *vs.* $\log C$ for bile salts shows a minimum in the presence of impurities. So, this tensiometric graph reveals that recrystallization does not completely remove the impurity.

The change in the CMC value for bile salt type bio-surfactants in the presence of various additives is relatively small[40,41] compared to conventional surfactants. The obtained CMC value for NaDC and NaC is lower in the presence of Cyt *C* compared to that in its absence, *i.e.*, the aggregation process of bile salts becomes facile in the presence of Cyt *C*. This may be due to the presence of an overall positive charge on Cyt *C* at a fixed pH of 7.4 (the iso-electric pH of Cyt *C* is 9.6), and this positive charge minimizes the electrostatic repulsion between the negatively charged head groups of cholates and

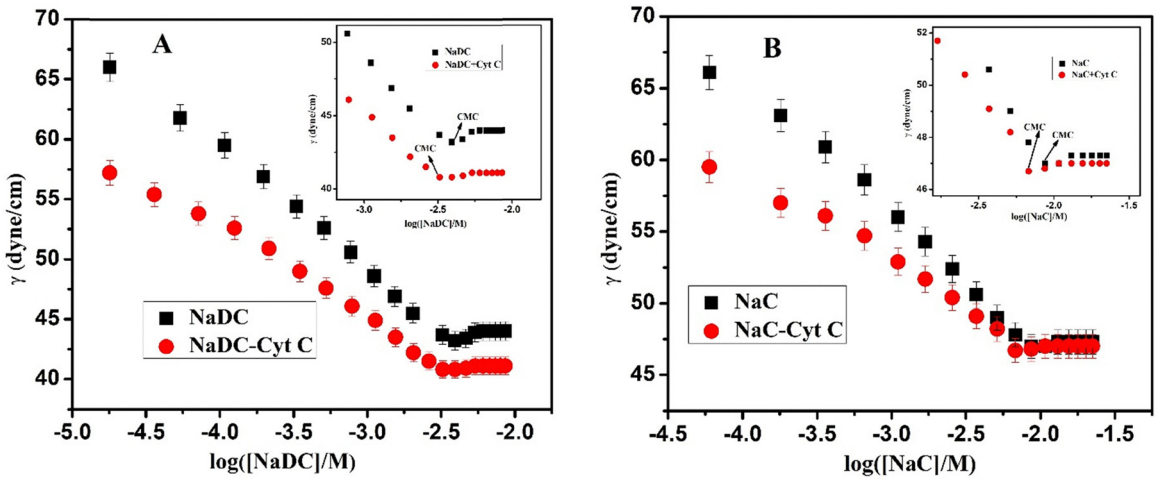

Fig. 1 Tensiometric profile of bile salt surfactants (NaDC and NaC) in the absence and presence of heme protein Cyt-*C* (5 μM) (A) for sodium deoxycholate (NaDC) and (B) sodium cholate (NaC) in phosphate buffer medium (pH 7.4) at 298 K (inset plot presents the tensiometric profile on a smaller scale).

deoxycholate monomers, which in turn makes the micellization process facile. Since protein molecules also have a large hydrophobic residue, hydrophobic–hydrophobic interaction between the bile salts and proteins is also responsible for lowering the CMC value in the presence of protein molecules.[42]

To gain more perception about the Cyt *C* and sodium cholate/deoxycholate interaction, the interfacial parameters were calculated at the air/liquid interface. The calculated parameters are depicted in Table S1 (ESI†).

It was noted that in the presence of Cyt *C*, the Π_{CMC} (surface pressure) value decreases for sodium cholate and deoxycholate compared to the pure one. This suggests that in the presence of Cyt *C*, the population of bile salts at the air/water interface decreases. The probable reason for the decrease in the population of bile salts at the interface may be the formation of a solubilized complex between the bile salts and proteins through both hydrophobic and electrostatic interactions, resulting in some bile salts going to the bulk from the interface by complex formation. As a result, there was a decrease in the Π_{CMC} value observed for bile salts in the presence of Cyt *C*.

The obtained Γ_{max} (Gibbs surface excess concentration) value and consequently A_{min} for pure bile salts are matched well with the literature-reported value.[43] From Table S1 (ESI†), it can be seen that in the presence of the Cyt *C* molecule, both sodium cholate and deoxycholate have a lower value of Γ_{max}, *i.e.*, surface excess concentration of bile salt decreases in the presence of Cyt *C*. The reduced efficiency of bile salts in populating the air/water interfacial monolayer in the presence of protein molecules suggests the possible formation of a solubilized Cyt *C*–bile salt complex at the monolayer. Consequently, the value of A_{min} for two bile salts is enhanced in the presence of Cyt *C*, suggesting the possible formation of the protein–bile salt complex. If we compare the Γ_{max} value of two pure bile salts, it can be seen that NaDC has a higher value than NaC. This phenomenon can be explained based on the hydrophilicity of the two bile salts. Due to the presence of an extra hydroxyl group, NaC is much more hydrophilic than NaDC. Since NaC is more hydrophilic than NaDC, it has a greater propensity to enter the bulk phase, which lowers its Γ_{max} value. The obtained A_{min} value for bile salts is much higher compared to conventional surfactants, suggesting that bile salts are loosely packed at the interface. Another important surface parameter is pC_{20}, which is indicative of the efficiency of the interfacial adsorption of amphiphiles. The greater value of pC_{20} suggests that the amphiphiles have a greater tendency to adsorb at the air/water interface. It can be seen from Table S1 (ESI†) that the pC_{20} of both bile salts decreases in the presence of Cyt *C*, *i.e.*, the interfacial adsorption efficiency of bile salts decreases in Cyt *C* medium. This suggests that the formed bile salt–Cyt *C* complex has a greater propensity to enter the bulk, resulting in some bile salts going to the bulk from the interface by complexation. The adsorption and micellization Gibbs free energy changes were calculated using the following equations.[44]

$$\Delta G^0_{mic} = RT \ln X_{cmc} \quad (2)$$

$$\Delta G^0_{ads} = \Delta G^0_{mic} - (\pi_{cmc}/\Gamma_{max}) \quad (3)$$

where X_{cmc} represents the critical micelle concentration of the mixture of two components at a given mole fraction. The standard free energy changes (ΔG^0_{mic} and ΔG^0_{ads}) are used to verify whether the process of micellization in the solution and the process of adsorption at the air/liquid interface are enhanced or not in the presence of protein molecules. The negative values of both ΔG^0_{mic} and ΔG^0_{ads} indicate that both processes are spontaneous in the medium. The ΔG^0_{mic} and ΔG^0_{ads} for pure bile-salt and bile salt/Cyt *C* systems are given in Table S1 (ESI†).

The values of adsorption-free energy change are significantly higher than those for micellization in both the presence and absence of the protein molecule, signifying that adsorption is the primary process, whereas micellization is secondary. Thus,

air/liquid interface adsorption is much more spontaneous than micellization in the solution. In the presence of protein molecules, both the standard free energy change of micellization and the energy change of adsorption are increased compared to the free bile salts. Since proteins and bile salts are oppositely charged, in the presence of proteins, the mutual repulsion between the similarly charged head groups of bile salts adsorbed at the interface is minimized, leading to more spontaneity of bile salt adsorption. The intermolecular or intramolecular hydrophobic interactions of bile salts and Cyt *C* are significantly favored, perhaps due to protein unfolding and surfactant–protein complex formation, resulting in the adsorption at the interface before micelle formation in the solution. Also, the standard Gibbs free energy value of micellization for both the surfactants in the presence of Cyt *C* is higher than that in its absence, indicating that micellization is favored in the presence of Cyt *C*. Since Cyt *C* has a charge that is opposite to that of bile salt, the presence of Cyt *C* molecules reduces the electrostatic repulsion between the charged head groups of bile salts, which leads to early micellization.

So, the tensiometric results validate the possible formation of the bile salt–Cyt *C* complex and also predict the nature of the formed protein–bile salt complex (loose/strong). The technique's sensitivity is reflected in its ability to detect minute variations in the CMC value of the bile salt in the absence and the presence of Cyt *C*. These findings support the conclusion that the surface activity of bile salts significantly improved in the presence of Cyt *C*.

3.2. Steady-state spectral analysis

UV-vis measurements. The original state of Cyt *C* shows a typical Soret band with maximum intensity at around 409 nm, which indicates the presence of methionine and axial ligands. In the presence of sodium cholate and deoxycholate, a change in the absorbance of the protein at 409 nm was recorded, shown in Fig. 2(A and B) (here we present the UV-vis spectra

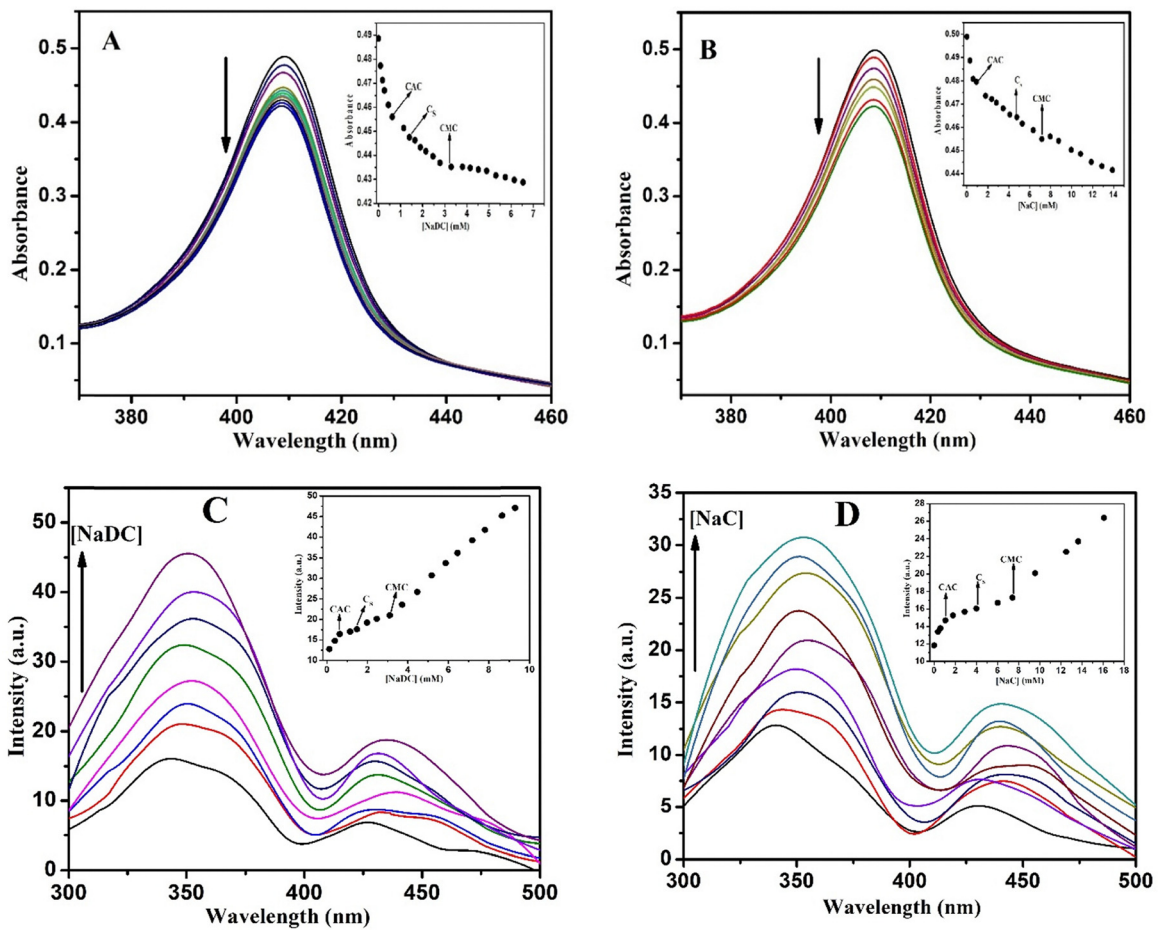

Fig. 2 Absorption spectra of Cyt *C* in the presence of various amounts of (A) NaDC (0, 0.08, 0.17, 0.62, 1.14, 2.46, 3.80, 5.31, 7.31, and 8.05 mM respectively) and (B) NaC (0, 0.29, 0.89, 1.77, 2.81, 4.08, 5.27, 7.14, 9.95, 10.88, 13.55, and 14.52 mM respectively) at 298 K (inset: plot of the variation in the absorbance of Cyt *C* (taking absorbance at 409nm) with concentrations of NaDC and NaC respectively). Steady-state fluorescence spectra of Cyt *C* in the presence of various amounts of (C) NaDC (0, 0.14, 0.93, 1.97, 3.21, 4.11, 5.99, and 9.55 mM respectively) and (D) NaC (0, 0.59, 1.77, 3.99, 6.01, 9.31, 12.49, 16.12, and 18.32 mM respectively) at room temperature (inset: changes in the fluorescence intensity of Cyt *C* with the concentration of NaDC and NaC, respectively).

on a smaller wavelength scale to clearly visualize the change in absorbance at 409 nm upon bile salt addition; the UV-vis spectra with a full wavelength scale are available in the supporting file in Fig. S1 (A and B), ESI†). From Fig. 2(A and B), it is seen that in the presence of sodium cholate and sodium deoxycholate, the maxima of the Soret band remain at 409 nm all over the bile salt concentration range analyzed, hence indicating the continuance of methionine ligation in Cyt *C*. Again, it is observed that when sodium cholate and deoxycholate are added to the protein solution, the absorbance of the Soret peak (at 409 nm) is reduced with each addition. The observed decrease in absorbance intensity may be attributed to the alteration in the electronic transition due to the protein unfolding near the heme environment.[45] The observed spectral variation may result from electrostatic perturbation or conformational adjustments induced by bile salt binding, as suggested by the docking-derived distances. Docking analysis suggests that although there is no direct co-ordination present between the bile salts and heme group of Cyt *C*, bile salts can indirectly influence the microenvironment of the protein through long-range electrostatic interaction. So, the bile salt-influenced uncoiling is driven by both non-polar (non-electrostatic) and electrostatic interactions.

The inset plot of Fig. 2(A and B) demonstrates a sharp decrease in absorbance, up to concentrations of 1.03 mM for sodium cholate and 0.59 mM for sodium deoxycholate. In this region, bile salt monomers bind to the different positively charged amino acid moieties of proteins *via* electrostatic and hydrophobic interactions. The structural alteration of the protein is significantly more pronounced in this region, resulting in a rapid decrease in absorbance. This zone is known as the critical aggregation concentration (CAC) zone of bile salt. At CAC, a small micelle-like cluster is formed with a lower aggregation number. Following CAC, the rate of decrease in the absorbance value of Cyt *C* slows down as the concentration of bile salts increases, reaching 4.73 mM for sodium cholate and 1.41 mM for sodium deoxycholate. In this region, the backbone of the protein is saturated by the bile salts. This region is known as the saturation concentration (C_S) zone. After C_S, the decrease in the absorbance becomes much slower up to CMC, suggesting that in this region the structural change of Cyt *C* is not so prominent. In this region, the protein-surface-bound bile salt monomers started to form aggregates among themselves. Following that, the change in the absorbance value of Cyt *C* becomes negligible with the bile salt concentration. In this case, free bile salt micelles are formed in solution, which have no significant effect on protein structure.

The above observation suggests that the structural modification of Cyt *C* occurs mainly in the presence of free bile salt monomers, and micelles do not play many roles in it. Also, three distinct breakpoints (CAC, C_S, and CMC) could be readily identified using absorbance measurements (Table 1), although surface tension measurements did not provide this information. Since the spectroscopic measurements are more sensitive to identifying the minute change in the protein structure, the interaction zone of bile salts and Cyt *C* is easily observed from UV-vis measurements. So, the binding isotherm obtained from UV-vis measurements suggests that the interaction of bile salts and Cyt *C* takes place in three critical zones.

Table 1 Transition concentration of bile salts in the presence of heme protein Cyt *C* (5 μM) obtained from absorbance measurements at 298 K

System	CAC (mM)	C_S (mM)	CMC (mM)
NaDC-Cyt *C*	0.59	1.41	3.18
NaC-Cyt *C*	1.03	4.73	7.18

The UV-vis results provide precise insights into the bile salt-Cyt *C* interaction, and the spectrum alterations correspond to expected structural changes. The main breakpoints (CAC, C_S, and CMC) were easily recognized in UV-vis spectra, demonstrating the technique's sensitivity to small structural changes. These data support the hypothesis that bile salt monomers have a greater impact on protein conformational changes than bile salt micelles.

Fluorescence analysis. Fluorescence emission is used to study the tertiary structural changes of Cyt *C* in the presence of bile salts (NaDC/NaC). This is presented in Fig. 2C and D, respectively. In Cyt *C*, the major fluorescence is given by tryptophan (Trp 59); apart from this, a small fluorescence is also observed for the porphyrin residue of the protein.[46] In native Cyt *C*, the emission intensity is very low compared to other globular proteins. This low fluorescence in native Cyt *C* is due to energy transfer from the fluorophore (Trp 59) to the adjacent heme group of the porphyrin ring, leading to a decrease in the fluorophore (Trp 59) emission.

In Cyt *C*, the tryptophan residue (Trp 59) is attached to one of the propionic groups of heme. This aromatic Trp 59 residue is mainly responsible for giving the emission spectra of Cyt *C*; however, the emission intensity is considerably low due to the proximity of the heme group to Trp 59, which results in a Förster energy transfer between Trp 59 and the heme group, starting from the former to the latter, thus diminishing the emission of the fluorescence spectra.[47,48] As the separation between the heme group and Trp 59 increases, an increase in the intensity of the fluorescence spectra of the protein can be seen.[49] As a result, molecular expansion around heme is frequently detected using the phenomenon of change in fluorescence emission intensity.

Fig. 2C and D show that native cytochrome *C* exhibits a prominent emission peak around 342 nm, which can be attributed to tryptophan fluorescence. In addition, a separate emission peak is observed near 432 nm, which likely arises from porphyrin fluorescence and is typically weak and largely quenched due to the strong absorption properties of heme. With increasing concentrations of both the bile salts, the fluorescence intensity of Cyt *C* also increases. This may be attributed to the unfolding of proteins by interacting with the bile salts. When the protein unfolds, the separation between the Trp 59 residue and the heme group increases, thus reducing the extent of Förster energy transfer between them, which in turn increases the fluorescence intensity, concurrently with a loss in the tryptophan structure.

Ahluwalia and his co-workers[50] observed that when the concentration of the anionic surfactant Sodium Dodecyl Sulfate (SDS) increases, fluorescence intensity also increases to a greater extent. The same type of observation was reported by Singh *et al.* for the interaction of the long-chain imidazolium ionic liquid surfactant with Cyt *C*.[51] Anionic biosurfactants, sodium cholate and deoxycholate, manifest an analogous observation. In addition to the increased fluorescence intensity of Cyt *C*, the presence of bile salts caused a notable red shift in the emission maxima. The red shift in the emission maxima is caused by an increase in the polarity of the microenvironment surrounding the fluorophore (tryptophan 59) following unfolding and exposure to the solvent.[52] Initially, the tryptophan group was inside the hydrophobic cavity of proteins, where it was in a less polar medium, but after it unfolded, it became exposed to the polar solvent. Therefore, the red-shifting is caused by a variation in polarity surrounding the fluorophore (Tr 59) moiety. The molecular docking-based distance calculation suggests that no direct coordination between the heme group and the bile salt is present. So, the long-distance electrostatic force and hydrophobic interaction are primarily responsible for this tertiary structural variation observed from steady-state fluorescence measurements.

The inset plot of Fig. 2C and D depicts the change in the fluorescence intensity of Cyt *C* with various concentrations of sodium cholate and deoxycholate. From this figure, three well-defined breakpoints corresponding to CAC, C_S, and CMC of the bile salts in the presence of Cyt *C* are observed. Here, a rapid increase in fluorescence intensity was observed up to CAC. In this region, the bile salt monomer bounds to the various positively charged sites of protein, which were already discussed in the UV-vis analysis. After CAC, a plateau region is found, which is known as C_S. In this region, the bile salt monomer covered the entire protein surface. Following this, a notable rise in fluorescence intensity was seen up to CMC once more. Here, past the CMC, a continuous increase in the fluorescence intensity was observed. Different factors may contribute to the rise in protein fluorescence intensity beyond CMC: (1) in aqueous buffer medium, protein exists in both monomeric and aggregated forms (as evidenced by DLS data). In the presence of bile salt micelles, protein–protein aggregation may be disrupted due to electrostatic and hydrophobic interactions between the oppositely charged micelle and protein molecules, and the protein monomer is uniformly distributed on the oppositely charged micelle surface. As a result, the percentage of monomeric protein molecules that emit fluorescence may rise in the system, resulting in increased fluorescence. (2) The hydrophobic heme moiety can be solubilized in the hydrophobic cavity of the bile salt micelle. The solubilization of heme in micelles can increase the distance between heme and Trp59, reducing energy transfer between Trp59 and heme and increasing fluorescence.[53] The results of the breakpoints (CAC, C_S, and CMC) matched well with the values obtained from absorbance measurements. So, the binding isotherm obtained from UV-vis measurements of bile salts and Cyt *C* interaction is well reproducible from the steady-state fluorescence measurements.

3.3. Benesi–Hildebrand plot analysis

A quantitative analysis of bile salts (sodium cholate and deoxycholate) interacting with Cyt *C* was carried out using the Benesi–Hildebrand equation, which indicates the stoichiometry at play in receptor–ligand interactions.[54]

$$\frac{1}{(I-I_0)} = \frac{1}{(I_1-I_0)} + \frac{1}{(I_1-I_0)k_b[\text{bile salt}]} \quad (4)$$

In this case, I_0 and I represent the fluorescence emission intensity of Cyt *C* in the absence and presence of bile salts; I_1 is the limiting fluorescence emission intensity, and k_b is the binding constant, respectively. When $\frac{1}{(I-I_0)}$ is plotted against the concentration of bile salts, it gives the Benesi–Hildebrand plot (Fig. 3A and B). A prominent linear pattern can be seen on the graph, indicating a 1 : 1 interaction[44,55,56] of bio-surfactants (sodium cholate and deoxycholate) with Cyt *C*. Based on the slope and intercept of the plot, we can calculate the binding

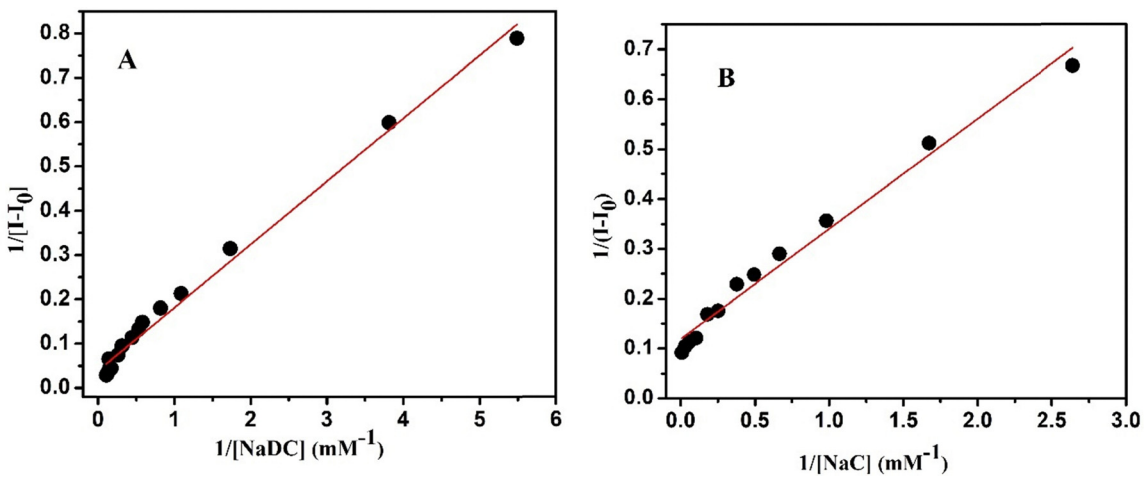

Fig. 3 Benesi–Hildebrand plot of $1/(I - I_0)$ against 1/[bile salt] for binding of Cyt *C* with bile salts (A) for NaDC and (B) NaC.

Table 2 Binding constant (k_b) and standard Gibbs free energy change (ΔG^0) of bile salt interaction with Cyt *C*, determined using the Benesi–Hildebrand plot at room temperature

System	k_b (M^{-1}) × 10^{-3}	$-\Delta G^0$ (kJ mol^{-1})
NaDC-Cyt *C*	0.75	16.40
NaC-Cyt *C*	0.41	14.90

constant (k_b) and standard Gibbs free energy change (ΔG^0), which results in 0.75 × 10^3 M^{-1} and −16.40 kJ mol^{-1} for sodium deoxycholate and 0.41 × 10^3 M^{-1} and −14.90 kJ mol^{-1} for sodium cholate respectively (Table 2). Considering the value of the binding constant and the negative Gibbs free energy, it is evident that bile salts and Cyt *C* interact quite attractively. For the NaDC–Cyt *C* system, the binding constant and Gibbs free energy are much higher than that for NaC-Cyt *C*, indicating that the NaDC–Cyt *C* interaction is stronger than the other one. Although the charges of the two bile salts are identical, the fundamental cause of the differences in binding energy and binding constant value is the hydrophobicity of the two bile salts. Since NaDC is inherently more hydrophobic than NaC, it interacts with Cyt *C* more strongly than the latter. The aforementioned findings, therefore, imply that bile salts' hydrophobicity is important for the interaction between bile salts and Cyt *C*.

3.4. Modification in the secondary structural conformation

To probe the alterations in secondary (far-UV) and tertiary (mid-UV) structures of biological macromolecules, CD spectroscopy is often used as a very efficacious tool.[45] Fig. 4A and B shows far-UV spectra of Cyt *C* in the presence of sodium cholate and deoxycholate, respectively, at different concentrations. Table S2 (Supplementary Section) (ESI†) presents the changes in the secondary structure of the protein, calculated utilizing secondary structure analysis software. In the native state, Cyt *C* significantly features the α-helix structure, which is characterized by two major negative peaks at around 208 nm (corresponding to π–π* transition) and 220 nm (corresponding to n–π* transition).[57,58] The contribution of the α-helical structure is around 38%, which correlates well with the value reported in the literature.[45]

Fig. 4(A and B) shows that the negative ellipticity value of Cyt *C* gradually decreased with increasing concentrations of sodium cholate and deoxycholate. The decrease in negative ellipticity at 208 and 220 nm suggests that Cyt *C* is losing its α-helical structure over time. The spectral alterations indicate partial unfolding or structural loosening of the protein, not a complete transformation to the β-sheet, as suggested by the CD spectra. This unfolding is probably caused by electrostatic interactions between positively charged lysine residues close to the heme crevice of Cyt *C* and the negatively charged carboxylate groups of bile salts. The local helical environment may be disturbed by such binding, which could destabilize the hydrogen bonding network and cause a detectable decrease in α-helicity. Additionally, a modest conformational rearrangement is supported by the slight blue shift of the CD band from 220 nm to 218 nm, corresponding to a 2 nm blue shift, which could be the result of reorganization of the tertiary packing or a change in the local polarity surrounding aromatic residues. The change in the secondary structure of proteins in the presence of bile salts is relatively less compared to conventional surfactants. Mukherjee *et al.*[31] found that HSA experiences just a 5% secondary structural change in the presence of bile salts. Mohanty *et al.*[32] also found that BSA undergoes only a 3% secondary structural change in the presence of bile salt NaDC. This minor alteration in the CD spectra of proteins in the presence of bile salts is mostly due to the unique steroidal structure of bile salts as compared to conventional surfactants, which contain a long hydrophobic chain. This long hydrophobic chain of conventional surfactants can easily permeate the numerous hydrophobic pockets of proteins, causing a significant secondary structural change, resulting in a substantially greater change in CD spectra in conventional surfactants compared to bile salt-type surfactants.

Overall, the CD data indicate that sodium deoxycholate and cholate have a mild but specific interaction with Cyt *C*,

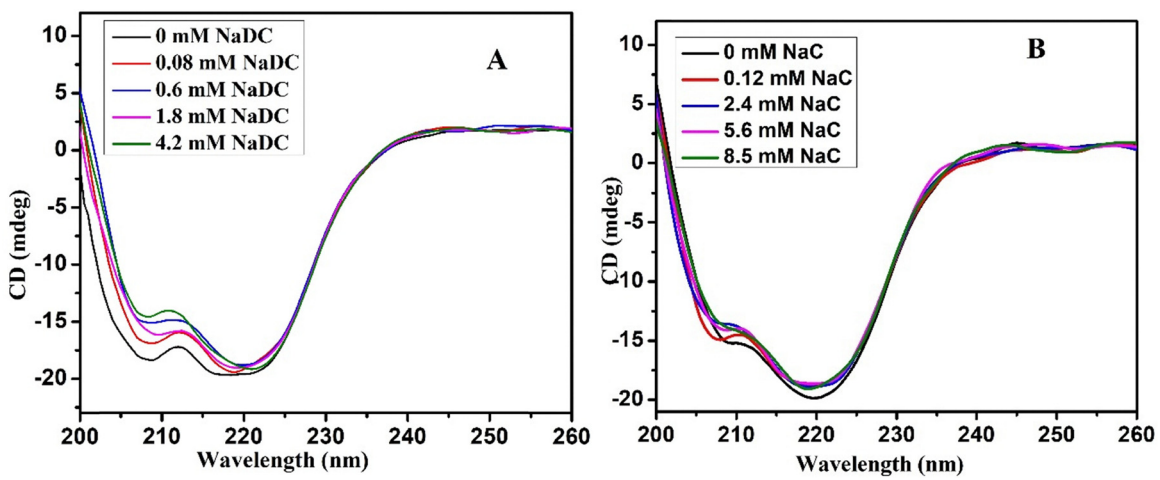

Fig. 4 CD spectra of Cyt *C* at various concentrations of bile salts: (A) NaDC and (B) NaC. [Cyt *C*] = 2.5 μM in phosphate buffer medium (pH 7.4) at 298 K.

resulting in a moderate decrease in the amount of α-helical content without inducing full unfolding. The interactions appear to be primarily electrostatic and sterically constrained due to the bile salts' rigid steroidal framework. However, a contrary observation was made by Singh and his colleagues while studying the interaction between the Cyt *C* protein and long-chain imidazolium ionic liquid.[51]

3.5. Dynamic light scattering (DLS) measurements

In the presence of ligands, DLS measurements can accurately predict protein–ligand interactions based on the changes in the hydrodynamic diameter of the protein.[59] The variation in the hydrodynamic diameter of Cyt *C* in the presence of NaDC and NaC is presented in Fig. 5(A and B). In its native state (pH 7.4), Cyt *C* exhibits two peaks with hydrodynamic diameters (D_h) of around 4.96 nm and 120 nm (Fig. 5A and B). Among them, the smaller one corresponds to the monomeric form of the protein, and the larger one corresponds to the aggregate form.[60] Based on the solution NMR structure, Bensi *et al.* calculated Cyt *C*'s diameter to be 3.6 nm.[61] Our result of a hydrodynamic diameter of ∼4–5 nm is consistent with the structural NMR investigation, given that the hydration layer thickness is approximately 0.6 nm.[62]

In the native state, the monomeric form makes a major contribution, while that of the aggregated form is minor. The diameter (D_h) of the monomeric form of Cyt *C* has been observed to increase in the presence of bile salts (NaDC and NaC). The increase in the diameter of the monomeric form could be due to a number of factors: (1) the denaturation of Cyt *C* in the presence of bile salts causes swelling in the protein structure; (2) when bile salts are added, the protein aggregates into oligomers from its monomeric state. In the presence of sodium deoxycholate, there is a remarkable enhancement in the hydrodynamic diameter of Cyt *C* from 4.96 nm to 10.54 nm, whereas a smaller increase for sodium cholate (4.96 nm to 6.42 nm) is observed, thus suggesting that NaDC is more efficient in forming aggregates and inducing the structural change of Cyt *C* compared to NaC. In a similar way, the hydrodynamic diameter (D_h) of the aggregated peak increased in the presence of NaDC/NaC. Here, both the intensity and the D_h of the aggregated peak were enhanced. The possible formation of the bile salt–Cyt *C* complex may be responsible for the increase in the diameter and intensity of the aggregated peak. However, in the presence of a very low concentration of NaDC, a decrease in the diameter of the aggregated peak was observed. This may be justified by the disruption of protein–protein aggregation by oppositely charged NaDC. Fig. 5A shows that in the presence of NaDC, in addition to the monomeric and aggregated hydrodynamic peak of Cyt *C*, there is also a peak at ∼1 nm. Sarkar *et al.*[60] observed that, in addition to monomeric and aggregated peaks, Cyt *C* shows a hydrodynamic peak at 0.6 nm in the presence of denaturing agents, urea and guanidine chloride (GdnCl). The hydrolysis of some amino acids of Cyt *C* in the presence of denaturants is one of the potential causes of the peaks in the solutions around 0.6 nm proposed by them. In the buffer solution, they measured the hydrodynamic diameter of the amino acid tryptophan and obtained a prominent peak at 0.8 nm. Based on this observation, they concluded that the peak at 0.6 nm may be due to the hydrolysis of some amino acids of Cyt *C*. So, the hydrodynamic peak around 1 nm of Cyt *C* in the presence of NaDC may be caused by the hydrolysis of some amino acid residues of proteins. Such types of hydrolysis peaks of Cyt *C* are not observed in the presence of NaC, suggesting that NaDC acts as a more powerful denaturant compared to NaC. Thus, it may be inferred that NaDC functions as a relatively potent denaturant agent for Cyt *C* in comparison to NaC because of its high hydrophobicity.

Additionally, the Benesi–Hildebrand plot shows that the k_b value for the NaDC–Cyt *C* system is higher than that for the NaC–Cyt *C* system, indicating that NaDC binds more strongly with Cyt *C* and leads to more structural alteration and aggregate formation with Cyt *C* compared to NaC.

Therefore, DLS results are corroborated with Benesi–Hildebrand plots. Therefore, it can be concluded that the enhancement of the hydrodynamic diameter of Cyt *C* in the presence of

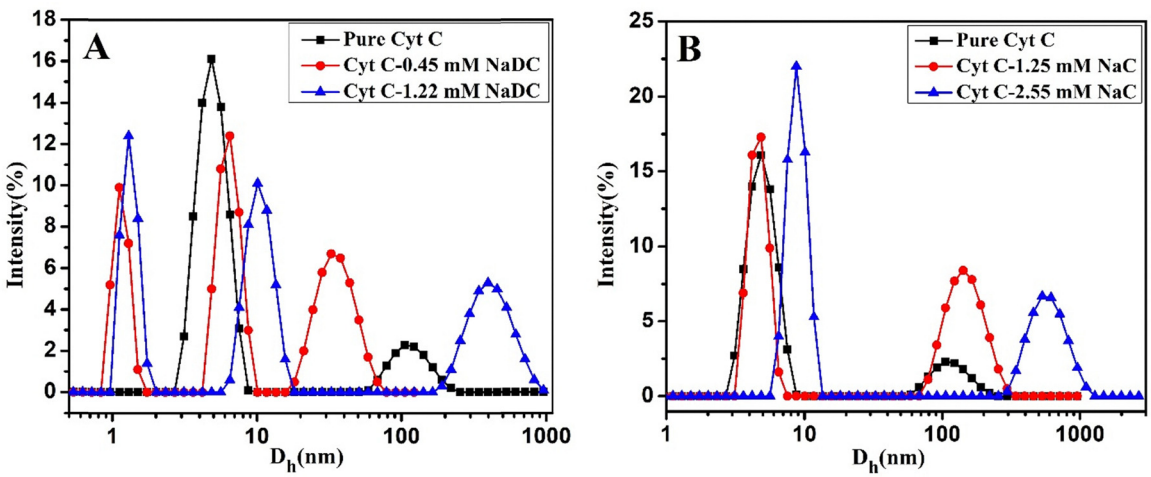

Fig. 5 Variation in the hydrodynamic diameter (D_h) of Cyt *C* in the presence of different concentrations of NaDC (A) and NaC (B), respectively.

bile salts suggests that the protein is unfolded and aggregated, and the results obtained from DLS measurements are consistent with those from various other measurements.

3.6. Microcalorimetry analysis (ITC)

One of the most important and sensitive methods for assessing the energy-related aspects of protein–ligand interaction is isothermal titration calorimetry (ITC). Fig. (6A and B) show the calorimetric profiles (*i.e.*, enthalpogram) of the binding of bile salts (NaDC and NaC) with Cyt *C*. The reported calorimetric profiles are derived by deducting the heat of dilution of bile salts in the buffer medium for an accurate analysis. Here, the 'one set of sites' binding model has been used to fit the enthalpogram.

The endothermic region dominates the sodium deoxycholate titration curves. It was observed that endothermicity increased with increasing NaDC concentration in Cyt *C* solutions up to a point and then began to decrease upon further increasing the bile salt concentration (Fig. 6A). The breakage of the H-bond (one of the most significant forces responsible for the secondary structure of proteins) during the interaction of the surfactant with the protein molecules may account for the increase in endothermicity observed with increasing sodium deoxycholate concentration.[63] Here, after reaching a maximum point (designated as CMC), there was a fall in the endothermicity of the NaDC–Cyt *C* ITC curve observed upon further increasing NaDC concentration. The latter half of the plot of NaDC titration in Cyt *C* is similar to the pure NaDC titration in a buffer medium (Fig. S4 in the supplementary section, ESI†), which signifies that the latter half of NaDC titration in Cyt *C* is due to the formation of free micelles after the formation of the Cyt *C*–NaDC complex. Our ITC profile of pure NaDC titration in buffer solution agrees well with the literature.[64]

It is interesting to notice that sodium cholate showed the opposite trend (Fig. 6B). In this instance, the reaction profile's lower panel exhibits exothermic characteristics, crosses zero, and eventually reaches the endothermic domain (upper panel). The cause of endothermicity has already been discussed (NaC). Exothermicity can be explained by the electrostatic/van der Waals interaction between the positively charged amino acid residues of Cyt *C* and the negatively charged groups of the bile salts.[65] The ITC profile of two bile salts (NaDC/NaC) is considerably different in the presence of Cyt *C*. The first portion of the enthalpogram (up to micellization) for the interaction of two bile salts with Cyt *C* follows a very consistent pattern. Here, exothermicity first progressively declines when bile salts (NaDC/NaC) are added, indicating that the bile salt monomer binds to the highly energetic sites of Cyt *C via* both hydrophobic and electrostatic contacts. Following their CMC point, two bile salts with Cyt *C* have different ITC profiles. The interaction of NaDC with Cyt *C* after the CMC point showed a progressive decrease in endothermicity, whereas NaC showed a modest rise in endothermicity. Therefore, during the formation of the free micelle, the ITC profile of the interaction between two bile salts and Cyt *C* differs. Even though the two bile salts (NaDC and NaC) have fairly similar structures, their micellization processes differ because of their varying hydrophobicity. As a result, the ITC profile of two bile salts alters during free micelle formation, resulting in a distinct ITC profile of the two-bile salt in the Cyt *C*–bile salt interaction.

With the NaDC–Cyt *C* system, the heat change for micellization $\left(\Delta H^{\circ}_{\text{micelle}}\right)$ is 388.5 J mol^{-1}, while it is 585.9 J mol^{-1} for the NaC–Cyt *C* system. The heat change of micellization $\left(\Delta H^{\circ}_{\text{micelle}}\right)$ for both the bile salts in the presence of Cyt *C* is endothermic in nature. There may be various factors responsible for these endothermic heat changes:

3.6.1. Disruption of structured water (hydration shells). In the solution phase, both the Cyt *C* and bile salts are usually surrounded by ordered water molecules. When bile salts form micelles in the presence of Cyt *C*, some of the structured water molecules are liberated into the bulk solution. The process of

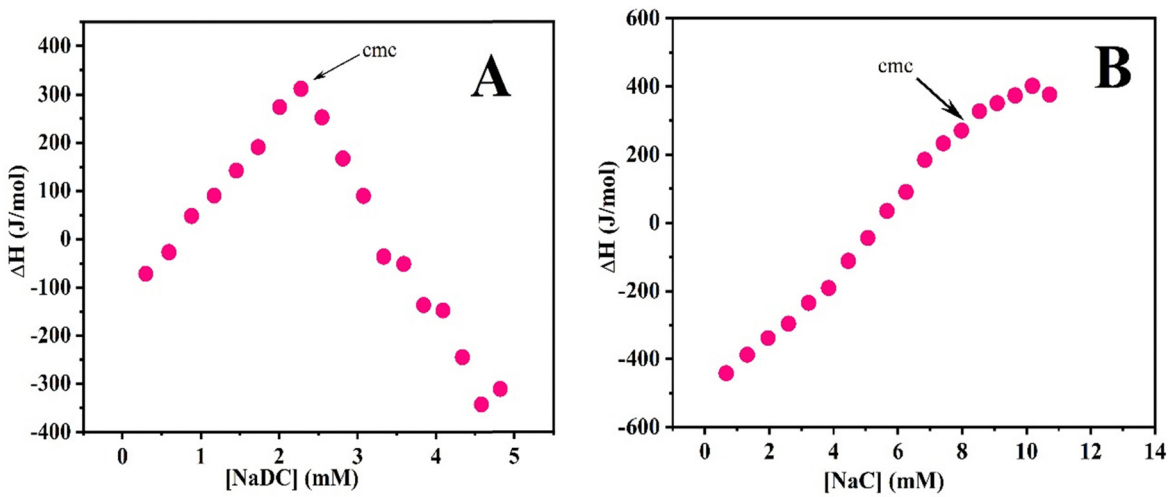

Fig. 6 Plot of integrated heat data after correction of heat of dilution of bile salts against the concentration of the bile salt, for the binding of NaDC (A) and NaC (B) to Cyt *C* at 298.15 K in phosphate buffer, pH 7.4.

breaking these hydration shells is endothermic since it needs energy.

3.6.2. Unfolding or rearrangement of protein structure. Bile salt interactions can lead to partial unfolding or structural changes in Cyt *C*. This unravelling or rupture of intramolecular bonds (such as hydrogen bonds, van der Waals forces, *etc.*) absorbs heat and contributes to the endothermic nature.

Despite the endothermic heat change, the micellization process is spontaneous due to the positive enthalpy change. Thus, the micellization process is driven by entropy. The release of water molecules during the interaction of bile salts with Cyt *C* (the water molecules that surround the protein and bile salts) enhances the system's overall entropy, making the entire process entropically favorable.

The greater positive value of enthalpy change suggests a lower negative value of Gibbs free energy, *i.e.*, the process is less spontaneous in nature. So, from the enthalpy change of micellization, it is clearly seen that the interaction process between sodium deoxycholate and Cyt *C* is more spontaneous than sodium cholate. This discrepancy in the enthalpogram between the two bile salts is mainly caused by the presence of a hydroxyl group in sodium cholate's 7th position, which leads to a difference in the hydrophobicity of the two bile salts and the resulting micellization process. So, from ITC measurements, it is also clear that the hydrophobicity of bile salts is the main governing factor of bile salts and Cyt *C*. It was observed from different techniques that sodium deoxycholate binds with Cyt *C* more effectively than sodium cholate, and calorimetric titration confirms this observation.

3.7. Cyclic voltammetry (CV) measurements

Cyclic voltammetry measurements were used to investigate the effect of bile salt ligands on the redox properties of the electron transport protein Cyt *C*. Typical cyclic voltammograms of Cyt *C* (10 μM) in 20 mM phosphate buffer solution in the native state and in the presence of bile salts (NaDC and NaC) are shown in Fig. 7A and B. From the figure, it was observed that Cyt *C* in its native state has distinct oxidation–reduction (redox) peaks observed on the Pt electrode at a scan speed of 50 mV s^{-1}. The major peak was oxidative at −0.634 V, and the corresponding reductive peak was at −0.96 V with respect to SCE. Separation of peak potential (ΔE_P), *i.e.*, the difference between the peak potential values of the cathode and anode, was ΔE_P = 0.538 V. These redox peaks correspond to redox reactions at the electrochemical center of Cyt *C* with a formal potential (E°) of −0.313 V regarding the reference electrode.[66] There was a dramatic change in the oxidation peak current of Cyt *C* in the presence of bile salts (NaC and NaDC). Treatment of Cyt *C* with sodium cholate increased the oxidative peak current (both above and below its CMC). Since proteins are hydrophobic macromolecules, they can bind to surfactant molecules through hydrophobic interactions. Due to the sodium cholate adsorption layer on the Pt electrode, more Cyt *C* adheres to the electrode surface. Furthermore, in the presence of NaC, the orientation of Cyt *C* on the electrode surface could change, resulting in increased electron transfer as a result of the increased peak current.[67]

Interestingly, an opposite observation was found for sodium deoxycholate. In this case, the peak current dropped as the surfactant concentration rose (above and below CMC). The formation of an electro-inactive Cyt *C*–NaDC complex explains this peak current drop. As a result, the electrical activity of Cyt *C* on the electrode surface is globally reduced, disrupting the peak current.[68,69] Cyclic voltammetry measurements, therefore, strongly support complex formation between Cyt *C* and bile salts (NaC and NaDC), which is also consistent with fluorescence, CD spectroscopy, DLS, and ITC studies. Cyclic voltammetry measurements show that the interaction of NaC and Cyt *C* is very different from that of NaDC.

3.8. Morphology analysis of bile salt–Cyt *C* complexes (AFM)

Atomic force microscopy (AFM) has further validated the aggregate formation between the bile salts (NaDC/NaC) and Cyt *C*. The AFM technique has become an essential tool over other

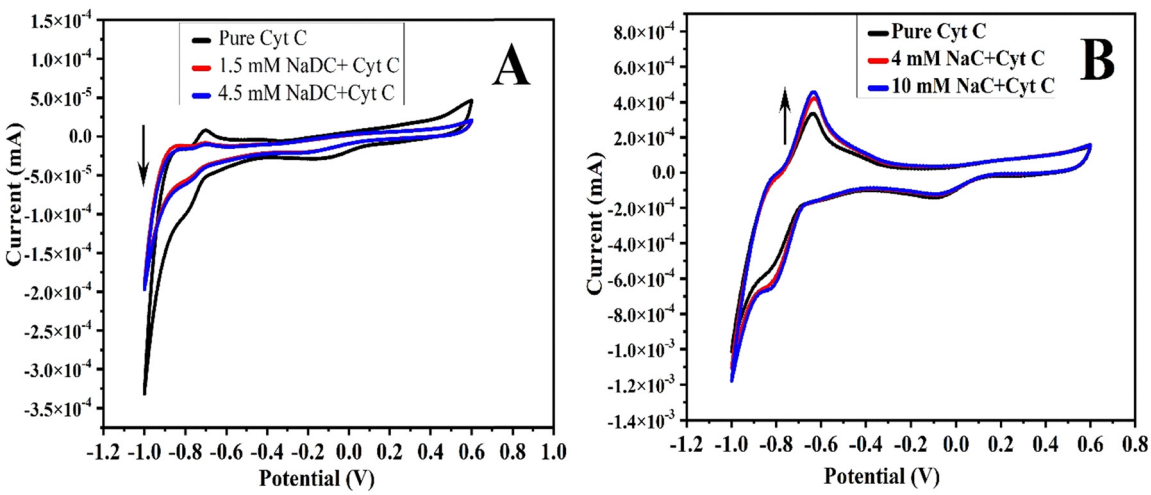

Fig. 7 Cyclic voltammogram of Cyt *C* (10 μM) in the presence of bile salts, above and below its CMC values: (A) NaDC and (B) NaC at 298 K and pH 7.4.

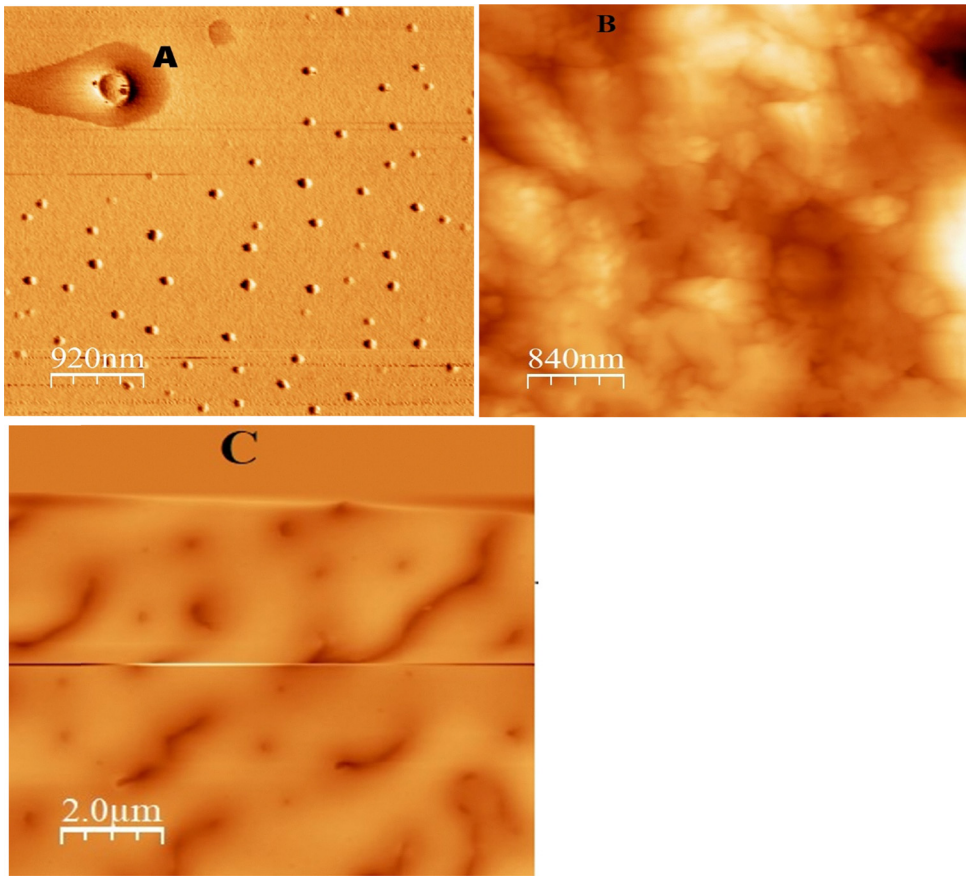

Fig. 8 2-Dimensional AFM topographic images of Cyt *C* in the absence and presence of bile salts (A), pure Cyt *C*, (B) 4.5 mM NaDC, and (C) 8.5 mM NaC at pH 7.4 and ionic strength 10 mM.

techniques because it provides precise and direct information about the creation, structural changes, dynamics, topography, and molecular interaction patterns of bio-macromolecules.[70]

Fig. 8 presents the AFM topographic images of free Cyt *C* (Fig. 8(A)) and its mixed system with NaDC/NaC (Fig. 8(B and C)). According to the AFM micrograph, free Cyt *C* shows star/sphere-like images. Upon the addition of bile salts, Cyt *C* exhibits a large aggregated structure. Cyt *C* shows lump-like aggregates in the presence of NaDC. Bhat *et al.* reported this type of lump-like AFM micrograph for the free hemoglobin.[71] Again, an entirely different micrograph was observed for Cyt *C* in the presence of NaC. In this case, a uniform sheet-like aggregated morphology was observed. At pH 7.4, Cyt *C* has a slightly positively charged surface (because Cyt *C* has an isoelectric pH of about 9.6), which enhances the adsorption of negatively charged NaDC/NaC on its surface. In this case, the negatively charged small micelle cluster of NaDC/NaC bound to the backbone of Cyt *C* results in morphological alteration.

3.9. Molecular docking analysis

Molecular docking is an ideal method to find the binding location and energy of a small molecule (ligand) inside a biomacromolecule. The protein structure has many ridges and grooves that attach small molecules. The blind docking method enables us to search over the entire protein surface simultaneously, minimizing the energy of the peptide conformations. Fig. 9A–D show that NaDC and NaC bind to Cyt *C*. The amino acid residues directly involved in the interaction of NaDC with Cyt *C* are – Ala 57, Ala 58, Gly 62, Pro 61, Gly 65, Thr 63, and Lys 4, and those involved in interaction with NaC are Ala 77, Ala 76, Phe 79, Lys 80, Gln 83, Ala 57, Phe 59, Gly 60, Ile 72, and Trp 73. The values of free energy obtained from the docking studies are -0.091 kcal mol^{-1} for NaDC and -0.079 kcal mol^{-1} for NaC, which are slightly different from the experimentally obtained values. This is probably because the crystal structure of the protein in the solid state differs from that in the solution where the experiments are carried out. The obtained negative free energy value theoretically predicts that the interaction of bile salts with Cyt *C* is a spontaneous process. The calculated value of negative free energy for the interaction of NaDC with Cyt *C* is greater than that for NaC, suggesting that NaDC interacts more strongly with Cyt *C*. Mukerjee *et al.*[31] observed a similar pattern in which the docking calculated negative free energy value for the interaction of NaDC with HSA was larger than that for NaC. However, the predicted free energy change for the bile salt–HSA system was more than that of the bile salt–Cyt *C* system. The experimental results already

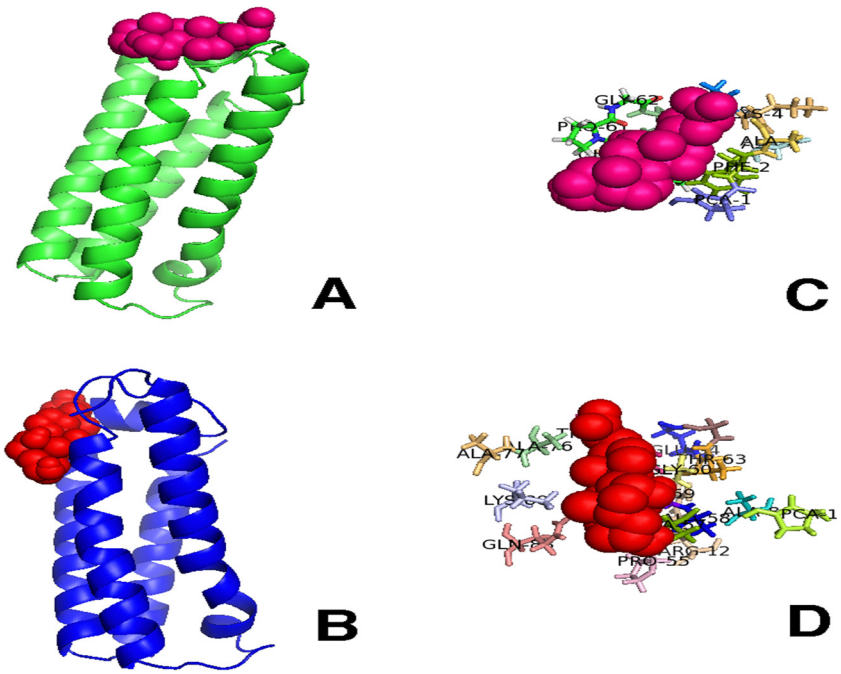

Fig. 9 The lowest energy binding modes of NaDC (A) and NaC (C) with Cyt *C*, respectively. The structure of Cyt *C* is displayed as ribbons and tubes. Close-up views of binding sites of Cyt *C* with NaDC (B) and NaC (D) corresponding to (A) and (C), respectively, and the selected amino acid residue is represented by a line model structure.

show that NaDC has a higher binding affinity towards Cyt *C* than NaC; theoretical calculations largely validate these results. The calculated distances from the heme moiety of Cyt *C* to the bound bile salts were approximately 14.4 Å for NaDC and 11.0 Å for NaC, respectively. These docking results revealed that both bile salts preferentially bind to surface-accessible regions of Cyt *C*, away from the heme group. These distances suggest that the interaction does not involve direct coordination of bile salts with the heme iron of Cyt *C*, but may still influence the local electrostatic environment or protein conformation through long-range interaction. A similar kind of observation was found by Bhat *et al.*,[72] where the interaction of hemoglobin was studied with two cleavable gemini surfactants. In that docking calculation, 15 Å and 19 Å distances were observed between the heme group of hemoglobin and the two gemini surfactant residues, respectively. There, long-term electrostatic and hydrophobic interactions have been suggested, which are responsible for the conformational change of hemoglobin by gemini surfactants.

Although the present molecular docking results point to a possible interaction between the *Alcaligenes* species Cyt *C* and NaDC/NaC, it is crucial to note that these conclusions are entirely computational in nature and do not have direct experimental support. Without radioligand binding assays, surface plasmon resonance, or other biophysical studies, it is impossible to draw definitive conclusions on the binding affinity or specificity of these interactions. Therefore, the current molecular docking data should be viewed as a preliminary hypothesis-generating tool rather than confirmatory evidence of molecular interaction. In light of these considerations, we acknowledge the limitations of our study and emphasize the need for future experimental investigations to validate our computational findings. In the literature, a lot of such types of studies are available where molecular docking is used as a preliminary tool to predict protein–ligand interaction without any experimental validation.[31,72,73]

4. Conclusions

This study thoroughly examined the molecular interaction between cytochrome *C* and two bile salts (NaDC/NaC) using a variety of complementary techniques, including tensiometry, UV-vis spectroscopy, fluorescence spectroscopy, circular dichroism (CD), dynamic light scattering (DLS), cyclic voltammetry (CV), isothermal titration calorimetry (ITC), atomic force microscopy (AFM), and molecular docking analysis. The overall results suggest that bile salts effectively alter the physicochemical properties, structural integrity, and electrochemical characteristics of Cyt *C*. Tensiometry investigations show that the interfacial activity of the bile salts improves significantly in the presence of Cyt *C*, implying the possible formation of a bile salt–protein complex at a certain critical micellar concentration. UV-vis spectroscopy and fluorescence experiments indicate that the bile salt interacts significantly with Cyt *C* at three distinct concentration points, causing the partial unfolding of the protein structure. The binding constant value (k_b) for the interaction of NaDC with Cyt *C* is much higher compared to NaC, signifying that the higher hydrophobicity of NaDC plays an important role in the binding process. CD results revealed a reduction of the α-helical structure of Cyt *C* upon exposure to

the bile salt medium, consistent with the destabilization of the protein structure. The DLS study confirms the alteration in the Cyt *C* size and possible formation of protein oligomers in the bile salt medium. ITC results give thermodynamic evidence of the spontaneous binding of the two bile salts with the Cyt *C* protein. Electrochemical evidence (CV analysis) suggests that the presence of NaDC reduces the oxidative peak current of Cyt *C* due to the formation of an electro-inactive complex between Cyt *C* and NaDC. However, in the presence of NaC, the peak current increases, suggesting that sodium cholate can enhance the electron transfer process at the electroactive center of Cyt *C* by changing its orientation around the electrode surface. AFM findings further validate the Cyt *C*–bile salt complex formation. Molecular docking analysis theoretically predicted the potential binding sites and binding energies of interactions between bile salts and Cyt *C*, and the data obtained supported the experimental results.

Overall, this study indicates the usefulness of multi-techniques for analysing protein–amphiphile interactions and sheds light on how bile salts influence the structure and function of Cyt *C*. These findings will be highly essential in the cell apoptosis process, and also the bile salt–protein interaction study will be useful in a variety of biological and pharmacological applications.

Future research may investigate this interaction utilizing structurally various bile salts or using other heme proteins, as well as high-resolution techniques such as NMR, SANS, and CDC-PAT, to get deeper mechanistic insights.

Conflicts of interest

There are no conflicts of interest to declare.

Data availability

In this manuscript, all the data are measured and collected using different instruments and presented. No data from the literature have been used.

Acknowledgements

R. S. and R. B. thank CSIR, India, for a senior research fellowship.

References

1 A. P. Davis, Cholaphanes steroids as structural components in molecular engineering, *Chem. Soc. Rev.*, 1993, **22**, 243–253.
2 J. Tamminen and E. Kolehmainen, Bile acids as building blocks of supramolecular hosts, *Molecules*, 2001, **6**, 21–46.
3 L. Mrózek, L. Dvořáková, Z. Mandelová, L. Árová, A. Řezáčová, L. Plaček, R. Opatřilová, J. Dohnal, O. Paleta, V. Král and P. Drašar, Investigation of new acyloxy derivatives of cholic acid and their esters as drug absorption modifiers, *Steroids*, 2011, **76**, 1082–1097.
4 S. Mishra and S. Patel, Design, synthesis, and anti-bacterial activity of novel deoxycholic acid-amino alcohol conjugates, *Med. Chem.*, 2020, **16**, 385–391.
5 D. Brossard, L. El Kihel, M. Clément, W. Sebbahi, M. Khalid, C. Roussakis and S. Rault, Synthesis of bile acid derivatives and in vitro cytotoxic activity with pro-apoptotic process on multiple myeloma (KMS-11), glioblastoma multiforme (GBM), and colonic carcinoma (HCT-116) human cell lines, *Eur. J. Med. Chem.*, 2010, **45**, 2912–2918.
6 R. Li, C. S. Santos, T. B. Norsten, K. Morimitsu and C. Bohne, Aqueous solubilization of photochromic compounds by bile salt aggregates, *Chem. Commun.*, 2010, **46**, 1941–1943.
7 N. Kundu, D. Banik, A. Roy, J. Kuchlyan and N. Sarkar, Modulation of the aggregation properties of sodium deoxycholate in presence of hydrophilic imidazolium based ionic liquid: Water dynamics study to probe the structural alteration of the aggregates, *Phys. Chem. Chem. Phys.*, 2015, **17**, 25216–25227.
8 F. Le Dévédec, D. Fuentealba, S. Strandman, C. Bohne and X. X. Zhu, Aggregation behavior of pegylated bile acid derivatives, *Langmuir*, 2012, **28**, 13431–13440.
9 B. K. Paul, N. Ghosh and S. Mukherjee, Direct insight into the nonclassical hydrophobic effect in bile salt:β-cyclodextrin interaction: Role of hydrophobicity in governing the prototropism of a biological photosensitizer, *RSC Adv.*, 2016, **6**, 9984–9993.
10 R. Li, E. Carpentier, E. D. Newell, L. M. Olague, E. Heafey, C. Yihwa and C. Bohne, Effect of the structure of bile salt aggregates on the binding of aromatic guests and the accessibility of anions, *Langmuir*, 2009, **25**, 13800–13808.
11 D. M. Small, S. A. Penkett and D. Chapman, Studies on simple and mixed bile salt micelles by nuclear magnetic resonance spectroscopy, *Biochim. Biophys. Acta, Lipids Lipid Metab.*, 1969, **176**, 178–189.
12 D. M. Small, P. P. Nair and D. Kritchevsky, *The bile salts*, Plenum Press, New York, 1971.
13 J. M. Ridlon, D. J. Kang and P. B. Hylemon, Bile salt biotransformations by human intestinal bacteria, *J. Lipid Res.*, 2006, **47**, 241–259.
14 G. Li and L. B. McGown, Model for bile salt micellization and solubilization from studies of a 'polydisperse' array of fluorescent probes and molecular modeling, *J. Phys. Chem.*, 1994, **98**, 13711–13719.
15 C. J. O'Connor and R. G. Wallace, Physico-chemical behavior of bile salts, *Adv. Colloid Interface Sci.*, 1985, **22**, 1–111.
16 D. L. Foster and R. H. Fillingame, Energy-transducing H+-ATPase of Escherichia coli. Purification, reconstitution, and subunit composition, *J. Biol. Chem.*, 1979, **254**, 8230–8236.
17 Y. Banno, Y. Yada and Y. Nozawa, Purification and characterization of membrane-bound phospholipase C specific for phosphoinositides from human platelets, *J. Biol. Chem.*, 1988, **263**, 11459–11465.

18 S. Zhuang, Q. Li, L. Cai, C. Wang and X. Lei, Chemoproteomic Profiling of Bile Acid Interacting Proteins, *ACS Cent. Sci.*, 2017, **3**, 501–509.

19 C. M. Cremers, D. Knoefler, V. Vitvitsky, R. Banerjee and U. Jakob, Bile salts act as effective protein-unfolding agents and instigators of disulfide stress *in vivo*, *Proc. Natl. Acad. Sci. U. S. A.*, 2014, **111**(16), E1610–E1619.

20 O. Toke, Structural and Dynamic Determinants of Molecular Recognition in Bile Acid-Binding Proteins, *Int. J. Mol. Sci.*, 2022, **23**(1), 505.

21 Y. Banno, Y. Yada and Y. Nozawa, Purification and characterization of membrane-bound phospholipase C specific for phosphoinositides from human platelets, *J. Biol. Chem.*, 1988, **263**, 11459–11465.

22 D. L. Foster and R. H. Fillingame, Energy-transducing H + -ATPase of Escherichia coli. Purification, reconstitution, and subunit composition, *J. Biol. Chem.*, 1979, **254**, 8230–8236.

23 M. C. Di Gregorio, J. Cautela and L. Galantini, Physiology and physical chemistry of bile acids, *Int. J. Mol. Sci.*, 2021, **22**, 1–23.

24 M. C. Di Gregorio, L. Travaglini, A. D. Giudice, J. Cautela, N. V. Pavel and L. Galantini, Bile Salts: Natural Surfactants and Precursors of a Broad Family of Complex Amphiphiles, *Langmuir*, 2019, **35**, 6803–6821.

25 J. Cautela, B. Stenqvist, K. Schillen, D. Belic, L. K. Mansson, F. Hagemans, M. Seuss, A. Fery, J. J. Crassous and L. Galantini, Supracolloidal atomium, *ACS Nano*, 2020, **14**, 15748–15756.

26 G. Du, D. Belić, A. Del Giudice, V. Alfredsson, A. M. Carnerup, K. Zhu, B. Nyström, Y. Wang, L. Galantini and K. Schillén, Condensed supramolecular helices: The twisted sisters of DNA, *Angew. Chem.*, 2022, **134**, e202113279.

27 K. Li, Y. Li, J. M. Shelton, J. A. Richardson, E. Spencer, Z. J. Chen, X. Wang and R. S. Williams, Cytochrome *c* deficiency causes embryonic lethality and attenuates stress-induced apoptosis, *Cell*, 2000, **101**, 389–399.

28 D. Chandra, S. B. Bratton, M. D. Person, Y. Tian, A. G. Martin, M. Ayres, H. O. Fearnhead, V. Gandhi and D. Tang, GIntracellular nucleotides act as critical prosurvival factors by binding to cytochrome *C* and inhibiting apoptosome, *Cell*, 2006, **125**, 1333–1346.

29 B. Zhivotovsky, S. Orrenius, O. T. Brustugun and S. O. Døskeland, Injected cytochrome *C* induces apoptosis, *Nature*, 1998, **391**, 449–450.

30 A. Maloyan, A. Sanbe, H. Osinska, M. Westfall, D. Robinson, K. I. Imahashi, E. Murphy and J. Robbins, Mitochondrial dysfunction and apoptosis underlie the pathogenic process in α-B-crystallin desmin-related cardiomyopathy, *Circulation*, 2005, **112**, 3451–3461.

31 N. Ghosh, R. Mondal and S. Mukherjee, Hydrophobicity is the governing factor in the interaction of human serum albumin with bile salts, *Langmuir*, 2015, **31**, 1095–1104.

32 S. Mohanty, S. S. Mishra, N. Kuldeep, J. Maharana and U. Subuddhi, Insight into the Effect of Submicellar Concentrations of Sodium Deoxycholate on the Structure, Stability, and Activity of Bovine and Human Serum Albumin: An Interesting Comparison between Single and Double Tryptophan Proteins, *Langmuir*, 2024, **40**, 5228–5244.

33 F. Zsila, Circular dichroism spectroscopic detection of ligand binding induced subdomain IB specific structural adjustment of human serum albumin, *J. Phys. Chem. B*, 2013, **117**, 10798–10806.

34 K. Singh and S. Chauhan, Interactional behavior of sodium cholate and sodium deoxycholate in the presence of ceftriaxone sodium: volumetric, compressibility, viscometric, and proton nuclear magnetic resonance studies, *J. Chem. Eng. Data*, 2020, **65**, 4536–4546.

35 T. Janek, P. Czeleń, E. J. Gudiña, L. R. Rodrigues and Ż. Czyżnikowska, Biomolecular interactions of lysosomotropic surfactants with cytochrome *c* and its effect on the protein conformation: A biophysical approach, *Int. J. Biol. Macromol.*, 2019, **126**, 1177–1185.

36 A. Srivastava, J. Dey and K. Ismail, Interaction of tetracaine hydrochloride with sodium deoxycholate in aqueous micellar phase and at the surface, *Colloids Surf., A*, 2015, **466**, 181–188.

37 F. M. Menger, On the Structure of Micelles, *Acc. Chem. Res.*, 1979, **12**, 111–117.

38 T. Chakraborty, I. Chakraborty, S. P. Moulik and S. Ghosh, Physicochemical and conformational studies on BSA - Surfactant interaction in aqueous medium, *Langmuir*, 2009, **25**, 3062–3074.

39 K. Matsuoka, J. Lee and Y. Moroi, Micellization of bile salts and solubilization into the micelles, *J. Surf. Sci. Technol.*, 2010, **26**, 105–136.

40 K. Kumar and S. Chauhan, Surface tension and UV–visible investigations of aggregation and adsorption behavior of NaC and NaDC in water–amino acid mixtures, *Fluid Phase Equilib.*, 2015, **394**, 165–174.

41 S. Chauhan, V. Sharma, K. Singh, M. S. Chauhan and K. Singh, Influence of lactose on the micellar behaviour and surface activity of bile salts as revealed through fluorescence and surface tension studies at varying temperatures, *J. Mol. Liq.*, 2016, **222**, 67–76.

42 J. Aslam, I. H. Lone, N. R. E. Radwan, M. F. Siddiqui, S. Parveen, R. B. Alnoman and R. Aslam, Molecular Interaction of Amino Acid-Based Gemini Surfactant with Human Serum Albumin: Tensiometric, Spectroscopic, and Molecular Docking Study, *ACS Omega*, 2019, **4**, 22152–22160.

43 R. Vashishat, R. Sanan and R. K. Mahajan, Bile salt-surface active ionic liquid mixtures: mixed micellization and solubilization of phenothiazine, *RSC Adv.*, 2015, **5**, 72132–72141.

44 A. Srivastava, H. Uchiyama, Y. Wada, Y. Hatanaka, Y. Shirakawa, K. Kadota and Y. Tozuka, Mixed micelles of the antihistaminic cationic drug diphenhydramine hydrochloride with anionic and non-ionic surfactants show improved solubility, drug release and cytotoxicity of ethenzamide, *J. Mol. Liq.*, 2019, **277**, 349–359.

45 P. Bharmoria, T. J. Trivedi, A. Pabbathi, A. Samanta and A. Kumar, Ionic liquid-induced all-α to α+ β conformational transition in cytochrome *c* with improved peroxidase activity in aqueous medium, *Phys. Chem. Chem. Phys.*, 2015, **17**, 10189–10199.

46 D. Löwenich and K. Kleinermanns, Porphyrin fluorescence dominates UV photoemission of folded cytochrome *c*, *Photochem. Photobiol.*, 2007, **83**, 1308–1312.

47 U. K. Singh and R. Patel, Dynamics of Ionic Liquid-Assisted Refolding of Denatured Cytochrome *c*: A Study of Preferential Interactions toward Renaturation, *Mol. Pharm.*, 2018, **15**, 2684–2697.

48 A. Zaragoza, J. A. Teruel, F. J. Aranda, A. Marques, M. J. Espuny, A. Manresa and A. Ortiz, Interaction of a Rhodococcus sp. Trehalose Lipid Biosurfactant with Model Proteins: Thermodynamic and Structural Changes, *Langmuir*, 2012, **28**, 1381–1390.

49 D. Hamada, M. Hoshino, M. Kataoka, Y. Goto and A. L. Fink, Intermediate Conformational States of Apocytochrome *c*, *Biochemistry*, 1993, **32**, 10351–10358.

50 U. Ahluwalia, S. M. Nayeem and S. Deep, The non-native conformations of cytochrome *c* in sodium dodecyl sulfate and their modulation by ATP, *Eur. Biophys. J.*, 2011, **40**, 259–271.

51 U. K. Singh, M. Kumari, S. H. Khan, H. B. Bohidar and R. Patel, Mechanism and Dynamics of Long-Term Stability of Cytochrome *c* Conferred by Long-Chain Imidazolium Ionic Liquids at Low Concentration, *ACS Sustainable Chem. Eng.*, 2018, **6**, 803–815.

52 U. K. Singh, M. Kumari and R. Patel, Dynamics of cytochrome *c* in surface active ionic liquid: A study of preferential interactions towards denaturation, *J. Mol. Liq.*, 2018, **268**, 840–848.

53 W. Liu, X. Guo and R. Guo, The interaction between hemoglobin and two surfactants with different charges, *Int. J. Biol. Macromol.*, 2007, **41**, 548–557.

54 B. K. Paul, A. Samanta and N. Guchhait, Exploring hydrophobic subdomain iia of the protein bovine serum albumin in the native, intermediate, unfolded, and refolded states by a small fluorescence molecular reporter, *J. Phys. Chem. B*, 2010, **114**, 6183–6196.

55 M. Kumar, A. Bhardwaj, D. Elahi, O. G. Singh, S. K. Singh, M. K. Gatasheh, M. Irfan, N. Singh and A. Srivastava, Counterion association of ionic drugs with sodium tetradecyl sulfate in the aqueous medium, *ACS Omega*, 2023, **8**, 45942–45951.

56 A. Srivastava, O. Yañez and P. Cantero-López, Mixed micellization of bile salts and transglycosylated stevia and enhanced binding and solubility of non-steroidal anti-inflammatory drugs using mixed micelle, *J. Mol. Liq.*, 2020, **311**, 113341.

57 P. Manavalan and W. C. Johnson, Sensitivity of circular dichroism to protein tertiary structure class, *Nature*, 1983, **305**, 831–832.

58 L. Banci, I. Bertini, J. G. Huber, G. A. Spyroulias and P. Turano, Solution structure of reduced horse heart cytochrome *c*, *J. Biol. Inorg. Chem.*, 1999, **4**, 21–31.

59 S. K. Chaturvedi, E. Ahmad, J. M. Khan, P. Alam, M. Ishtikhar and R. H. Khan, Elucidating the interaction of limonene with bovine serum albumin: A multi-technique approach, *Mol. BioSyst.*, 2015, **11**, 307–316.

60 R. Sarkar, A. K. Shaw, S. S. Narayanan, F. Dias, A. Monkman and S. K. Pal, Direct observation of protein folding in nanoenvironments using a molecular ruler, *Biophys. Chem.*, 2006, **123**, 40–48.

61 L. Banci, I. Bertini, H. B. Gray, C. Luchinat, T. Reddig, A. Rosato and P. Turano, Solution structure of oxidized horse heart cytochrome *c*, *Biochemistry*, 1997, **36**, 9867–9877.

62 S. K. Pal, J. Peon and A. H. Zewail, Biological water at the protein surface: dynamical solvation probed directly with femtosecond resolution, *Proc. Natl. Acad. Sci. U. S. A.*, 2002, **99**, 1763–1768.

63 M. Akram and I. A. Bhat, New insights into binding interaction of novel ester-functionalized m-E2-m gemini surfactants with lysozyme: A detailed multidimensional study, *RSC Adv.*, 2015, **5**, 102780–102794.

64 S. Das, P. Roy, P. Saha Sardar and S. Ghosh, Addressing the interaction of stem bromelain with different anionic surfactants, below, at and above the critical micelle concentration (cmc) in phosphate buffer at pH 7: physicochemical, spectroscopic, & molecular docking study, *Int. J. Biol. Macromol.*, 2024, **271**, 132368.

65 N. Keswani and N. Kishore, Calorimetric and spectroscopic studies on the interaction of anticancer drug mitoxantrone with human serum albumin, *J. Chem. Thermodyn.*, 2011, **43**, 1406–1413.

66 M. Negahdary, S. A. Sadeghi, M. H. michak, S. R. Zarchi, F. Salahi, N. Mohammadi, E. Azargoon and A. Sayad, Direct electron transfer of cytochrome *C* on cadmium oxide nanoparticles modified carbon paste electrode, *Int. J. Electrochem. Sci.*, 2012, **7**, 6059–6069.

67 Y. Wu and S. Hu, Voltammetric investigation of cytochrome *c* on gold coated with a self-assembled glutathione monolayer, *Bioelectrochemistry*, 2006, **68**, 105–112.

68 S. Mahajan, R. Sharma and R. K. Mahajan, An investigation of drug binding ability of a surface active ionic liquid: Micellization, electrochemical, and spectroscopic studies, *Langmuir*, 2012, **28**, 17238–17246.

69 R. Sharma, A. Kamal and R. K. Mahajan, A quantitative appraisal of the binding interactions between an anionic dye, Alizarin Red S, and alkyloxypyridinium surfactants: A detailed micellization, spectroscopic and electrochemical study, *Soft Matter*, 2016, **12**, 1736–1749.

70 S. R. Cohen and A. Bitler, Use of AFM in bio-related systems, *Curr. Opin. Colloid Interface Sci.*, 2008, **13**, 316–325.

71 I. A. Bhat, B. Roy and P. Hazra, Conformational and solution dynamics of hemoglobin (Hb) in presence of a cleavable gemini surfactant: Insights from spectroscopy, atomic force microscopy, molecular docking and density functional theory, *J. Colloid Interface Sci.*, 2019, **538**, 489–498.

72 I. A. Bhat, B. Roy and P. Hazra, Conformational and solution dynamics of hemoglobin (Hb) in presence of a cleavable gemini surfactant: Insights from spectroscopy, atomic force microscopy, molecular docking and density functional theory, *J. Colloid Interface Sci.*, 2019, **538**, 489–498.

73 S. Rudra, S. Dasmandal and A. Mahapatra, Binding interaction of sodium-N-dodecanoyl sarcosinate with hemoglobin and myoglobin: Physicochemical and spectroscopic studies with molecular docking analysis, *J. Colloid Interface Sci.*, 2017, **496**, 267–277.

I&EC research
Industrial & Engineering Chemistry Research

pubs.acs.org/IECR

Article

Comparative Study of the Aggregation Behavior of Some Ionic Surfactants with Nonionic Triton X-114 in Water and a Water/2,2,2-Trifluoroethanol Mixture

Rajesh Banik, Bipin Bihari Mondal, Raju Sardar, and Soumen Ghosh*

Cite This: *Ind. Eng. Chem. Res.* 2024, 63, 3057−3071

Read Online

ACCESS | Metrics & More | Article Recommendations

ABSTRACT: The influence of 2,2,2-trifluoroethanol (TFE) on the micellar properties of ionic surfactants hexadecyltrimethylammonium bromide (CTAB), hexadecyltrimethylammonium *p*-toluenesulfonate (CTAT), sodium dodecyl sulfate (SDS), *N*-lauroylsarcosine sodium salt (SDDS), and nonionic surfactant Triton X-114 (TX-114) in aqueous solutions was studied using tensiometry, electrical conductivity, fluorimetry, time-resolved fluorescence, and microcalorimetry. With increasing concentrations of TFE, the micellar charge densities of the ionic head groups decrease, causing a decrease in the critical micelle concentration (CMC) of ionic-surfactant solutions (SDS, SDDS, CTAB, and CTAT) in micellar solutions. However, for nonionic surfactant TX-114, the polar headgroup undergoes some conformational changes causing an increase in the value of CMC. Time-resolved fluorescence decay measurements were done to get evidence of penetration of TFE molecules into the stern layer of the micelle. The micellar aggregation number declines with increasing concentration of solvent, indicating a higher concentration of mixed solvent reducing the number of monomers needed for micellization for ionic surfactants, whereas for nonionic TX-114, it indicates some structural changes of the molecule forming the micelle in the presence of TFE.

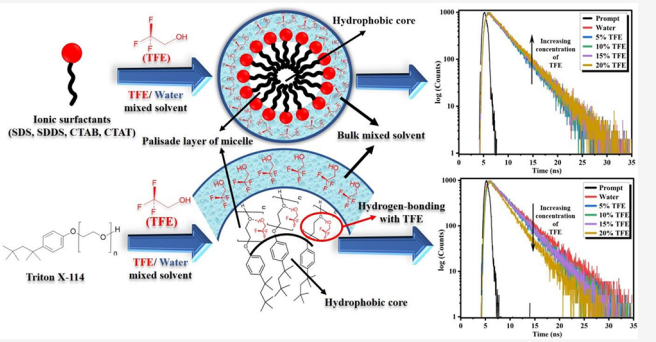

1. INTRODUCTION

In recent years, a broad community of surface chemists has shown a great deal of scientific interest in the physicochemical modifications of surface-active agents in an attempt to improve the functionality of surfactant formulations. In this context, various additives, including salts,[1] solvents,[2] polymers,[3] drugs,[4] etc., have been introduced to the micellar environment of amphiphilic systems to achieve the desired features with various industrial importance in cosmetics,[5] food products,[6] enhanced oil recovery,[7] and pharmaceuticals.[8] Among all the additives, nonaqueous alcohol solvents have been examined mostly in amphiphile-water-solvent ternary systems using both theoretical and experimental approaches.[9−17] The exceptional solubilizing and hydrogen bonding potential of alcohols distinguish them as solvents of choice.[18] Moreover, alcohols possess a dual character of serving as either cosurfactants or cosolvents as a motif to modify the critical micelle concentration (CMC) in the self-assembly of amphiphilic systems.[19] The present study has opted to use 2,2,2-trifluoroethanol (TFE), a fluorinated alcohol,[20,21] due to its great demand as a cosolvent in molecular biology, particularly during the denaturation process of proteins.[22,23] More importantly, TFE has been extensively reported in the literature in elucidation of the secondary structures of biological macromolecules, including polypeptides and proteins.[24,25] The presence of electron-withdrawing trifluoromethyl (CF_3) group in TFE imparts unique qualities as a solvent compared to other conventional alcohols.[26−28] TFE has the advantage of being highly soluble in water, irrespective of having a hydrophobic $-CF_3$ terminal. Fatima et al.[29] has performed a comparative analysis to investigate the effects of TFE and ethanol solvents on the thermal stability of an ionic liquid 1-ethyl-3-methylimidazolium dicyanamide ([EMIM]-[DCA]) in a TFE/ethanol binary mixture. TFE has been reported as a solvent medium in many organic synthesis reactions.[30,31] Nevertheless, there has not been substantial attention on surfactant aggregation in TFE solvent.[32,33]

Surfactants,[34,35] also known as surface-active agents, are widely recognized for their ability to self-assemble into various

Received: June 16, 2023
Revised: January 22, 2024
Accepted: January 22, 2024
Published: February 12, 2024

https://doi.org/10.1021/acs.iecr.3c02040
Ind. Eng. Chem. Res. 2024, 63, 3057−3071

PCCP

ROYAL SOCIETY OF CHEMISTRY

PAPER

View Article Online
View Journal

Cite this: DOI: 10.1039/d4cp03264k

A physicochemical investigation of the complex formation by β-cyclodextrin with Triton X-100 and Triton X-114 and their aggregation behaviour in aqueous solution: an experimental approach

Rajesh Banik, Raju Sardar, Bipin Bihari Mondal and Soumen Ghosh *

The complexation behavior and binding affinity of Triton X-100 (TX-100) and Triton X-114 (TX-114) with β-cyclodextrin (β-CD) were extensively studied in an aqueous medium using a comprehensive suite of experimental techniques. These techniques allowed for the evaluation of key physicochemical parameters, including critical micelle concentration (cmc), aggregation number (N_{agg}), Stern–Volmer constant, and particle size distribution. These metrics were instrumental in understanding the underlying mechanism of the host–guest interaction between β-CD and Triton-X. Dynamic light scattering (DLS) data provided strong evidence for the formation of inclusion complexes, demonstrating significant hydrophobic interactions between the hydrophobic regions of Triton-X and the cavity of β-CD. The disruption of micellar structures, caused by β-CD encapsulating the hydrophobic moieties of the surfactants, was clearly observed. This process also resulted in an increased CMC, further underscoring the impact of β-CD on the aggregation behavior of the surfactants. To quantify the interaction, the Benesi–Hildebrand method was utilized to determine the stoichiometry and binding constants of the β-CD/Triton-X complexes. The results confirmed a well-defined 1 : 1 binding mode, indicating the precise incorporation of the surfactant's hydrophobic tails into the β-CD cavity while leaving the hydrophilic regions exposed to the aqueous environment. This selective binding mechanism alters the thermodynamics of micellization and disrupts the native micellar equilibrium of the surfactant systems. This systematic and comparative investigation is among the few studies that thoroughly examine the interactions between Triton-X surfactants and β-CD. Such research not only enhances our understanding of these complexes, but also reveals their significant potential for various applications. In drug delivery, for example, β-CD/Triton-X complexes can improve the solubility, stability, and bioavailability of hydrophobic drugs. In supramolecular chemistry, these complexes serve as model systems for studying host–guest interactions and self-assembly processes. Furthermore, their ability to modulate surfactant behaviour opens avenues for their use in material science, cosmetics, and industrial formulations, where precise control over micelle formation and aggregation is essential. This study underscores the versatility and utility of β-CD in interacting with non-ionic surfactants, offering insights that can be applied to other amphiphilic systems and paving the way for innovative applications in diverse fields.

Received 19th August 2024,
Accepted 23rd January 2025

DOI: 10.1039/d4cp03264k

rsc.li/pccp

Introduction

Cyclodextrins (CDs) are macrocyclic oligosaccharides which are linked by α-1,4glucosidic bonds.[1] Discovered by French chemist Antoine Villiers in 1891 as a potato-starch fermentation by-product, cyclodextrins are truncated cone-shaped oligosaccharides classified as α-, β-, or γ-CDs, containing six, seven, or eight α-(1–4) D-glucopyranose units, respectively. β-Cyclodextrin (β-CD), with seven glucose units, has a toroidal shape and a hydrophilic exterior.[2] Cyclodextrins possess unique structural properties that enable them to selectively bind organic molecules within their cavities, forming stable host–guest inclusion complexes with exceptional molecular and enantioselectivity.[3] These oligosaccharides have a cone-shaped structure with an internal cavity size ranging from 4 to 8 Å, depending on the number of glucose units in the macrocycle. The structure consists of two rims: the smaller, referred to as the primary rim or head, and the larger, known as the secondary rim or tail. The outer surface is hydrophilic due to the presence of hydroxyl (O–H) groups, while the inner cavity is hydrophobic, characterized by inward-oriented C–H bonds. Additionally, the non-bonding electron pairs of oxygen atoms in the glycosidic bonds

Centre for Surface Science, Physical Chemistry Section, Department of Chemistry, Jadavpur University, Kolkata-700032, West Bengal, India.
E-mail: gsoumen70@hotmail.com

Journal of Molecular Liquids 411 (2024) 125684

Contents lists available at ScienceDirect

Journal of Molecular Liquids

journal homepage: www.elsevier.com/locate/molliq

An inclusive comparison regarding aggregation of surface active ionic liquid and conventional surfactant with a cationic dye Acridine Red exposed in view of spectroscopic and theoretical study

Sumanta Bandyopadhyay, Rajesh Banik, Raju Sardar, Soumen Ghosh *

Centre for Surface Science, Physical Chemistry Section, Department of Chemistry, Jadavpur University, Kolkata 700032, India

ARTICLE INFO

Keywords:
Acridine Red
SDS
Surface active ionic liquid
Interaction
Spectroscopy
Theoretical study

ABSTRACT

The investigation was conducted on the interaction of acridine red (AR) with sodium dodecyl sulfate (SDS) and 1-butyl-3-methyl imidazolium octyl sulfate (BMImOS) in both premicellar and post micellar concentrations. The interaction between AR and room temperature ionic liquid (RTIL) 1-butyl-3-methyl imidazolium bromide (BMImBr) was studied to understand the effect of imidazolium cation on micellization. Spectroscopic experiments, such as UV–visible absorption spectroscopy, steady-state fluorescence spectroscopy, time-resolved fluorescence spectroscopy, and dynamic light scattering, have been introduced. Various important parameters like spectral shifts, anisotropy, and aggregation number have been determined spectroscopically. However, a fresh insight into density functional theory calculations has also been provided. The observed results have been explained in terms of the aggregation behavior of the amphiphiles. A prominent redshift accompanied by a change in intensity is observed in the presence of surfactant and SAIL. However, in the case of BMImBr, no such spectral shift has been observed; only a decrease in spectral intensity highlights the quenching ability of the imidazolium cation. Average lifetime also provides some additional information regarding the difference in the formation of aggregates by SDS and BMImOS, which is further established from particle size density obtained from DLS. The salt like role of 1-butyl-3-methyl imidazolium cation also has been logically explained by anisotropy measurement and the determination of aggregation number. Using Gauss View 5.0 and Gaussian 09 package, the energy of optimization of each set of amphiphiles along with dye has been determined to follow the interaction at the molecular level. TDDFT calculations have also been performed to determine the structure of HOMO and LUMO.

1. Introduction

In the past few decades, the interaction of ionic dye and ionic surfactants having the same or opposite charges generated a significant amount of coverage and discussion due to its widespread applications in various fields like textiles dying [1,2], food [3–5], photography [6], printing ink, hair coloring [7], sustainable wastewater treatment [8,9], etc. Moreover, besides those industrial applications, surfactant dye association is important in various analytical and pharmaceutical fields like spectrophotometric determination of metal ions [10], biological transportation [11], medicinal photosensitization [12,13], etc. Surfactants are used in drug delivery [14–16], food processing [17,18], petroleum industries [19,20], and traditional household products like detergents [21]. Despite the above-mentioned usefulness, surfactants are hazardous to the environment [22,23]. In recent eras, room temperature ionic liquids (RTILs) have had a promising future due to their unique physical properties such as low melting point, negligible vapor pressure, high viscosity, thermal stability, inclusive electrochemical window, and less toxic environmental effect [24–27]. The presence of these particular features allows these solvents to be classified as green solvents. Ionic liquids with long alkyl chains are surface active ionic liquids (SAILs), a combination of ionic liquid and a short-chain surfactant moiety. SAILs have been used extensively in fuel [28,29], nanoparticle synthesis [30,31], catalysis [32,33], advanced material fabrication [34,35], drug delivery [36,37], polymerization [38,39], separation, and extraction processes [40,41]. However, SAILs containing 1-alkyl-3-methyl imidazolium cations have shown much prospect for academic and industrial purposes [42]. This work utilizes sodium

* Corresponding author.
E-mail address: gsoumen70@hotmail.com (S. Ghosh).

https://doi.org/10.1016/j.molliq.2024.125684
Received 18 May 2024; Received in revised form 1 August 2024; Accepted 2 August 2024
Available online 3 August 2024

Journal of Molecular Liquids 433 (2025) 127953

Contents lists available at ScienceDirect

Journal of Molecular Liquids

journal homepage: www.elsevier.com/locate/molliq

Aggregation and characterization of the microenvironment of solvatochromic eosin yellow dye in the presence of zwitterionic, cationic, and anionic surfactants: A spectroscopic and theoretical approach

Sumanta Bandyopadhyay, Rajesh Banik, Raju Sardar, Soumen Ghosh *

Centre for Surface Science, Physical Chemistry Section, Department of Chemistry, Jadavpur University, Kolkata 700032, India

ARTICLE INFO

Keywords:
Eosin yellow
Zwitterionic surfactant
Solubilization of dye
Stern layer
Zeta potential
DFT

ABSTRACT

This study explores the interactions between the anionic dye eosin yellow (EY) and various amphiphiles, specifically focusing on a newly synthesized zwitterionic surfactant called N-dodecyl-N, N-dimethyl-2-ammonio-1-ethanecarbonate (C_{12}DmCB), along with sodium lauryl sarcosinate (SLAS), sodium deoxycholate (NaDC), and cetyl trimethyl ammonium chloride (CTAC). The investigation encompasses both premicellar and postmicellar concentrations. By utilizing advanced techniques such as conductometric titration, UV–visible absorption spectroscopy, steady-state fluorescence spectroscopy, time-resolved fluorescence spectroscopy, and dynamic light scattering (DLS) measurements, this research aims to provide a comprehensive understanding of the behavior and properties of these interactions. We have effectively determined several vital parameters through spectroscopic analysis, including spectral shift, Stokes shift, and anisotropy. This contributes significantly to our understanding of the underlying phenomena. Recent findings from density functional theory calculations have effectively integrated into this work. Moreover, particle size and zeta potential of the studied system have been determined regarding the colloidal stability of each EY-surfactant system. The observed results can be thoughtfully interpreted in light of the differing aggregation behaviours of amphiphiles, which contributes to a nuanced understanding of their interactions. By utilizing Gauss View 5.0 and Gaussian 09, we have effectively optimized the energy of each amphiphile-dye combination, allowing us to uncover critical insights into their molecular interactions. Furthermore, the implementation of TDDFT calculations has provided us with a comprehensive analysis of the HOMOs and LUMOs, enhancing our understanding of these complex systems. C_{12}DmCB, a zwitterionic surfactant, stabilizes EY most effectively by creating a more protective microenvironment than all other amphiphiles. CTAC, being an oppositely charged surfactant concerning EY, provides extra stability to the EY-CTAC system. However, a very prominent spectral shift in UV–visible absorption and steady-state fluorescence spectroscopy denoting an increment in the average lifetime of EY-C_{12}DmCB establish the stable system.

1. Introduction

Since the beginning of the 20th century, the surfactant-dye association has had a supreme increasing interest due to its vast applications in the fields of textiles [1,2], cosmetics [3,4], food [5–7], and the photographic industry [8]. Surfactants are a special class of amphiphiles with a hydrophilic polar head group and a hydrophobic non-polar tail group consisting of mainly long-chain alkyl groups. Considering the charge of the hydrophilic group, classification of surfactants is into four types: cationic, anionic, non-ionic, and zwitterionic. It also has a self-association property when its concentration is on or above its critical micellar concentration (CMC) [9]. However, the interaction of the dyes with surfactants also serves a valuable contribution in various analytical and pharmaceutical fields, such as spectrophotometric determination of metal ions [10–12], biological transportation [13–15], characterization of drug delivery [16,17], medicinal photosensitization [18], etc. Moreover, from an environmental point of view, the dye-surfactant association also has an important use in wastewater treatment [19,20]. The association mechanism of oppositely charged dye-surfactants assembly depends on some parameters, especially, the electrostatic force of attraction created between two oppositely charged species [21,22], the van der Waals force of attraction generated between the hydrophobic

* Corresponding author.
E-mail address: gsoumen70@hotmail.com (S. Ghosh).

https://doi.org/10.1016/j.molliq.2025.127953
Received 25 December 2024; Received in revised form 17 May 2025; Accepted 10 June 2025
Available online 11 June 2025